Res Electricae Magdeburgenses
MAgdeburger FOrum zur Elektrotechnik

Power and Energy Student Summit 2019

9 – 11 July 2019
Otto von Guericke University Magdeburg

Conference Program

MAFO
Band 77

Supported by

50hertz

PSI

MR

SIEMENS
Ingenuity for life

OPAL-RT
TECHNOLOGIES

avacon

In cooperation with

Young EnergyNet

Res Electricae Magdeburgenses
Magdeburger Forum zur Elektrotechnik, Jg. 2019, Band 77, 2019

Impressum

Herausgeber:
Prof. Dr.-Ing. habil. Martin Wolter, Otto-von-Guericke-Universität, Institut für Elektrische Energiesysteme, Universitätsplatz 2, 39106 Magdeburg

V.i.S.d.P.:
Sebastian Helm, Otto-von-Guericke-Universität, Institut für Elektrische Energiesysteme, Universitätsplatz 2, 39106 Magdeburg

Bearbeitung:
Sebastian Helm, Institut für Elektrische Energiesysteme
Jonte Dancker, Institut für Elektrische Energiesysteme
Martin Fritsch, Institut für Elektrische Energiesysteme
Tamara Schröter, Institut für Elektrische Energiesysteme

ISBN: 978-3-944722-84-9
DOI: 10.24352/UB.OVGU-2019-086

Magdeburg, 2019
Druck: docupoint GmbH
Otto-von-Guericke-Allee 14, 39179 Barleben

PESS 2019 Conference Team

Conference Chair

Prof. Dr.-Ing. habil. Martin Wolter

Organization Team

- Sebastian Helm
- Tamara Schröter
- Marc Gebhardt
- Nicola Könnecke
- Jonte Dancker
- André Richter
- Christian Klabunde
- Eric Glende
- Martin Fritsch

Contact

sebastian.helm@ovgu.de
0391/67 51068

Table of content

I General Theme

The conference is organized especially for students in the area of electric power systems. The focus for participating students lies on gaining experience in the preparing, publishing and presenting research topics. Furthermore, the conference provides a stage for discussion of these topics with a technical audience. Throughout the conference renowned researchers and experts will support and supervise the students.

The conference main topics are as follows:

Renewable Energy

- Photovoltaic systems
- Wind turbines
- Storage systems
- Virtual power plants

High Voltage Technology

- Asset Management
- Diagnosis
- High-voltage tests
- Insulation coordination

Grid Control and Network Planning

- Network Modeling
- Network Dynamics
- Neutral Pint Treatment
- Network Calculation
- Power Quality

Power Quality

- Voltage quality
- AC- and DC-filter
- Flicker
- Compensation

HVDC and FACTS

- Power Converter Topology
- Basic Design
- Multi-terminal systems
- Modulation Methods

Protection Technology

- Wide Area Protection
- Protective behavior while grid restoration
- Protection Strategies
- Adaptive Protection Systems
- Protection Coordination

II Venue

The conference will be held at the Lukasklause. The Lukasklause is only a few minutes walking from the University and can be found in the northeastern corner of the Madgeburger town walls.

Magdeburg is inextricably linked with one technical invention: The Magdeburger Halbkugel were used by **Otto von Guericke**, born 1602 in Magdeburg, to prove the existence of air pressure. The combined force of 16 horses was not sufficient to tear both metal hemispheres apart, which were only held together by a vacuum. Otto von Guericke is seen as a pioneer in the field of experimental physics. He also invented the air pump and barometer. Besides his research, he participated in the negotiations on the Peace of Westphalia ending the Thirty Years War as the mayor of Magdeburg. Today he is the namesake of the university, which is a central pillar of the research landscape in the region.

The prominent landmark in the city is the **cathedral**, which is the first gothic building in Germany. Built in 1209, the cathedral emerged from a roman building, which was built by Kaiser Otto I in 937 AD. Within the cathedral you can find the burial ground of the emperor and founder of the Holy Roman Empire. Another impressive medieval building is the monastery “Unser Lieben Frauen” and the old town hall with its famous “Golden horseman”, the first freestanding equestrian monument in Northern Europe.

After Magdeburg was mostly destroyed in the last days of World War II, the city has become a modern and lively city since 1989. New landmarks joined the historic building such as the Grüne Zitadelle, the last and largest building of the Austrian artist Friedensreich Hundertwasser. Other buildings were discovered and restored or rebuilt, such as the Festung Mark the Bastion Kleve. These mighty fortifications state Magdeburg’s historic importance.

III Conference Dinner

In the evening of July 9, you will have the opportunity for a further scientific exchange with your fellow students in a relaxed atmosphere. We invite you to have Italian specialties at the "Lago di Garda" situated in close vicinity to the university. Here, a buffet awaits you composed of different meals from the Italian cuisine.

Lago di Garda
Universitätsplatz 10
39104 Magdeburg

IV How to Get There by Public Transport

Starting at the Hostel, walk to the road „Breiter Weg“. There you turn right and you will see the tram station. Take the tram into the direction “Messegelände” which will take you to the station “Askanischer Platz”. From there you walk towards the Elbe. Turn right at the Schleinufer and after a couple of minutes you reach the conference venue.

Line	Stop	Direction	Stations	Travelling time
5	Leiterstraße	Messegelände	6	9 min

V Activities

Substation Wolmirstedt

At the substation in Wolmirstedt, you will find an important electric node in the transmission system connecting Eastern and Western Germany. In the year 1989, the first 380 kV transmission line connected Helmstedt with Wolmirstedt. This transmission line was the first part of the connection between Helmstedt and Berlin. Furthermore in the past, the longest 380 kV transmission line with a length of 287.4 km was connected to the substation. During the tour at the substation, you will visit a control room, which is now out of order.

In the future, the substation will be connected via an HVDC link to Isar in Bavaria. The link named DC5 will have a total length of 580 km and a nominal power of 2 GW. The main task of the link will be the transmission of electricity from regions with a high penetration of renewables in Eastern Germany to the load centers in the south. The launch is planned for 2025.

Evening Event

On Wednesday July 10 starting from 7 pm, we invite all participants to a barbecue at the Elbauenpark. Here you can get into touch with other participants while having sausages, steaks and different salads. Furthermore, alcoholic and non-alcoholic drinks will be provided. Because it is on the other side of the Elbe, we offer to go there as a group.

VI Program

Time	Tuesday	Wednesday	Thursday
09:00 AM - 09:30 AM		**Opening day 2** Presentation MR	**Session 4** Special Topic´s
09:30 AM - 10:00 AM		**Session 1** Grid control and planning	
10:00 AM - 10:30 AM			
10:30 AM - 11:00 AM			
11:00 AM - 11:30 AM		Coffee break	Coffee break
11:30 AM - 12:00 PM		**Session 2** Renewable Energies	IEEE PES Best Master Thesis Award 2019
12:00 PM - 12:30 PM	Check-In hotel		PESS Award
12:30 PM - 01:00 PM			Guided tour Substation Wolmirstedt
01:00 PM - 01:30 PM		Lunch break	
01:30 PM - 02:00 PM	"Welcome" and submission of posters		
02:00 PM - 02:30 PM	Opening Prof. Dr.-Ing. habil. Martin Wolter	**Poster presentation 2** Posterno. 21 - 39	
02:00 PM - 03:00 PM	Presentation PSI Presentation 50Hertz Presentation of bronze sponsors		
03:00 PM - 03:30 PM			Closing Prof. Dr.-Ing. habil. Martin Wolter
03:30 PM - 04:00 PM	**Poster presentation 1** Poster 1 - 20	**Session 3** High Voltage Technology / HVDC and FACTS	
04:00 PM - 04:30 PM			
04:30 PM - 05:00 PM			
05:00 PM - 05:30 PM	Guided Lab tour PSI control room / Opal-RT HIL-simulator		
05:30 PM - 06:00 PM			
06:00 PM - 06:30 PM			
06:30 PM - 07:00 PM			
from 07:00 PM	Evening event 1	Evening event 2	

Time	Tuesday, 9 July 2019
from 12:00 PM	Check-In hotel
01:30 PM - 02:00 PM	"Welcome" and submission of posters
02:00 PM - 02:30 PM	Opening Prof. Dr.-Ing. habil. Martin Wolter
02:30 PM - 03:30 PM	Presentation PSI Software AG Presentation 50Hertz Transmission GmbH
03:30 PM - 05:00 PM	**Poster/Company presentation 1** (Session Chair: Avacon AG) Posters 1 - 20
05:00 PM - 06:00 PM	Lab tour PSI control room / Opal-RT HIL-simulator
from 07:00 PM	Lago di Garda

Time	Wednesday, 10 July 2019
09:00 AM - 09:30 AM	**Opening day 2** Presentation Maschinenfabrik Reinhausen GmbH (MR)
09:30 AM - 11:00 AM	**Session 1** - Grid control and planning (Session Chair: PSI)
	- Yuelin Zeng, Stability Analysis in Inverter-dominated Distribution Grids with Aggregate Models for Network Reduction
	- Julian Berger, An analysis of the price behavior of the Intraday Continuous Market
	- Pengpeng Li, A mixed integer linear programming for the day-ahead electricity market with wind power generators
	- Marc Rene Lotz, Three Phase Unbalanced Power-Flow calculation
	- Hermann Kraus, Automated use of wired measures in grid planning for solving current and voltage band problems
11:00 AM - 11:30 AM	Coffee break
11:30 AM - 01:00 PM	**Session 2** - Renewable Energies (Session Chair: 50Hertz)
	- Katrin Schulte, Predicting the local generated photovoltaic power by creating a forecast model using artificial neural networks and verifying the model with real data
	- Jonathan Ulbrich, Analysis of potentials for battery electric vehicles for the implementation of V2G-technologies
	- Steffen Kubik, Optimization of micro CHP systems through the integration of batteries A theoretical analysis
	- Cassandra Klonz, Modeling and experimental validation of a unitized regenerative fuel cell
	- Friederike Thomas, Robust and Optimized Voltage Droop Control consindering the Voltage Error
01:00 PM - 02:00 PM	Lunch break
02:00 PM - 03:30 PM	**Poster-/Company-presentation 2** (Session Chair: OPAL-RT) Posterno. 21-39
03:30 PM - 05:00 PM	**Session 3** - High Voltage Technologies and HVDC (Session Chair: MR)
	- Jan Wiesner, Life-cycle analysis of the climate impact of present high-voltage direct current transmission systems
	- Christoph Rohr, Development of an Automated Tool to Generate Test Cases for Preventive and Curative HVDC Methods
	- Anton Chupryn, Coupling of energy storage devices with the automotive high voltage grid via power electronics
	- Bartlomiej Tomasz Madura, Four-quadrant DC converter analysis for hoisting machine drive applications
	- David Schmidt, Monitoring and Automation of Transformer Drying
from 07:00 PM	Barbeque at the Elbauenpark

Time	Thursday, 11 July 2019
09:00 AM - 11:00 AM	Session 4 - Special Topic´s (Session Chair: Siemens)
	- Stephan Balischewski, Multifunctional use of battery storages in distribution grids
	- Iryna Chychykina, Comparison of different Redispatch optimization strategies
	- Gabriela Freitas Gomes da Fonseca, Electric Boat Propulsion with Archimedean Screw
	- Ankit Singh, Development of an Economic Power Plant Optimization Model for Profit Maximization
	- Muhammad Tayyab, Flexible tariffs for optimal operation of storage in a microgrid
	- Raphael Houben, Integrated Optimization of Large Scale Power and Gas Flow Problems
	- Martin Fritsch, A new approach for variable valve control of single-cylinder engines with a single camshaft
11:00 AM - 11:30 AM	Coffee break
11:30 AM - 12:00 PM	IEEE PES Best Master Thesis Award 2019 - Sebastian Schwarz, Parallel Optimiziation in Demand Response Architectures Challenges, Requirements, Applications
12:00 PM - 12:30 PM	PESS Award
12:30 PM - 03:00 PM	Guided tour Substation Wolmirstedt
03:00 PM - 03:30 PM	Closing Prof. Dr.-Ing. habil. Martin Wolter

VII Sponsor description

We operate the transmission grid in northern and eastern Germany and secure the electricity supply for around 18 million people. The 50Hertz extra high voltage grid has a circuit length of about 10,200 kilometers – that is the distance from Berlin to Rio de Janeiro. 50Hertz maintains lines, cables and substations through efficient maintenance, expands its grid to meet demand and ensure the electrical balance between energy consumers and power generators. With around 1,100 employees at ten locations, our team ensures constant availability of electricity in Berlin, Brandenburg, Hamburg, Mecklenburg-Western Pomerania, Saxony, Saxony-Anhalt and Thuringia. 50Hertz is a leader in the secure integration of renewable energies: More than half of the annual average consumption in our grid area originates from renewable sources - and it is constantly growing. The 50Hertz transmission grid is part of the European interconnected grid and is directly connected to the neighbouring countries Poland, the Czech Republic, Denmark and in the near future also Sweden. We maintain a constant exchange with our partners. By openly discussing the challenges of grid adaptation and by offering a reliable infrastructure we are actively working towards a successful energy transition in a sustainable world.

As an independent software company, PSI Software AG has been a technology leader for process control and information systems since 1969. Around the world, the PSI software products ensure reliable and efficient energy supply as well as optimized production and logistics processes. The PSI Energie EE business unit provides systems for monitoring and controlling all types of energy networks, asset service optimization (service restoration, maintenance, and crisis management), and systems for achieving maximum automation in the liberalized energy market. PSI Software AG develops intelligent solutions for efficient support of the daily operations of utilities. Flexible use for various utility types. Maximum performance and intuitive operation. PSIcontrol is a high-end control system which works reliable even in extreme network fault situations. It effectively supports network management with fault localization as well as with fast and comprehensive service restoration. Using PSIcontrol provides new options for the increase in productivity demanded today. PSIcommand offers powerful functions for maintenance management, crisis management and planned outage management. The PSIpassage product family provides innovative solutions to network operators for their tasks in the liberalized energy market.

Maschinenfabrik Reinhausen GmbH (MR), based in Regensburg, Germany, and 43 subsidiaries and 5 affiliated companies around the world enjoy success in the global niche markets of electrical energy technology. The company is mainly family-owned and is now managed by the fifth generation of the family. MR is the global market leader in power transformer regulation. MR tap changers and de-energized tap-changers adjust the transmission ratio of the primary to the secondary transformer winding in order to adapt to changing load ratios and, together with innovative sensors, electronics, and information and communication technology thereby help to ensure a reliable power supply around the world. Project planning is also undertaken for turnkey solutions for the non-reactive operation of critical industrial applications and supply security in power distribution grids facing increasingly fluctuating feed-in. Other parts of the business deliver stationary and mobile test and measurement technology systems for high-voltage devices or manufacture composite hollow insulators and fiber glass-reinforced plastics for products subject to high mechanical and electrical loads. Customers include manufacturers of high-voltage equipment and systems, transmission and power distribution grid operators, and large electricity users in heavy industry. Business is driven by global population growth, the expansion of infrastructure in developing countries and emerging markets, reinvestments in industrialized nations, feed-in from renewable energies, and industrial applications which respond sensitively to fluctuations in electricity quality.

Siemens AG (Berlin and Munich) is a global technology powerhouse that has stood for engineering excellence, innovation, quality, reliability and internationality for more than 170 years. The company is active around the globe, focusing on the areas of power generation and distribution, intelligent infrastructure for buildings and distributed energy systems, and automation and digitalization in the process and manufacturing industries. Through the separately managed company Siemens Mobility, a leading supplier of smart mobility solutions for rail and road transport, Siemens is shaping the world market for passenger and freight services. Due to its majority stakes in the publicly listed companies Siemens Healthineers AG and Siemens Gamesa Renewable Energy, Siemens is also a world-leading supplier of medical technology and digital healthcare services as well as environmentally friendly solutions for onshore and offshore wind power generation. In fiscal 2018, which ended on September 30, 2018, Siemens generated revenue of €83.0 billion and net income of €6.1 billion. Further information is available on the Internet at www.siemens.com.

OPAL-RT TECHNOLOGIES

OPAL-RT TECHNOLOGIES provides open real-time digital simulators to design, test and validate complex controls for electrical, electro-mechanical and power electronic systems. This Hardware-in-the-Loop (HIL) approach is widely used for power systems studies by engineers and researchers at leading manufacturers, utilities, universities and research centres around the world.

More than a simple supplier, OPAL-RT Germany GmbH, created two years ago, fosters research cooperation with German universities.It allows the university to benefit from an industrial partner during a call for projects and benefit from OPAL-RT support during the project phase. It allows OPAL-RT to partner with leading research institutions to develop industry-leading real-time simulation technology, and simultaneously grow an R&D team in Germany. OPAL-RT Germany GmbH is glad and proud to collaborate with a lot of electrical engineering departments in German universities as well as a lot of Fraunhofer institutes. OPAL-RT vision is to democratize real-time simulation to make the imagination the only limit to complex system design.

avacon

Full of energy. For the people in the region.

We are your partner for regional energy solutions and connect people via our intelligent energy networks from the North Sea coast to southern Hessen. As one of the largest regional energy service providers in Germany, we bring energy exactly where millions of people need it. Fast, reliable, efficient and environmentally friendly. We are your partner for regional energy solutions in the fields of electricity, gas, water, heating, cooling, mobility and lighting. Our intelligent energy networks connect people from the North Sea coast to southern Hesse, Lower Saxony and Saxony-Anhalt.

With around 2,100 employees and around 190 apprentices, the Avacon-group is one of the largest employers and trainers in the region and is also a relevant economic factor. On average, 700 million euros flow into the regional economic cycle every year in the form of taxes, orders and wages. In this way we make a contribution to economic growth and set impulses for companies in the region.

Parameter Tuning by Neural Network for Digital Twins of Inverter

X.Song, H.Cai, YL. Zeng, T. Jiang, S. Schlegel, D. Westermann
song.xinya@tu-ilmenau.de

Abstract—**This paper proposed the innovative methods based on the neural network (NN) to build the digital twins (DT) of the inverter model. The proposed methods can be divided into two groups: firstly, an online-parameterized tuner for the PI controller is formulated through backpropagation (BP) algorithm; and secondly an NN-based identifier is used to approximate the nonlinear functional dynamics of the targeted control loop of the inverter. The design of PI tuner is based on the deviation between the output of the model and the reference output from measurement data. Then, according to the difference, the tuner can calculate the appropriate parameter of the current and voltage controller to track the dynamic behaviour of the reference model. The NN identifier is, however, to replicate the dynamic character of the reference model by NN which is initially trained offline with extensive test data and afterward is applied to online tuning.**

Index Terms- neural network, digital twins, backpropagation, PI tuner, NN identifier

INTRODUCTION

A growing number of power inverters are being used to feed renewable energies into the grid. Because of the switching processes, the harmonic oscillations are also brought into the power system [1]-[3]. To guarantee the stability of the network and the success of its operation, it is crucial to investigate the interaction between the parallel-connected inverters and the distribution grid. The paper initially focuses on the modelling of the inverter and the network to simulate the possible dynamic in inverter and network. To enhance the precision of the model, the parameter tuning will be considered to build the digital twins (DT) [6] of the inverter based on the measurement data from the reference model. The original concept of DT could be dated back to 2002 in the presentation about the formation of a Product Lifecycle Management (PLM) from the University of Michigan, which it was referred to as the Mirrored Spaces Model. [7] The first adoption of Digital Twin as a conceptual basis used as a simulation of a vehicle or system that uses the best available physical models to mirror the life of its flying twin, which implies that a highly-detailed simulation model can reproduce its physical behaviour as close as possible. [6],[7]. In electrical and electronic area, they are, with the development of computer simulation, dependent on the simulation models for the understanding the dynamics of power system. The modelling technology has been evolved from an access to mathematical and computing experts to a standard tool in an engineer's portfolio, which is afterwards developed as a support tools to solve the problem like the validation and testing for system. Because of its autonomous, adaptive and intelligent rectification of parameters, artificial intelligence (AI) is becoming increasingly significant [7]-[9]. This paper uses one of the AI methods, the neural network (NN) [10], to build, firstly, a PI tuner for the parameterization of the controller of the inverter model. Because of the adaptive character [10] of NN, the PI tuner can dynamically rectify the controller according to the response of measurement data. On this account, the NN will be built to tune the controller automatically according to the deviation of the targeted model and the measurement data of the reference model in the control loop of inverter. By using backpropagation algorithm (BP) [11], the gradient that is applied to the calculation of weights to be used in the network can be computed as to minimize the error between model and the measured data of reference model. For the sake of evaluation of this method, the parameter estimation, which also aims to rectify the parameter of the control loop of the inverter, will be presented in this paper.

Another application of NN in this paper is on account of its self-learning ability [12]. The performance of NN has increased significantly in new research domains such as neurobiology, bioinformatics. Moreover, neuropsychology has also become increasingly demanding, particularly at the interfaces of biology and medicine with computer science [10]-[12]. The aim is to create an exact replication of the natural networking of neurons and thus, for example, to draw inferences about the functioning of the brain. In contrast to the mapping of neurons, the technical application has no longer concentrated on the biological plausibility of the networking and activity of NN, instead in automation technology on the stability and real-time performance of the application. With the enormous measurement data, the NN is trained offline by using the training algorithm of supervised learning [11]. The NN can be regarded as an identifier, which could be used online to replicate the dynamic behaviour of reference inverter.

The purpose of this paper is to build a DT of the inverter by using the parameter tuning method. Accordingly, the structure of this work can be arranged as follows: In chapter II, the inverter model which will be tuned is built firstly based on the differential equations described in AC side and DC side. To maintain the targeted current and voltage, an overlaid voltage and an underlaid current control loop are designed. The initial parameter of the inverter model can be calculated by the optimum process, which will also be described in chapter II. Afterward, the theoretical fundamentals of parameter tuning strategy will be presented in chapter III. Then, the tuning process will be operated and the simulation results with the new parameter can be demonstrated in chapter IV. Finally, this paper concludes with a summary of the main points.

SIMULATION MODEL

A precise model for investigating the influence of the effect caused by the parallel-connected inverter is required [3]. With regards to the modeling concept [4] focused in this chapter, the model of inverter including its overlaid control loop is operated. To simplify the modeling procedure, the states and the topology considered are transformed from natural coordinates to αβ coordinates. Furthermore, the transformation from αβ coordinates to dq coordinates for the control of the states is executed [5].

Fig. 1 illustrates the topology of the inverter circuit, which connect with the voltage source of the grid. The circuit is shown in natural coordinates and includes a three-phase inverter with an intermediate voltage circuit, RL filter circle, and a capacity.

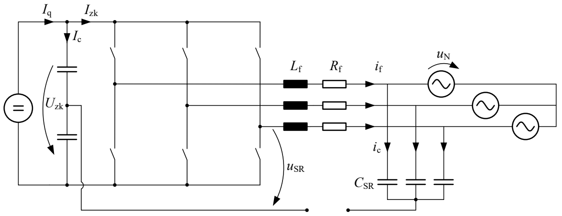

Fig. 1: Topology of Inverter model with the ideal switch

To model the dynamic process by using the differential equations, the system behavior is first converted to vector coordinates (αβ coordinates).

$$\underline{\vec{u}}_{\mathrm{SR}} = R \cdot \underline{\vec{\imath}}_{\mathrm{f}} + L \cdot \dot{\underline{\vec{\imath}}}_{\mathrm{f}} + \underline{\vec{u}}_{\mathrm{N}} \tag{1}$$

Here $R = R_{\mathrm{f}} + R_{\mathrm{N}}$, $L = L_{\mathrm{f}} + L_{\mathrm{N}}$

$$I_{\mathrm{q}} = I_{\mathrm{c}} + I_{\mathrm{zk}} = I_{\mathrm{zk}} + C \cdot \dot{U}_{\mathrm{zk}} \tag{2}$$

To associate the AC and DC, the power relationship of both sides is used here:

$$P_{\mathrm{AC}} = P_{\mathrm{DC}} \tag{3}$$

with $P_{\mathrm{DC}} = I_{\mathrm{zk}} \cdot U_{\mathrm{dc}}$, $P_{\mathrm{AC}} = \frac{3}{2} \cdot \underline{\vec{\imath}}_{\mathrm{f}} \cdot \underline{\vec{u}}_{\mathrm{SR}}$, $\underline{\vec{u}}_{\mathrm{SR}} = \underline{\vec{v}} \cdot \frac{U_{\mathrm{zk}}}{2}$

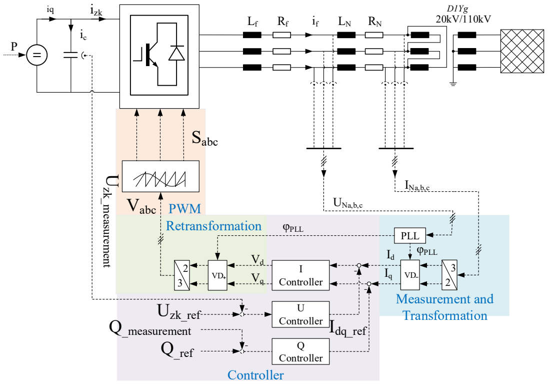

Fig. 2: Equivalent block diagram of inverter model

According to the above conditions, the power relationship can be rewritten:

$$I_{\mathrm{zk}} \cdot U_{\mathrm{zk}} = \frac{3}{2} \cdot \underline{\vec{\imath}}_{\mathrm{f}} \cdot \underline{\vec{u}}_{\mathrm{SR}} = \frac{3}{4} \cdot \underline{\vec{\imath}}_{\mathrm{f}} \cdot \underline{\vec{v}} \cdot U_{\mathrm{zk}} \tag{4}$$

Then,

$$I_{\mathrm{zk}} = \frac{3}{4} \cdot (V_{\alpha} I_{\mathrm{f}\alpha} + V_{\beta} I_{\mathrm{f}\beta}) \tag{5}$$

From αβ coordinates to dq coordinates for controlling process: With these functions, the diagram can be shown with the control loop in Fig.2

PARAMETER TUNING STRATEGY

To research the interaction between inverter and grid, simulation will be the prior choice because of its reasonable price and safe research environment. This, however, exists in the difference between the real network and the simulation results, which can cause the imprecision of the analysis, see Fig.3.

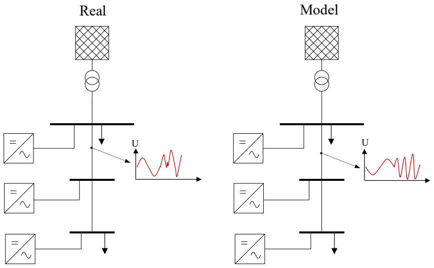

Fig. 3: Difference between the measurement data and the simulation results

On account of this, the parameterization should be applied to the model to tune the parameter. It is determined to decrease the deviation between the model and the measurement data from the grid. In this paper, two parameter tuning's methods will be used to build DT of inverter.

A. PI tuner through neural network

According to the BP algorithm, an illustration of the relevant procedure for the setup of the neural network for the parameterization of the PI controller is then presented. The form for the digital PI controller [33] is as follows:

$$u(k) = u(k-1) + K_{\mathrm{p}} \cdot \big(e(k) - e(k-1)\big) + K_{\mathrm{i}} \cdot e(k) \tag{6}$$

The structure of applied neural network in PI tuner can be shown in Fig. 4.

There are three inputs, two outputs and five hidden neurons. The states for further computations are collected in the input layer. The input variable is defined as:

$$O_{\mathrm{i}}^{(1)} = x(i), \mathrm{i} = 1,2,3 \tag{7}$$

Between the input layer and the hidden layer, the input states are transmitted by the weighted factor. Then, the input value of the hidden layer is calculated:

$$net_{\mathrm{j}}^{(2)}(k) = \sum_{\mathrm{i}=0}^{3} W_{\mathrm{ij}} \cdot O_{\mathrm{i}}^{(1)}, \mathrm{j} = 1,2,\dots,5 \tag{8}$$

Fig.4 obviously reveals that the output of the hidden layer is determined by function f_1 , which is called the activation function. The output value after the activation function is defined as:

$$O_{\mathrm{j}}^{(2)}(k) = f_1(net_{\mathrm{j}}^{(2)}(k)), \mathrm{j} = 1,2,\dots,5 \tag{9}$$

Similarly, the input and output value of output layer are:

$$net_{\mathrm{l}}^{(3)}(k) = \sum_{\mathrm{i}=0}^{3} W_{\mathrm{jl}} \cdot O_{\mathrm{j}}^{(2)}, \mathrm{l} = 1,2 \tag{10}$$

$$O_{\mathrm{l}}^{(3)}(k) = f_2\left(net_{\mathrm{l}}^{(3)}(k)\right), \mathrm{l} = 1,2 \tag{11}$$

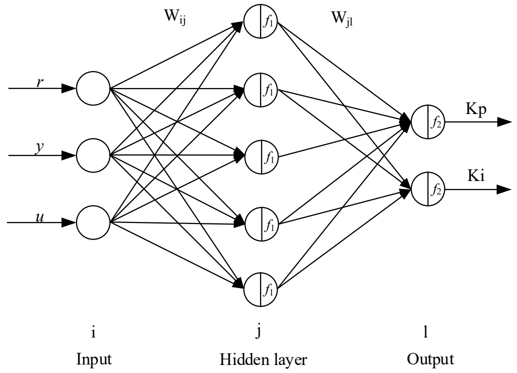

Fig. 4: Structure of neural network in PI tuner

To search for the optimized parameters, the gradient regression method is used. Before the computation, the evaluation function must be determined in the first place. In this paper, the evaluation function for the optimization process is described as:

$$E(k) = \frac{1}{2}(r(k) - y(k))^2 \tag{12}$$

The weight matrix is rectified by the gradient regression method through the (24):

$$\Delta W_{\mathrm{jl}}(k) = -\eta \cdot \frac{\partial E(k)}{\partial W_{\mathrm{jl}}} + \alpha \cdot \Delta W_{\mathrm{jl}}(k-1) \tag{13}$$

Here, η is the learning rate and α means the inertial parameters. From the equation, the change of weight matrix has a correlation with the evaluation function. Consequently, in order to calculate the new weight matrix, the following differential equation should be computed first:

$$\frac{\partial E(k)}{\partial W_{\mathrm{jl}}} = \frac{\partial E(k)}{\partial y(k)} \cdot \frac{\partial y(k)}{\partial u(k)} \cdot \frac{\partial u(k)}{\partial O_{\mathrm{l}}^{(3)}(k)} \cdot \frac{\partial O_{\mathrm{l}}^{(3)}(k)}{\partial net_{\mathrm{l}}^{(3)}(k)} \cdot \frac{\partial net_{\mathrm{l}}^{(3)}(k)}{\partial W_{\mathrm{jl}}} \tag{14}$$

In (14),

$\frac{\partial net_{\mathrm{l}}^{(3)}(k)}{\partial W_{\mathrm{jl}}} = O_{\mathrm{j}}^{(2)}, \frac{\partial u(k)}{\partial O_1^{(3)}(k)} = e(k) - e(k-1), \frac{\partial u(k)}{\partial O_2^{(3)}(k)} = e(k),$

The change of the weight matrix can be determined by the equations mentioned above:

$$\Delta W_{\mathrm{jl}}(k) = \alpha \cdot \Delta W_{\mathrm{jl}}(k-1) + \eta \cdot \delta_{\mathrm{l}}^{(3)} O_{\mathrm{j}}^{(2)}(k) \tag{15}$$

with $\delta_{\mathrm{l}}^{(3)} = e(k) sgn(\frac{\partial y(k)}{\partial u(k)}) \cdot \frac{\partial u(k)}{\partial O_{\mathrm{l}}^{(3)}(k)} \cdot f'_2(net_{\mathrm{l}}^{(3)}(k))$

Through the same procedure, the changes of the weights of the hidden layer is as follows:

$$\Delta W_{\mathrm{ij}}(k) = \alpha \cdot \Delta W_{\mathrm{ij}}(k-1) + \eta \cdot \delta_j^{(2)} O_i^{(1)}(k) \tag{16}$$

$$\delta_j^{(2)} = f'_1\left(net_j^{(2)}(k)\right) \cdot \sum_{l=1}^{2} \delta_l^{(3)} \cdot W_{jl}(k), \tag{17}$$

According to the mentioned above, two PI controllers are used to stabilize the voltage and current, which means that two PI tuners will be used to parameterize the inverter. Each tuner picks up the measured data from the demonstrator and the output of model of each control loop. The output of each tuner is the optimized K_{p} and K_{i}, see Fig.5.

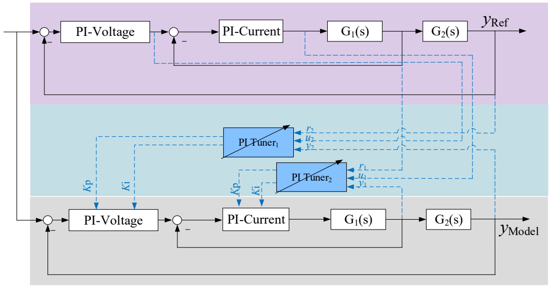

Fig. 5: Structure of neural network in PI tuner

B. Neural network(supervised learning)

In supervised learning, an external supervisor is used to provide the network with the required response to each input or the deviation of the actual from the correct output [10]-[12]. According to the deviation, the modification of the network is carried out via the learning rules. The size of the errors determines the weight configuration, which is varied and adapted to the current learning progress. After updating the adjusted weight parameters, a performance improvement should be achieved. Another goal is to minimize the network error as much as possible. The general graphical representation of the supervised learning procedure is shown in Fig.6

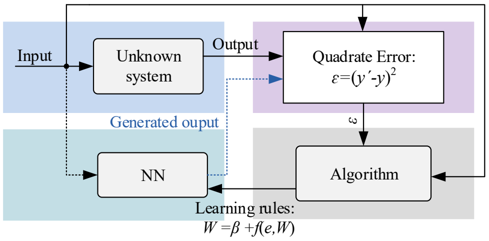

Fig. 6: Structure of supervised learning

Based on the theoretical explanation mentioned above, the voltage control loop and the current control loop of the reference model can be replicated by the NN identifier, the general idea of which can be observed in Fig.7. To replicate the reference model, three neural networks are designed to imitate the voltage controller, the current control loop and the controlled plant of the overlaid control loop. Based on the measurement data of the input and the output from the reference model, these three NN will be trained firstly according to the supervised learning process. The selection of the number of hidden neurons of NN has no exact criterium. In this work, the NN with 15 hidden neurons, after testing, exerts the best performance. To build the DT, the objective is that the state variables of the model are the same as in the reference model.

The simulation results by NN-identifier will be presented in the following chapter. For the sake of comparing these methods, the Root-Mean-Square-Error (RMSE) [10] of the state will be calculated to justify the similarity between the simulation results and the measurement data, see Table 1.

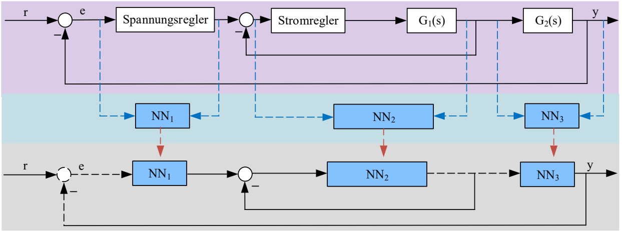

Fig. 7: Concept of application of NN identifier to build DT

PARAMETER TUNING AND SIMULATION

In this chapter, the validation process is firstly operated to testify whether there exists the deviation between the simulation results and the measurement data exists. The difference between the model and the reference model is investigated by comparing the dynamic behaviour. From this difference, the parameter tuning methods are correspondingly used to rectify the parameters in order to build the DT to replicate the dynamic process of the reference model. The general idea for the parameterization can be shown in Fig.8. As the explanation above, the parameters in the model are rectified according to the deviation between the simulation model and the measurement data from the reference model.

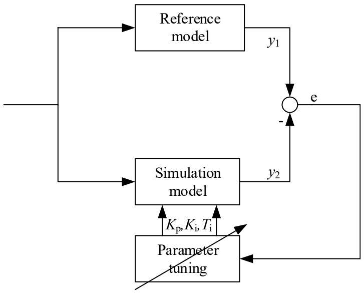

Fig. 8: General ideal of parameter tuning

By changing the operation point of the inverter, the active and reactive power curve of the reference model and the simulation model at PCC are presented as follows.

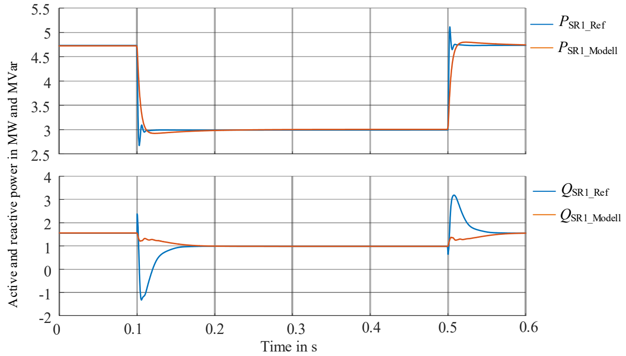

Fig. 9: Validation with active and reactive power at PCC

From Fig.9, it is obvious to see that the deviation between the reference model (blue) and the simulation model (orange) is sized during the changing process than at the steady period. Additionally, at the balancing procedure, the reference model can, however, reach the new operating point more quickly, which means that the parameter or the structure of the reference model differs from the simulated model. Except for state of the grid, the control loop of the converter should also be observed. According to the explanations in the front chapter, the amplitude of the voltage is determined by the regulated DC link voltage and the magnitude of the current is also defined by the current control loop. The following diagram illustrates the output of the overlaid voltage loop.
The actual value of the DC link voltage in Fig.10 clearly shows at 0.1s and 0.5s that the response time of the reference model is slower than the simulated model. In this regard, the DC link voltage of the reference model needs about 0.3s to reach the new steady state after the operating point changes, while the model needs only about 0.02s. It should be noted that the dynamic difference between these two models exists from 0.1s when the change occurs.

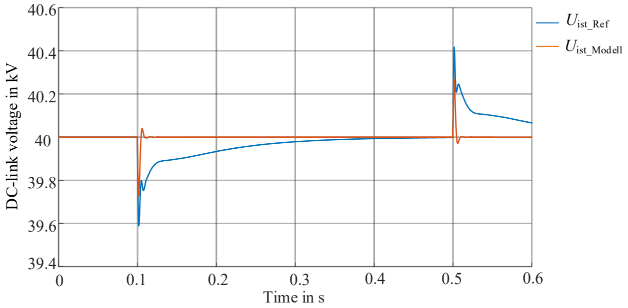

Fig. 10: Validation with DC link voltage of inverter

As exhibited in Fig.11, it should be pointed out that the amplification of the current controller is too small, which leads to the lower peak at the changing point

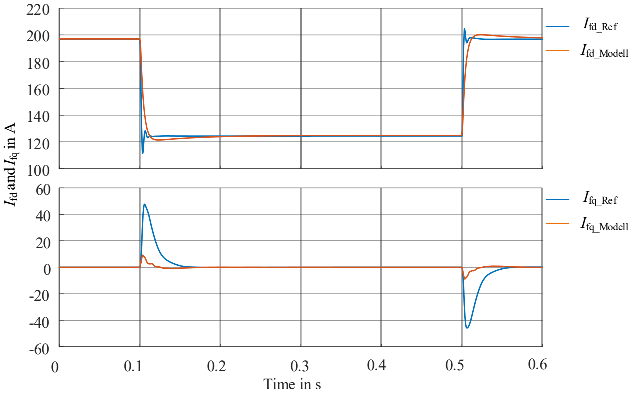

Fig. 11: Validation with output of current control loop on d and q axis of inverter

Besides, it can be observed that, on q axis, the integral parameter is too large, which has a smaller duration to reach the new steady point. Based on validation results, it is necessary to take the parameterization into account to reduce the deviation between them. As the explanation in chapter 3, four methods can be used into parameterization, and the simulation results after the tuning are in following.

1) *PI tuner*

In this paper, three controllers including DC link voltage controller, the current controller on axis d and current controller on axis q are parameterized separately. For this purpose, altogether six parameters are needed to be tuned in three controllers. The curve of the voltage controller is shown in Fig.12. It can be clearly seen that the controller parameters vary with the change in the DC link voltage (see Fig.12) and that the curves have the same dynamic behaviour.

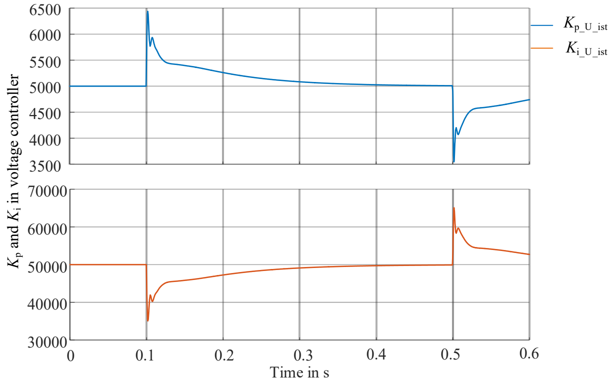

Fig. 12: $\boldsymbol{K}_{\mathbf{p}}$ and $\boldsymbol{K}_{\mathbf{i}}$ of voltage controller by PI tuner based on the validation

With PI tuner, the state of the model, after parameterization, is closer to the reference model (see Fig.13). It reveals the state of active and reactive power by changing the operating point of the simulation model and the measurement data. Compared to the validation results, the active power curve is more closely matched to the reference model.

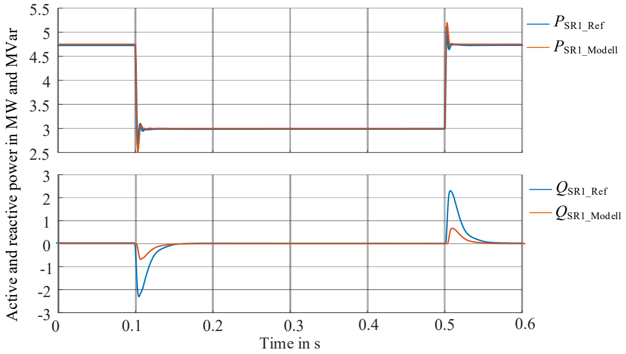

Fig. 13: Active and reactive power after parameter tuning by PI tuner

Despite the small deviation in the balancing process, the RMSE of the active power can reach 84.93%. However, the difference of the reactive power is bigger than that of the active power. Nevertheless, the behaviour of the reactive power in the dynamic process between 0.1s and 0.5s is identical.

As explained in Chapter 2, the dynamic behaviour of the three-phase voltage is determined by the DC link voltage. To build the DT, the DC link voltage dynamics between the parameterized model and the reference model should match with each other firstly. The DC link voltage plot is shown in Fig.14. This clearly indicates that the dynamic response between two curves (orange and blue line) is quite similar.

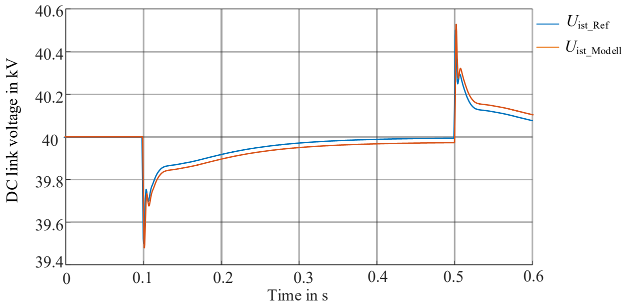

Fig. 14: DC link voltage after parameter tuning by PI tuner

In comparison with validation results, the output of the current control loop can better match the reference model after parameterization by the PI tuner (see Fig.15).

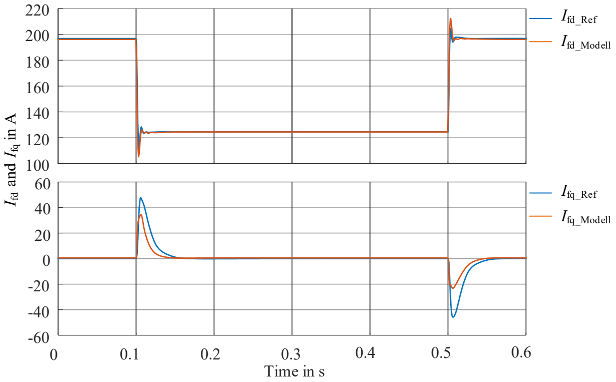

Fig. 15: $\boldsymbol{I}_{\mathbf{fd}}$ and $\boldsymbol{I}_{\mathbf{fq}}$ after parameter tuning by PI tuner

After the operation point changes, the behaviour during the dynamic process of the simulation model with the new parameters can better track the reference model. The figure below shows that despite the similar dynamic behaviour there exists still a deviation between these two curves. The maximum value of the orange line is about 36A, while at the same time the maximum value of the blue line is about 50A. As a result, it takes a longer balancing time of reference model to reach the steady state.

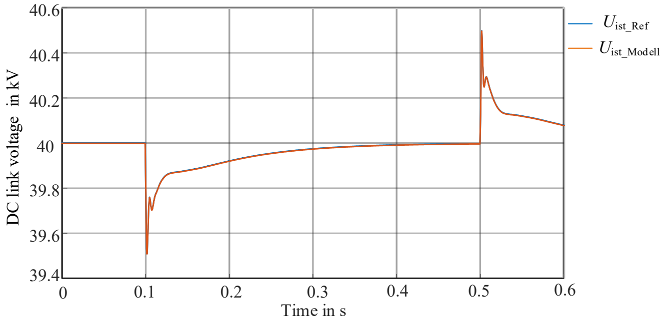

Fig. 16: DC link voltage after parameter tuning by NN

1) Neural network

Fig.16 shows the output of the voltage loop. The result illustrates that the two curves are identical, i.e. the voltage loop modeled by the NN is highly similar to the reference model. From the Tab.1, it can be also known that the RMSE of the simulation model, which is built through the NN, can reach 99.3%.

Then, the underlaid current loop will be observed, which is simulated by the NN_2 (see Fig.7). To train these three NN, there are 200.000 data accumulated from the reference model. The output of NN_2 is shown in the following Fig.17.

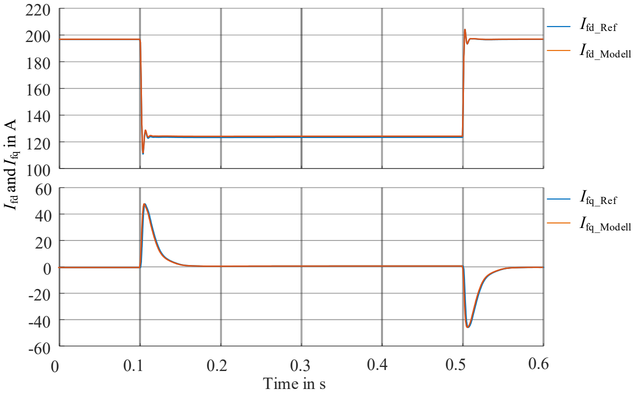

Fig. 17: $\boldsymbol{I_{fd}}$ and $\boldsymbol{I_{fq}}$ after parameter tuning by NN

To compare the results of these four methods, Tab.1 indicates us the RMSE of state and the output of the control loop, which represents the similarity grad between the reference model and the tuned model. From the table, the highest precise rests in the model tuned through NN. The similarity of the DT and reference model can reach over 97% on an average.

Tab. 1: Comparison of simulation results after parameter tuning

	U_{DC}	U_{SR1}	I_{fd}	I_{fq}	P	Q
PI	82,56%	88,37%	81,45%	80,33%	84,93%	79,78%
NN	99,5%	99,1%	97,77%	98,8%	97,65%	98,76%

CONCLUSION

To investigate the impact caused by the decentralized renewable generation, the simulation is firstly taken into consideration before the application. Thus, this paper has firstly built an inverter model to research the existing dynamic interaction between the distribution grid and the inverter. By comparing the simulation result and the testing data, there is, however, the deviation between simulation results and the measurement data from the reference model, which can lead to the inaccuracy of the research results. To improve the precision of the model, the tuning method has been applied, see Table 2.

Tab. 2: Comparison of different parameter tuning's methods

Method	advantage	disadvantage
PI tuner	• online parameter tuning • intelligent and self-learning • little training data	• lowest precision • only tuning of K_p and K_i
NN	• highest precision of these four methods • better identifier than system identification • online tuning	• Huge amount of data for the training process • NN transfer function without tuning the exact parameter

PI tuner aims to tune the controller's parameter of the overlaid voltage control loop and the underlaid current control loop on d and q axis for the tracking of reference inverter model. In contrast to parameter estimation, the PI tuner can merely rectify the controller's parameter which result in a lower precision. NN identifier utilizes the neural network to replicate the dynamic behaviour by training the NN with the measurement data from the reference model. By contrast with the PI tuner, the NN identifier can effectively build the DT of the inverter, which is over 97% the same as the reference model.

REFERENCES

[1] A. Y. Liu, P. H. Lan, and H. H. Lin, "An IEEE 1547-Based Power Conditioner Test System for Distributed Energy Resources," *EPE*, vol. 05, no. 04, pp. 945–949, 2013.

[2] Tao Yang, "Development of dynamic phasors for the modelling of aircraft electrical power systems," Ph.D. dissertation, University of Nottingham.

[3] I. Hauer, A. Naumann, M. Stotzer, and Z. A. Styczynski, "Communication interface requirements during critical situations in a Smart Grid," in *2012 3rd IEEE PES Innovative Smart Grid Technologies Europe (ISGT Europe)*, Berlin, Germany, op. 2012, pp. 1–7.

[4] M. Motoyama *et al.,* "Erratum to "Improving the Power Generation Performance of a Solar Tower Using Thermal Updraft Wind" [Energy and Power Engineering Vol. 6 No. 11 (October 2014) 362-370]," *EPE*, vol. 07, no. 06, pp. 255–257, 2015.

[5] F. Jenni and D. Wüest, Eds., *Steuerverfahren für selbstgeführte Stromrichter*. Zürich, Stuttgart: Vdf, Hochsch.-Verl. an der ETH Zürich; Teubner, 1995.

[6] F. Biesinger, D. Meike, B. Kras und M. Weyrich, „A Case Study for a Digital Twin of Body-in-White Production Systems General Concept for Automated Updating of Planning Projects in the Digital Factory" in *2018 IEEE 23rd International Conference on Emerging Technologies and Factory Automation (ETFA)*, Turin, Sep. 2018 - Sep. 2018, S. 19–26.

[7] F. Biesinger, D. Meike, B. Krass, M. Weyrich, "A Digital Twin for the Production Planning based on Cyber-Physiscal Systems",*CIRP ICME 18-12th CIRP Conference on Intelligent Computation in Manufacturing Engineering*, 2018.

[8] R. Rosen, G. von Wichert, G. Lo, K. D. Bettenhausen, "About The Importance of Autonomy and Digital Twins for the Future of Manufacturing." in ScienceDirect; IF AC Papers Online CONFERENCE PAPER ARCHIVE, pp. 567-572, 2015

[9] S. S. Haykin, *Neural networks: A comprehensive foundation / Simon Haykin,* 2nd ed. Upper Saddle River, N.J.: Prentice Hall; London : Prentice-Hall International, 1999.

[10] S. Kamalasadan, G. Swann, and A. A. Ghandakly, "A novel radial basis function neural network based intelligent adaptive architecture for power system stabilizer," in *Proc. North Amer. Power Symp.*, 2009,

[11] pp. 1489–1496. K. Reinisch, Analyse und Synthese kontinuierlicher Regelungs- und Steuerungssysteme 3. Aufl.-Berlin.

[12] A. Zell, *Simulation neuronaler Netze,* 4th ed. München [u.a.]: Oldenbourg, 2003.

Stability Analysis in Inverter-dominated Distribution Grids with Aggregate Models for Network Reduction

YL.Zeng, T. Jiang, S. Schlegel, D. Westermann
Power Systems Group
Technische Universität Ilmenau
Ilmenau, Germany

***Abstract*— Recently, model reduction has become a major analysis technique for large energy systems. The structure of distribution grids is becoming increasingly complex, because of the growing use of inverters. However, inverters influence the stability of distribution grid. This paper discusses which factors have influences on the grid stability and what kind of influences there are. Besides, the paper comes up with a network reduction method, so that the model of inverter-dominated grid can be simplified in structure in order to create an efficient grid model. By maintaining the input-output characteristics of the networks, the aggregate model is useful for analyzing small signal stability. Based on the aggregate model, this paper investigates the stability boundary of an inverter-dominated distribution grid with regard to the interaction of the parameters in the grid.**

***Index Terms*: small signal stability, inverter-dominated distribution grid, network reduction, stability boundary**

I. INTRODUCTION

In order to analyze system stability, the distribution grid will be tested by an event. This event can be a small change of working point. As a result, stability can be investigated from the dynamic behavior of the distribution grid. However, the event impacts not only the distribution gird, but also other grids of lower or higher voltage level, that are connected to the distribution gird. As shown in Fig. 1, the underlaying and overlaying grids could be influenced by the event A accordingly. Then event B and event C would be created in overlaying and underlaying grids which can be seen as a result of the impact from event A. They could also have an influence on the distribution grid. In this paper, the interaction between distribution grid and its overlaying and underlaying grids on the stability of the distribution network will be simulative examined. If the interaction is confirmed to be exist, the stability study of the distribution grid will be conducted with the consideration of the interaction.

For the simulations, using the detailed structure of high-voltage, the medium voltage and the low voltage grid causes the increasing requirement of calculation time, the calculation ability and storage space due to the large number of state variables and grid elements [1, 2]. To reduce the simulation time, the network reduction is applied in the stability analysis [2, 3]. This paper introduces a network reduction method that simplifies the structure of overlaying and underlaying networks without distorting the character of dynamics.

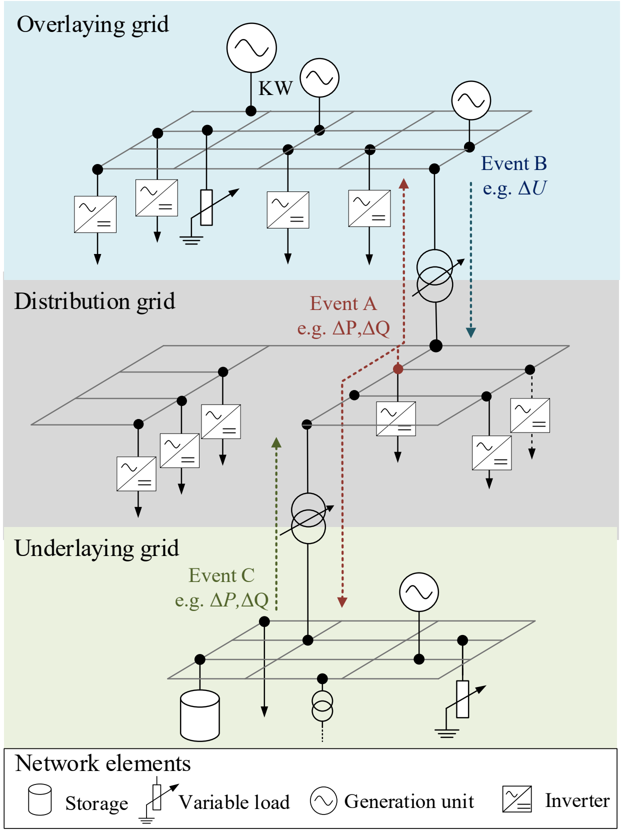

Fig. 1: Interactions with the superposed and underlaying grid

This paper focuses further on the stability of the distribution network with consideration of the network parameters. The network parameters of the distribution network also influence the stability [4]. Furthermore, the stability of distribution grid can be influenced not only by the its own parameters, but also by the parameters from other neighboring networks, which are connected to the distribution grid. This paper investigated the interaction of the parameters on the stability and searched a stability boundary. The stability boundary would be an important indicator for selection of network parameters.

This paper is divided into four parts. Chapter 1 presents the motivation and background of the work. In chapter 2, the network models, the reduction methods are presented. The concept, test model and results of the stability study according to scenarios are presented in Chapter 3. Chapter 4 shows the summary.

II. NETWORK REDUCTION TO INVESTIGATE THE SMALL-SIGNAL STABILITY

A simulation using the detailed grid model takes several hours. The network reduction with using aggregate model is a solution to reduce the simulation time, at the same time the dynamics of the network is substantially emulated. The concept of aggregate model is shown in Fig. 2.

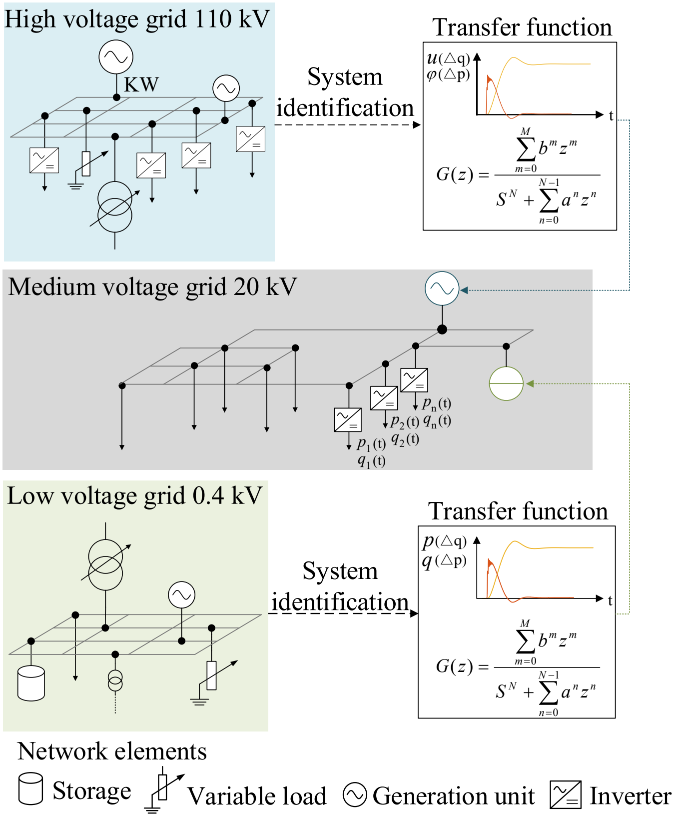

Fig. 2: Network reduction by using the aggregate model

As shown in Fig.2, the dynamic behaviors of the underlaying and overlaying networks are simulated by transfer functions, which can be determined by system identification. The response of the aggregate model under a small excitation signal change is identical to the original system, retains main original characteristics but simplifies the structure. Instead of using the detailed network structure, the aggregate models of the low and high voltage girds will be integrated with the medium voltage grid for further stability study. The following sections describe two reduced network models.

A. Aggregate model to emulate the overlaying network

An ideal high voltage network is often modelled as an ideal voltage source [4]. In this paper, a controlled voltage source is used to build the aggregate model of a high voltage network, in order to obtain a controllable and precise response.

The aggregate model is constructed to contain two parts, one simulates the stationary behavior and the other builds the dynamic behavior under small excitation signal change.

The state variables which are important or observed for the investigation can be selected as input or output of the aggregate model. In this paper, the inputs are the operating points while the outputs are the voltage response. The stationary behavior is an unchanged voltage value that can be measured in the simulation using detailed model. The dynamic response is simulated by transfer functions. The topology of the aggregate model is shown in Fig. 3.

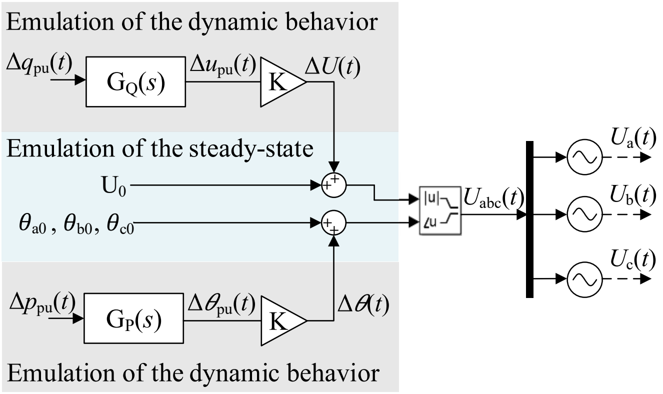

Fig. 3: Topology of the aggregate model of overlaying network

The gray area shows the emulation of the dynamic behavior and the blue area includes the simulation of the stationary behavior of the overlaying network. The input signals $\Delta p_{pu}(t)$ and $\Delta q_{pu}(t)$ denotes the operating point change on the medium-voltage network in per unit (pu) value. The use of pu value has the advantage that they are relative to a reference, thus it is identical for both the overlaying and underlaying networks. The transfer functions $G_Q(s)$ and $G_P(s)$ are

$$G_P(s)=\frac{\Delta\theta_{pu}}{\Delta P},\ G_Q(s)=\frac{\Delta u_{pu}}{\Delta Q}$$

and gain factors K serves, on the one hand, to convert the pu value into absolute value, on the other hand, to adapt the output values when implementing the transfer functions.

The steady-state voltage amplitude U_0 and the steady-state voltage angle θ_0 for the respective phase indicate the stationary behavior of the voltage. After combining the dynamic response with the static response, the output is turned into a complex voltage signal, which drives the voltage sources. The voltage sources produce the corresponding electrical signal.

B. Aggregate model to emulate the underlying grid

To simulate the underlaying network, a controlled power source model is constructed as an aggregate model. The controlled current source feeds the same active and reactive power as the low-voltage grid. The aggregate model is also modeled in two parts for emulation of the dynamic and stationary behavior. The dynamic behavior of the underlaying network is modeled by transfer functions.

The input signal of the transfer functions is the voltage change Δu_{pu} at the overlaying grid and the output signals are the change of the active and reactive power. The topology is presented in Fig. 4.

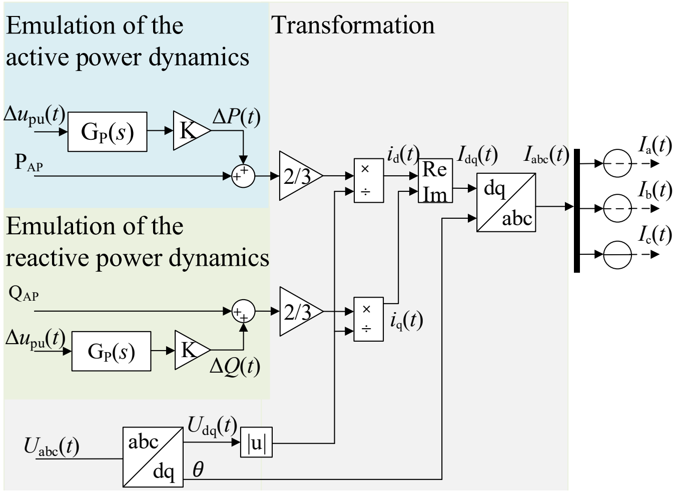

Fig. 4: Topology of the aggregate model for underlaying network

The active and reactive power dynamics are determined by the composition of the stationary operating points P_{AP} and Q_{AP} by the transfer functions

$$G_P(s) = \frac{\Delta P}{\Delta u_{pu}}\ ,\ G_Q(s) = \frac{\Delta Q}{\Delta u_{pu}}$$

To build the power source, the active current i_d and the reactive current i_q are calculated on the relationship between active power, reactive power and voltage. The current is then converted into three phase current i_{abc} by the inverse-Park transformation.

III. INVESTIGATION OF THE SYSTEM STABILITY

The investigation is performed under several scenarios. In each scenario, one predetermined parameter is observed and varies. The test model is excited with a small excitation signal. In this paper, the excitation signal is a step signal, so that the transfer function can be easily determined by the corresponding output response and the step signal.

For example, in the basic model, in which all parameters are unvaried, the transfer function can be determined with the small voltage excitation by 0.1 p.u. and the active power caused by it. The transfer function is shown as follow:

$$TF = \frac{-8.76\times10^{10}s^3 - 6.93\times10^{15}s^2 + 2.98\times10^{19}s - 1.30\times10^{21}}{s^4 + 9.30\times10^3 s^3 + 2.52\times10^8 s^2 + 9.08\times10^{10}s + 6.74\times10^{13}}$$

There are four poles of this transfer function, and the dominant pole plays a significant role for stability analysis. A dominant pole is the one of all the poles of transfer function which has the greatest effect on the system stability. In this transfer function the dominant pole is -0.0177-0.0489i.

According to change of position of the dominant pole, a fitting curve can be created to record the movement of the pole and to predict the stability boundary. When the fitting curve intersects with the imaginary axis, a stability boundary is found. If the imaginary axis and the fitting curve do not intersect, the test system remains stable as the parameter changes. Fig. 5 shows the topology of the test model. On the 110kV high voltage level, two medium voltage networks connected in parallel are fed by one transformer. The two medium-voltage networks are each connected in parallel with three inverters. In a medium voltage branch, the parameters are varied and the interactions on the stability of the second medium-voltage string are investigated. Table I shows the scenarios for seeking the stability boundary.

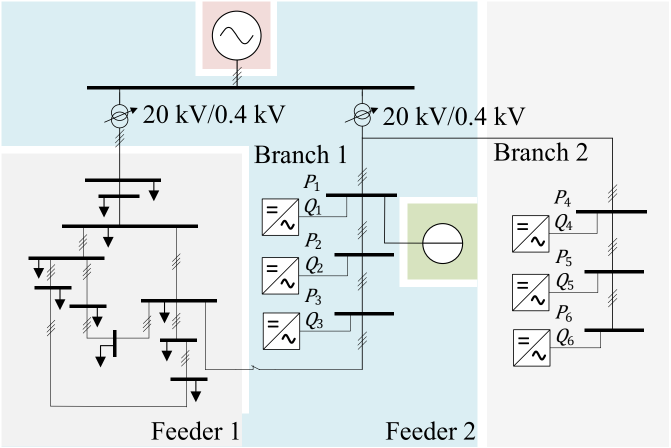

Fig.5: Topology of the test model Internet

TABLE I OVERVIEW OF THE SCENARIOS

Scenario	Description	Scenario-Caption
Grid elements	*R* of transmission line	Scenario L_R
	L of transmission line	Scenario L_L
	C of transmission line	Scenario L_C
	R/X-Ratio of transmission line	Scenario L_R/X
	Z of transmission line	Scenario L_Z
	R/X-Ratio of transformer	Scenario T_R/X
inverter parameters	Operation point	
	Active power of inverter	Scenario AP_P
	Reactive power of inverter	Scenario AP_Q
	Number of inverters	Scenario AN
	Inverter-Filter R_F	Scenario F_R
	Inverter-Filter L_F	Scenario F_L
Controller parameters	Current controller	
	Current controller K_P	Scenario I_P
	Current controller K_I	Scenario I_I
	Voltage controller	
	Voltage controller K_P	Scenario U_P
	Voltage controller K_I	Scenario U_I
	Reactive power controller	
	Reactive power controller K_P	Scenario Q_P
	Reactive power controller K_I	Scenario Q_I

The selected parameter in each scenario is created as the product of a variation factor and a base value. The variation of the parameter is achieved by changing the variation factor while the base value remains the same. The investigation of the interactions takes place according to the structure of Table I in three sections: Grid elements, inverter parameters and controller parameters.

Since the dynamics of the high voltage and low voltage networks may change due to the variation of parameters, the transfer functions should be updated. However, this is time-consuming because the update of transfer function requires adjustment of variable iteratively. In this paper, four indicators are introduced to determine if an update of the transfer functions should be performed or not. If the differences of four indicators are less than 5%, the transfer functions would not be updated, and the present transfer functions are kept. If a change of indicators exceeds 5%, the transfer functions must be updated, and the updated transfer functions are used for further investigation. This saves simulation time while maintaining the accuracy of the simulation.

IV. STABILITY LIMIT OF THE INTERNET

In Fig.6, Fig.7 and Fig. 8 the interactions of the grid elements, inverter parameters and controller parameters are presented.

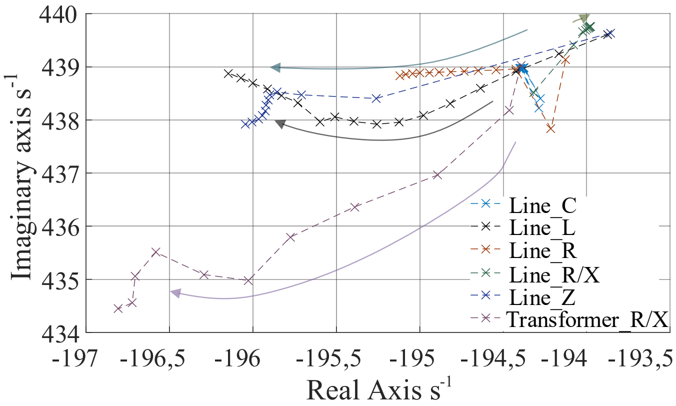

Fig.6 Movement of the dominant pole according to the variation of the grid elements parameters

The increase in the R/X ratio of the transmission line has a stabilizing influence on the grid stability, therefore overhead lines are preferable, due to their larger R/X ratio. With increasing transmission line impedance, the distribution network remains stable. In contrast, the grid stability has a negligible interaction with the line capacitance and R/X ratio of the transformer.

According to Fig. 7, it is obvious that grid stability decreases with an increasing number of connected inverters. That is why the distribution network with lots of inverters must be intensively monitored. The inductive component of the filter has a destabilizing effect on the system stability. An increasing filter resistance shows a stabilizing influence. However, it is lower compared to the filter inductance. In comparison with operating point, other inverter parameters have relative less effects on the grid stability, which means that the active and reactive power of inverters have the largest impact on the grid stability. And The controller parameters have the greatest effect on the grid stability against other parameters, see Fig. 8.

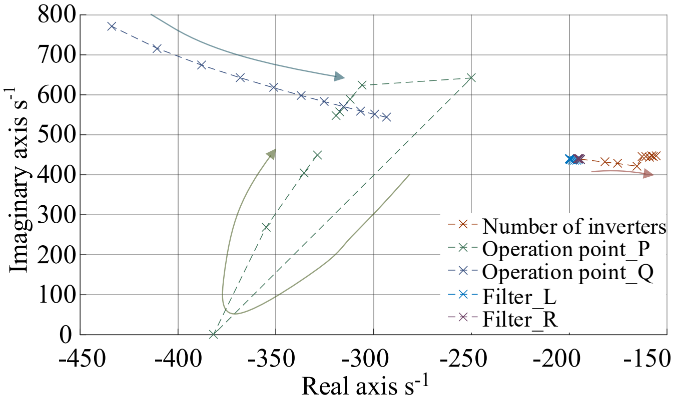

Fig.7 Movement of the dominant pole according to the variation of the inverter parameters

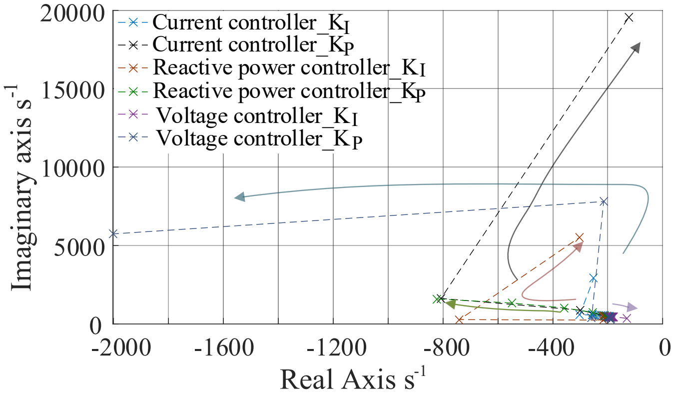

Fig. 8 Movement of the dominant pole according to the variation of the controller parameters

The integral and proportional component of the voltage controller and the integral component of the reactive power controller have a destabilizing effect. Meanwhile, the proportional portion of the reactive power controller and both portions of the current regulator have a stabilizing character by increasing value.

V. SUMMARY

In this paper, the dynamics of the underlaying and overlaying networks were simulated by means of network reduction methods with using aggregate models. The calculation time is less, because the state variables in aggregate model are reduced due to a simplified structure.

The results of the stability study show that the controller parameters have the greatest influence on the grid stability. Then follow the inverter parameters. The parameters of the network elements have the smallest influence on the network stability. The interaction of the control parameters and a central control method to coordinate the controller parameters should be examined in future work.

REFERENCES

[1] V. Crastan und D. Westermann, Elektrische Energieversorgung 3: Dynamik, Regelung und Stabilität, Versorgungsqualität, Netzplanung, Betriebsplanung und -führung, Leit- und Informationstechnik, FACTS, HGÜ, 3. Aufl. Berlin: Springer, 2012.

[2] T. Laurent, Vierpoltheorie und Frequenztransformation: Mathematische Hilfsmittel für systematische Berechnungen und theoretische Untersuchungen elektrischer Übertragungskreise. Berlin, Heidelberg: Springer Berlin Heidelberg, 1956.
[3] G. Ziegler, Digitaler Distanzschutz. Hoboken: Wiley-VCH, 2008.
[4] M. Kraiczy, M. Braun, T. Stetz, J. Brantl und S. Schmidt, Untersuchung der Wechselwirkungen zwischen der lokalen Spannungsregelung des Umspannwerks-Transformators und der lokalen Blindleistungsregelung dezentraler Erzeugungsanlagen im Verteilungsnetz, 2013.

Three Phase Unbalanced Power-Flow Calculation for Pre-Validation of Topology Changes in a Laboratory Grid

Marc René Lotz
Institute for Electrical Systems and Automation Technology (IfEA)
Ostfalia University for Applied Sciences
Wolfenbüttel, Germany
m.lotz@ostfalia.de

***Abstract*—This paper introduces an algorithm to calculate the power-flow of a power system with three phases including possible imbalances at fundamental frequency. Transmission lines are modelled with their pi-section equivalent circuits with a mutual ground impedance and capacitive coupling. The algorithm will be validated using Simscape, showing that it accurately computes the power-flow. The power-flow calculation is then performed with an experimental setup of a laboratory grid, a scaled transmission system, to depict the reliability of the grid for future research. At last, a procedure will be developed to incorporate the power-flow calculation into the existing control of the laboratory grid to pre-validate topology changes.**

***Index Terms*—power-flow studies, power-flow calculation, unbalanced three phase power system, laboratory grid, transmission system, pre-validation, topology change**

I. INTRODUCTION

This paper introduces an algorithm to calculate the power-flow of a power system with three phases including possible imbalances at fundamental frequency. Imbalances imply non-symmetrical power-injections, voltages and admittances in general, as shown later on with the experimental setup.

After this introduction as Chapter I, Chapter II briefly explains the definitions made for the power-flow calculation of an unbalanced power system at fundamental frequency, up to the numerical solution. Transmission lines are modelled with their pi-section equivalent circuits, including capacitive coupling between the phases and a mutual ground admittance.

Chapter III gives an overview of the laboratory equipment, including a grid of a scaled transmission system, generators, loads, power hardware, and a real-time simulator for controlling the transmission system, acquiring measurements and performing the power-flow calculation.

In Chapter IV, an experimental setup is presented, firstly, to validate the power-flow calculation using Simscape, and secondly, to show that it accurately calculates the state of the laboratory grid, which also means that the grid is a sufficient model of a transmission system.

After that, Chapter V provides a first attempt of a procedure to incorporate the power-flow calculation into the existing control of the laboratory grid to pre-validate topology changes. This enables the user or an external application to evaluate wether switching operations result in inapplicable states beforehand. The whole procedure and the control is performed on a real-time simulator.

A conclusion on the results and future work is then drawn in Chapter VI.

II. POWER-FLOW CALCULATION

A. *Preliminary*

Consider a stationary three phase power system at fundamental frequency with $n \in \mathbb{N}_{>0}$ nodes. Every node consists of three phases and one neutral, which makes a total of four lines per node. Each line of a node i can be connected to another line of another node j with a constant and complex admittance. The admittances between two nodes form a pi-section equivalent circuit of a transmission line with a mutual ground admittance and capacitive coupling between the phases. Fig. 1 shows the equivalent circuit, similarly depicted in [1] and [2], of two nodes i and j.

To identify every admittance $\underline{y}$ of Fig. 1, and for the purpose of including all possible connections in the future, the following notation

$$ {}_{b_{ij}}\underline{y}^{\lambda_1 \lambda_2}_{k_1 k_2} \tag{1} $$

is used, where $\Lambda = \{0, 1, 2, 3\}$ is the set of lines, with the subset of phases $P = \{1, 2, 3\}$ and $\lambda_1, \lambda_2 \in \Lambda$; $K = \{1, 2, \ldots, n\}$ is the set of nodes with $k_1, k_2 \in K$; and b_{ij}, with $i, j \in K$ and $i \neq j$, is the branch between the two nodes i and j, written as $b_{ij} = ij$. Identification of the branch is important to distinguish the admittances modelling capacitive coupling if there is more than one node connected to the considered node. The nodal phase voltage of a phase $\alpha \in P$ is expressed as $\underline{u}^{\alpha}_{i} = u^{\alpha}_{i} \cdot \exp\left(\mathrm{j} \cdot \delta^{\alpha}_{i}\right)$. To avoid division by zero, the following definition is made.

$$ \underline{z}_{ij} = \begin{cases} \sum\limits_{\forall \lambda \in \Lambda} {}_{ij}\underline{y}^{\lambda\lambda}_{ij} & i \text{ and } j \text{ connected} \\ 1 & i \text{ and } j \text{ not connected} \end{cases} \tag{2} $$

It is then possible to describe the phase currents and the neutral current at node i with (3) and (4).

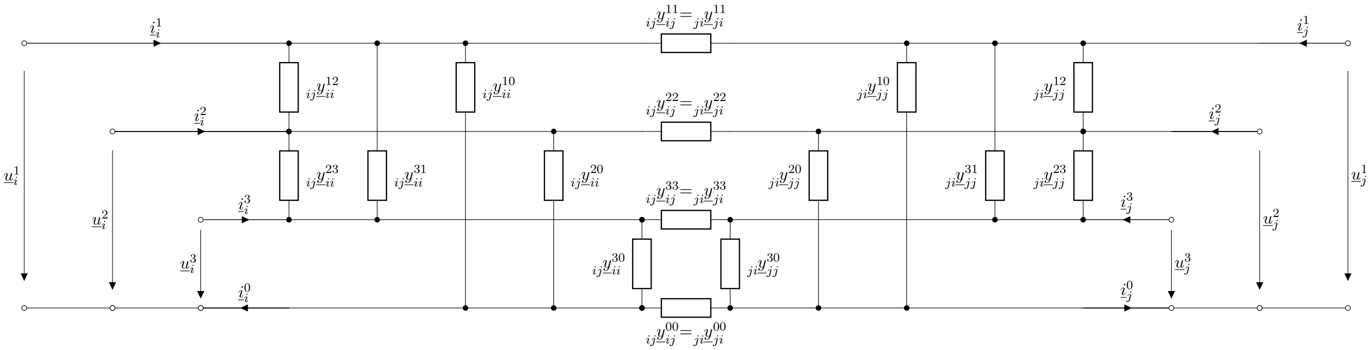

Fig. 1. Three Phase Equivalent Circuit of Two Connected Nodes

$$
\begin{aligned}
\underline{i}_i^\alpha = \underline{u}_i^\alpha \cdot \sum_{\substack{j=1\\ j\neq i}}^{n} &\left(\sum_{\substack{\forall\lambda\in\Lambda\\ \lambda\neq\alpha}} \left({}_{ij}\underline{y}_{ii}^{\alpha\lambda} \right) + \underline{z}_{ij}^{-1} \cdot {}_{ij}\underline{y}_{ij}^{\alpha\alpha} \cdot \sum_{\substack{\forall\lambda\in\Lambda\\ \lambda\neq\alpha}} \left({}_{ij}\underline{y}_{ij}^{\lambda\lambda} \right) \right) \\
&- \sum_{\substack{\forall p\in P\\ p\neq\alpha}} \left(\underline{u}_i^p \cdot \sum_{\substack{j=1\\ j\neq i}}^{n} \left({}_{ij}\underline{y}_{ii}^{\alpha p} + \underline{z}_{ij}^{-1} \cdot {}_{ij}\underline{y}_{ij}^{\alpha\alpha} \cdot {}_{ij}\underline{y}_{ij}^{pp} \right) \right) \\
&- \sum_{\substack{j=1\\ j\neq i}}^{n} \left(\underline{u}_j^\alpha \cdot \underline{z}_{ij}^{-1} \cdot {}_{ij}\underline{y}_{ij}^{\alpha\alpha} \cdot \sum_{\substack{\forall\lambda\in\Lambda\\ \lambda\neq\alpha}} \left({}_{ij}\underline{y}_{ij}^{\lambda\lambda} \right) \right) \\
&- \sum_{\substack{\forall p\in P\\ p\neq\alpha}} \left(\sum_{\substack{j=1\\ j\neq i}}^{n} \left(\underline{u}_j^p \cdot \underline{z}_{ij}^{-1} \cdot {}_{ij}\underline{y}_{ij}^{\alpha\alpha} \cdot {}_{ij}\underline{y}_{ij}^{pp} \right) \right)
\end{aligned}
\tag{3}
$$

$$
\begin{aligned}
\underline{i}_i^0 = \sum_{\forall p\in P} &\left(\underline{u}_i^p \cdot \sum_{\substack{j=1\\ j\neq i}}^{n} \left({}_{ij}\underline{y}_{ii}^{p0} + \underline{z}_{ij}^{-1} \cdot {}_{ij}\underline{y}_{ij}^{pp} \cdot {}_{ij}\underline{y}_{ij}^{00} \right) \right) \\
&- \sum_{\forall p\in P} \left(\sum_{\substack{j=1\\ j\neq i}}^{n} \left(\underline{u}_j^p \cdot \underline{z}_{ij}^{-1} \cdot {}_{ij}\underline{y}_{ij}^{pp} \cdot {}_{ij}\underline{y}_{ij}^{00} \right) \right)
\end{aligned}
\tag{4}
$$

Complex nodal power for each phase is calculated by (5).

$$\underline{s}_i^\alpha = \underline{u}_i^\alpha \cdot \left(\underline{i}_i^\alpha\right)^* \tag{5}$$

At a node i, complex power can be injected by means of power generation or dissipation, e.g. by generators or loads. This injected power is equal to the nodal power, as seen in (6).

$$\underline{s}_{\text{inj},i}^\alpha = \underline{s}_i^\alpha \tag{6}$$

The sum of all currents at the neutral of every node i needs to be incorporated with (7).

$$\underline{\sigma}_i^0 = \underline{i}_i^0 - \sum_{\forall p\in P} \left(\underline{i}_i^p\right) \tag{7}$$

B. System of Equations

Aim of the power-flow calculation is to compute the complex nodal voltages $\underline{u}_i^\alpha$ of the phases with known injected powers $\underline{s}_{\text{inj},i}^\alpha$. Because there are four vertices of a linear electric network per node with a complex number as the weight of these vertices, it is necessary to set up $8n-2$ linearly independent equations to get a sufficient solution to the power-flow. Beside these constant power nodes, there has to be one slack node $s \neq i$ for balancing power with known complex nodal voltage. Other node types, like constant absolute voltage and active power nodes, are not considered in this scope.

The variables of one phase α of the slack node s are written as a vector with

$$\boldsymbol{x}_s^\alpha = \begin{pmatrix} p_{\text{inj},s}^\alpha & q_{\text{inj},s}^\alpha \end{pmatrix}^T \tag{8}$$

to define the slack node variable vector as

$$\boldsymbol{x}_s = \begin{pmatrix} \boldsymbol{x}_s^1 & \boldsymbol{x}_s^2 & \boldsymbol{x}_s^3 \end{pmatrix}^T. \tag{9}$$

Similar definitions hold for the constant power nodes.

$$\boldsymbol{x}_i^\alpha = \begin{pmatrix} u_i^\alpha & \delta_i^\alpha \end{pmatrix}^T \tag{10}$$

$$\boldsymbol{x}_i = \begin{pmatrix} \boldsymbol{x}_i^0 & \boldsymbol{x}_i^1 & \boldsymbol{x}_i^2 & \boldsymbol{x}_i^3 \end{pmatrix}^T \tag{11}$$

This gives, with $s = 1$ as an example, the complete variable vector

$$\boldsymbol{x} = \begin{pmatrix} \boldsymbol{x}_{s=1} & \boldsymbol{x}_{i=2} & \boldsymbol{x}_{i=3} & \dots & \boldsymbol{x}_{i=n} \end{pmatrix}^T. \tag{12}$$

For the constant power nodes and the slack node, using $k \in K$, the following equations are defined.

$$f_{k,1}^\alpha = \Re\{\underline{s}_k^\alpha\} - p_{\text{inj},k}^\alpha \tag{13}$$

$$f_{k,2}^\alpha = \Im\{\underline{s}_k^\alpha\} - q_{\text{inj},k}^\alpha \tag{14}$$

To get a solution to the power-flow, additional equations for a node i are necessary.

$$f_{i,1}^{0} = \Re\{\underline{\sigma}_i^0\} \tag{15}$$

$$f_{i,2}^{0} = \Im\{\underline{\sigma}_i^0\} \tag{16}$$

With $\lambda \in \Lambda$ and

$$\boldsymbol{f}_i^{\lambda} = \begin{pmatrix} f_{i,1}^{\lambda} & f_{i,2}^{\lambda} \end{pmatrix}^T, \tag{17}$$

the vector of a constant power node is composed of

$$\boldsymbol{f}_i = \begin{pmatrix} \boldsymbol{f}_i^0 & \boldsymbol{f}_i^1 & \boldsymbol{f}_i^2 & \boldsymbol{f}_i^3 \end{pmatrix}^T. \tag{18}$$

Given the vectors

$$\boldsymbol{f}_s^{\alpha} = \begin{pmatrix} f_{s,1}^{\alpha} & f_{s,2}^{\alpha} \end{pmatrix}^T, \tag{19}$$

$$\boldsymbol{f}_s = \begin{pmatrix} \boldsymbol{f}_s^1 & \boldsymbol{f}_s^2 & \boldsymbol{f}_s^3 \end{pmatrix}^T, \tag{20}$$

the complete vector of all nodes, again with $s = 1$ as an example, is as follows.

$$\boldsymbol{f} = \begin{pmatrix} \boldsymbol{f}_{s=1} & \boldsymbol{f}_{i=2} & \boldsymbol{f}_{i=3} & \cdots & \boldsymbol{f}_{i=n} \end{pmatrix}^T \tag{21}$$

C. Numerical Solution

The numerical solution of $\boldsymbol{f}(\boldsymbol{x}) = \boldsymbol{0}$ is performed with the Newton-Raphson method, based on [3], with the nomenclature of [4]. The iteration is given by

$$\boldsymbol{x}^{(\nu+1)} = \boldsymbol{x}^{(\nu)} - \boldsymbol{J}_f^{-1}(\boldsymbol{x}^{(\nu)}) \cdot \boldsymbol{f}(\boldsymbol{x}^{(\nu)}), \tag{22}$$

with $\nu = 0, 1, 2, \ldots$ as the iteration index. The index $\nu = 0$ denotes the initial value of $\boldsymbol{x}$. Rewritten as

$$\boldsymbol{J}_f(\boldsymbol{x}^{(\nu)}) \cdot \Delta\boldsymbol{x}^{(\nu+1)} = -\boldsymbol{f}(\boldsymbol{x}^{(\nu)}) \tag{23}$$

with the definition

$$\boldsymbol{x}^{(\nu+1)} = \boldsymbol{x}^{(\nu)} + \Delta\boldsymbol{x}^{(\nu+1)}, \tag{24}$$

the iteration can be stopped when $\|\Delta\boldsymbol{x}^{(\nu+1)}\|_\infty < \varepsilon$ with ε as an arbitrarily small value. The Jacobian is given by

$$\boldsymbol{J}_f = \begin{pmatrix} \frac{\mathrm{d}\boldsymbol{f}_{s=1}}{\mathrm{d}\boldsymbol{x}_{s=1}} & \frac{\mathrm{d}\boldsymbol{f}_{s=1}}{\mathrm{d}\boldsymbol{x}_{i=2}} & \cdots & \frac{\mathrm{d}\boldsymbol{f}_{s=1}}{\mathrm{d}\boldsymbol{x}_{i=n}} \\ \frac{\mathrm{d}\boldsymbol{f}_{i=2}}{\mathrm{d}\boldsymbol{x}_{s=1}} & \frac{\mathrm{d}\boldsymbol{f}_{i=2}}{\mathrm{d}\boldsymbol{x}_{i=2}} & \cdots & \frac{\mathrm{d}\boldsymbol{f}_{i=2}}{\mathrm{d}\boldsymbol{x}_{i=n}} \\ \vdots & \vdots & \ddots & \vdots \\ \frac{\mathrm{d}\boldsymbol{f}_{i=n}}{\mathrm{d}\boldsymbol{x}_{s=1}} & \frac{\mathrm{d}\boldsymbol{f}_{i=n}}{\mathrm{d}\boldsymbol{x}_{i=2}} & \cdots & \frac{\mathrm{d}\boldsymbol{f}_{i=n}}{\mathrm{d}\boldsymbol{x}_{i=n}} \end{pmatrix}. \tag{25}$$

The initial values of $\boldsymbol{x}$ should be set as

$$p_{\mathrm{inj},s}^{\alpha} = -\sum_{\substack{i=1 \\ i \neq s}}^{n} p_{\mathrm{inj},i}^{\alpha}, \tag{26}$$

$$q_{\mathrm{inj},s}^{\alpha} = -\sum_{\substack{i=1 \\ i \neq s}}^{n} q_{\mathrm{inj},i}^{\alpha}, \tag{27}$$

for the slack node, and $\underline{u}_i^{\alpha} = \underline{u}_s^{\alpha}$ for the other nodes.

Fig. 2. Laboratory Grid

TABLE I
TRANSMISSION LINE
ADMITTANCES IN PER UNIT

Admittances	50 km	100 km
${}_{ij}\underline{y}_{ij}^{\alpha\alpha}$	$1.437 - \mathrm{j} \cdot 15.986$	$0.720 - \mathrm{j} \cdot 8.001$
${}_{ij}\underline{y}_{ij}^{00}$	$1.547 - \mathrm{j} \cdot 20.932$	$0.706 - \mathrm{j} \cdot 10.476$
${}_{ij}\underline{y}_{ii}^{\alpha 0}$	$\mathrm{j} \cdot 0.011$	$\mathrm{j} \cdot 0.023$
${}_{ij}\underline{y}_{ii}^{\alpha\beta}$	$\mathrm{j} \cdot 0.004$	$\mathrm{j} \cdot 0.008$

Fig. 3. Real-Time Simulator OPAL OP5600

III. LABORATORY EQUIPMENT

The laboratory grid is a scaled model of a 220 kV transmission system with $U_{\mathrm{r}} = 220$ V, $S_{\mathrm{r}} = 2$ kVA and $f_{\mathrm{base}} = 50$ Hz, including twelve transmission line models with their pi-section equivalent circuits, representing lengths of 50 km and 100 km. Fig. 2 shows the whole grid. The normalised transmission line admittances are presented in Tab. I, where $\beta \in P$ and $\beta \neq \alpha$.

There are two busbars, each feeding up to three different sections of the grid independently. Switches, modelling circuit breakers and disconnectors, can be controlled remotely via a real-time simulator and a SCADA system.

Two 12 kVA generators can be connected to the grid at any node, either to generate or to dissipate power. The same holds for the 15 kVA Triphase Power Module, which also gives the possibility to model renewables and HVDC components, for example. Resistors and inductors of different values model appropriate loads and can also be connected to any node of the grid.

Control of the generators and the power hardware, acquisition of measurements, and the power-flow calculation is performed with the OPAL OP5600 real-time simulator, shown in Fig. 3, which has two cores of an Intel Xeon E5-2667 v3 3.2 GHz CPU activated.

Overall, the equipment provides an extremely flexible model

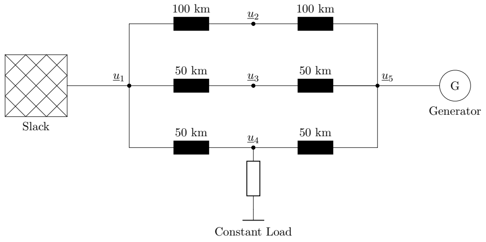

Fig. 4. Grid of the Experimental Setup

of a transmission system – the kind of many experimental setups, like [5] – for validation purposes, e.g. of modern controller designs, and impacts of grid development and faults on power system stability. Unlike utility-setups, all experiments can be designed and repeated arbitrarily at wish. The scaling of the laboratory grid provides transients of reasonable values to validate simulation and real field results in particular.

IV. EXPERIMENTAL SETUP

The experimental setup used for validating the presented power-flow calculation consists of a grid with $n = 5$ nodes, as shown in Fig. 4. The normalised line admittances of the 50 km and 100 km transmission line models are the ones presented in Tab. I.

The results will later be compared related to [6], but without considering different methods of solving algorithms and the computation performance. This is because time constraints are irrelevant for this setup.

A. Validation Using Simscape

The grid of Fig. 4 is modelled in Simulink using the Simscape toolbox with MATLAB R2015a SP1 32 Bit with a step size of $T_\mathrm{s} = 1\ \mu\mathrm{s}$. Transmission lines, capacitive coupling and the mutual ground admittances are modelled with Series RLC Branches. Power generation is done with Controlled Current Sources, power dissipation with Series RLC Loads. The slack voltages are generated with AC Voltage Sources and Series RLC Branches of $R = 1\ \mathrm{m}\Omega$. Measurements are carried out with RMS and Power blocks. The slack nodal voltages and the injected power of the other nodes are then used to perform the power-flow calculation.

In both balanced and unbalanced cases, the relative difference between calculated and simulated nodal voltages with $\varepsilon = 10^{-6}$ was less than 10^{-2} %, the absolute difference was less than 10^{-4} per unit. The same applies to the injected reactive power at the slack node. Relative difference of active power at the slack node was 10^{-2} %, and the absolute difference was 10^{-4} per unit respectively.

This shows that the power-flow calculation accurately computes the state of the experimental grid in Simscape, which means that it can be used to validate the laboratory grid configuration.

B. Validating the Laboratory Grid

The laboratory grid is configured to represent the experimental setup shown in Fig. 4. The measurements used for the power-flow calculation are presented in Tab. II. To illustrate the capability of modelling unbalanced power systems, phase one of the constant load does not dissipate any power. Measurements are acquired with Gossen Metrawatt A2000 devices.

Again, the measured values are used to calculate the power-flow with $\varepsilon = 10^{-6}$. These values are presented in Tab. III. Tab. IV shows the differences d and relative changes c_r according to (28) and (29), with x_calc as a calculated and x_meas as a measured value, both in per unit.

$$d = x_\mathrm{calc} - x_\mathrm{meas} \tag{28}$$

$$c_\mathrm{r} = \frac{x_\mathrm{calc} - x_\mathrm{meas}}{x_\mathrm{meas}} \tag{29}$$

The results show that the relative change of the nodal voltages is less than $\pm 1\ \%$, which is negligible, considering measuring errors, deterioration of capacitances, contact resistances, component parameter scattering, and, most importantly, the results of the validation using Simscape with general deviations.

While the relative difference of injected active and reactive power at the slack node is significantly higher, the absolute difference shows that there is no considerable distinction. This gives the conclusion that the laboratory grid is an accurate model of a stationary three phase and unbalanced transmission system.

V. IMPLEMENTATION ON A REAL-TIME SIMULATOR

The real-time simulator is used for control of the generators, the power hardware and the switches of the laboratory grid, and for processing measurements, thus providing a flexible development and simulation environment, e.g. as a rapid control prototyping platform. For a feasible pre-validation of topology changes, the power-flow calculation is implemented on the real-time simulator. The following procedure is executed. For the procedure itself, real-time is not a requirement.

1) Detect topology change request
2) Evaluate new topology state
    a) Calculate admittances
    b) Measure slack voltages and injected nodal power
    c) Combine with nodal power injection of requested topology
    d) Calculate power-flow
3) Detect limit violations
4) Respond to topology change request

A topology change can be requested by the user or an external application. Among the request, the weighted adjacency matrix has to be provided as an input to the procedure. The weights represent the length of the transmission lines, connecting two nodes.

Every node of the laboratory grid has to be uniquely identified with this adjacency matrix. With twelve transmission line models, there is the possibility to define up to 24 nodes. This is important to assign every node, considered in the power-flow, the correct information about the power injection.

TABLE II
LABORATORY GRID MEASUREMENTS USED
FOR THE POWER-FLOW CALCULATION IN PER UNIT

α	u_1^α	$p_{\mathrm{inj},2}^\alpha$	$q_{\mathrm{inj},2}^\alpha$	$p_{\mathrm{inj},3}^\alpha$	$q_{\mathrm{inj},3}^\alpha$	$p_{\mathrm{inj},4}^\alpha$	$q_{\mathrm{inj},4}^\alpha$	$p_{\mathrm{inj},5}^\alpha$	$q_{\mathrm{inj},5}^\alpha$
1	0.5882	0	0	0	0	0	0	0.2425	−0.1355
2	0.5832	0	0	0	0	−0.0555	0	0.2560	−0.1355
3	0.5814	0	0	0	0	−0.0555	0	0.2525	−0.1385

TABLE III
LABORATORY GRID MEASUREMENTS AND
VALUES OF POWER-FLOW CALCULATION

MEASURED VALUES IN PER UNIT							CALCULATED VALUES IN PER UNIT						
α	$p_{\mathrm{inj},1}^\alpha$	$q_{\mathrm{inj},1}^\alpha$	u_2^α	u_3^α	u_4^α	u_5^α	α	$p_{\mathrm{inj},1}^\alpha$	$q_{\mathrm{inj},1}^\alpha$	u_2^α	u_3^α	u_4^α	u_5^α
1	−0.235	0.0125	0.5918	0.5877	0.5882	0.5868	1	−0.2414	0.0193	0.5893	0.5868	0.5870	0.5839
2	−0.1980	0.0195	0.5855	0.5810	0.5773	0.5805	2	−0.1993	0.0210	0.5835	0.5810	0.5787	0.5774
3	−0.1965	0.0235	0.5836	0.5791	0.5800	0.5795	3	−0.1958	0.0240	0.5821	0.5797	0.5813	0.5765

TABLE IV
DIFFERENCE AND RELATIVE CHANGE OF
MEASURED AND CALCULATED VALUES

DIFFERENCE IN PER UNIT							RELATIVE CHANGE IN PERCENT						
α	$p_{\mathrm{inj},1}^\alpha$	$q_{\mathrm{inj},1}^\alpha$	u_2^α	u_3^α	u_4^α	u_5^α	α	$p_{\mathrm{inj},1}^\alpha$	$q_{\mathrm{inj},1}^\alpha$	u_2^α	u_3^α	u_4^α	u_5^α
1	−0.0064	0.0072	−0.0026	−0.0010	−0.0013	−0.0030	1	2.73	57.86	−0.43	−0.17	−0.21	−0.51
2	−0.0016	0.0019	−0.0020	0.0001	0.0014	−0.0031	2	0.79	9.71	−0.34	0.02	0.24	−0.53
3	0.0000	0.0009	−0.0016	0.0005	0.0012	−0.0032	3	0.02	3.92	−0.27	0.09	0.21	−0.55

To calculate the power-flow, a node has to exist in the new topology, which means that the adjacency matrix has to be adapted to these existing nodes. The admittances are then calculated and stored in a multi-dimensional structure. It is also necessary to measure the slack voltages – and if not present in the new topology, to define a slack node – and the nodal power injections. This information also has to be provided by the user or an external application, if the power injections of the new topology differ from that of the current topology.

After the power-flow calculation, the results have to be compared to limits, e.g. the maximum line current or the minimum nodal voltage. This leads to the decision wether the topology change request is acceptable or not, sent to the user or the external application.

While the procedure is straightforward to implement, for example, with a MATLAB Function block, it is important to exclude this procedure from the real-time execution to not negatively influence the other processes demanding real-time.

VI. CONCLUSION

This paper presented an algorithm to calculate the power-flow of unbalanced three phase power systems with all necessary definitions. Validation with Simscape showed that it precisely computes the stationary state of a power system at fundamental frequency. Thus, the power-flow calculation has been used to validate the state of a laboratory grid with an experimental setup. The results illustrated that the grid accurately represents a transmission system with reliable transmission line parameters.

Even though implementing the power-flow calculation on a real-time simulator is not meaningful, the provided solution combines control of the transmission system and pre-validation of topology changes on the same platform. Another advantage is that there is the possibility to build a predictive simulation environment, as pictured in [7, pp. 52–53].

Among that, future work should be invested in defining different node types, e.g. to model renewables and dc grids as in [8], which greatly affect grid development of power systems. It should also be considered to calculate the power-flow on an external device, which makes it necessary to define suitable interfaces for communication between the real-time simulator and external hardware. Application of state estimation techniques, based on the unbalanced power-flow calculation, could lead to research in the field of modern controller designs incorporating the power system state. Basics on static-state estimation are given in [9], a review on dynamic state estimation techniques is outlined in [10]. Also based on the unbalanced three phase model, it should be considered to calculate transients for pre-validation of topology changes.

REFERENCES

[1] J. A. Peralta, F. de Leon, and J. Mahseredjian, “Unbalanced multiphase load-flow using a positive-sequence load-flow program,” *IEEE Transactions on Power Systems*, vol. 23, no. 2, pp. 469–476, 2008.

[2] R. M. Ciric, A. P. Feltrin, and L. F. Ochoa, “Power flow in four-wire distribution networks-general approach,” *IEEE Transactions on Power Systems*, vol. 18, no. 4, pp. 1283–1290, 2003.

[3] W. Tinney and C. Hart, “Power flow solution by newton’s method,” *IEEE Transactions on Power Apparatus and Systems*, vol. PAS-86, no. 11, pp. 1449–1460, 1967.

[4] G. Engeln-Müllges, K. Niederdrenk, and R. Wodicka, *Numerik-Algorithmen: Verfahren, Beispiele, Anwendungen*, 10th ed., ser. Xpert.press. s.l.: Springer-Verlag, 2011. [Online]. Available: http://gbv.eblib.com/patron/FullRecord.aspx?p=645640

[5] A. S. Meliopoulos, G. J. Cokkinides, S. Mohagheghi, Q. B. Dam, R. H. Alaileh, and G. K. Stefopoulos, “A laboratory setup of a power system scaled model for testing and validation of ems applications,” in *IEEE Bucharest PowerTech, 2009*, L. Toma, Ed. Piscataway, NJ: IEEE, 2009, pp. 1–8.

[6] M. Abdel-Akher, K. M. Nor, and A. Rashid, “Improved three-phase power-flow methods using sequence components,” *IEEE Transactions on Power Systems*, vol. 20, no. 3, pp. 1389–1397, 2005.

[7] *IEEE P3002.2/D9, September 2017: IEEE Approved Draft Recommended Practice for Conducting Load-Flow Studies of Industrial and Commercial Power Systems*. [Place of publication not identified]: IEEE, 2017.

[8] M. Baradar and M. Ghandhari, “A multi-option unified power flow approach for hybrid ac/dc grids incorporating multi-terminal vsc-hvdc,” *IEEE Transactions on Power Systems*, vol. 28, no. 3, pp. 2376–2383, 2013.

[9] A. Abur and A. G. Exposito, *Power System State Estimation: Theory and Implementation*, ser. Power Engineering (Willis). Hoboken: Marcel Dekker Inc, 2004.

[10] M. R. Karamta and J. G. Jamnani, “A review of power system state estimation: Techniques, state-of-the-art and inclusion of facts controllers,” in *International Conference on Electrical Power And Energy Systems (ICEPES-2016)*. Piscataway, NJ: IEEE, 2016, pp. 533–538.

Life-cycle analysis of the climate impact of present high-voltage direct current transmission systems

Jan Wiesner
Master student Elektromobilität
Technical University of Chemnitz
Chemnitz, Germany
jan.wiesner@s2013.tu-chemnitz.de

Prof. Dr.-Ing. Josef Lutz
Chair of Power Electronics and EMC
Technical University of Chemnitz
Chemnitz, Germany
josef.lutz@etit.tu-chemnitz.de

***Abstract*— Modern high-voltage direct current distribution networks are mostly assessed from a cost perspective. The objective of this study is to compare the technologies' impact on global warming over its complete lifespan. A software tool was created that allows the investigation and simulation of different grids using variable parameters. Results indicate that present high-voltage direct current transmissions with overhead lines and more than 376 kilometers length emit less greenhouse gas equivalents than their high-voltage alternating current counterparts over their service life. Findings did also reveal that common understanding regarding costs of high-voltage cable and overhead lines needs to be reassessed.**

***Keywords*— high voltage direct current, global warming potential, life-cycle-analysis, overhead lines, cable, laying**

I. INTRODUCTION

The existential threat of man-made global warming and the resulting climate change is one of the greatest challenges of our time. The continuous expansion of fluctuating energy sources places demands on European distribution networks, which play a key role in an energy system with 100 % renewable electricity due to the increasing distances between producers and consumers. Large site-dependent generation centers are built offshore with high expansion rates [1]. A future grid must connect them with the consumers in remote agglomerations. Megatrends such as electromobility and sector coupling pose additional challenges. High voltage alternating current (HVAC) transmission is only suitable to a limited extent for such functional network that spans long distances and incorporates submarine and cable connections. High-voltage direct current (HVDC) transmissions offer the advantages needed for such Pan-European network. Previous work has mainly dealt with the costs and comparison of network advantages of HVDC and HVAC. With the use of large quantities of energy-intensive raw materials in voltage-sourced converter stations of HVDC installations, it must be ensured that such system does not cause higher greenhouse gas emissions over its life cycle than conventional HVAC systems. In this paper, the global warming potential (GWP) of components of both technologies is investigated.

In the course of the current political discussion on network expansion in Germany, citizens protest planned overhead lines. Therefore, in many places underground cabling is being discussed [2]. The German government decided that new HVDC lines built near residential areas should be designed as underground cables in order to increase public acceptance [3]. The commissioned network operators point to significantly higher costs due to the laying of the cables. According to them, underground cables are 4 to 8 times more expensive than HVDC overhead lines [4]. A study by the Research Centre for Energy Economics, which examined existing projects, found an average cost factor of 5.9 between HVDC underground cable and overhead line systems during the last years. The price for HVDC overhead line transmissions was between 700 € and 1400 € per kilometer and kilowatt [5]. The investments for underground cables amounted to 1200 € to 16000 € per kilometer and kilowatt [5].

The present study attempts to provide assertions for the two types of transmission from a life-cycle-assessment point of view, allowing to compare the use of energy-intensive materials and the system costs.

II. METHODOLOGY

A. Scope

This life-cycle analysis (LCA) serves to identify the potential environmental impacts, using a cradle-to-grave approach. In order to compare the lifecycles of technologies, both the emissions caused by the materials used and the losses during operation of the system were considered. Necessary manufacturing processes and their energy requirements, transports and the resulting greenhouse gases are included. The losses were determined for terminal stations and transmission lines of a system. The study forms a comparative life cycle assessment that compares several products. System boundaries were created to limit the scope of it. Central components are two terminal stations, and the transmission in between them. Therefore, only the losses in the internal HVDC transformers are covered. Any existing transformer-substations and their losses for coupling to other networks are not included for neither HVAC nor HVDC in order to create comparability across all systems. Since the scope of a life cycle analysis can be increased to infinity from the raw material to the end-of-life of a product by the available resolution of the data, the analysis is limited to the significant emission factors, if possible. Due to the data sets mentioned in section II B, a very high level of detail was achieved for the assessment of emissions by the materials used in the HVDC converter stations. In addition to the extraction, processing and transports of raw materials for HVAC and HVDC systems, the analysis also includes losses of the transmitted energy caused by lines and terminal stations or compensation devices. The recycling of each system is included as an end-of-life-scenario and is then offset against the material-emissions. Transport routes of materials were assumed to be 500 km, unless detail information by suppliers was available. The final assembly of components or installation processes of terminal stations and overhead lines are not included in the calculation, since the needed data would lead to inadequate estimates or extensive calculations for each individual component. The considered HVDC bipolar cable system was analyzed without metallic return, as no data were available from the manufacturer and estimated to be not significant. The losses in the terminal converter stations are assumed for operation at 100 % load but are listed as free parameters to take more precise data into account in the future. Only overhead lines were considered for 400 kV HVAC technology because of the strong need for compensation and the associated inefficiency of cables [6]. Due to the system boundaries, no effects of transmissions on the overall grid stability have been considered.

To communicate the results of the GWP, this paper uses a functional unit: a transmission system for transporting 2 GW of electrical power over 400 km with 8760 full load hours per year was considered. The assumed emission factor of the electricity is 534 g of CO_2 equivalent per kilowatt hour electricity (CO_{2eq}/kWh_{el}) which represents specific electricity-generated emissions in Germany in the year 2015 [7]. All parameters can be changed in the created tool (see section II C).

B. *Data base*

The material compositions with exact mass and material specifications for the components of the HVDC Bipolar ± 500 kV terminal stations with voltage-sourced converters (VSC) were provided by a leading technology company. The company revealed achieved recycling rates for each separate material. Also, precise power loss data were obtained for the full-bridge and half-bridge converter stations. For further calculations, the worst-case losses in the converter terminal stations were assumed. The HVAC systems were evaluated based on [8].

C. *Used life cycle assessment software*

For the study on GWP of HVDC VSC transmissions the „E3 Database“ software was used which obtains data mainly from the "ecoinvent V3" database. The author has been trained in the software and instructed by Ludwig-Bölkow-Systemtechnik GmbH (LBST). After programming a changeable data set (LCA tool), the results of the research were analyzed and illustrated in detail. The LCA tool allows the user to investigate the CO_{2eq} footprint of HVDC VSC in direct comparison with 400 kV HVAC distribution systems. Parameters such as the emission factor of the transmitted energy, the number of full load hours and transmission distances can be varied. The variation of transmitted power, amount of terminal stations and their rated power enable the time-efficient calculation of the climate impact of a future grid.

D. *Sensitivity analysis*

The following results focus on the climate impact in CO_{2eq} over the life cycle (CO_2 footprint). A sensitivity analysis was conducted to measure how sensitive the resulting CO_{2eq} balances react to changes in the input parameters. It was found that the total CO_{2eq} emissions are very sensitive to the generation emissions of the transmitted electricity. This is due to the relatively large operating losses in terminal stations (operation emissions) and transmission lines compared to emissions caused by materials used to build the systems (material emissions). There is no change in the qualitative results when changing the electricity emission factor with virtually emission-free generation (emission factor of 30 g CO_{2eq}/kWh_{el}) or pure coal powered generation (emission factor of 800 g CO_{2eq}/kWh_{el}). The same applies to realistic changes of system utilization rates.

III. IMPLEMENTATION AND RESULTS

A. *Emissions of HVDC terminal stations*

The life cycle analysis for HVDC VSC terminal stations revealed the emissions distribution shown in Fig. 1. The large proportion of operating emissions accounts for more than 99 % of total emissions over the service life of the terminal stations when the emission factor of 534 g CO_{2eq}/kWh_{el} [7] is used. Initial concerns, that the use of large quantities of energy-intensive silicon and packaging technology would lead to a relatively high GWP, can thus be denied.

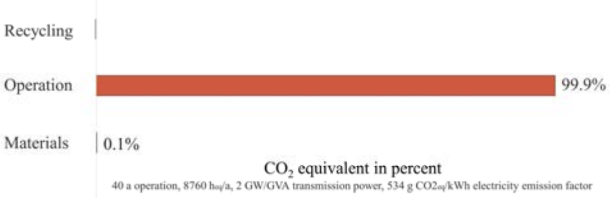

Fig. 1: Share of emissions of HVDC voltage sourced full bridge converter stations

Data from the manufacturer show that half-bridge (HB) IGBT modules are used for HVDC VSC cable connections in the converter stations, since error handling for short-circuits does differ as is the case with overhead lines. For overhead lines, full-bridge IGBT modules (FB) were assessed, as they offer better fault handling than half-bridge modules. It must be said that it is also possible to use half-bridge converters in overhead line transmissions according to the manufacturer. This comes with significantly worse system behavior in response to temporary DC line faults and increased component load.

B. *Emissions of overhead line transmissions for HVDC*

A common ACSR Pheasant conductor with a cross-section of 726.8 mm² per quad-bundle and pole was evaluated. The maximum permanent operating temperature of 80 °C and resulting resistances [9] as defined by DIN EN 50182 for the overhead conductors were used for power loss assessment on the HVDC overhead line system. A ± 500 kV bipolar HVDC overhead line, capable of transmitting 2 GW of electrical power, uses two of these four-bundle ropes. The material composition for foundations, masts, conductor cables and insulators of the overhead lines was provided by the company partner and used for climate impact analysis with the E3database. The material emissions with considered recycling-scenario amount to 56 t CO_{2eq}/km of such bipolar HVDC overhead line system.

C. *Emissions of cable transmissions for HVDC*

At time of the study, DC cable products with cross-polymer (XLPE) insulation were on the market that were approved for a voltage level of 525 kV [10]. One advantage of this technology is the significantly lower weight per kilometer of cable and the lower number of conductors required due to the higher power density, which results in fewer transports and longer cable sections with fewer connection sleeves [11]. The use of highly recyclable materials [12] and the absence of oil-soaked paper insulation also decreases the environmental impact of XLPE technology compared to mass impregnated cables (MI) which were previously used for underground cabling. In the following, it is assumed that future projects will be carried out with plastic insulated XLPE cables. Products for higher voltage ranges are to be expected in the next few years that will displace MI technology from ± 800 kV HVDC transmission applications [13].

An XLPE cable with 2000 mm² copper conductors was evaluated in accordance with the manufacturer's specifications for 2 GW [10]. Since cable manufacturers and suppliers keep a low profile about material compositions of products, these were determined using graphics from [10]. The given cross-sectional area of the copper conductor of 2000 mm² was used to determine the diameter of the conductor and, subsequently, the total area of the cable.

Based on this data, the CO_{2eq} for the materials used could be determined using E3database software. According to [14], marine and underground cables with XLPE technology are almost identical in construction, the differences in the sheath layer, the material composition of which depends strongly on the planned location, were marginal within the results of the calculation.

The recycling rates for individual materials specified by the company partner for the terminal stations were applied for XLPE cables as well. After taking the recycling scenario into account, a total of 63 t CO_{2eq}/km of bipolar system are emitted for extracting and transporting the materials for the two cables. The calculations on the climate impact of cable couplings according to data from [11] were also carried out. The advantage of the lower weight of XLPE cables makes it possible to use longer cable sections. One drum can carry 1.2 km which reduces the number of required couplings [15]. It is assumed that their CO_{2eq} footprint is significantly determined by the insulation material. According to this, the couplings result in emissions of 3.4 t CO_{2eq}/km of bipolar conductors.

In total, 66.4 t CO_{2eq}/km are emitted for supplying all materials of the bipolar ± 500 kV XLPE cables with couplers (recycling of the cable and couplers included).

The manufacturer specifies a maximum operating temperature for the insulation of 70 °C. Following this, the resistance at 70 °C is assumed for these most unfavorable operating conditions when the load is 2 GW. The same worst-case scenario applies to the resistances of the conductors on the overhead lines under consideration, where 80 °C is permissible as a permanent operating temperature according to DIN EN 50182.

D. *Uncertainty about the cost ratio of high-voltage overhead lines and underground cabling*

After the first interim results on the material emissions of cables and connection couplings, doubts arose about the prevailing tenet of the cost distributions between overhead lines and underground cabling. A rather similar CO_2 footprint for the material supply of 56 t CO_{2eq}/km for HVDC overhead lines versus 66 t CO_{2eq}/km for underground cables was proven. It can be assumed that the use of materials and the associated greenhouse gas emissions are in some direct relation to the costs. It was therefore decided to carry out an additional investigation on the climate impact of the XLPE cable installation, to possibly explain the price factor of 4 to 8 between the two routing options [4]. The research was carried out by W. Weindorf from the project partner Ludwig-Bölkow-Systemtechnik GmbH. His study [16] examines not only the delivery of the couplings but also several installation methods with trencher, excavator and laying-plough (Föckersperger installation system). Due to the lowest specific greenhouse gas emissions per kilometer of cable installation, the laying-plough was included in this study. The consideration includes laying without crossing of infrastructure. Both cables can be laid in one process [17]. The chosen installation solution can be used for high-voltage cables of 525 kV and offers a productivity of up to 1500 m/h (excluding coupler installation) [17]. According to the supplier, it can be used in almost any terrain, including rock [17]. According to the manufacturer of the XLPE cable, it is possible to lay the cables close (0.5 m between cables) and at a depth of 1.5 m [10]. Under these conditions and assumed 1 K*m/W average thermal resistance of the ground, a permanent transmission power of 2 GW is possible [10]. The worst-case emissions to be expected during laying were calculated at a diesel-consumption of 185 l/km. This assumes very impassable terrain and high stress on the tractor [17]. Fig. 2 shows the Foeckersperger laying principle.

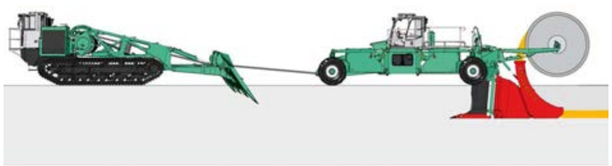

Fig. 2: Elements of Foeckersperger cable laying system, from [17]

In addition to the material emissions of the cables, emissions of 1.18 t CO_{2eq}/km by laying the cables with a plough and 0.067 t CO_{2eq} for transporting the couplers to the construction site occur [16]. It was found that in total, 67.6 t CO_{2eq}/km are emitted for the bipolar ± 500 kV HVDC cable system. This number includes the material supply emissions as well as the installation and recycling of the cables.

In 2005, cable manufacturer ABB published the results of a life cycle analysis between a first generation HVDC underground cable and a three-phase overhead line [18]. The differences in mass and CO_2 emissions can be adapted to the comparison between HVDC-XLPE cable and HVDC overhead line and confirm the correlations observed in this study. A common price factor of 4 to 8 between the two routing options [4] [5] appears to be exaggerated. When considering existing correlations between GWP of materials and cost for products, the price difference between both transmission options must be found in the installation process, which seems unlikely. Further research is needed to reassess price estimations by grid operators. It should nevertheless be noted that projects such as the construction of a high-voltage transmission system depend heavily on the geographical conditions. The experience of the grid operators must therefore be considered. It is possible that the cost difference to the detriment of a cable route is due to the installation effort of the cable under worst conditions. An assessment of crossings with other structures requires a case-by-case analysis and therefore cannot be easily evaluated in detail. For undercrossing of any kind with cables, a very economical method is available in the form of the horizontal flush drilling technique (HDD drilling technique) [19]. The sensible combination of horizontal flush drilling technology and cable ploughing is known as the plague-and-plow method. In Germany, 15 % of HDD and 85 % of cable ploughing work are realistic [19]. Investigations into the laying of underground cables, which were previously carried out, were almost always based on laying in open trenches [19]. As already mentioned, this paper examines trenchless cable laying using a plough. Then, the laying costs amount to only 10-30 €/m [21]. After extending the scope of this study, the material supply and laying of the HVDC cable as well as the material supply and delivery of the cable sleeves were considered. In the case of overhead lines, only material supply was considered. The installation with motorized rams, the casting of the foundation with the help of concrete mixers, the delivery by truck, the stacking of the mast elements with one or more mobile cranes as well as the clamping of the conductor cables are necessary work steps when installing an overhead line [22]. Due to the high degree of mechanization involved in erecting the masts and foundations, local emissions from the combustion of fossil fuel are likely. It is also possible to estimate a large transport requirement for concrete, conductor wires and steel elements. By way of comparison, the mass ratios of about 4:1 between overhead lines (with foundations) and cables must be observed [9] [10]. The emissions caused by the transport of overhead line components are thus to be expected far higher than those caused by the delivery of cable segments and couplings. Since the mass of overhead line components is more than 4 times higher than a cable (including foundations) [9] [10], it is plausible that the greenhouse gas emissions associated with material transport are even higher than the GHG emissions of all machines that would be used for cable ploughing and the sporadic use of HDD drilling technology. Since the emission of CO_{2eq} for the installation of an overhead line or cable route (no materials, only the installation process) depends largely on the energy consumption of the construction machinery used, it becomes clear that the installation process of an overhead high-voltage line for an HVDC system, using conventional fuels, must cause higher emissions than the laying of underground cables. Further research is needed to quantify the difference accurately. For this study it became clear that the influence of installation of components is insignificant, as the impact category is the use phase of the components.

E. Emissions of overhead line transmissions for HVAC

For the HVAC 400 kV reference system, two complete overhead line tracks are required for the desired transmitted active power of 2 GW [8]. An existing Finch product (4x564/72) was selected for these conductors [23]. Since the diameter differs by only 2 mm compared to the Pheasant conductor, which was analyzed in the HVDC overhead line, it is assumed that the material emissions of such Pheasant conductor are very similar to those in the HVDC overhead line. HVAC overhead lines use one conductor rope per phase and system [22]. In addition to twice the number of masts and foundations, six bundled conductor cables are therefore required for two HVAC overhead lines. Material supply emissions are thus 2.7 times higher than for a comparable HVDC line. This results in material emissions of 150.6 t CO_{2eq}/km of HVAC overhead line system for 2 GW with considered recycling scenario. The losses on a HVAC line system are divided into voltage-dependent losses P_{vu} and current-dependent losses P_{vi}. Per unit length factors R', G' and Q' of the routing [8] were included. The maximum permanent operating temperature of 80 °C as defined by DIN EN 50182 for the overhead conductors is used for power loss assessment. Losses per kilometer P_{loss} on the HVAC overhead lines are therefore calculated as:

$$P_{loss} = 2 \bullet 0.099 \text{ MW} \tag{1}$$

Required reactive power is provided by STATCOM technology for three-phase overhead line systems in the evaluation. STATCOM enables additional network stabilization and was therefore assessed. One of the used Cascaded Multilevel Inverter (CCMLI) causes 185 kW losses for 24 MVA control power [24]. Relative to the assessed transmission active power of 2 GW, the losses amount to about 0.77 %. It is also necessary to consider the corresponding supply transformer, which in total leads to losses of up to 1.4 % (related to the active transmission power) [25]. The effect on the HVAC GWP is based on the assumption that a STATCOM for a 2 GW system of 400 km has a similar CO_2 balance as three transformers of the VSC technology.

F. Comparison of HVAC and HVDC emissions

The use of a 400 km HVDC VSC system with full bridge modules (FB) and overhead lines over 40 years results in a 3.5 % reduction in greenhouse gas emissions compared to further use of an existing three-phase HVAC system as it can be seen in Fig. 3. The reduction over 40 years corresponds to 0.64 Mt CO_{2eq} under the German electricity mix in 2015 [7]. The life cycle analysis shows that the total emissions of a 400 km ± 500kV HVDC VSC with XLPE cables amount to 13.4 Mt CO_{2eq} and are thus 6.7 Mt below the amount of CO_{2eq} emissions that would result during 40 years of operation of an existing HVAC line (see Fig. 3). As already mentioned, half-bridge modules (HB) are mainly used for cable transmission in HVDC VSC systems. This results in lower operating losses in the terminal stations and a saving of almost 4 Mt CO_{2eq} (see Fig. 3) compared to the full bridge (FB) HVDC VSC, which is considered for overhead line systems in this study.

For all assessed systems it was noticed that the largest amount of CO_{2eq} is emitted due to operational losses. The supply and transport of materials is of insignificant impact to the overall GWP of HVAC or HVDC installations under given parameters. These findings accord to other current studies which conclude that the effect category is the operational phase of power distribution products [26].

After analyzing the total emissions of individual systems, it is important to determine the beneficial minimum transmission length of an HVDC system when considering building a multi-terminal distribution network. This distance, at which the construction of an HVDC link would be associated with lower emissions than a HVAC line, is set as the break-even point. For HVAC systems, one of the evaluated STATCOMs per 400 km was included and their emissions were scaled linearly accordingly.

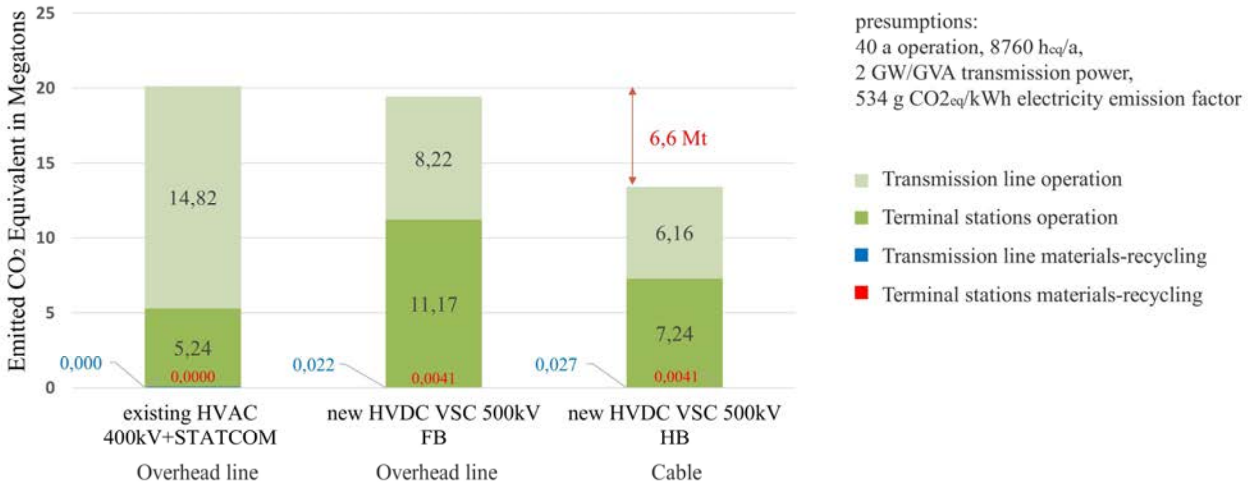

Fig. 3: Results of life cycle assessment, comparison of HVAC and HVDC transmissions

This results in a break-even distance of 376 km for the ± 500 kV HVDC VSC with overhead line under given parameters. The emission break-even for a cabled ± 500 kV HVDC VSC system over of a 400 kV three-phase HVAC system when transmitting 2 GW occurs already at 208 km transmission distance. For reasons of climate protection, it is therefore advisable to replace an existing three-phase HVAC overhead line system with a VSC HVDC using overhead lines or cables to transmit 2 GW over 40 years. The cable system most significantly reduces the GWP due to usage of half-bridge converters. In addition to the grid benefits of HVDC VSC with cable routing, the replacement would also make a major contribution to achieving the climate protection targets.

G. *Emissions of an fictive HVDC VSC Supergrid*

The investigation of a meshed supergrid for regenerative supply of Europe was carried out using the LCA tool. The scenario is based on the expansion map published by [28], which is cost-optimized and uses a mix of expansion of HVAC and new installation of HVDC technology. Based on the findings gained during this present study, the extension and construction of HVAC lines is significantly more harmful to the climate than comparable HVDC systems (see section III F). It is recommended to carry out future projects at distribution network level with HVDC VSC technology to meet climate targets. Fig. 4 shows the scenario from [27] adapted by Professor J. Lutz with additional HVDC connections marked in light blue. His adaption uses only DC links, which make AC expansion from [27] obsolete (marked in red). The resulting multi-terminal grid is seamless and is not interrupted by HVAC transmissions. Markers have been added for each link and for the location of half-bridge (H) and full-bridge (V) terminal stations for calculations with the LCA tool. This altered scenario was assessed by the author with the LCA tool based on the findings of the GWP of HVDC VSC installations. Additionally, materials, recycling and losses for two HVDC breakers per HVDC link are included into the calculation. Connections along coasts were implemented as undersea cables along the coastlines.

The GWP balance for such HVDC network results in 1110 Mt CO_{2eq} over 40 years when considering parameters as mentioned in section II A. The climate impact of an equivalent distribution network using only fictive expansion of HVAC overhead-line transmissions was determined using the LCA tool for comparison. The GWP balance for such comparable HVAC network with solely overhead lines amounts to 1571 Mt CO_{2eq} including scaled STATCOMs. This corresponds to an additional output of 461 Mt CO_{2eq} over 40 years, comparable with emissions from 2.5 average German 1 GW power plants in 2015 (at 534 g CO_2/kWh_{el} [7]).

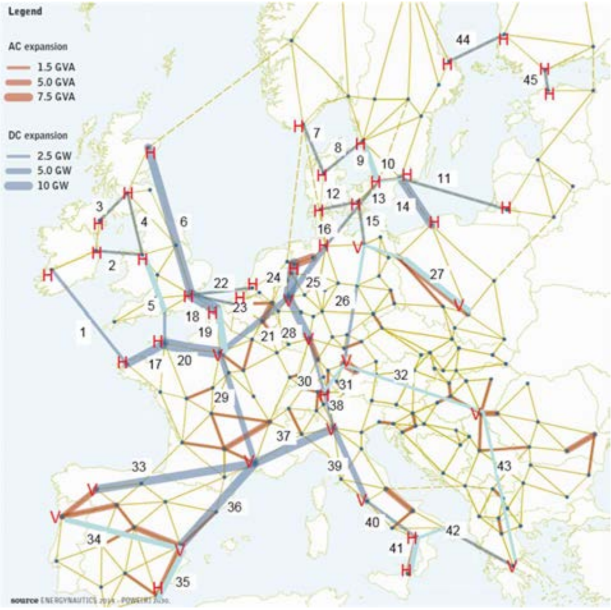

Fig. 4: European distribution network scenario from [27], adapted from Prof. Dr. Lutz with additional HVDC connections (light blue)

IV. CONCLUSIONS

It was found that HVDC VSC installations above certain transmission distances cause lower emissions of CO_{2eq} over their lifecycle than equivalent HVAC installations. The advantage becomes particularly clear with cabled HVDC VSC transmissions, as cabling and the use of half-bridge converters result in significantly reduced losses. It has been found that material emissions are currently of little influence. Emissions caused by operational-losses in terminals and transmission-lines dominate. For this reason, the advantage of the HVDC VSC is also independent of whether a new HVAC connection is built or an existing one is replaced.

In the course of the study, no explanation could be found for the previously prevailing opinions on cost relationships between overhead line construction and underground cable deployment, despite more in-depth investigations into cable laying. The emissions caused by the installation of XLPE cables and the installation of the overhead line are estimated to be in the same magnitude and to have little impact on the total emissions of transmission systems under a given current emission factor. Based on these results, it is advisable, within the framework of further investigations, to assess the extent to which the laying of HVDC transmission lines underground causes higher costs than equivalent overhead lines. However, determined differences between the carbon footprints of HVDC cable and overhead line systems generally recommend cabling for reasons of climate protection today. It was further found that a continental multiterminal network with HVDC has a lower GWP in comparison to equivalent network extensions with HVAC technology. A result that should be taken into account to reach ambitious European climate targets.

ACKNOWLEDGMENT

The author thanks Dipl.-Ing. Menia Meier-Möbius and Prof. Dr.-Ing. Josef Lutz for the support and supervision of this work.

REFERENCES

[1] International Energy Agency, ‘Offshore Wind – tracking clean energy progress', 2017. [Online] Available: https://www.iea.org/tcep/power/renewables/offshorewind/. [Accessed: 14- March- 2019].

[2] Deutschlandfunk, ‘Erdverkabelung verschlingt Milliarden', 2016. [Online] Available: https://www.deutschlandfunk.de/netzausbau-nach-dem-atomausstieg-erdverkabelung-verschlingt.769.de.html?dram:article_id=356492. [Accessed: 14- April- 2017].

[3] German government, ‘Erdkabel statt Freileitung’, 2015. [Online] Available: https://www.bundesregierung.de/breg-de/aktuelles/erdkabel-statt-freileitung-388676. [Accessed: 14- March- 2019].

[4] Newspaper inFranken with quote of project manager of Tennet, ‘Tennet-Projektleiter: Erdkabel vier- bis achtmal so teuer’, 2015. [Online] Available: https://www.infranken.de/regional/bad-kissingen/nur_saalezeitung/tennet-projektleiter-erdkabel-vier-bis-achtmal-so-teuer;art156736,927399. [Accessed: 14- April- 2017].

[5] Anika Regett, Kristin Wachinger, Florian Samweber, Simon Köppl “Kurzgutachten zum Kostenvergleich Stromtransport” Forschungsstelle für Energiewirtschaft e.V., p. 21, 2014.

[6] David Schmidt “Gleichstrom-Unterwasserkabel zwischen Skandinavien und Mitteleuropa” Technical University of Berlin, p.4-5, 2007.

[7] German environmental agency Umweltbundesamt, ‘Strom- und Wärmeversorgung in Zahlen’, 2015. [Online] Available: https://www.umweltbundesamt.de/themen/klima-energie/energieversorgung/strom-waermeversorgung-in-zahlen#Kraftwerke. [Accessed: 22- June-2016].

[8] Prof. Dr.-Ing. habil. B. R. Oswald “Verlust- und Verlustenergieabschätzung für das 380-kV-Leitungsbauvorhaben Wahle – Mecklar in der Ausführung als Freileitung oder Drehstromkabelsystem” University of Hannover, p. 2-3, 2007.

[9] Robert Rotkait “Methodik zur Erarbeitung des CO2 Fußabdruckes eines Hochspannungs-Gleichstromübertragungssystems” Technical University of Chemnitz, p. 30, 2015, unpublished.

[10] Stefan Habild “Erdverkabelung im Bereich der HGÜ-Leitungen” ABB group, p. 22-25, 2015.

[11] ABB Newspaper “ABB about - 525kV unterirdisch transportiert” ABB group, p. 13, 2015.

[12] Prysmian Group Newspaper, ‘Breakthrough HVDC cable technology for power transmission grids’, 2016. [Online] Available: https://www.prysmiangroup.com/en/en_2016_PR_PLaser525kV.html [Accessed: 14- April- 2017].

[13] N. MacLeod, M. Callavik, M. Boden, M. Dhesi, R. Huuva, N. Kuljaca, F. Schettler, CIGRE‘A Technological Roadmap for the Development of the European Supergrid’, 2015. [Online] Available: https://library.e.abb.com/public/323e5c246dee456c8219f05d9b58ae55/A%20Technological%20Roadmap%20for%20the%20Development%20of%20the%20European%20Supergrid.pdf [Accessed: 14- April-2017].

[14] ABB Newspaper “525kV extruded HVDC cable system”, ABB group, p. 4, 2015

[15] ABB Group, ‘XLPE-Gleichstromkabel für mehr als 500 kV - ein wichtiger Baustein für die Energiewende’, 2015 [Online] Available: http://www.abb.de/cawp/seitp202/553c6c3095ef68a2c1257dd9004672dd.aspx [Accessed: 14- April- 2017].

[16] Werner Weindorf, “Energieaufwand und Emissionen aus der Kabelverlegung,” Ludwig-Bölkow-Systemtechnik, 2016, unpublished.

[17] Foeck Walter Foeckersperger GmbH, ‘Verlegepflüge’, 2016 [Online] Available: https://www.foeck.com/de/produkte/verlegepflug/ [Accessed: 20- März- 2018].

[18] ABB Newspaper “Unsichtbar und umweltschonend”, ABB group 2005.

[19] D. H. Bayer, ‘Erdkabel oder Freileitung’, 2005 [Online] Available: https://www.nodig-bau.de/praxisberichte/tis_6-2007_42_46_Erdkabel_Freileitung.pdf [Accessed: 14- April- 2017].

[20] TenneT TSO GmbH, ‘HGÜ-Erdkabel’,2015 [Online] Available: http://www.tennet.eu/fileadmin/user_upload/Our_Grid/Onshore_Germany/Allgemein/151022_HGUE_Erdkabel_1_.pdf [Accessed: 14- April- 2017].

[21] Foeck Walter Foeckersperger GmbH, ‘Ökologie und Ökonomie, Die 7 Gründe, warum das FOECK-Verlegepflugsystem die fortschrittlichste und günstigste Art ist, Kabel/Rohre ins Erdreich zu verlegen’, 2016 [Online] Available: https://www.foeck.com/de/unternehmen/oekologie-und-oekonomie/ [Accessed: 14- April- 2017].

[22] TenneT TSO GmbH, ‘Freileitungen im Bau’, 2016 [Online] Available: http://www.tennet.eu/fileadmin/user_upload/Our_Grid/Onshore_Germany/Allgemein/15-240_Freileitungen_im_Bau-V7_FINAL.pdf [Accessed: 14- April- 2017].

[23] Midal-Kabel GmbH, ‘ACSR metric Conductor datasheet’, 2015 [Online] Available: https://www.midalcable.com/sites/default/files/ACSR-metric.PDF [Accessed: 14- April- 2017].

[24] K. Fujii; U. Schwarzer; R.W. De Doncker “Comparison of Hard-Switched Multi-Level Inverter Topologies for STATCOM by Loss-Implemented Simulation and Cost Estimation” IEEE 36th Power Electronics Specialists Conference, p. 7, 2005.

[25] S.Fassbinder “Efficiency and loss evaluation of large power transformers” European copper institute, 2013.

[26] Raquel Santos Jorge, Troy R. Hawkins, Edgar G. Hertwich, “Life cycle assessment of electricity transmission and distribution-part 1: Power lines and cables”, The International Journal of Life Cycle Assessment 17(1):9-15, 2011.

[27] Greenpeace e.V. “powE[R] 2030 - a european grid for 3/4 renewable electricity by 2030”, 2014.

Monitoring and Automation of Transformer Drying

D. Schmidt
Omexom Hochspannung GmbH
Schulstraße 124,
Walsrode, Germany
david.schmidt@omexom.com

M. Koch
University of Applied Sciences Magdeburg-Stendal
Breitscheidstr 2,
Magdeburg, Germany
maik.koch@hs-magdeburg.de

***Abstract*: This paper introduces the application of the dielectric response analysis to automate and optimize a paper insulation drying process. First the need for drying of paper insulation is indicated by the problems caused due to water contamination. Then the drying process in general will be outlined in this paper. To measure the amount of water within the paper insulation, the dielectric response analysis and its properties are presented. Normally, water concentration in paper insulation can be measured before and after the drying process. However, in the following case study a dielectric response analyser is installed to measure the water concentration continually during the drying process. It sends the gathered data to the oven control unit for optimizing the drying process and saving time and energy.**

I. INTRODUCTION

As moisture in oil-paper insulated power transformers causes various detrimental effects, manufacturers and repair workshops proceed insulation drying with outmost care, however this process consumes time and energy and often causes a bottleneck in the production process.

Residual moisture after production and repair is considered as a contribution to the overall moisture contamination and due to the autocatalytic effects to the dangerous effects of water: Decrease of dielectric withstand strength, accelerated cellulose aging and emission of bubbles at high temperatures [1], Fig. 1. Therefore, a thorough removal of moisture is desired in the drying process. For achieving this, the following means are commonly applied:

- Heating to 120°C,
- Application of successive vacuum phases,
- Fine vacuum for several hours up to days,
- Vapour phase drying for very large power transformers.

If at all moisture is measured during oven drying, this is done via observance of the separated water vapor during the vacuum phases. A direct measurement of remaining moisture in paper is impossible during the drying process. Most commonly, the drying process depends on experiences, not on actual observations. Several reasons evoke interest in optimizing this process:

- As vacuum ovens are costly, they cause a bottleneck in the production process of oil-paper insulations,
- Depending on the ambient humidity and the raw materials condition, the drying time needs to be adjusted,
- Shortening the drying time saves energy costs,
- Customers require an initial moisture content of the insulation of less than 1 %, but preferably 0.5 %.

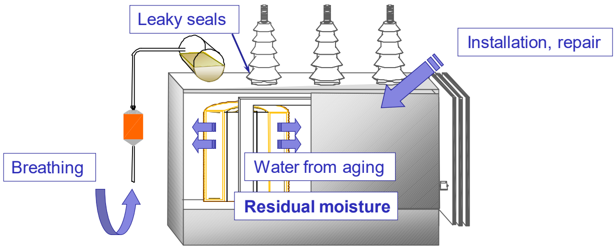

Fig. 1. Sources of moisture contamination for oil-paper insulated power transformers

Monitoring the drying process increases the insulation quality and saves costs and is therefore of benefit for the manufacturer as well as the operator of oil-paper insulated equipment.

As a solution, this paper utilizes dielectric response analysis for monitoring the drying process of oil-paper insulations. Dielectric response methods have been developed to deduce moisture in paper and pressboard from dielectric properties like polarization currents and dissipation factor [2]. The dielectric response as capacitance and dissipation factor is measured across a very wide frequency range, typically 1 kHz to 0.1 mHz. Moisture content is calculated by fitting a model to the real dielectric response. As an earlier paper described the creation of a data base [3], this paper shows the practical implementation in combination with automation and control of the drying oven.

II. DRYING OF OIL-PAPER INSULATION SYSTEMS

A. *Premise*

To reduce the water concentration in paper insulation, first it is required to bring heat Q into the active parts to rise the water vapor pressure within the paper. Second, the pressure of the surrounding air needs to be reduced to evaporate the water out of the paper into the air and get out of the plant while evacuating. After refuelling the oven with dry air, the temperature can reach its maximum so the water vapour pressure reaches its maximum too. After reaching the maximum temperature, the oven is set to fine vacuum where the pressure is reduced to 0,01 mbar. During this phase, a big part of the water evaporates into the air cooling the active parts of the transformer. Because of the cooling, the water vapor pressure drops within paper, so a remaining part of water stays in the insulation. To continue the drying process, the transformer needs to heat up again [4].

B. Heating up

The heat transfer for heating of material to be dried is characterized by the following equation:

$$\dot{Q} = \frac{dQ}{dt} = \alpha \cdot A \cdot (T_2 - T_1) \qquad (1)$$

With:

α - heat-transfer coefficient
$\dot{Q}$ - heat to be transferred
A - transfer surface
$(T_2 - T_1)$ - temperature difference between temperature of medium and surface Pressure reduction

With rising temperature the water vapor pressure in the paper insulation is rising as shown in Fig. 2 and by the different in pressure between the water vapour pressure within and outside of the paper Δp, the water starts to diffuse in the surrounding air.

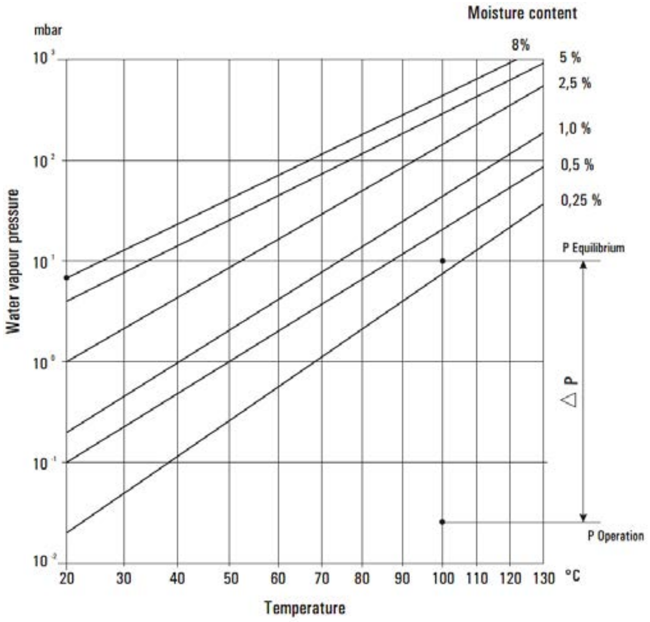

Fig.2. Water vapour pressure within the paper during heating up.

C. Pressure reduction

With water diffusing into surround air, the relative saturation of the air rises until the water vapour pressure in the air is to nearly equal to the water vapour pressure in the paper. To continue the drying process during the heating, the air will be exchanged by a pressure reduction followed by refilling the oven with dried air.

D. Fine Vacuum

When the temperature reaches its peak, the heater turns off and the vacuum pump switched on to reduces the air pressure down to 0.01 mbar. The different from the water vapor pressure between paper and air is now high enough to overcome the binding forces between the water and the cellulose, therefore the water can leaves the paper via diffusion. The surrounding air gets wet but is pulled out of the oven via vacuum pump.

E. Further heating and fine vacuum

During evacuation of the water in the paper, the transformer is cooling, because of the loss of evaporation heat, so the water vapour pressure of the remaining water drops until no more diffusion takes place. Too dry further, a second or third cycle of heating up and fine vacuum is needed, so the oven is filled with dry air and the heat is turned on again.

F. Unloading

Usually the drying process is stopped when the estimated water content is safely low enough. The dried transformer stayed into the oven until its temperature is low enough due to the water attraction of a warm and dry paper insulation. After unloading, the transformer is closed and refilled with oil under vacuum. Finally the water content of the finished transformer is measured.

III. MOISTURE ANALYSIS

Moisture content is calculated by fitting a model to the real dielectric response. Using the so called XY-model [2], a dielectric response is calculated under consideration of the insulation geometry, temperature, oil (if present) and moisture content. A fitting algorithm aligns the dielectric response of the data base to that of the real transformer and automatically delivers the water content of the cellulose material as well as the moisture saturation, Fig. 3.

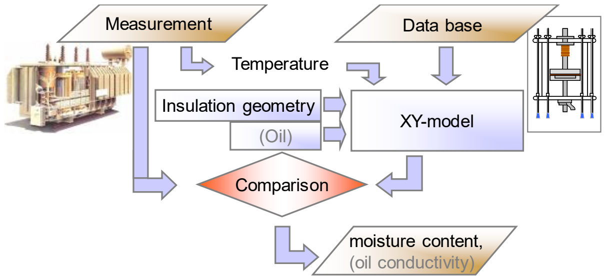

Fig. 3. Calculation of the moisture content as based on comparison of the insulations dielectric response to a modelled dielectric response

Being part of the data base for the modelled dielectric response, Fig. 4 depicts exemplarily the dissipation factor over the very wide frequency range of 10 kHz to 10 µHz for non-impregnated pressboard of HD quality. The graph for 0 % water content has been extrapolated from measurements at 0.3 % water content. With increasing water content, the losses in the material increase as well.

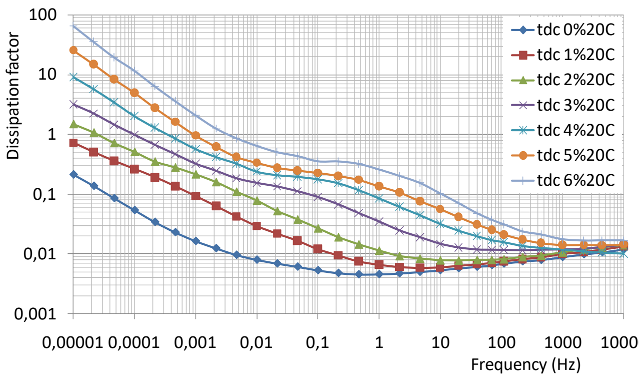

Fig. 4. Dissipation factor over frequency for non-impregnated pressboard samples at 0; 1; 2; 3; 4; 5 and 6 % water content at 20°C

IV. CASE STUDY AT MIEBACH ELEKTROTECHNIK GMBH

Miebach Elektrotechnik GmbH is a company, which repairs power transformers and large coils. After opening one power transformer, its paper insulation gets wet by the water of the surrounding air, so it needs to get dried after maintenance. For this purpose, Miebach uses an hot-air-vacuum-oven. Due to the many different sizes and water contents the time and the number of heating and vacuum cycles different for each transformer. To avoid a risk of too much water left in the insulation, the transformer usually was dried way longer than needed. This increased the amount of energy and time used to dry. The solution for this problem was to implement an automation, which controls the oven and stops the drying process when the water content, given by the dielectric response analyser, is low enough. In the following, the automation and the results of the monitoring is presented.

A. *Automation*

The oven is controlled by a programmable logic controller (PLC). The plc sets all units for heating and vacuum as shown in figure 1. It gets the information of temperature and pressure within the oven and lead them to a PC. The dielectric response analyser measures the tan δ of the transformer insulation via heat and vacuum resisted bushing. It sends the information of the tan δ to the pc. With temperature and tan δ a program on the pc can calculate the water content within the paper and gives the information back to the plc. If the water content is below a certain amount, the plc will stop the drying process.

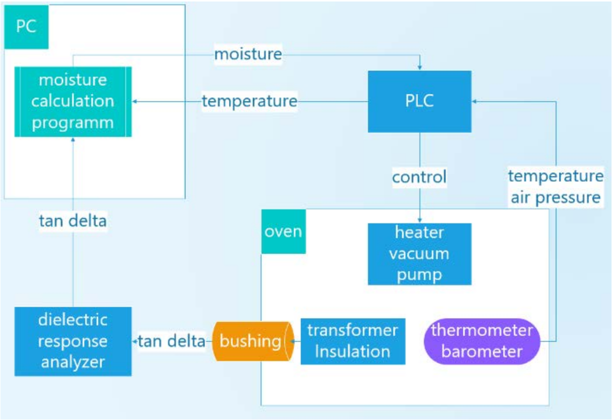

Fig. 5. concept for automation of the oven

B. *PLC- programming*

To execute the course of drying given in chapter II the PLC is programmed as follows. In Fig a simple flowchart is given. Every phase begins and by appropriate handover conditions (HC 0 to HC 98). Each phase is assigned a combination of control states. Next a simplified description of the main phase is presented:

- Heating up: After initiating the plant is set to heating up. There for the heater is set to on and all valves are open.
- HC 1: pressure reduction = true
  temperature > 45 °C
- HC 41: pressure reduction = false
- Pressure reduction: in this phase the heater stays switched on but all valves are closed and the vacuum pump is started to reduce the pressure down to 30 mbar. By reaching 30 mbar, the pump is switched off and the valves were set open.
- HC 21: temperature > 64 °C
- Vacuum: all valves are closed and the vacuum pump is switched on.
- HC 5: Pressure < 25 mbar
- Fine vacuum: additionally the roots pump is switched on to reduce the pressure further down to 0,01 mbar.
- HC 67: Moisture > target moisture
  number cycles < max number cycles
  number cycles = number cycles +1
- HC 98: Moisture < target moisture
  number cycles = max number cycles
- Unload: all valves stay closed. The vacuum and roots pumps were switched off. The transformer stays in the oven until it cools down enough and the operator opens the oven to unload.

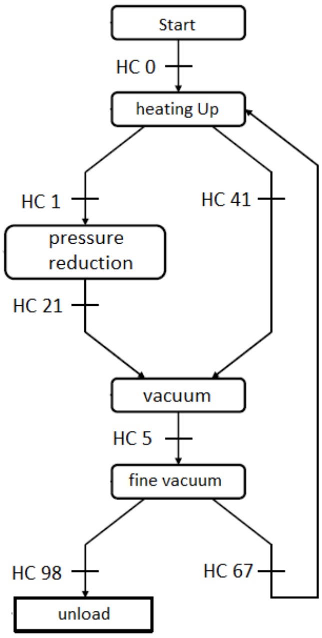

Fig. 6. simplified Petri net for drying program

C. *Case 25 MVA Transformer*

The first transformer drying controlled by the plc and monitored by the dielectric response analyser, was a 25 MVA transformer.

Fig. 7. Dried 25 MVA transformer

The drying took 7 days and consist of one pressure reduction during heating up and two times fine vacuum.. To measure the water content within the paper during the drying process, the dielectric response analyser Dirana from Omicron was used.

Fig. 8. Dielectric response analyser Dirana from Omicron

One measurement required 30 minutes and was repeated after 6 hours. All tan delta measurements during transformer drying are shown in Fig. 9. After the target moisture of 1.5% was reached, the plc stops the drying process and the transformer was left in the vacuum for about 3 days losing another 0.3 % moisture. With the information about temperature pressure and moisture gained, the process can now be followed more closely.

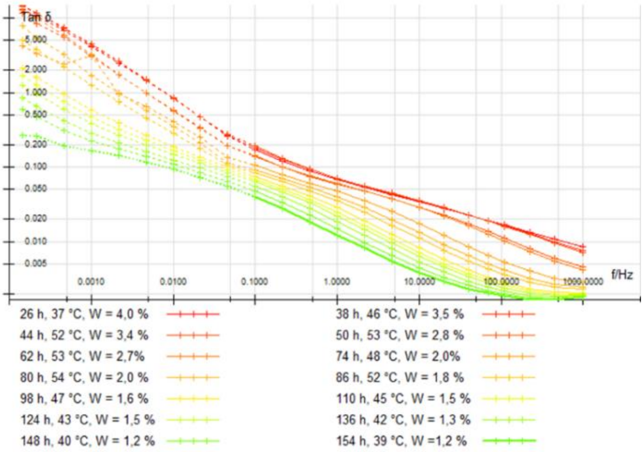

Fig. 9. All tan delta measurements during 25 MVA transformer drying

D. *Interpretation*

Using all tan delta measurements the course of drying as shown in Fig. 10 can be generate and could be used to interpret the drying process.

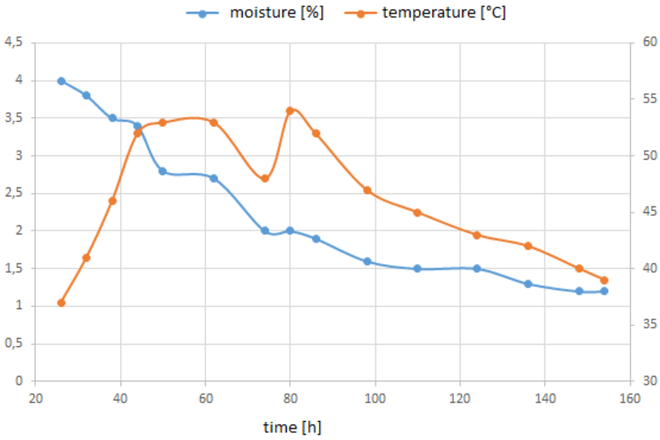

Fig. 10. Course of drying

During the first heat up, the temperature rise until 54°C the water vapour pressure in the paper rise. The water evacuates out of the paper into the air until the water vapour pressure and the air equal after approximately 44 hours. The Water content drops from 4 % to 3.4 %.

To continue the drying process, the wet air must be exchanged by a pressure reduction. After 44 hours by a pressure reduction the water content fell from 3.4 % until 2.6 %. After 68 hours the first fine vacuum was executed. Because of the water vapour pressure different of approximately 15 $mbar$ between paper and surround air, water was pressed out of the paper, so the water content drops from 2.6 % to 2.0 %.

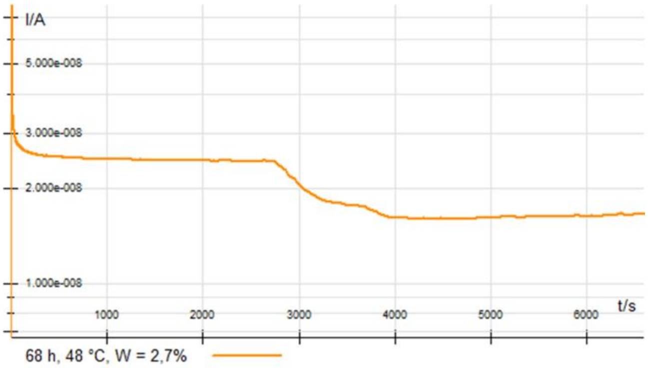

Fig. 11. Disrupted PDC- measuring

During the fine vacuum the PDC measuring was disrupted. The polarisation current drops after 3000 s from 0.25 nA to 0.16 nA as shown in Fig. 11. The drop in current can be explained by cooling of the transformer during evaporate of the water. The dc conductivity drops also because of the lower amount of water. This could lead to errors during the Fourier transformation, when the polarisation current is transformed from time to frequency domain. After the change of the water content is saturated, dry air was let into the oven to heat up the plant again. The second cycle of heating up and fine vacuum lead to a measured water content of 1.2 %, so the oven could stay in fine vacuum until the insulation gets cold enough to unload.

E. Energy Savings

The operator of the plant indicates that before the new automation system, it took two weeks and approximately 200 litres of oil to dry one 25 MVA transformer. Now, with the new monitoring and automaton system, the oven needs only one week and 100 litres of oil. If one litre mineral oil has about 11 kWh, the energy-saving is about 110 kWh or 50 %. Thus, with every drying process, 317 kg of carbon dioxide are not emitted.

V. SUMMARY

The challenging requirements for the low water content in oil-paper-insulation can only be achieved by adequate drying. To estimate the correct amount of time and heat for drying proved to be a challenge. With dielectric response measurement it was possible to measure the moisture in paper insulation during the drying process.

A programmable logic controller was used to control the oven. It gets information about temperature and pressure and transfers it to a personal computer. The dielectric dissipation factor tangent delta of the paper insulation was measured through a water and heat resisting bushing by the dielectric response analyser Dirana and provided to the PC. A moisture calculation program on the PC used temperature and tan delta to calculate the information about moisture content to a PLC, which terminated the drying process if the target moisture was reached.

The dielectric response analyser monitored the drying process. Primarily the gained information could be used to shorten the amount of energy and time used to dry paper insulation adequately. Secondly by collecting all information about certain transformers and there drying features, the understanding of the drying process could be improved.

REFERENCES

[1] Sokolov et al., “Moisture Equilibrium and Moisture Migration within Transformer Insulation Systems” Cigré Working Group A2.30, *Technical Brochure 359*, Paris 2008

[2] S. M. Gubanski, et al., “Dielectric Response Diagnoses for Transformer Windings” *CIGRÉ Task Force D1.1.14, Technical Brochure 414,* Paris, 2010

[3] M. Koch, S. Raetzke, S. Tenbohlen, „Monitoring the Oven Drying Process of Power Transformers by Dielectric Response Analysis”, Conference Proceedings of Condition Monitoring and Diagnosis 2010, Tokyo 2010

[4] Helmut Strzala, “Vapour Phase Vacuum Drying” Heidrich in House Seminar, 2000

Development of an Automated Tool to Generate Test Cases for Preventive and Curative HVDC Methods

Christoph Rohr, Florian Sass, Student Member, IEEE, Tom Sennewald, Student Member, IEEE, Dirk Westermann, Senior Member, IEEE
Power System Group
Technische Universität Ilmenau
Ilmenau, Germany
E-mail: christoph.rohr@tu-ilmenau.de

Abstract— **The expansion of renewable energies and the growing decentralized infeed into the AC grid are causing an increased utilization of the transmission grid and require the transport of electrical energy over long distances. The expansion of the grid is an important issue to further ensure secure grid operation. The high voltage direct current (HVDC) solution based on voltage-sourced converter (VSC) technology is suitable to support the AC network to guarantee system stability. Equipment outages within the AC grid can cause line overloads that can be compensated by an overlay HVDC system. To demonstrate this, test cases for a given grid must be generated which contain critical outage scenarios. The developed algorithm is able to automatically generate cases to demonstrate the supporting function of an HVDC overlay system. The procedure is based on sensitivity factors, which are required for the developed variable selection methodology. The algorithm can thus generate scenarios with the desired properties, taking resource limits into account.**

Keywords—AC-HVDC-systems, Operational security, n-1 security, test cases

I. INTRODUCTION

The energy transition pushed by politics and the innovations demanded by the Renewable Energy Sources Act (EEG) pose major challenges for the energy sector in Germany. The resolution [1] resulted in an increasing shift from fossil fuels such as coal, oil, natural gas and nuclear energy to environmentally friendly renewable energies such as wind power and photovoltaics. Due to the uncertainties in energy production resulting from the nature of weather-related renewable energy sources and the spatial distance between energy production and energy consumers, the existing grid structure must be both expanded and used more efficiently [2]. In order to ensure the security of supply and avoid transmission bottlenecks, transmission system operators rely on redispatch measures. In recent years, an increasing frequency of such interventions in the active power operating points has been observed. Network operators in Germany such as TenneT, for example, reported costs of over one billion euro for redispatch measures in 2017 [3]. In order to keep the redispatch measures and network expansion requirements to a minimum, network expansion in Germany is based on the so-called NOVA principle (network optimization before expansion [4]).

One of the most promising technologies for grid expansion is high-voltage direct current transmission (HVDC) based on the Voltage Source Converter technology (VSC). DC transmission causes lower losses than equivalent AC transmission over the same distance and thus offers a practicable solution especially for large transmission distances [5], [6]. The technology allows the construction of multi-terminal HVDC systems or even meshed HVDC grids. These can contribute to the necessary grid expansion and enable the connection of large offshore wind farms [7]. Such an HVDC grid can be operated in parallel to the existing AC system. Self-guided converters (VSC) can connect the two grids at different nodes. Such a superimposed DC grid can not only improve the quality of the current energy transmission, but also improve the overall system security. Parallel operation of both networks only makes sense if network security is also considered in combination. There are already existing studies for this, e.g. [8], [9].

In the course of this approach to relieve the AC grid, a benchmark system was developed [9] as a testbed for algorithms to improve the overall system security such as SCOPF methods.. The benchmark system composes two kinds of information: the grid topology and the load and generation scenario.

The subject of this paper is the development of an automatic algorithm that can create different cases for a network with a given topology to prove the aforementioned improvement of the overall system safety. The generation of these cases should be automatic and applicable to any system. The test cases from [9], [10] are used as a basis for the scenarios to be generated. Congestions are implemented to create cases that can validate the operational planning methods of the system as well as possible. A distinction is made between congestions caused by generator, line or VSC outages.

The approaches chosen to develop the scenarios are presented in section II. Building on this, section III deals with the development of the method used for this purpose. Subsequently, the numerical results and conclusions are presented in sections IV and V.

II. BASICS

A. Sensitivity factors

The Power Transfer Distribution Factor (PTDF) shows how the power flow on a branch l changes when the power is supplied to a node i and taken from a reference node (II.1) [11]. The PTDF is determined using a transaction as described above. The exchange does not take place directly between two nodes, as from an economic point of view, but the actual power flow is distributed throughout the entire network according to the physical topology of the network. This is expressed by equation (II.2).

$$PTDF_l^i = \frac{\Delta P_i}{\Delta P_l} \tag{II.1}$$

$$\Delta p_{ij} = \begin{bmatrix} b_{ij,1} z_{ij,1} \\ \vdots \\ b_{ij,n_z} Z_{ij,n_z} \end{bmatrix} \Delta\delta = \underbrace{\begin{bmatrix} b_{ij,1} z_{ij,1} \\ \vdots \\ b_{ij,n_z} Z_{ij,n_z} \end{bmatrix} B^{-1}}_{PTDF} \Delta p = PTDF \Delta p \tag{II.2}$$

A part of the power from the infeed point does not flow directly to the reference point, but also takes the path via other nodes and thus via the corresponding lines. The PTDF now expresses how the power flow is distributed in the network. This is repeated until the PTDFs of all lines are determined in relation to a transaction. The PTDFs together describe how a current transaction between two nodes affects all network branches.

If the calculation is performed for all lines and transactions, the result is a PTDF matrix that shows the distribution of the energy fed into the individual lines. It is important that a start and end node are defined for each line.

Like the PTDF, the Load Outage Distribution Factor (LODF) is a sensitivity factor and indicates changes of the power flow on a line *k* in the event of an outage of a line *l* [11], [12]. As previously mentioned, this means that in the event of a line outage, the power flow is distributed according to the new conditions in the network. If power previously flowed through a line, which is now considered as an outage, the power flow in the other lines increases accordingly.

III. AUTOMATED GENERATION OF CONTINGENCY SCENARIOS

As described in the introduction, the goal of this paper is to create an algorithm that automatically generates contingency scenarios for any power system with defined topology. The cases enable, through their different contingency types, the testing of different HVDC operation methods by incorporating critical contingencies (criCo) into the system. Regarding the N-1 criterion, critical contingencies are outages that result in the violation of any defined security criterion. The following violations are considered overloads:

- Violation of the AC voltage range from 1.1pu - 0.95pu
- Utilization of a single line over 100%

In order to identify criCos, power flow calculations must be performed in the course of a contingency analysis

If there are critical contingencies in a network, it should be checked whether these can be solved with curative measures. A distinction is made between curative HVDC OPF and curative generator OPF. This distinction is made between the two curative measures, since generator OPF (redispatch measures) cause economic costs, whereas HVDC OPF (adjustments of the VSC operating points) cause no costs except the investment costs. An OPF algorithm is used for these calculations. As basis for the new test cases, the initial scenarios described in [9], [10] are used.

A. Definition of Critical Contingencies Types

To ensure that the generated cases cover as many different types of critical contingencies as possible, critical contingencies are defined in advance, as shown in Tab. 1.

A classification is made between different cases of outages and effects. The outages are divided into generator outages (gen_out), line outages (line_out/intcon_out) and VSC outages (VSC_out), whereas the effects generated by the outages include voltage band violations (volt_vio) and line overloads (line_vio/intcon_vio). Furthermore, the lines of the system are divided into lines and interconnectors (intcon) connecting two control zones.

The table serves as a defined framework in which the functionality of the algorithm can be checked. The algorithm to be designed is universally applicable to every system. Therefore, several control zones (CZ) were assumed in the table. Voltage range violations (volt_vio) are considered and generated in the work, but are not checked for their feasibility, since reactive power optimization lies outside the scope of the paper.

Tab. 1: List of critical contingencies being implemented

Outage		**Effect**	
Location	**Type**	**Location**	**Type**
CZ a	gen_out	CZ b / CZ c	line_vio
CZ a	gen_out	CZ a	line_vio
CZ a	gen_out	CZ a	volt_vio
CZ a	gen_out	CZ a – CZ b	intcon_vio
CZ a	gen_out	CZ a – CZ c	intcon_vio
CZ a	line_out	CZ b / CZ c	line_vio
CZ a	line_out	CZ a	line_vio
CZ a	line_out	CZ a – CZ b	intcon_vio
CZ a	line_out	CZ a – CZ c	intcon_vio
CZ a- CZ b	intcon_out	CZ a – CZ c	intcon_vio
CZ a- CZ c	intcon_out	CZ a – CZ b	intcon_vio
CZ a	line_out	CZ a	volt_vio
CZ a	VSC_out	CZ b / CZ c	line_vio
CZ a	VSC_out	CZ a	line_vio
CZ a	VSC_out	CZ a	volt_vio
CZ a	VSC_out	CZ a – CZ b	intcon_vio
CZ a	VSC_out	CZ a – CZ c	intcon_vio

B. Selecting the control parameters

To design cases with the defined properties from the previous section, a control parameter must be selected. On the one hand, the active power components of the loads would be a conceivable degree of freedom, on the other hand, the active power operating points of the VSC converters and the generators would also be possible as degree of freedom. The control parameter P_{gen} was selected, since the loads in the system are assumed to be constant. Another reason for selecting the active power of generators as the degree of freedom of the algorithm is that the adjustment of the active power reflects redispatch measures. The approach of sensitivity factors could also be further pursued, since the degree of freedom P_{gen} is directly related to the transactional consideration of PTDF and LODF. As described at the beginning of this paper, the expansion of renewable energies leads to a decentralized infeed in the AC-system. As a result, the generator nodes are distributed more evenly in the topology of the grid and can thus influence large parts of the electrical grid with their active power operating points. P_{gen} thus forms the general control parameter which must be distinguished from the control variable, which is the generator whose effective power operating point is going to be adapted.

C. Algorithm design

In order for the algorithm to edit the cases automatically and independently, it must find the control variables with whose changes it can generate the desired congestion. The algorithm should be able to independently find generation operating points that lead to critical contingencies during a contingency analysis. The selection of these control variables represents the greatest challenge of this approach. To find the correct control variables, the dependencies of the components are examined. This is done by means of sensitivity factors.

With regard to this approach, the algorithm described later on using the flow chart in Fig. 1 is developed. The program is divided into five modules. The five modules contain the following points and are described in more detail in the next sections.

- Initialization: Import of system data and grid properties

- Contingency analysis: determination of outages that result in a violation of security constraints (critical contingencies)

- Selection of control variables: Selection of the control variables on the basis of the load factor, load change and sensitivity factors of the corresponding network element.

- Adaptation of control variables: Adjustment of the selected control variables by an iterative process

- Solvability check: Checking the solvability of critical contingencies by a CSCOPF

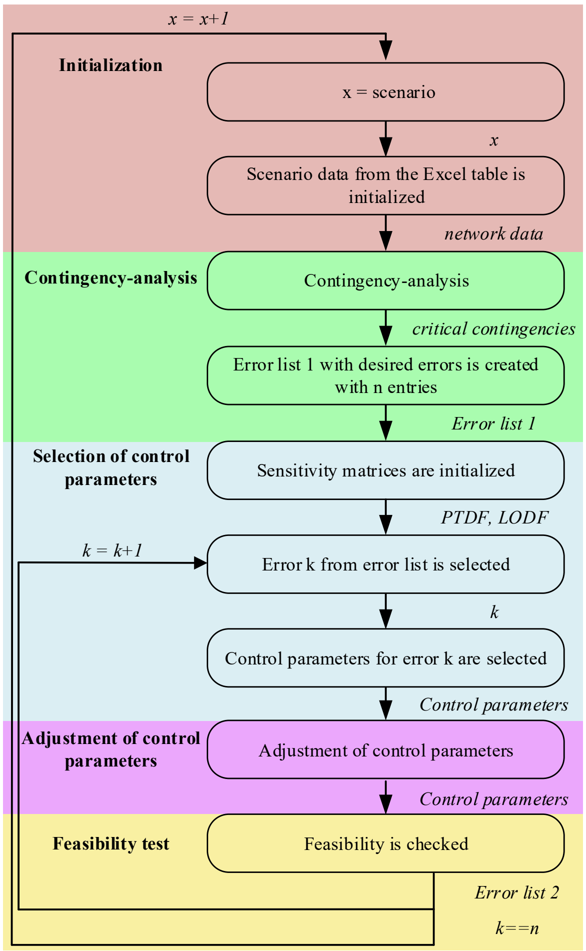

Fig. 1: Structogram of the developed algorithm

The algorithm starts by initializing the network data. Consecutive a contingency analysis is then performed to determine the existing critical contingencies ($criCo_{ist}$). The results of the power flow calculations are checked for violations of the defined limits, such as voltage range and line loading. If a limit violation occurs, the contingency is marked as critical. The advantage of the reduced consideration of only critical contingencies instead of all possible occurring contingencies is that the computing power can be drastically reduced in the following modules.

The critical contingencies are passed on to the next module, which categorizes the critical contingencies and classifies them. In this way it can be determined which critical contingencies are already contained in the initial scenario and no longer need to be generated. The module uses the critical contingencies that have already occurred to create a list that contains information about which critical contingencies still need to be generated (error list 1).

After the list of critical contingencies still to be generated ($criCo_{soll}$) has been created, the PTDF and LODF sensitivity matrices are initialized. They contain the PTDF and LODF of all lines for all transaction options. Once the sensitivity matrices have been created, the first case is selected from error list 1 and the function for determining the control variable being adjusted is started.

To select a control variable, information on the location, type and trigger of the violation is first retrieved from the list of $criCo_{soll}$. A distinction is made between whether the cause of the violation is a line, generator or VSC outage. Furthermore, a distinction is made between the two types of violations to be generated: voltage range violation and line overload. In the further course of the control variable selection, the lines or network elements interesting for the contingency generation are examined for three selected criteria:

1. largest change of the value being considered, voltage or power, in comparison to the base case scenario.
2. minimum difference between the value taken into account and the limit to be exceeded.
3. maximum absolute value of the sensitivity factors.

The first characteristic can be used to determine which network element will be reacting the most to changes. The second characteristic serves to find the grid element which is closest to its limits. In the third and last selection criterion, the network element which can be influenced by changes the most is found.

The three attributes are determined for each network element being investigated and stored in a three-dimensional matrix. In order to select the network element that is to be overloaded, the stored matrix is sorted according to the three properties and thus three different sequences are defined. The scores of the network elements in the generated sequences are summed up. This results in a numerical evaluation of the network elements, in which the network element with the lowest evaluation value is selected, since it comes closest to fulfilling the three criteria. The criteria are all weighted with the same priority.

Once the network element of interest has been selected , the sensitivity factors define the control parameters that has the biggest impact on the respective equipment. The control parameters are stored in priority order in a control parameter matrix.

Once the control variables have been selected, they are transferred to the next function in order to adapt them. A start value for the change being made is calculated. Starting with the calculated start value, the selected control variable is changed. The network data with the changed control variable are examined with a contingency analysis. The resulting critical contingencies are compared with the critical contingency to be implemented. If the desired critical contingency has not yet been reached, but the control variable is still within its operating limits, the initial value calculated before is increased iteratively until the desired critical contingency occurs. If the critical contingency occurs without any limit violation, the new values of the grid data are stored in a table.

An list with the existing contingencies is generated from the new grid data. The new contingency list (error list 2) is compared with the old contingency list (error list 1). The algorithm checks whether no previously existing contingencies have been lost due to the creation of the newly introduced critical contingencies. If all entries in error list 2 are correct, it is checked whether the built-in contingencies can be solved. For this, a CSCOPF with different optimization variants is carried out. The CSCOPF algorithm introduced in [13] is used for these optimizations. With regard to the developments, a distinction is made between two optimization variants. In the first variant, the effective generator power P_{gen} is chosen as degree of freedom, because it represents the currently common redispatch measures. In the second optimization, the CSCOPF is performed with the active power of the VSCs (P_{VSC}) and the DC-sided voltage (U_{DC}) as optimization parameters in order to show the solvability of the critical contingency cases with the future method of adjusting the VSC operation points. This has the advantage that, in contrast to redispatch measures, it is cost neutral.

The CSCOPF algorithm only makes a statement as to whether a critical contingency can be solved or not. Since the CSCOPF does not perform reactive power optimization, critical contingencies with a voltage band violation are not investigated.

The now modified Excel table functions as a further starting point for the implementation of the next critical contingency from error list 1 and the algorithm starts over at the selection of the control variable.

IV. NUMERICAL CASE STUDY

This section reviews the derived methodology. The algorithm developed is checked for functionality by means of a numerical simulation with the reference network presented before. The functionality of the developed algorithm is determined by the implemented critical contingencies, which were predefined before (Tab. 1).

The 67-node network presented in [9] serves as the AC-DC hybrid network at which the investigations take place. It consists of an AC network, which is superimposed by an HVDC network and connected to it at eight nodes via VSCs. The AC network consists of 67 nodes connected by 102 lines. Furthermore, the AC network is divided into three control zones (CZ), which are connected to each other via AC interconnectors. The maximum load of the system amounts to 11817 MW, which is divided between the control zones. The superimposed HVDC network consists of nine nodes and has two designs. The first design, the network is meshed, in the second the network is set up with point-to-point connections and one multi-terminal connection. The connection points between the AC and DC grids are the eight onshore VSCs, three in each CZ and one VSC for connecting the offshore wind farm. There is no (n-1) security in the reference grid. This applies to both superimposed grids, AC and DC. The critical outages that lead to overloads of network elements include the failures of AC and DC lines as well as converters and generators. For AC and DC lines, a load of more than 100 % is considered critical. The prerequisites for the generated scenarios are that all bottlenecks present in the grid can be eliminated by corrective measures. This means that there must be no structural bottlenecks.

The table Tab. 1 forms the basis for the evaluation of the results of the algorithm. The aim is to implement each critical contingency from Tab. 1 automatically using the methodology described and then to check its solvability using a CSCOPF with various optimization parameters (P_{Gen}, U_{DC}, P_{VSC}). The following table (Tab. 2) exemplary shows the results of the implementation through the algorithm, on the basis of line outages.

The individual outages are listed vertically. The lines are described by start and end nodes, as defined in [9]. The effects are listed horizontally. The classification takes place equivalent to the first column. The coloured cells make a statement about the solvability of the critical contingency. Again a distinction is made between the two optimization variants with the different optimization parameters. The first optimization variant is executed with P_{Gen} as the optimization parameter, whereas the second optimization variant is executed with the optimization parameters P_{VSC} and U_{DC}. If the critical contingency could be successfully solved by the CSCOPF, it is marked with a color. Green stands for solvability through optimization with P_{Gen}. If the cell is colored blue, the contingency can be solved by adjusting the VSC operating points (P_{VSC} and U_{DC}) and if the cell is yellow, the failure can be solved both ways.

The result table (Tab. 2) shows the critical contingencies that arise when a line outage in a control area triggers a line overload in the same control area. Tab. 4.1 shows that the critical contingencies could be implemented with the desired properties. As described in the legend, the solvability of the critical contingency is represented by the coloring. It is noticeable that there is not only one critical contingency with the desired properties, but that there can occur also several others. This is due to the fact that by adjusting the control variable to violate a security, the corresponding network element must be brought close to its overload limit in order to be susceptible to outages. Since the network element is then susceptible to outages, this can cause it to overload not only at the individual desired outage, but also at other outages.

Tab. 2: Solvability of line outages with line overloads in the same CZ

Outage \ **Effect**	**4-19**	**10-22**	**26-40**	**39-43**	**41-42**	**43-44**	**56-58**
4-14		🟨					
10-22	🟨						
19-23		🟨					
32-40			n.a.				
40-41				🟩	🟩	🟩	
43-44				🟨			
62-66							🟨

🟦 P_{VSC} 🟩 P_{Gen} 🟨 P_{VSC} / P_{Gen}

This effect can be seen, for example, in the case of AC line 10-22, which overloads in several outage-cases.

Furthermore, it can be seen in one case that no statement (n.a.) can be made for its solvability. This is due to the fact that in the event of this outage, a voltage band violation also occurs in addition to the line overload. As the CSCOPF does not have reactive power optimization, the solvability of these cases is not considered in this paper.

The developed algorithm was able to implement the critical contingencies caused by line outages with the previously defined attributes in Tab. 1. Thus, the functionality of the control variable selection and the control variable adaptation could be confirmed. The algorithm was able to select the correct control variables using the selection criteria and it was able to adapt them successfully. All critical contingencies, which did not contain voltage band violations, could be solved. This was to be expected, since the control variable adaptation works with the operating points of the generators and thus normally does not generate any structural, unsolvable critical contingencies.

V. CONCLUSION

Due to the increasing decentralized infeed and the change from fossil to renewable energies, there will be a greater utilization of the electrical energy network. In addition to grid expansion, the focus is on more efficient usage of the grid. One promising concept is the use of AC-HVDC hybrid networks. It can also be used to relieve the increasing redispatch measures. A combined consideration of HVDC and AC system also requires an extended consideration of the (n-1) criterion. Suitable test scenarios are required in order to test the operational management methods of such electrical networks. The goal of this paper is the development of an algorithm, which is able to independently create cases for a given grid-topology. Therefore several approaches were considered, which allow a targeted creation of such scenarios. The methodology developed in the work is based on the approach of sensitivity factors and serves to select suitable control variables for the scenario generation. Once a suitable selection has been made, the scenario is adapted and tested for its solvability using curative measures. Exceptions to this are voltage band violations, as these require reactive power optimization. Due to the complexity of the topic, this was not done within the scope of this work. The special feature of the algorithm is that it is generally applicable for every system. With the generated cases, operational management methods of AC-HVDC hybrid networks can be tested, for example to reduce redispatch costs or avoid bottlenecks. To demonstrate the advantages of the AC-HVDC network, critical contingencies have been implemented by the algorithm. The grid, on which the developed algorithm was tested, is considered with two different designs of the superimposed HVDC grid. In the first variant, the AC reference network is superimposed with a meshed HVDC network. The second variant considers the superposition of the AC reference network with three point-to-point and one multi-terminal HVDC connections. The numerical results proved the functionality of the algorithm and gave a summarizing overview of the generated scenarios.

Further consideration of combined AC-HVDC networks and HVDC operational management methods is a promising area of development. With regard to the algorithm described here, further investigations could be undertaken with regard to an improved and more stable selection of the control parameters in the area of contingency screening and contingency filtering. So-called severity indices can contribute to a further optimization of the algorithm. As mentioned before in the summary, the solvability of voltage band violations was not considered. At this point, the methodology could be further expanded. A reactive power optimization with combined consideration would complete the curative SCOPF. In addition to a curative SCOPF, a preventive SCOPF of critical contingencies is another conceivable approach that can be pursued in the future.

REFERENCES

[1] Gesetz für den Ausbau erneuerbarer Energien (Erneuerbare-Energien- Gesetz - EEG 2017): EEG, 2014.

[2] D. van Hertem, M. Ghandhari and M. Delimar, “Technical limitations towards a SuperGrid — A European prospective,” in IEEE International Energy Conference and Exhibition (EnergyCon), 2010: 18 - 22 Dec. 2010, Manama, Bahrain, Piscataway, NJ: IEEE, 2010.

[3] DPA and Tennet, Stromnetzbetreiber Tennet meldet Rekordkosten für Noteingriffe. Available: https://p.dw.com/p/2qBIn (2018, Nov. 20).

[4] 50Hertz Transmission GmbH, Amprion GmbH, TenneT TSO GmbH, TransnetBW GmbH, Netzentwicklungsplan. Available: https://www.netzentwicklungsplan.de/sites/default/files/paragraphs-files/kapitel_5_netzanalysen_nep_2012_0.pdf.

[5] Carl Barker, Gunnar Asplund, Kerstin Lindén and Andree Marzin, et al, “HVDC Grid Feasibility Study,” 2013.

[6] “Combined AC/DC Transmisson Systems – Benefits and prospects of innovative multilevel VSC Technologies,” no. 115-2014_0166, 2014.

[7] L. Xu, B. W. Williams and L. Yao, “Multi-terminal DC transmission systems for connecting large offshore wind farms,” in 2008 IEEE Power & Energy Society general meeting: Pittsburgh, PA, 20 - 24 July 2008, Piscataway, NJ: IEEE, 2008.

[8] F. Linke, F. Sass and D. Westermann, “Preventive Parameterization of DC Voltage Control for N-1 Security of AC-HVDC-systems,” in 20th Power Systems Computation Conference: PSCC2018 Dublin : June 11-15, 2018, University College Dublin, Dublin, Ireland, Piscataway, NJ: IEEE, 2018.

[9] F. Sass, T. Sennewald, A.-K. Marten and D. Westermann, “Mixed AC high-voltage direct current benchmark test system for security constrained optimal power flow calculation,” IET Generation, Transmission & Distribution, vol. 11, no. 2, pp. 447–455, 2017.

[10] B. Sc. Johannes Kayser, “Entwicklung von Erzeugungs-Szenarien für das 67 Knoten AC-HVDC Test System,” Technisch-wissenschaftliches Spezialseminar, Elektrische Energieversorgung, Technische Universität Ilmenau, Ilmenau, 2017.

[11] R. Vykuka and L. Nohacova, “Sensitivity factors for contingency analysis,” in 2015 16th International Scientific Conference on Electric Power Engineering (EPE): 20 - 22 May 2015, Hotel Dlouhé Stráně, Kouty nad Desnou, Czech Republic, Piscataway, NJ: IEEE, 2015.

[12] C. S. Song, C. H. Park, M. Yoon and G. Jang, “Implementation of PTDFs and LODFs for Power System Security,” Journal of International Council on Electrical Engineering, vol. 1, no. 1, pp. 49–53, 2014.

[13] M. Sc. Tom Sennewald, “Ein Preventive Security Constrained Optimal Power Flow (PSCOPF) Verfahren für ein AC-HGÜ-Verbundnetz,” Masterarbeit, Fachgebiet Elektrische Energieversorgung, Technische Universität Ilmenau, Ilmenau, 2016.

An analysis of the price behavior of the Intraday Continuous Market

Julian Berger, Tankut Yalcinoz and Krzysztof Rudion
Institute of Power Transmission and High Voltage Technology (IEH)
University of Stuttgart
Stuttgart, Germany
st153617@stud.uni-stuttgart.de, tyalcinoz@ieee.org and rudion@ieh.uni-stuttgart.de

Abstract— **The ongoing efforts to increase and integrate the share of renewable energies across Europe pose a challenge to both the grid and the trading system. In Germany, the "Intraday Continuous Market" is used to adjust short-term deviations between electricity demand and consumption in order to avoid the more expensive use of "Balancing Power". This study analyses the price behavior for the 15-minutes contracts in the "Intraday Continuous Market" in terms of their cyclical behaviors (hourly, daily, seasonally) and the appearance of extreme prices. Besides, the influence of exogenous parameters (solar-, onshore wind infeed and load) is analyzed. In this study, the dataset of prices of 15-Minutes contracts from the "Intraday Continuous Market" of the EPEX SPOT over the period from 1 January 2015 to 31 August 2018 is used for analyzing the common bidding zone of Germany, Austria and Luxembourg. The naturally occurring solar ramps during peak hours as well as the contract duration in the various markets explain the typical "Zig Zag Pattern" of the "Intraday Continuous Price" for 15 minutes contracts. In general, the price level is dependent on the daily load profile and thus also on the seasons. Regarding the number of occurrences of extreme prices, it can be stated that both the load profile and the infeed from onshore wind energy have significant influence.**

Keywords—intraday continuous market, EPEX SPOT Market, onshore wind, outliers

I. INTRODUCTION

In the early 1990s, the process of liberalization of the power sector in Europe began. The monopolistic and state-controlled system was reshaped to increase flexibility and efficiency. The main objective of the liberalization process was to increase competition among market participants in the generation and distribution of electricity. The idea of deregulating markets has been applied in many sectors in recent years. However, some basic characteristics distinguish them from the energy sector.

Most importantly, the produced electricity cannot be stored economically, and production and consumption must always be balanced [1]. With the introduction of the "Erneuerbare Energien Gesetz" (EEG) in Germany, two very effective incentives for the promotion of energy from renewable energy sources (RES) were created. On the one hand, the EEG guarantees a fixed feed-in tariff and the right to feed their electrical powers primarily into the grid, and on the other hand, unlike conventional power plants, production depends on the weather conditions [2]. Therefore, it makes sense to divide the power production into "Variable Renewable Energy Sources" (VRE) and "Controllable Electricity Production" (CEP) [3].

With a higher share of VRE, it is becoming increasingly important to improve the accuracy of forecasts of VRE in order to predict the amount of power which must be generated by CEP to meet the demand. As the trading system was introduced the share of VRE in total electricity generation was small compared to the CEP. Therefore, it was enough to predict demand and adjust production. To fit the requirements of an increasing share of infeed from VRE, both the duration between placing a bid and the physical delivery and the duration of the traded products have been shortened in order to be able to react on deviations in the short term. Therefore, market participants can take advantage of precise short-term forecasts of the infeed from VRE and the expected load to either trade with a lower risk of forecast errors or correct trading errors made at an earlier point in time (e.g., at the "Day Ahead Market") [4].

In this study, an analysis of the price behavior of the "Intraday Continuous Prices" is carried out. The data are identified first and then analyzed with a closer look at the cyclical behavior (daily, weekly and yearly), distribution of outliers and time-varying volatility changes. After that, the impact of exogenous factors (infeed from onshore wind, solar and the load) on the price and especially on the occurrence of extreme prices is explained

II. ANALYSE OF DATA

The growing infeed from VRE increased the need to make the trading system more flexible. For this reason, the "15-Minutes Intraday Call Auction" was introduced at the EPEX Spot in 2011. There are 96 15-minute Intraday Call Auctions each day. This process is like the "Day Ahead Auction" and allows to finer balance between supply and demand, especially to adapt the demand to the supply during peak hours with the occurring solar ramps. After the closing of the "Intraday 15-Minutes Auction Market" further deviations can be adjusted at the "Intraday Continuous Market." The underlying principle of the "Intraday Continuous Market" differs from the pricing at the "Day Ahead Market". Traders at the "Intraday Continuous Market" can put their offer, including whether they want to buy or sell a certain amount of energy for a certain price at any time. As soon as a buy offer matches a sell offer the trading is concluded. The supplier would be paid exactly the price he bid for the quantity transacted. In most cases, this price corresponds more closely to his marginal costs. In contrast at the “Day Ahead Market” supplier would have been paid “Day Ahead Price” regardless of his actual bid as long as it was at or below [4].

In this paper, the used data consist of quarter-hourly prices of the 15-minutes contracts of the “Intraday Continuous Market” at the EPEX SPOT Market for the bidding zone, which includes Germany, Austria, and Luxembourg. The values, which are listed as “Weighted Average Prices,” are determined for each 15-minute delivery period. Cross border trades are considered in this calculation. The data consist of a total of 128544 samples of the period between January 1, 2015, and August 31, 2018, and corresponds with 1339 days with 96-time steps for each day.

Fig. 1 shows the prices over the whole time span. The orange line visualizes the monthly average of the “Intraday Continuous Price.” It differed from a minimum average of 21.7253 in February 2016 to a maximum of 54.8537 in January 2017. For the given timespan there is neither a clear trend observable nor a clear seasonal behavior regarding the monthly average. For further analysis, the characteristics of the Intraday Continuous and monthly average prices are shown in the following Table I. The standard deviation of 18.9172 shows that a large share of prices is relatively close to the mean. Moreover, the high value for the “Kurtosis” is an indicator of extreme price occurrences in both directions. The skewness for Intraday Continuous prices is calculated as 0.2088811. The value is low and slightly positive, which means that prices above average are more likely than prices below average.

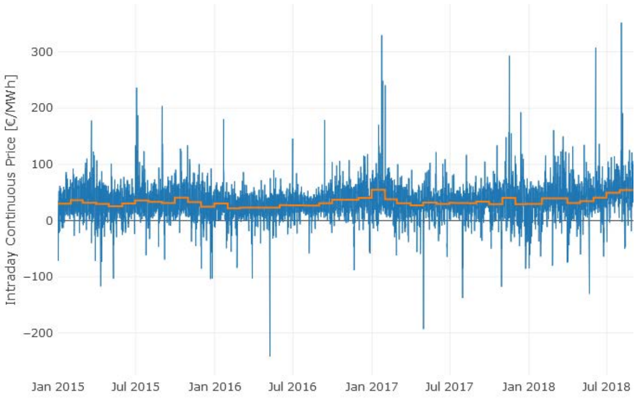

Fig. 1. Prices for the period from 1 January 2015 to 31 August 2018 of the 15-minutes contracts at the EPEX “Intraday Continuous Market” (blue) and their monthly average price (orange)

TABLE I. CHARACTERISTICS OF THE DATA

	Intraday Continuous	*Monthly Average*
Mean	33.1096 €/MWh	33.1118 €/MWh
Std. Deviation	18.9172	7.3993
Min. Value	-241.83 €/MWh	21,73 €/MWh
Max. Value	352.22 €/MWh	54.8537 €/MWh
Skewness	0.2088	1.1650
Kurtosis	12.9454	1.4952

Moreover, data of the infeed from onshore wind, solar and the load profile is used. This data is provided by the “ENTO-E Transparency Platform” and is also available for the given period and as quarter-hourly data. For all data, the daylight savings and the leap year in 2016 must be taken into consideration. Therefore, all data are converted to “Coordinated Universal Time (UTC).”

III. ANALYSIS OF THE PRICE BEHAVIOR

The price of the “Intraday 15-Minutes Continuous” contracts follow a “Zig-Zag Pattern” [2]. This pattern appears in the used data and is shown in Fig. 2. Thereby the pattern depends on the season and the peak- or off-peak hours of each day. Three full cycles of the seasons are used, starting with spring in 2015 and ending with winter in 2018.

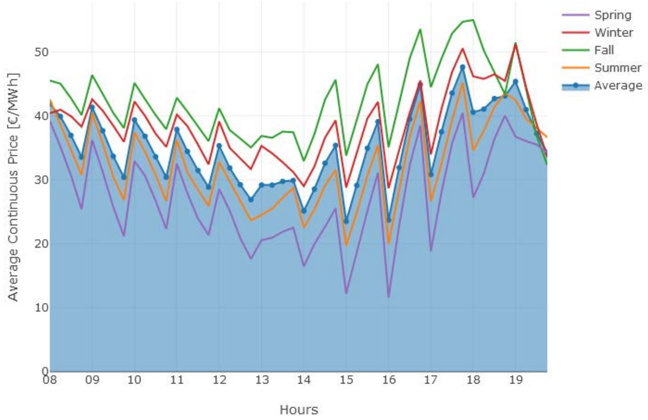

Fig. 2. Quarter hourly average of the “Intraday Continuous Price” of all seasons for peak hours

During the peak hours, the pattern shows a high at every first quarter of a full hour during the time from 8 am to 12 am as shown in Fig. 2. After the peak, the values decrease over three consecutive steps. Between 12 am and 2 pm the price behavior is varying depending on the season. For winter and fall, the behavior is the same as the peak in the first quarter; for summer and spring, the behavior changes during this time of the day. After 2 pm the prices are increasing over each full hour and have their peak during the third quarter. Until 6 pm this behavior stays the same for all seasons, besides the average price level. The prices for spring and summer are below the average, in contrast to winter and fall. This is explained firstly by the higher demand during winter and fall and secondly by the lack of infeed from solar energy, which has a lowering effect on the price. The dependency of the price on the solar infeed during the peak hours is also explained in [2] and is furthermore shown in Fig. 3.

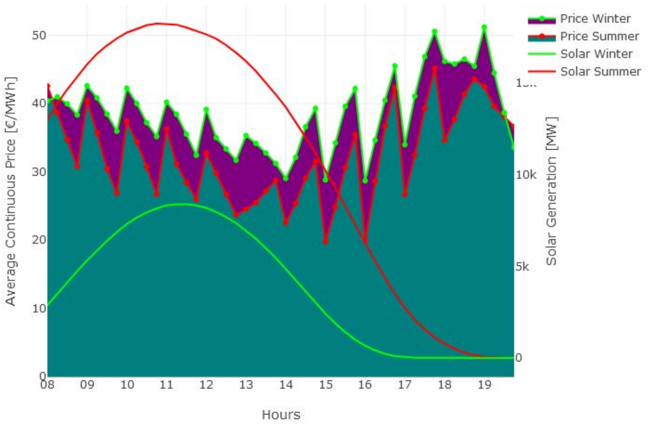

Fig. 3. Comparison of the average "Intraday Continuous Price" and average load profile during peak hours for summer and winter

The solar energy suppliers sell their produced energy in the "Day Ahead Market" for the full hour of the following day, which equals the average of the four quarters. As the sun goes up, buying pressure prevails in the first quarter of every hour because the hourly average cannot be reached. While the ongoing hour, the buying pressure is weakened because more and more solar power can be produced, therefore the price decreases until a new full hour starts as shown in Fig. 3 [2]. In contrast, in the second half of the day, the behavior shows the opposite pattern. As the sun goes down, the selling pressure appears during the first quarter of the hour and changes to buying pressure in the fourth quarter. As a result, the "Zig-Zag Pattern" appears. Between 1 pm and 2 pm, a contrary price behavior occurs. For summer the price increases (red) and for winter the price decreases (green) during this time. After that, the price follows the same pattern for both seasons.

It is likely that the difference between the highest and lowest price within each hour of the day is greater at times where the solar infeed is higher and consequently higher in summer than in winter. The fact that the difference of the average prices during the first and the second quarter (8 am to 12 am) and the third and fourth quarter (2 pm to 6 pm) of each hour is greater during summer than winter, as seen in Fig. 2 and also in Fig. 3 strengthens this statement, because of the higher the difference the greater the buy/sell pressure.

It can be seen from Fig. 2 and Fig. 3 that even if the forecasts of load and generation on which the pricing at the "Day Ahead Market" is based, are completely accurate, the price will nevertheless follow the "Zig-Zag Pattern," because it is depended on the natural ramping effect of the solar production. Moreover, it is likely that the volatility during each hour of the day is dependent on the difference between the "Day Ahead Market" contract and the 15-minutes contracts which are used to finer adjust the power balance.

It becomes evident that there is a relationship between the load and the "Intraday Continuous Price". The price level follows the load curve, especially during peak hours. When the loads are high, prices reach their highest levels around 7 am and around 6 pm as depicted in Fig. 4.

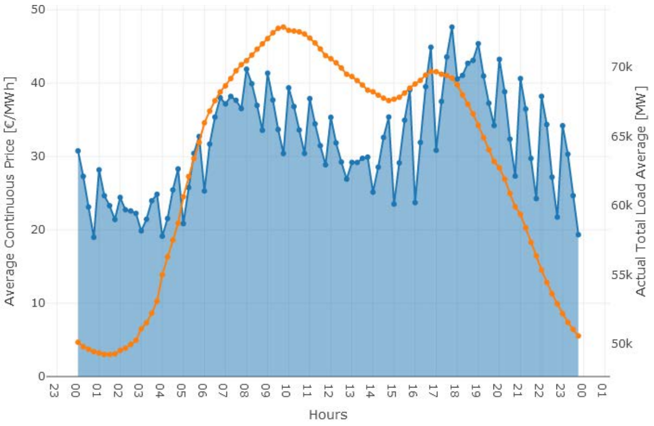

Fig. 4. Quarter hourly average of the "Intraday Continuous Price" (blue) and the "Actual Total Load" (orange)

This dependency can be specified by comparing different days of the week in accordance with their load profile. For this reason, the average of the business days (from Monday to Friday) are compared to the average of Saturday and Sunday. In Fig. 5 the "Intraday Continuous Prices" for business days (blue), as well as for Saturdays (red) and Sundays (green) are drawn against their corresponding load profile. The basic "Zig-Zag Pattern" is clearly observable in Fig. 5, just varying between the average price levels for each day. The price level on Sunday is below average and below any other day of the week. It can be explained by the fact that the demand for electricity on Sundays is lower than on any other day of the week.

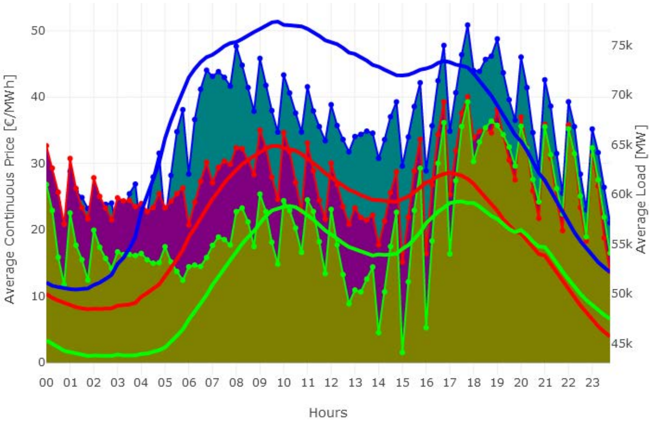

Fig. 5. Quarter hourly average of the "Intraday Continuous Price" and the "Actual Total Load" for business days (blue), Saturdays (red) and Sundays (green)

The relationship between the load level and the price level for each category (business days, Saturdays, Sundays) seems to be the strongest during the early peak hours, where the differences between the load profiles are the highest. In the late hours of the day, as the load profiles are approaching each other the same occurs for the "Intraday Continuous Prices". Moreover, it can observe that a low load level has a more significant influence on the volatility of the prices. The differences within an hour between the highest and lowest price are highest on Sunday, especially in the second half of peak hours.

IV. OUTLIERS

Extreme prices occur at times when the difference between demand and supply is highest. In general, it can be stated that extremely high prices occur at times when the supply cannot fulfill the demand. Moreover, low or negative prices occur at times when the supply exceeds the demand [4]. The prices at the “Day Ahead Market” and the “15-Minutes Intraday Auction” are set for the following day, and they are based on the given forecast information at this time. The “Merit Order can explain the extreme price occurrence in the "Day Ahead Market". With a very inelastic demand in combination with a very steep supply curve, the price could reach very fast high values [5]. That means if it is foreseeable that the supply will not fit the demand on the following day, the price will increase. However, there is still enough time to adjust either demand or supply in the “Intraday Market”. When the "Intraday 15-minute Auction Market” opens, more information about the current situation is available and the duration of the contracts is shorter, allowing supply to be more closely matched to demand.

Because the prices at the “Day Ahead Market” and the “Intraday 15-minutes Auction Market” are set for the next day, only the forecasts of demand and supply are available at this moment. Therefore, using real data in order to explain the price behavior in these two markets is not effective [2]. The real conditions are not available at the time when the pricing takes place. After that, only the “Intraday Continuous Market” can correct deviations. In the “Intraday Continuous Market,” the duration between setting the bid and executing the trade is shorter. Therefore, nearly the real conditions of supply and demand are available and can be considered to set the price. That means that extreme prices are more likely to occur in the “Intraday Continuous Market,” which is confirmed in Table II because the market participants have to react in short to avoid the use of the costlier “Balance Market.”

There is no established definition for extreme values [6]. Further on all appearances of negative prices and all prices above the doubled mean of the time series are counted as extreme values.

TABLE II. EXTREME PRICES

	Negative Prices	*Positive Outliers*
Intraday Continuous	4019	4003
Intraday 15-min. Auction	3153	3425
Day Ahead	496	625

It can be stated that the higher the extent of correction between the “Intraday 15-Minutes Auction” and the “Intraday Continuous Market”, the higher the impact on the price. This can lead to both, higher price volatility and higher extreme values. Forecast errors from VRE, unforeseeable issues like the short-term failure of any power plant or trading behavior of some market participants can be the reason why the correction is necessary. A higher share of VRE in the power mix should increase the number of extreme price occurrences, due to possible forecast errors [2]. High level of wind production (onshore, due to a higher installed power in contrast to offshore), in combination with low load, is seen as the driving factor behind negative prices [7, 8, 9].

A. *Outliers overall*

The following Fig. 6 shows the number of occurrences of extreme prices for every month over the given period from January 1st, 2015 to August 31, 2018. Moreover, the monthly average of the onshore wind generation and the average load for every month are given.

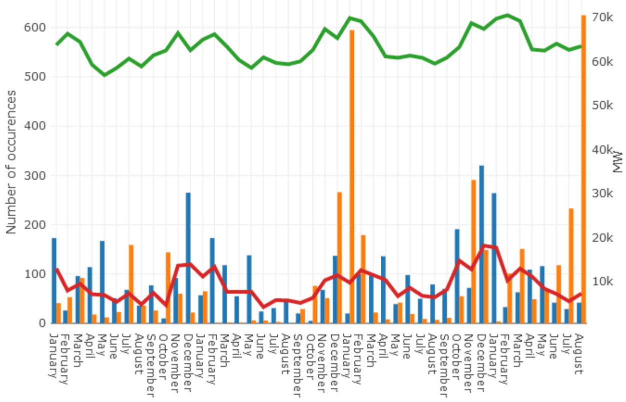

Fig. 6. The occurrence of negative prices (blue bar), positive outliers (orange), the monthly average of load (green) and onshore wind generation (red)

The two months in which negative prices occur most frequently are December 2015 and December 2017 with 265 and 320 occurrences. The third highest number of negative prices is 264 for January 2018. Consequently, it can be stated that negative prices seem to occur more frequently in the winter months, where the share of onshore wind is higher compared to other seasons. Due to the lower share of solar energy in the generation of VRE during winter, the infeed from VRE mainly consists of less predictable onshore wind energy, which leads to increased occurrence of extreme prices. The lower electricity demand in December 2015 and 2017 (due to the Christmas holidays) compared to other winter month with a simultaneous high infeed from onshore wind explains the high occurrence of negative prices. For the rest of the year especially during summer, an increasing infeed from onshore wind often leads to a higher occurrence of negative prices and a decreasing infeed to a smaller number of negative prices. In general, during summer the occurrences of both the negative prices and the positive outliers, are very low. It could be explained by the fact that the more predictable infeed from solar has a higher share than the infeed from the wind.

The numbers of positive outliers seem to be more unpredictable since the most and second most frequent occurrences are in January 2017 with 595 and August 2018 with 625 occurrences. Both are more than twice as high as in the third highest month of December 2017 (266). The events cannot be assigned to a specific season, but the most positive outliers are seen in the winter months of 2017 and 2018.

B. *Outliers by hours of the day*

As a next step, the occurrences of extreme prices are analyzed for every hour a day. The data is further rearranged for that purpose. Fig. 7 shows the average occurrence of negatives prices (blue) as well as the positive outliers (orange) for each hour of the day for the whole period. Moreover, the average load over one day is plotted into the graph.

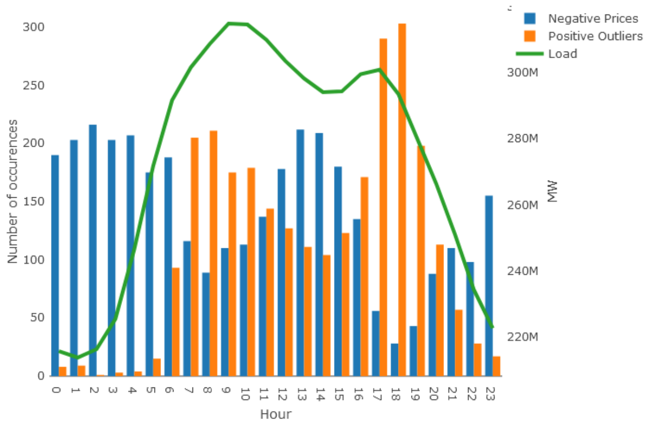

Fig. 7. The occurrence of negative prices (blue), positive outliers (orange), and the daily average of load (green)

It becomes apparent that there is a positive correlation between positive outliers and high demand. During peak hours, with increasing/decreasing load, the occurrence of positive outliers also increases/decreases. The peaks of both are between 7 am – 10 am and 4 pm – 7 pm. When the load during peak hours reaches a low level, there is also the lowest number of positive outliers. In general, positive outliers are much more likely to occur during peak hours.

Negative prices show the opposite behavior during peak hours. With decreasing load, the number of negative prices increases until the load reaches a low level. During the off-peak hour, negative prices occur more regular. It could be explained by the fact that the demand for electricity is much lower. Low demand in combination with a high infeed from VRE could explain this behavior. For that reason, the onshore wind infeed is plotted into the graph and is shown in Fig 8.

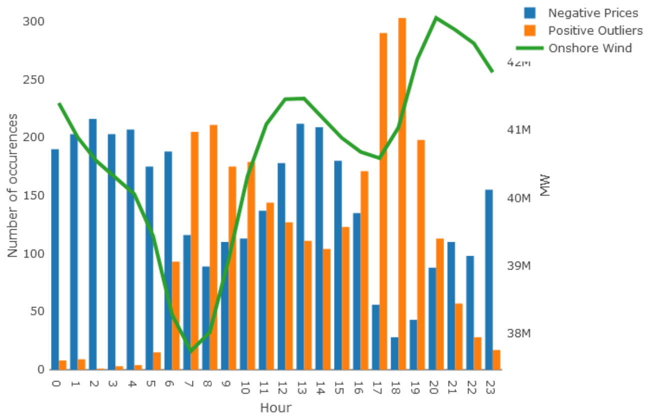

Fig. 8. The occurrence of negative prices (blue), positive outliers (orange), and the hourly average of onshore wind generation (green)

While the onshore wind generation increases between 8 am and 1 pm, the occurrence of negative prices increases to a similar extent as seen from Fig. 8. The same is observable for the late hours of the day (6 pm to 11 pm). Between 6 am and 12 am both the number of negative prices and the onshore wind generation increases. For the peak hours, the number of negative outliers reaches a peak at the same time as most solar infeed is expected. This high amount of solar energy in addition to the high infeed from onshore wind could lead to an oversupply and therefore to increasing prices. In general, it can be said that negative prices occur more frequently in times of high onshore wind infeed.

V. CONCLUSION

This paper presented an analysis of prices at the EPEX SPOT “Intraday Continuous Market” of 15-minutes contracts. Firstly, the data set is described and introduced and then analyzed due to its seasonal behavior during peak hours. The reason for the characteristic “Zig-Zag Pattern“ is explained, as well as the impact of the infeed from solar energy. The naturally occurring solar ramps during peak hours have a significant impact on the price. In the time when the sun rises, high prices occur in the first quarter of every hour. After the sun has reached the highest point, the lowest prices for every hour can be observed in the first quarter. It can be stated that the different contract lengths of the products at the “Day Ahead Market” and the “Intraday Markets” are the reason for this pattern. The prices set in the “Day Ahead Market” for one hour does not fit the real production conditions. When the sun goes up/down the produced energy in the first quarter of each hour is lower/higher than the expected average of the Day Ahead contracts because of the angle between the PV system and solar radiation. It leads to a price peak/low in the first 15-minutes of every hour.

Next, the dependence of the price level on the load profile by the example of days of the week is analyzed. On Sundays where the demand is lower compared to every other day of the week, the average prices are the lowest and besides the difference between the prices within each hour is the greatest. A close correlation can be observed between the prices of the 15-minutes contracts at the “Intraday Continuous Market” and the load profile.

Concerning the outliers, it can be stated that both the negative prices and the extremely high prices occur most frequently in the "Intraday Continuous Market" in comparison to the "Day Ahead Market" and the "Intraday 15 minutes Auction Market". It can be found that the infeed from VRE especially from onshore wind, have a significant impact on the number of occurrences of outliers in the "Intraday Continuous Market". Negative prices happen more likely at times of low load and high onshore wind feed-in. In contrast at times with a high load and low infeed from onshore wind, high prices occur more often. Therefore, most of the negative prices appear during winter.

ACKNOWLEDGMENT

Tankut Yalcinoz would like to thank the Philipp Schwartz Initiative, which was launched by the Alexander von Humboldt Foundation and the German Federal Office, for their support.

REFERENCES

[1] AGGARWAL, Sanjeev Kumar ; SAINI, Lalit Mohan ; KUMAR, Ashwani: Electricity price forecasting in deregulated markets: A review and evaluation. In: International Journal of Electrical Power & Energy Systems 31 (2009), Nr. 1, S. 13–22

[2] KIESEL, Rüdiger ; PARASCHIV, Florentina: Econometric analysis of 15-minute intraday electricity prices. In: Energy Economics 64 (2017), S. 77–90

[3] PAPE, Christian: The impact of intraday markets on the market value of flexibility — Decomposing effects on profile and the imbalance costs. In: Energy Economics 76 (2018), S. 186–201

[4] MARTIN, Henry ; OTTERSON, Scott: German Intraday Electricity Market Analysis and Modeling Based on the Limit Order Book. In: 2018 15th International Conference on the European Energy Market (EEM) : 27-29 June 2018. Piscataway, NJ : IEEE, 2017, S. 1–6

[5] PARASCHIV, Florentina ; ERNI, David ; PIETSCH, Ralf: The impact of renewable energies on EEX day-ahead electricity prices. In: Energy Policy 73 (2014), S. 196–210

[6] HAGFORS, Lars Ivar ; KAMPERUD, Hilde Hørthe ; PARASCHIV, Florentina ; PROKOPCZUK, Marcel ; SATOR, Alma ; WESTGAARD, Sjur: Prediction of extreme price occurrences in the German day-ahead electricity market. In: Quantitative Finance 16 (2016), Nr. 12, S. 1929–1948

[7] KETTERER, Janina C.: The impact of wind power generation on the electricity price in Germany. In: Energy Economics 44 (2014), S. 270–280

[8] NICOLOSI, Marco ; FÜRSCH, Michaela: The Impact of an increasing share of RES-E on the Conventional Power Market — The Example of Germany. In: Zeitschrift für Energiewirtschaft 33 (2009), Nr. 3, S. 246–254

[9] ZIEL, Florian: Modeling the impact of wind and solar power forecasting errors on intraday electricity prices. In: 2017 14th International Conference on the European Energy Market (EEM) : 6-9 June 2017, Dresden, Germany. Piscataway, NJ : IEEE, 2017, S. 1–5

Application of dynamic line rating in the grid planning process

Fahad Mansoor
Otto-von-Guericke University
Germany

Dr. Roland Bauer
IEEE Member
Germany

Dr. Georgios Papaefthymiou
Elia Grid International
Germany

Rena Kuwahata
Ampacimon
Belgium

Dr. Marc Osthues
Elia Grid International
Germany

Abstract—**This paper presents a methodology for the incorporation of Dynamic Line Rating (DLR) in the grid planning process. Based on the CIGRE methodology for transmission line ampacity calculation, a tool is developed in MATLAB for the assessment of the DLR potential based on historical meteorological data. Based on these ampacity estimates and detailed N-1 load flow calculations, the key drivers behind line loadings were analyzed. Our results show that the ampacity potential should be analyzed together with the power flow profiles in order to assess for which lines higher ampacity potential temporally coincides with increased line loadings. Further, the investigation of the change of ampacity potential along studied lines shows the existence of "hotspot segments", with minimum ampacity. These segments are the natural candidates for the implementation of DLR monitoring devices and further local analysis. Finally, regional ampacity potential maps for whole Germany are presented, which can be used as indication for the target areas for grid expansion and for the transmission line route planning.**

Keywords—dynamic line rating, renewable integration, transmission grid planning, congestion management.

I. INTRODUCTION

In order to make the power system more sustainable, safe and eco-friendly, countries are shifting from fossil fuels and nuclear power towards variable renewable energy sources (VRES) such as solar and wind. Renewable generators are built in areas with high wind and solar resources, which are often far from large demand centers. The northern areas of Germany have a high wind power potential, while load centers are located in the south. As shown in [1], average wind speeds are 40% higher in the North than in the South; it is therefore more economical to build wind power plants in the North and transport the power to the load centers. As a result, 70% of the wind generation potential is concentrated in the north of the country. However, the expansion of the transmission grid did not follow at the same pace, and together with offshore wind infeed as a result, congestions appear at the transmission system level in the north-south directions. Due to these congestions, there has been increased need for redispatching, incurring additional costs [2]. Since the construction of new lines is a lengthy process, transmission line monitoring with regard to weather effects provides an alternative solution to increase the transmission grid capacity, especially as a temporary measure until the transmission grid if finally upgraded.

The transmission line ampacity or the static line rating (SLR) is usually calculated considering weather conditions in such a way to be always on the sure side. For example, for European lines the usual parameters are 35°C ambient temperature, 0.6 m/s wind speed and 900 W/m^2 solar irradiation [3]. This leads to conservative values of the ampacity. Dynamic Line Rating (DLR) allows monitoring of the impact of actual weather conditions and the assessment of the weather depended line ampacity. Due to the cooling of lines in case of high winds and low ambient temperatures, transmission line conductors are allowed in many instances to carry more current than the SLR.

Related literature highlights the potential of DLR as an enabler for the integration of renewables [4–8]. On one hand it increases the grid capacity that can be available to the market by increasing the ampacity of the grid. On the other hand, it helps Transmission System Operators (TSOs) to reduce costs for utilization of assets. For instance, with increased grid capacity the need for redispatch decreases and thus the operational costs (OPEX) decrease. Also, the incorporation of DLR in short and mid-term grid planning time horizons can reduce capital costs (CAPEX) for TSOs by reducing the number of new lines to be built. But it must be carefully differentiated between the methodology to assess the long term grid expansion needs (as done in [19]) and the more operational advantages of DLR.

A lot of work has already been done to explore the highlighted benefits of DLR. In [11] the authors have presented a two-stage stochastic optimization model to combine the benefits of DLR forecasting with uncertainties in wind generation and line outages. Their results show that the stochastic framework enables DLR to be optimally utilized, offering cost savings and better integration of wind while avoiding the over-estimation of reserves by sharing the reserve capacity over multiple sources of uncertainty. To use an online DLR the impact of higher currents towards neighboring infrastructure and the legal situation has carefully to be taken into account. The effect on adjacent infrastructure and the deviation of electrical parameters from the initial legal approval cannot be neglected. While implementing a DLR monitoring system, a basic question arises about the optimal placement of monitoring devices. In [9, 10] it is shown that heuristic based approach gives far better results than a standard equidistant approach. In particular, reference [9] shows that the heuristic based approach gives monotonic results and addition of new critical spans always increases the quality of DLR monitoring systems whereas equidistant monitoring produces confusing results. Therefore, the prediction of critical spans or sections of a line for DLR monitoring is very important. The potential of redispatch mitigation in Northern Germany using DLR is shown in [12]. Results show that DLR is most useful in winter months when wind speeds are generally high and the need of redispatch is increased. They show that in the North the wind in-feed and DLR values are highly correlated and redispatch requirements can be significantly reduced even if DLR monitoring system is implemented only on selected lines.

In [10] DLR has been applied to the optimal management of transmission networks. DLR has been incorporated in an optimal power flow problem and the power flow is optimized based on increased transmission system capacity due to DLR. The results show that DLR was able to improve overall system capacity by 96% on hourly basis and only 1 line remained overloaded out of 4 critical lines in peak hours. Reference [13] has incorporated DLR into a transmission expansion planning problem using a stochastic model. The study shows that, using DLR, the number of required new lines decrease with increasing load levels in the system and the total cost of new lines together with the DLR installations is lower than the cost of lines without DLR. However, they have only studied fixed Right-of-Ways (RoW) for transmission system expansion which, first, ignores the fact that there might be potentially good areas with favorable weather conditions available for DLR. Secondly, it can force the line to be built in areas with sub-optimal weather conditions thus not utilizing the full benefit of DLR investment. This issue is addressed by other researchers using large-eddy and CFD simulations to consider the effect of weather conditions over a particular terrain. In [14] a CFD analysis of an area was done where new onshore wind farms have to be connected with existing 132 kV grid via a new overhead line. The results showed that the optimal route of an 89 MVA overhead line allow wind farm of 140 MW rating to be connected to the grid with a predicted constraint of 1.1% of energy yield.

However, in meshed grid the power flows are much more complicated, and the loading of a line can be due to several factors which correlate with weather parameters and other underlying factors in different ways, as power flows can also be due to injections from other types of power plants. The main contribution of this paper is to analyze the different factors correlating the line loading and the available potential by DLR. The analysis presents in a detailed way, whether DLR values can mitigate the congestion of the lines for future years. This is beneficial to both existing and planned lines. For existing lines, this analysis helps prioritizing the installation and implementation of DLR systems, while for new lines it assists in prioritizing the project execution and mid-term investment planning for the TSO based on the expected benefits from DLR.

Also, heat maps for individual lines show that there are always some specific regions of the line which are most critical and should be the focus of measurement devices for optimal monitoring of the whole line. This approach is cost effective as compared to the equidistant approach of monitoring device installation.

II. METHOD

A. CIGRE approach to calculate DLR

CIGRE and IEEE represent the two most reputed methods for ampacity calculation of a transmission line conductor. The two methods differ in the consideration for solar heating and convective cooling calculations, however, they provide similar results and the choice of one method depends upon the available input and the required complexity [15, 16].

In this paper, the CIGRE method was chosen because the available input data already contained the solar irradiation values thus it was more feasible to use the simple approach of the CIGRE model. Also, this study was done for a TSO therefore the preferred approach of the regulator has been adopted.

The CIGRE method [17] establishes the heat balance of the conductor as the heat gained by the conductor equal to the heat loss:

$$\text{Heat gain} = \text{Heat loss}$$
$$\mathrm{P_J + P_S + P_M + P_i = P_C + P_R + P_W} \tag{1}$$

where P_J is the Joule heating, P_S is the solar heating, P_M the magnetic heating, P_i the corona heating, P_C the convective cooling and P_R and P_W are the radiative and evaporative cooling. The corona heating P_i can be normally considered irrelevant for rating purposes as the convective effects are more important. The evaporation effect P_W is ignored for being rare and difficult to assess, and the magnetic heating P_M is often included in the increasing effect of the conductor resistance so that the general equation gives:

$$\mathrm{P_J + P_S = P_C + P_R} \tag{2}$$

. All the equations used are from [17] unless otherwise specified.

$$\mathrm{P_S = \alpha_S I_T D} \tag{3}$$

The solar heating P_S is defined by the absorptivity of the surface of the conductor α_S, the global irradiation intensity I_T and the outer diameter of the conductor D . The convective cooling P_C of the conductor is due to the flowing wind and can be calculated as:

$$\mathrm{P_C = \pi\lambda_f(T_S - T_a)Nu} \tag{4}$$

where λ_f is the thermal conductivity of the air, T_S is the conductor surface temperature, T_a is the ambient temperature of air and Nu is the Nusselt number. The equations to calculate the thermal conductivity of the air and the Nusselt number can be seen in [17].

$$\mathrm{P_R = \pi D\sigma_B\varepsilon_s[(T_S + 273)^4 - (T_a + 273)^4]} \tag{5}$$

Equation (5) represents the radiative cooling of the conductor which depends upon the conductor diameter D, the Stefan-Boltzmann constant σ_B, the emissivity of the conductor surface ε_s and the surface and air ambient temperatures.

$$\mathrm{P_J = I_{AC}^2 k_j R_{DC}(1 + \alpha(T_{av} - 20))} \tag{6}$$

Equation (6) is taken from [18] which gives the heat generated in the conductor due to the flow of current known as Joule heating. Here I_{AC} is the current through the line, k_j is the skin effect factor, R_{DC} is the DC resistance of the conductor, α is the linear temperature coefficient of resistance and T_{av} is the average conductor temperature.

B. Implementation of the model in MATLAB

The complete system of equations was implemented in MATLAB to create a tool which takes as input the weather parameters for whole Germany. The available weather parameters included wind speed at 10 m height, ambient temperature and solar irradiation for all the weather points in Germany having a resolution of 7×7 km. The data for weather year 2012 was used for the base case analysis since this has also been used by previous grid development plans.

Also, the year 2012 was hotter as compared to adjacent years thus giving a conservative estimate of DLR values. A distance matrix using minimum distance approach was created to allot the nearest weather point to each transmission tower of a certain line. Using the output of the distance matrix, the relevant hourly ampacity vectors were extracted from the 8784×7884 matrix resulting in an 8784×nWP matrix for a specific line. A minimum from this matrix for each hour gives the hourly minimum ampacity value for the whole line. A histogram of this vector tells which weather points occur most frequently as the minimum ampacity points and thus act as an ampacity bottleneck for the line. If this histogram is divided in different levels of occurrence frequency, then a heat map of the line can be created as shown in Fig. 7. The whole workflow is shown in Fig. 1.

III. RESULTS

Detailed load flow studies were conducted on the future grid development scenarios for the years 2021, 2023 and 2030. In order to assess the variability in the system power flows, the analysis was performed in hourly resolution for the full year (8760 hourly snapshots). In parallel, detailed N-1 analyses were performed for the critical system snapshots, leading in practice to detailed N-1 analysis of almost half of the snapshots[1]. The models used were extensive grid models for the whole European grids and the interconnecting area. The grid models were driven by the market models which provided the generation schedule for thermal power plants, renewable infeed schedules and loads. In long-term investment planning the potential of an operational DLR has to be carefully checked, there are too many effects affecting the load flow. In [19] a methodology to handle this uncertainty is presented.

Table I shows the bottleneck energy for each line. This indicates the total amount of energy that needs to be managed for the whole year using redispatch or other measures for each line. It gives an indication of both the duration and the severity of the overloads. The table indicates that the overloading is generally high for the years 2021 and 2023. Therefore, this will be the ideal time for the implementation of DLR when increase in grid capacity is strongly desired. For year 2030, the bottleneck energy is lower because there of the less congestions due to the expected implementation of the already identified grid expansion projects.

A. *Driver analysis*

Fig. 2 shows the duration curves for line 1 where it can be seen that there exists overloading for the years 2021 and 2023. The maximum value is the same quantity specified by the bottleneck energy in Table I. From Fig. 2, it can be seen that the DLR curve is higher than the loading curves which means that DLR is able to remove these congestions, but the duration curve is not the best identifier of this information as it has no information about time dependency. To accurately analyze the time correlation between DLR and line loadings the scatterplots are presented. Fig. 3 shows the scatter plot for line 1 for DLR and line loading of the year 2021. Here it can be seen that there are many points above the horizontal line of static rating, but all are below the diagonal which means DLR can remove these congestions. This scatter plot also tells us the correlation between the two quantities which is +0.609 according to the corrcoeff function of MATLAB. The high correlation value suggests that the DLR and loading of the line has a common driver which is wind and thus DLR strongly supports the ampacity of this line when it is required. The correlation coefficient is calculated for the DLR values and the N-0 loadings of the lines.

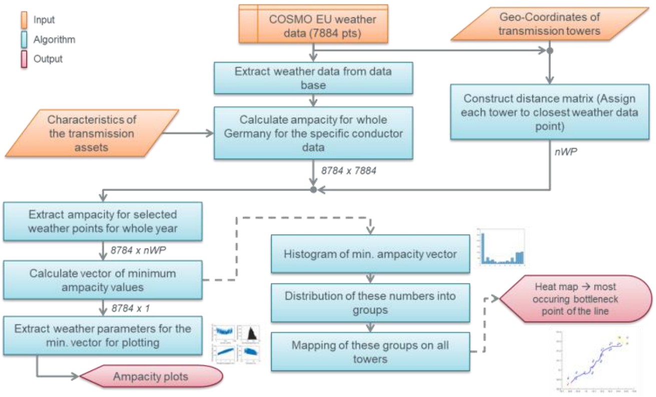

Fig. 1 Workflow of the MATLAB toolbox

TABLE I. N-1 LOAD FLOW RESULTS FOR SELECTED LINES

Line #	**Bottleneck energy per line (GWh)**		
	2021	***2023***	***2030***
1	392	52	-
2	1.4	205	0.8
3	51	187	-
4	0.9	35	4.5
5	489	352	-

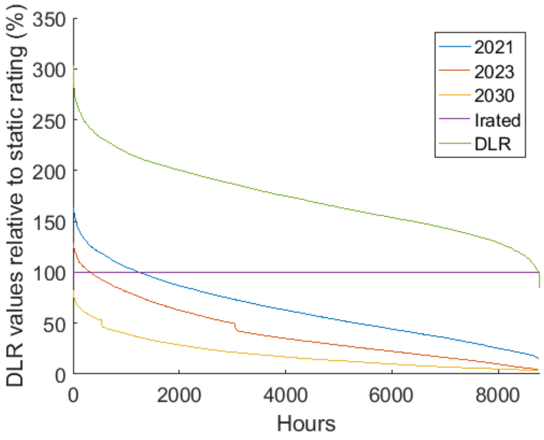

Fig. 2. Loading and DLR potential duration curves for line for future years

Next, in Fig. 4 the scatter plot for line 2 has been shown between DLR and line loadings of 2023. From this figure it can be seen that there are some loadings which are even above the diagonal, this means that DLR is not able to fully remove the overloading of this line. The points in Fig. 4 also show a horizontal trend which means there is little to no correlation between the two quantities. The correlation coefficient calculated is equal to -0.152 which means that wind is not the common driver between the DLR values and the loadings of line 2.

---

[1] In cases results for the full set of snapshots are presented (e.g. duration curves or scatter plots), we combine results from N-1 security assessment and base load flow. This leads to discontinuity of duration curves or to empty areas in scatter plots. Correlation coefficients are estimated based on the use of full set of load flow calculations.

In Fig. 4, it can also be seen that there are some points which lie in the bottom left triangle. This is the area where the line loading is below the static rating but higher than the diagonal of DLR. If a line is loaded in this condition considering only the static rating, then it is susceptible to physical damage because the conductor surface temperature will exceed its limit. Thus, via this analysis DLR shows the instances when this situation could occur and highlights the risk which is neglected if only static rating is considered.

In order to examine other possible drivers behind the loadings of line 2, an analysis with the coal in-feed of the whole country is done as shown in Fig. 5. The correlation coefficient calculated for this case is +0.297 which shows the correlation between the line loadings and the coal in-feed. This implies that due to the absence of a common driver between line loading and DLR, the ampacity gains provided by DLR might not be timely matched for line 2. In this case, further investigations on the drivers for this line would be required. Based on the results of the driver analysis, these lines can be classified into different groups as under:

1) Strong positive correlation

Those lines which show good positive correlation between DLR and loadings will come under this group, therefore line 1 is a suitable candidate. The strong positive correlation suggests that the DLR and loadings have a common driver i.e. wind and therefore in times of high wind, DLR will be able to increase the ampacity of the line when strongly needed. Thus, the implementation of DLR monitoring devices should be done on a priority basis on such lines to reap maximum benefit of DLR.

2) Weak or negative correlation

Line 2 is a member of this group as the correlation between DLR and line loadings was negative for line 2. This means that wind is not the common driver between DLR and loadings of line 2 and the correlation with the coal in-feed shows that it has better correlation with coal power. However, DLR was still able to remove 98% of the overloading of line 2. Thus, the installation of DLR monitoring devices can be delayed for such lines and the ampacity values from predictions and forecasts can be used instead. This offers a flexibility option for the TSO for better investment planning. But to decide on the transmission needs, the often rapid changes and uncertainties in the general scenario framework whether there are still coal fired power plants or whether there are more renewables have to be taken into account.

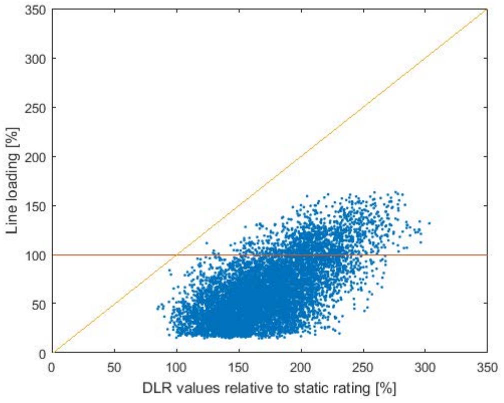

Fig. 3. Scatter plot of DLR vs. line loading of year 2021 for line 1

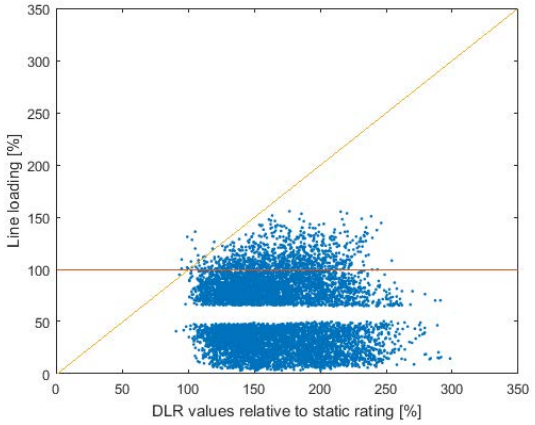

Fig. 4. Scatter plot of DLR vs. line loading of year 2023 for line 2

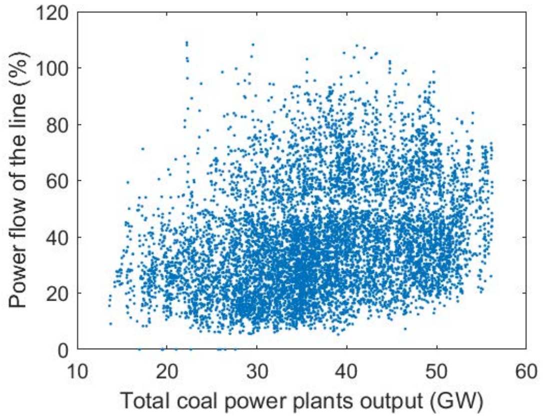

Fig. 5. Scatter plot of loading of line 2 with the coal in-feed

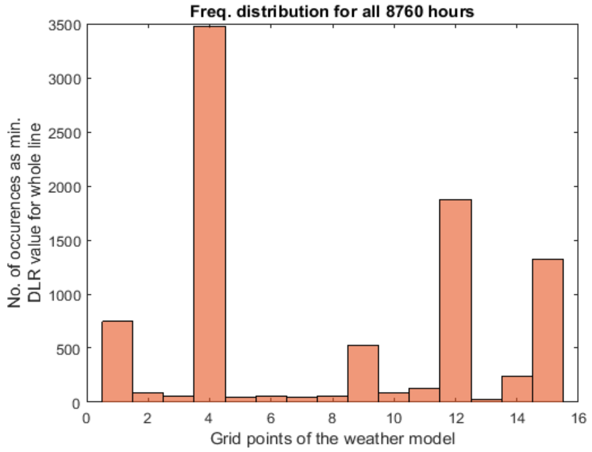

Fig. 6. Histogram of weather points for line 4 giving minimum DLR values for the whole year

B. *Heat maps*

In this section heat map is discussed for the individual lines. As discussed previously, Fig. 6 shows the histogram of the weather stations having minimum ampacity. From the figure, weather point 4 occurs as the minimum ampacity point for almost 3500 hours of the year. This means this point is the ampacity bottleneck for the line 40% of the time of the year. Using this information, the line can be color coded to show the hottest and coolest points of the line as shown in Fig. 7. This figure helps in the optimization of the DLR monitoring device placement and a heuristic rule can be made for this placement. Research shows that placement using a heuristic rule is more efficient as compared to equal length placement of sensors [9].

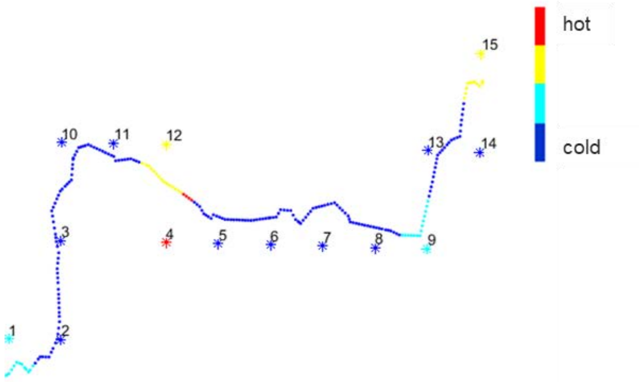

Fig. 7. DLR heat map of line 4 showing the ampacity bottlenecks

IV. CONCLUSION

This paper has presented a tool and a methodology to incorporate DLR in the grid planning process suitable for short and mid-term tasks. It highlights the importance of considering the DLR potential along with line loading values and establishes that such kind of analysis should be done to evaluate the impact and role of DLR in the grid expansion process. The case study was conducted for the German grid where it was shown how DLR minimizes redispatch, unlocks new market potential and removes congestions from the lines.

DLR also highlights the risk when SLR is not so conservative and may allow line loading above the physically allowable limit.

This paper also shows that driver analysis is an important tool in a quick prioritizing the lines for DLR implementation. The scatter plots of line loadings with factors such as wind and coal in-feed show that the lines can be divided into two broad categories. For the lines which show strong and positive correlation between DLR and line loading, indicates that wind is the common factor between the two. For such lines it is a win-win situation to install DLR measurement devices in a high priority as DLR will offer high ampacity gains exactly when it is needed. The other category is when the correlation between line loading and DLR is weak. For such lines wind might not be the common driver and as shown for line 2 coal in-feed had a better correlation with line loading. This means that DLR ampacity gains will not temporally coincide with the line loadings and therefore the implementation of DLR on such lines can be delayed providing better investment planning for the TSO. However, it should be noted that even for this line DLR was able to remove 98% of the congestions.

Also, a concept of heat maps was given in this paper for individual lines. The heat maps for individual lines shows the bottleneck points for ampacity on these lines and allow the optimized placement of DLR sensors for special weather years.

REFERENCES

[1] T. Unnerstall, *The German Energy Transition*. Berlin, Heidelberg: Springer Berlin Heidelberg, 2017.

[2] Enerquire, *German electricity market in 2017.* [Online] Available: https://www.enerquire.com/blog/german-electricity-market-in-2017-records-for-battery-storage-and-redispatch. Accessed on: 21-Oct-18.

[3] BNetzA, *Gründsätze für die Ausbauplanung des deutschen Übertragungsnetzes.* [Online] Available: https://www.50hertz.com/Portals/1/Dokumente/Netz/ÜNB-Planungsgrundsätze_Juli%202018.pdf?ver=2018-10-26-150403-247. Accessed on: 24-Jan-19.

[4] S. Karimi, P. Musilek, and A. M. Knight, "Dynamic thermal rating of transmission lines: A review," *Renewable and Sustainable Energy Reviews*, vol. 91, pp. 600–612, 2018.

[5] A. Michiorri *et al.,* "Forecasting for dynamic line rating," *Renewable and Sustainable Energy Reviews*, vol. 52, pp. 1713–1730, 2015.

[6] A. Michiorri and P. C. Taylor, Eds., Forecasting Real-time ratings for electricity distribution networks using weather forecast data: CIRED, 2009.

[7] US Department of Energy, "Dynamic Line Rating Systems for Transmission Lines," Apr. 2014. [Online] Available: https://www.smartgrid.gov/files/SGDP_Transmission_DLR_Topical_Report_04-25-14_FINAL.pdf. Accessed on: 10-Jan-19.

[8] Puffer R., Schmale M., Rusek B., Neumann C., and Scheufen M., "Area-wide dynamic line ratings based on weather measurements," *CIGRE*, 2012.

[9] M. Matus *et al.,* "Identification of Critical Spans for Monitoring Systems in Dynamic Thermal Rating," *IEEE Trans. Power Delivery*, vol. 27, no. 2, pp. 1002–1009, 2012.

[10] J. Duque, D. Santos, A. Couto, and A. Estanqueiro, "Optimal management of power networks using a dynamic line rating approach," *REPQJ*, vol. 1, pp. 584–589, 2018.

[11] F. Teng *et al.,* "Understanding the Benefits of Dynamic Line Rating Under Multiple Sources of Uncertainty," *IEEE Trans. Power Syst.*, vol. 33, no. 3, pp. 3306–3314, 2018.

[12] T. Ringelband, M. Lange, M. Dietrich, and H.-J. Haubrich, "Potential of improved wind integration by dynamic thermal rating of overhead lines," in *2009 IEEE Bucharest PowerTech*, Bucharest, Romania, 2009, pp. 1–5.

[13] J. Zhan, W. Liu, and C. Y. Chung, "Stochastic Transmission Expansion Planning Considering Uncertain Dynamic Thermal Rating of Overhead Lines," *IEEE Trans. Power Syst.*, p. 1, 2018.

[14] D. M. Greenwood, G. L. Ingram, and P. C. Taylor, "Applying Wind Simulations for Planning and Operation of Real-Time Thermal Ratings," *IEEE Trans. Smart Grid*, pp. 1–11, 2015.

[15] Wroclaw University of Technology, Wroclaw, Poland, *The differences between IEEE and CIGRE heat balance concepts for line ampacity considerations*: IEEE, Sep. 2010.

[16] A. Arroyo *et al.,* "Comparison between IEEE and CIGRE Thermal Behaviour Standards and Measured Temperature on a 132-kV Overhead Power Line," *Energies*, vol. 8, no. 12, pp. 13660–13671, 2015.

[17] J. Iglesias and F. Jakl, *Guide for thermal rating calculations of overhead lines: Working group B2.43*. Paris: Cigré, op. 2014.

[18] J. Rodriguez Alvarez, J. Azurza Anderson, and C. Franck, "Validation of a Thermal Model for Overhead Transmission Lines at High Conductor Temperature," 2016.

[19] German TSOs, "*Grundsätze für die Ausbauplanung des deutschen Übertragungsnetzes*", 50Hertz, Amprion, TenneT, Transnet BW, July 2018

Economic transmission network expansion planning considering rescheduling of generation

Fabian Lukas, Tobias Deß
Institute of Electrical Energy Systems
Friedrich-Alexander-University of Erlangen-Nuremberg (FAU)
Erlangen, Germany
fabian.lukas@fau.de, tobias.dess@fau.de

***Abstract*—Efficient grid development is crucial for a successful integration of renewable energy sources (RES) in power systems. While the transmission grids are getting more complex a need for advanced network expansion planning methods is rising. This paper introduces an automated two-part process of identifying cost-efficient grid expansion measures. The tool determines the cost optimum between grid expansion investments and costs for rescheduling of power generation (redispatch) in order to minimize the overall system costs. With the help of load flow optimizations (LFO) the resultant costs for redispatch were calculated. The decision-making process of the optimization strategy was tested in a modified Garver's six-bus network. The simulation results demonstrated that the proposed approach is capable of reinforcing the transmission grid economically to meet reliability criteria and additionally to seek the cost optimum between further grid expansion and redispatch costs.**

***Index Terms*—transmission network expansion planning, automated grid planning, redispatch, NOVA principle.**

I. INTRODUCTION

With the ambitious German goals of reducing the emission of greenhouse-gases by 80% until 2050, the power production landscape is changing fast. The remaining German nuclear plants will be shut down until 2022 and only recently the phasing out of coal energy production by 2038 was recommended by a governmental committee. These missing amounts of conventional power need to be compensated by renewable energy sources (RES). Whereas the installed capacities of wind and solar power are growing constantly, the expansion of the German transmission network is hesitating. The slow expansion progress is due to long planning processes and a lack of social acceptance for new expansion measures. The insufficient grid development leads to increasing operational challenges for the transmission system operators (TSO). Network congestions and interventions for rescheduling of power generation (redispatch) are occurring more frequently. Redispatch implicates increased costs of power production due to deviations from a merit order supply. Additional costs for power plant operators need to be compensated by the TSOs. Hence the costs for end consumers are rising. Commissionings of selective expansion measures show the beneficial effects on reducing the occurrences of network congestions and redispatch costs in practice. In order to identify these cost beneficial measures, improved processes are needed for evaluating and comparing different expansion paths. There is existing literature about various approaches for solving the transmission network expansion planning (TNEP) problem. Reference [1] gives an overview about different solving methods, treatment of constraints and planning horizons. In most cases the aim is to minimize investment costs for the addition of transmission lines subjected to the constraints of security thresholds. Many papers analyze the optimal transmission expansion on a short-term view without considering operational costs. The focus of this paper lays on the economic expansion with the use of redispatch for a long-term planning horizon. Standardized test systems like Garver's six-bus network [2] are used for testing purposes in specialized literature. This approach employs Garver's initial grid topology extended by various potential expansion measures to display the outcome of the grid planning tool. The paper is structured as follows. Section II describes the methodology and simplifications that were made for identifying optimized economic grid expansion paths. Section III presents the test system in which the planning tool was verified. Details about the input data and simulation results are given. Finally in Section IV, a conclusion about this approach for network expansion planning is drawn.

II. METHODOLOGY

The objective of the automation process is finding the system cost optimum between grid expansion investments and redispatch costs. While solving this optimization problem the constraints of a reliable power system i.e. meeting loading thresholds are given. Due to a prioritization of dependable supply over economic efficiency, the process is divided into two iterative optimization loops that are completed successively. The flow chart in figure 1 shows the iterative process of the network expansion strategy. First, mandatory expansion measures are identified to solve all congestions (at least) with the use of redispatch. The second process seeks for the cost optimum between investment costs of further expansions and redispatch costs drawn to a certain period of time. A reinforcement process of adding and evaluating grid expansion measures is introduced.

A. Input Data

The inputs of the process are a model of a grid in critical state, a catalog of potential grid expansion measures and data of clustered load flow points. The purpose of clustering the

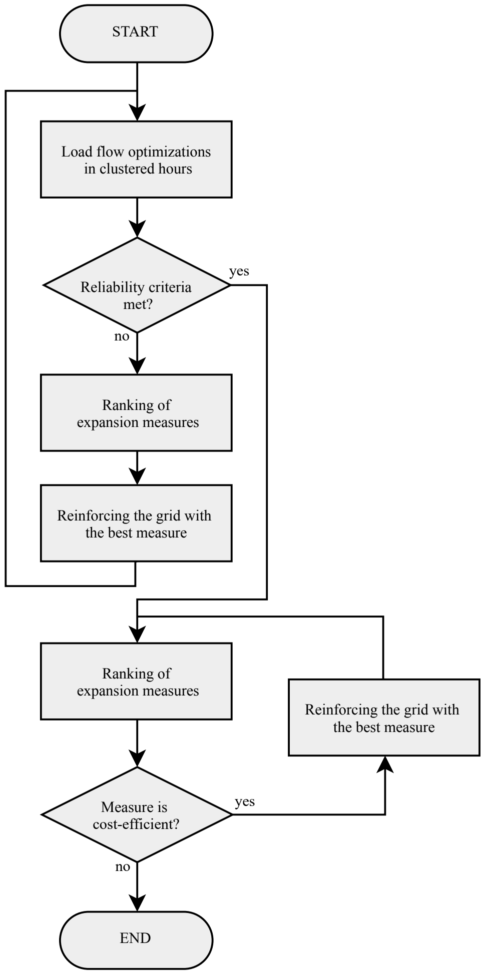

Fig. 1. Two-phase process of economic grid expansion

load flow time series of the intended year is the reduction of calculation effort while keeping information of the critical load flow hours. The decisive hours, in which load thresholds are violated, represent the yearly hours of operational interventions. The load flow data follow from power flow calculations with data of power generation and consumption and its allocation to the network buses. A catalog of grid expansion measures is needed to evaluate the different variants of grid expansions. It is now possible to run representative load flow calculations for the whole year by calculating only the clustered hours and extrapolate these hours to the full year.

B. Process

At the start of the process, a load flow optimization (LFO) with the constraint of meeting the reliability criterion is calculated for every clustered hour. The reliability criterion for a transmission line is set to 70% of its rated current. This is a common simplification for the n-1 criterion that was used in studies for transmission grid planning to ensure network security [3], [4]. It suggests that a line utilization of more than 70% will likely also cause n-1 violations. The main reason for the usage of this simplification is the saving of computing time.

TABLE I
CLUSTERED DATA OF REPRESENTATIVE LOAD FLOW HOURS

Hour	Frequency	PV [MW]	Wind [MW]	Load [MW]
14.02. 23:00	998	0	1350	4605
04.10. 09:00	1196	1148	142	4989
08.06. 21:00	1065	0	283	4918
01.09. 15:00	1082	297	1575	6202
08.08. 05:00	786	175	253	4100
07.09. 14:00	862	1192	437	6038
03.12. 20:00	508	0	1419	5822
25.05. 21:00	1355	0	228	4054
30.05. 17:00	520	211	1380	4938
11.03. 18:00	398	0	39	6149

A standard n-1 analysis would require load flow calculations for every possible outage of transmission components. The results are analyzed with regard to remaining congestions. If rescheduling the generation doesn't solve the congestions in all clustered hours, grid expansion is the mandatory implication. To find the most cost beneficial grid expansion measures the algorithm starts with a ranking of measures. The implementation of a fitness factor (FF) is necessary to compare the measures effectivenesses. The benefit of a measure is defined in equation 1.

$$FF = \left(\Delta \sum_{l=1}^{n_{lines}} P_l \right) \cdot \frac{1}{c_{inv}} \tag{1}$$

P_l describes the power of a transmission line, that can't be transferred due to occurring overloads, accumulated for one year by using the extrapolated clustered hours. The sum of overload power for the number of existent transmission lines n_{lines} represents a performance index for the transmission grid. Furthermore it is an indicator for redispatch costs as this amount of power needs to be rescheduled to meet the reliability criterion. The difference in ΣP_l with and without addition of the expansion measure based to the measures investment costs c_{inv} is equivalent to the fitness factor. The highest scoring measure is now added to the transmission grid, a new LFO is calculated and the overload criterion is evaluated again. This process repeats until there are no more violations of the 70%-criterion. This represents a state in which remaining transmission congestions can be solved by redispatching the power feed-in of the reinforced transmission grid. The first iterative process is finished and the identified expansion measures are stored. When this point is reached a second iterative process starts. This procedure seeks the economic optimum between investment costs for grid expansions and redispatch costs for a certain period. The yearly redispatch costs c_{RD} are determined by LFO calculations in the clustered hours for the intermediate transmission grid. The sum of redispatch costs of each clustered hour c_n multiplied by its occurring frequency $f_{cluster}$ represents the redispatch costs of the whole year.

$$c_{RD} = \sum_{n=1}^{n_{cluster}} c_n \cdot f_{cluster} \tag{2}$$

A new ranking of the remaining expansion measures is started. The economic benefit of the highest scoring measure is now determined by calculating the operational redispatch costs after adding the measure.

The difference in yearly redispatch costs with and without the measure displays the operational saving Δc_{RD} due to the enforcement measure. By means of a current value calculation, the economic value of a measure for its expected lifetime T can be determined. The discount rate i and the instant of time t are necessary for calculating the discounting factor $(1+i)^t$. This allows comparing the value of future and today's payments. The comparison of the operational savings and the investment costs c_{inv} decides whether the measure is cost-efficient or not.

$$eco = \left[\sum_{t=1}^{T} \frac{\Delta c_{RD}}{(1+i)^t}\right] - c_{inv} \tag{3}$$

If the expansion measure is cost beneficial ($eco > 0$) the iteration process continues and a new ranking will be started. Practically speaking, the investment costs for a new expansion measure will amortize by the savings of operational costs in its lifetime. This optimization process acts like a hill-climbing algorithm that allows steps in the right direction i.e. adding measures that are reducing the overall costs in its lifetime. For avoiding local cost minima, the algorithm allows "bad steps" to check whether there might occur a bigger step up after a step down. Thus the algorithm checks if a combination of measures is cost-efficient while one or more of its individual measures are not cost beneficial. The optimization iteration breaks if a counter for non-beneficial steps reaches a certain threshold. Non-cost-efficient measures then get removed from the stored list of grid reinforcement measures.

C. Output Data

If the iteration end is reached, an optimized combination of grid reinforcement measures is the output. An overview of the identified measures, their investment costs and the course of operational redispatch costs is given.

III. APPLICATION TO GARVER'S SIX BUS SYSTEM

A modified Garver's six-bus test system is implemented in the network calculation software INTEGRAL7 [5]. Garver's initial grid topology was employed and enlarged with different expansion measures.

The test system involves six buses, seven existing lines and two potential new construction line between buses 4-5 and 1-3. The electricity generation results from conventional energy sources and RES. Via multiplication factors the hourly amount of generation is distributed proportionally to the installed capacity among the generation units of the respective energy source. The capacities of generation and load are shown in table II.

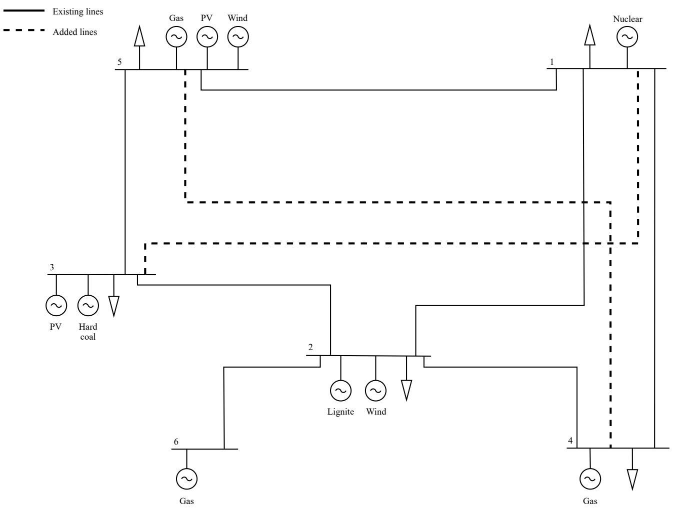

Fig. 2. Topology of a modified Garver's network

TABLE II
INSTALLED CAPACITIES OF GENERATION AND LOAD

Renewable Energy	4747 MW
Photovoltaic Power	2891 MW
Wind Power	1856 MW
Conventional Power	4007 MW
Load	7473 MW

The courses for renewable generation and load are based on historical data of 2015 scaled down to the installed capacities. The dispatch of generation is adjusted to merit order supply. The marginal costs of conventional power plants were calculated from data published by the Federal Network Agency [6]. The calculations contain costs for fuels, CO_2 certificates, specific operation and maintenance costs. The marginal costs were assumed as shown in table III.

TABLE III
MARGINAL COSTS FOR CONVENTIONAL POWER PLANTS

Power plant	**Marginal costs [€/MWh]**
Nuclear	4.07
Lignite	11.69
Hard coal	16.20
Gas	23.03

A linear approach for the redispatch cost modeling was implemented into the grid model. This approach implies a linear cost behavior when power plants increase or decrease their generation as a result of redispatch. Consequently the compensation that power plant operators receive for the additional generation of 1 MWh is equal to the amount they have to pay back to the TSOs for reducing their generation by 1 MWh. This approach is based on the assumption that marginal costs of conventional power plants are mainly dominated by fuel costs. This modeling allows calculations of redispatch costs from the marginal costs of redispatching power plants during LFOs.

The catalog of grid expansion measures includes the following options for grid reinforcement and reconstruction:

- Replacing of aluminum conductor steel-reinforced cable (ACSR) of existing overhead lines with high temperature low sag conductors (HTLS)
- Construction of double circuit transmission lines in new traces

Optimizing and reinforcing existing structures are generally cheaper than the construction of new lines. Due to the fitness factor being drawn to the investment costs of the measure, optimization and reinforcement are the preferred options for the planning tool. This supports the NOVA principle of grid planning, which suggests the application of grid optimization and reinforcement prior to the extension of the grid. This procedure is commonly used by German TSOs for reasons of social acceptance, economic feasibility and faster planning processes. The cost assumptions for the different expansion measures are taken from [7] and shown in table IV.

TABLE IV
INVESTMENT COSTS FOR POTENTIAL EXPANSION MEASURES

Expansion measure	Measure type	Investment costs [€/km]
Replacement of 380-kV ACSR conductors with HTLS conductors	Reinforcement	0.6 million
Construction of a 380-kV double circuit line in a new trace	Construction	2.2 million

Having gathered all information about the grid topology, power generation and load courses, marginal costs and potential expansion measures, the optimization algorithm was embedded in INTEGRALs programming environment QtScript. The tool was now able to add and evaluate different expansion paths. The resulting measures from both optimization phases are shown in table V.

TABLE V
IDENTIFIED EXPANSION MEASURES AND COSTS

Iteration cycle	0	1	2	3	4
Expansion measure	-	R2-4	R2-3	R3-5	R1-5
Investment costs [Mio. €]	0	7.5	15	22.5	30
Redispatch costs [Mio. €]	-	-	-	859	34
Total costs [Mio. €]	-	-	-	881.5	64
Reliability criteria met	✗	✗	✗	✓	✓

The first optimization loop was finished with the end of iteration cycle three, when the reliability criteria were met. Hence the reinforcement of transmission lines between the buses 2-4, 2-3 and 3-5 was identified. Subsequently the tool checked if further expansion measures amortized their investment costs in their assumed lifetime. A period of 40 years was assumed, which is a common lifetime for new transmission lines. With an interest rate set to 2%, the current value of potential expansion measures was calculated. The reinforcement of line 1-5 was proposed to reduce the redispatch costs from 859 million euro to 34 million euro over the period of 40 years.

IV. CONCLUSION AND OUTLOOK

The proposed approach for network expansion planning aims for minimal total cost of reliable transmission, which represents the desirable condition for electricity consumers. Therefore investment costs for network expansion and operational expenses for rescheduling of generation are evaluated. The results in a modified Garver's network show, that the tool identifies expansion measures that solve network congestions and reduce operational costs. The suggested solution is an expansion path that minimizes the overall costs, consisting of expansion investment costs and redispatch costs, on a long-term perspective. In summary, this straight-forward approach can be a supportive tool for economic expansion planning of transmission networks.

In the next step the tool will be applied to the German transmission grid within the scope of the interdisciplinary research project KOSiNeK (Combined Optimization, Simulation and Grid Analysis of the German Electrical Power System in an European Context) [8]. The application in KOSiNeK will show the tool's transferability to a larger scale of transmission networks.

REFERENCES

[1] I. Alhamrouni, A. Khairuddin, M. Salem and A. Alnajjar, "Review on Transmission Expansion Planning Models," AMM (Applied Mechanics and Materials), vol. 818, pp. 129–133, January 2016.

[2] L. Garver, "Transmission Network Estimation Using Linear Programming," IEEE Transactions on Power Apparatus and Systems, vol. PAS-89, pp.1688–1697, October 1970.

[3] Bundesnetzagentur, "Acknowledgement of the grid development plan 2030 (2017)" (German title: "Bestätigung des Netzentwicklungsplans Strom für das Zieljahr 2030"), Bonn, December 2017.

[4] Forschungsstelle für Energiewirtschaft e.V. (FfE), "Merit Order Grid Expansion 2030 (MONA 2030)" (German title: "Merit Order Netz-Ausbau 2030 (MONA 2030)"), Munich, September 2017.

[5] Forschungsgemeinschaft für Elektrische Anlagen und Stromwirtschaft GmbH (FGH), "Interaktives Grafisches Netzplanungssystem (INTEGRAL), Version 7".

[6] Bundesnetzagentur, "Monitoring report 2018" (German title: "Monitoringbericht 2018"), Bonn, February 2019.

[7] Grid Development Plan 2030, "Cost estimations" (German title: "Kostenschätzungen"), February 2019.

[8] R. German, M. Pruckner, D. Steber, M. Luther, T. Graber, A. Martin, C. Thurner, "Combined Optimization, Simulation and Grid Analysis of the German Electric Energy System in an European Context (KOSiNeK) - Presentation of the project and first results," Integration of Sustainable Energy Expo & Conference (iSEnEC), Nürnberg, 2018.

Low-cost Grid Connected Micro Inverter with Minimum Number of Components

Dayana Granford Ruiz
University of Kassel
Kassel, Germany
granforda@gmail.com

Prof. Dr.-Ing. habil Peter Zacharias
Chair of Electric Power Supply Systems
(KDEE-EVS)
University of Kassel
Kassel, Germany
peter.zacharias@uni-kassel.de

Abstract—**The goal of this paper is to propose new low-cost topology inverter connected to the grid. The topology of the inverter consists in a basic design with minimal components which it can be easily founded in the market. The topology feasibility is validated through a 57.5 W first prototype and it was simulated and constructed. A PV-module is used as a generator for this microinverter.**

Keywords—Micro inverter, PV-Module, optocouple, Total Harmonic Distortion (THD), transformer.

I. INTRODUCTION

Currently, the energy generation models are driven by the use and exploitation of fossil resources. The creation of fossil products dates back millions of years due to a photo synthetic process, from which fossil resources were produced [2]. However, since last years it has been seen the necessity to create new methods of energy generation. It has been noticed that the current ways of generating energy, are not viable for the future, because every day there is an unstoppable rise in prices in natural resources such as oil, gas, and coal due to its depletion. In addition, the consequences of the excessive use of fossil resources have been observed, examples of which are: glacial melt, rising sea levels and, especially, the immoderate changes in the environment [1].

Fortunately, the solutions have been offered from the field of Renewable / Regenerative Energies. Currently, are of great significance, the energy by biomass, wind, tidal, geothermal and photovoltaic [1]. This last one is has been considered as the most promising in the field of the renewable energy because of its fast growth and high levels of investment around the world.

The photovoltaic energy consisting in capturing solar energy and convert it into electricity hat caught the attention in that point that the research on photovoltaic solar energy has increased in the recent years [3]. The PV system is classified according to its power level in different sizes [4]: Small (Power < 350 W), medium (Power < 10 kW, Power < 500 kW), and large (Power < 850 kW) [4]. Additionally, PV solar systems are modular. PV solar systems can achieve a maximum module efficiency of 22 %, while average can be assumed 15 % - 17 %, meaning that at STC (Standard Test Conditions) they can deliver an output power of 150 - 200 W_p / m^2.

As PV systems deliver DC power, the use of inverters are necessary. Inverters can be classified in strings inverter, micro inverters. Considering many of modules with 1 - 2 m^2 area, string inverters should be integrated into modules with a power range of 150 - 450 W. In the case that the original DC power from every module into AC power is converted, this presents problems like a lot of wiring with DC power and the mismatching of modules in larger PV generators [5].

For that reason, the *"Microinverters",* a combination of a PV module with a grid connected inverter [6], whose characteristics are the small size and lower power rating, usually rated at 190 - 250 W are presented as module integrated for PV systems. They are rated for a single panel, and tie in parallel with the rest of a system, converting the DC power from each panel to AC individually and tie it together before feeding into the grid [5]. However, several problems hinder a real break through the microinverter's approach:

- Specific costs
- Long term reliability
- Total efficiency
- Safety aspects

The specific costs of a microinverter rises with the increment of the power. The reason comes mainly due to the requirements for grid connection and safety, which cause effects that not decreases with rated power increment. On the other hand, the long-term reliability is affected as the number of devices increases, because this high number of devices have a negative impact on the Mean Time Between Failures (MBTF) and the Failures in Time (FIT) rates. [5]

For that reason, the question arises how far the number of implemented electronic devices may be reduced without the violation of the existing standards. In this research, a new microinverter topology is proposed, in which the main goal is to achieve a simple design (minimum number of components), low costs and easy maintenance.

II. APPROACH FOR THE SOLUTION

The PV generator works as a current source without any control with the grid voltage according to the solar irradiation. A rectangular current produced by this generator can be delivered to the grid by only applying a pole commutator in combination with transformer.

The operation principle of the circuit consists of these steps for the positive cycle: 1) as the voltage coming from the grid has not exceeded the threshold voltage coming from the Zener diode branch, the topology does not work because the MOSFET is off. The voltage presented in this circuit is the open circuit voltage coming from the PV module. 2) The voltage of the grid starts to increase and suddenly exceed the threshold voltage of the Zener-diode 2; the circuit starts to operate, here the MOSFET 1 is activated. When this happens, the voltage of the grid gives the voltage of the circuit. 3) As the voltage of the grid continuous to rise, the voltage of the circuit reaches the peak-voltage of the grid. 4) As the voltage coming from the grid starts to decrease, it starts to be smaller than the voltage coming from the threshold voltage (Zener 2), and the circuit for this cycle ends to operate, here the MOSFET 1 is off. The open circuit voltage of the PV module again gives the voltage of the circuit.

Again, those steps are repeated for the negative cycle, but here the threshold voltage comes from Zener 1 and MOSFET 2 is activated/deactivated. The MOSFET 1 / MOSFET 2 receive the information at its gate input due to the optocoupler 1 (Emitter 1 / Receiver 1) and optocoupler 2 (Emitter 2 / Receiver 2). Fig. 1 reveal the low-power microinverter proposed.

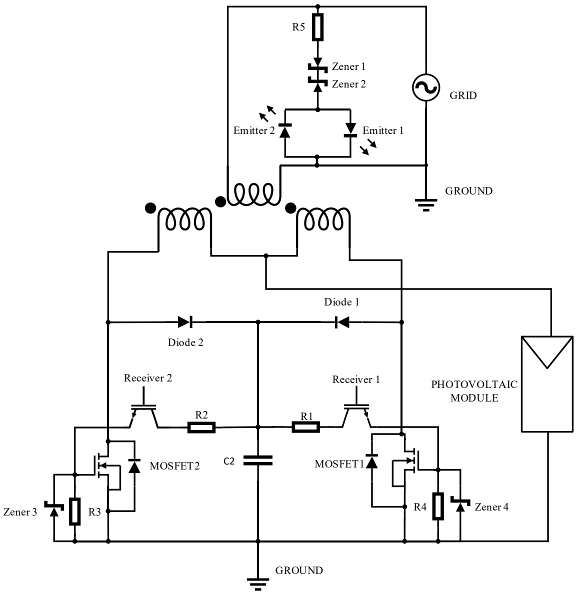

Fig. 1. Microinverter topology proposed.

III. COMPLYING THE MICROINVERTER INTO THE GRID

In order to feed the grid with the current coming from the microinverter, it must to comply the maximum permissible harmonic content for the current and the voltage according to the standards.

A. Current Harmonic Distortion

According to the international standard DIN EN 61000 3 - 2, the micro inverters can be classified in different classes depending on the active input power. For this case, this micro inverter is assumed to be class A and that means that for harmonics orders which are bigger than 1, its RMS value has to be kept below the limit within DIN EN 61000 3 - 2. Table I despites the permissible values for the Harmonic Distortion of the Current (THD_i):

TABLE I. MAXIMUM PERMISSIBLE HARMONICS CLASS A [12]

Harmonic Limits for class A			
Odd		***Even***	
n	Max [A]	n	Max [A]
3	2.3	2	1.08
5	1.14	4	0.43
7	0.77	6	0.3
9	0.4	8 ≤ n ≤ 40	0.23 x 8 / n
11	0.33		

The evaluation of the harmonic content is made through the Fourier analyses, delivering the series for a rectangular wave [7]:

$$i(t) = \frac{4I_d}{\pi}\sum_{\nu=1}^{\infty}\frac{cos\nu\alpha}{\nu}\cdot sin(\nu\omega t), \tag{1}$$

Where I_d is the input current, $\alpha=\omega t$ is an angle with zero current, ν is the order of the harmonic. At the same time, rectangular function despites a normalized content of the basic harmonics (g) given by equation 2:

$$g = \frac{I_1}{I_{tot}} = \sqrt{\frac{4^2{I_d}^2cos^2\alpha}{2\pi^2{I_d}^2\left(1-\frac{2\alpha}{\pi}\right)}} = \frac{4cos\alpha}{\sqrt{2\pi(\pi-2\alpha)}}. \tag{2}$$

Equation 2 is showed in Fig. 2 and it indicates that the fundamental harmonic has a maximum content if ${}^{\alpha}/_{\pi} = {}^{1}/_{6}$. At this value, g is approximately 0.96. Assuming this condition, the THD_i is:

$$THD_i \approx \frac{\sqrt{1-g^2}}{g} = \frac{\sqrt{1-0.96^2}}{0.96} = 0.292, \tag{3}$$

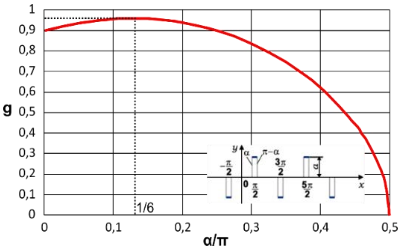

Fig. 2. Content of the basic harmonics in comparison to the zero current angle.

Now, the first idea leads to consider that the third harmonic content can be controlled by adjusting the angle with zero current (α) [13]. Equation 4 belongs to the Fourier series when the angle with zero current is equal to $\frac{\pi}{6}$. At this angle the third harmonic can be reduced.

$$i(t) = \frac{4I_d}{\pi}\sum_{\nu=1}^{\infty}\frac{1}{\nu}cos\left(\nu\frac{\pi}{6}\right)\cdot sin(\nu\omega t), \tag{4}$$

For satisfying this condition, a zener diode is used for controlling the duty cycle of the circuit and at the same time compensating the value of the third harmonic.

$$V_{DZ} = \sqrt{2}\cdot 230\,V\cdot sin(\alpha), \tag{5}$$

Applying equation 5, a value of V_{DZ} = 162.5 V is obtained.

B. Voltage Harmonic Distortion

The other limit concern the maximum allowed Total Harmonics for the Voltage (THD_u). According to the standard EN 50160 as a single-phase grid impedance can be as Z(ω)=0.4Ω+jω·0.796 mH assumed. That leads to the equation 6:

$$U_\nu = \left|Z_{grid}\right|\cdot I_\nu = I_\nu\cdot\sqrt{(0.4\ \Omega)^2+(\nu\cdot 0.25\ \Omega)^2}, \tag{6}$$

Where I_ν is the current produced by the microinverter at the order ν=1, 2, 3, 4... Delivering the equation 7 for the calculation of the THD_u:

$$THD_u = \frac{\sqrt{\sum_{\nu=2}^{\infty}\left({U_\nu}^2\right)}}{U_{1\_grid}}\cdot 100\ \% \ < \ 8\ \%, \tag{7}$$

Where U_{1_grid} is the main voltage at the connection point of the grid impedance (230 V). Equation 7 refers that the value of 8 % cannot be exceed. In Fig. 3 can be observed that the standard also gives a limit of permissible effective value for the single harmonics at unloaded connection point.

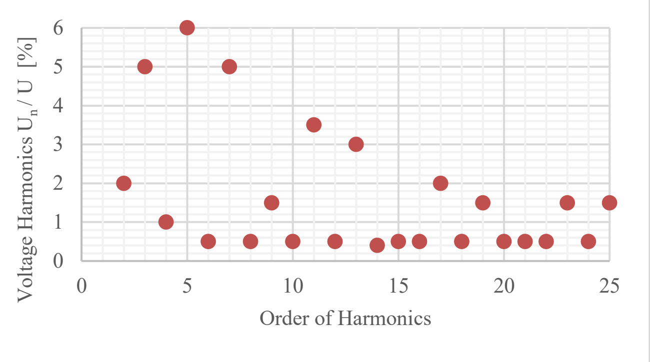

Fig. 3. Permissible Harmonics for the Voltage at a point interconnection grid [11].

These values for the single order of harmonics of the voltage cannot be exceeded too.

IV. TECHNICAL IMPLEMENTATION FIRST PROTOTYPE

Some requirements need to be satisfied in order to implement a new topology. One requirement for this approach is that the island operation is not treated. Instead, grid controlled converter is used, meaning that if the voltage disappears, the operation is not possible anymore.

A. Photovoltaic Characteristic

For this paper the Shell Solar SQ175 - PC PV module is used.

TABLE II. SPECIFICATIONS OF THE SHELL SOLAR SQ175 - PC PV MODULE [9]

Characteristics	**Values**
Open Circuit Voltage, (V_{oc}) [V]	44.6
Voltage at Maximum Power Point, (V_{mpp}) [V]	35.4
Short Circuit Current, (I_{sc}) [A]	5.43
Current at Maximum power point, (I_{mpp}) [A]	4.95
Maximum Power at STC [W]	175
Number of cells connected in series	72
Temperature coefficient of I_{sc}, (α) [mA/°C]	0.8
Temperature coefficient of V_{oc}, (β) [mV/°C]	-145
Temperature coefficient of P_{mpp} (Γ) [%/°C]	-0.43

The I-V characteristic of a PV generator in principle follows the so-called Shockley equation. For an ideal PN - diode [10]:

$$I_F = I_S\left(e^{U_{AK}/n\cdot\frac{k\cdot T}{q_e}} - 1\right), \tag{8}$$

In equation 8 I_F is the forward diode current, I_S is the diode saturation current, U_{AK} is the voltage across the diode, kT/q_e is the Boltzmann constant times the temperature divided by the electron charge and n is the ideality factor or the emission constant of the diode. The equivalent circuit for a PV generator is showed in Fig. 4:

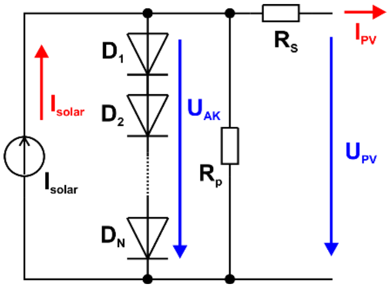

Fig. 4. Equivalent Circuit for the PV Module.

A PV generator consists of several diodes in series having a leakage current. A simple PV generator model can be found as N diodes in series with a parallel resistor (R_p) and a series resistor (R_s). For that reason, the new equation would be:

$$I_{PV} = I_S\left(e^{U_{AK}/N\cdot n\cdot\frac{k\cdot T}{q_e}} - 1\right) + \frac{U_{AK}}{R_p} + I_{solar}, \tag{9}$$

This Equation 9 contains 4 unknown parameters since I_{solar} is taken as the short circuit of the PV generator. In [8] can be found for the Shell Solar SQ175 - PC PV module the following values: $I_S = 1.2\,nA$, $R_s = 0.7\,\Omega$, $R_p = 196.2\,\Omega$, $N = 72$ and $U_T = 2.01\,V$. Using these parameters and the Equation 9, the PV generator is simulated as is denoted in Fig. 5:

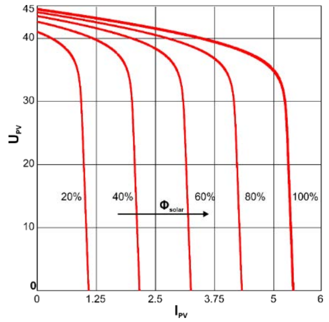

Fig. 5. Output characteristic of the Module Shell Solar SQ175 - PC at STC according to the parameters of [8].

B. *The Transformer*

Using the PV module itself as a current source, the transformer grid voltage must be below the MPP voltage at any time. This current source is temperature depending and the values changes depending on the radiation and the weather conditions, especially in Germany where the existence of seasons affects the operation of the PV module, giving other values of V_{mpp}, V_{oc}, I_{sc}. Considering this, the V_{oc}, I_{sc} and V_{mpp} can be expressed at different operating temperatures as [8]:

$$V_{oc,T} = V_{oc}[1 + \beta_{V_{oc}}(T - T_0)], \tag{10}$$

$$I_{sc} = I_{sc}[1 + \alpha_{I_{sc}}(T - T_0)], \tag{11}$$

$$V_{mpp,1} = \frac{V_{mpp,STC}\cdot V_{oc,T}}{V_{oc,STC}}, \tag{12}$$

Where β_{Voc} is the temperature coefficient of V_{oc}, α_{Isc} the temperature coefficient of I_{sc}, T_0 is the temperature at Standard Conditions (STC) (20 ° C), and T the new temperature of the module. The values $\beta_{V_{oc}}$ and $\alpha_{I_{sc}}$ are provided by the technical datasheet of the PV module [9]. Assuming that in summer the module temperature achieves a value of 70 ° C and in winter a value of - 20 ° C and using the (10), (11), (12) showed above, the temperature values are revealed in Table III.

TABLE III. NEW VALUES OF V_{OC}, V_{MPP}, I_{SC}, PSTC WITH THE CHANGE OF THE TEMPERATURE IN THE PV MODULE

STC (20 ° C)	**(T-T0)**	**V_{oc}**	**V_{mpp}**	**I_{sc}**	**P/PSTC**
	[° C]	**[V]**	**[V]**	**[A]**	**[%]**
Summer	50	37.45	29.7	5.47	21.5
Winter	- 40	50.5	40.08	5.4	17.2

With the V_{mpp} value, the transformer ratio can be calculated as:

$$\frac{N1}{N2} = \frac{\sqrt{2}\cdot 230\,V}{29.7\,V} > 10.94, \tag{13}$$

After denoting the number of turns ratio, a toroid three windings transformer with 20 turns of ratio is taken for a first validation of the circuit. This line frequency transformer is characterized by the resistance core (R_p), magnetization component in the core (X_p), resistance at the primary winding (R_{s1}), resistance at the secondary winding (R_{s2}), reactance of the primary winding (X_{s1}) and reactance of the secondary winding (X_{s2}). Those values can be founded in Table IV and are included in the simulation.

TABLE IV. PARAMETERS TOROID CORE TRANSFORMER

Toroid Core	**L_m**	**R_p**	**L_{s1}**	**L_{s2}**	**R_{s1}**	**R_{s2}**
	[H]	**[kΩ]**	**[mH]**	**[mH]**	**[Ω]**	**[Ω]**
	15.1	10.2	0.45	1	4.25	11.2

V. SIMULATION RESULTS

The topology from the Fig. 1 was simulated with the help of the software Plecs. Fig. 6 despites the current to the grid generated by the PV module:

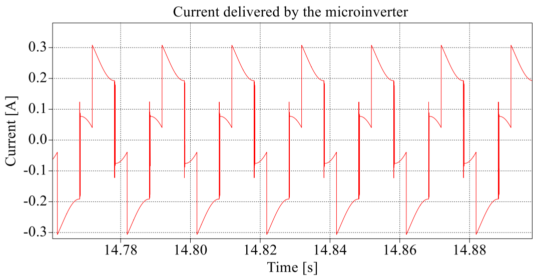

Fig. 6. Current delivered by the microinverter to the grid.

This device has a RMS current value of 194.9 mA. According to the simulation, Fig. 7 and Fig. 8 indicate the content of harmonic generated by this microinverter:

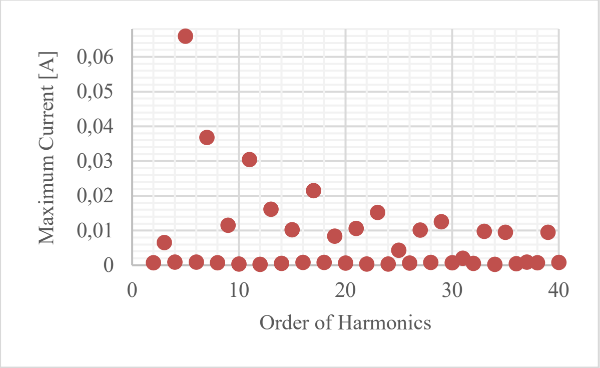

Fig. 7. Maximum Current in [A] per Harmonics given by the Micro Inverter.

Where it can be seen that the influence of the third harmonic is 0.0064 A and the rest of the harmonics have an influence which is lower than the permissible effective value of current accepted by the DIN EN 61000 3 - 2 in table I. Fig. 8 despites the single harmonic content of the voltage:

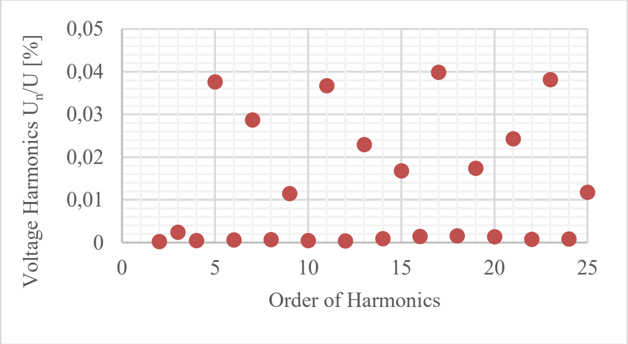

Fig. 8. Maximum Voltage in [%] per Harmonics given by the Micro Inverter.

With a total THD_u injected to the grid of 0.117 %. Fig. 8 demonstrate that the value for THD_u given by the micro inverter is lower as permissible voltage harmonics accepted by the EN 50160 (see Fig. 3).

VI. CONSTRUCTION FIRST PROTOTYPE

A first 57.5 W attempt of the micro inverter was constructed. In Fig. 9 can be seen the implementation of the new inverter topology connected into the grid, together with the devices from section II, toroid transformer and the PV module, which it was at the top of the roof.

Fig. 9. Implementation of the Micro Inverter into the grid.

Fig. 10 indicates the current injected to the grid with the help of the oscilloscope, with a RMS value of 119 mA.

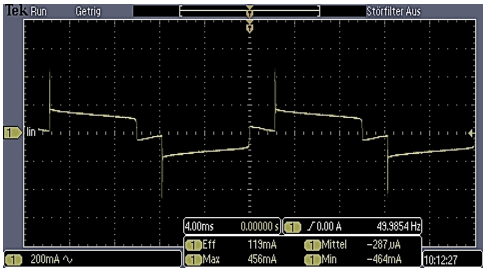

Fig. 10. Current of the Micro Inverter into the grid.

VII. CONCLUSIONS

In this research a topology with minimum device number of PV inverter connected into the grid is proposed. To feed the grid with the current generated by the PV inverter, some standards are considered for the content of harmonics. The Total Harmonic Distortion of this device needs to be accomplished according to the IEC 61000 3 - 2 / EN 50160. As those standards cannot be violated, a simulation is run to prove it. Some compensation of the harmonics is done by parametrising. For the third harmonic Zener diodes of 162.5 V are calculated. According to the simulation, it was observed that the value from the single harmonics of the current are within the range demanded by the norm. This can be checked if the Table I is compared with the values showed by Fig. 7. Furthermore, the THD_u equals to 0.117 %, which value is lower than the 8 % indicated by the standard. This makes one advantage of this PV inverter, demonstrating how easy is to design and construct a PV inverter with a simple design and minimal devices without the violation of the existing standards. Another advantage is that the control of de duty cycle is made through these Zener-diodes and at the same time it makes the compensation of the harmonics. For approximating the simulation most possible to the reality, the PV module was simulated with its real values of resistances, thermal voltage, open circuit voltage, short circuit current, saturation current, and on the other hand, the values of inductivities, resistances, of the transformer were found it. A 57.5 W first topology was constructed and an experimental setup with 20 turns of ratio transformer has been tested to prove the simulations.

REFERENCES

[1] K. Mertens. “Photovoltaik: Lehrbuch zu Grundlagen, Technologie und Praxis”. In *Einleitung: Wozu Photovoltaik?*, Ed. München: Carl Hanser Verlag, Germany, 2013, pp. 17-18.

[2] S. Krauter. “Solar electric power generation”. In *Introduction: CO_2-emissions by humankind*, Ed. Heidelberg: Springer-Verlag, 2006, pp. 4.

[3] P. Goncalves and M. Orestes, “Photovoltaic solar energy: Conceptual framework”, In *Elsevier LTD Renewable and Sustainable Energy Reviews 74*, pp. 590-601, March 2017.

[4] S. Kouro, J. Leon, D. Vinnikov and L. Franquelo, “Grid-connected photovoltaic systems”, *IEEE Industrial Electronics Magazine,* pp. 47-61, March 2015.

[5] “Micro inverters for residential solar arrays”, Solar Expert, ExpertSure, 2019, [Online]. Available: https://www.expertsure.com/uk/home/micro-inverters-for-residential-solar-arrays/. [Accessed: 19-feb-2019].

[6] S. Baekhoej, J. Pedersen and F. Blaabjerg, “A review of single phase grid-connected inverters for photovoltaic modules”, *IEEE Transactions on Industry Applications*, vol. 41, no. 5, pp. 1293-1303, September 2005.

[7] C.Y. Liu, J.G. Zhu and V.S. Ramsdem, “Minimization of total harmonic distortion for square wave voltage source inverters”, *Research Gate,* March 2014.

[8] T. Ma, H. Yang and L. Lu, “Development of a model to simulate the performance characteristics of crystalline silicon photovoltaic modules/strings/arrays”, *Elsevier LTD Solar Energy 100*, pp. 31-41, December 2014.

[9] Shell Solar, “Shell PowerMax solar modules for grid-connected markets: Ultra 175-PC/165-PC”, first edition 2004.

[10] K. Mertens. “Photovoltaik: Lehrbuch zu Grundlagen, Technologie und Praxis”. In *Aufbau und Wirkungsweise der Solarzelle*, München: Carl Hanser Verlag, Germany, 2013, pp. 97-101.

[11] *Merkmale der Spannung in öffentlichen Elektrizitätsversorgungsnetzen,* EN Standard 50160.

[12] *Electromagnetic compability,* DIN EN Standard 61000-3-2.

[13] D. Hart, “Electronica de Potencia”. In *Control de Armonicos y de Amplitud,* Ed. Madrid: Pearson, Spain, 2001, pp. 327-330.

Influence of Protection Systems on the Vertical Grid Operation in Distribution Networks

H. Cai, X. Song, T. Jiang, J. Kircheis, S. Schlegel, D. Westermann
Power Systems Group
Technische Universität Ilmenau
Ilmenau, Germany
teng.jiang@tu-ilmenau.de

***Abstract*— The energy revolution, which has been forced by law, is leading to a change in the energy sector. Energy generation is moving from centralized large-scale power stations in the upper grid levels to decentralized small generators in distribution networks. The Renewable Energy Act prescribes that electricity from renewable sources can be fed into the grid ahead of conventional power. In addition, conventional power plants must reduce production in times of excess supply. Along with this reduction, there is a lack of sources for providing system services. Here, new potentials are searched for the distribution network level. For these potentials to be exploited, new concepts are needed to ensure safe network operation. The investigations in this work are focused on how the provision of system services from the distribution network level will be limited by network protection in the future. Because there are comprehensive protection concepts and a wide range of protection devices, an overview of the basics of protection systems is created. To identify the influence of the protection systems, a possible concept for detection of influences of protection systems has emerged. A simulation in a low-voltage grid has been implemented as part of this work and serves to test the proposed concept.**

***Index Terms*—distribution network, system service, protection system.**

I. INTRODUCTION

THE power supply is the foundation for prosperity and progressing of a highly developed country. Since the nuclear disaster in Fukushima, the energy revolution has been considered in recent years [1]. The conventional centralized power supply through the large-scale power plants is gradually being replaced by a decentralized energy supply through renewable energy generators [2]. Accordingly, this development has effects on all grid levels because the previously unidirectional load flow from the upper grid levels to the lower grid levels changes into a bidirectional exchange of energy between the grid levels [2]. This exchange between the levels, however, means that previous concepts of network operation management and monitoring of system parameters and equipment must be changed in order to meet the new requirements.

The change due to the increased feed-in from renewable energies, as can be seen in Fig. 1.1, leads to new grid conditions. The volatility of renewable energies leads to constantly fluctuating load flows, depending on weather conditions [2]. For example, to maintain a stable frequency despite these constant changes in the grid, the imbalance between production and consumption must be compensated [5]. This imbalance leads to a deviation of the basic frequency defined in the European network system. If the deviations from this frequency are too large, this can result in damage to equipment and dangerous conditions [6]. The network operators, therefore, make use of the possibility of system services to avoid such harmful consequences. One example of this is power-frequency control. This regulation consists of primary, secondary and tertiary management. The various types of power serve, on the one hand, the purpose of protecting the frequency in the event of a fault from excessive deviations and on the other hand, of returning it to its setpoint value. An imbalance in the power grid can be either positive or negative. On the one side, power plants can, therefore, be out of operation, on the other hand also large loads due to disturbances in the grid [5]. To ensure sufficient positive and negative compensate power in the future, it is considered to be retrieved from the distribution grid level [2]. For this project to succeed, new concepts are required, including vertical network operation [7]. However, the influence of the protective systems on this concept is so far uncertain. [2].

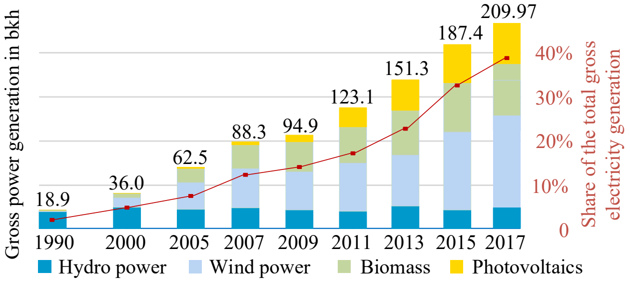

Fig. 1: Electricity generation from renewable energies in Germany from 1990 to 2017 according to [3], [4]

The previous research has usually been carried out in two directions. On the one hand, the issue about how decentralized power generation plants can contribute to system services was investigated. [2], [8]-[12]. On the other hand, it was researched how grid protection concepts can be adapted and optimized to changes in the feed-in situation in order to continue to enable secure grid operation [13]-[18]. In System Services 2030, it is repeatedly pointed out that there is a specific need for research to investigate the interactions between protection concepts and the planned potential realization of system services from the distribution grid level [2]. The present work is based on this point and intended to show a preliminary approach to the investigation of this influence. The aim of this thesis is to develop a concept to detect influences on the vertical network operation and minimize these influences by suitable methods.

This paper is divided into five parts. The first chapter presents an overview of the current network operation in Germany and the novel approach of vertical network operation for the management of electrical networks. The second chapter is devoted to the concept of recognizing possible influences caused by network protection and incorporating this insight into operational management, particularly in power-frequency control using the secondary power control. After that, the influence of overcurrent protection devices on the low-voltage level when activate secondary control power is investigated by simulation in order to test the effectiveness of the concept recommended in the third chapter. A summary of the conclusions drawn from this work is given in the end chapter. The possibilities for improvement of the investigations are also dealt with as well.

II. VERTICAL OPERATION

In the following chapter, how current studies and publications investigate the changing significance of the distribution network in electrical energy supply with regard to network protection will be discussed. The influences of the increasing number of decentralized energy supply in the distribution network will be explained and then the current problems that occur during network expansion will be examined. This chapter will demonstrate that it is necessary to prepare the future distribution networks for vertical grid operation.

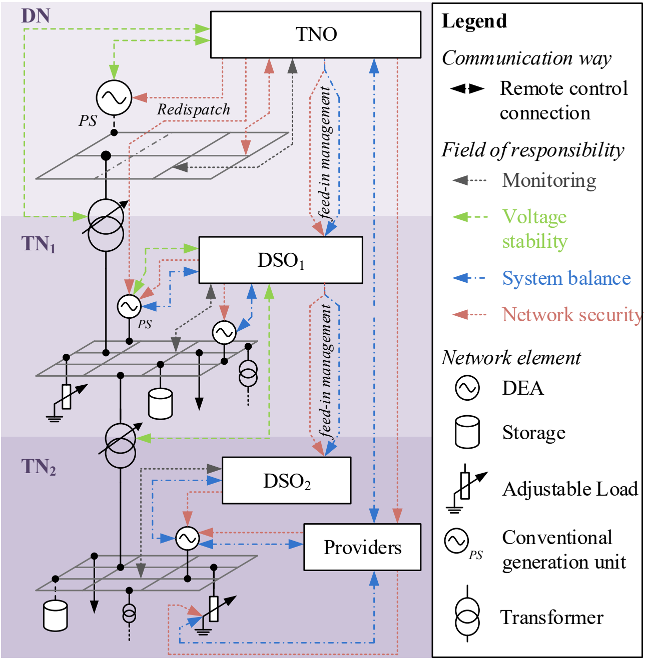

Fig. 2: Overview of existing responsibilities and interactions of participants [1]

The vertical operation is a concept for the coordination of grid operating services at different grid levels. It unites the advantages of two network operation approaches. First is the hierarchical method and the second is the centralized approach. The focus of vertical network operation is on the aggregation, utilization, and coordination of operational flexibility across the various grid levels. The responsibilities of the grid given by the regulations, as described in this section, are not involved. The approach is based on the fundamental principle that the relevant local grid operator can take part in the control. The requirement here is that the measures introduced by the transmission grid operator should not lead to a deterioration of the grid condition. The grid instance is established, which can realize the interaction between the participants of the grid operation as shown in Fig. 2. This grid instance is referred to as the aggregator. In order to fulfil the system services as described in Chapter 1, the aggregator and the transmission system operator have various options at their disposition [7].

It should be mentioned that in this approach the possibility of direct access by the transmission system operator to the technical units is facilitated. The advantage of vertical grid operation in contrast to other grid operation is the straightforward integration into the existing grid operation management system. The responsibilities and competencies with regard to the measures and tasks described in Fig. 3.3 remain untouched. The legal limits defined by the EnWG and EEG are also taken into account.

III. CONCEPT FOR AVODING OF PROTECTION INFLUENCES

The following chapter presents a concept for recognizing grid congestion caused by grid protection at an early time in the case of a demand for system services from the distribution grid using the example of secondary control power. The concept is based on vertical network operation.

In the future, transmission and distribution system operators and aggregators will, therefore, need an opportunity to verify whether the control power, as stated in the quantities offered, can also be freely supplied at the time of the retrieval. If restrictions occur due to limitations in the grid, e.g. on account of disturbances, utilization of operating resources at their limits or due to overloading of the grid and associated topology shifts due to protection trips, such restrictions must be recognized and then identified. In the following, an approach is presented how limitations by the protection systems in the grid to the provision of system services can be identified using the example of secondary control power. It is also discussed how the individual participants in the energy sector can deal with this acquired information.

If a fault occurs, for example, due to a power plant failure or the disconnection of a large load in the grid, an imbalance occurs in the system. This imbalance leads to a deviation of the mains frequency from its nominal value. The power-frequency control reacts to this deviation and, if possible, restores the balance between supply and consumption. Since this balancing must take place promptly, the operations are mostly automatic. In order to respond, for example, by adjusting the switchable loads or the feed-in of renewable energy systems in the distribution grid, the current grid status must be checked. This network status includes the current switching positions of disconnectors and circuit-breakers, the load of the grid and the current parameters of the protection technology. According to [19], each distribution system operator is responsible for its respective grid area by obtaining detailed information.

If control power, according to the proposals, is requested using the tenders defined on the market, possible restrictions in the grid may be identified on the basis of the forecasts made in step 7. In order to minimize the inaccuracies of the forecasts, this investigation is repeated in step 11 in order to identify possible problems with the current state of the grid when providing the compensation power.

Tab. 1: Information exchange between operators and distribution system operators according to DistributionCode [19].

Information on operational planning	Information on operational management
• feed-in schedules • reactive power capability • Start-ups and shutdowns	• Measured values for currents, voltages, powers • Limited values for active and reactive power • Switch positions and step controller positions • protection signals • Start-up and shutdown of the technical unit

In this case, the transmission system operator or its control equipment defines the setpoint of the control power for frequency. This set point is forwarded to the operators and the distribution system operators by the aggregator. The operator transmits the set point to the technical units. Based on the behavior of the technical units, the distribution system operator can carry out a load flow calculation of its network based on the current status. An exchange of information between the operators of the technical units and the distribution system operator is necessary in order to obtain information on the current state of the grid. According to [19], it is required to provide information as listed in Tab. 1 in the 110kV grid. Thus, it will be necessary in the future to exchange system services in the lower voltage levels between plant operators and distribution grid operators in order to retrieve system services from the distribution grid.

At the same time, the distribution grid operator also informs the plant operators if there is a fault in the grid. In addition, it informs which generation plants should not increase their feed-in during this period in order to avoid e.g. a tripping protection. The detection of such grid faults requires a further expansion of automation and information technology so that the operational management tasks required of the distribution grid operator can be fulfilled. According to the Distribution Code [19], these tasks include monitoring and adherence to the system variables current and voltage, controlling the switching state and operating the necessary measuring and counting devices. The distributor is thus obliged to collect the information required for the load flow calculation.

If the distribution network operator has carried out the load flow calculation (LFR) with current parameters of the grid, further system parameters can now be determined. These system parameters, for example, voltage and current, are used by the protection systems in the grid as protection criteria. In order to present this clearly, a state vector protection for the current state of the protective devices and a state vector for the current state of the grid can be determined. In order to present this clearly, a state vector $\boldsymbol{x}_{\text{protection}}$ for the current state of the protective devices and a state vector $\boldsymbol{x}_{\text{grid}}$ for the current state of the grid are generated for the respective connection. The status of the network refers to the system dimensions.

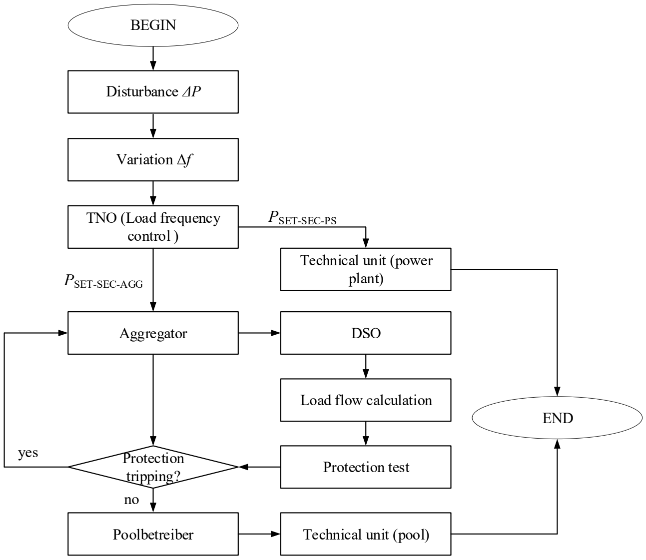

Fig. 3: Flowchart of the proposed concept

After the system parameters have been identified, a test is carried out using a function to verify whether protective devices are tripped. When a tripping occurs and at what time, and what maximum transfer power is possible at the network connection point without causing a change in the topology, it is returned to the aggregator as a reset value. The aggregator must decide, according to the result of the reset value, whether it is necessary to distribute the setpoint to other operators based on a set value in order to provide the secondary control power. This distribution may be necessary to avoid any tripping of the protective devices and therefore to provide the control power without changing the topology. It should be mentioned here that the distribution grid operator does not transmit the status and parameters of its own grid, only if there are problems with the protection systems in its grid area and the amount of secondary balancing power that can be provided from its grid area at the grid connection point. The network security and data protection of the own grid has a high priority here. The transmission network operator is not included, which is similar to the previous procedure described in Chapters 2. It issues an invitation to tender for the quantity of balancing power required on the market at a fixed price and the respective supplier must ensure that the available quantities are provided in accordance with its capabilities.

The advantage of the proposed concept is that it can be used in planning as well as in operational management. In the pre-qualification phase, the aggregator and the distribution grid operator can determine how much power can be retrieved, and it is also possible to test the current state of the grid when providing the secondary control power. In this way, possible faults with regard to the mentioned problems in chapter 2 can be detected by decentralized supply to the protection systems and hence, allow the smooth operation of the power-frequency control.

The disadvantage in the dynamic considerations include the inaccuracies of the model and the delay caused by the load flow calculation. These make the dynamic processes t<1s, which is impossible or even unrealistic. This means that, according to the present concept, no investigations can be carried out with regard to the provision of primary control power.

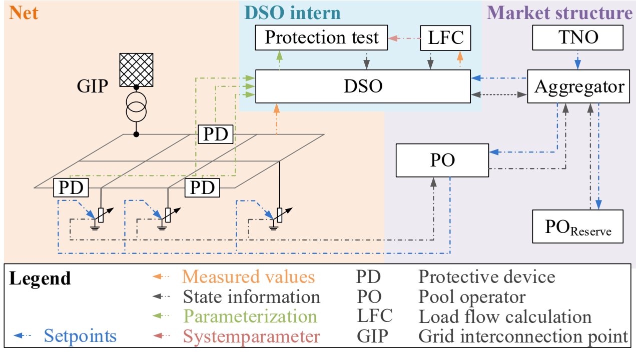

Fig. 4: Concept for effects of protection

IV. SIMULATION

The reference grid is needed to test the proposed approach and to monitor the impact of a protection tripping on the provision of system services. The medium voltage reference network according to Cigré Benchmark Systems for Network Integration of Renewable and Distributed Energy Resources European Configuration [45] is used. This represents, as shown in Fig. 4, an urban cable network (grey background) with a rural environment with overhead lines (green background). There are 15 nodes at which possible loads can be parameterized. The grid is operated as a closed ring (in Fig. 4 the red T stands for an open isolator and the green T for a closed isolator), as is usual in medium voltage with regard to (n-1) safety [7].

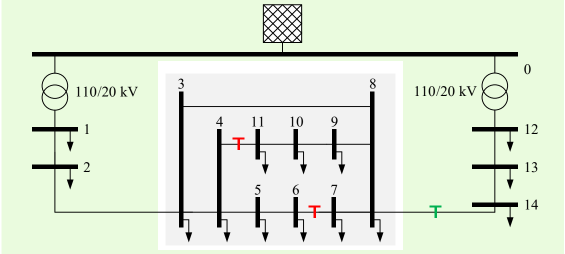

Fig. 5: Reference grid for medium voltage Cigré Benchmark System European Configuration according to [7], [45]

In the medium-voltage field, the protection systems are required to have a high degree of supply reliability and the requirements must be met by the plants and protection systems. In addition, research on the effects of decentralized feeders in accordance with [15] has been improved to such an extent that protection tripping due to overload will not occur, even when system services are provided from this voltage level. Therefore, the consideration of the low-voltage grid was extended, since here loads, for example, electric cars in private households, no permission is required, and neither is a load sharing between household and grid operator. In Europe, low-voltage networks are mainly designed as radial networks. Due to the geographical extent and the low density of loads in rural areas, low-voltage networks in Germany are designed as radial networks. The designs can vary between underground cables and overhead lines. A low-voltage network is normally fed by a local transformer. The above conditions are illustrated in the low-voltage network according to [45] [7]. The reference network, as shown in Fig. 5, contains 19 nodes, 12 of which are designed as cable distributors to which no loads are connected.

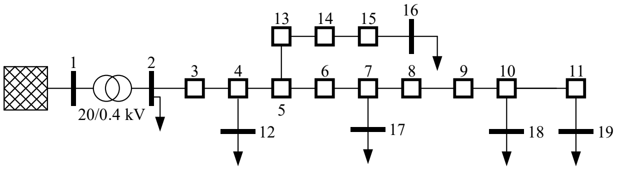

Fig. 6: Reference grid for low voltage Cigré Benchmark System European Configuration according to [7], [45]

Thus, five loads can be estimated in this network, which can also contain storage and electric vehicles as well as decentralized injection units. According to [2], these will in future be able to provide power supply and will be referred to as technical units as proposed by [7]. The parameterization of the networks and the loads they contain is based on the investigations, which is carried out in [7].

The threshold values are selected previously based on the maximum load according to [7] by a load flow calculation and the resulting current flows in the conductors since the protection in low-voltage networks is designed for the maximum load [6]. A distance of 1.6 between the threshold values is selected on the basis of selectivity. This ensures selective triggering [36]. The selected safety devices according to this principle are shown in Tab. 5.2. The NH protections are selected as full-range protections (label g). This means for lines on the basis of the nominal current rules described above and for the local network transformer (gTr) by selection from dimensioning tables.

To ensure the setpoint value as accurately as possible, it is transmitted to the technical units, which comes from a model in that a disturbance can be applied to a control area in Germany and from this, the frequency curve, as well as the primary control power and the secondary control power, can be calculated. The primary control power is provided here by a power plant model and the secondary control power by a pool of electric vehicles, which can be used for charging on the one hand and for feeding on the other hand. The setpoint for power change is taken from the value for the pool and scaled to a maximum change of ΔP_{max}=10kW per electric vehicle in order to obtain a feasible value for a vehicle in the low-voltage grid [47]. Depending on the scenario, these are distributed among the nodes in order to investigate the behaviour of the network shown in Fig. 5.2 and the protective elements contained in it. In the assessed scenarios, the electric vehicles are regarded as loads in the state of charge instead of as generators.

In the future, the power supply will be dominated by decentralized generation plants and new storage facilities [2]. These innovations are to be found mainly at the distribution grid. New challenges are brought with them, for example, new load conditions of the grid. In this chapter, various scenarios are used to test whether the concept presented can work. This test is carried out by the simulation explained in the previous chapter. The main task here is to analyze the transfer power at PCC including the triggering at the nodes of the low-voltage grid level.

Tab. 2: Selected and validated scenarios

Scenario	Load	Electric vehicles	Connection node for electric vehicles
A	low load	0	-
B	low load	1	12
C	low load	3	12, 16, 17
D	low load	5	12, 16, 17, 18, 19
E	heavy load	0	-
F	heavy load	1	12
G	heavy load	3	12, 16, 17
H	heavy load	5	12, 16, 17, 18, 19

The scenarios presented in Tab. 2 for a fault of P=3000MW at t=0 s are more closely examined. A positive P means that negative control energy is required. Negative regulation power can either be generated by reducing the feed-in or by increasing the load. Since in prospective scenarios, the power generated by renewable energies should not be reduced as far as possible, just as it is now decided by the EEG, an intelligent load management based on the example of electric vehicles is considered in this paper. This means that if generation is too large, it will be used to charge storage facilities in the grid [2]. In the simulation, 10 pools of electric vehicles with a total power of P_{EVges}=500 MW are simulated. This corresponds to 50,000 electric vehicles with a charging capacity of P_{EV}=10 kW.

When the load factor is 100%, it can be assumed as the heavy load. These loads were taken from [7]. Accordingly, the load factor of 20% will be assumed similar to [11]. In the condition of the heavy load and a technical unit at node 12, as the simulation in scenario F, the protective element F4-12 is stimulated and triggered, as shown in Fig. 6. The activation of the technical unit results in the rising of conductor current at t=25.3 s due to the load increase. The excitation occurs at t=48 s since the maximum current has arrived. The gradient of the phase current becomes smaller after the excitation and the phase current reaches a stationary terminal value. Since the maximum value is still overstepped, the protection system is triggered after the set delay time of 5 seconds. The triggering happens at time t=53.1 s.

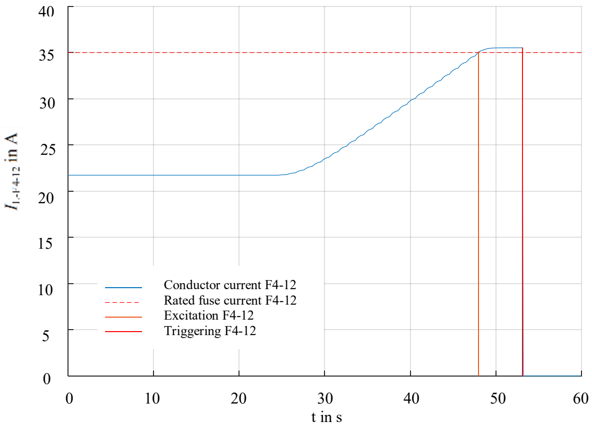

Fig. 7: Scenario F: Triggering of the protection system F4-12

In scenario H, in contrast to scenario F, two additional technical units are activated at nodes 18 and 19. As in scenarios F, the triggering by protective element F4 12 is expected. The protective elements F7 8, F4 12 and F10 18 were excited by an overcurrent during activation of the technical units. The protective element F4 12 is excited at time t=47.8 s, the difference of 0.2 s seconds is due to the sampling by the S function. Like the previous scenarios, this protective element is triggered in the case of a heavy load. The protective element F10 18 is also triggered at the time t=48.2 s. According to the selectivity, the protective element F7 8 is excited, but the other protective elements are triggered, causing the protective element to reset.

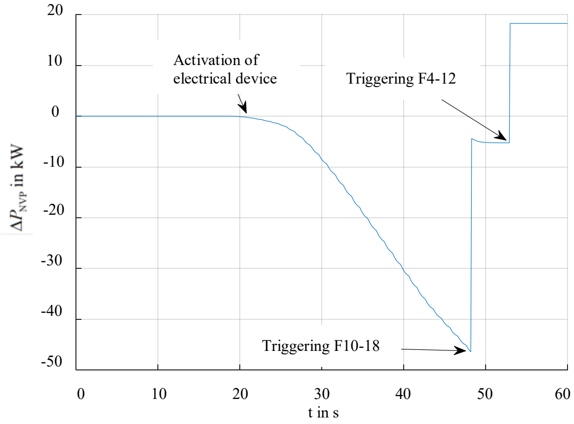

Fig. 8: Scenario H: Power Change at PCC

Due to the two triggering operations, the change in power results in a stepped curve from the time of the first triggering. As shown in Fig. 7, the power at the PCC drops here on the basis of the setpoint up to the triggering of the protective element F10 18. Here the power change at the PCC climbs from 46.25 kW to 4.42 kW, which corresponds to the connected load and the power change of the technical unit.

This is followed by a further reduction of the load since at node 12, the load continues to follow the setpoint. Then, similar to the other heavy load cases with load increase, the load at node 12 is reduced by triggering the protective element F4-12.

The triggering of the protective devices of individual branches can affect the frequency stability. According to the current selectivity setting by using the nominal current, the protective device on the power supply unit is excited, but not triggered. The results of the simulation are clearly presented in Tab. 3. The heavy load scenarios can be assumed to be the worst case. Thus, the probability of impact is fairly low. The charging of more than two electric vehicles simultaneously in a low-voltage grid with only one jet is currently still regarded as improbable, but trends towards more electric vehicles can be recognized and such a load should be expected in the future [49].

Tab. 3: Evaluation matrix der Simulation

🟧	Trigger	**Scenario**							
🟩	Excitation	**A**	**B**	**C**	**D**	**E**	**F**	**G**	**H**
▨	Normal operation	**low-load**				**heavy-load**			
Protective device	**F1-2**	▨	▨	▨	▨	▨	▨	▨	▨
	F2-3	▨	▨	▨	▨	▨	▨	▨	▨
	F4-5	▨	▨	▨	▨	▨	▨	▨	▨
	F4-12	▨	▨	▨	▨	▨	🟧	🟧	🟧
	F5-6	▨	▨	▨	▨	▨	▨	▨	▨
	F5-13	▨	▨	▨	▨	▨	▨	▨	▨
	F7-8	▨	▨	▨	▨	▨	▨	▨	🟩
	F7-17	▨	▨	▨	▨	▨	▨	▨	▨
	F10-11	▨	▨	▨	▨	▨	▨	▨	▨
	F10-18	▨	▨	▨	▨	▨	▨	▨	🟧

V.CONCLUSION

The simulated scenarios led to the conclusion that the protective devices in the low-voltage grid are primarily designed for the event of a fault. In order to observe a triggering of these protection elements, the grid must be heavily overloaded. The proposed concept can help the distribution system operator to detect such overloads and the effects of the protective devices before providing the secondary control power from his own system. In the scenarios at the nodes to which a controllable load can be connected, it was used to increase the load in the network until a triggering occurs. The influence of this triggering can be observed based on the power at the PCC point and thus, it can be connected between the distribution system operator and the aggregator. The aggregator now has the option of correcting the setpoint for this distribution network for the power change at which there is no influence by the protection systems. So that the available secondary control power can be used completely for power-frequency control. According to the principle, the secondary control power would be operated from a reserve pool. This would ensure that the setpoint requested by the transmission system operator can be fulfilled. In the low-load scenarios, there was, as expected, no effect from the protection systems. Here, the system dimensions were shown in the prescribed ranges. The voltage moves within a tolerance band of ±10 % around the nominal voltage and the conductor currents did not excite or trigger the protective devices.

The applicability of the approach can be verified by the simulation. In order to provide sufficient secondary control power in the future, it is necessary to resort to the capacities in the distribution grid. The processing of current measurement data in the grid and their use for operational planning is a meaningful method to react to changes in the distribution grid. In this way, it is possible to identify tendencies towards endangered states at an early time and to implement suitable preventive measures to ensure system stability. To achieve this with the increasing volatility of the feeding components and changing loads, it is necessary to take the protection measures within the grid in considerations. With the help of the approach, the influences of the protective devices can be identified and eliminated. Thus, it is possible to react preventively to current restrictions caused by the grid conditions. Furthermore, it is also possible to carry out simulations in the intra-day area by integration into a dynamic model in order to identify tendencies to endangered states in plant management.

REFERENCES

[1] R. Schwerdfeger: “Vertikaler Netzbetrieb,” Ph.D. dissertation, Dept..Power System. Ger., Univ. TU Ilmenau, 2016.

[2] Cao, Wenchao; Zhang, Xuan; Ma, Yiwei; Wang, Fred: Stability criterion and controller parameter design of radial-line renewable systems with multiple inverters. In: 2016 IEEE Applied Power Electronics Conference and Exposition (APEC). Long Beach, CA, USA, pp. 2229–2236.

[3] Chen, Jikai; Ma, Xiuwei; Li, Yang: Dynamic interaction analysis of two-parallel active power filter. In: 2016 China International Conference on Electricity Distribution (CICED). Xi'an, China, pp. 1–5.

[4] He, Jinwei; Li, Yun Wei; Bosnjak, Dubravko; Harris, Brent (2013): Investigation and Active Damping of Multiple Resonances in a Parallel-Inverter-Based Microgrid. In: *IEEE Trans. Power Electron.* 28 (1), pp. 234–246.

[5] Wang, Xiongfei; Blaabjerg, Frede; Wu, Weimin (2014b): Modeling and Analysis of Harmonic Stability in an AC Power-Electronics-Based Power System. In: *IEEE Trans. Power Electron.* 29 (12), pp. 6421–6432.

[6] Wan, Cheng; Huang, Meng; Tse, Chi K.; Ruan, Xinbo (2015): Effects of Interaction of Power Converters Coupled via Power Grid. A Design-Oriented Study. In: *IEEE Trans. Power Electron.* 30 (7), pp. 3589–3600.

[7] Yu, Yanxue; Li, Haoyu; Li, Zhenwei: Impedance modeling and stability analysis of LCL-type grid-connected inverters with different current sampling schemes. In: 2016 IEEE 8th International Power Electronics and Motion Control Conference (IPEMC 2016 - ECCE Asia). Hefei, China, pp. 974–981.

[8] Parker, Stewart Geoffrey; McGrath, Brendan P.; Holmes, Donald Grahame (2014): Regions of Active Damping Control for LCL Filters. In: *IEEE Trans. on Ind. Applicat.* 50 (1), pp. 424–432.

[9] M. Schärfenberg, *Untersuchung der Wechselwirkungen zwischen leistungselektronisch integrierten Netzelementen im Verteilernetz*, Masterarbeit, Ilmenau, 2017.

[10] M. Schärfenberg, T. Jiang, S. Schlegel, D. Westermann, „Development of a Voltage-dependent Stabilizer for a converter dominated distribution grid“, ISGT Europa, Turin, 2017.

[11] S. Yang, F. Schaller, B. Schönfeld, S. Schlegel, B. Fischer, T. Jiang, S. Nicolai, S. Prinz, M. Malsch, D. Westermann, P. Bretschneider, „A cross voltage-levels simulation approach for interaction analysis in converter-dominated distribution networks “, Bonn, 2017.

[12] Y. Liu, *Untersuchung der Wechselwirkungen in Verteilnetzen mit hohem Anteil umrichtertechnologiebasierter Erzeuger und Lasten*, Ilmenau, 2016.

[13] Cigré Working Group B4.57, “Guide for the Development of Models for HVDC Converters in a HVDC Grid,” Cigré, 2014

[14] CIGRE, "Benchmark Systems for Network Integration of Renewable and Distributed Energy Resources", Task Force C6.04.02, 2010

A comparative study of various modulation techniques for grid-connected and standalone 3L-NPC converter

Bazil Nawaz, Mohamed Abdelrahem, Ralph Kennel
Institute for Electrical Drive Systems and Power Electronics, Technical University of Munich (TUM)
E-mail: bazil.nawaz@tum.de, mohamed.abdelrahem@tum.de, ralph.kennel@tum.de

***Abstract*—This paper presents the operation and control of a three level neutral point clamped inverter under commonly used modulation techniques. First, simulations for standalone inverter with various modulation techniques are investigated in terms of their switching frequency, inverter input voltage and modulation index. Then, a grid and filter is connected and most of the modulation techniques are simulated for voltage oriented control, which controls the power injected in the grid. A harmonic analysis is made in each case and the objective is to check which modulation technique results in the lowest THD.**

Keywords—SPWM, SVM, CBSVPWM, THIPWM, VOC, 3L- NPC, standalone 3L-NPC, grid connected 3L-NPC

I. INTRODUCTION

Over the years, renewable energy sources such as wind, biomass and PV are increasing their share of energy supply. Especially, wind power which reached a staggering 600 GW by the end of 2018, seeing an increase of installed capacity by about 10% for 2 years in a row [1]. These growing renewable energy trend has demanded more high voltage and high power as the cost per unit of the system drops at higher ratings (for example 3 kV offshore wind energy system). Therefore, as the voltage level of the power converter has to increase to medium voltage, multilevel inverters become a more attractive solution.

In comparison to a 2-level inverter, multi-level topology has better properties such as reduced voltage stress on the switches (half of the DC link voltage in case of 3L-NPC), lower switching losses, better output waveform quality with improved harmonics. In multi-level inverters, 3L-NPC has caught a lot of attention in literature due to being more economical and easier to implement compared to higher level inverters. [2] – [7]

A general 3L-NPC is shown in figure 1 and the three possible levels and operation are shown in the table I.

Table I. Switching states of the 3L-NPC

V_{yo}	S_{x1}	S_{x2}	S_{x3}	S_{x4}
$+V_{dc}/2$	ON	ON	OFF	OFF
$-V_{dc}/2$	OFF	OFF	ON	ON
0	OFF	ON	ON	OFF

The main issue for a 3L-NPC that can arise is controlling the neutral point voltage, which varies according to the modulation technique used. The imbalance of neutral voltage arises due to dead time, asymmetrical loads, variation in timing of gate signals and tolerances of the capacitors [8] – [9]. For a fair comparison of all the modulation techniques, it will be assumed that the neutral point voltage is controlled and equivalent to 0 V. So, instead of the capacitors, C_1, and C_2, DC voltage sources of equal values will be used.

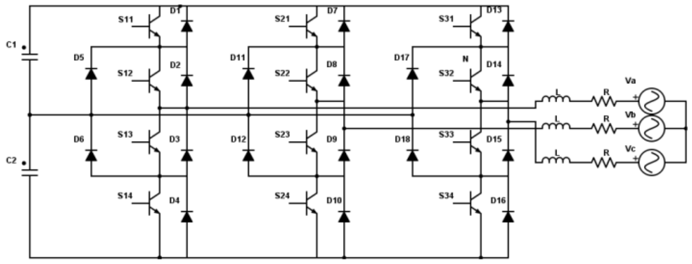

Fig. 1. A general 3L-NPC inverter

II. MODULATION TECHNIQUES OF A 3L-NPC

There are various methods to control the fundamental voltage generated by the 3L-NPC. It is well known that the performance of the inverter depends on its modulation strategy. The switching losses and harmonic contents in particular are of utmost interest. To control the switching pattern of the switches most commonly used techniques will be implemented and tested in Simulink.

A. Sinusoidal pulse width modulation (SPWM)

The principle of SPWM involves comparing a reference/modulation signal (sine wave) which is desired at the output of the inverter to a high frequency triangular wave (carrier wave). In our case, two gating signals are required as S_{x1} and S_{x3} are complementary to each other, as are S_{x2} and S_{x4}. For two gating signals, one sine wave and two carrier signals are chosen. Figure 2 shows the waves that will be compared. The upper triangular wave can be labelled as ‘c_1’, lower one as ‘c_2’ and modulation signal as ‘m_1’. Table II shows the algorithm that will be used to control the switches.

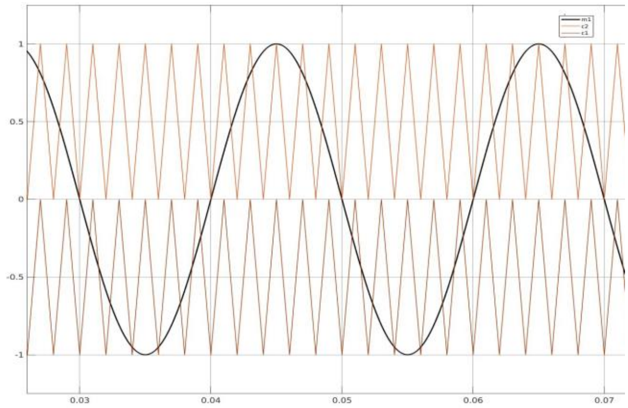

Fig. 2. SPWM technique

Table II. Algorithim to control the switches

Logic	**Switch state**
$m_1>c_1$	S_{x1} ON
$m_1<c_1$	S_{x3} ON
$m_1>c_2$	S_{x2} ON
$m_1<c_2$	S_{x4} ON

Another important parameter is the amplitude modulation index (m) which is the ratio of the amplitude of the waves. If the modulation index is greater than 1 the system is in the over-modulation range. Conversely, it would be in under-modulation region.

$$m_1 = A\sin(\omega t) \tag{1}$$

Where A = amplitude of the sine wave, ω = angular frequency of the sinusoidal wave

$$m = A / K \tag{2}$$

Where K= amplitude of a triangular wave
Thereby the output voltage of the inverter is related as

$$V_o = mV_{dc} \tag{3}$$

Where V_{dc} is the DC link input voltage.

B. *Third harmonic injection pulse width modulation (THIPWM)*

THIPWM involves injecting a third harmonic signal to the modulating signals of the SPWM to get rid of the third harmonics of the output current/voltage. The modulating signals are mathematically represented as given in equation

$$\begin{aligned} m_1 &= 1.15\sin(\omega t) + 0.19\sin(3\omega t) \\ m_2 &= 1.15\sin(\omega t - 2\pi/3) + 0.19\sin(3\omega t) \\ m_3 &= 1.15\sin(\omega t + 2\pi/3) + 0.19\sin(3\omega t) \end{aligned} \tag{4}$$

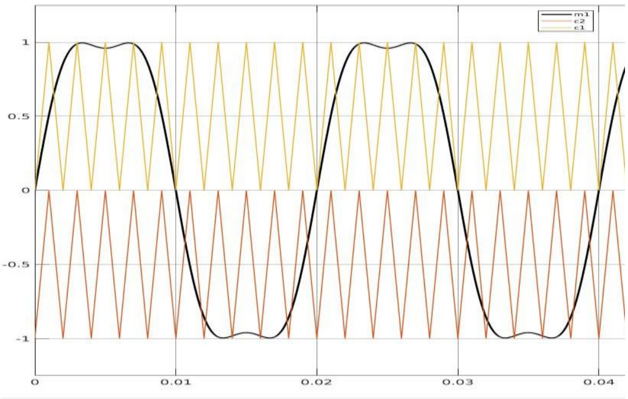

Fig. 3. THIPWM technique

Furthermore, a dq transformation of the modulating signal shows a 15% increase in the amplitude, which means 15% extension in the modulation range as compared to SPWM.

C. *Space vector modulation (SVM)*

The 3L-NPC has a total of 19 vectors and 27 switching states in the α-β frame. The frame consists of a hexagonal structure which can be divided into 6 sectors. Each sector consisting of 4 regions as shown in the figure below. [10]

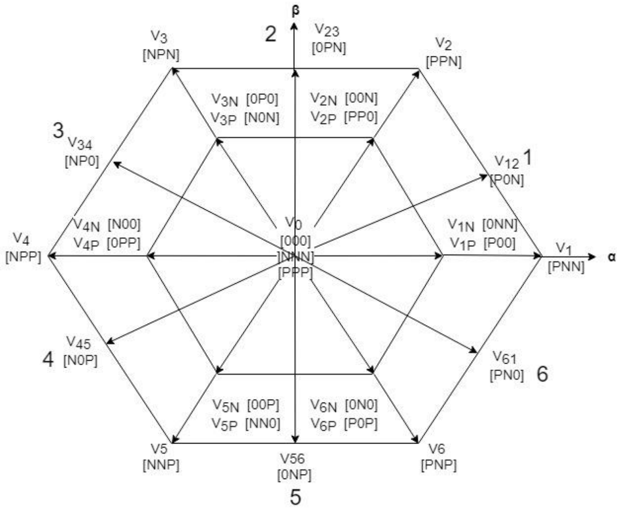

Fig. 5. 3L-NPC space vector diagram

At a sampling time, T_s, the reference voltage vector can fall into one of the sectors and one of the regions. This vector can be synthesized by the three nearest voltage vectors and the dwell time can be calculated [10]. All 27 switching states are assigned to the vectors according to their definition. The nearest three voltage vector could be a vector in $V_0 - V_{18.}$ V_0 is called the zero vector and there are three of them, which are assigned 3 switching state each. $V_1 - V_6$ are called small vectors which are assigned 2 switching states each, example, $V_7 - V_{12}$ are called medium vectors and are assigned 1 switching state each. The remaining vectors are called large vectors and are also assigned 1 switching state each. Using the volt-second balance principle the following equations can be derived:

$$V_{ref}T_s = T_aV_x + T_bV_y + T_cV_z \tag{5}$$

$$T_s = T_a + T_b + T_c \tag{6}$$

$$m = V_{ref}\sqrt{3} / V_{dc} \tag{7}$$

Assuming the vector falls in one of the sectors, then depending on the region it falls in Ta, Tb, Tc can be found as mentioned in table IV.

After the dwell time calculation, the switching sequence is designed as shown in table III. The design needs to give the lowest switching step per period in order to minimize the switching losses. For example, if the reference voltage vector falls in region 1 of sector 1, the nearest three voltage vectors would be V_0,V_1,V_2 which corresponds to 7 switching states (3 from zero vector and 2 each from the two medium vectors). The design for sector 1 is shown in the table below, a similar design pattern is used for other sectors.

Table III. Switching sequence design

Switching sequence	
Region 1	V_{0N}- V_{1N} – V_{2N} - V_{0O} – V_{1P} – V_{2P} - V_{0P}
Region 2	V_{2P} – V_{1P} – V_7 – V_{2N} – V_{1N}
Region 3	V_{1N} – V_{13} – V_7 – V_{1P}
Region 4	V_{2N} – V_7 – V_{14} – V_{2P}

D. Carrier based space vector pulse width modulation (CBSVPWM)

The CBSVPWM is implemented in practice to reduce the switching losses caused by other modulation techniques. Moreover, the computation burden involved with lookup tables, dwell time calculations and switching sequence design is also overcome by implementing this method as it involves finding a zero sequence vector which is added in the modulation signal to achieve similar switching as the space vector modulation but with reduced switching losses as discussed in [10]. Figure 4 shows a block diagram of the method to be implemented.

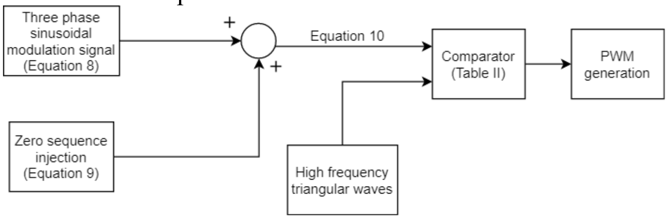

Fig. 6. CBSVPWM PWM generation block diagram

The equations defining the three phase modulation signals are as follows.

$$m_1 = m\sin(\omega t)$$
$$m_2 = m\sin(\omega t - 2\pi/3) \qquad (8)$$
$$m_3 = m\sin(\omega t + 2\pi/3)$$

Where, m = amplitude modulation index and ω=angular frequency

The zero sequence injection voltage that needs to be added to the modulating signals can be calculated as follows:

$$m_0 = -\frac{\min(m_1, m_2, m_3) - \max(m_1, m_2, m_3)}{2} \qquad (9)$$

The modulating reference signal that would be compared to the high frequency carrier waves is as follows:

$$m_1^* = m_1 + m_0$$
$$m_2^* = m_2 + m_0 \qquad (10)$$
$$m_3^* = m_3 + m_0$$

Figure 7 shows the non-sinusoidal modulating signal and carrier wave that will be compared. Table II shows the algorithm used to control the switches.

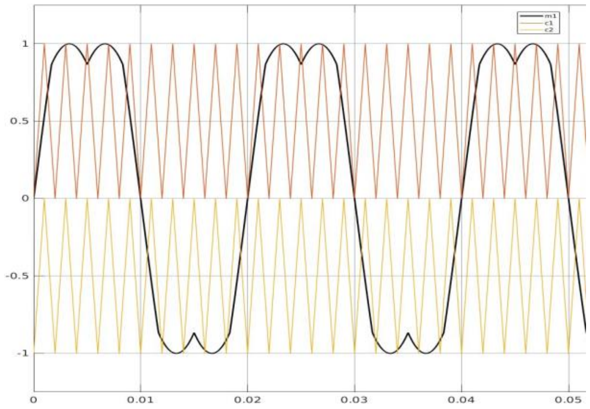

Fig. 7. The carrier and modulation wave being compared in Simulink

III. VOLTAGE ORIENTED CONTROL (VOC)

Up to now, the load connected at the output of the inverter was not discussed. For this simulation, it has been assumed that a grid is connected to the output and the active power injected into the grid needs to be controlled. The most commonly used control techniques are voltage oriented control (VOC) and direct power control (DPC). The purpose of these control techniques is to control the active and reactive power injected into the grid. A block diagram of the system to be simulated on Simulink is shown in figure 8. DPC uses a switching table in combination with hysteresis controller, instead of PI controller and PWM. [3] Since, the modulation techniques mentioned before need to be compared, only voltage oriented control would be considered in this paper.

The filter type used would be an L-filter and use of other filter types would be part of future work. The IEEE 519-2014 standards highlighted in table V and VI will be set as the standard for this simulation. Using Clark's transformation at the three output voltage, the angle can be obtained. Park's transformation is done to easily calculate the reference current vectors. Equation 11 shows the relationship between the active power, reactive power and current vectors [3].

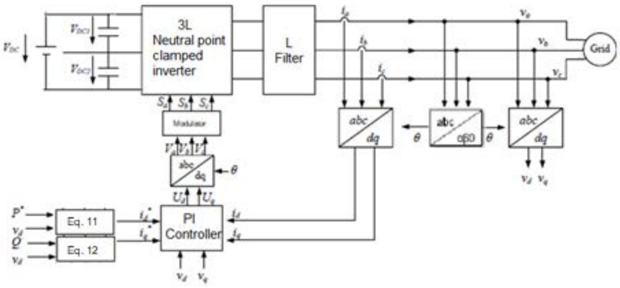

Fig. 8. Voltage oriented control technique block diagram

$$P = \frac{3}{2}(v_d i_d + v_q i_q) \qquad (11)$$

$$Q = \frac{3}{2}(v_q i_d - v_d i_q) \qquad (12)$$

Table IV. Dwell time calculation

Region	Ta	Tb	Tc
1	$T_s\,[2m\sin(\pi/3-\Theta)]$	$T_s\,[1 - 2m\sin(\pi/3+\Theta)]$	$2T_s m\sin(\Theta)$
2	$T_s\,[1 - 2m\sin(\Theta)]$	$T_s\,[2m\sin(\pi/3+\Theta) - 1]$	$T_s\,[1 - 2m\sin(\pi/3-\Theta)]$
3	$2T_s\,[1 - m\sin(\pi/3+\Theta)]$	$2T_s m\sin(\Theta)$	$T_s\,[2m\sin(\pi/3-\Theta) - 1]$
4	$T_s\,[2m\sin(\Theta) - 1]$	$2T_s m\sin(\pi/3-\Theta)$	$2T_s\,[1 - m\sin(\pi/3+\Theta)]$

In our case, we will not inject any reactive power to the grid (Q=0). Furthermore, by aligning the d-axis with the grid voltage vector, $v_q = 0$. Putting these assumptions into perspective, the equations can be simplified to as follows.

$$P = \frac{3 v_d i_d}{2} \tag{13}$$

$$i_q = 0$$

$$Q = -\frac{3 v_d i_q}{2} = 0$$

The equations above show that the reactive power is proportional to the q-component of current vector, whereas the active power is proportional to the d-component of the current vector.

The PI controller would be designed using the modulus optimum technique, the sampling time would be set to 50 µs, the parasitic resistance would be assumed to be 50 mΩ. The back calculation coefficient K_b would be set to 1, considering the anti-windup calculation. Design parameters would be selected using the following equations depending on the inductance value for each filter keeping the standard chosen in mind. [3]

$$T_k = L_{filter} / R \tag{14}$$

$$K_p = L / 3T_{sample}$$

$$K_i = K_p / T_k$$

Table V. Voltage distortion limits

Bus voltage V at PCC	**Individual harmonic (%)**	**Total harmonic distortion THD (%)**
V ≤ 1.0 kV	5.0	8.0
1 kV < V ≤ 69 kV	3.0	5.0
69 kV < V ≤ 161 kV	1.5	2.5
161 kV < V	1.0	1.5

*High-voltage systems can have up to 2.0% THD where the cause is an HVDC terminal whose effects will have attenuated at points in the network where future users may be connected

IV. RESULTS

For the first part, the 3L-NPC will be tested with a resistive-inductive load before using the voltage oriented control technique to see how each modulation technique compares to one another. In the second part, a grid would be connected as load and the voltage oriented control technique would be implemented using SVM, SPWM and CBSVPWM modulation techniques. Finally, the required filter inductance would be compared for each case.

A. Harmonic analysis – Standalone inverter

As seen in figure 9, the THD remains almost constant for input voltages of up to 10 kV for both phase currents and line to line voltages for all modulation techniques apart from SVM technique. Additionally, the THD remains constant for carrier frequencies up to 70 kHz for line to line voltages. The THD drops linearly as the inverter input voltage increases for both phase current and line to line voltage in SVM technique. For all remaining cases during under-modulation the THD decreases exponentially with increasing carrier frequency and modulation index. SVM shows the lowest THD, while SPWM shows the highest. During over-modulation CBSVPWM shows the lowest THD and in SVM the THD increases as the carrier frequency or modulation index increases.

Table VI. Current distortion limits

Maximum harmonic current distortion in percent of I_L						
Individual harmonic order (odd harmonics)[a, b]						
I_{SC}/I_L	3 ≤ h < 11	11 ≤ h < 17	17 ≤ h < 23	23 ≤ h < 35	35 ≤ h < 50	TDD
< 20[C]	4.0	2.0	1.5	0.6	0.3	5.0
20 < 50	7.0	3.5	2.5	1.0	0.5	8.0
50 < 100	10.0	4.5	4.0	1.5	0.7	12.0
100 < 1000	12.0	5.5	5.0	2.0	1.0	15.0
>1000	15.0	7.0	6.0	2.5	1.4	20.0

[a] Even harmonics are limited to 25% of odd harmonic limits above.

[b] Current distortion that result in a dc offset, e.g., half-wave converters, are not allowed.

[c] All power generation equipment is limited to these values of current distortion, regarding of actual I_{SC}/I_L where

I_{SC} = maximum short-circuit current at PCC

I_L = maximum demand load current (fundamental frequency component) at the PCC under normal operating conditions

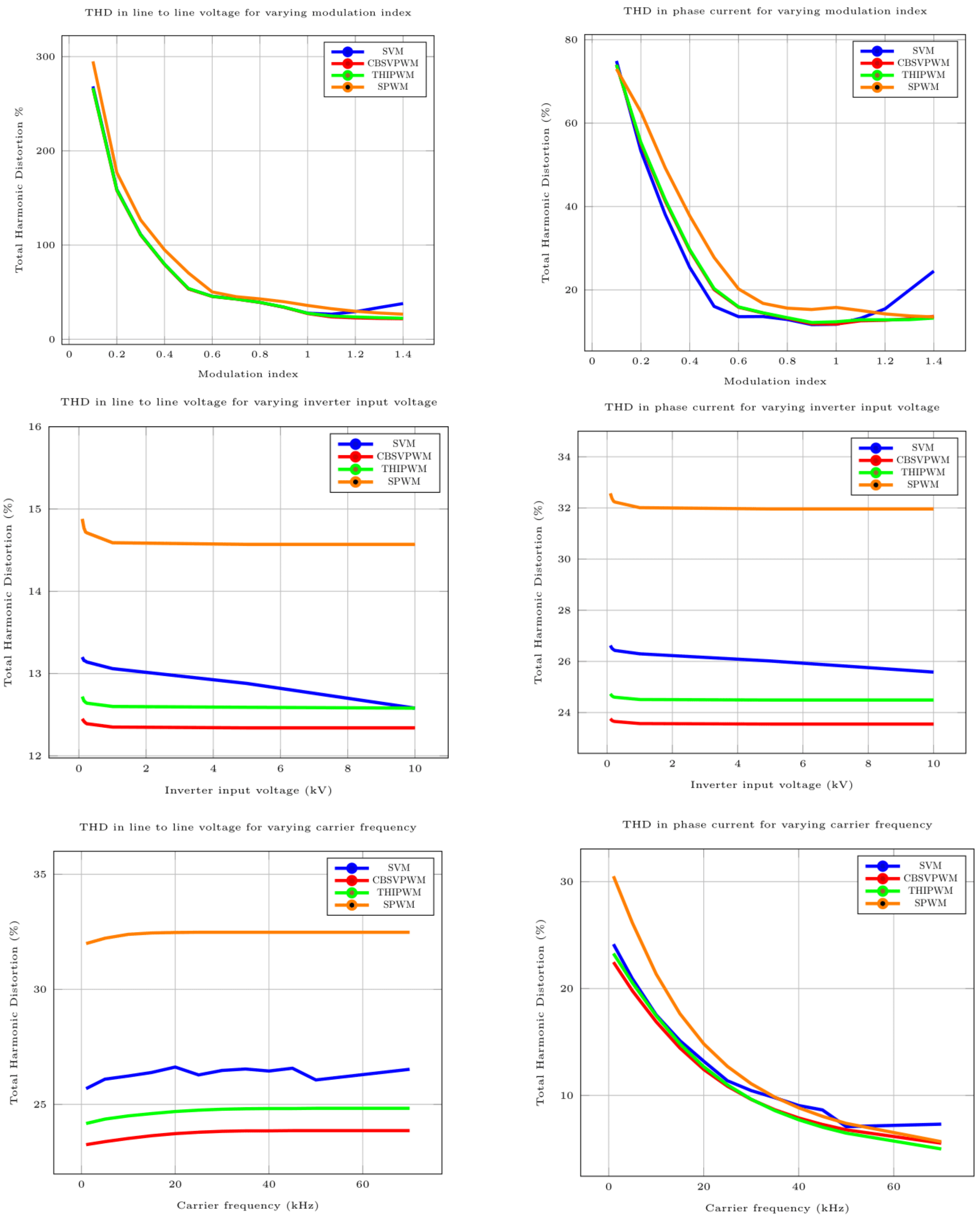

Fig. 9. THD in line to line voltage and phase current for various modulation index, inverter input voltage and carrier frequency

B. *Dynamic performance – VOC*

The power reference of the VOC is changed from 6 kW to 4 kW at 0.5s, as shown in figure 10. The controller reacts quickly and changes the output power to the reference value in about 1 ms for SPWM and CBSVPWM. However, it takes around 200 ms for SVM to reach the reference value. Hence, the control algorithm implemented shows good dynamic performance for SPWM and CBSVPWM.

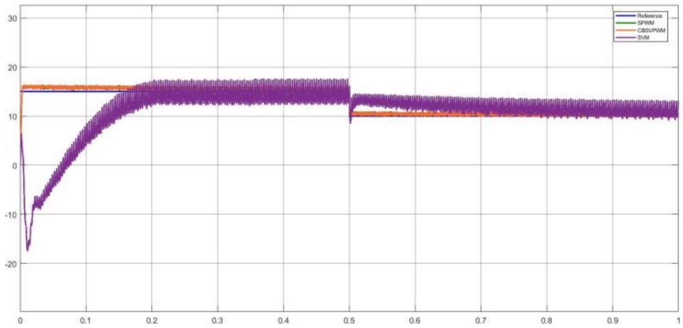

Fig. 10. Controller dynamic performance to changes in active power

C. *Harmonic analysis – VOC*

The simulations are made for 10 kW rated power. As seen by figure 11 SPWM and CBSVPWM show similar harmonic content, but the existence of even harmonics require a filter of 35 mH to stay within the standard chosen before. For SVM, a 110 mH filter is required, however the only dominant harmonic are the 5th and 7th order. This is because the operation of the VOC is in over-modulation region and the SVM performs poorly there as discussed before. The even harmonics are quite low in this case.

V. CONCLUSION

In this paper, commonly used modulation techniques for a 3L-NPC were implemented and simulated as a standalone and grid connected VOC inverter. In standalone inverter, the impact of carrier frequency, modulation index and inverter input voltage on THD of the line to line voltage and phase current was investigated. Firstly, SVM showed the lowest THD in under-modulation, whereas CBSVPWM showed the lowest THD in over-modulation. Secondly, the carrier frequency showed no significant impact on the THD of the line to line voltage for all modulation techniques. There was exponential decrease in THD of the phase current with increasing carrier frequency for all modulation techniques. Lastly, increasing the inverter input voltage up to 10 kV had no significant impact on the THD for all modulation techniques apart from SVM. There was a linear decrease in THD of both line to line voltage and phase current for SVM technique.

For grid connected VOC inverter, SVM showed poor dynamic performance, whereas SPWM and CBSVPWM showed good dynamic performance. SPWM and CBSVPWM phase current harmonic content were the lowest for an L-filter. For these two techniques, apart from odd harmonics, there are also even harmonics present in the phase currents which further deteriorate there steady state performance. To stay within the chosen IEEE standards, a high inductance is required for both these modulation techniques to attenuate these even harmonics. Furthermore, as seen in the results section, only 5th and 7th order harmonics are dominant and deteriorate the steady state performance of SVM. Consequently, other filters types such as LCL filter need to be tested to see if SVM technique can come close to the performance of a SPWM/CBSVPWM. This would be part of future work. For this study, under grid connected 3L-NPC converter, SPWM and CBSVPWM techniques showed the best performance.

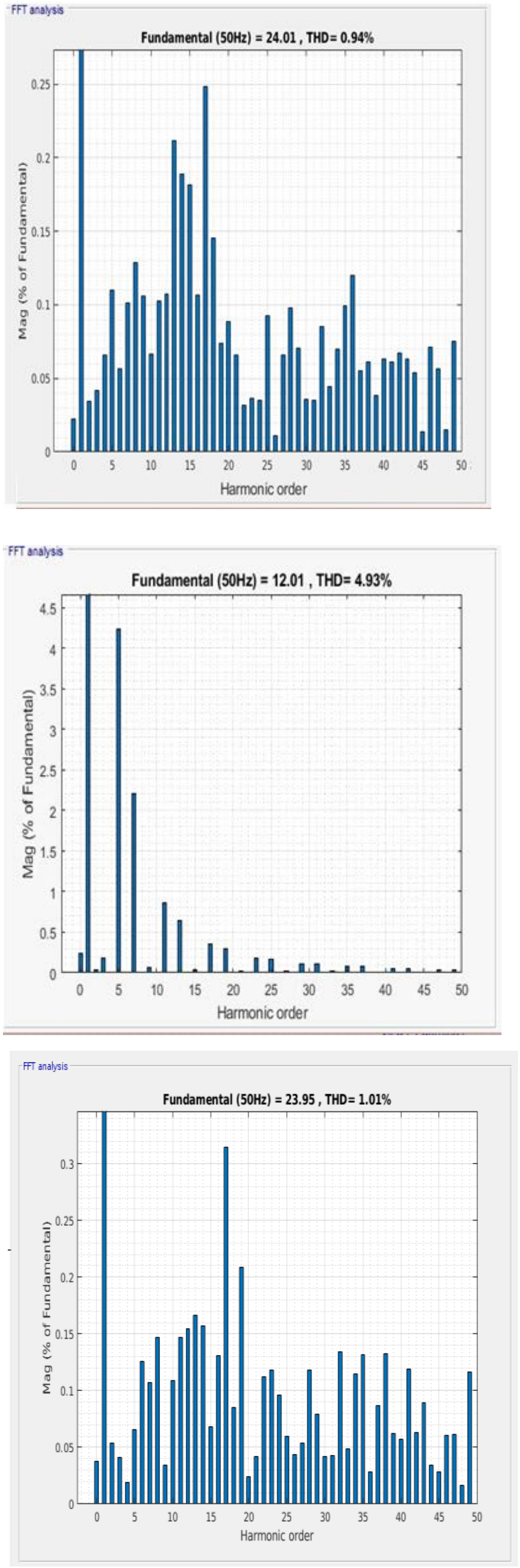

Fig. 11. FFT of SPWM, SVM and CBSVPWM phase currents respectively

REFERENCES

[1] "Wind Power Capacity Worldwide Reaches 600 GW, 53,9 GW added in 2018" Feb. 25, 2018 [online] Available at: https://wwindea.org/blog/2019/02/25/wind-power-capacity-worldwide-reaches-600-gw-539-gw-added-in-2018/ [Accessed 19 Apr. 2019].

[2] J. Rodriguez, S. Bernet, B. Wu, J. O. Pontt, and S. Kouro, "Multilevel voltage-source-converter topologies for industrial medium-voltage drives," *IEEE Trans. Ind. Electron*., vol. 54, no. 6, 2007.

[3] S. Alepuz, S. Busquets-Monge, J. Bordonau, J. Gago, D. Gonzalez, and J. Balcells, "Interfacing renewable energy sources to the utility grid using a three-level inverter," *IEEE Trans. Ind. Electron*., vol. 53, no. 5, 2006. J. M. Carrasco, E. Galvan, R. Portillo, L. G. Franquelo, and J. T. Bialasiewicz, "Power electronic systems for the grid integration of wind turbines," in *Proc. IECON*, 2006.

[4] J. M. Carrasco, E. Galvan, R. Portillo, L. G. Franquelo, and J. T. Bialasiewicz, "Power electronic systems for the grid integration of wind turbines," in *Proc. IECON*, 2006.

[5] F. Blaabjerg, R. Teodorescu,M. Liserre, and A. V. Timbus, "Overview of control and grid synchronization for distributed power generation systems," *IEEE Trans. Ind. Electron*., vol. 53, no. 5, 2006.

[6] T. Atalik, M. Deniz, E. Koc, C. Gercek, B. Gultekin, M. Ermis, and I. Cadirci, "Multi-dsp and -fpga based fully-digital control system for cascaded multilevel converters used in facts applications," *IEE Trans Ind. Inf.*, vol. PP, no. 99, p. 1, 2012

[7] J. R. Rodriguez, J.W. Dixon, J. R. Espinoza, J. Pontt, and P. Lezana, "PWM regenerative rectifiers: State of the art," *IEEE Trans. Ind. Electron*., vol. 52, no. 1, 2005.

[8] Lange, A., Zimmermann, M. and Piepenbreier, B. "Neutral Point Balancing for Three-Level Neutral Point Clamped Inverters Under Light Load Conditions" *IEEE 21st International Conference on Electrical Machines and Systems (ICEMS),* 2018

[9] Sprenger, M., Barth, T., Alvarez, R., Tannhaeuser, M. and Bernet, S. "Experimental verification of direct dead-time Control and DC-link neutral-point balancing of a three level neutral-point-clamped (3L-NPC) VSC" *IEEE Energy Conversion Congress and Exposition*, 2013

[10] Kitidet, H. and Kumsuwan, Y. "Reduction of switching step/commutation using unipolar CB-SVPWM for three-level NPC inverters" *IEEE 13th International Conference on Electrical Engineering/Electronics, Computer, Telecommunications and Information Technology (ECTI-CON)*, 2016

[11] Yin, H. and Dieckerhoff, S. "Experimental comparison of DPC and VOC control of a three-level NPC grid connected converter" *IEEE 6th International Symposium on Power Electronics for Distributed Generation Systems (PEDG), 2015*

Setpoint Adaption of DC Converters Integrated in AC Systems using Security Constrained Optimal Power Flow

Elisabeth Heusinger, Alexander Raab
Institute of Electrical Energy Systems
Friedrich-Alexander-University Erlangen-Nuremberg (FAU)
Erlangen, Germany
elisabeth.heusinger@fau.de, alexander.raab@fau.de

***Abstract*—The electrical grid is becoming more complex due to the increased use of renewable energies. For this reason, utilities have long demanded real-time monitoring and remote control of power grid elements. This can involve substations, intelligent devices, Grid-Boosters, capacitor banks or other physical facilities. At present, (n-1)-security in the power grids is ensured by over-dimensioning the equipment and this separately in the AC grid and DC system. Coupling the two systems provides diverse redundancy, which results in significantly higher network utilization and a considerable reduction in network expansion. In this paper the mentioned coupling is realized by the application of Voltage Source Converters (VSC-MMC). By adapting the active power set-points of VSC-MMC stations support and stabilization of the electrical system in case of a fault scenario is ensured. The corrective actions are based on a Security Constraint Optimal Power Flow (SCOPF). After successful fault detection, the operating point of the High Voltage Direct Current (HVDC) is changed to a set-point, which was prior calculated for this specific scenario. The adaptation of the VSC set-points increases the overall system's security by reducing the number of critical contingencies.**

***Keywords*—(n-1)-security, diverse redundancy, AC-HVDC systems, corrective control, OPF, power system stability**

I. INTRODUCTION

Due to the increased share of renewable energies in the overall energy mix, there are major changes in power transmission. Since renewable energy generation fluctuates, the existing grid must be expanded to handle the high power fluctuations. In addition, generation no longer takes place near the load centres, but decentralised depending on the potential of renewables. Accordingly, in the future the existing transmission grid will undergo a high level of grid expansion, which cannot be achieved solely by selective additions to individual lines [1].

Due to the growing distances between generation and consumption, the power losses of the AC system increase and prove to be uneconomical in this case. High voltage direct current (HVDC) transmission is used as a profitable solution. The operational management of an extended DC system and its integration into the existing AC grid offers new possibilities such as long distance bulk power transmission and providing operational security. There are two different ways to connect an HVDC system to the existing AC grid: Point-to-Point (P2P)-connectors or a meshed overlay DC grid. Both methodologies are tested in PSS®Netomac and discussed in this paper. The challenge of DC interconnections is that DC converters do not respond automatically to power flow alterations. Therefore, the converter stations have to adapt fast to fault scenarios by adjusting their operating points. The determination of the converter set-points is based on an Optimal Power Flow (OPF) calculation [2]. Using both systems, AC and DC, for preventing critical disturbances opens up new possibilities in redundancy, the so-called divers redundancy [3]. If the HVDC are implemented with Voltage Source Converter (VSC) using Modular Multilevel Converter (MMC)-Technology, active and reactive power can be controlled independently of each other. In this way, the described HVDC can actively intervene in the load flow resulting in intelligent automated power supply and mitigate today's security restrictions [4].

In this paper the active modification of the system management during a fault scenario is discussed. The corrective measures are based on active power set-point adjustment of the converter set-points. For this purpose, after successful fault identification, a previously calculated active power set-point is activated locally at the HVDC converter station. In this way, the grid is supported and stabilized during failure using load flow controlling equipment. The use of controllable VSC converters avoids critical disturbances in the transmission grid by fast adaptation of the power set-points. Due to that, the aim is to prevent long-term equipment overload, which reduces the risk of subsequent cascaded failures and in the worst case blackouts.

Since the expansion of the transmission grid is not only costly, but also leads to resistance in the population, alternatives must be found that can reduce the extent of grid expansion [5].

II. CORRECTIVE MEASURES

This section presents an alternative type of redundancy that allows better use of the existing grid and provides a comparison with the conventional principle of redundancy. Afterwards, the applied optimization calculations are presented and explained.

A. System management

Different grid characteristics must be considered during grid planning. These include grid security and reduction of disturbances, good voltage stability, high supply reliability and also high availability. In order to meet these requirements, the distribution grid is based on the principle of (n-1)-security. This principle defines the fact that the failure of one operating device must not overload the remaining grid, even during maximum transmission and supply tasks. The (n-1)-safe operation is ensured by the redundancy of the equipment in the grid, which is generally not operated at full capacity in undisturbed operation [6], [7].

The outage of any component must not result in exceeding either voltage limits or equipment load limits. Grid expansion based on the conventional preventive (n-1)-principle results in high investment costs. This is due to the fact that the grid must have sufficient transmission capacities and power reserves even in the event of a failure and must be expanded accordingly [5]. As an alternative diverse redundancy can be used to stabilize the existing grid and avoid the expensive construction of additional power plants. For this purpose, the existing AC grid is e.g. overlayed with a DC system. This method is characterized by lower costs than those estimated by previous planning. Different disturbances in the system can cause either power deficits or power peaks in the grid. By providing diverse redundancy and adapted control, the grid topology is changed so that the power flow can be adjusted, optimized and thus overloaded components can be supported [8]. In contrast to conventional redundancy, it is possible with diverse redundancy to intervene in the load flow and thus not disturb the stable equilibrium as depicted in Fig. 1.

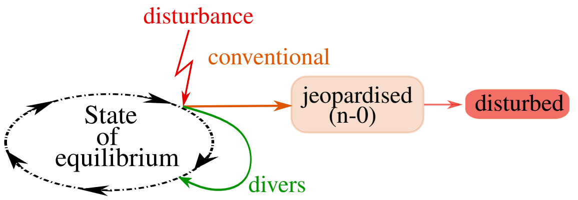

Fig. 1: Conventional and divers redundancy

Load flow controlled actuators are used to guarantee diverse redundancies. There are two different procedures for optimizing grid stability, which can be classified in preventive and corrective. Both measures are based on the Security Constraint Optimal Power Flow (SCOPF). Corrective actions use the flexibility provided by the HVDC terminals to allow the system to respond in the event of a fault. As Fig. 2 shows, corrective measures are particularly characterized by the fact that the transmission lines can be used to very high capacity in the normal state. Fast actions in the load flow compensate short-term overloads and thus avoid critical loads. Due to the limiting load integral ($\int i^2 \mathrm{d}t$ or I^2t) of transmission lines, a short-term overload is feasible before strong mechanical or thermal stresses occur due to the rising temperature [9]. Corrective measures enable a more efficient operation of the system, since the components can be used at higher loads than permitted by preventive measures, while fulfilling the requirements of the safety standards. Although the corrective measures are computationally more complex than the preventive measures, generally, significantly more economical results are achieved [10].

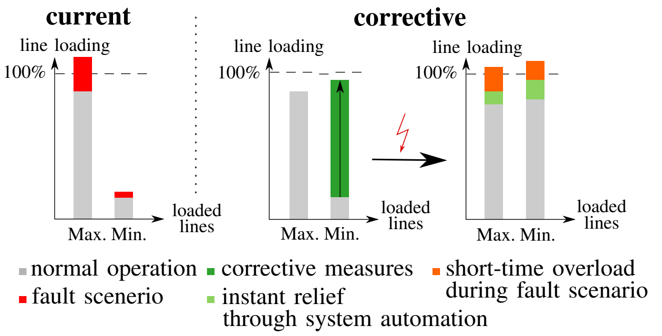

Fig. 2: Corrective measures to reduce critical disturbances

This paper proposes a Preventive Security Constrained Optimal Power Flow (PSCOPF) that will be used to adjust the active power set-points of the VSCs for the corrective actions.

B. Security constrained optimal power flow

In PSS®Netomac two optimization methods are defined as Powell or Quasi-Newton algorithm. Both optimization algorithms are based on the Newton-Raphson method. The OPF calculation is performed based on a failure analysis. A general optimization problem (1) is solved for every fault scenario and also operating points of the converter stations of the overlaid DC grid must be calculated in steady-state operation. The OPF extends the existing load flow, which enables the optimization of the operational behaviour of an electrical grid. Therefore, optimized operating points of an existing system are calculated by minimizing any objective function F.

$$\min_{x}(F(\mathbf{u},\mathbf{x})) \tag{1}$$

$$F = P_{\text{losses}} = I^2R \tag{2}$$

The decision vector $\mathbf{x}$ describes the resulting system state (3) and with $\mathbf{u}$ available degrees of freedom of the system are defined. In this paper, the transmission losses in the AC grid are used as the objective function (2) [8].

$$\mathbf{x} = [\mathbf{p}_{\text{VSC}}^{\mathsf{T}} \quad \mathbf{u}_{\text{DC}}^{\mathsf{T}}] \tag{3}$$

The controlled variable $\mathbf{x}$ is adapted for the optimization of the AC grid, which is formed by the active converter power $\mathbf{p}_{\text{VSC}}$ and the DC node voltage $\mathbf{u}_{\text{DC}}$ [2].

If the inverter stations are operated decoupled from the AC grid, the DC grid is not affected by disturbances in the AC grid. For this reason, only the AC grid is examined in this paper, whereby the calculation of $\mathbf{x}$ is constrained to the optimization of $\mathbf{p}_{\text{VSC}}$.

In addition to the objective function, several constraints must be set up and fulfilled. These are divided into equality conditions g (4) and inequality conditions h (5):

$$g_k(\mathbf{x}_k, \mathbf{u}_k) = 0, \quad k \,\epsilon\, [0, AF] \tag{4}$$

$$h_k(\mathbf{x}_k, \mathbf{u}_k) \leq 0, \quad k \,\epsilon\, [0, AF] \tag{5}$$

For instance, the limits of voltages or operating equipment can be seen. The abbreviation *AF* indicates the number of all fault scenarios to be simulated. With $k = 0$, the grid is defined in its initial state without faults.

Using fault analysis, a SCOPF calculation provides corrective values for the operating points of the active converter power.

III. METHODOLOGY FOR DIVERSE REDUNDANCY

This section provides an overview of the overall system, followed by a description of the individual steps of the methodology.

A. *Overall structure*

As depicted in Fig. 3, the relevant process contains three instances. In order to activate corrective actions after contingencies, different steps are implemented:

- Fault detection: For each critical disturbance specific and crucial values are saved in an offline look up table.
- Identification of fault scenarios: Each fault scenario has to be clearly identified. For this purpose an offline table with precalculated values is used.
- Adjustment of active power set-points: Calculation of corrective set-points of the VSC-converter based on SCOPF.

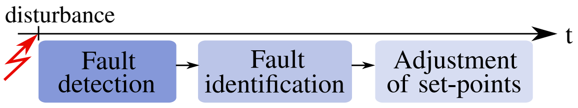

Fig. 3: Structure of the methodology

In case of a failure, the first step is the fault detection. This step only provides information regarding whether a fault has occurred. In the same section, the fault is solved and the line on which the scenario takes place is switched off. The failure is then allocated to a specified scenario and provides information about the location and type. This step is named fault identification. In the last step, a corrective action is performed after the successful identification, whereby the power set-points are adapted to the fault scenario by the HVDC [11].

All calculations are based on a contingency analysis. After a dynamic simulation of all critical failure scenarios, the characteristic values are saved in an offline table and stored locally at each HVDC converter control as shown in Fig. 4. Both, fault detection and identification are based on voltage and current measurements. In order to analyze and supervise the load flow, signals must be measured locally in the grid. Various input variables are important for fault detection, which can be obtained using time-synchronized Phasor Measurement Units (PMU). For grid supervision, PMUs are installed locally on important busbars in the power grid. With this measuring device the complex amplitude of various signals such as current and voltage can be gathered digitally at specified times. Afterwards, the data is then transmitted to a central unit, the Wide Area Monitoring System (WAMS) [12]. In the local and also central assessment of the fault scenario, two measured variables are evaluated:

- Maximum deviation of the voltage angles $\Delta\delta_i$
- Maximum current deviation $\Delta i_{i,j}$

The voltage angle $\Delta\delta_i$ and the currents $\Delta i_{i,j}$ of all lines between the busbars j and bus i where the HVDC is connected are monitored. Finally, the two measured parameters are represented in (6) using the variable x.

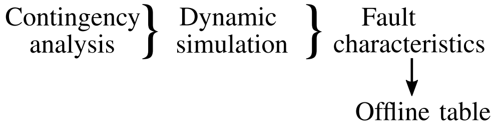

Fig. 4: Generation of offline tables based on contingency analysis

B. *Fault detection*

Fig. 5 shows the fault detection procedure. The process is based on a time domain simulation of an exemplary fault scenario. If the signal exceeds the tolerance upper limit or falls below the lower threshold (x_{limit}), a fault is detected for this signal. After exceeding the tolerance band (x_{TB}), a fault is recorded and the maximum deviation of the input variable from the initial state is determined within a defined time window Δt. If a value for each variable is outside the tolerance band, the Δx values of each signal, that can be calculated with

$$\Delta x = \max_{t=t_0 \ldots t_0+\Delta t} \{x(t_0) - |x(t)|\} \tag{6}$$

The Δx values are then stored in an offline table at each converter station. However, a distinction is made between online

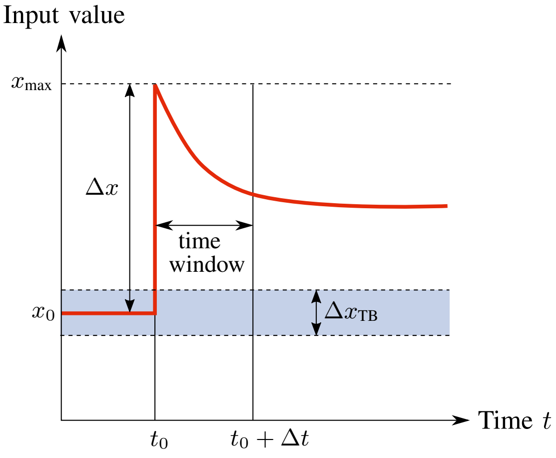

Fig. 5: Principle of the fault detection [13]

and offline calculations. Offline signifies that an contingency is simulated in advance, online indicates the real-time failure that must be identified. This method is first performed offline and then online.

C. *Identification of the fault scenario*

If a fault occurs in the system during real system operation, the maximum deviation Δx_{online} within a defined time window is determined first. In the next step, this value is compared with the fault characteristics of the offline table. Thus, an event can be assigned to each input variable that is measured online. Using a decision algorithm, a specific fault scenario can be identified.

D. *Adjustment of set-points*

In this paper, the HVDC is simulated as a P-Generator or P-Load, depending on whether active power is fed in or consumed. A phasor simulation (RMS) is performed with the main focus on the operational management concept. Based on the failure list, an OPF calculation is performed for each possible fault scenario. As a result, the corrective operating points are determined, then saved in an offline table.

Successful fault identification leads to the initiation of corrective actions. The appropriate $P_{\text{VSC,corr}}$ value is assigned to the fault scenario and used as the new P_{VSC} value of the HVDC. Fig. 6 shows the basic procedure for activating a corrective measure of the HVDC.

In the first step, compliance regarding the tolerance limits of the input variables must be checked. This is validated with the request $|\Delta\delta_{\text{u}}| > |\Delta\delta_{\text{limit}}|$. In case this inequality is not fulfilled, no fault is detected and the HVDC keeps working with its stationary operating point. If the tolerance limit is not complied with, the next step is to check the different input variables. The maximum deviations of the measured variables Δx_{online} are compared with the previously calculated $\Delta x_{\text{offline}}$ variables from the offline table. If each comparison of the fault characteristics results in a match, the fault scenario is clearly identified. Thus, a comparison of Δx_{online} with $\Delta x_{\text{offline}}$ is successful if

$$\Delta x_{\text{offline}} - \Psi_{\text{tol}} \leq \Delta x_{\text{online}} \leq \Delta x_{\text{offline}} + \Psi_{\text{tol}} \tag{7}$$

is fulfilled. The $P_{\text{VSC,corr}}$ can then be adjusted at the converter station. However, a fault identification that failed does not influence the P_{VSC} value.

IV. CASE STUDY

The presented methodology is implemented and tested in PSS®Netomac using phase-based simulation for the evaluation. The overall online process is divided into only a few steps, which are schematically shown in Fig. 7.

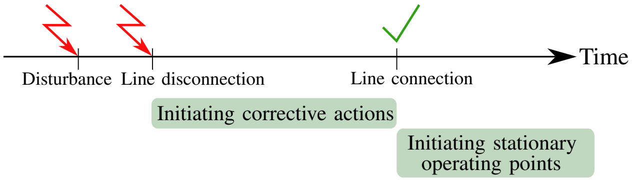

Fig. 7: Schematic overview of he procedure in the test grid

In this simulation model, a three-phase short-circuit occurs in the middle of line 04-14 (Fig. 8) after 3 s. This is interrupted after 100 ms by a line switch-off. The fault line is switched on again after 20 s in order to restore the initial state after fault clearance. During disconnection of the disrupted line, the active power operating points of the converter stations are adapted to the new grid situation as a corrective measure to ensure safe grid operation even in the event of a contingency.

A. *Test grid IEEE39*

The New England IEEE 39 Bus test system is used and expanded with DC-Technology extensions. Since the DC network is not affected by interference in the AC network, only the AC network is investigated. Two different methods to

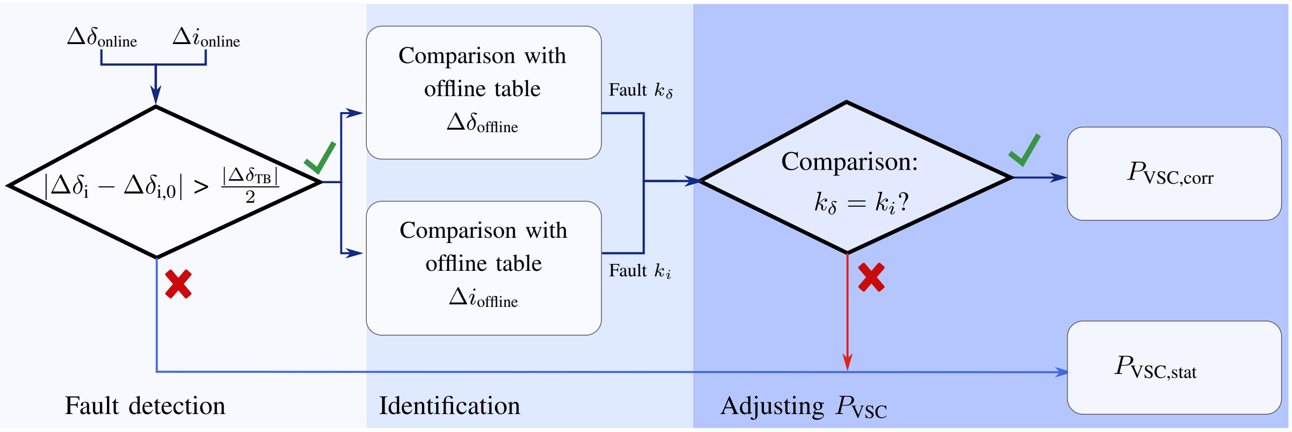

Fig. 6: Processing method of measured values

combine AC and DC systems are defined as point-to-point-interconnectors and meshed overlay HVDC grid and is shown in Fig. 8.

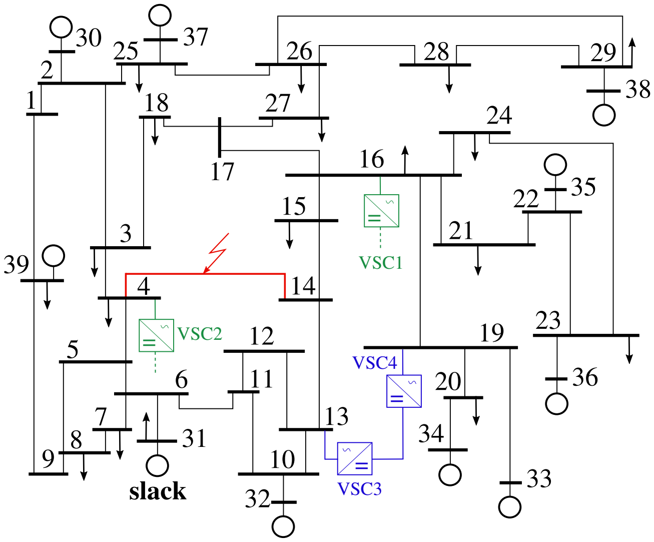

Fig. 8: New-England-Test grid with an overlay HVDC grid (green) and P2P-interconnectors (blue) and 3-phase short-circuit on line 04-14

To determine the influence of a connected DC system to an AC system according to the (n-1)-principle the load pattern is set such way that the AC-lines are highly loaded during undisturbed operation whereby the thermal limit current must not be exceeded. The dynamic models of the generators are controlled by an Automatic Voltage Regulator (SEXS), a Turbine-Governing System (TGOV1) and a Power System Stabilizer (PSS2A). In the further procedure a fault analysis is carried out in order to determine several fault scenarios in which critical overloads of different transmission lines occur. After calculating corrective converter power set-points for the relevant contingencies, the critical scenarios can be prevented by adjusting the determined P_{corr} values.

Various test cases are investigated with the focus on relieving overloaded lines in order to prevent cascaded equipment outages up to blackouts. In the presented methodology, the use of VSC-MMC converters is assumed, resulting in decoupling of both grids, so that the reciprocal support of AC and DC grids can be realized by adapting the power converter set-points.

B. Comparison of three scenarios

Three applied scenarios can be differentiated as summarized in Table I. The reference grid is provided by the original AC test grid without HVDC technology and represents scenario 1. The other two scenarios have a DC system expansion and differ in the adjustment of the active power set-points of the VSC converters. Here, the individual converter stations are considered to detect the occurring fault locally and then assign it to a specific fault case.

TABLE I: DEFINITION BY CASES

Scenario	**Converter**
1	-
2	Maintaining of P_{stat}
3	Adjustment of P_{corr}

Two extreme cases are investigated. In scenario 1, not a single converter station identifies the fault scenario, in scenario 2 each station classifies the scenario successfully.

For all cases, the dynamic behavior of the slack is observed. Figure 9 shows that the generator is in a stable initial state at the beginning of the simulation, then it is accelerated out of its initial state and oscillates to a new stable state. After reconnecting the line, the generator returns to its initial state.

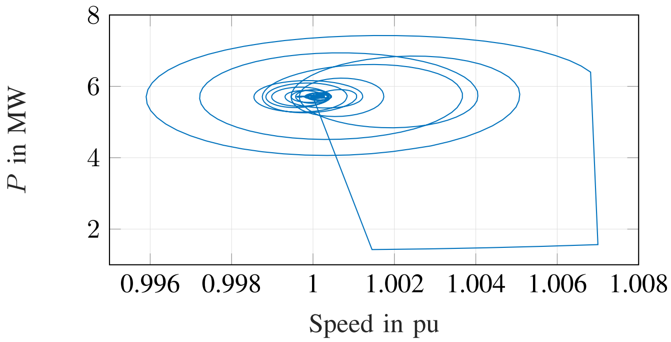

Fig. 9: Stability investigation on the slack

Due to the closed curve, a reliable operation can be assumed even during the disturbed grid operation. In the second scenario, the converter stations are not adjusted and maintain their stationary value P_{stat} as depicted in Fig. 10(a). This is the case if the fault scenario is not clearly identified. In scenario 3, the power set-point is adjusted after successful fault identification as shown in Fig. 10(b). After a fault occurred on line 04-14, all four converter stations detect the same fault, which ensures clear fault identification. Thus, the pre-calculated corrective power set-points P_{corr} can be adjusted immediately at the stations. The characteristics of the active power set-points of each converter station for the scenarios with DC system expansion are shown in Fig. 10.

The thermal limit current of the transmission line, shown in Fig. 11, is 1.2 kA. Any current above this limit is equivalent to a line overload. This current flow is therefore in the critical area. At the beginning of the test case, the stationary state exists whereby scenario 2 and 3 differ by ΔI from scenario 1. The HVDC connections actively control the load flow and increase the load on the less loaded lines, this explains the difference ΔI.

If the fault occurs at line 04-14, the current flow is highest in scenario 2, since no corrective measures are performed. In contrast to scenario 1 without HVDC, the line is already more loaded overall. In scenario 1 and 2, the current exceeds

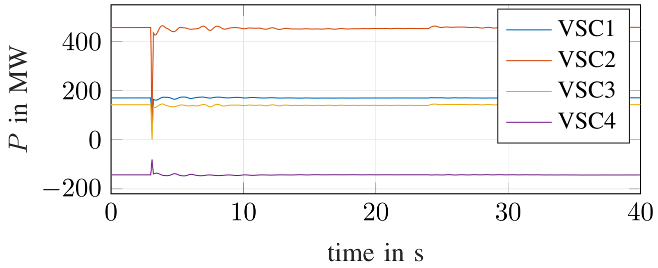

(a) Scenario 2: Maintaining of P_{stat}

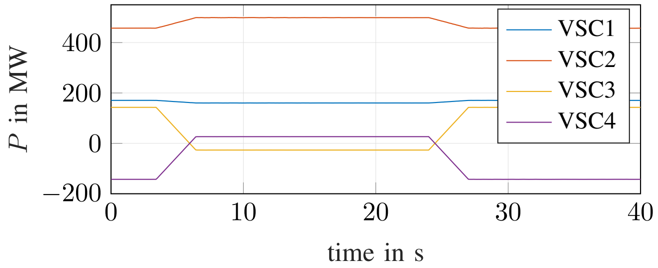

(b) Scenario 3: Adjustment of P_{corr}

Fig. 10: Active power characteristics of the HVDC stations

the thermal limit current, which leads to line overload. In scenario 3 however, the HVDC with active power adjustment can increase the load on the line in the fault-free case and thus transfer more energy, since P_{corr} prevents the line from being overloaded after the fault has occurred. This ensures (n-1)-safety even during a fault scenario. In this test case, HVDCs thus enable corrective measures to be taken in the power flow to support system stability.

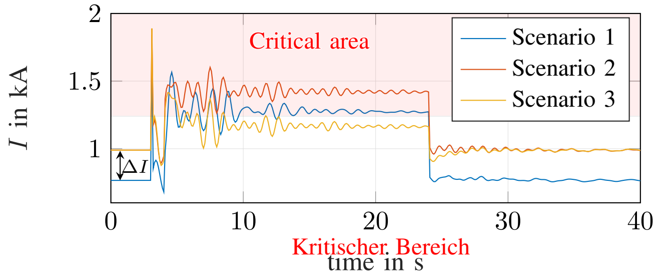

(a) Current caracteristics over time on line 05-06

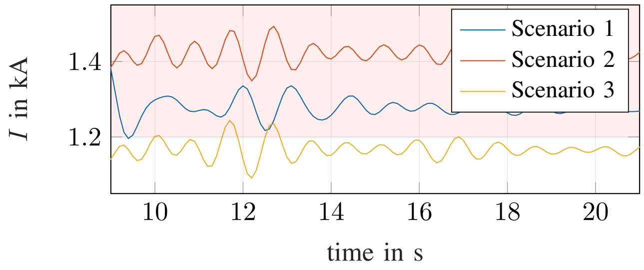

(b) Zoomed view of the current between second 9 and 21

Fig. 11: Current characteristic over time on line 05-06 in case of a fault on line 04-14

V. CONCLUSION

This paper deals with the coordination of VSC active power set-points to provide diverse redundancy for an AC-HVDC-system using corrective measures. The presented methodology is designed in PSS®Netomac to actively intervene in the load flow using VSC-MMC in order to stabilize the grid. For this purpose, the ability of VSC-MMC to control active and reactive power independently of each other is used. Thus, the active power operating points of the HVDC can be adjusted according to the fault scenario in the grid. With regard to minimizing transmission losses, an SCOPF calculation was carried out in order to find suitable set-points of the converter stations. Alternatively to the used Newton method, the optimization could also be implemented using an intelligent algorithm. Various evolutionary algorithms such as differential evolution can be applied, which are able to determine even better corrective set-points for the converter stations. Despite higher cable loads, it can be seen that the HVDC guarantees (n-1)-safe grid operation through active power set-point adjustment. From the presented results of the pre-defined scenarios it is clear that a VSC-MMC as a connection to a higher-level DC grid according to the designed model is suitable for corrective use. Consequently bottlenecks in the grid are prevented, the AC system is strengthened and possible blackouts avoided. The resulting possibility of higher utilization of the currently used equipment reduces the planned, upcoming grid expansion significantly.

REFERENCES

[1] Bundesnetzagentur, “Netzausbau: Ausbau der Höchstspannungsnetze,” 21.08.2018.

[2] A.-K. Marten, F. Sass, D. Westermann, *Fast local converter set point adaption after AC grid disturbances based on a priori optimization*. 2015.

[3] T. Sennewald, F. Sass, D. Westermann, “A preventive security constrained optimal power flow for mixed AC-HVDC-systems,” in *13th IET International Conference on AC and DC Power Transmission (ACDC 2017)*, Institution of Engineering and Technology, 2017.

[4] P. HOFFMANN, “Automatisierte Systemführung,” 2017.

[5] Amprion, TenneT, TransnetBW, 50Hertz, “Glossar: Netzentwicklungsplan,” 01.07.2018.

[6] I. KASIKCI, *Planung von Elektroanlagen: Theorie, Vorschriften, Praxis*. Berlin: Springer Vieweg, 2., aktualisierte und erw. aufl. ed., 2015.

[7] Amprion, TenneT, TransnetBW, 50Hertz, *Netzentwicklungsplan Strom 2030, Version 2017 - Zweiter Entwurf der Übertragungsnetzbetreiber*. 2017.

[8] D. NELLES, *Netzdynamik: Elektromechanische Ausgleichsvorgänge in elektrischen Energieversorgungsnetzen*. Berlin and Offenbach: VDE-Verl., 2009.

[9] G. HEROLD, *Ein- und Ausschaltvorgänge, Überspannungen, Grundprinzipien des Selektivschutzes*, vol. 4 of *Elektrische Energieversorgung*. Wilburgstetten: Schlembach, 2003.

[10] R. WIGET, E. IGGLAND, G. ANDERSSON, “Security constrained optimal power flow for HVAC and HVDC grids,” in *Power Systems Computation Conference (PSCC), 2014*, (Piscataway, NJ), pp. 1–7, IEEE, 2014.

[11] F. Sass, A. Rothstein, V. Staudt, D. Westermann, “Critical contingency management based on characteristic fault pattern for AC-HVDC-systems,” in *ACDC 2017*, (Stevenage, England), IET, 2017.

[12] A. G. Phadke and J. S. Thorp, *Synchronized Phasor Measurements and Their Applications*. Boston, MA: Springer US, 2008.

[13] A.-K. MARTEN, *Operation of meshed high voltage direct current (HVDC) overlay grids*, vol. 12 of *Ilmenauer Beiträge zur elektrischen Energiesystem-, Geräte und Anlagentechnik*. Ilmenau: TU Ilmenau Universitätsbibliothek, 2015.

Electric Boat Propulsion with Archimedean Screw

Gabriela Freitas G. da Fonsêca
Center of Competence for Distributed
Electric Power Technology (KDEE)
Energy Supply Technology (EVS)
University of Kassel
Kassel, Germany
gabrielafreitas@uni-kassel.de

Prof. Dr.-Ing. habil. Peter Zacharias
Center of Competence for Distributed
Electric Power Technology (KDEE)
Energy Supply Technology (EVS)
University of Kassel
Kassel, Germany
peter.zacharias@uni-kassel.de

This paper presents the development of an innovative solution to the problem of energy efficiency and energy storage for electric or hybrid boats. Using the principles of an Archimedean screw it was possible to design a new propulsion system for boats with a lower energy consumption and high efficiency.

Keywords—archimedean, screw, boat, electric, hybrid, battery.

I. INTRODUCTION

For different reasons a change towards electric drive in propulsion can be observed in maritime applications. Electric motors offer silent and clean movement of boats and ships in harbors and protected regions. Even big ships are using more and more hybrid solutions decoupling electric power production and propulsion. The starting point for the presented research idea was a task to change the propulsion of a boat with a weight of several tons from diesel to electric drive. In principle only the diesel engine has to be replaced by an electric motor. A major problem is the power consumption of boats and the limited energy density in batteries.

Table 1 shows a comparison of the weight between the diesel and electric drive with the same power for this project. The power density (power per weight) of electric motors is higher than of combustion engines. But the energy density of the storage is different in both cases and influences travel range. For larger distances refueling of the batteries must be considered, since the number of battery modules to be used are limited due to the total weight of the boat and the space on it available. Thus, the task initiated a general system review to find an optimum system design.

TABLE I. ELECTRICAL AND DIESEL SYSTEM COMPARISON

	Diesel	Battery
Energy weight	0.08 kg/kW	4 kg/kW
Engine	Motor 2.5 kg/kW	Motor 2.2 kg/kW Inverter 0.75 kg/kW
	2.5 kg/kW	2.95 kg/kW
Storage	Tank 0.01 kg/kW	Charger 0.5 kg/kW

II. MOTIVATION

A. The Energy Problem

Large scale storage of electric energy directly is impossible due to the small energy density in electric and magnetic field. This is important especially for moving systems, since weight of the storage has to be carried. Thus, all storages use another energy form for storage which in case of electric demand is converted into electric energy. High efficiency of this conversion is important. Combustion engines achieve circa 40% while efficiency of batteries is 85-95%. To illustrate the different storage density batteries are compared in Fig. 1. In this case the theoretical lift altitude for the approaches are compared. This can be calculated by answering the question: To what altitude a storage can be lifted by using the stored energy at 100%. This makes sense since the storage itself has to be moved too. There is a big gap between density of batteries of petrol or diesel. Even considering the higher efficiency of electric drives this gap cannot be closed.

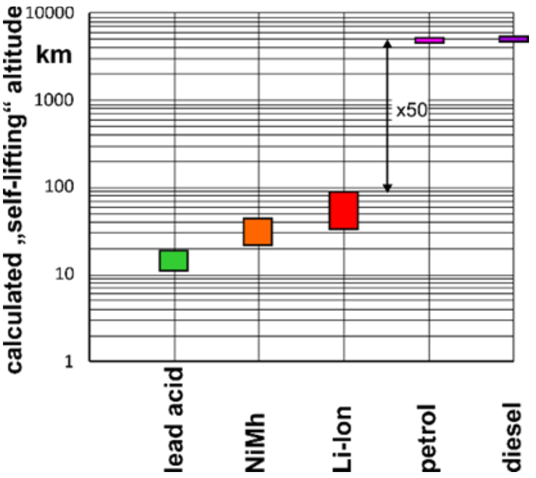

Fig. 1. Comparison of batteries and fuel with the "self-lifting" altitude.

B. Propulsion Basics of Boats

The principle of basic operation of a boat is shown in Fig. 2. The axis of the boat is coupled to the engine, which when triggered, causes the propeller to begin to rotate. The more gas is delivered to the engine, the greater the number of rotations of the engine, thus, the greater the number of rotations of the propeller which leads to the increase of speed of the boat. The rudder located behind the propeller is responsible for steering the boat, that is, allows the boat to move to the right or left.

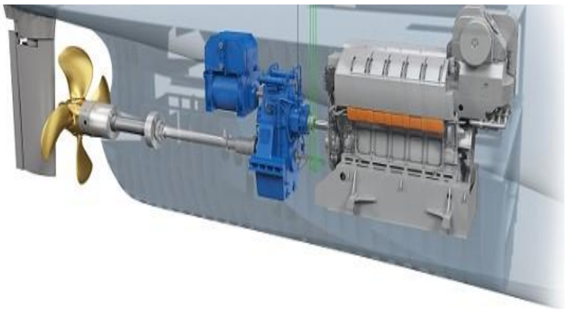

(a)

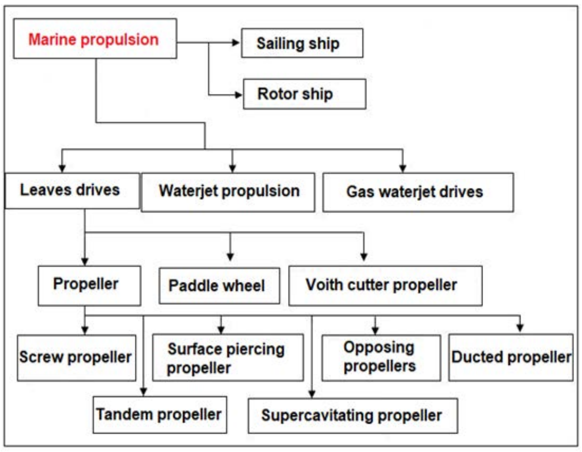

(b)

Fig. 2. (a) Basic mechanisms of a boat [1]; (b) Classification of marine propulsion [1], as amended.

The development of such a system involves not only the electric part but also the mechanical part, especially the fluid mechanics. Due to the movement of the boat under water, several physical forces are generated which often creates a resistance to the movement of the boat, thus requiring more engine power. That is, the system must be developed considering all possible events present in the environment in which it operates: rivers, seas and oceans. As is known, these means do not present a linear behavior which makes the design of marine drive systems more complicated, since it must be ensured that the system has sufficient power and energy to move independently of the flow and water adversities.

Fig. 3. Boat used to implement the eBoot project, model Rhapsody 29.

C. Energy Needs

With the objective of developing a boat completely powered by electricity, it is necessary to use different sources of energy, in order to obtain the greatest possible autonomy of travel without recharging and the minimum emission of CO_2. Thus, the sources of energy considered here were: Battery, Photovoltaic, fuel cell and gas generator. Thus, the system formed by them, would enable the generation of energy and recharge the battery while the boat was in motion. However, for such a design, the weight and size limitation of the boat make the development of this system very complicated, because the greater the distance to be traveled, the more energy is needed and consequently the greater the weight of the system. Several calculations were made in order to estimate the energy required according to the range of the boat. Fig. 4 shows the results of optimization calculations of a hybrid system, related to its weight and reach at a constant speed, for each result there is the required quantity of each energy source.

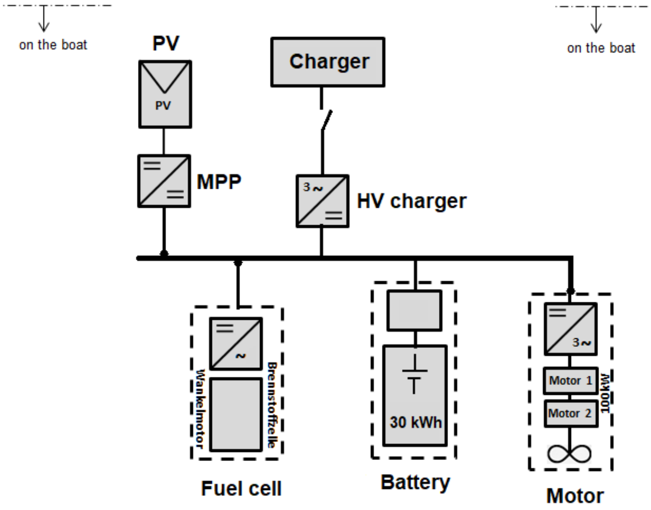

Fig. 4. Design of a hybrid system.

D. Necessary Power for Electric Boat Propulsion

At low Reynolds numbers, *Re* in the lower speed range, the necessary feed force F_{prop}, which depends on the speed of the boat, can be determined according to the law of Stokes.

$$F_{prop} = c_w A_z \frac{1}{2} \rho v^2 \tag{1}$$

Where, v is the speed, ρ the density of water, A_z the boat cross section and c_w is the value of boat shape.

The integration results in the required performance is:

$$P = \int F_{prop}\, dv = \frac{1}{6} c_w A_z \rho v^3 \tag{2}$$

Consequently, at low speeds, it is necessary very little power to move a boat. In contrast to land vehicles, the Coulomb friction plays practically no role. As a result, even very small forces are enough for a continuous drive. This is called the "displacement drive". This mechanism works up to a speed v_{v_max} at which bow wave and stern wave "touch". This maximum speed can be estimated according to the (3).

$$\frac{v_{v\_max}}{\left[\frac{km}{h}\right]} \approx 4{,}5 \sqrt{\frac{l_{wl}}{[m]}} \tag{3}$$

In other words, the longer the boat, the higher the maximum speed v_{v_max} at displacement drive. If this speed is exceeded, the boat hull floats on the bow wave and there is increasingly „gliding ride". The transition between the two forms of transport is very power consuming. Therefore, it is generally true for long distances that boat speeds of > 0.44 · v_{v_max} are not cost effective because of the increased fuel consumption. In the present case, therefore, such an estimated maximum cruising speed is 6.5 km/h. Although achieving the glide travel requires high drive power, a further increase in speed can be achieved with less power increase. Based on some measurements power consumption of the boat can be estimated with the approximation formula:

$$P_{el} \approx 26.8\,W * \left(\frac{v}{k/m}\right)^3 \qquad (4)$$

With a battery of 32 kWh one can expect the traveling range depending on velocity as depicted in Fig. 5. It becomes clear, that only a hybrid power solution (additional fuel cell or gas genset, see Fig. 5 results in an enough travel range.

$$S = t * v = \frac{32\,kW}{26.8\,W * \left(\frac{v}{k/m}\right)^3} \qquad (5)$$

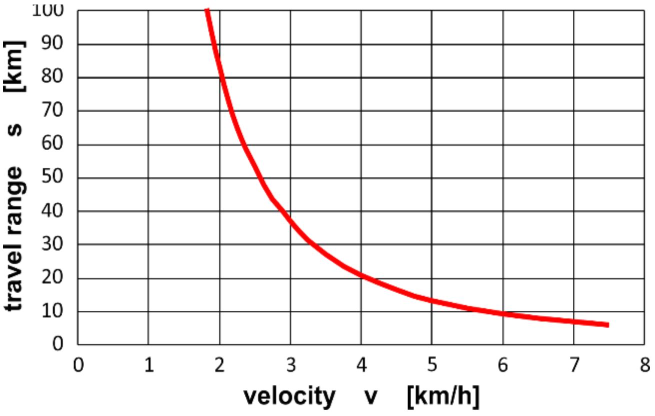

Fig.5. Calculated travel range of the boat at constant speed.

As you can see, the weight of energy is very high. Considering that the vessel in question weighs approximately 4.5 tones, it is practically impossible to obtain a system with a high range and autonomy.

III. DEVELOPMENT

The following is the solution developed for this problem, which is the solution on which this project is based.

A. *The Archimedean Screw*

The Archimedean screw is considered to be in in different applications already 5000 years. As an example, it is a very robust system for conveyance of liquids and dry bulk goods like grain and granulated materials. Recently it became of interest even for small hydro energy production. In principle the energy conversion is similar to a propeller [1] but situated in a tube. Propeller consist of 2 until 8 wings located in one plane around the axis. Since water is an incompressible liquid these wings carve into water and cause a force into axis direction. The higher the number of rotor blades the lower is the required rotation speed for the axis.

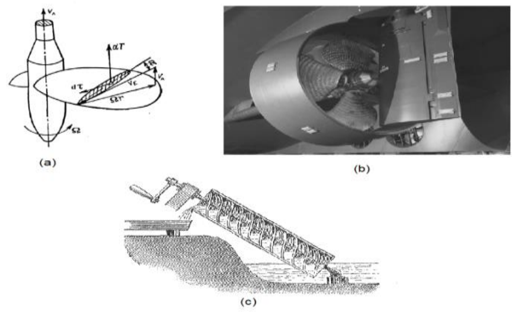

Fig. 6. (a) Scheme of the screw propeller [1], (b) Ducted propeller [1], (c) Archimedean screw [1].

In a similar way it is possible to design an Archimedean screw whose operation resembles a propeller and can be used as a propulsion system for boats. In this way, the development of this system would allow that, with a smaller number of rotations of the engine, the boat would start moving, that is, the system would require less engine power, which would result in a lower energy expenditure. Thus, the use of an Archimedean screw as a propulsion system would provide greater energy efficiency, greater range and the use of a completely electric system.

B. *Mathematical Modeling*

As already mentioned, the design of a propulsion system from an Archimedean screw depends not only on the electrical part but also on the mechanical part, being a dependent part of the other. Due to this, the mathematical modeling of this system becomes a fundamental tool for the project, therefore, the Archimedean screw can be designed in optimized dimensions.

It is possible to find in the literature works describing the design of an Archimedean screw, as the work presented by Kotarba [3], however, most of them are oriented to applications with grains and have a totally vertical structure or with a certain inclination. Although not appearing, these factors are fundamental to the development of calculations. In this project, the Archimedean screw is used totally horizontally, without any degree of inclination with respect to the ground, the material that it transports is the water and it is totally immersed in it, that is, in the bottom of the boat. In figure 6 it is possible to see the forces that act in a grain when it is moving inside an Archimedean screw.

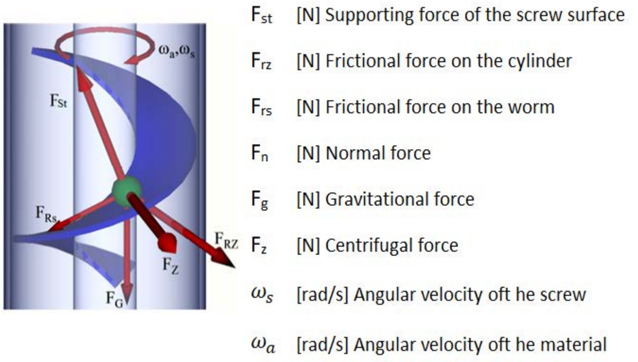

Fig. 7. Division of forces present in a single grate within an Archimedean screw [2].

In this work, several equations were developed in order to model the system whose material in flow was water and together with that, to model so that the water according to the movement of the Archimedean screw allowed the greatest possible propulsion.

The system in question has the following characteristics:

- Steady flow.
- Incompressible flow.
- Uniform flow.

In a simplified and direct way, the following equations were developed in order to design an Archimedean screw with the highest efficiency possible for this application. The angle between the forces is given by:

$$\beta_1 = tg^{-1}\left(\frac{frz}{frs}\right) \tag{6}$$

$$\beta_2 = tg^{-1}\left(\frac{fst}{frs}\right) \tag{7}$$

Thus, we can obtain the resulting forces:

$$F_1 = \sqrt{f_z^2 + f_{rz}^2 + 2 * f_z * f_{rz} * cos(\beta_1)} \tag{8}$$

$$F_2 = \sqrt{f_{st}^2 + f_{rs}^2 + 2 * f_{st} * f_{rs} * cos(\beta_2)} \tag{9}$$

$$F_3 = \sqrt{F_1^2 + F_2^2} \tag{10}$$

Since F_g is the gravitational force inside the cylinder, we obtain the equation of the impulse from the calculation of the resultant force:

$$F_R = \sqrt{F_3^2 + F_g^2} \tag{11}$$

With the modeling of the finished mechanical part, the development of the energy balance equations was started. The calculated efficiency of the system is given by (7) which is dependent on the R value of the resistors and the A value of the area of the Archimedean screw.

$$\eta = \frac{1}{1+\frac{2A^2}{\rho}\Sigma R} \tag{12}$$

The work done by Archimedean screw is given by:

$$W = A * p_{dy} * t * w \tag{13}$$

Where p_{dy}, t and *w* refer to the dynamic power, time and velocity of the flow respectively. Having both equations in hand it is easy to obtain the energy balance E_S equation:

$$E = \frac{W}{\eta} \tag{14}$$

$$E_s = \frac{1}{d^2}\left(\frac{M*l}{2} + a * V^3 * R_n\right) \tag{15}$$

Where, M is the system torque, l the length of the Archimedean screw, d diameter, V volume and R_n the resistors involved in the system. Many of these resistances are impossible to calculate theoretically, others such as the impulse tensile strength and the resistance caused by the pressure have already been calculated.

With the development of the equations that model the propulsion system from an Archimedean screw, it was realized that the optimal shape for an Archimedean screw would be a conical shape where the propellers will vary in size along their axis. That is, the important thing is that each end presents a different diameter to have a decrease of the value of the resistors and with that a decrease of the spent energy.

C. Prototype

With the modeling done, three Archimedean screw with different distances between each propeller were modeled in 3D and later printed, in order to use them for assembly of the prototype. As can be seen in Fig. 7.

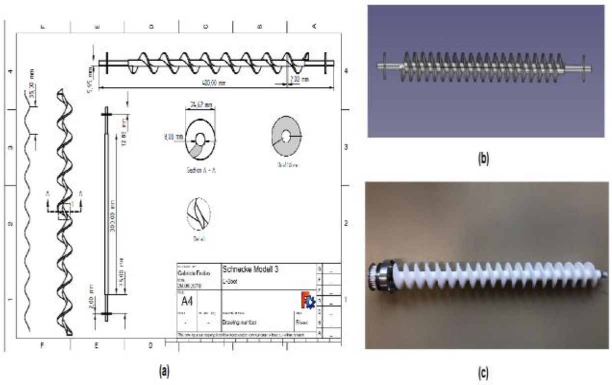

Fig. 8. (a) Dilution of the 3D model made in Freecad software; (b) 3D model; (c) Archimedean screw printed on a 3D printer.

With the Archimedean screw the prototype was assembled according to Fig. 8. In it, there was a small electric motor, in it the Archimedean screw was coupled, and the control was done remotely, that is to say there was a receiver that evaded the signal received from the control to the motor. By control the direction and speed were controlled. Every system was powered by a Li-Ion battery.

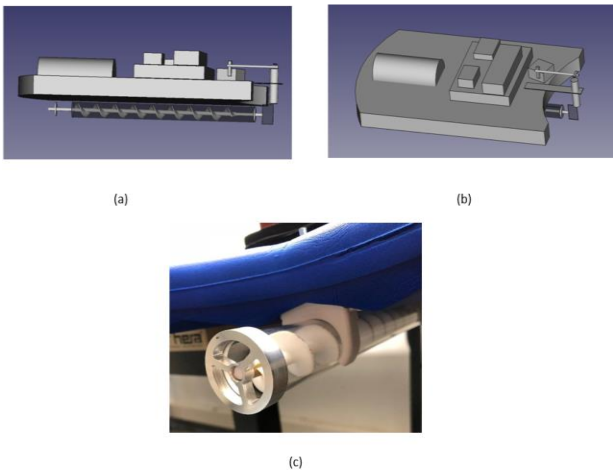

Fig. 9. (a) Side view of the prototype; (b) top view of the prototype; (c) Bearing and acrylic cylinder.

In possession of the prototype several tests of force and energy expenditure were made. With them it was possible to identify what each structural part of the Archimedean screw influences in the mechanical and energetic result and it was also possible to verify if the developed equations were correct.

IV. EXPERIMENTAL SETUP AND RESULTS

The tests carried out so far have confirmed the accuracy of the developed equations related to the mechanical forces present in the Archimedean screw. When comparing the theoretical results with the practical ones one can perceive the similarity between them according to Fig. 10.

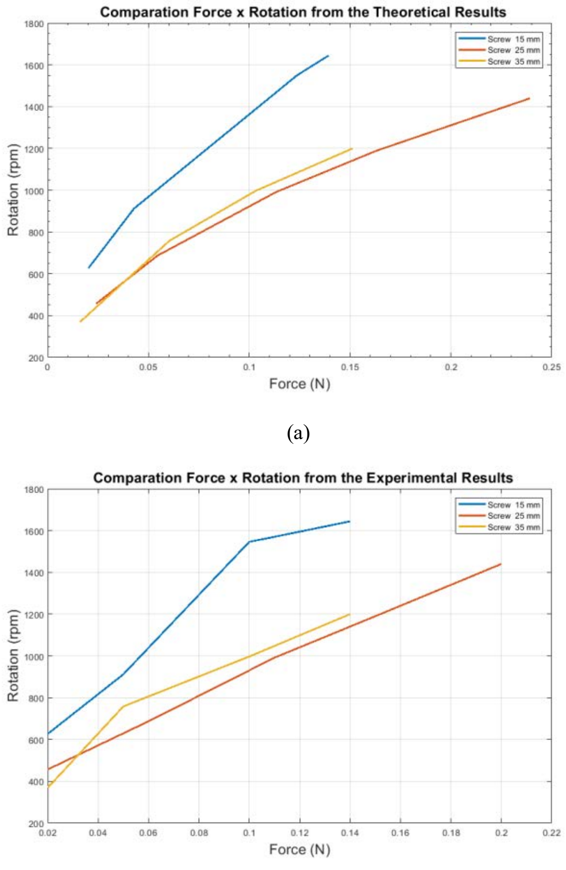

(a)

(b)

Fig. 10. Comparison between the theoretical results (a) and the experimental results (b).

From these initial tests it was possible to conclude that the greater the distance between the propellers present in the Archimedean screw the greater the angle between the main axis and the propeller which improves the performance of the system. In the tests performed, the Archimedean screw whose distance between the propellers was 35 mm showed a better performance with respect to the others.

The next tests to be performed will serve to prove the new conic model proposed here and will be done together with the Department of Hydraulic Engineering and Water Management of the University of Kassel where not only the prototype of the boat will be in motion but there will also be a flow of water , thus simulating for example a river.

Fig. 11. Hydraulic Engineering Hall of the Department of Hydraulic Engineering and Water Management of University of Kassel.

With these tests it is expected to confirm the veracity of the system modeling, the proposal of the new model of this screw and to demonstrate the greater efficiency of this system compared to other existing ones, according to the study present in [1] shown in Fig. 12.

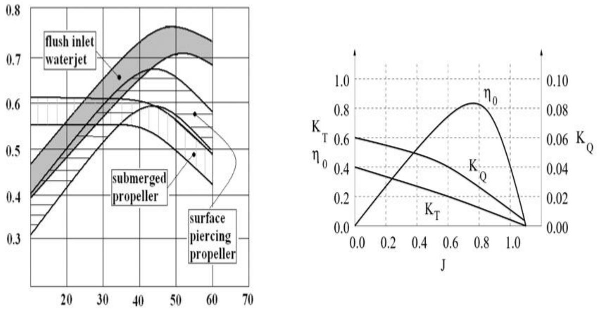

Fig. 12. Efficiency of propulsion systems (Paxis/Pvessel] at different vessel velocity (kn) [1, 2].

Unlike the actuator disc a propeller requires that the power be input into the fluid via a shaft and thus must apply torque to the fluid. To balance this torque the flow must contain tangential velocity, or swirl, to counteract this torque. The kinetic energy in the swirl velocity, if not recovered by a stator or downstream blade row, is lost. Therefore, the efficiency of an ideal propeller will be less than an actuator disc efficiency. For a propeller in uniform flow this ideal efficiency can be computed given the coefficient, J, and the thrust coefficient, Ct [4].

In aeronautics and marine hydrodynamics, the advance coefficient, J, is the ratio of the freestream fluid speed to the propeller or rotor tip speed. When a propeller-driven vehicle is moving at high speed relative to the fluid, or the propeller is rotating slowly, the advance ratio of its propeller(s) is a high number; and when it is moving at low speed, or the propeller is rotating at high speed, the advance ratio is a low number [5].

As mentioned, future tests will determine the efficiency of this system. However, simulations have already been made and show that the system's behavior resembles that shown in Fig. 13 with great efficiency values.

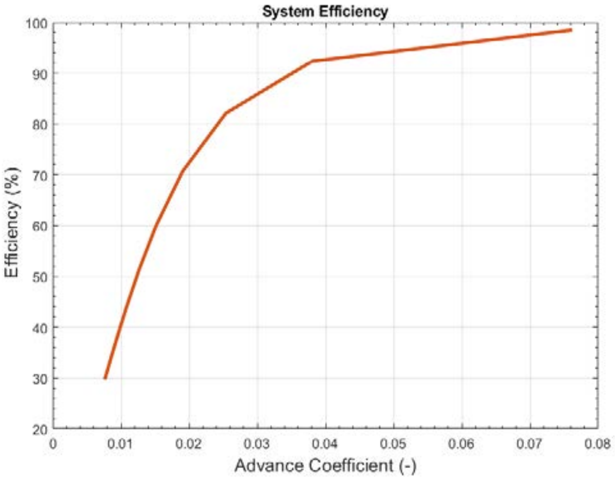

Fig. 13. Simulated results for 3 blades and 7 turns of the helix with constants with ideal values.

If the above mentioned topics are confirmed, it will be possible to develop a boat drive system, totally powered and with greater efficiency that will result in a better use of the energy stored in the batteries or any other sources of energy that the boat has.

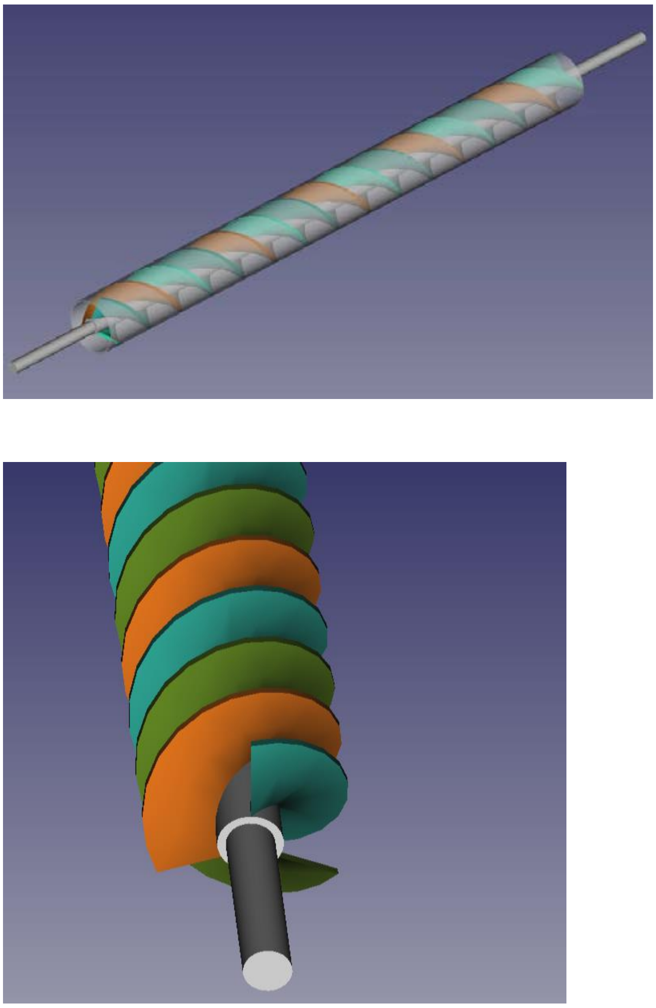

Fig. 14. Future screw to be used for the tests.

REFERENCES

[1] N. Kornev, Propellertheorie, Fakultät für Maschinenbau und Schiffstechnik, Universität Rostock, 2009.

[2] M. Kotarba, Beitrag zur Auslegung von Senkrechtschneckenförderern für den Schüttguttransport, Technischen UniversitÄt Bergakademie Freiberg,2013.

[3] Chris B. Mckesson, PE John J. Mcmullen associates Inc., „Hull Form and Propulsor Technology for High Speed Sealift“, 1997.

[4] M. Kotarba, Beitrag zur Auslegung von Senkrechtschneckenförderern für den Schüttguttransport, Technischen Universität Bergakademie Freiberg, 2013

[5] A.H. Techet, 2.016 Hydrodynamics, Massachusetts Institute of Technology, 2005.

[6] Prof. Z. S. Spakovszky. "11.7.4.5 Typical propeller performance" MIT turbines, 2002.

Structural function and operation of a cluster-based energy management system

Timo Alexander Hertlein
Siemens AG
Hochschule Coburg
Erlangen, Germany
timo-alexander.hertlein@hs-coburg.de

Prof. Dr. Christian Weindl
Hochschule Coburg
Coburg, Germany
christian.weindl@hs-coburg.de

Tobias Blenk
Hochschule Coburg
Coburg, Germany
tobias.blenk@hs-coburg.de

Dr. Ivana Mladenovic
Siemens AG
Erlangen, Germany
ivana.mladenovic@siemens.com

***Abstract*—The power grids are increasingly facing great challenges due to the steadily rising share of regenerative and volatile feed-in. Thus, the requirements on operation management and network planning to ensure the necessary balance between load and feed-in are progressively challenging. On the other hand, the ancillary services that ensure supply stability and quality have to manage every critical situation independent of the feed-in circumstances. In order to fulfil these requirements several solutions such as centralized, cellular or blockchain-based systems have been created, researched and tested. In this paper a novel concept called Energy Cluster Service System (ECS) that supports the localization of the energy management by means of targeted stimulation (monetary incentives) of the network actors is presented. An additional feature of the ECS-System is the realization of the power flow management under consideration of the actual state of the power equipment and its prognosticated aging rapidity for given loading situations.**

Keywords—power system control, load flow control, energy management, power system management, energy cluster system

I. INTRODUCTION

The over decades developed centrally structured power grid has been historically designed for a demand-based transmission and distribution of electricity from large-scale power plants located in the area of major loads, [1]. The resulting vertical load flow no longer meets the current demands and circumstances in the power networks resulting from the gradually increasing share of regenerative energy sources. According to [2], most of renewables feed-in the distribution network, causing a change from only vertical to periodically vertical and horizontal load flow. Moreover, the permanent development and realization of the energy transition, which is fixed by legal regulations and international agreements, will even intensify the mentioned network situation.

In order to enable the further integration of renewables and simultaneously to retain the reliability of the energy supply, it is necessary to take the measures in timely manner to appropriately prepare the networks for the future developments and challenges. Besides the grid expansion this can be realized through the adaption of consumption patterns to current generation characteristics of renewables, [2], which is in comparison to grid expansion a cost-effective alternative. One possible concept presented and discussed in this article is given by the Energy Cluster Service System which is cluster-based, hierarchical and works with monetary incentives.

II. THE ECS-SYSTEM

A. *Fundament of the ECS-System*

The ECS-System represents an innovative, economically viable and socially acceptable approach for the realization of the energy transition. It is founded on technical solutions – local balancing of power generation and consumption – within defined grid areas (clusters) by means of local and dynamical monetary incentives.

This can be realized by billing tariff models consisting of fixed and flexible components, which are able to adapt dynamically to actual network load situations. These targeted monetary incentives will be offered to the subordinary subnetwork or network users that are willing to participate in the ECS-System, further called participants, to support the network operation and hence, to adapt their generation or consumption behavior.

In this way the monetary incentives, that are limited by previously defined economic areas (to avoid for example socially intolerable extreme values or prices), allow participants to generate economic benefits for supporting public power supply. On the other hand, the local balancing of consumption and generation results in decreased loading of the power equipment leading to the extension of average expected lifetime of power components, which means a shift of the replacement investments for the network operator [3-6].

B. *Integration of the ECS-System in the grid*

ECS is mainly integrated into the energy supply system at the distribution points within the energy network, such as substations, transformer stations or grid distribution boxes. The technological clusters that are hierarchically oriented to the energy supply system are defined and stretched out over available feeder up to the participants in a consequential manner.

At these gird nodes so-called ECS-Nodes are implemented, which provide the necessary data-related services. The structural integration of the ECS-System into the power network, with its different voltage levels and actors, is shown in Fig. 1.

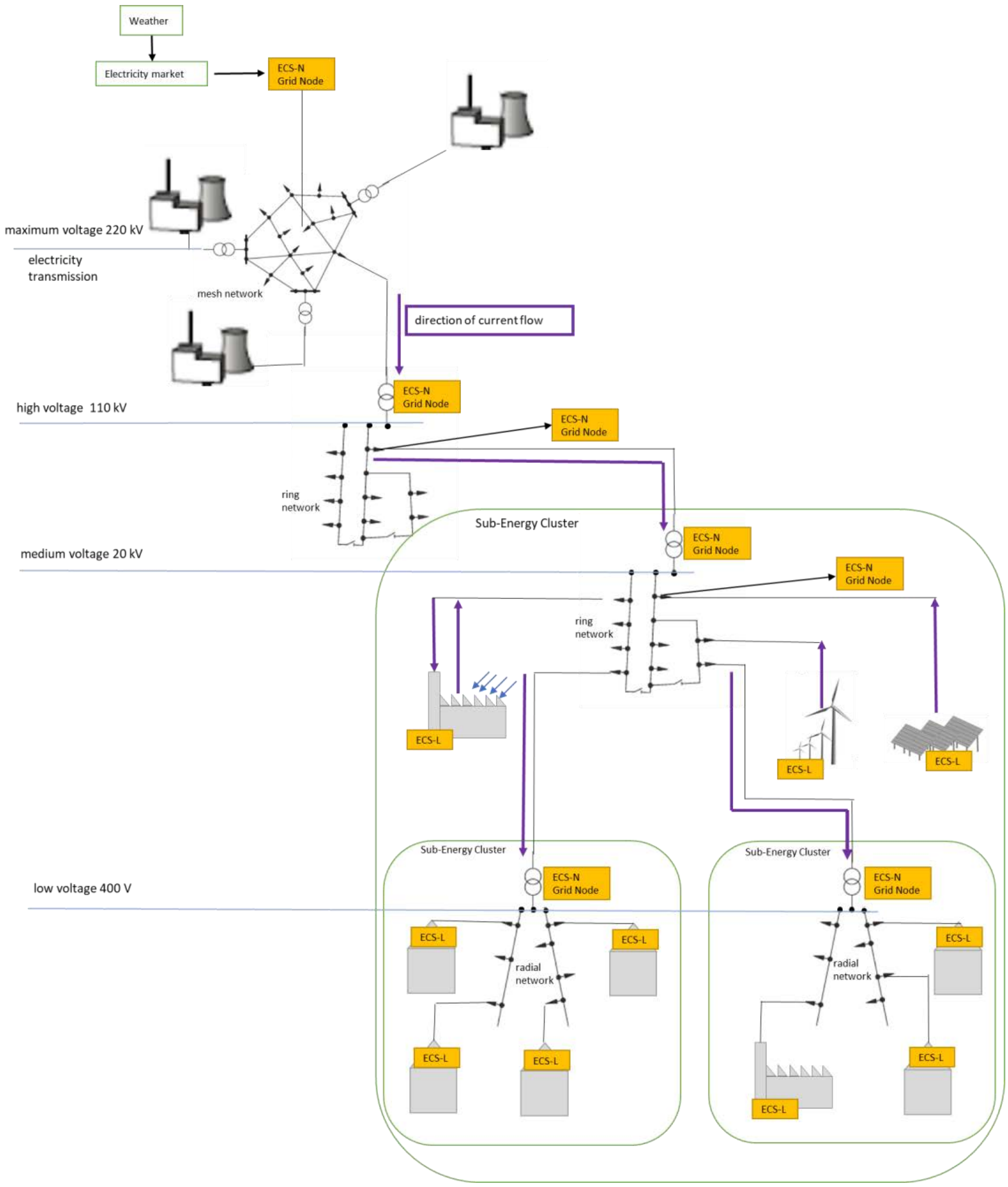

Fig. 1. Structural integration of the ECS-System into the electrical energy supply network

The ECS-Nodes are intended to enable a comprehensive detection, acquisition and assignment of energy flows within certain areas, the clusters, of the power grid. Each cluster can contain several sub-clusters. The ECS services and the technical implementation by compact server systems are realized in such a way that they can be used universally and uniformly for any voltage level and network topology. An individual distinction between the functioning of the ECS-Nodes exists only at the level of the end participants (ECS-L, Fig. 1), all other ECS-Nodes (ECS-N, Fig.1) have a uniform functionality. Therefore, two different ECS-Node types with a different task are defined: the ECS-N and the ECS-L node.

ECS-N nodes are installed at distribution nodes such as substations or transformer stations. Their tasks generally include measuring and processing important network state parameters as currents, voltages and powers at the installation point, creating monetary incentives and forwarding of the most important data, e.g. the calculated monetary incentives for further processing in the downstream ECS-Nodes. The creation of monetary incentives correlates the loading of the appropriate power equipment belonging to the associated cluster.

ECS-L nodes are installed at or within the consumption and/or generation end nodes, where they can directly control the load situation. Only this node type owns the information about accessible and controllable systems as well as the control conditions that are predefined by the end participant. Even more, only this node type can directly or indirectly conduct this switching actions according to determined requirements by the participant.

C. *Functionality of the ECS-System*

The functionality of the ECS-System is based on an established unidirectional informational structure, top-down following the hierarchy of the power network. Fig. 2 shows the schematic representation of the information transfer between the ECS-Nodes. The receiver (Receiver-Node) reads the read-only information continuously or in particular intervals from the clearly predefined superordinate ECS-Node servers (Sender-Node). Due to the explicit assignment of the sender and receiver in the data hierarchy and due to the continuous and unidirectional information flow, network and load data or participant information cannot be externally manipulated or observed and accessed in detail. Even without further measures, such as encryption or channel coding, problems regarding the protection of data privacy could be largely excluded. Therefore, an increased acceptance for participation can be expected.

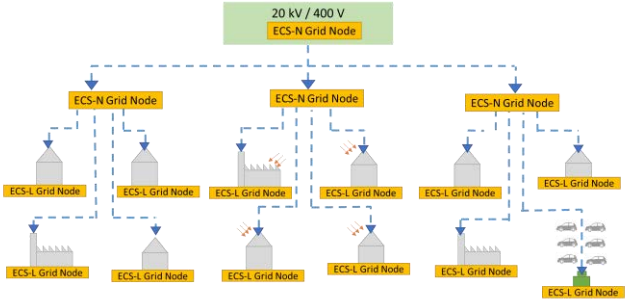

Fig. 2. Schematic presentation of the transmission (the arrows symbolize the respective reading flow of information by subordinate ECS-Nodes)

The information to be transmitted consists of the measured values, the estimated power and the monetary incentives aimed to influence the behavior of the participants according to the actual network situation. The incentives represent a monetary valuation of the network load indicators. Hence, the energy load flow in the network can be optimized by means of economic terms.

Depending on the nature and extend of the network load, e.g. load due to high local consumption or massive feed-in, the incentives will be evaluated. The monetary compensation for a flexible use of the participants' facilities and their responsive feed-in or feed-out are reflected in surcharges and discounts on pre-agreed tariffs, i.e. the monetary compensation for active feed-in or feed-out. Each ECS participant can define in which way his flexibility may be used to support the ECS-System, i.e. can exactly define the mode of operation of its own facilities. The monetary incentives, especially in the case of storage systems, can also include the weather forecast for a more exact evaluation and therefore for more efficient management of the storage facility.

In order to build up a motivation for a specific cluster, the incentives from hierarchically superordinate network nodes are needed and have to be cumulated. The motivation from the assigned Sender-Node (ECS-Node) will be used from the Receiver-Node by summing up to the indicators of its own cluster load condition in order to build up its own motivation. In this way, the motivations within the cluster structures will be accumulated up to the end node, i.e. nodes with direct consumption and/or infeed. Depending on the validation of the motivation, the appropriate load action will be initiated. As a result of a holistic (wide area) load consideration (from the hierarchically superordinate network nodes to the considered node), a load reduction along the network can be achieved.

The voluntary participant of the ECS-System determines its own participation conditions which can be changed at any time. This means that each participant determines the availability of the flexibility potentials himself and furthermore, under which economic conditions this may be activated or must be deactivated. For example, it is possible to set an individual threshold value that determines to which economic conditions electrical energy should be stored in or also stored out.

III. SIMULATION OF NETWORK LOAD

A. *Description oft the model environment and control*

In order to analyze the effect of the ECS-System on the power network, a simulation environment was developed, where the load of the network and its components can be examined with or without an impact of the ECS-System.

The scenarios used in the simulation are based on realistic data regarding the development of the energy landscape within typified network structures. For this purpose, the scenario framework 2019 – 2030 approved by the Federal Network Agency and a project called "Merit Order Netz-Ausbau 2030" conducted by the German Research Center for Energy Economics (Forschungsstelle für Energiewirtschaft e.V), were used, [7, 8]. Both studies analyze and describe possible developments of diverse influencing factors (e. g. development of storage technologies and systems) on the energy supply and distribution system. Here, the research focus is on distribution systems - low and medium voltage networks with their typical network topologies.

For the model description, two typical network structures have been selected, a radial network structure and a network with a long feed line. These structures were used for the further network simulations. Fig. 3 is a schematic representtation of the examined radial network, and Fig. 4 the investigated long feed line.

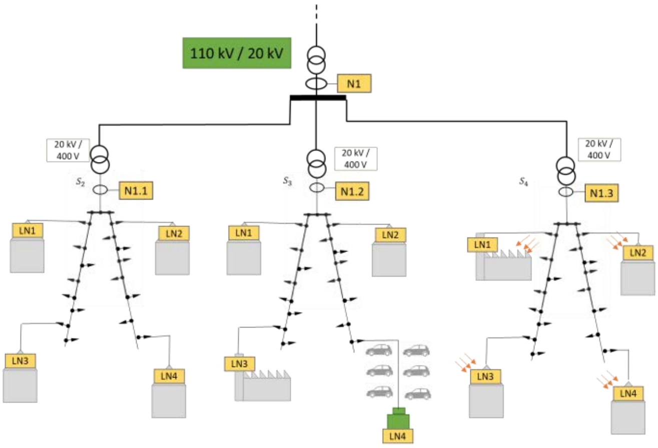

Fig. 3. Typed radial network as the basis of the network simulation

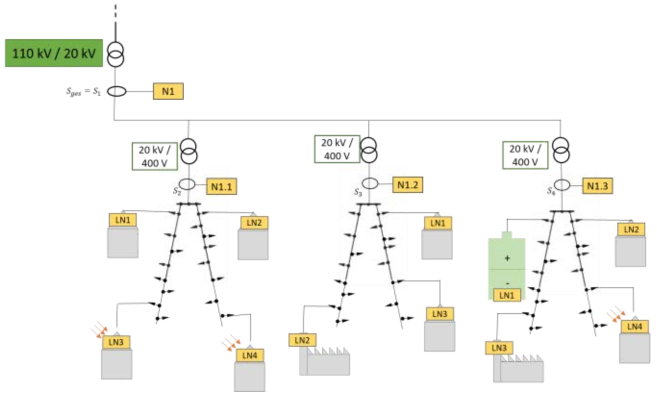

Fig. 4. Typed feed line as the basis of the network simulation

Both network structures consist of three different subnetworks, which are identified through their ECS-Nodes. For the electricity landscape in each of the subnetworks, realistic development of renewable energies and relevant technologies, based on mentioned studies, were used. The goal is to develop diverse subnetworks, which are differentiable, heterogeneous and consistent.

The participants in each subnetwork are divided into different groups, depending on their types (residential unit, diverse kinds of commercial enterprises, industry and agriculture), and technologies (electric vehicles, photovoltaic system, wind power station, variable storage systems). By a selective determination of the amount of available types and technologies in the subnetworks, different network areas, such as rural or urban networks, can be represented.

Fig. 5 provides information on the essential configuration parameters within the simulation and its way of operation.

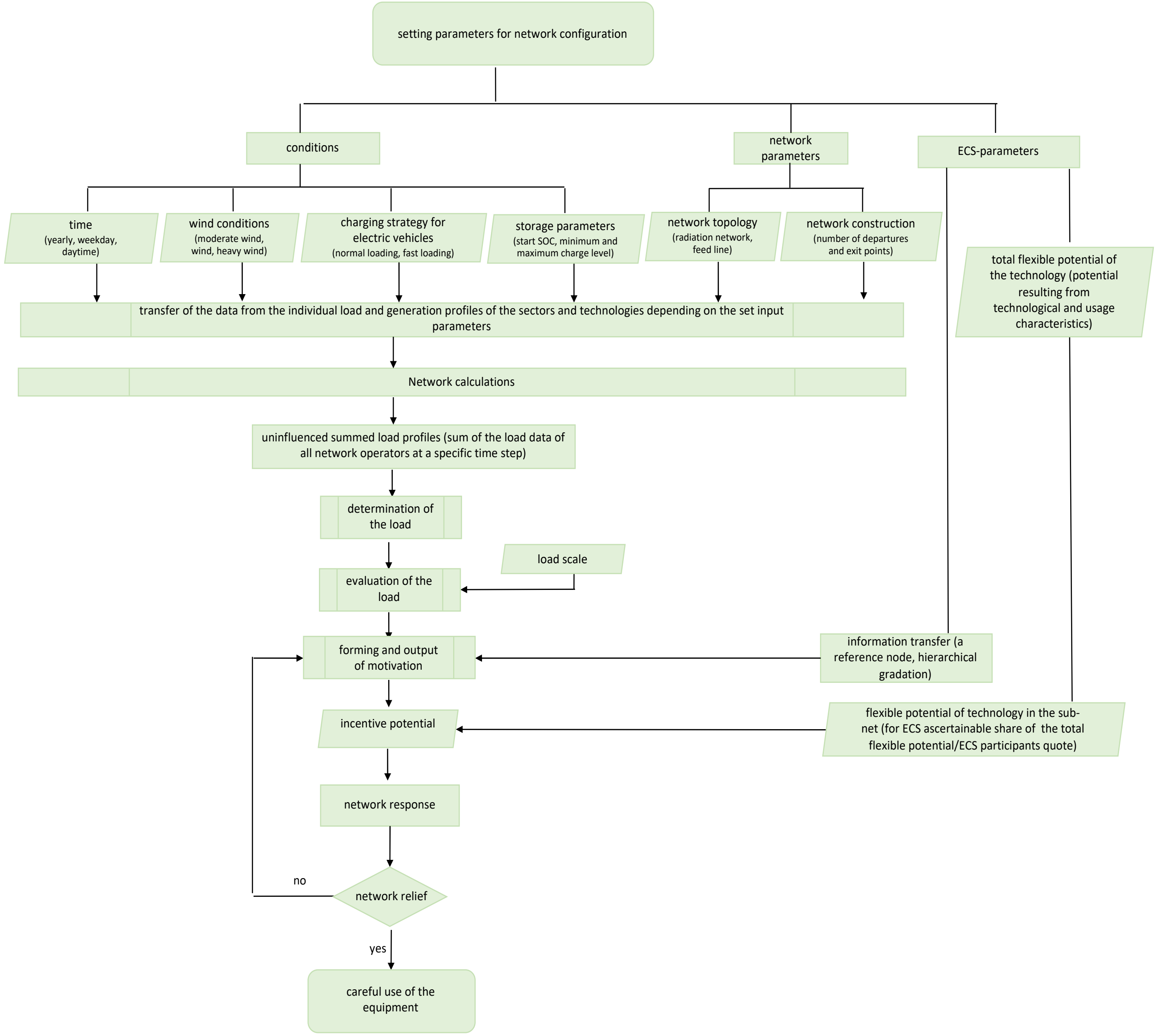

Fig. 5. Control of the ECS-System for network simulation

Different scenarios can be generated by suitable selection of various parameters, like wind conditions, charging strategies of electric vehicles, storage parametrization and also the grid topology, as shown in fig. 5. They also can be varied by use of different time dependencies. Time dependencies refer to the time of day, type of the day, season and also to the reference year. The differences in the energy landscape of the reference years 2019 and 2030 allow a comparison of the actual and the future network situation.

The data basis used in the simulation includes the daily load profiles for each type or technology, which are either standard load profiles of the Federal Association of Energy and Water Industry (BDEW) or anonymized and realistic daily load or daily generation profiles from the real network. The daily profiles differ between working day, Saturday and Sunday as well as between summer, winter and transition period. In addition, the flexible potential that is available in the individual subnetworks and the flexible potential, available to the ECS-System, can be specified separately. Using the mentioned settings, it is possible to address the area, the technological as well as social differences, e. g. acceptance of the ECS-System by the population. Regarding the configuration parameters and the specification of the participating groups for each subnetwork, the profiles will be selected and considered for the calculations. The results of the simulations for each ECS-Node (Nodes N1, N1.1, N1.2 and N1.3 in the figures 3, 4) are finally: a summarized load profile and respective currents and voltages. The resulting load profiles and the calculated network parameters determine the unaffected load situation which is assessed by a self-defined load scale.

The network load, as shown in the following figures, is determined by the loads of the cables and transformers used in the lower and medium voltage grids. All of the other network equipment is usually also affected by load-dependent aging characteristics, but they can be neglected for a first-time assessment of the effects on the network load and the functionality of the ECS-System. The load scale is aligned to the results of ageing studies and analyses of paper insulated lead covered cables, which are still very present in the distribution networks. According to this studies, thermal loads higher than 30% of the nominal cable load cause remarkable ageing of the cables and therefore will be regarded as starting point for the intervention of the ECS-System, [3-6].

As already shown, the assessment of the network load forms the basis for the monetary incentives, which are intended to influence ECS participants' usage behavior. Due to the continuously conducted processes of measurement and calculating as well as the valuation of the network load, the effect of the ECS-System is directly reflected in the measured values. If the initial situation does not change sufficiently, monetary incentives can be increased in order to integrate more flexible potential and thus further relieve the different load flows in the network.

B. *Results of the simulation*

For the simulation, two different network areas were examined: rural/suburban and urban network. The main difference in the network structures is given by network topology and structure of the end user.

For the purpose of this article a rural and radial power network area for the year 2030 was analyzed. It consists of 180 households and several commercial enterprises, as well as several agricultural businesses. According to the developments of the installed photovoltaic and wind systems as well as storage systems and registered electrical vehicles, [7-10], there are over 80 photovoltaic systems, 30 electrical vehicles, 10 heat pumps and more than 40 household storage systems in the considered network. Every type and technology is characterized by the profiles mentioned before.

The load flow simulation of the described network, structured as in Fig. 3, in the time span of 24 hours in a summer season with and without impact of the ECS-System is carried out.

Fig 6. shows exemplarily the effect of the ECS-System at the ECS-N1 node (Fig. 3). The load of the power equipment, in this simulation of the cable systems, is shown in relation to the cable nominal load.

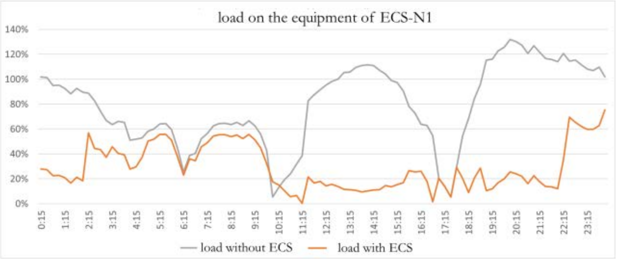

Fig. 6. Network load at the grid node of the ECS-N1 node with and without the use of the ECS-System

The grey graph indicates the load on the equipment without the influence of the ECS-System. The high load at between 10 am and 4 pm results from the increased feed-in of photovoltaic systems. The increasing load at the end of the day can be traced back to the high energy consumption of electric vehicles that are being charged at home at that time. The maximal cable load of 132% is reached at around 8 pm.

The orange graph shows the affected load profile of the power equipment due to the use of the ECS-System. It is important to mention, that the ECS-System just intervenes when the load of the equipment exceeds 30% as described before.

The main effects of the reduction of the cable loads is achieved through the appropriately scheduled and adapted interaction between photovoltaic feed-in, charging of the storage systems charging the electrical vehicles. In this way the maximal load of the cables of 70% is reached at around 10:30 pm (time when the storage systems do not support charging of the electrical vehicles anymore).

In this way and with the impact of the ECS-System the maximal cable load is reduced from 132% to 70%. Moreover, the maximum load is shifted from the middle of the day to night hours.

The load curve of the subnetwork 1 (N1.1), which characterizes a residential area, is shown in Fig. 7.

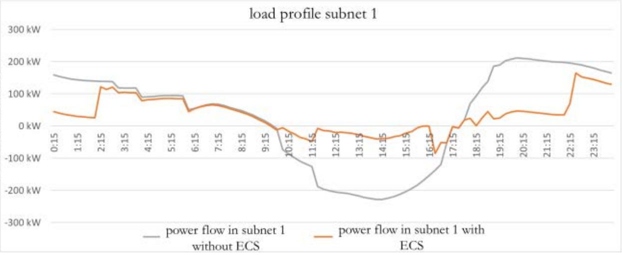

Fig. 7. Load profile at the grid node of the first subnetwork (N1.1) with and without the use of the ECS-System

The grey graph in Fig. 7 shows the unaffected load profile at N1.1 node (from Fig. 3). The negative power results from the reverse of the power flow into the medium voltage network. The orange graph demonstrates the significant reduction of the negative load as well as the reduction of the maximal consumption in the considered node using the ECS-System. The sudden increase of the load at around 10 pm is a result of the already discharged storage systems in an appropriate subnetwork at that time, which means that the needed power has to be delivered in conventional way from the power system. The resulting gradients and maximum loads can be further significantly reduced by an application of a sophisticated and forward-looking optimization of the use of storage systems by the ECS-System.

Fig. 8 shows the load on the equipment, i.e. the cables, in the subnetwork 1 (from Fig. 3).

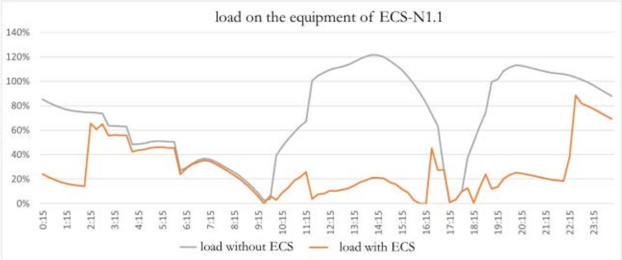

Fig. 8. Network load at the grid node of the first subnetwork (N1.1) with and without the use of the ECS-System

Fig. 8 demonstrates a remarkable reduction of the power equipment load in the subnetwork N1.1 through the application of the ECS-System, similarly to Fig. 6.

IV. CONCLUSION

By the application a cluster-based Energy Cluster Service System, the load of the network components and thus the load on the structural components of the power systems can be reduced significantly. As described, the ECS-System and its clusters are hereby hierarchically oriented on the given supply structure of the energy system.

The main goal of the simulation was to prove the functionality and effect of the ECS-System and here especially to validate the creation and transmission of the load dependent monetary incentives. For this purpose, high flexibility, as well as high acceptance and participation have been assumed. Hence the results shown in this article represent an optimal case of the effect of the ECS-System.

For the further analyses and further improvement of the ECS-System the simulation parameters will be selectively adjusted finally to reach a realistic reflection of the power system.

The options and the feasibility of load reductions are particularly important when considering the gradually increasing volatile feed-in to the public electricity network from distributed energy sources over the next few years. Economically and technologically alternatives to grid expansions or network enhancements are absolutely essential. By applying the ECS-System, the maximum load and thus the necessary grid expansion can be reduced to a minimum or largely extended in many areas.

The active motivation of a local balance between production and consumption can thus be used to minimize network expansion costs and reduce the load on superordinate networks and equipment. Additionally, an extended average lifetime of the power system components is to be expected, which should also allow a significant postponement of important replacement investments in the longer term.

REFERENCES

[1] P. Würfel, Unter Strom: die neuen Spielregeln der Stromwirtschaft, 2nd ed., Wiesbaden: Springer, 2017, p. 28.

[2] F. Joos, Hrsg., Energiewende – Quo vadis? Beiträge zur Energieversorgung., Wiesbaden: Springer Vieweg, 2015, p. 25, 28.

[3] I. Mladenovic, Ch. Weindl: Empiric Approach for Criteria Determination of Remaining Lifetime Estimation of MV PILC Cables, A chapter in Dielectric Material, ISBN 979-953-307-1016-8, InTech, DOI: 10.5772/51490, 2012

[4] Dr. Christian Weindl: Verfahren zur Bestimmung des Alterungsverhaltens und zur Diagnose von Betriebsmitteln der elektrischen Energieversorgung, Habilitationsschrift im Fachgebiet Elektrische Energieversorgung, Technische Fakultät der Friedrich-Alexander-Universität Erlangen-Nürnberg, 2012

[5] I. Mladenovic, Ch. Weindl: Developments in the Diagnostics of MV PILC Cables, IEEE Electrical Insulation Magazine, January/February 2012

[6] I. Mladenovic, „Determination of the Remaining Lifetime of Paper Insulated Lead Covered Cables based on the Diag-nostics of Partial Discharges and the Dissipation Factor,“ Dissertation, Erlangen, 2012.

[7] Bundesnetzagentur, „Genehmigung des Szenariorahmens 2019-2030“, 15-Jun-2018.

[8] Forschungsstelle für Energiewirtschaft e.V., Szenario-Analyse – potenzielle zukünftige Rahmenbedingungen für den Netz-Ausbau, 2017.

[9] Nationale Plattform Elektromobilität, „Fortschrittsbericht 2018 – Markthochlaufphase“, Mai-2018, S. 51.

[10] Agora Energiewende, „Stromspeicher in der Energiewende“. Sep-2014, S. 106ff.

Application of a Dynamic State Estimation Method for a Real-time Simulated Distribution System

Jan-Niklas Ceschlaw, Rajkumar Palaniappan, Annika Brüggemann, Björn Bauernschmitt, Christian Rehtanz
Institute ie^3, TU Dortmund University
Dortmund, Germany
jan-niklas.ceschlaw@tu-dortmund.de

***Abstract*—With the advent of distributed energy generation and ambiguous directions of power flow, state estimation (SE) becomes a very important topic in distribution networks. The requirement of a dynamic algorithm that can perform SE with respect to changes in in-feed, loads and network topology is becoming increasingly important. This paper presents the implementation of a SE algorithm for a dynamic grid model running on a real-time simulator (RTS). The work includes simulating suitable measurements on the RTS as well as the preparation of the measurement data for the use in an algorithm for both static and dynamic SE. The available static case is used for implementing the dynamic SE. The optimal location and number of the measurements for the network are also analyzed. In order to validate the implementation, the results of the SE are compared to the actual measurements directly available at the RTS. The work is done as a preliminary proof of concept that is extended in the context of the i-Automate project at the institute ie^3.**

***Index Terms*—observability analysis, state estimation, smart grids, real-time simulation, software-in-the-loop**

I. INTRODUCTION

The institute ie^3 works on implementing protection and control functions on a standardised platform in the project i-Automate. These algorithms are currently being validated in hardware-in-the-loop simulations and will later be tested in real-world conditions. The detailed system concept and its implementation on KoCoS measurement devices have been published in [1].

The voltage control developed in this context [2] depends on measurements taken from several points of the grid. However, measuring all points in a distribution grid is impractical and improbable. State Estimation (SE) offers a way to obtain an estimate for the system state by computing the voltage phasors of all buses based on a limited set of measurements [3]. It is typically performed at the control center level. The speciality of the planned implementation is to have a dynamic SE and smart grid functions on the same hardware device which is located at the substation level. A dynamic SE executes automatically as soon as new measurement data is available to make allowance for the dynamic changes in the grid. The first step to achieve this is to implement a dynamic SE with measurements obtained from the real-time simulator (RTS) that simulates the grid. This includes the transfer of measurement data for the SE as well as the optimal location of the measurements in a modified Cigré low voltage network model. This simple grid model allows for a more comfortable research while the results obtained are then applicable for the real-world distribution grid associated with i-Automate.

Research shows the use of RTS in combination with SE for validating protection and control functions, such as the validation of a voltage control in [4] or a fault detection using phasor measurement units (PMUs) in [5]. In comparison to the work in [6] that presents the implementation of a real-time SE on a RTS, this paper makes use of a SE program that is running on a host computer.

The paper starts with an introduction to SE in chapter II. The RTS is introduced in chapter III and the grid setup is explained in chapter IV. The usage of the available algorithm for a dynamic SE is explained in chapter V. The results of the dynamic simulation are dealt with in chapter VI and the paper finishes with a conclusion and outlook in chapter VII.

II. STATE ESTIMATION

A SE calculates the voltage phasor at each system node for the system state with the highest probability. The calculation is based on the available set of measurements and the topology information of the network. According to Abur [3] the term SE accumulates several functions. Before an estimate for the system state is computed, an observability analysis is performed based on the information provided by the topology processor and available measurement data. The SE can proceed only when the system is observable. The detection and identification of bad data is also a task of the SE algorithm.

A. Weighted Least Squares SE

The weighted least squares (WLS) method is formulated in [3] and [7]. It is based on equation 1 which relates the vector of measurements z to the state vector x by using the measurement functions h. The state vector of a system contains the real and imaginary part of all nodal voltages. The measurement errors are presented by e. It is assumed that the errors have a normal distribution and are independent.

$$z = h(x) + e \tag{1}$$

The weighting matrix W is the inverse of the covariance matrix R which is the diagonal matrix of the standard deviation σ of the measurement errors e. The elements of the weighting matrix represent the accuracy of the measurement.

The residuals $r_i = z_i - h_i(x)$ in function $J(x)$ (equation 2) are weighted accordingly.

$$J(x) = \sum_{i=1}^{m} W_i r_i^2 = [z - h(x)]^T R^{-1} [z - h(x)] \qquad (2)$$

The SE minimizes the objective function J by iteratively solving the normal equations (5) for the state update Δx^{k+1}.

$$G(x) = H^T(x^k) R^{-1} H(x^k) \qquad (3)$$

$$H(x) = \frac{\partial h(x)}{\partial x} \qquad (4)$$

$$G(x^k)\Delta x^{k+1} = H^T(x^k) R^{-1} [z - h(x^k)] \qquad (5)$$

B. State Estimation algorithm

A Matlab algorithm for WLS SE using Cartesian coordinates was developed as part of a dissertation at the institute ie^3 [8]. It allows the use of a specific measurement set and has a graphical user interface (GUI). It also includes an observability analysis and bad data processing. Essential functions like providing measurement and network data to the SE algorithm, starting the observability analysis or performing SE are done via the GUI. The measurement data is provided to the algorithm as text files. Other relevant data including the network topology and the start values for the state vector at the first iteration should also be available. The measurements that shall be used for SE as well as several parameters (weighting, precision) can be selected in the GUI. The algorithm uses iterative solution of the normal equations and the observability analysis is based on the numerical method with branch variables as described in [3].

III. REAL-TIME SIMULATOR

The requirement for a simulation in real-time using a fixed time step is that the time needed to solve the equations is shorter than the fixed time step. This enables the simulation to imitate the dynamic properties of the physical system. An overrun occurs when the computations cannot be finished within one time step. [9]

The RTS OP5600 from OPAL-RT is used for real-time simulation. An overview of its technical data is given in [10]. The simulator is controlled by the software RT-LAB [11] running on the host computer.

A Simulink model is prepared for real-time simulation by making use of the blocks provided by the Artemis library. The model can be distributed on subsystems that are decoupled by using Artemis Distributed Parameter Lines (DPL) or Stublines in order to reduce its complexity and to set it up for parallel execution. These Artemis blocks model a transmission line and enable the parallel execution on different cores by introducing a delay of one time step. A further decoupling of the system using State Space Nodal (SSN) blocks can be necessary for complex networks with a lot of switches. By making use of the SSN method the memory needed for the pre-calculated state space matrices of the network can be limited. [12], [13]

The internet standard of the User Datagram Protocol (UDP) [14] is used for the connection to the host computer. The UDP standard does not provide a guarantee that a sent package reaches its destination. UDP packages do not necessarily arrive in the same order in which they were transmitted. There is also no duplicate protection available. This means that it is possible to receive several copies of the same UDP package. [15]

IV. MODIFIED CIGRÉ LOW VOLTAGE NETWORK MODEL

A grid model in Simulink runs on the RTS containing two branches, each of them representing a Cigré low voltage (LV) benchmark network, as shown in Fig. 1.

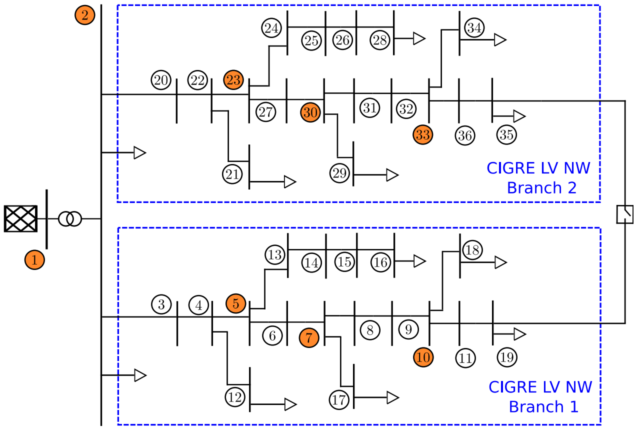

Fig. 1. Measurement configuration

The model has a switch located between bus 19 and 35. The grid is connected to a fixed 20 kV network via a two-winding transformer. The topology data needed for SE is acquired via a Cigré LV benchmark model in PowerFactory [16]. The model is extended as in Fig. 1. The measurement configuration that is obtained in section IV-C is given in Fig. 1. The measurement points are marked orange. The Cigré transformer is replaced with a transformer whose parameters are defined in table I.

TABLE I. Comparison of the transformers

	Cigré transformer	**used transformer**
Type	20/0.4 kV Dyn5	20/0.4 kV Yy0
Nominal apparent power S	0.5 MVA	0.8 MVA
Resistance R1	0.01 pu	0.00875 pu
Inductance X1	0.04 pu	0.05936 pu

A. Measurements

In order to acquire the measurements needed for SE, the Simulink model is built up with measurement subsystems. An artificial error of 1 % is added to all the measurements. The following measurements are provided:

- voltage magnitude at node i (ph-ph, RMS)
- voltage phase angle at node i
- three-phase real power flow from node i to node j
- three-phase reactive power flow from node i to node j

Every node is equipped with measurements in Simulink and all available data is sent to the host computer via UDP. The selection of which of the measurements are used for the SE is done at the host computer. This allows to test different measurement configurations without the need for time consuming changes to the Simulink model. All measurements of the same type (voltage, power flows, etc.) are stored in a single vector in a defined order. That makes it easy for applications on the host computer to determine which node or branch the received measurements belong to. The first datum of every sent UDP package contains a time stamp that indicates the simulation time of the RTS, allowing a time-wise differentiation of packages. The remaining data of a package contains the measurement values. The model on the RTS is configured to send a new set of measurement data to the host computer every 20 seconds.

B. Eliminating overruns and usage of Stublines

The Simulink model was initially configured for a fixed time step of $T_s = 50\,\mu s$. Adding the measurement subsystems and the UDP functionality made the computing power no longer sufficient to run the model without overruns. The time step is therefore raised to $T_s = 200\,\mu s$ to eliminate overruns.

Since the model chosen is complex, it has to be split into multiple subsystems. Stublines are used for the connection of power lines between the different subsystems. The transmission lines modelled by the Stublines between two subsystems have no equivalent in the network model and thus have a parasitic effect on the simulation. The impedances are not known by the SE and their influence on the simulation results has to be constrained. There are two ways taken into consideration to achieve this. It is either possible to remove the Stublines and use the SSN method instead or to modify the model parameters. Since the correct implementation of the SSN method still needs to be figured out for this implementation, the second possibility is used for now. A Stubline is located between the transformer and each branch so that the transformer and the two branches are simulated in their own respective subsystems. The default transformer ratio leads to a higher than expected voltage magnitude at the end of the Stublines if these are connected to ground via a high resistance. Therefore the transformer ratio is lowered to regain the expected voltage of 400 V.

C. Optimal selection of measurement points

Having measurement devices at all possible nodes is too expensive and impractical. Therefore the preparation of SE on the real-world grid requires a strategy for the optimal placement of measurements. The following concept for the Cigré network can be transferred to the real-world distribution grid that is much larger and more complex.

1) Default model: Determining which measurements are best used for the SE is achieved by using a concept developed in [8]. A ranking of all possible measurement locations is generated by computing the product of the path length and the loads connected at that node. The measurement points are ranked by their influence on the estimation quality. As starting point to find the optimal measurement configuration, [8] proposes to use the main station of the network as first measurement location. Other measurement points are added starting with the node of highest ranking. Once a node is added, all the neighbouring nodes are removed from the set of possible locations.

Since the goal is to have the number of measurements used for SE as minimum as possible, an observability check is performed after adding a new measurement point to the set. The virtual nodal power measurements of nodes without loads (P=Q=0) are assumed to be known. When the system is fully observable, no more measurements are added. If a node i is defined as a measurement point, the voltage magnitude U_i, the nodal powers P_i and Q_i as well as all outgoing line power flows P_{ij} and Q_{ij} are known and used for SE calculation. The resulting configuration for the model is given in Fig. 1.

2) Variant 1: In the following sections, two variants of network topologies are discussed. In variant 1, the connection between node 5 and 6 is disconnected (e.g. due to a fault). The switch at the end is closed to restore power supply to all parts of the network. The parameters of the newly introduced line closed by the switch are set to be equal to the line between node 5 and 6. For this reconfigured network, measurements in already observable parts of the network are to be added when following the ranking order. These measurement points, marked with double circles in Fig. 2, can be beneficial for the estimation quality but make no difference for observability.

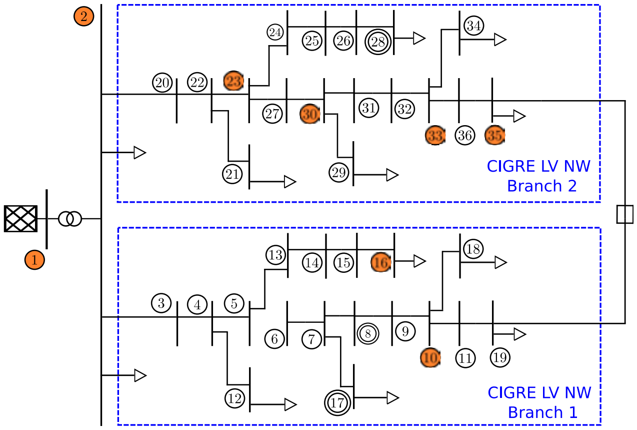

Fig. 2. Measurement configuration - variant 1

For the reconfigured network, only one measurement point is sufficient for the remaining part of the first branch that is still directly connected to the busbar at node 2. This measurement is now at node 16 since its impact on the estimation quality is greater there than at node 5. In comparison to the default model, the measurement at node 10 remains and one is added at node 35.

3) Variant 2: The second variant features the removal of station 17 and increasing all loads in branch 2 by 10 kVA (excluding the load at node 2). The former load at node 17 is added to the load supplied by node 12. Loads that have changed in comparison to the default configuration of the network are marked green in Fig. 3. Because of the increased load at node 12, the measurement at node 5 shifts to node 4. Since the total load has only increased in the second network branch, the distribution of measurement points in the ranking

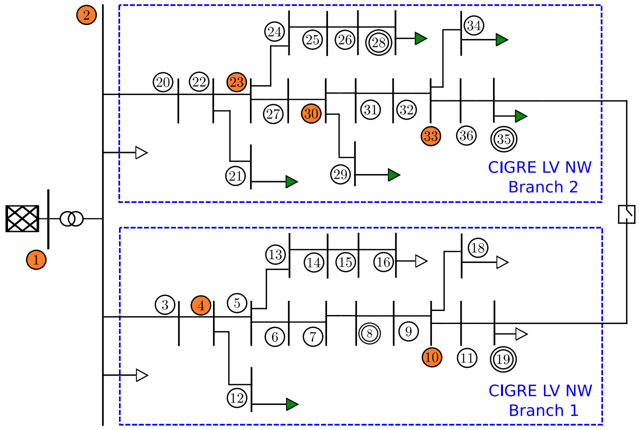

Fig. 3. Measurement configuration - variant 2

is no longer equal for both branches like it was the case for the default network model.

V. Dynamic SE

A. Processing of the measurement data

One of the major tasks of this paper is to execute the functional implementation of the SE algorithm on a continuous basis. In this regard, a new set of measurement values is received at the host computer every 20 seconds via UDP, prompting an updated SE. The host computer runs a Simulink model that listens to the ports and writes the received measurement data in the Matlab workspace. A script has been developed to process this data and output it in text files as required by the SE algorithm. The flowchart in Fig. 4 gives an overview about the process implemented.

There are some nodes in the network that are not connected to any loads. Since there is no nodal power measurement available at these nodes, it is necessary to find the corresponding node for each of the received power measurements. For all nodes without a load a virtual power measurement of zero can be set. To achieve this, the script automatically determines all end nodes of the network and makes the assumption that there is a load connected. The indices of the remaining nodes are provided by the user. Further, the index of the node which is connected to the fixed grid needs to be given to the script. All input data can be found in the white boxes in Fig. 4.

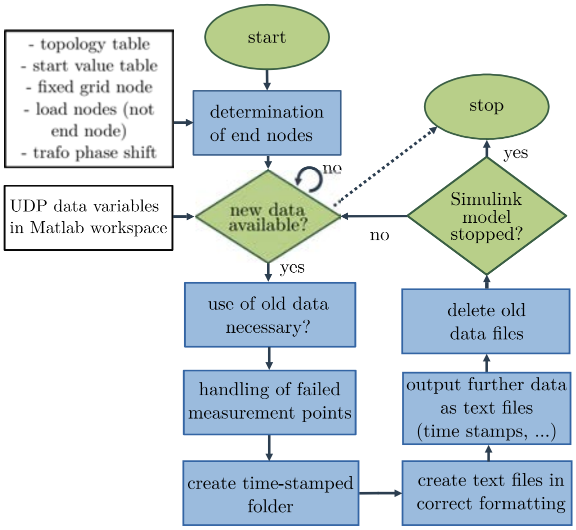

Fig. 4. Algorithm flowchart

The SE algorithm also needs PMU measurements. The data provided by the measurement subsystems enables the script to calculate the real and imaginary part of the complex nodal voltages and line currents. Before performing these calculations, the measured phase angles affected by the transformer phase shift are corrected. The correction is necessary because the SE algorithm does not consider the transformer phase shift in its calculations.

B. Unavailability of measurement data

In this implementation, the exactness of the measurements or bad data detection are not considered. Although, it checks for data which is unavailable or outdated. If a measurement data package does not arrive, an old time stamp is detected. In this case, previously received data is used for the SE algorithm. The implementation is also capable of replacing the values of unavailable measurement points with the last data that was successfully transmitted. For this replacement to work, it is required that a measurement point outputs the value ”NaN” (Not a Number) for all its measurements. The output of the script consists of the measurement data as well as information regarding the time stamps, the existence of old data and the indices of unavailable measurement points.

C. Implementation of dynamic SE

The dynamic SE executes automatically when new measurement data is available on the host computer. It is implemented by using the existing SE algorithm [8]. As mentioned, this static SE includes a GUI for user interaction, where a user input triggers a callback function. An automated system is created to achieve an autonomous execution of these functions. It triggers the callbacks without any user interaction every time new measurement data files are detected. Since there is no measurement configuration done by the user when running dynamic SE, a fixed configuration is defined in the SE code for the purpose of this implementation. The GUI is enhanced with a button to choose a static run of the SE or to start the dynamic SE. The time stamps of the measurements as well as the indices of unavailable measurement points are displayed in the GUI. It can also be checked if old data had to be used due to an unreceived UDP package.

VI. Results

In order to verify the implementation, the output of the SE algorithm available as complex voltage phasors is compared with the actual measurements available at the RTS. The preconfigured SE parameters (convergence constraint, weighting, etc.) and the measurement configuration as given in Fig. 1 are used. A flat start is applied for the state vector at the first iteration. This means that the real part of the complex voltage phasors equals 1 pu and the imaginary part is 0 pu. Since the complete system cannot be displayed, the nodes with the highest error percentages are chosen.

A. Static network

As a first step, the SE algorithm is run on the default model without any dynamic changes. The errors on the real part e_i and imaginary part f_i of the complex voltages at the nodes with maximum error are shown in Fig. 5 and Fig. 6.

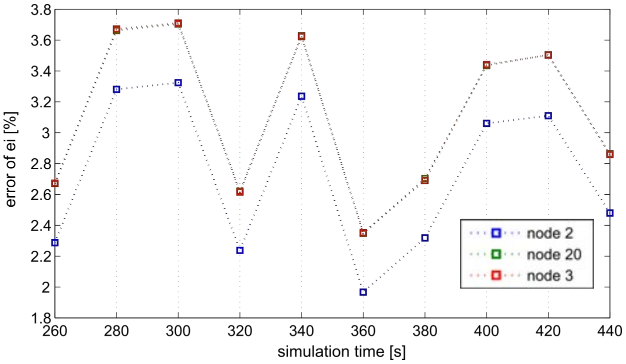

Fig. 5. Estimation error of e_i for different nodes in the static network

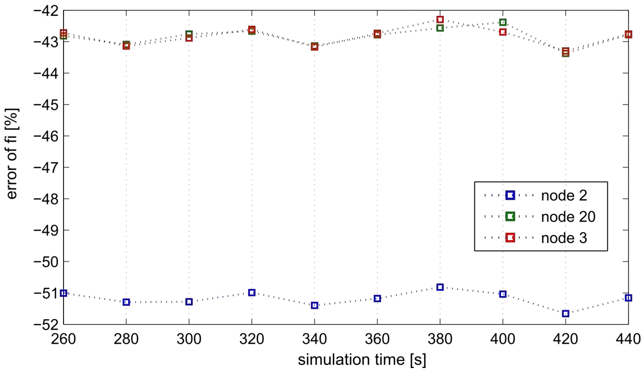

Fig. 6. Estimation error of f_i for different nodes in the static network

The results show an average estimation error of 3 % for the real part e_i of the complex voltages. The estimation quality of the imaginary part f_i has an average of −32 % and is therefore quite poor. The undertaken corrective measures are not able to minimize the influence of the Stublines satisfactorily. This is because the SE does not know about this parasitic impedance. A check of the power flow shows that the reactive power flow is not as expected. The capacitive influence of the Stublines is high enough to invert the power flow. The node connected to the fixed grid is now injecting reactive power into the grid. It is found that introducing an additional inductive load as well as adding additional measurement points to the estimation does not improve the results. The results for the nodes 2, 3 and 20 are the most influenced by Stublines since these nodes are directly connected to them. The estimation errors for these nodes over a course of ten datasets (simulation time from 260 to 440 seconds) are given in Fig. 5 and Fig. 6.

B. Dynamic network

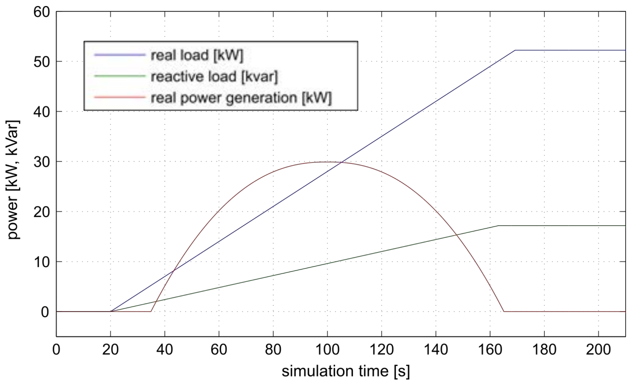

Fig. 7. Dynamic load and power generation at node 29

The static load at node 29 is replaced with a dynamic load and a decentralized generator (DG) according to Fig. 7 to create a dynamic operation of the system. The estimation errors over time are documented in Fig. 8 and Fig. 9. The measured voltage at node 29 has its peak at $t = 80\,s$. This is due to node 29 becoming an injection node for a period of time around $t = 80\,s$ when the power generation is greater than the power consumed by the load. Regarding the estimation errors it is important to note that the dynamic process introduced at node 29 has an impact on the estimation quality. When the power generation stops after approximately 160 seconds, the

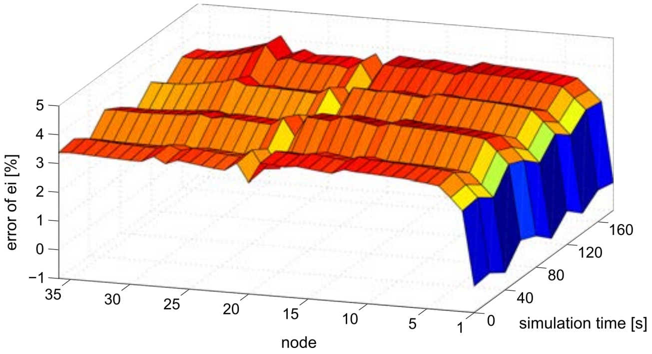

Fig. 8. Estimation error of e_i for different nodes in the dynamic network

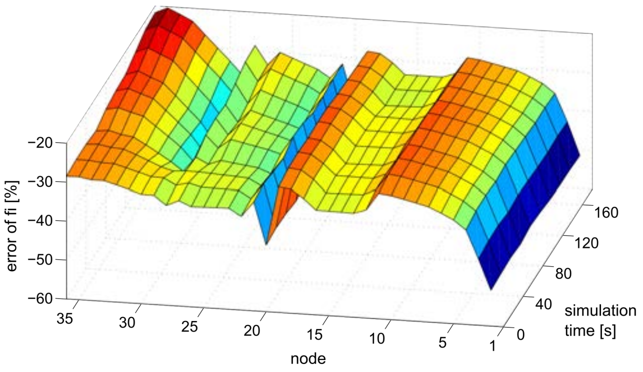

Fig. 9. Estimation error of f_i for different nodes in the dynamic network

error of the real part at node 29 raises above $4\,\%$. While the power generation increases, the error of the imaginary part at node 29 also raises from $-32\,\%$ at the beginning of the simulation to its peak of $-41\,\%$ at $t = 120\,s$. In general the behaviour of the errors in Fig. 8 is quite homogeneous with the reference node 1 being the only exception. The observations that have been made for the nodes 2, 3 and 20 in the static network are still applicable.

VII. CONCLUSION AND OUTLOOK

The application of a SE algorithm for a distribution grid model running on the RTS has been presented in this paper. This is done as an initial test to show that SE can run in quasi-dynamic and dynamic conditions using the RTS. To facilitate this, measurement data is sent from the RTS to the host computer to be used in a dynamic SE. An optimal measurement point configuration for SE has also been investigated. The validation of the results has shown some major problems regarding the use of Stublines in the model which enable the RTS to perform a parallel execution. The large estimation errors lead to the realization that Stublines are not suitable to get usable SE results for the used network. It is advised to implement the SSN method for future tasks.

Since this is a preliminary implementation, some assumptions are made which are not close to real-world applications. For example, a 3-phase SE is not done, which could be an advancement to the existing implemenation applicable in distribution grids. There are several other ways in which the implementation presented in this paper can be researched further. It can be useful for future applications to enhance the used WLS SE with more sophisticated SE methods, for example by using an adaptive SE as proposed in [17]. Further tasks can also include the step towards a transient SE. This means considering the effect of a synchronous generator connected to the grid between two execution cycles of dynamic SE and how SE can be used to understand the occurring transients. In future versions of the measurement processing, pseudo measurements could be used for failed or unavailable measurement points. The replacement with the latest data that was successfully transmitted is not optimal since these values are static and only represent an outdated overview of the system. As described, all nodes of the network model in Simulink are equipped with measurements. This will not be feasible with large systems. Hence the simulation should only include the measurements that are needed for SE.

After the first studies presented in this paper, a SE program was further developed in C++. The program which also incorporates several other smart grid functions shall be deployed on a KoCoS measurement device for use in a real-world distribution grid. The real-time voltage values at the local substations will be measured with the devices. These values will be sent to the central controller. With the decentralized values from the different points of the network, the central controller will run the SE algorithm. A voltage control algorithm is applied based on the current system state. The proposed voltage control only considers the voltages at specific points in the grid while the voltages of the unmeasured nodes are unknown. By introducing a SE, the effect of voltage control on all system nodes can be observed. Before moving on to the field, the implementation is currently being validated in the lab by using a hardware-in-the-loop setup with the central controller and the RTS.

REFERENCES

[1] B. Bauernschmitt, R. Palaniappan, D. Hilbrich, C. Rehtanz: *Modular Configurable and Testable Automation Architecture for future Active Electrical Energy Grids*, UPEC, 2018, DOI: 10.1109/UPEC.2018.8541947

[2] R. Palaniappan, D. Hilbrich, B. Bauernschmitt, C. Rehtanz: *Co-ordinated voltage regulation using distributed measurement acquisition devices with a real-time model of the Cigré low-voltage benchmark grid*, IET Gener. Transm. Distrib., 2019, Vol. 13 Iss. 5, pp. 710-716, DOI: 10.1049/iet-gtd.2018.5300

[3] A. Abur, A. Gómez Expósito: *Power System State Estimation - Theory and Implementation*, New York: Marcel Dekker, Inc., 2004

[4] K. Christakou, M. Pignati, R. Rudnik, S. Sarri, J.-Y. Le Boudec, M. Paolone: *Hardware-in-the-loop Validation of the Grid Explicit Congestion Notification Mechanism for Primary Voltage Control in Active Distribution Networks*, Power Systems Computation Conference (PSCC), 2016

[5] M. Pignati, L. Zanni, P. Romano, R. Cherkaoui, M. Paolone: *Fault Detection and Faulted Line Identification in Active Distribution Networks Using Synchrophasors-Based Real-Time State Estimation*, IEEE Transactions on Power Delivery, vol. 32, no. 1, February 2017

[6] A. Chandra, A. K. Pradhan, A. K. Sinha: *PMU Based Real Time Power System State Estimation using ePHASORsim*, National Power Systems Conference (NPSC), 2016

[7] A. Gómez-Expósito, A. Abur, A. De La Villa Jaén, C. Gómez-Quiles: *A Multilevel State Estimation Paradigm for Smart Grids*, Proceedings of the IEEE 99 (2011), no. 6, p. 952-976

[8] K. Görner: *Analyse und Anwendung der zeitsynchronisierten Zeigermessung*, Dissertation, Reihe ie3 - TU Dortmund, 1st ed., Sierke Verlag, 2017

[9] J. Bélanger, P. Venne, J.-N. Paquin: *The What, Where and Why of Real-Time Simulation*, Planet RT (October 2010), no. 1, p. 37-49

[10] OPAL-RT: *OP5600*, http://www.opal-rt.com/simulator-platform-op5600/, last checked: 30.05.2019

[11] OPAL-RT: *RT-LAB*, http://www.opal-rt.com/software-rt-lab/, last checked: 30.05.2019

[12] OPAL-RT: *Artemis User Guide Version 6.1*, 2008, https://www.researchgate.net/file.PostFileLoader.html?id=57b2a9d3b0366dfee75e0183&assetKey=AS%3A395586898546692%401471326674861, last checked: 30.05.2019

[13] OPAL-RT: *Artemis-SSN: State-Space Nodal (SSN) A nodal admittance solver for SimPowerSystems*, Real-Time Conference 2013, http://www.opal-rt.com/wp-content/themes/enfold-opal/pdf/L00161_0368.pdf, last checked: 30.05.2019

[14] J. Postel: *User Datagram Protocol: RFC 768*, https://tools.ietf.org/html/rfc768, version: August 1980, last checked: 30.05.2019

[15] L. Eggert, G. Fairhurst: *Unicast UDP Usage Guidelines for Application Designers: RFC 5405*, https://tools.ietf.org/html/rfc5405, 2008, last checked: 30.05.2019

[16] Cigré: *Benchmark systems for network integration of renewable and distributed energy resources*, Paris: Conseil international des grands réseaux électriques, 2014, 978-285-873-270-8

[17] J. Zhang, M. Momtazpour, G. Welch, S. Rahman: *Secure and Adaptive State Estimation for a PMU-equipped Smart Grid*, IEEE 15th International Conference on Environment and Electrical Engineering (EEEIC), 2015

A mixed integer linear programming for the day-ahead electricity market with wind power generators

Pengpeng Li, Tankut Yalcinoz and Krzysztof Rudion
Institute of Power Transmission and High Voltage Technology (IEH)
University of Stuttgart
Stuttgart, Germany
st152704@stud.uni-stuttgart.de, tyalcinoz@ieee.org, rudion@ieh.uni-stuttgart.de

***Abstract*—Currently, with the rapid development of renewable energies on the electricity market, the integration of renewable energies into the electricity grid as power plant units has become a significant development trend. This paper presents the optimal market model with the economic dispatch and unit commitment based approaches in the day-ahead electricity market and analyses the effects of the uncertainty of wind power on the next day's electricity market. In this paper, a mixed integer linear programming (MILP) algorithm is used to solve the unit commitment (UC) and economic dispatch (ED) problem. Three case studies with different load demands are performed for this study, and the proposed method is verified on the IEEE 30-bus system with six conventional power plants and three wind power generators.**

Keywords—Day-ahead electricity market, renewable energy sources, mixed integer linear programming, economic dispatch, unit commitment

I. INTRODUCTION

Today, large amounts of electricity are traded in day-ahead markets where market participants can transparently exchange electrical energy for each hour of the following day. The day-ahead market is the centralized trading platform that uses "one day" as the trading time for market organization, where market participants can more accurately sell or buy electricity based on generation capacity and the price at which they will trade [1][7].

Renewable energies are those energies which are obtained from natural sources such as sunlight, wind, hydroelectric power, biomass, and geothermal energy, etc. As environmentally friendly electrical energy sources, the rapid development of renewable energy sources brings not only remarkable energy security and economic benefits but also a reduction in environmental pollution. In recent years, many countries have begun to rely more and more on renewable energy sources.

As a kind of renewable energy, wind energy has attracted a lot of attention and support worldwide. Wind energy has many advantages, such as cleanliness at low operating costs, like any other renewable energy source that encourages governments to share more of their wind energy. On the other hand, wind power also has the variability of renewable energy sources, as its speed is naturally stochastic, leading to uncertainty and intermittent wind power output [3]. Furthermore, the uncertainty of renewable energy sources should be taken into account while making a day-ahead clearing trading plan [7].

The economic dispatch refers to the procedure for allocating electricity generators, the aim of which is to maintain the set of power plant dispatch points with the lowest operating costs while meeting the power demand, subject to transmission and operating conditions.

The unit commitment problems aim to determine the optimal scheduling of generator units over several time intervals with different power demands under different constraints and environments. The optimal time series is the one that guarantees a feasible system operation with the least possible losses and minimum operating costs in order to maximize welfare [2][4]. Many optimization approaches have been applied to solve the unit commitment problem such as Lagrangian relaxation (LR) method [8], simulated annealing approach [9][10] and the priority list method [11].

This paper suggests a day-ahead electricity market model for wind power producers and aims to give a perspective on the impact of the variability of renewable energies on the day-ahead electricity market. The economic dispatch and the unit commitment to deal with the time sequences problem for power plants and wind power generators in the day-ahead electricity market are investigated. In this project, the mixed-integer linear program method is proposed to solve the unit commitment problem. The proposed model is tested on the IEEE 30-bus system.

II. PROBLEM FORMULATION

In the day-ahead electricity market problem, the market model integrated with the wind power generators attempts to find the optimum power sharing of the power plants. Generally, the solution of the market model is obtained by solving the economic dispatch problem combined unit commitment approach.

The MATPOWER user's manual emphasized that minimizing the cost f(x) of generation is equivalent to maximizing social welfare [6]. The objective function of the market clearing model, subject to several constraints, can be described as equation (1):

$$\begin{aligned} \min_{P_{i,t},\ \forall i,t} \Big(& \textstyle\sum_i^{N_G} \sum_t^T c_i \cdot P_{i,t} + \sum_i^{N_G} \sum_t^T c_{i,t}^v \cdot v_{i,t} \\ & + \textstyle\sum_i^{N_G} \sum_t^T c_{i,t}^w \cdot w_{i,t} \Big) \end{aligned} \tag{1}$$

where $P_{i,t}$ denotes the dispatch power output of the i-th conventional generator at time t; $v_{i,t}$ and $w_{i,t}$ are the startup and shutdown status of i-th conventional generator at time t respectively; c_i, $c_{i,t}^{v}$ and $c_{i,t}^{w}$ present the operating, startup and shutdown cost of the i-th generator at time t respectively and N_G is the number of generators.

Constraints

These below equations present the constraints that must be satisfied in the day-ahead market clearing model.

a) Power balance equation of the system

$$\textstyle\sum_{i\in I} P_{i,t} + \sum_{j\in J} W_{j,t} - D_t = 0 \tag{2}$$

where $W_{j,t}$ denotes the output of the j-th wind power producer at time t; D_t is the load at time t.

b) Power limits and commitments of a conventional generator

$$0 \le u_{i,t} \le 1 \tag{3}$$

$$u_{i,t}P_i^{min} \le P_{i,t} \le u_{i,t}P_i^{max} \tag{4}$$

where $u_{i,t}$ presents binary commitment state for the i-th unit at time t; P_i^{min} and P_i^{max} are the maximum and minimum output limit of the i-th conventional generator.

c) Power limits of wind power producer

$$W_j^{min} \le W_{j,t} \le W_j^{max} \tag{5}$$

where W_j^{min} and W_j^{max} present the maximum and minimum output limit of the j-th wind power producer

d) Startup and shutdown events

$$u_{i,t} - u_{i,(t-1)} = v_{i,t} - w_{i,t} \tag{6}$$

$$0 \le v_{i,t} \le 1 \tag{7}$$

$$0 \le w_{i,t} \le 1 \tag{8}$$

e) The ramping constraint of the conventional generator

$$R_{D,i} \le P_{i,t} - P_{i,(t-1)} \le R_{U,i} \tag{9}$$

where $R_{D,i}$ and $R_{U,i}$ denote the ramping-down and ramping-up limits of the i-th conventional generator at time t, respectively.

III. MILP-BASED UC/ED PROBLEM

In this paper, the proposed algorithm based on the mixed-integer linear program is applied to solve the economic dispatch and unit commitment problem. In this study, only active powers are considered, and since wind energy belongs to the renewable energy sources, the costs of wind energy are assumed to zero in the simulation studies, and their allocations within the corresponding power intervals in the market model are randomly generated. The variables of the day-ahead unit commitment, such as the generator status, start-up, and shut-down status, are binary. The procedures for solving the problem are composed mainly of these steps:

- Initialization and input data of conventional generators, renewable energy sources, and loads.
- Create wind power allocations randomly between the lower and upper bounds.
- Establish the market model with unit commitment and economic dispatch to find the generator allocations for each period.
- Print and plot the results of the market model problem.

In this work, the period of 24 hours is selected for the unit commitment problem. For step 1, since this algorithm is continuous, all initial states are set to On, and the initial assignments are set to the mean of the maximum and minimum values of the scheduled generators. For step 2, wind power is a kind of renewable energy sources; hence, all the costs of wind power are considered as zero. The wind power allocations are randomly created in the maximum and minimum range.

IV. SIMULATION RESULTS

The IEEE 30-bus system with six conventional generators and three wind power producers is tested in the case studies. The load data of the IEEE 30-bus system is given in [7], and the transmission data consists of 41 branches, as found in [6]. The mixed-integer linear program method is applied for solving the economic dispatch and unit commitment problem. In this work, the proposed method is carried out in Matlab.

TABLE I. gives parameters of the conventional generator. c_i, $c_{i,t}^{v}$ and $c_{i,t}^{w}$ are the coefficients of generating, startup and shutdown costs, respectively. P^{max} and P^{min} are the maximum and minimum output limits of generators. R_U and R_D refer to the ramp-up and down limits [5][7].

TABLE I. PARAMETERS OF CONVENTIONAL GENERATORS [5][7]

Bus	**Gen**	c_i **(€/MWh)**	$c_{i,t}^{v}$ **(€)**	$c_{i,t}^{w}$ **(€)**	c_i^{inc} **(€)**	c_i^{dec} **(€)**	P^{max} **(MW)**	P^{min} **(MW)**	R_U **(MW/h)**	R_D **(MW/h)**
1	G_1	30	70	30	26	32	100	30	12	12
2	G_2	38.5	50	60	20	23	100	30	12	12
13	G_3	41.25	70	275	20	25	70	20	6	6
22	G_4	37.087	30	60	28	37	60	18	6	6
23	G_5	42	20	200	33	35	50	15	5	5
27	G_6	34.5	40	60	34	38	30	15	5	5

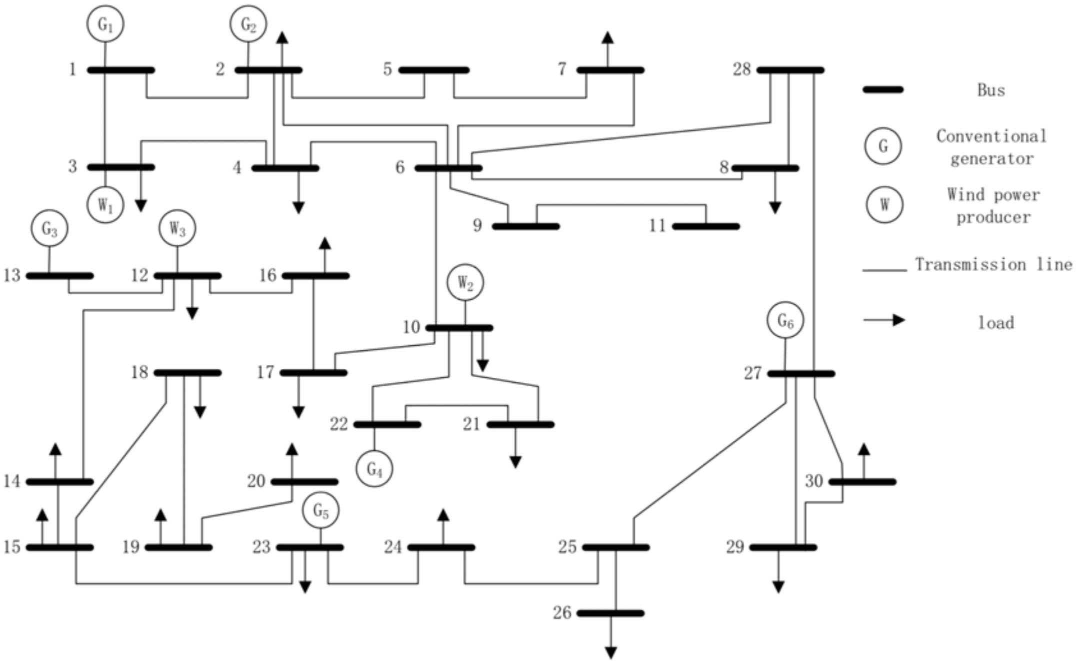

Fig. 1. The IEEE 30-bus system [7]

TABLE II. , TABLE III. and TABLE IV. give the maximum and minimum output limits of wind power generators from [7], which are the crucial components of the uncertainty set. Uw and Lw are the upper and lower bounds, respectively.

TABLE II. WIND POWER GENERATOR I FORECAST OUTPUT INTERVALS (MW) [7]

Time	**1h**	**2h**	**3h**	**4h**	**5h**	**6h**	**7h**	**8h**
Uw	9.97	15.00	21.56	20.42	18.57	16.69	8.91	9.11
Lw	0.26	9.18	11.64	15.44	16.03	5.70	6.92	5.32
Time	**9h**	**10h**	**11h**	**12h**	**13h**	**14h**	**15h**	**16h**
Uw	3.67	4.01	0.00	0.50	0.00	2,79	4.15	5.86
Lw	0.63	0.00	0.00	0.00	0.00	0.00	0.00	1.61
Time	**17h**	**18h**	**19h**	**20h**	**21h**	**22h**	**23h**	**24h**
Uw	11.84	23.72	22.04	28.70	29.18	29.44	29.48	29.48
Lw	3.77	14.21	13.13	23.21	21.55	17.42	17.26	19.24

TABLE III. WIND POWER GENERATOR II FORECAST OUTPUT INTERVALS (MW) [7]

Time	**1h**	**2h**	**3h**	**4h**	**5h**	**6h**	**7h**	**8h**
Uw	26.22	21.11	17.37	5.56	5.52	25.59	36.76	32.63
Lw	16.87	9.85	7.82	0.00	0.11	7.77	21.40	23.85
Time	**9h**	**10h**	**11h**	**12h**	**13h**	**14h**	**15h**	**16h**
Uw	22.92	16.34	5.57	3.49	0.67	2.80	0.00	0.00
Lw	18.04	2.28	0.00	0.00	0.00	0.00	0.00	0.00
Time	**17h**	**18h**	**19h**	**20h**	**21h**	**22h**	**23h**	**24h**
Uw	0.00	0.23	9.04	12.62	22.53	25.84	26.18	0.00
Lw	0.00	0.00	2.65	10.02	13.49	19.62	17.80	0.00

TABLE IV. WIND POWER GENERATOR III FORECAST OUTPUT INTERVALS (MW) [7]

Time	**1h**	**2h**	**3h**	**4h**	**5h**	**6h**	**7h**	**8h**
Uw	5.41	10.38	15.67	16.75	21.92	18.98	5.01	5.14
Lw	0.14	4.60	10.69	12.26	20.19	2.21	3.97	2.33
Time	**9h**	**10h**	**11h**	**12h**	**13h**	**14h**	**15h**	**16h**
Uw	2.63	7.05	0.00	0.00	0.00	0.00	4.15	2.73
Lw	0.01	0.00	0.00	0.00	0.00	0.00	0.00	0.00
Time	**17h**	**18h**	**19h**	**20h**	**21h**	**22h**	**23h**	**24h**
Uw	12.50	29.34	35.48	27.51	29.38	29.47	29.47	29.47
Lw	3.87	14.01	30.70	19.63	17.38	22.70	29.29	29.44

A. Case 1: Original Data

The case study 1 studies the power system based on the original data of the IEEE 30-bus system as well as the load in [7].

Fig. 2 gives the commitment status of conventional units and Fig. 3 shows the allocations of both conventional generators and wind power producers. Fig. 4 demonstrates the operation costs for case study 1.

In Fig. 3, the solid lines with different colors present the generator and wind power allocations. The red dash-dot line shows the total demand and the green is the total supply.

According to the figures, the supply can fully meet the demand during this day. It is evident that the generator 1 has highest dispatching power over multiple time intervals because of its cheapest cost. The generator 5 keeps on until the peak time has passed due to its high shutdown cost, although the most expensive operating cos. As for the generator 6, since its operating, the startup and the shutdown costs are lower than other conventional generators, it will be turned on and off firstly when needed. The total demand is higher in the middle of the day, especially at 13 h and 15 h, and so is the total cost. All the generators turn on in these periods in order to meet the demand.

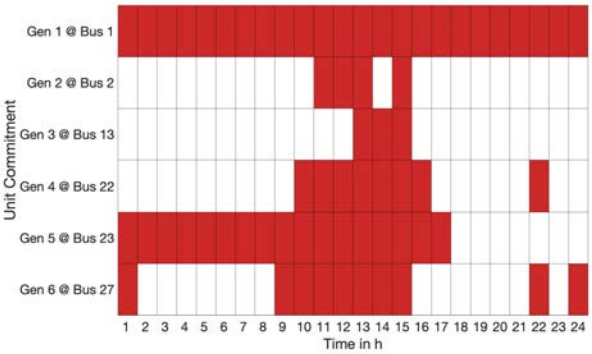

Fig. 2. Generator Status for Case Study 1

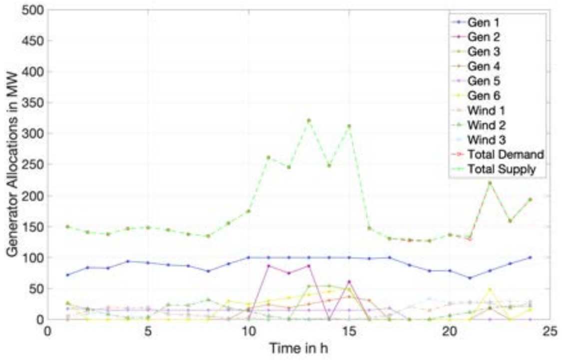

Fig. 3. Generation Allocations for Case Study 1

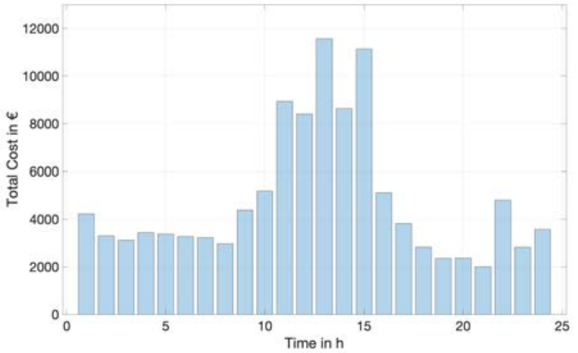

Fig. 4. Total Cost for Case Study 1

After 17 h, the wind power gradually increased. Between 18 h and 21 h, there is the only unit 1 turned on. From 16 h to 18 h, because of the gradually reduced demand, unit 6 was turned off first, and unit 5 was the last. Only unit 1 kept on for 18 h to 21 h duration. At 17 h, unit 5 offered 18.36 MW output and unit 1 full-power output for the demand. At the next period, unit 5 turned off, and the wind power generators provided 28.58MW more than in the previous period. However, from 17 h to 18 h, the demand went down by only 1.78 MW. As shown in Figure 3, the supply exceeds the demand at 18 h due to the ramp limitation of Unit 1, leading to the overproduction. Similarly, due to the increase in wind energy and the ramp limitation from Unit 1 from 20 h to 21 h, there is still unnecessary power production. However, as shown in Fig. 4, although the supply at 21 h is more than at 20 h, it costs less, thanks to the zero cost of wind. During peak hours, the utilized wind energy is lowest, which makes the power plants need to provide more energies.

B. Case 2: Increase of the Load Demand

In this case study, the load demand is increased to analyze the performance of the day ahead market model. The demand for every bus is increased by 5%.

The conventional generator status are shown in Fig. 5 and Fig. 6 illustrates the allocations of both conventional generators and wind power producers. Fig. 7 shows the operation costs for case study 2.

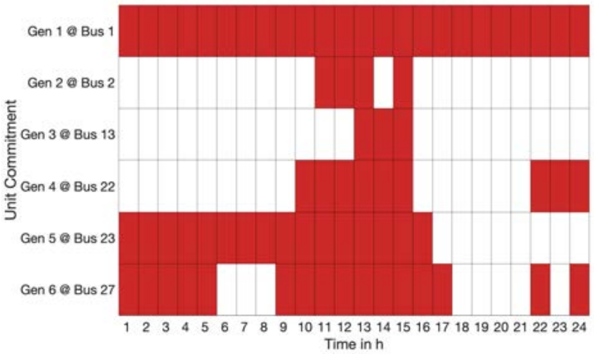

Fig. 5. Generator Status for Case Study 2 with 5% Increase of Load Demand

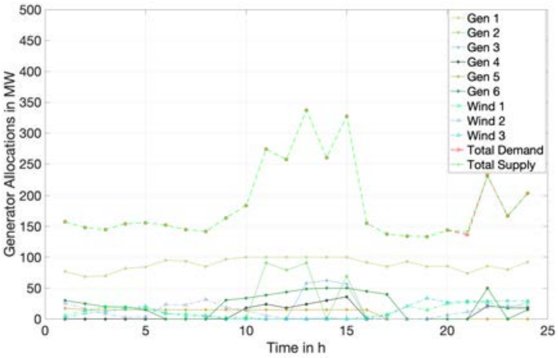

Fig. 6. Generation Allocations for Case Study 2 with 5% Increase of Load Demand

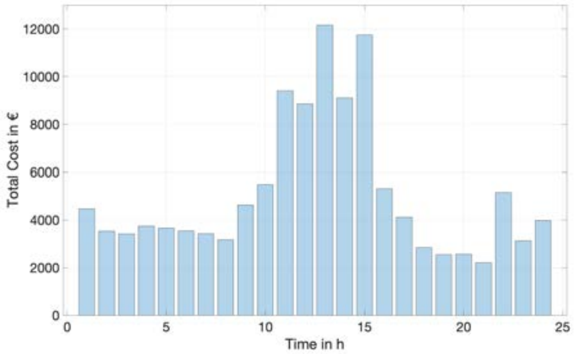

Fig. 7. Total Cost for Case Study 2 with 5% Increase of Load Demand

It is apparent in Fig. 5 that unit 6 is turned on to support higher demand when needed. In contrast to case study 1 (Fig. 2), in this case study, unit 6 is switched off at least from 16 h to 18 h to meet the high demand, which means that unit 1 generates more electricity to meet the high demand. However, same as case study 1, there is merely unit 1 kept on from 18 h to 21 h duration. According to Fig. 6, it is only at 21 h that supply exceeds demand, which did not result in excessive losses compared to the case study 1 as seen in Fig. 3.

As in case 1, wind power producers can only provide a small amount of energy compared to conventional power plants during peak hours.

C. *Case 3: Decrease of the Load Demand*

In the case study 3, the load demand is decreased to analyze the performance of the day ahead market model. The demand for every bus is decreased by 5%.

Fig. 8 presents the generator status of power plants. It is clear that the decrease in power demands will lead to fewer generators being used than case study 2 as seen in Fig. 5. Fig. 9 gives the allocations of both conventional generators and wind power generators. Fig. 10 shows the operation costs for case study 3.

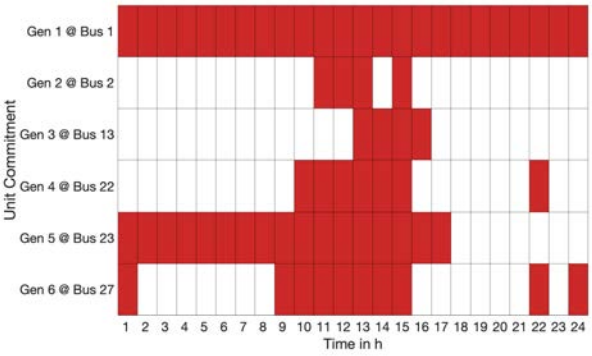

Fig. 8. Generator Status for Case Study 3 with 5% Decrease of Load Demand

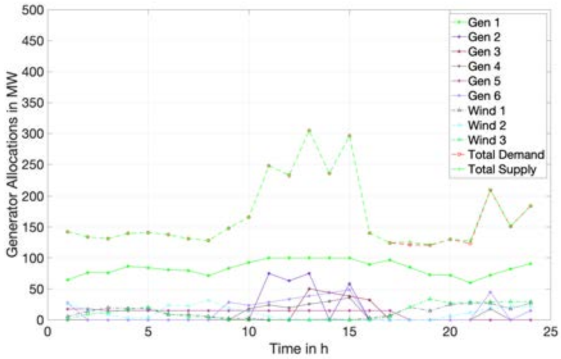

Fig. 9. Generation Allocations for Case Study 3 with 5% Decrease of Load Demand

According to Fig. 9, the differences between supply and demand at 18 h and 21 h are even more significant than in case study 1 as observed in Fig. 3, which will lead to more unnecessary losses. Similar to case 1, only unit 1 and 5 are turned on at 17 h, and the energy provided by unit 5 is limited, which leads to the high dependence of supply on unit 1. At 18 h, unit 5 is shut down because of the less supply, and there is a significant increase in wind energy. At the same time, due to ramp constraints, unit 1 cannot be adjusted to exactly meet the demand, which causes unnecessary losses at this period.

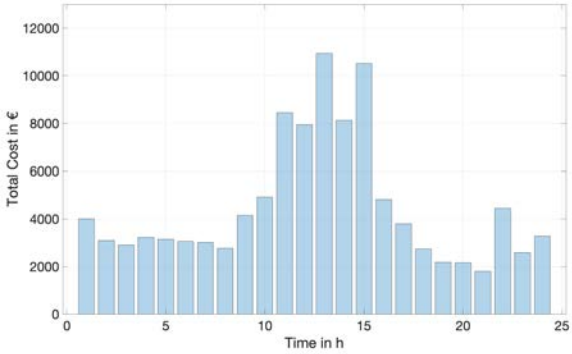

Fig. 10. Total Cost for Case Study 3 with 5% Decrease of Load Demand

D. *The Effect of the Wind Power Utilization*

Wind energy plays a vital role in the dispatch at the off-peak period. However, one of the disadvantages of wind generation is the variability of wind, and wind energy changes over time and places. The utilization of wind power in the cases is shown in Fig. 11.

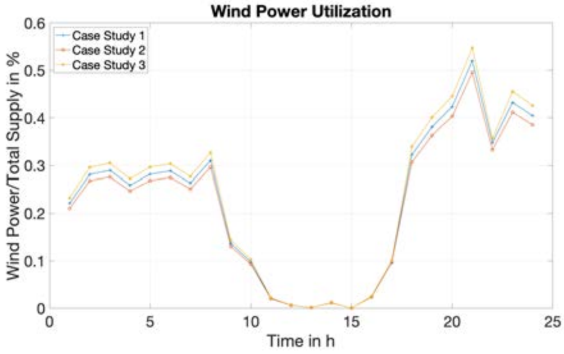

Fig. 11. Wind Power Utilization

It is clear that the lower wind power utilization happens for 11 h to 16 h duration, which is a period of high demand. Before 9 am, wind power utilization is between 20% and 30%. It is higher after 18 h, and even at 21 h, wind power utilization is up to 50%. One important reason for this result is that wind energy varies during the day, generally providing less power at peak times. As can be seen from Fig. 11 that the supply is more dependent on wind power in less demand because of the lower cost.

V. CONCLUSION

This paper proposed a day-ahead electricity market model considering the variability of renewable energy and attempted to provide a view on the effect of the uncertainty of renewable energy on the electricity market. The mixed-integer linear program method is proposed to solve the unit commitment and economic dispatch problem. The proposed model was fruitfully applied for solving the economic dispatch and the unit commitment to deal with the time sequences problem for power plants and wind power generators in the day-ahead electricity market. The proposed model is tested on the IEEE 30-bus system.

The test results demonstrate that due to the cheap cost the wind power producers play a vital role in the dispatch of the allocations of generating units during the next day. However, besides the significant advantages, wind power will change over time and places, which will lead to unpredictable consequences, such as overload on the transmission line. Further research should focus on the impact of renewable energy sources on the congestion in the transmission line for the secure operation of power systems.

ACKNOWLEDGMENT

Tankut Yalcinoz would like to thank the Philipp Schwartz Initiative, which was launched by the Alexander von Humboldt Foundation and the German Federal Office, for their support.

REFERENCES

[1] Mehdi Madani, “Revisiting European day-ahead electricity market auctions: MIP models and algorithms,” Louvain School of Management, March 2017.

[2] B. Saravanan, Siddharth Das, Surbhi Sikri, D. P. Kothari, “A solution to the unit commitment problem -- a review,” Frontiers in Energy, vol. 7, pp. 223–236, June 2013.

[3] M.H. Alham, M. Elshahed, Doaa Khalil Ibrahim, Essam El Din Abo El Zahab, “A dynamic economic emission dispatch considering wind power uncertainty incorporating energy storage system and demand side management,” Renewable Energy, vol. A96, pp. 800–811, October 2016.

[4] Kenneth Van den Bergh, Kenneth Bruninx, Erik Delarue, William D’haeseleer, “A Mixed-Integer Linear Formulation of the Unit Commitment Problem,” University of Leuven, April 2014.

[5] Vijay K. Prajapati, Vasundhara Mahajan, “Grey Wolf Optimization based Energy Management by generator rescheduling with renewable energy resources,” 2017 14th IEEE India Council International Conference (INDICON), pp.1–6, December 2017.

[6] Ray D. Zimmerman, Carlos E. Murillo-Sánchez, “MATPOWER User’s Manual,” Version 7.0b1, October 2018.

[7] Hongze Li, Xuejie Wang, Fengyun Li, Yuwei Wang and Xinhua Yu, “A Robust Day-Ahead Electricity Market Clearing Model Considering Wind Power Penetration,” Energies 2018, 11, 1772, July 2018.

[8] A. Merlin, P. Sandrin, “A New Method for Unit Commitment at Electricite de France,” IEEE Transactions on Power Apparatus and Systems, vol. PAS-102 , pp.1218–1225, May 1983.

[9] A. H. Mantawy, Youssef L. Abdel-Magid, Shokri Z. Selim, “A Simulated Annealing Algorithm for Unit Commitment,” IEEE Transactions on Power Systems, vol. 13, pp.197–204, February 1998.

[10] F. Zhuang, F.D. Galiana, “Unit Commitment by Simulated Annealing,” IEEE Transactions on Power Systems vol. 5, pp.311–318, February 1990.

[11] Yang Tingfang, T. O. Ting, “Methodological Priority List for Unit Commitment Problem,” 2008 International Conference on Computer Science and Software Engineering, pp.176–179, December 2008

Predicting the local generated photovoltaic power by creating a forecast model using artificial neural networks and verifying the model with real data

Katrin Schulte, Michael Kelker, Jens Haubrock
University of Applied Sciences Bielefeld
Institute for Technical Energy Systems
Bielefeld, Germany
katrin.schulte@fh-bielefeld.de

Abstract—**In order to increase the share of power generated by decentralised photovoltaic (PV) systems in the charging current for electric vehicles (EV), it is necessary to predict the power generated from a single PV system. This paper presents a forecast model for predicting the locally generated PV power. The model consists of artificial neural networks (ANN), which predict the solar irradiation and a mathematical PV model, which calculates the generated PV power from the predicted irradiance. The model was trained and validated with historical weather data. In training, the model achieved a deviation of 43.92 W/m^2 and in validation 50.36 W/m^2. With freely available weather forecasts, the forecast model predicts irradiation for a local area. For this purpose, the model was tested on a real PV system. In this test, the forecast model achieved a percentage error of the PV power of 6.58 % on sunny days to 16.19 % on cloudy days.**

Keywords— Photovoltaic, Irradiance Forecast, Photovoltaic Power Prediction, Neural Network

I. INTRODUCTION

Electric vehicles (EV) can make a contribution to climate and environmental protection if they are charged with electricity from renewable energies. The sector coupling between the electrical grid and the mobility sector is an important step in the energy system transformation [1]. In the typical German electricity mix, the share of renewable energies is 36 % [2]. If the EV is charged with the electricity mix, they are not much more climate-friendly than vehicles with combustion engines [3]. Accordingly, the share of renewable energies in the charging current of EV must be increased. As part of the Fit2Load research project funded by the state of North Rhine-Westphalia (NRW) and the European Union (EU), a fleet of commercial vehicles for delivery traffic is to be converted to electromobility. The aim is to charge the EV with the highest share of renewable energies as possible. A photovoltaic (PV) system on the rooftop of the company provides this charging current.

One problem, however, is the volatility of PV generation. In order to be able to use the electricity from the decentralised PV systems to charge the EV for delivery transport, a daily and short-term forecast of the expected electricity generation for a single PV system is required. The generated power depends on the solar irradiation on the PV system. This irradiation is changing permanently during the day and during the year due to the different positions of the sun and, above all, due to the changing cloud cover during the day. Weather forecast data are usually only available for larger regions. Therefore, the Fit2Load research project requires a power forecast for a decentralised PV system that provides the charging current for the EV. With a charging management system, the EV will be charged on the basis of the PV power forecast in a way that the share of the PV in the charging current is maximised.

For this purpose, a forecast model based on an artificial neural network (ANN) had been developed for the power generated by a PV system. A model for predicting solar irradiation had been trained and validated with historical weather data. A mathematical PV model converts the predicted solar irradiance into the generated PV power. Afterwards, the developed forecast model had been tested on a real PV system equipped with measurement units by forecasting the generated power and comparing it with the measurement. For the forecast, open weather data are used.

II. METHODOLOGY

The forecast model consists of two parts: A. the irradiation forecast model and B. the mathematical model of the PV system. The irradiation forecast model is carried out by an artificial neural network (ANN) trained with historical weather data. On the basis of a weather forecast, the ANN predicts the solar irradiation. The PV model then uses the predicted irradiation and technical data of the PV system to calculate the power generated by the system.

A. Irradiation forecast model

Artificial neural networks (ANN) are a branch of artificial intelligence (AI). They illustrate the human brain and deal with the processing of information according to the model of the neural system [4]. Information is processed in parallel by a large number of neurons that are connected to each other. By activation signals, the information about connections between the neurons is passed on [4]. In contrast to the human brain, modern computers perform tasks one after the other and not in parallel [5]. Tasks such as pattern recognition, speech recognition or prognosis cannot be solved by conventional programs but can be solved by humans through their ability to learn and the interconnection of neurons in the brain [5]. Therefore, ANN are developed and trained so that they can solve problems on the basis of the learned knowledge.

ANN have already been successfully used to predict solar irradiance, as for example in [6] or [7]. However, the developed models were not tested on a real PV system. In [8] a forecast model for the prediction of the PV Power has already been developed in Matlab. It has been tested on a real PV system but with only a few test data.

1) Structure of the ANN for the irradiation forecast:

ANN is developed using the deep learning framework Keras for Python [9]. With Keras, a variety of deep learning models can be developed and trained and is therefore suitable for the development of an ANN for irradiation prediction.

The structure of the developed ANN is shown in Fig. 1. A feed-forward net is used, which consists of connected layers that pass the input values forward through the net. The input layer consists of eight neurons, the hidden layer of 80 neurons and the output layer of two neurons. After several tests, this structure was selected as the best variant. The linear ReLu function (Rectified Linear Units) is used as the activation function. Negative values are set to zero in the ReLu function. This enables the ANN to predict any positive values. As loss function, the mean square error (MSE) between true value and output from the ANN is used. This is minimized during training.

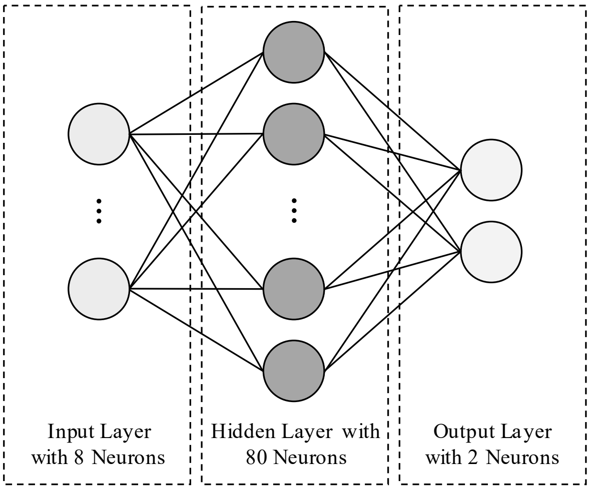

Fig. 1. Structure of the artificial neural network for the irradiance forecasting

2) Training and validation data:

To train the ANN, historical data on solar irradiation and various historical weather data from the German Weather Service (Deutscher Wetterdienst (DWD)) are used. The DWD provides a large amount of measured climate data in different resolutions from various weather stations. Different weather stations have been tested for their suitability for ANN training. The weather station in Braunschweig was selected due to the extensive data basis. In order to train the ANN, the hourly resolution data sets were first processed and the hours in which no solar irradiation is given (e.g. at night) were removed.

The neurons of the input layer of the ANN correspond to the number of weather data selected to train the ANN. As shown in Fig. 2, the input data include wind speed, wind direction, temperature, air pressure, humidity, cloudiness, sun elevation, and sun azimuth. The two neurons of the output layer corresponding to the global and diffuse irradiation. The solar irradiation consists of direct and diffuse radiation. While the direct radiation $\Psi_{d,h}$ comes directly from the direction of the sun, the diffuse radiation $\Psi_{df,h}$ is caused by scattering in the atmosphere and does not have a defined direction [10]. Direct and diffuse irradiation together result in the global irradiation $\Psi_{g,h}$ on the horizontal earth surface according to (1).

$$\Psi_{g,h} = \Psi_{d,h} + \Psi_{df,h} \tag{1}$$

The direct irradiation is calculated after the transformation of (1) from the global and diffuse irradiance predicted by the ANN. The hourly resolution measurement data from 2012 to 2016 are used as training data and the measurement data from 2017 as validation data.

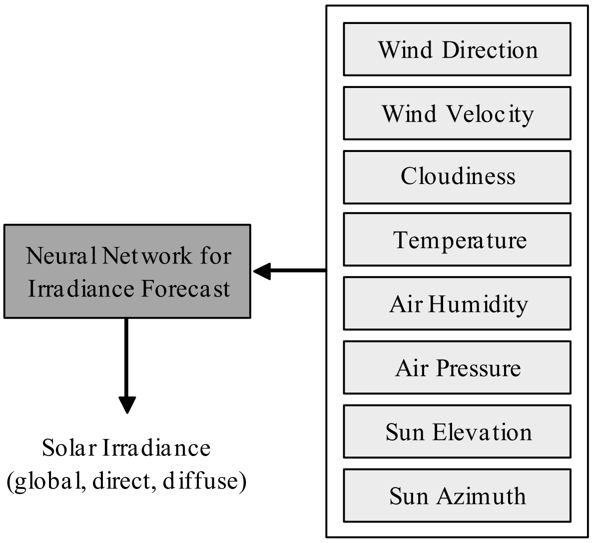

Fig. 2. Overview of the irradiation forecast model

3) Training of the ANN for the irradiation forecast:

Because the input data has different dimensions, it is first standardized before the training. For this purpose, the mean value μ of all input data of a weather characteristic is subtracted from each input value X and divided by the standard deviation σ. Thus the data of a weather characteristic have the mean value 0 and the standard deviation 1. The normalized data X_n are calculated by this method according to (2) [9]. Therefore, this normalization is also performed for the training data and the validation data.

$$X_n = \frac{X - \mu}{\sigma} \tag{2}$$

A total of ten ANN (Model 1 - 10) were created with the same architecture because the networks are usually never parameterized the same during the training. By calculating the mean value of the output from all ten networks, the predicted solar irradiation is computed.

During the training, several epochs are running through, during which the loss function is minimized by adjusting the parameters in the ANN. As can be seen in Fig. 3, the MSE decreases in both, training and validation, with each epoch.

Overfitting occurs when the training loss continues to decrease but the validation loss increases again [9]. Then the ANN adapts too much to the training data and cannot be generalized to unknown data like the validation data. To avoid this, training is monitored and stopped when the validation error begins to increase. For Model 1, this was the case after 31 epochs (see Fig. 3).

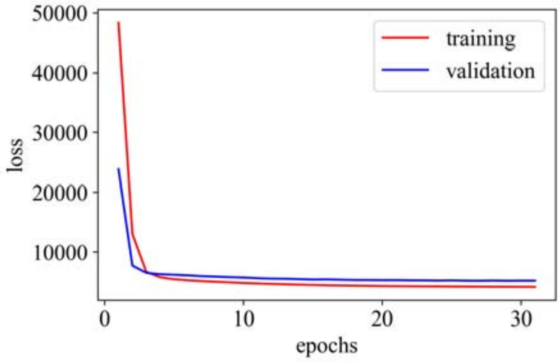

Fig. 3. Mean square error as loss function during training and validation exemplary for Model 1

During the training, the mean absolute error (MAE) and the root mean square error (RMSE) were monitored. The MAE describes the difference between prediction and target value. The RMSE is the root of the MSE and indicates the average amount by which the forecast deviates from the target value. Table I shows the loss function as MSE, the MAE and the RMSE as a mean for all generated ANN for training and validation. On average, the trained ANN have an MAE between prediction and measurement of irradiance of 43.92 W/m^2 and an RMSE of 64.28 W/m^2. The MAE and the RMSE with 50.36 W/m^2 and 71.91 W/m^2 are slightly higher in validation than in training.

TABLE I. MEAN ACCURACY OF ALL ANN (MODEL1-10)

	Loss/ MSE	MAE (W/m^2)	RMSE (W/m^2)
Training	4246.56	43.92	64.28
Validation	5295.83	50.36	71.91

The trained ANN act as an irradiation forecast, which can predict the irradiation by a weather forecast. The data from a freely available weather forecast website is used for this purpose. For this reason, the training input parameters of the ANN are only measurement data that are also available for a local forecast.

B. Photovoltaic model

In order to calculate the PV power from the irradiance predicted by the neuronal networks, the following parameters must be considered: Efficiency of the PV system, area of the PV module, tilt angle, orientation and the module temperature. The technical data of a PV system required in the mathematical PV model to calculate the power are shown in Fig. 4.

Due to the measured values from the DWD, the solar irradiance is related to a horizontal surface. Therefore, the radiance on a horizontal surface must first be converted to an arbitrarily oriented surface. The global irradiance on a tilted surface $\Psi_{g,t}$ defined in [10, 11] is composed of the direct irradiance $\Psi_{d,t}$ and diffuse irradiance $\Psi_{df,t}$ on a tilted surface and a part that is reflected from the ground $\Psi_{r,t}$ according to (3).

$$\Psi_{g,t} = \Psi_{d,t} + \Psi_{df,t} + \Psi_{r,t} \tag{3}$$

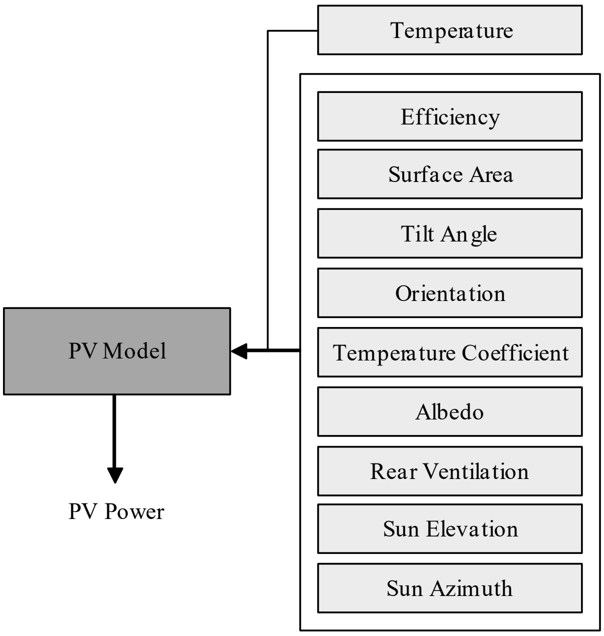

Fig. 4. Overview of the PV model

For this conversion, the angle of incidence θ between the direct solar radiation and the surface normal of the PV system in [10] using (4) is required. The angle of incidence depends on the position of the sun and the tilt angle β and orientation of the PV module. The orientation of the PV module is described by the azimuth angle α_z (south: $\alpha_z = 0°$, west: $\alpha_z = 90°$, east: $\alpha_z = -90°$). The position of the sun is defined by the sun elevation γs and the sun azimuth α_s (north: $\alpha_s = 0°$, east: $\alpha_s = 90°$, south: $\alpha_s = 180°$, west: $\alpha_s = 270°$). Both sun elevation and sun azimuth are determined by the position of the observer as well as the season and the time of day. Sun elevation and azimuth are calculated by the formulas in [10].

$$\begin{aligned}\theta = \arccos(&-\cos\gamma_s \cdot \sin\beta \cdot \cos(\alpha_s - \alpha_z) \\ &+ \sin\gamma_s \cdot \cos\beta)\end{aligned} \tag{4}$$

The direct irradiance $\Psi_{d,t}$ on a tilted area defined in [10, 11] results from the direct horizontal irradiance $\Psi_{d,h}$ multiplied by a geometric factor of sun elevation and angle of incidence according to (5).

$$\Psi_{d,t} = \Psi_{d,h} \cdot \frac{\cos\theta}{\sin\gamma_s} \tag{5}$$

The diffuse irradiance $\Psi_{df,t}$ on a tilted area is given in [10, 11] by (6) with the tilt angle β of the PV system. An isentropic approach is assumed.

$$\Psi_{df,t} = \Psi_{df,h} \cdot \frac{1}{2} \cdot (1 + \cos\beta) \tag{6}$$

For the calculation of the reflected irradiance $\Psi_{r,t}$ on a tilted area from the global horizontal irradiance $\Psi_{g,h}$ defined in [10, 11] according to (7) the albedo coefficient A is required. If the Albedo cannot be measured, there is a table in [10] for different environments. An isotropic approach is also used.

$$\Psi_{r,t} = \Psi_{g,h} \cdot A \cdot \frac{1}{2} \cdot (1 - \cos\beta) \qquad (7)$$

The efficiency of a PV system depends on the module temperature. As the temperature rises, the generated PV power decreases. The temperature of the PV module $\vartheta_{\text{module}}$ results from the ambient temperature $\vartheta_{\text{ambient}}$, the irradiation and a constant of proportionality c for the type of the installation of the PV module defined in [10] by (8). The type of installation is important because of the rear ventilation. There is also a table in [10] for factor c for different installation variants.

$$\vartheta_{module} = \vartheta_{ambient} + \frac{c \cdot \Psi_{g,t}}{1000 \frac{W}{m^2}} \qquad (8)$$

The generated PV power P_{PV} is calculated in [10] from the global radiation on an arbitrarily tilted surface $\Psi_{g,t}$, the PV area A_{PV}, the efficiency η_{PV} of the PV module and a correction factor for the module temperature Λ according to (9). The efficiency here is assumed to be constant in a first approximation.

$$P_{PV} = \Psi_{g,t} \cdot \eta_{PV} \cdot A_{PV} \cdot \Lambda \qquad (9)$$

The correction factor for the module temperature is given by (10). The temperature coefficient ψ_T indicates the percentage by which the power decreases or increases based on the temperature under Standard Test Conditions (STC) 25°C.

$$\Lambda = 1 + (25°C - \vartheta_{module}) \cdot \psi_T \qquad (10)$$

III. RESULTS

After training and validation of the developed model to predict the generated PV power, the model is tested with real data. For this purpose, the irradiation at the location of a PV system is predicted and the generated PV power is calculated with technical data of the system. Weather data from a weather forecast website for a district in Bielefeld, where the PV system is located, is used to forecast irradiation. These must first be normalized on the basis of the training data before being read into the ANN. The technical data of the PV system are shown in Table II. The system is located on a completely free mounting with a ground of clean concrete (Albedo, Rear Ventilation). With this data, the PV power is calculated from the predicted irradiation. The prognosis of the generated PV power is then compared with the real measurement of the PV system.

TABLE II. TECHNICAL DATA OF THE PV SYSTEM

Nominal Power	**Surface Area**	**Efficiency at STC**
2240 W	13.31 m^2	16.8 %
Temperature Coefficient	**Tilt Angle**	**Orientation**
0.47 %/K	30°	South (0°)

The weather forecast was read daily and hourly into the ANN, so that in addition to the daily forecast local fluctuations can be detected by hourly updates. Due to the hourly resolution of the forecast, the 15-minute measured values of the PV system were also averaged to one hour for better comparability. A total of 61 days were tested between January and May 2019. In this period 7 days were sunny, 12 days partly cloudy and 42 days cloudy.

Table III shows the average values for the MAE, the RMSE and the normalized MAE (nMAE) between the measured and predicted global irradiance for the three day types sunny, partly cloudy and cloudy for the daily forecast and the hourly updated forecast. The MAE is normalized because the values for morning and evening irradiation are different from noon and between months. To do this, the MAE is divided by the maximum interval length on a corresponding day. Table IV shows the same values for PV power.

TABLE III. GLOBAL IRRADIANCE ACCURACY FOR DIFFERENT DAY TYPES

Day Type	**MAE (W/m^2)**	**RMSE (W/m^2)**	**nMAE (%)**
Sunny DU[a]	35.45	68.53	5.99
Sunny HU[b]	36.23	65.04	6.07
Partly cloudy DU[a]	52.73	90.60	9.86
Partly cloudy HU[b]	52.42	88.66	10.12
Cloudy DU[a]	43.25	72.92	12.64
Cloudy HU[b]	41.40	69.47	12.36

a. DA = Daily Updated Forecast

b. HU = Hourly Updated Forecast

TABLE IV. PV POWER ACCURACY FOR DIFFERENT DAY TYPES

Day Type	**MAE (W)**	**RMSE (W)**	**nMAE (%)**
Sunny DU[a]	127.18	241.11	6.71
Sunny HU$_b$	123.79	225.87	6.58
Partly cloudy DU[a]	193.15	348.04	11.40
Partly cloudy HU[b]	193.16	349.81	11.62
Cloudy DU[a]	164.31	283.17	16.19
Cloudy HU[b]	156.18	268.16	15.65

On sunny days, the MAE is lower for both irradiation and power than on partly cloudy or cloudy days. On cloudy days, the MAE is lower than on partly cloudy days, as the solar irradiation on cloudy days is lower in total due to the cloudiness. The percentage deviation between predicted and measured irradiance is between 5.99 % on sunny days and 12.64 % on cloudy days. For PV power this value is between 6.58 % and 16.19 %.

In order to visualize this, one from each day type was selected to display the PV power over the day. Fig. 5 shows the predicted and measured PV power on a sunny day. Fig. 6 is a partly cloudy day and Fig. 7 is a cloudy day. The blue curve shows the measured values, the orange curve and the green curve the forecast values. For the orange curve, the forecast was made one day in advance because the weather forecast provides weather data for the next 24 hours. For the green curve, the forecast was updated hourly with the current weather forecast data.

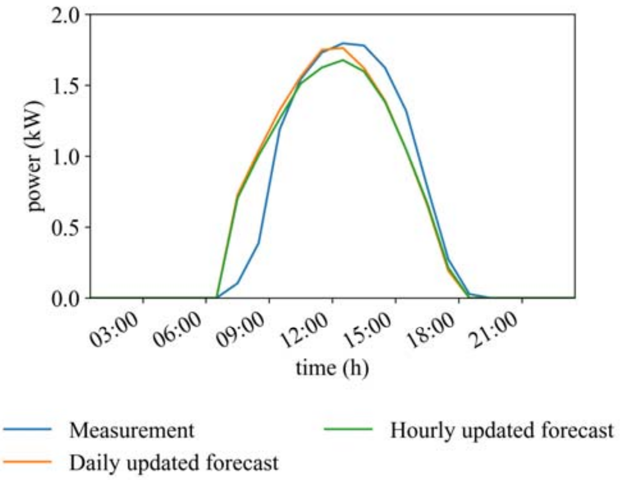

Fig. 5. PV Power on a sunny day (22 March 2019)

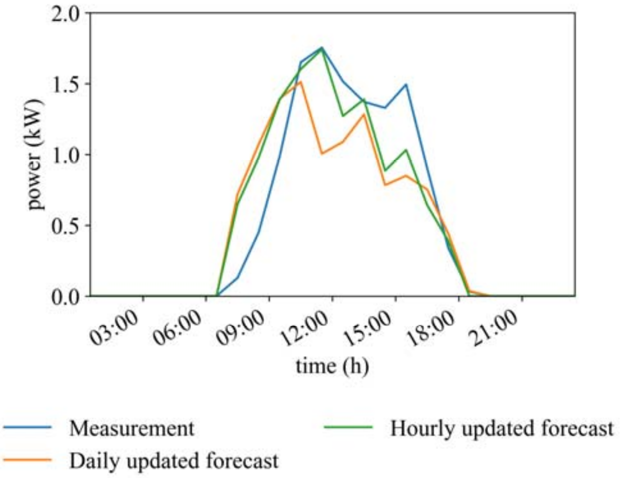

Fig. 6. PV Power on a partly cloudy day (24 March 2019)

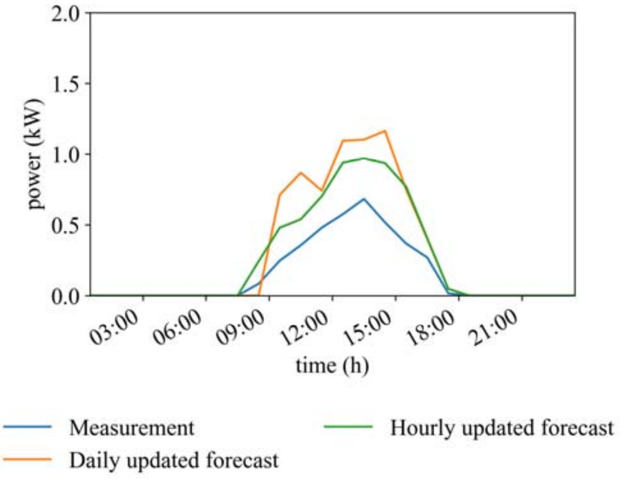

Fig. 7. PV Power on a cloudy day (20 February 2019)

In Table V-VII the MAE, the RMSE and the nMAE for the global irradiation and the PV power are shown for the three days under consideration. On a sunny day, the MAE and RMSE are again lower than on the partly cloudy and cloudy day. Due to the hourly update, on the partly cloudy and cloudy day the deviation between the measurement and the forecast for both irradiance and power is less. The hourly update improves the accuracy of the prediction model.

TABLE V. ACCURACY ON A SUNNY DAY (22 MARCH 2019)

Global Irradiance	**MAE (W/m^2)**	**RMSE (W/m^2)**	**nMAE (%)**
DU[a]	38.46	66.20	6.11
HU[b]	39.67	65.42	6.31
PV Power	**MAE (W)**	**RMSE (W)**	**nMAE (%)**
DU[b]	99.31	205.20	5.53
HU[a]	101.82	199.60	5.67

TABLE VI. ACCURACY ON A PARTLY CLOUDY DAY (24 MARCH 2019)

Global Irradiance	**MAE (W/m^2)**	**RMSE (W/m^2)**	**nMAE (%)**
DU[a]	60.86	98.65	9.81
HU[b]	45.09	70.47	7.27
PV Power	**MAE (W)**	**RMSE (W)**	**nMAE (%)**
DU[b]	185.91	317.00	10.60
HU[a]	125.80	228.57	7.17

TABLE VII. ACCURACY ON A CLOUDY DAY (20 FEBRUARY 2019)

Global Irradiance	**MAE (W/m^2)**	**RMSE (W/m^2)**	**nMAE (%)**
DU[a]	43.10	69.72	15.97
HU[b]	28.39	49.92	14.79
PV Power	**MAE (W)**	**RMSE (W)**	**nMAE (%)**
DU[b]	181.62	285.89	21.92
HU[a]	123.19	200.65	21.10

The results show that the forecast already works very well on sunny days. The deviations are only small and therefore acceptable. When it gets cloudy, the deviations between measurement and forecast are greater. This is due to the dependency on a local weather forecast. The weather forecast predicts the cloudiness for an area and not for an exact position where the PV system is located. Therefore, it is difficult to predict cloud cover exactly at one location.

IV. CONCLUSION

A forecast model had been developed for predicting the local solar irradiation and a mathematical model based on it was developed to calculate the power generated by decentralised PV systems. It consists of artificial neural feed-forward networks, which were trained with historical weather data from the DWD. The historical weather data from the DWD were also used for validation. During training, the model reached a mean absolute error of 43.92 W/m^2. During validation, the model has shown a deviation of 50.36 W/m^2.

Furthermore, the forecast model was tested under real conditions. The irradiation at the location of a real PV system was forecast with a local weather forecast website. The predicted irradiation was converted into the generated PV power with the mathematical PV model and compared with the measurement of the PV system. A total of 61 days were tested between January and May 2019. The days were divided into sunny, partly cloudy and cloudy day types. In this period 7 days were sunny, 12 days partly cloudy and 42 days cloudy. The mean deviation of global irradiance varies from 35.45 W/m^2 on sunny days to 52.73 W/m^2 on cloudy days. The forecast reaches similar deviations in the real test as in the training as well as in the validation. This deviation corresponds to a percentage deviation of 5.99 % on sunny days to 12.64 % on cloudy days. The deviation of the generated PV power is between 123.79 W on sunny days and 193.16 W on cloudy days. The percentage error of the power ranges from 6.58 % to 16.19 %. Overall, the deviations are smaller on sunny days, resulting in a more accurate forecast on sunny days.

In addition, it was investigated whether an hourly update of the forecast by detecting short-term local fluctuations improves the accuracy of the model. On three exemplary days of each day type, smaller deviations were achieved by an hourly update.

In order to improve the developed forecast model, new elements will be added to the mathematical model of the PV system. The aim is to map the PV system better so that the percentage error of the power is even closer to the percentage error of the irradiation. Furthermore, inaccuracies caused by real weather forecasts for local regions can be reduced by using satellite images. Artificial Neural networks for image recognition can help to detect the cloud movements above the PV system. This allows the cloudiness to be predicted for exactly one location where a PV system is located.

REFERENCES

[1] P. Komarnicki, J. Haubrock and Z. A. Styczynski, Elektromobilität und Sektorenkopplung. Springer-Verlag, 2018.

[2] German Federal Ministry of economics and energy (BMWi), “Erneuerbare Energien in Zahlen”. Druck und Verlagshaus Zarbrock, September 2018.

[3] German Federal Ministry for the Environment, Nature Conservation, Construction and Nuclear Safety (BMU), “Wie umweltfreundlich sind Elektroautos?”. Druck- und Verlagshaus Zarbrock, July 2018.

[4] R. Kruse, C. Borgelt, C. Braune, F. Klawonn, C. Moewes and M. Steinbrecher, Computational Intelligence: Eine methodische Einführung in Künstliche Neuronale Netze, Evolutionäre Algorithmen, Fuzzy-Systeme und Bayes-Netze. Berlin Heidelberg New York: Springer-Verlag, 2015.

[5] Z. A. Styczynski, K. Rudion and A. Naumann, Einführung in Expertensysteme. Berlin Heidelberg: Springer-Verlag, 2017.

[6] S. P. Durrani, S. Balluff, L. Wurzer and S. Krauter, “Photovoltaic yield prediction using an irradiance forecast model based on multiple neural networks,” in Journal of Modern Power Systems and Clean Energy, pp. 255-267, 2018.

[7] K. P. Moustris, K. A. Kavvadias, A. I. Kokkosis and A. G. Paliatsos, “One day-ahead forecasting of mean hourly global solar irradiation for energy management systems purposes using artificial neural network modeling,” Mediterranean Conference on Power Generation, Transmission, Distribution and Energy Conversion, 2016.

[8] M. Kelker, K. Schulte, D. Hansmeier, F. Annen, K. Kröger, P. Lohmann, J. Haubrock, “Development of a forecast model for the prediction of photovoltaic power using neural networks and validating the model based on real measurement of a local photovoltaic system”, 13th IEEE PowerTech, June 2019, Milano.

[9] F. Chollet, Deep Learning mit Python und Keras. Frechen: mitp Verlag, 2018.

[10] V. Quaschning, Regenerative Energiesysteme. München: Hanser verlag, 2015.

[11] V. Wesselak and T. Schabbach, Regenerative Energietechnik. Berlin Heidelberg: Springer-Verlag, 2009.

The influence of the leasing model on the distribution of electric vehicles in the field of company fleets

Lisa Nienaber, Jens Haubrock
University of Applied Science Bielefeld
Institute for Technical Energy Systems
Bielefeld, Germany
lisa.nienaber@fh-bielefeld.de

***Abstract*—The transition to e-mobility is influenced by various factors. The importance of technology development and the effects by the actions of the politics are widely known, but what impact does a financing option like leasing have on the distribution of electric vehicles [EV]. The commercial sector is in this field an important market who represent 65% of all new registered EVs in Germany. This paper deals with the question, in which way the leasing model has an influence on the decision of companies, to invest in EVs. To investigate this question the basic conditions of the leasing model was outlined, and then top barriers of the e-mobility development stated and analyzed. As the final step the two topics were set in context and a non-representative survey among lessees and car manufacturer representatives was conducted, comparing the theoretical finding with the practical experience. It was shown, that with the leasing model the customer can save its liquidity and does not have to bear the burden of an expensive investment. Furthermore, the car can be given back at the end of the contract duration and the customer has no issues with the liquidation value or the further maintenance of the car. This gives him secure data to plan for the future and the flexibility to keep up with the fast development of this technology. Leasing can be seen as one of the main drivers for the distribution of electric vehicle**

Keywords*— *leasing, e-mobility, financing, costs, barriers, company fleets

I. INTRODUCTION

E-mobility is a topic of great importance in today´s society. Up until today, e-mobility has developed rapidly and the technology has improved continuously. Due to this evolution, cars with electronic powertrain have gained sufficient market maturity and are able to compete with conventional vehicles.

With the current state of development, companies have the opportunity to upgrade their fleets with EV. The commercial costumers represent an important sales market for the distribution of electric vehicles. They represented in 2017 almost 65% of the new registrations of electric vehicles and 58% of the hybrid vehicles [Fig. 1]

The decision on switching to electric drive is not only affected by technical reasons but also financial aspects. A new vehicle is always a long-term investment and the company has to verify if they have the necessary liquidity to bear the costs.

This paper investigates the question, whether or not the leasing model has an influence on the company´s decision for choosing an EV for their fleet provided

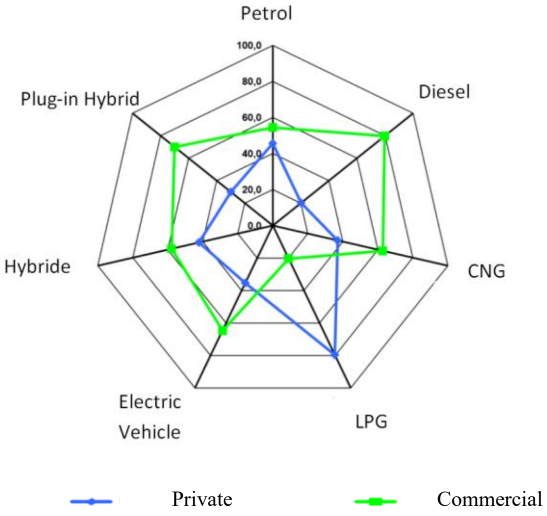

Fig. 1. New registration of vehicles in 2017 in % [1]

II. LEASING

Leasing is a form of financing, giving the leasing object [LO] to the lessee in exchange for an agreed payment to the lessor. The lessee is accountable for the maintenance of the LO and must take responsibility for possible damages. In return, he obtains the purchase right and the financing function[2]

There are different varieties of how the leasing contract can be defined. First, there is a distinction between mobile and immobile leasing objects. Due to the fact that this paper is about the leasing of vehicles, only the mobile leasing objects will be covered in the following lines. The major aspect is the composition of the parties involved in the contract. A leasing contract can be concluded between

- lessee and the car manufacturer,
- lessee and the lessor or
- lessee, lessor and the car manufacturer.

The most common way is the last-mentioned combination Normally, the future lessee gets in contact with the car producer and selects a car.

If leasing is chosen as the finance option a lessor company is being contacted. They can then decide whether they approve the treaty or not. If so, the lessor pays the purchase price for the LO and thereby covers the investments costs. The lessee can save his liquidity and use this capacity for other investments. Nevertheless, the leasing object will be sent directly to the lessee who has to check it for damages.

In the case of an undamaged vehicle, the lessor will be informed, and he will then pay the bill to the manufacturer. The LO is now in possession of the lessee but it stays the property of the lessor. [2]

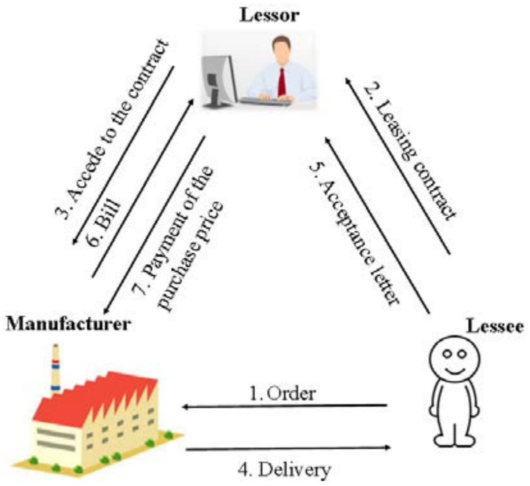

Fig. 2. Three dot relationship [3]

The lessor receives monthly payments which in sum must cover his investment costs so that the investment amortizes itself.

The investment costs consist of the purchase price, financing costs as well as risk and profit margins. There are two different amortization options. The first is the full amortization, meaning that the sum of the monthly payments covers all the costs after the duration of the contract. [2]

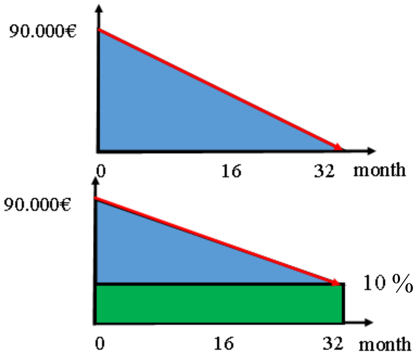

Fig. 3. Full and part amortisation with 10% residual value [4]

The part amortization can be performed as a kilometre or as a residual value settlement. In both cases, the lessee is obliged to cover the financial gap of the lessor to the full amortization. At the beginning of a contract with a kilometre settlement, the contracting parties determine a kilometre distance the car is allowed to drive during the contract period. If the limit is exceeded, a defined extra kilometre rate has to be paid. [2] This option is very popular due to its predictability and its transparent costs.

During the contract negotiations with a residual cost settlement, the value of the LO at the end of the contract is predicted and agreed on. At the end of the contract period, the car is examined, and the value is assessed. In very few cases the value matches the one set at the beginning. If there is a negative prize gap the lessee has to cover the costs. In case of a positive prize gap, the lessee receives in most cases a share of about 75% of the profit. [5]. This more unpopular option involves the danger of incalculable costs due to uncertain evaluations and possible damages.

Depending on the choice of amortization there can be different agreements regarding the subsequent actions. In the case of a full amortization contract, the contracts partners can choose between three options. First, a contract with no further option means the LO has to be given back to the lessor. Second a contract with a purchase option, in which case the lessee can but does to have to buy the car. And the last option is a contract extension under new conditions. If a part amortization was chosen, there are three different options, as well.

The contract with offer privilege contains a purchase obligation for the lessee, but he does not have the right to buy the car. Means, if a car is above its estimated value, the lessor can keep it instead of selling it to the lessee. Another option is that the lessor sells the car and if the retail price is higher than the remaining value the lessor needs for his full amortization, the difference is shared and the lessor receives up to 75% of the value. A last option is a contract with an undefined time period. During an irredeemable time zone of 40% of the usual use period, the lessee cannot cancel the contract. Afterwards, he is free in his decision when to end the contract. In any case, the difference between remaining costs and retail prize have to be paid by the lessee. .[2].

III. CHALLENGES OF THE E-MOBILITY

Since 2010 the number of new registered EV steadily increased in Germany from 541 to 36.061 in 2018, but this still makes up only a small proportion of 1% of all newly registered vehicles (3,44 million). [6][7]. There are diverse reasons for this small percentage

A study [4] from 2018 investigated the top 5 barriers for the development of the e-mobility in Germany. It was found out, that the biggest impact comes from the insufficient coverage of good charging points, followed by the high prices, the inactivity of the industry, the battery performance and finally the lack of motivation to try something new

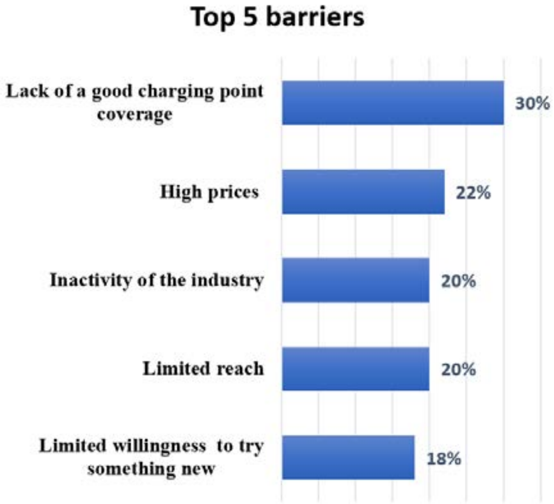

Fig. 4. Top 5 barriers for the development of e-mobility in Germany [8]

The results of this study make obvious, that for the customer the topics convenience and security are of immense importance. The network of charging points is still under expansion but to this day it cannot provide equal coverage as the petrol station network. In further investigation, this argument will be neglected, first because the financing option has no direct impact on the network of charging points and second because the focus is on fleets of companies. It is assumed, that if a company invest in EV it will also invest in a charging park who is sufficient for powering their own fleet.

Another driving factor is the higher price for EV in comparison to internal combustion engine vehicle [ICEV] due to the high costs of the battery. The costs of batteries are predicted to decline in the next years which will lead to a convergence of the vehicle prices. How long this will still take is uncertain. Besides the dropping cost for battery their performance is improving, extending the maximum distance an EV can cover.

The e-mobility development was underestimated by many car manufacturers whereby the variety of models accessible on the market is still limited. Even if the customer wants to switch to electric mobility, there is often not a suitable solution for their needs.

Another problem, especially for commercial clients, is the uncertain development of electric mobility. Which powertrain technology will have a leading position in the future depends on different influence factors. The following Fig. 5 shows as an example the different market shares of the powertrain technologies depending on the extent of the climate goal regulations.

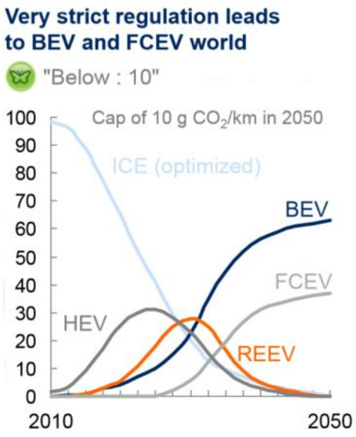

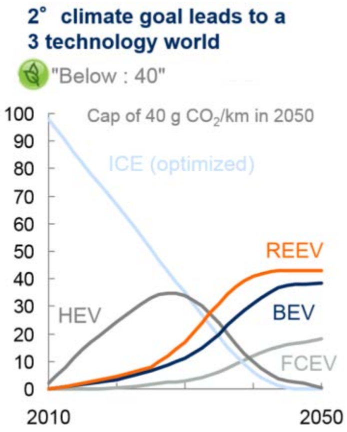

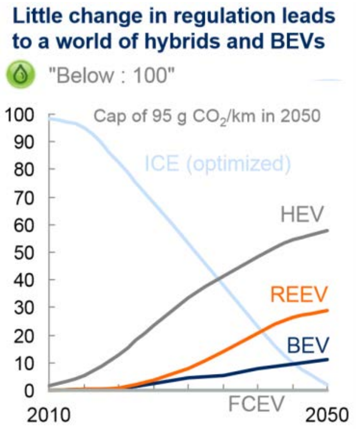

Fig. 5. Market share of powertrain units produced globally in % [9]

Companies need secure data to do investments in the future. Strategic planning starts at five years. It is hard to predict how the technology will develop over the next couple of years and which technology will succeed.

Additionally, there are very few historic data calculations can be based on. This makes it hard for a company to plan and to invest. An accurate plan is important for economic success.

IV. SOLUTIONS WITH THE LEASING MODEL

Obviously, the leasing model is not the solution for all the barriers of the e-mobility. Especially on the technological requirements like battery performance and charging duration, it has no direct impact on.

Nevertheless, there are aspects of the leasing model which make the investment in EV more attractive. A major aspect is the absorption of costs by the lessor. The lessee is not affected by the high initial purchase costs and can save its liquidity. This makes this investment much less dangerous.

Furthermore, the lessee stays flexible. At the end of the contract, he can give the vehicle back to the lessor. This gives him the chance to switch to a newer and better model.

He is also protected from an incalculable prize drop. In the case that the technology will develop in the next couple of years so much that the old car has no sales market, there is no problem to get rid of the car.

Due to the fact, that in most cases new cars are leased, there is a minimal risk regarding the battery. In that time period of the leasing contract, the guarantee of the battery is still valid and in the case of a problem the manufacturer has to replace it.

In order to get a connection between theory and practical application, a non-representative survey was held among expert in the field. The survey was about the development of the e-mobility, the barriers that still exist and the importance of the leasing financing model as a part of the distribution. As a trigger for the recent increasing demand the political discussion and restrictions, e.g. diesel driving bans, as well as the media coverage of the topic, were determined. This led to a growing interest in the topic, motivating the costumers to overcome their scepticism regarding EV.

But the e-mobility is still in its early stage. The net of charging points is insufficient, the charging duration is in comparison to other powertrain options too long, the initial purchase price is too high, the selection of vehicle models is too small and often the representatives of the car manufacturer are not properly instructed or do not exist at all. This in sum makes the decision for e-mobility an uncertain journey for the customer.

The leasing model was seen by respondents as an option to make the EV more attractive. The government funding rate is more advantageous with the leasing model (percentage relates to the whole purchase price and not only to the prize difference like with debt financing) – cheaper. One major aspect was seen in inflexibility. The development of the e-mobility is unbelievable fast and the option of giving the car back to the lessor and having no realization risk, especially with regard to the battery, is a huge advantage

Altogether, the leasing model was regarded as one of the main drivers of the e-mobility.

V. CONCLUSION

The transition of our mobility is a major challenge of our time. There are many aspects influencing this development, but what impact does the financing option leasing have?

Leasing as a finance option is characterized by the distinction between possessor and owner of a LO. The lessee as the possessor uses the LO for the contract duration and has then the option to give the LO back to its owner, the lessor. In exchange, the lessee gives the lessor monthly compensation for expenses.

Two of the major barriers of the e-mobility are the high purchase price as well as the uncertain and fast development of this technology sector. Companies act with restraint to do an expensive investment with no certainty about the value in a few years.

Leasing is a solution due to the initial shift of purchase costs to the lessor and the option to give the car back to the lessor at the end of the contract duration. The company has no burden on its liquidity and no incalculable risk regarding the value of their car in the future.

The distribution of EV is still in its early stage and there are still many obstacles to be overcome. Leasing is one of the main drivers of the e-mobility and has an important part especially in the commercial customer market. Further research and more interviews with lessees, lessors and vehicle manufacturer should be conducted.

REFERENCES

[1] KBA: Fahrzeugzulassungen (FZ) Neuzulassungen von Kraftfahrzeugen nach Umwelt-Merkmalen Jahr 2017, lhttps://www.kba.de/SharedDocs/Publikationen/DE/Statistik/Fahrzeuge/FZ/2017/fz14_2017_pdf.pdf?__blob=publicationFile&v=2(24.05.19)

[2] Grundmann, W.: Leasing und Factoring. Formen, Rechtsgrundlagen, Verträge. Wiesbaden: Springer Fachmedien Wiesbaden 2019

[3] Ermschel, U., Möbius, C. u. Wengert, H. M.: Investition und Finanzierung. BA KOMPAKT. Berlin, Heidelberg: Springer Gabler 2016

[4] Kettner, T.: Vertragsformen des Leasing, WISU 2012-02,

[5] Finkenberg, A.: Finanzierung & Leasing im Autohaus. So funktioniert's! Marketing/Verkauf. München: Autohaus Buch & Formular 2011

[6] KBA. Anzahl der Neuzulassungen von Elektroautos in Deutschland von 2003 bis 2019*. https://de.statista.com/statistik/daten/studie/244000/umfrage/neuzulassungen-von-elektroautos-in-deutschland/ (zugegriffen am 26.05.19 13:14

[7] KBA, und VDA, und EurotaxSchwacke. Anzahl der Neuzulassungen von Pkw in Deutschland von 1955 bis 2019 (in Millionen). https://de.statista.com/statistik/daten/studie/74433/umfrage/neuzulassungen-von-pkw-in-deutschland/ (zugegriffen am 26.05.19)

[8] Statista: In-depth: eMobility 2019, Statista Mobility Market Outlook, 2019 https://de.statista.com/statistik/studie/id/49256/dokument/emobility/

[9] Mckinsey&Company : EVolution Electric vehicles in Europe: gearing up for a new phase?, 2014 https://www.mckinsey.com/~/media/McKinsey/Locations/Europe%20and%20Middle%20East/Netherlands/Our%20Insights/Electric%20vehicles%20in%20Europe%20Gearing%20up%20for%20a%20new%20phase/Electric%20vehicles%20in%20Europe%20Gearing%20up%20for%20a%20new%20phase.ashx

Implementation and Verification of Power Plant Models for Power System Restoration Studies

Felix Flatter
Department of Electrical and Computer Engineering
TU Kaiserslautern
Kaiserslautern, Germany
flatter@rhrk.uni-kl.de

***Abstract*—Increasing penetration of volatile renewable energy sources combined with rising dependency on electricity supply lead to an incremented risk of blackouts of the electrical transmission grid. Research on how to restore the transmission grid safely and securely after such a major disturbance is underway, e.g. in the form of controllers governing power generation. For studies on this topic, both detailed and customizable as well as manufacturer-generic power plant models may be required to develop and verify restoration plans and measures. In this paper, such models are presented and their adequacy is verified using specific simulation scenarios and examining the models' frequency response.**

Keywords—power system restoration, power plant operation, power plant models, model verification

I. INTRODUCTION

Renewable power generation, in Germany mainly from off- and onshore wind farms near the coast, is expected to be the predominant source of electricity in the future. Therefore, it will be necessary to transport electrical power from generation areas in the North to load centres in the South and West of Germany, adding strain to the already heavily loaded transmission grid. Under such circumstances, loss of large generation units, such as offshore wind farms, may lead to grid frequency fluctuations significant enough to trigger protective relays. In the worst case, this may lead to a partial or even complete blackout of the transmission grid. [1] By Commission Regulation (EU) 2017/2196 [2], Transmission System Operators (TSOs) are obligated to prepare measures to prevent blackouts as well as to restore the transmission grid after such events. One example of such measures is the application of controllers governing the real power generation of power plants aiming for frequency stability during Power System Restoration (PSR). For the development of such controllers a verification environment containing models of power plants typically used during PSR is necessary. This paper presents suitable power plant models for this task and a verification method in context to PSR. First, the basics of PSR are described to provide context for the reader. Next, the chosen literature models for steam, gas turbine, and hydro units and their block diagrams for software implementation are presented. At last, the models are examined by applying PSR-specific verification scenarios in Matlab SIMULINK®.

II. BASICS OF POWER SYSTEM RESTORATION

A. Transmission Grid States

Reference [2] defines five operational states for the transmission grid. In the *secure state* all grid parameters are within their limits and enough reserves are available to compensate for certain unavailabilities without violating system security limits. If frequency deviation from its nominal value reaches a predefined threshold or if said reserves are insufficient, the grid is in the *alert state.* The next worse grid state is the *emergency state,* in which at least one system security limit is violated, a vital system element is unavailable for more than 30 minutes, frequency deviation reaches a significant value or measures of the System Defence Plan are activated. The fourth grid state marks the worst case: in the *blackout state,* at least one half of a TSO's control area is unpowered or de-energised for more than three minutes. Once measures from the Restoration Plan are activated, the transmission grid is in the *restoration state*.

B. Restoration Strategies

In Europe, two major strategies for Power System Restoration are applied. All strategies follow the same sequence of power plant start-up, re-energization of the transmission lines and finally load pickup. [3]

With the *Top-Down-Strategy,* a sufficiently powerful neighbouring part of the affected transmission grid provides power to start up shut down power plants within the blacked-out grid area, and a basis for synchronisation for power plants in islanded operation to ensure quick reconnection of these plants. When all generation units are securely reconnected, other transmission lines can be re-energised, and all loads can be reconnected gradually. [3] The major advantage of this strategy lies in the stability provided by the large, interconnected transmission grid areas providing the necessary power reserves for PSR, so failure due to active or reactive power imbalance is unlikely.

In comparison, the *Bottom-Up-Strategy* that can be applied universally to all blackout scenarios utilises black-start capable or islanded-operating power plants to provide the necessary power to start up non-black-start capable power plants and to energise transmission lines. Once enough generation units are reconnected and ready, load pickup can begin. [3] Next to independency from external power, another major advantage of this strategy is that a PSR failure cannot affect other secure grid areas, causing a blackout to spread beyond its original extent. On the other hand, a disadvantage lies in the reduced stability and resilience of the small grid formed during PSR.

C. Black-start capabilities

The power-on of a power plant using only itself as a power source for operational and auxiliary facilities is called a black-start [4]. This capability is crucial for a plant's role during Power System Restoration, more so if a Bottom-Up-Strategy is to be applied. Technically, it is possible to provide every power plant with sufficient auxiliary power generation for it to be black-start capable, but cost-effectiveness justifies this only for units with moderate power demand during start-up.

Steam power plants, especially coal-fired units with coal mills, conveyers, and high-pressure pumps, require up to 10 % of their rated output power over a long period of time for secure power-on. With rated output power up to 1 GW, it becomes uneconomical to provide enough auxiliary generators on-site. These power plants are considered non-black-start-capable. [4]

In comparison to steam plants, gas turbine power plants have far less operational and auxiliary machinery, and power on much quicker, reducing the necessary start-up energy to a reasonable level that can be served by local auxiliary generation or battery storage. Energy sources using wind, solar or hydro power are in principle black-start capable as they usually transform primary energy directly to electrical energy and hence do not have operational or auxiliary facilities, except for control systems. [4 Gas turbine and (pumped) storage hydro power plants are today the preferred power plants used in transmission grid restoration.

D. *Load Pickup*

Grid frequency depends on the active power balance due to the conservation of energy. The rotating masses of turbines and generators store mechanical energy. If electrical power demand exceeds mechanical power supply (e.g. steam) to the turbine, the stored rotational energy is transformed into electrical energy in expense of rotational speed, i.e. the electrical frequency. Two control strategies are applied to react to frequency changes due to load loss or acquisition. First, frequency containment will stabilise the frequency to a level defined by droop. Then, frequency restoration returns the grid frequency to its nominal value by allocating secondary control reserves. [5] However, the control systems and turbines need time to follow the change in demand, hence a deviation from the nominal frequency at least for some time is inevitable. Therefore, loads must be picked up in an appropriate scheme to ensure compliance with frequency limits.

III. SELECTION AND IMPLEMENTATION OF POWER PLANT MODELS FOR POWER SYSTEM STUDIES

A. *Speed Governor*

A governor according to Fig. 1 is used in all models to generate a setpoint for either a valve opening or fuel flow. Table I describes its input parameters, of which the latter three have to be set by the simulation environment. It includes a droop d as well as an input filter with a time constant T_{PF} in the power error path. To calculate the output, a PI controller with proportional gain K_{PG} and integral gain K_{IG} is used. Parameters not listed in Table I are specified for each model individually.

Note that measured electrical power output P_{el} should be generated by the simulation environment. Connecting it to mechanical power output would disregard the generator and cause an error depending on the value of load damping D.

B. *Generator*

To convert mechanical power to rotational speed, the generator representation based on the swing equation according to [6] is used in all models. Depending on the mechanical power from the turbine and the electrical load, the frequency deviation is calculated. The structure is shown in Fig. 2, where H is the generator/turbine inertia constant, and D the load damping coefficient.

TABLE I. GOVERNOR INPUT PARAMETERS

Parameter	Description	Value
ω_{set}	Rotational speed setpoint Based on 50 Hz	1 p.u.
P_{set}	Output power setpoint Based on rated power output	0…1 p.u.
P_{el}	Measured electrical power output Based on rated power output	0…1 p.u.

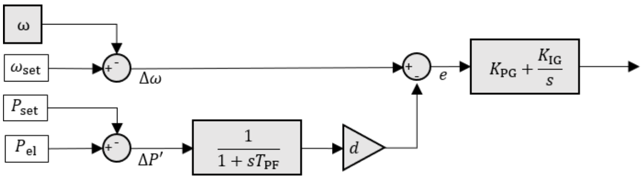

Fig. 1. Governor block diagram

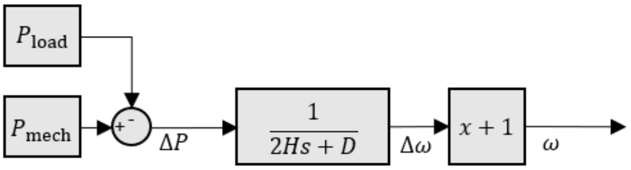

Fig. 2. Generator block diagram

C. *Steam Units*

Fig. 3 shows a modified version of the model for a single-shaft single-reheat steam power plant with a high-pressure (HP), an intermediate-pressure (IP), and a low-pressure (LP) turbine according to reference [7]. Table II states the model parameters, typical values and for per-unit values the per-unit base value.

For the purpose of this paper, the model has been simplified. The intercept valve (IV) has been omitted since it is not available in every steam power plant, and utilisation of the IV varies between plants. The boiler representation has been omitted in favour of a constant steam pressure p_{T} as it can be assumed that during grid restoration plant operators coordinate with grid operators to ensure steam production leading load pickup. Because the original model assumes an ideal turbine/generator set, a no-load full-speed steam flow $\dot{m}_{\mathrm{nl}}$ is introduced to represent internal losses.

The control valve (CV) position controller calculates the necessary CV position reference from set and output speed and set and output power. Then, the CV servo acts upon the CV position reference signal and outputs the actual CV position. CV position, main steam pressure, and no-load steam flow define the steam flow into the turbine set. First, steam flow reaches the high-pressure turbine and generates a fraction of the total mechanical power output. Afterwards, steam flows through the reheater and reaches the intermediate pressure turbine where it generates another fraction of the total mechanical power output. Steam then passes through the crossover into the low-pressure turbine where the third fraction of the total mechanical power output is generated. Because all turbines are mounted on the same shaft, the mechanical power of each turbine adds up and defines the electrical output power of the generator.

D. *Gas Turbine Units*

To represent a stand-alone gas turbine power plant, a model according to reference [8] was selected (see Fig. 4). The *Generator* block is implemented according to Fig. 2. Note that the governor from Fig. 1 was modified since the control loop already contains a PI controller.

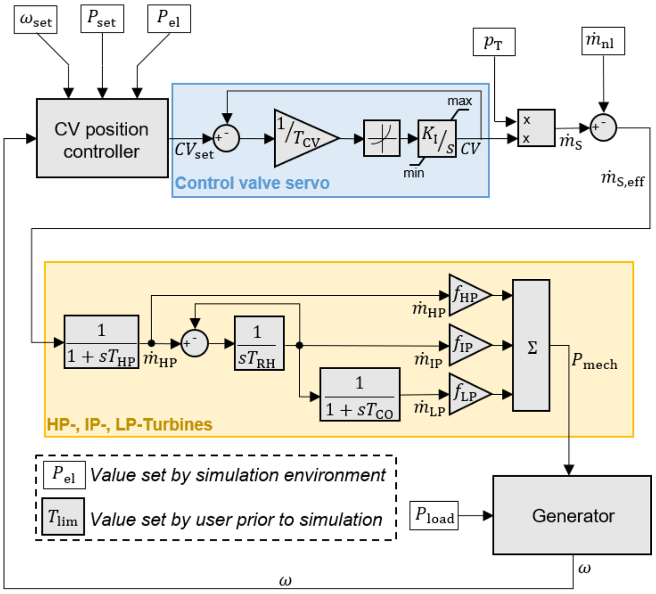

Fig. 3. Steam Turbine power plant model block diagram

Again, the model has been simplified.. First, the turbine characteristic curve, representing the frequency dependency of the maximum power output, was omitted. If necessary, a characteristic curve can be added to the model easily through a look-up-table in the h feedback path. Also, the fuel system reference feedback was not implemented since it varies with manufacturers and does not influence the model behaviour significantly. [8]

Of the three independent control loop branches for temperature, acceleration, and speed control, the speed control branch is dominant during normal operation. Within the speed control loop, speed error is limited to a pre-set band, which works as a rate limiter for the PI controller. The deadband helps with computation speed by cutting out very low turbine speed deviations. Temperature and acceleration control intervene only if pre-set exhaust temperature or turbine acceleration limits are exceeded. The lowest fuel system reference value r_{temp}, r_{acc}, or r_{speed} is selected by a minimum value select gate. To take compressor losses into account, a no-load full-speed fuel flow f_{nl} is subtracted from the total fuel flow f_{total}, resulting in the effective fuel flow f_{eff}. Whereas only the latter is available for electrical power generation, exhaust heat h, relevant for temperature control, corresponds to the total fuel consumption. The turbine gain A_{T} (1) scales the effective fuel flow to a full-range per-unit power output of the turbine.

Table III describes the model parameters, typical values and for per-unit quantities the per-unit base.

Turbine gain and temperature limit correspond to each other and must be calculated from other model parameters.

$$A_{\mathrm{T}} = \frac{1}{f_{\mathrm{fl}} - f_{\mathrm{nl}}} \tag{1}$$

$$T_{\mathrm{lim}} = \frac{1}{A_{\mathrm{T}}} + f_{\mathrm{nl}} \tag{2}$$

Note that the lower limit of the fuel reference must be lower than the no-load full-speed fuel flow because this difference represents the deceleration of the turbine through the compressor.

TABLE II. STEAM TURBINE MODEL PARAMETERS

Parameter	Description, per-unit base	Value
P_{load}	Electrical power demand (load) Based on rated output power	0…1 p.u.
p_{T}	Constant steam pressure Based on steam pressure for rated power output	1.02 p.u.[a]
$\dot{m}_{\mathrm{nl}}$	No-load full-speed steam flow Based on steam pressure for rated power output	0.01 p.u.
ω	Output rotational speed Based on 50 Hz	1 p.u. ± 0.05
d	Permanent Droop Based on rated output power and 50 Hz	0.05 p.u.
T_{PF}	Power feedback filter time constant	5 s
K_{PG}	Speed governor proportional gain	10
K_{IG}	Speed governor integral gain	0.5 s^{-1}
T_{CV}	Control valve servo time constant	0.1 s
K_{I}	Control valve position integrator gain	1 s^{-1}
min, max	Minimum/maximum gate opening	0 p.u., 1 p.u.
T_{HP}	High pressure steam bowl time constant	0.3 s
T_{RH}	Reheater time constant	7 s
T_{CO}	Crossover time constant	0.5 s
f_{HP}	Contribution of high pressure turbine to total mechanical power generation Based on rated power output	0.3 p.u.
f_{IP}	Contribution of intermediate pressure turbine to total mechanical power generation Based on rated power output	0.3 p.u.
f_{LP}	Contribution of low pressure turbine to total mechanical power generation Based on rated power output	0.4 p.u.
H	Intertia constant of turbine/generator set	9
D	Load Damping coefficient	1

[a] To allow for frequency containment and enhance stability, a value larger than 1 must be chosen.

E. Storage Hydro Units

For simplicity, storage hydro power plants are often modelled assuming an inelastic water column, neglecting travelling wave phenomena. However, these models have significant disadvantages not compensated for by the simple structure or quicker computation. For example, to account for all elastic properties of a long water column and long pipes, a non-linear model in combination with an elastic water column representation is necessary. For this paper, a model presented in reference [9] was selected. This model allows for convenient scaling due to its modular structure. Fig. 5 shows the tunnel and a first penstock in detail and indicates how other penstocks can be added to the same tunnel. *Gate position governor* and *Generator* are as shown in Fig. 1 and Fig. 2.

Table IV shows the model parameters, typical values and for per-unit values the corresponding base quantity.

The hydraulic surge impedance can be calculated according to reference [9]. Turbine gain is given by (3).

$$A_{\mathrm{T}} = \frac{1}{q_{\mathrm{fl}} - q_{\mathrm{nl}}} \tag{3}$$

Tunnel head is influenced by tunnel flow in two different ways. The zero-flow tunnel head of 1 p.u. is reduced by friction losses square to flow as well as by pressure surges through tunnel surge impedance and the hyperbolic tangent of the wave travel time, which together represent the wave transfer function.

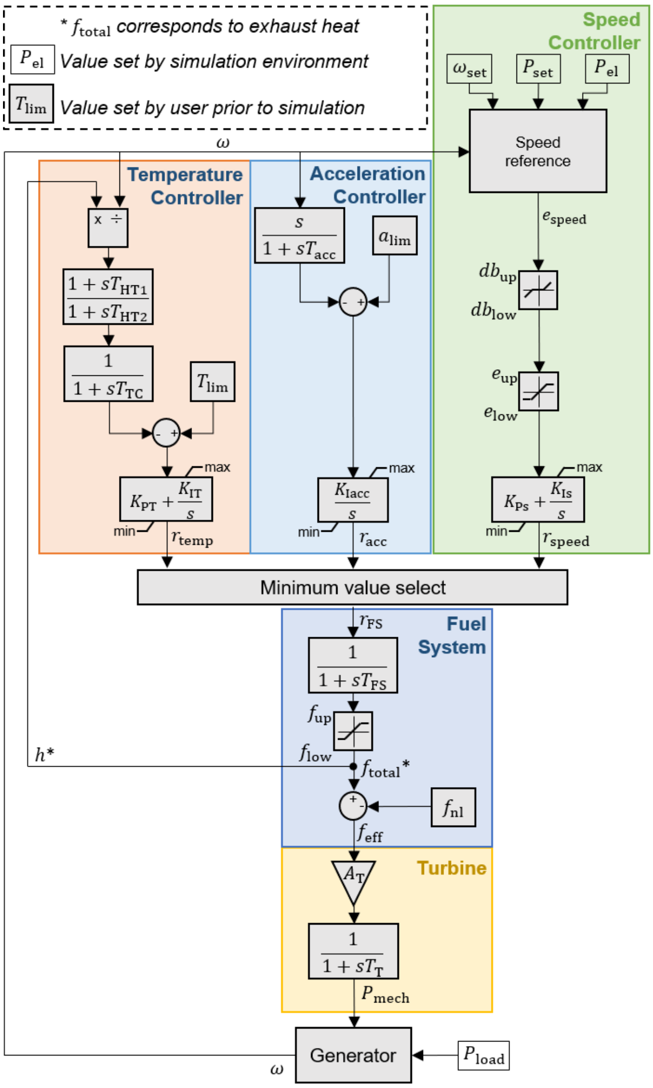

Fig. 4. Gas Turbine power plant model block diagram

Because the tunnel and penstock per-unit quantities are not based on the same absolute parameters, the per-unit penstock flows $q_{\mathrm{P}i}$ must be scaled to the contribution each penstock flow makes towards tunnel flow. To scale the per-unit penstock flows, a weight factor c_i is calculated for each penstock i (4). Then, each per-unit penstock flow q_i is multiplied with the weight factor (5). The sum of all weighted penstock flows q'_i gives the per-unit tunnel flow (6).

$$c_i = \frac{\overline{q}_{\mathrm{P}i}}{\sum_n \overline{q}_{\mathrm{P}n}} \tag{4}$$

$$q'_i = q_i c_i \tag{5}$$

$$q_{\mathrm{T}} = \sum_n q'_n \tag{6}$$

The gate position is calculated by the gate position controller from set and actual speed and set and actual power and then executed by the gate servo, resulting in a penstock flow corresponding to gate opening. The mechanisms of head loss and deviation due to surges also apply to the penstock, however, the initial penstock head is not 1 p.u. but the tunnel head. Penstock head multiplied with penstock flow and turbine gain give the mechanical output power of one hydro turbine. Turbine damping, inherent from turbine dynamics, counteracts speed deviations based upon power imbalance and gate opening which, assuming near constant speed, corresponds to mechanical power [9].

TABLE III. GAS TURBINE MODEL PARAMETERS

Parameter	Description, per-unit base	Value
P_{el}	Electrical power demand Based on rated output power	0…1 p.u.
ω	Output rotational speed	1 p.u. ± 0.05
d	Droop Based on rated power output and 50 Hz	0.05 p.u.
T_{PF}	Power feedback filter time constant	5 s
K_{PG}	Speed governor proportional gain[b]	1
K_{IG}	Speed governor integral gain[b]	0
$db_{\mathrm{up}}, db_{\mathrm{low}}$	Upper/lower deadband limit	±0.000015
$e_{\mathrm{up}}, e_{\mathrm{low}}$	Upper/lower error limit	±0.005
K_{Ps}	Speed governor proportional gain	10
K_{Is}	Speed governor integral gain	2 s^{-1}
a_{lim}	Acceleration limit setpoint	0.01
T_{acc}	Acceleration differentiator filter time constant	0.1 s
K_{Iacc}	Acceleration controller integral gain	10 s^{-1}
T_{HT1}	Heat transfer lead time constant	10 s
T_{HT2}	Heat transfer lag time constant	15 s
T_{TC}	Thermocouple time constant	2.5 s
T_{lim}	Temperature limit (2)	1.05 p.u.[c]
K_{PT}	Temperature controller proportional gain	1
K_{IT}	Temperature controller integral gain	0.2 s^{-1}
min max	Lower/upper fuel reference limit Based on rated fuel flow	0.15 p.u. 1 p.u.
T_{FS}	Fuel system time constant	0.5 s
f_{up} f_{low}	Upper/lowe fuel flow limit Based on rated fuel flow	1 p.u. 0 p.u.
f_{nl}	No-load full-speed fuel consumption Based on rated fuel flow	0.25 p.u.
A_{T}	Turbine gain (1)	1.35[c]
T_{T}	Turbine time constant	0.5 s
H	Turbine/Generator/Compressor inertia constant	6
D	Load damping coefficient	1

[b] The speed governor from Fig. 1 is not used in this model

[c] A margin was added to avoid numerical issues at full load

IV. VERIFICATION OF POWER PLANT MODELS FOR POWER SYSTEM RESTORATION STUDIES

A. Verification Scenarios

During PSR, power plant operation demands actions that cannot be compared to normal, everyday operation. To verify the applicability of the presented power plant models, several PSR-typical scenarios were implemented. Note that the simulated time intervals are chosen to regard the presentability of the scenarios and do not represent realistic time intervals during operation.

First, in *scenario 1* the characteristics of the plant controller are verified for each model. According to the droop formula (7), a change in either the power setpoint or the electrical load (ΔP) compared to the rated power P_{r} will result in a defined frequency deviation Δf from the nominal frequency f_{n}.

$$d = \frac{\Delta f \cdot P_{\mathrm{r}}}{\Delta P \cdot f_{\mathrm{n}}} \tag{7}$$

At $f_{\mathrm{n}} = 50\,\mathrm{Hz}$ and $d = 5\,\%$, a plant's electrical frequency is expected to drop to a steady-state value of $f = 47.5\,\mathrm{Hz}$ at $P_{\mathrm{load}} = 1\,\mathrm{p.u.}$ and $P_{\mathrm{set}} = 0\,\mathrm{p.u.}$ Fig. 6 shows the frequency response for the last step of a $\Delta P = 0.1\,\mathrm{p.u.}$-staircase series approaching $P_{\mathrm{load}} = 1\,\mathrm{p.u.}$

TABLE IV. STORAGE HYDRO MODEL PARAMETERS

Parameter	Description, per-unit base	Value
Z_{T}	Tunnel hydraulic surge impedance	0.6
T_{eT}	Tunnel wave travel time	0.642 s
f_{T}	Tunnel water head loss Based on tunnel length and rated flow	0.005 p.u.
$\overline{q}_{\mathrm{P\_fl}\_i}$	Absolute full-load flow in penstock i	
P_{el}	Electrical power demand Based on rated output power	0…1 p.u.
ω	Output rotational speed	1 p.u. ± 0.05
d	Droop Based on rated power output and 50 Hz	0.05 p.u.
T_{PF}	Power feedback filter time constant	5 s
K_{PG}	Speed governor proportional gain	5
K_{IG}	Speed governor integral gain	0.5 s^{-1}
K_{PS}	Gate servo gain	5
T_{PS}	Gate servo time constant	0.5 s
$r_{\mathrm{up}}, r_{\mathrm{down}}$	Maximum Gate opening/closing rate Based on rated gate opening	±0.2 p.u./s
e_{up} e_{low}	Upper/lower gate position limit	1.05 p.u. 0.001 p.u.
Z_{P}	Penstock hydraulic surge impedance	2.1
T_{eP}	Penstock wave travel time	0.148 s
f_{P}	Penstock water head loss Based on penstock length and rated flow	0.005 p.u.
q_{nl}	No-load full-speed water flow Based on rated flow	0.1 p.u.
A_{T}	Turbine gain (3)	1.15[d]
D_{T}	Turbine damping factor	0.5
H	Turbine/generator inertia constant	4
D	Load damping coefficient	1

[d] A margin was added to avoid numerical issues at full load

Next, in *scenarios 2* and *3* two PSR-typical load pick-up actions are simulated. In *scenario 2*, a 0.1 p. u. setpoint step followed by a 0.15 p. u. load step followed by a 0.05 p. u. setpoint step illustrate the case where the plant operator underestimates the load by 50% and adjusts the setpoint. Afterwards, in *scenario 3* a 0.1 p. u. setpoint step, followed by a -0.15 p. u. load step and a -0.25 p. u. . setpoint step describe the case that a load pick-up is expected but upon switching a significant load is lost. Fig. 7 through Fig. 10 show the frequency response of all three power plant models (*part a* at low load levels and *part b* at higher load level).

At last, *scenario 4* pictures the plants' responses to an unexpected significant load acquisition of 0.25 p.u. followed by an unexpected load loss of the same magnitude. Fig. 11 depicts the frequency response of all three power plant models at a low load level, typical for an early point during PSR.

B. Examination of Verification Results

1) Governor and Reaction Characteristics

As expected, each plant's governor counteracts the change in frequency and stabilises it for *scenario 1* at 47.5 after an inevitable dynamic frequency dip or spike.

Of the three modelled power plants, the steam power plant has the slowest, yet most stable reaction to load changes as it returns to a steady-state frequency smoothly. In comparison, the gas turbine and hydro power plant models react quickly to load steps but show oscillations with amplitudes up to 1 Hz before returning to the steady-state frequency. This behaviour is strongly influenced by the governor parametrisation which depends on the other model parameters that limit the speed a governor can stabilise the frequency.

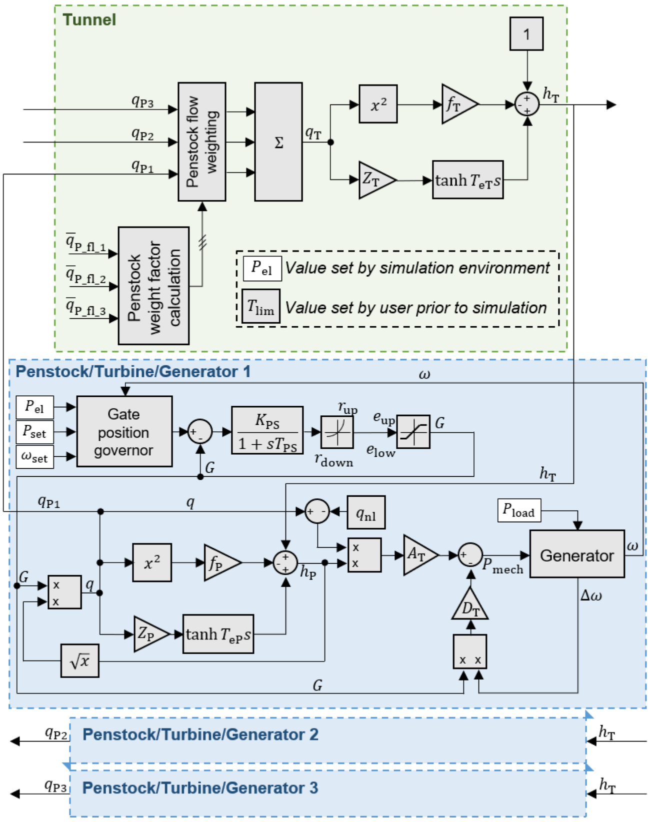

Fig. 5. Storage hydro power plant model block diagram

2) Reaction to large load changes

Upon large load pick-up, a significant frequency dip is, as expected, seen in *scenario 4* for all power plant models of which the gas turbine unit model shows the largest frequency excursion. The behaviour over time again depends on the generator dynamics, especially the inertia constant of the machine set, as well as the governor/turbine characteristics. The magnitude of the peak is also determined by the governor's ability to reduce power to the turbine quickly.

The behaviour of the gas turbine unit can be explained by the error limitation of the speed governor as well as the function of the acceleration control path. The intentional speed error limit e_{speed}, parametrised according to [8], functions as a rate limiter for the speed governor path PI controller and and thus prevents it from increasing or decreasing fuel flow quickly enough to counteract large speed deviations that cause an error signal $e_{\mathrm{speed}} > |0.005|$. The slow governor reaction then causes a higher frequency excursion. In addition, the acceleration controller cannot intervene quickly enough due to its setpoint that is parametrised to protect the turbine against significant turbine acceleration. To mitigate this issue, the magnitude of the speed control path error limit could be raised to allow for quicker control. This was, however, not done to maintain consistency of the model parameters to reference [8]. Reducing the acceleration limit setpoint may improve the model behaviour regarding large load changes but can also lead to stability issues when the limit is set so low that it is met under normal operating conditions.

3) Low/high load level differences

The comparison between responses on high and low load levels yields a significant difference in the behaviour of the hydro power plant. At low load levels, i.e. at low flow, the magnitude of the frequency excursions after load changes is moderate but rises to almost 1 Hz at higher load. This can be

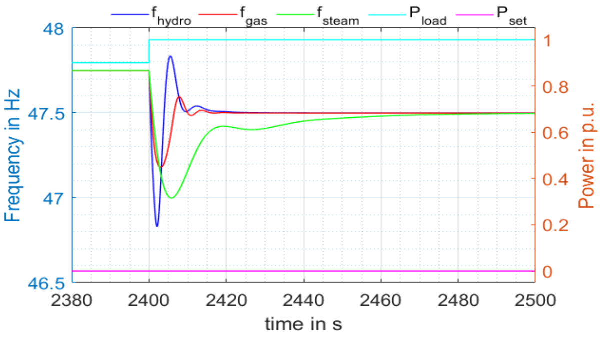

Fig. 6. Frequency response to *scenario 1*

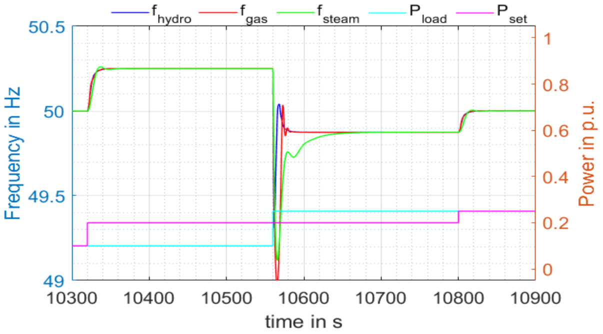

Fig. 7. Frequency response to *scenario 2a*

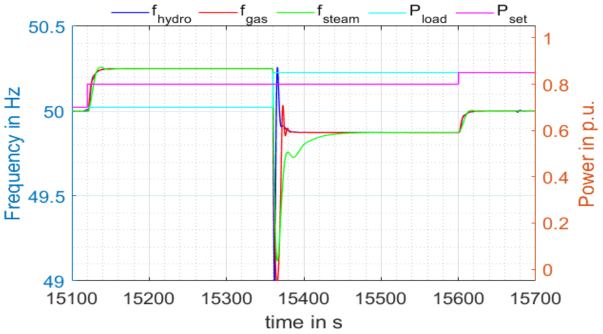

Fig. 8. Frequency response to *scenario 2b*

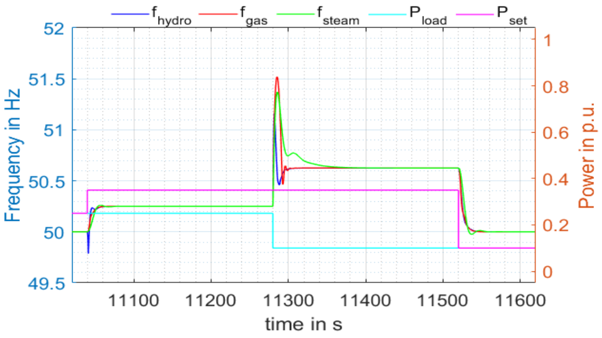

Fig. 9. Frequency response to *scenario 3a*

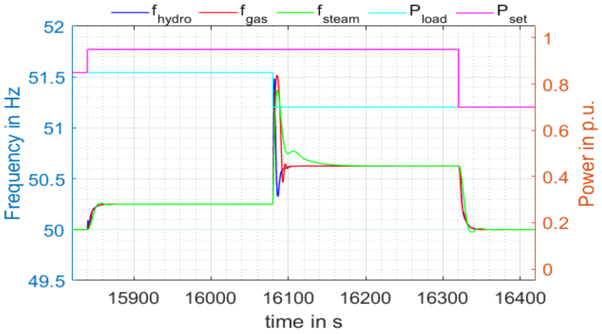

Fig. 10. Frequency response to *scenario 3b*

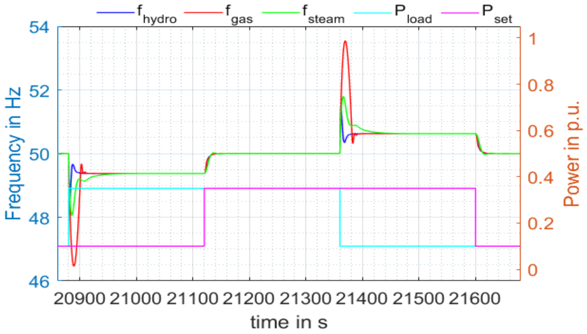

Fig. 11. Frequency response to *scenario 4*

explained by the nature of implementation the travelling wave transfer function in Fig. 5. The $\tanh(T_e s)$ blocks of the tunnel as well as the penstock only react to changes in their input, however, the magnitude of change is influenced by the bias value qZ. So, the response of these model paths changes with power output which correlates to gate position and thus flow.

Because the gas turbine and steam power plant model are strictly linear, their responses to load changes is expected to be equal at all load levels. Indeed, this expectation was confirmed by all simulation results.

V. CONCLUSION AND OUTLOOK

From the presented verification simulations, it can be concluded that the power plant models chosen from literaure are suitable for the use in power system restoration studies as the models behave as expected and offer enough options to specify important parameters. However, some modifications were necessary to enable all models to be applicable to the PSR-specific scenarios.

Not covered in this paper was the analysis of interaction between the plant models when connected to a grid. Also, as power generation from wind farms increases, the possibility of them participating in power system restoration has to be incorporated in future research.

REFERENCES

[1] Bundesministerium für Wirtschaft und Energie, “Systemsicherheit und Systemdienstleistungen”, [Online] available at https://www.bmwi.de/Redaktion/DE/Artikel/Energie/netz-und-systemsicherheit.html, Feb. 15th 2019

[2] Comission Regulation (EU) 2017/2196 of 24 November 2017 establishing a network code on electricity emergency and restoration.

[3] M. Krüger, H. Weber, W. Franke and R. Kirsch, „Wiederaufbau von Uebertragunsnetzen nach Großstörungen“, [Online] available at https://www.iee.uni-rostock.de/fileadmin/uni-rostock/Alle_IEF/IEE/Publikationen_EEV/Wiederaufbau_von_Uebertragungsnetzen_nach_Grossstoerungen.pdf, Feb. 18th 2019

[4] W. Sun, C.-C. Liu and S. Liu, “Black Start Capability Assessment in Power System Restoration” in 2011 IEEE Power and Energy Society General Meeting

[5] D. Oeding, B. R: Oswald, „Elektrische Kraftwerke und Netze“, 7. Aufl., Springer, 2011, ISBN: 978-3-642-19245-6

[6] P. Kundur, Power System Stability And Control, McGraw-Hill, 1994

[7] IEEE WG on Prime Mover and Energy Supply Models for System Dynamic Performance Studies, “Dynamic Models For Fossil Fueled Steam Units In Power System Studies”, in IEEE Transactions on Power Systems, Vol. 6, No. 2, pp. 753-761, May 1992

[8] CIGRE Task Force 25, Advisory Group 2, Study Committee 38, “CIGRE Technical Brochure on Modelling of Gas Turbines and Steam Turbines in Combined-Cycle Power Plants”, April 2003

[9] IEEE WG on Prime Mover and Energy Supply Modles for System Dynamic Performance Studies, “Hydraulic Turbine and Turbine Control Models for System Dynamic Studies”, in IEEE Transactions on Power Systems, Vol. 7, No. 1, pp. 167-179, February 1992

Experimental validation of the impact of module and circuit parameter scattering on the switching behaviour

Oelze, Maximilian
Otto-von-Guericke Universität
Magdeburg , Germany
maximilian.oelze@ovgu.de

***Abstract*— This paper deals with the determination of differences related to the switching performance of nominally identical power semiconductors which are based on gallium nitride (GaN). These GaN high electron mobility transistors (HEMTs) are investigated using a bridge leg topology with active gate driver control. At first, the parameter deviations of threshold voltage, on resistance and parasitic inductance are named via literature research. Structure and operating principle of the active gate drivers control for the improvement of switching performances are explained and compared to constant gate resistances. To evaluate the real parameter differences the influence of measuring devices on measurements was investigated. As a result this influence on gate-source-voltage and drain current is limited. Furthermore, the influence of parasitic inductance is analyzed. The potential parameter differences of power semiconductors at measurements were done with various operating points as well as input voltages. Thereby discrepancies of threshold voltage on resistance and the parasitic inductances within the power circuit are analyzed.**

Keywords—bridge leg topology, gallium nitride, GaN-HEMT, gate driver control, parameter deviation, turn on behavior

I. INTRODUCTION

The increase of the efficiency, the output power, switching speed breakdown voltage and thermal resistance are major requirements of the improvement of power electronic circuits. However, the improvement of power semiconductors based on silicon is has reached a limit. Therefore, new materials, so-called Wide-Band-Gap materials, are investigated [1]. That includes gallium nitride (GaN). GaN-semiconductors are subject to production emphasis, which causes parameter deviations by nominally identical components. In this paper, the divergent parameters are determined with literature research and the influence on the switching behavior are identified. The results of the literature research are presented in section II. Also, the influence of parasitic inductances and measuring instruments are investigated [2]-[3]. Section III deals with the measurement setup. Thereby, three nominally identical non-isolated DC/DC converters, which are assembled with GaN high-electron-mobility-transistors, are built. The special feature of the circuit is the active gate driver to control the power semiconductor, which improves the switching behavior and reduces electromagnetic disturbances and switching losses. The operating principle is also part of section III. The experimental results, where the boards are measured by different operating points, input voltages and gate resistor profiles, are shown in section IV. In section V the results of the literature research and the experiment are summarized.

II. RESULTS OF THE LITERATURE RESEARCH ON WIDE BANDGAP SEMICONDUCTORS

In literature parallel circuits of wide-bandgap semiconductors were under examination. Likewise, parameter deviations have an influences on parallel circuits of power semiconductors. Here, these results are helpful for the performed investigation. Power semiconductors based on GaN and silicon carbide (SiC) are investigated. SiC is also a new power semiconductor material and also has parameter deviations. Hence the results of SiC are usable for the investigation of parameter deviations of GaN.

A. Threshold-Voltage

In [2] SiC junction-field-effect-transistors, with parameter deviations, are investigated. Thereby deviations in threshold voltage are important. Fig. 1 shows the output characteristic of two nominally identical SiC-JFETs with a different threshold voltage. At a point with equal drain-source-voltage, the drain current deviates.

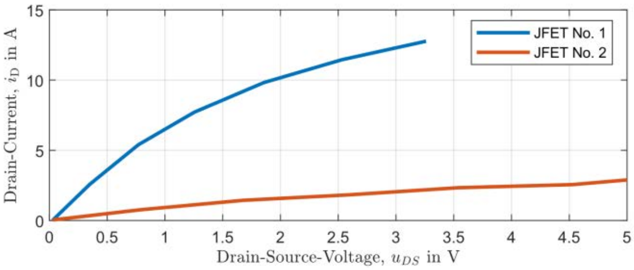

Fig. 1 Sequence of the drain current depending on the drain-source voltage on a gate-source voltage of -5V of two nominally identical SiC-JFETs [2].

In Fig. 2 the gate-source-voltage becomes attuned to -4 V. Because the different threshold voltage, JFET Nr.1 is conductive, while JFET Nr.2 is blocking. The parameter deviations causes one semiconductor to be conductive while the other semiconductor is still in blocking state.

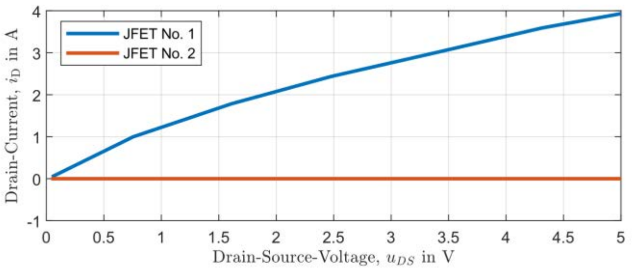

Fig. 2 Sequence of the drain current depending on the drain-source voltage on a gate-source voltage of -4V of two nominally identical SiC-JFETs [2].

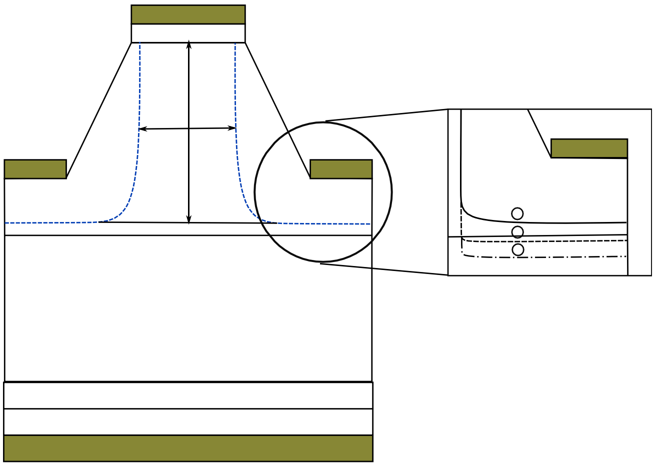

Fig. 3 Structure of a VJFET different spacings of the p-doped area to the N-drift region [4].

In [4] additional investigations with SiC vertical junction field effect transistor (VJFET) are presented. Thereby, the different spacings are shown in Fig. 3 between the p-doped area the N-drift region was varied. The effects of the different spacings are shown in Fig. 4.

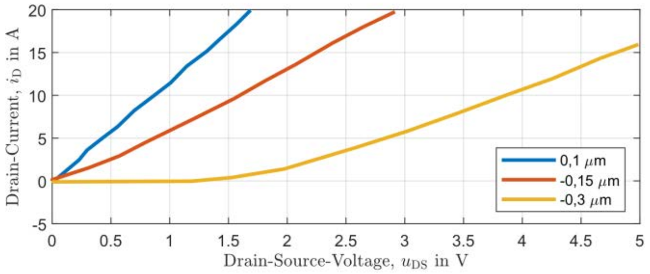

Fig. 4: Sequence oft the drain current depending on the drain-source voltage by different spacings of the p-doped area to the N-drift region [4].

The more the p-doped area reaches into the N-drift-region, the more is the increase of the drain current delayed. The deviations by the spacings change the threshold voltage. Even less geometrical deviations can change the output characteristics significantly. In [4] were differences von 100 nm described, which change the threshold voltage by 1 V.

B. On-state-Resistance

Another parameter with deviations between different power semiconductors is the on-state resistance. In [5] metal-oxide-semiconductor field effect transistors (MOSFETs) based on SiC were compared. The attributes of these MOSFETs were detected with a curve tracer. In Fig. 5 two MOSFETs with high on-state resistance were compared. MOSFET Nr.1 has a higher on-state resistance. There are deviations related to the current spike, but the current increase is roughly the same. Subsequently, the chronological sequence of the drain current of MOSFET Nr.1 is smaller, because the on-state resistance is higher.

C. Parasatic Inductance

Parasitic inductances also influence the switching behavior. These may be reduced by a thoughtful printed circuit board (PCB), but never complete avoided. Parasitic inductances and capacitance form oscillating circuits. Therefore, the real switching sequences ringing, compared to the ideal switching sequences.

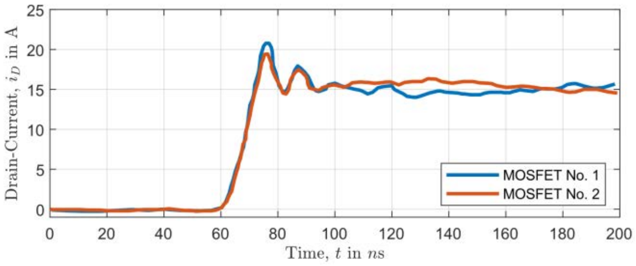

Fig. 5 Sequence of the drain current by different gate resistance [5].

A benefit of GaN power semiconductors is the higher switching speed. The result is a faster change of current related to the time. They increase the influence of parasitic inductances.

III. MEASUREMENT SETUP

For the investigation of parameter deviations by GaN power semiconductors, three identical boards with a non-isolated DC/DC converter were built. The bridge-leg topology was assembled with GaN-HEMTs.

A. Non-Isolated DC/DC Converter

Fig. 6 show the measurement setup. The setup works as a boost converter, so the energy flows from right to left. Gate and source of transistor T_1 are shorted so the transistor works as a diode. Transistor T_2 is driven by an active gate driver. Hence the gate resistor is variable during the switching process.

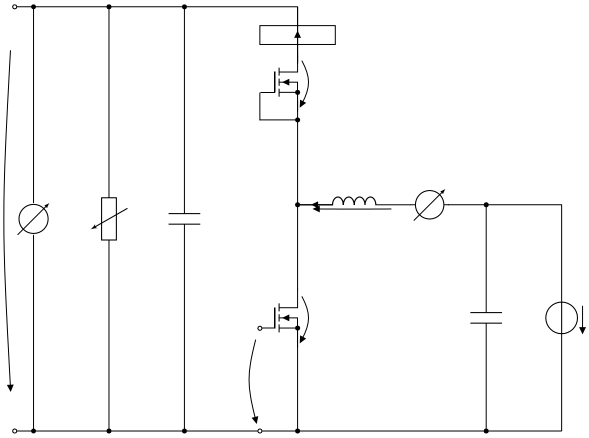

Fig. 6: Measurement setup of a non-isolated DC/DC converter.

This improves the switching behavior. The operating principle is explained more in section III.C. The gate-source- and drain-source-voltage of T2 is measured via two voltage probes. The choke current i_L is detected with a current clamp. A special feature is the detection of the drain current iD1. These were measured with the infinity-sensor. The sensor is more explained in section III-B. These values are visualized by an oscilloscope. The in- and output voltage were measured by multimeters. The DC-links consist of parallel connected capacitances with a value of 2µF-100nF. Hence the setup has a low impedance over a broad frequency range. The average choke current is adjusted by an externally connected load resistor. Three operating points are used for the experiment (5 A, 7 A, 9.5 A). Additionally, the gate resistor profile and the input voltage were changed (50 V, 115 V, 200 V).

B. Infinity Sensor

The infinity sensor is composed of a conducting path which covers two contrarily twisted loops. A current change induces a voltage induction which is measured by a voltage probe. The drain current is derived from the voltage integration over time. The infinity sensor has a small bandgap and less parasitic components [6].

C. Active Gate Driver Control

With the active gate driver control, it is possible to change the gate resistor during the switching operation. The gate driver allowed setting the optimal gate resistor at any time. This optimizes the switching behavior, without increasing switching losses [7].

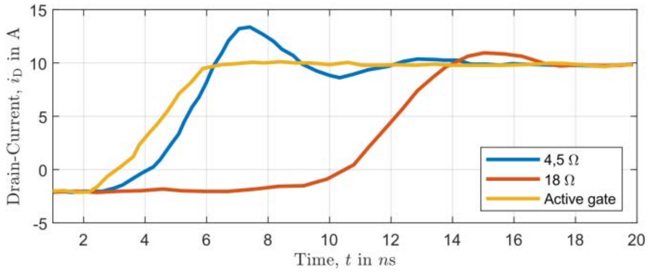

Fig. 7: Sequence of the drain-source voltage by different gate resistors [7].

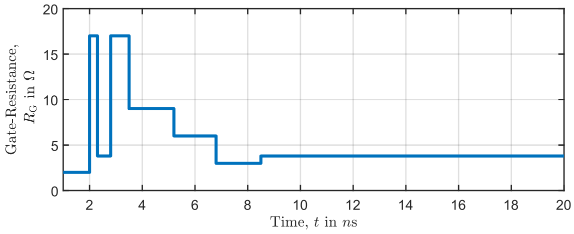

Fig. 8: Sequence of the gate resistance of the active gate driver [7].

A double pulse test is used in [7] to investigate the switching behavior of a power semiconductor. Fig. 7 and Fig. 8 show the sequence of the drain-source voltage with three different gate resistor sequences. At a gate resistor of 4,5 Ω, the voltage change is very fast, but a high voltage peak occurs. In comparison, the voltage change with 18 Ω is slower and the voltage peak is smaller. The voltage sequence of the active gate driver combines the benefits of both. The voltage change is fast and a voltage peak does not exist. Fig. 8 shows the sequence of the gate resistor of the active gate driver. In [7] was shown by different tests, that the switching behavior of the drain current also is improved. The additional losses because the added circuit for the active gate driver is negligible [7].

IV. EXPERIMENTAL RESULTS

To determine the influence of parameter derivations of power semiconductors, parasitic inductances and the influence of measuring instruments were three boards investigate by different operation points and input voltages. The following section deals with the on-switch behavior of a boost converter with GaN-HEMTs.

A. Switching Behaviour of a Boost-Converter with GaN HEMTs

For the investigation of the boost converter, an average choke current of 9.5 A was chosen. The control is done with a constant gate resistor of 4 Ω. Fig. 9 and Fig. 10 shows the sequences of the measured quantities. At first, the gate-source voltage starts to rise and reaches the threshold voltage at -9 ns. Then the drain current rises. The current change leads to a voltage induction because of the parasitic inductances of the commutation circuit. This voltage induction counteracted the drain-source voltage and causes the drop to the voltage plateau at -5 ns in Fig. 10.

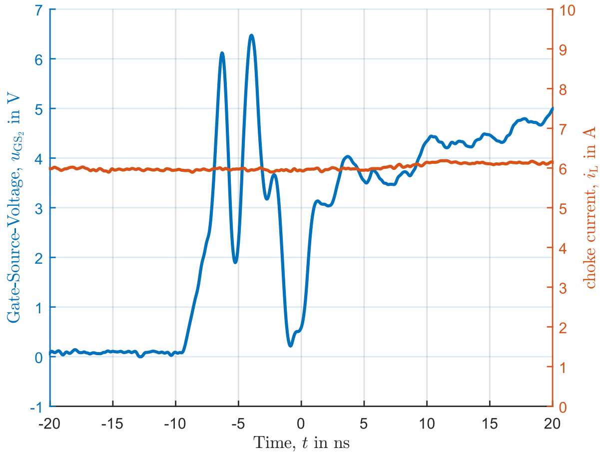

Fig. 9: Sequence of the gate-source voltage (blue) and the choke current (red) while switch-on.

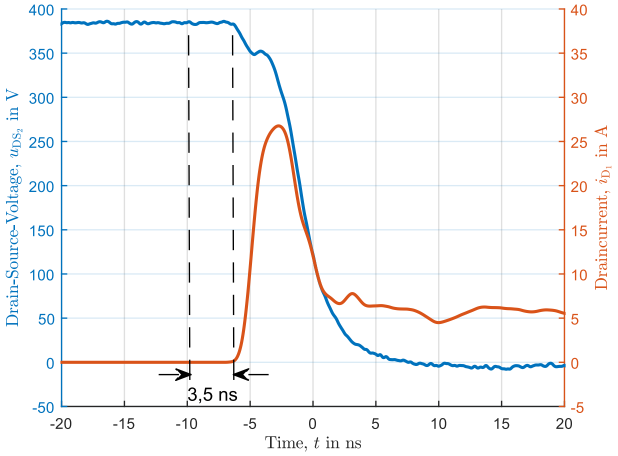

Fig. 10: Sequence of the drain-source voltage (blue) and the drain current (red)

The current change also causes oscillation. The output capacitance of the power semiconductor and the parasitic inductances form an oscillation circuit. This ringing overlapped the gate-source voltage. The drain current is shifted about 3.5 ns. Different cable length causes a shift of signal propagation delay. This was determined with the following equations:

$$v = \frac{c}{\sqrt{\mu_r \cdot \epsilon_r}} \tag{1}$$

$$\Delta t = \frac{l_2 - l_1}{v} \tag{2}$$

Where c is the speed of light while μ_r is the relative permeability (for copper around 1), v is the speed, Δt is the time difference and ϵ_r is the relative permittivity,. This depends on the dielectricum of the measuring cable. Normally polyethylene (PE) is used ($\epsilon_{r,PE}$=2.25). With the two lengths, l_1=1,3m and l_2=2m result in a time shift of 3.5 ns.

B. *Measuring Impact*

Before the determination of the influence of power semiconductors, the influence of the measurement instruments is investigated. The measurement setup was build up three times in a row. After each assembly, all parameters were measured. Therefore, the position of the probes changes a little bit. The position differences most influences the gate-source voltage. Fig. 11 shows the sequence of the gate-source voltage of the three measurements. The amplitudes of the single measurements spread. The oscillation frequency is identical. Only at the drain current spread at the current peak visible. The sequences of the drain-source voltage are identical. A second possibility to investigate the influence of measurement instruments is to compare measurements when all measurements are installed and when only one is installed. Even here, the gate-source voltage is most influenced (cf. Fig. 12). The other quantities are not or even less influenced. Summarizing only the gate-source voltage is influenced by the other measurement instruments.

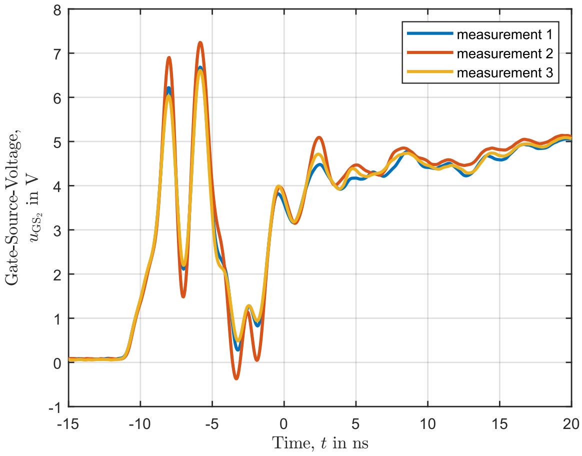

Fig. 11: Sequence of the gate-source voltage after repeated assembly and dismantling of the measurement setup.

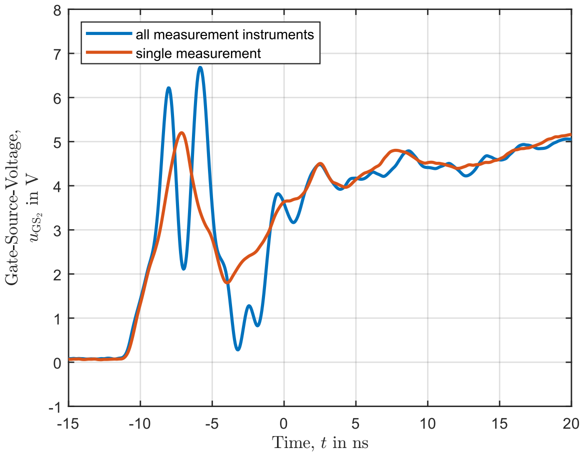

Fig. 12: Sequence of the gate-source voltage with all measuring instruments (blue) and as single measurement (red).

C. *Impact of parasatic Inductances*

For the determination of the influence of parasitic inductances, a gate resistor of 4 Ω is used for turn-on. Thereby the power semiconductor switches fast and the current change increases. This increases the influence of the parasitic inductance causes to the law of induction. Fig 13 shows, that there are differences between board three and the other boards.

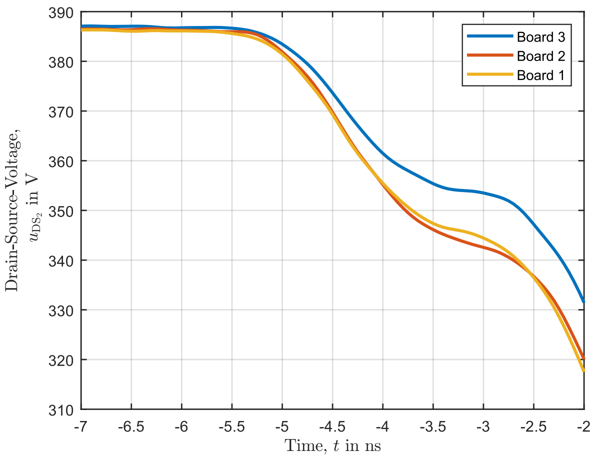

Fig. 13: Sequence of the drain-source voltage of all boards (fast switching).

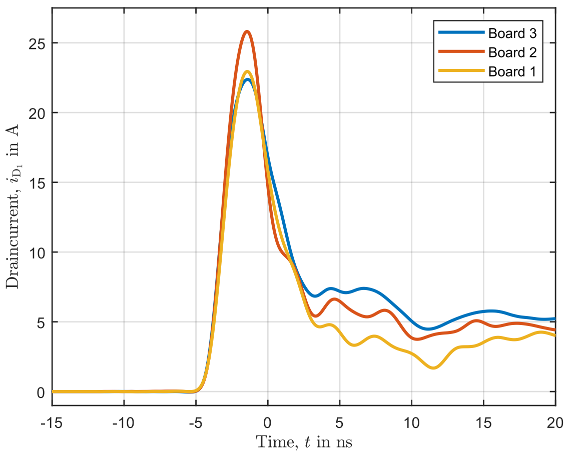

Fig. 14: Sequence of the drain current of all boards (fast switching).

The current change also causes oscillation. The output capacitance of the power semiconductor and the parasitic inductances form an oscillation circuit. This ringing overlapped the gate-source voltage. The drain current is shifted about 3.5 ns. Different cable length causes a shift of signal propagation delay. This was determined with the following equations:

$$L = \frac{\Delta U}{\frac{\mathrm{d}i}{\mathrm{d}t}} \tag{3}$$

The results vary widely and do not conform to Fig. 12. But this measurement method is inaccurate. For this reason, the resonance frequency of the oscillation circuit, consisting out of parasitic inductances and the output capacitance of the power semiconductor, was determined. The ringing caused by the oscillation circuit overlapped the gate-source voltage. Hence, the resonance frequency was determined with the gate-source voltage.

With the resonance frequency, the output capacitance out of the manual [8] (130 pF) and the following equation the oscillation circuit inductance was calculated:

$$L = \frac{1}{(2\pi \cdot f_r)^2 \cdot C} \tag{4}$$

The results of both methods are described in the following table:

Tab. 1: Increase of the drain current, voltage difference of the drain-source voltage, resonance frequency and resulting parasitic inductances of all Boards.

	Board 1	Board 2	Board 3
$^{di}/_{dt}$	11 A/ns	13,2 A/ns	12 A/ns
ΔU	40 V	42,3 V	32,7 V
L	3,6 nH	3,2 nH	2,7 nH
f_r	385,8 MHz	414,9 Mhz	387,1 Mhz
L_{SK}	1,31 nH	1,13 nH	1,3 nH

The deviation of the inductance determined with the resonance frequency are lower compared to the other inductances. But both results do not confirm with Fig. 12. The deviation of the power semiconductor not justified these gaps. Another possible cause for the differences in reference connection of the voltage probe („Pig-Tails"). The position of the reference connections was varied. This does not lead to a change of the drain-source voltage. So, a different layer structure of the PCB could be a reason.

D. *Impact of Power semiconducter*

To investigate the influence of the power semiconductor deviation to the switching behavior, different operating points and input voltages were adjusted. The presumption was, that different starting conditions emerge different parameters. Fig. 14 shows the gate-source voltage and the drain current by a choke current of 5 A. At a time of -9 ns the drain current increase. At this point, it is possible to determine the threshold voltage

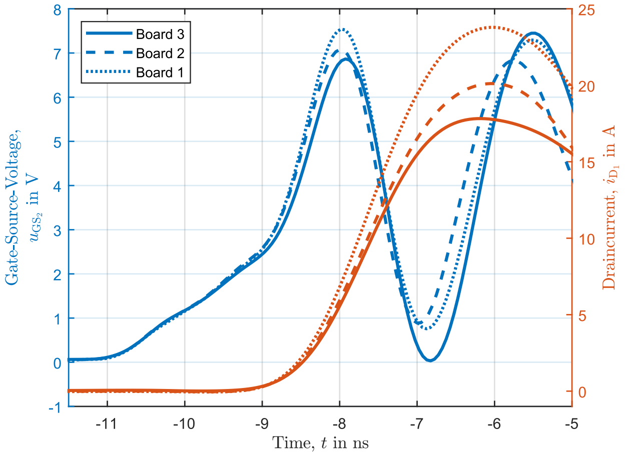

Fig. 15: Sequence of the gate-source voltage (blue) and the drain current (red) of all Boards at the time of -9 ns reach the threshold-voltage.

The threshold voltage of board 3 is 0,1 V smaller than the one from the other boards. As shown in the literature research, different threshold voltages cause changes concerning the output characteristics. Fig. 16 shows the sequence of the drain current at an average choke current of 5 A. The current increases show small deviations, during the current peaks have bigger differences. The differences in Fig. 16 are equal compared to the differences at other operating points. Because the different operating points do not affect the sequences, the input voltage was modified. Fig. 17 shows the drain-source voltage at an input voltage of 50 V.

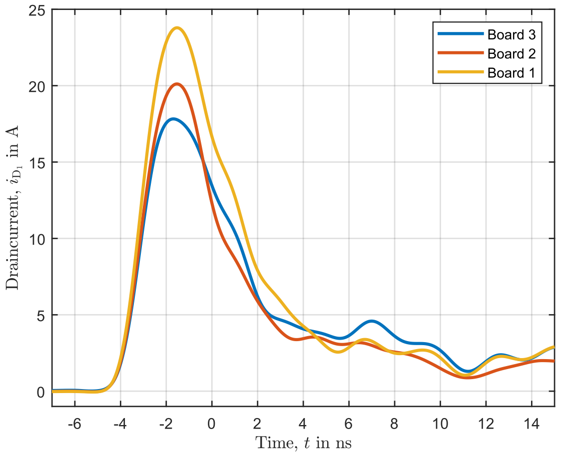

Fig. 16: Sequence of the drain current of all boards at a choke current of 5 A.

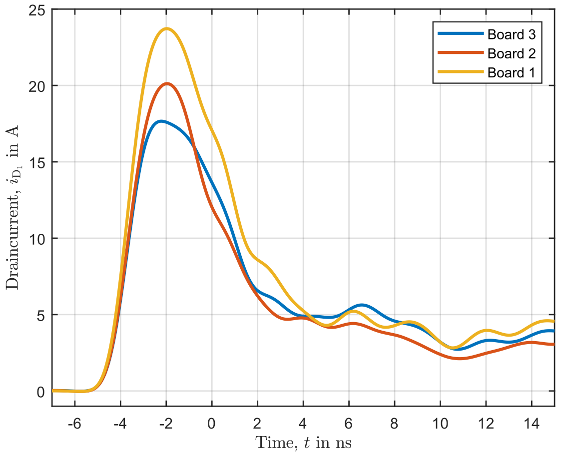

Fig. 17: Sequence of the drain current of all boards at a choke current of 7 A.

The influence if the induced voltage is higher because the relation from induced voltage and switched voltage is smaller. Also, the drain current increases are different. Fig. 19 shows the sequence of the drain current at an input voltage of 50 V. Compared to an input voltage of 200 V there are only fewer differences.

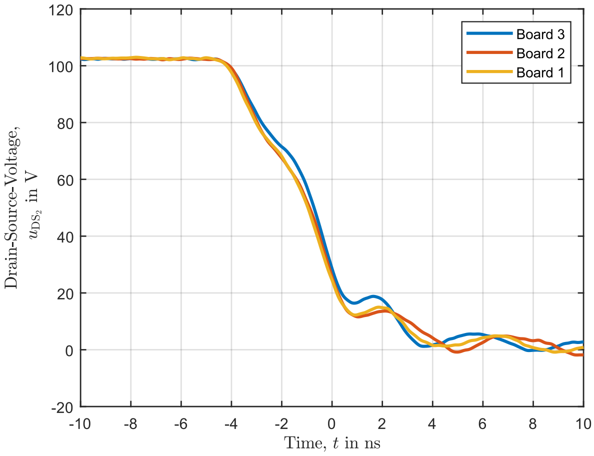

Fig. 18: Sequence of the drain-source voltage at a input voltage of 50 V.

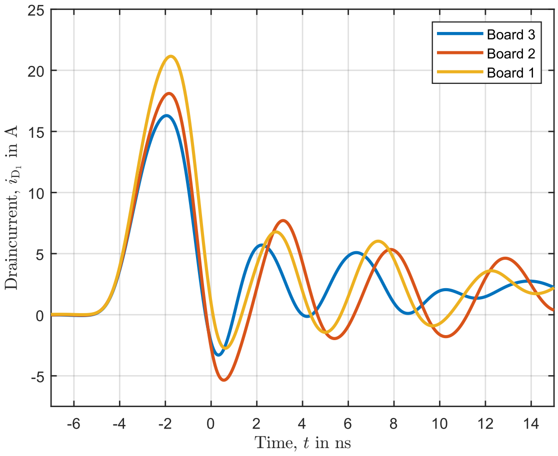

Fig. 19: Sequence of the drain current at a input voltage of 50 V.

V. CONCLUSION

In this paper it was determined, which parameter derivates by a GaN-HEMT. There are the threshold voltage, the on-resistance, and parasitic inductances, which vary. The circuit setup of a non-isolated DC/DC converter as a boost converter was explained. Special features like the infinity sensor and the active gate driver were elucidated. The experimental validation shows the influence of parameter deviation of power semiconductors on the turn-on behavior was investigated by different points of operation and input voltages. It was determined that the influence of measurement instruments is limited to the gate-source voltage. Also, different parasitic inductances were determined. But the differences were too large to be caused by the packages of the power semiconductor. Differences in the threshold voltage are determined, which have influences on the output characteristics. Different on-resistances could explain the derivation in the drain current. Primarily there were small differences in the current increases and larger differences in the current peak determined. At all operating points and all input voltages, these differences are equal. Summarizing, GaN-HEMTs have parameter derivations and these have an influence on the switching behavior, mainly to the drain current peak.

REFERENCES

[1] Millán, J. ; Godignon, P. ; Perpiñà, X. ; Pérez-Tomás, A. ; Rebollo, J.: A Survey of Wide Bandgap Power Semiconductor Devices. In: IEEE Transactions on Power Electronics 29 (2014) May

[2] Peftitsis, D. Baburske, R., Rabkowski, J. Lutz, J. Tolstoy, G. Nee,, H.: Challenges Regarding Parallel Connection of SiC JFETs. In IEEE Transactions on Power Electronics 28 (2013), March

[3] Reusch, D. Strydom, J.: Understandig the Effect of PCB Layout on Circuit Performance in a High-Frequency Gallium-Nitride-Based Point of Load Converter. In IEEE Transactions on Power Electronics 29 (2014), April

[4] Lim, J.; Peftitsis, D.; Rabkowski, J.; Bakowski, M.; Nee, H.: Anaylysis and Experimental Verification of the Influence of Fabrication Process Tolerances and Circuit Parasatics on Transient Current Sharing of Parallel-Connetet SiC JFETs. In IEEE Transactions on Power Electronics 29 (2014), May.

[5] Li, H.; Munk-Nielsen, S.; Pham, C. ; Beczkowski, S.;:Circuit mismatch influence on performance of paralleling silicon carbide MOSFETs. In 2014 16th European Conference on Power Electronics and Applications.

[6] Wang, J.; Hedayati, M. H.; Liu, D.; Adami, S.; Dymond, H. C. P.; Dalton, J. J. O.; Stark; B. H.: Infinity Sensor:Tempearature Sensing in GaN Power Devices using Peak di/dt. In 2018 IEEE Energy Conversion Congress and Expostion (ECCE).

[7] Dymond, H.C.P.; Wng, J.; Liu, D.; Dalton, J.J.O.; McNeill, N.; Pamunuwa, D.; Hollis, S. J.; Stark, B.H.: A 6,7-GHz Active Gate Driver for GaN FETs to Comabt Overshoot, Ringing, and EMI. In IEEE Transaction on Power Electronics 33 (2018), Jan

[8] Systems, GaN: GS66516 Top-side colled 650 V E-mode GaN transistor Prelimiary Datsheet, 2018

Coupling of energy storage devices with the automotive high voltage grid via power electronics

M.Sc. Anton Chupryn
Institute for Electric Power Systems
Otto-von-Guericke-University
Magdeburg, Germany
e-mail: anton.chupryn@ovgu.de

Prof. Dr.-Ing. Andreas Lindemann
Institute for Electric Power Systems
Otto-von-Guericke-University
Magdeburg, Germany
e-mail: andreas.lindemann@ovgu.de

***Abstract*—This paper addresses the design of a concept for the automotive high voltage grid using a power electronic DC/DC converter. A structure of the high voltage automotive system with a short time energy storage and the basic principles of its operation with the corresponding waveforms are described. Based on this an outlook on further development is given.**

I. INTRODUCTION

A fast growing e-mobility sector causes a high demand of novel power electronic solutions that follow financing of new e-drive developing projects in the world, as well as in Germany [1]. For the new powertrain a power range of more than 12 kW is not unusual [2], this fact forces the implementation of high voltage (HV) grid for automotive solution in terms of reducing the current and consequently the thermal load of the system. Along with this fact a part of market of wide bandgap semiconductors is growing quickly every year [3]. The use of gallium nitride (GaN) semiconductors, which represent a class of wide bandgap materials, could bring benefits of increased efficiency and reduced volume of the power electronics of the e-vehicle [4]. A performed investigation of the automotive high voltage grid with a short time energy storage in form of a double layer capacitor (DLC) [5] allows to implement both: a HV grid and the GaN technology in one modular DC/DC converter for electric cars, as well as to develop the basis for further e-mobility projects.

II. CONCEPT

An automotive high voltage grid with double layer capacitor for short time energy storage has been investigated. The concept foresees to use a DLC to provide power for acceleration or store energy generated during recuperative braking. Thereby the DLC is intended to cover the peak currents related to rapid changes of the speed. This will reduce cycling of the high voltage (HV) battery. The power flow between HV grid and DLC needs to be controlled by a power electronic DC/DC converter. The corresponding setpoints are provided by a master controller (μC). It will communicate through a CAN-interface. Figure 1 shows the concept.

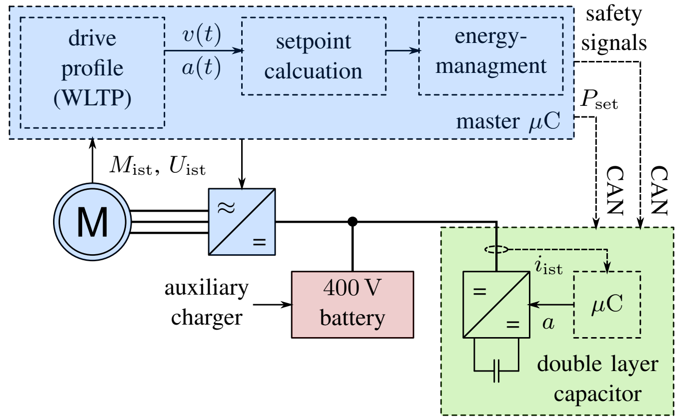

Fig. 1. Block diagram of the concept ”Genial” structure with energy storage [6]

III. PARTS OF THE SYSTEM

An automotive high voltage (HV) grid with double layer capacitor (DLC) for short time energy storage has been investigated.

A. Short term energy storage

The DLC serving for short term energy storage has been dimensioned with regard to the ”Worldwide Harmonized Light Vehicles Test Procedure” (WLTP) [7] : This standard defines a speed profile which depicts a city, overland and highway trip. Based on the given speed profile, acceleration, kinetic energy and maximum as well as average driving power have been calculated, using typical parameters such as the weight of the car. These relations are shown in Fig. 2.

To determine the size of the DLC, its nominal voltage needs to be defined. The voltage of the HV grid can be in the range between 200 V and 400 V depending on the state of charge of the HV battery. When using a phaseleg topology as DC/DC chopper - cf. section III-B - the voltage of the DLC always needs to be lower. Based on the aforementioned analysis and the availability of DLCs the ”Maxwell BMOD0165 P048 C01” [8] with a capacitance of 165 F and a maximum voltage of 48 V per module was chosen. A serial connection of five such modules results in an total capacitance of 33 F and a nominal

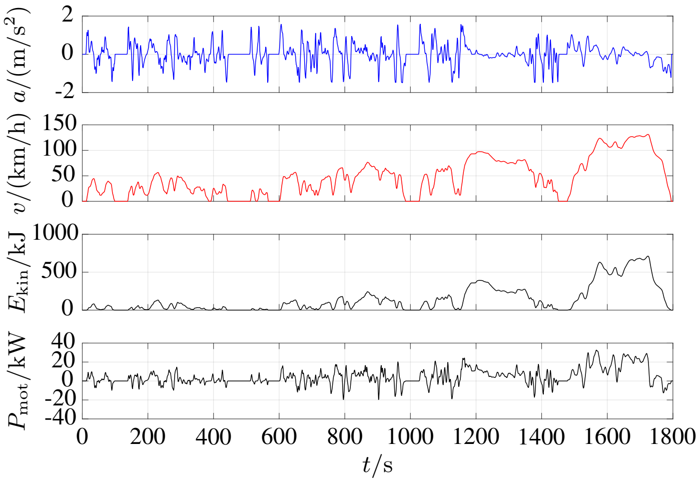

Fig. 2. Waveforms of acceleration and speed in the WLTP [6]

voltage of 240 V respectively which meets the requirements; in particular the DLC can deliver the energy required for most accelerations defined in WLTP.

B. DC chopper

Due to the aforementioned specifications of the DLC and the requirements derived from WLTP [7], the DC/DC converter was designed for a rated power of 10 kW. For the converter a modular interleaved structure [9][10], in which each module is a complete DC/DC converter, was chosen. Such a structure as depicted in Fig. 3 allows to increase the control dynamic, to decrease the voltage and current ripple and to increase efficiency under partial load conditions [10].

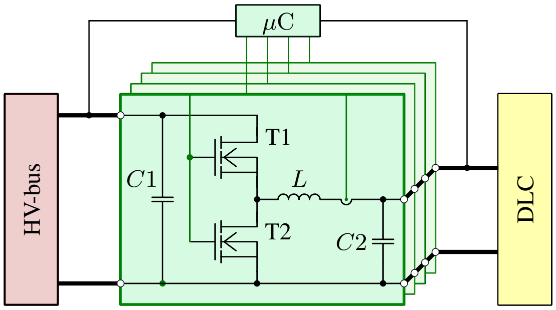

Fig. 3. Block diagram of the energy storage with modular DC/DC converter [6]

As already mentioned in section III-A the phaseleg topology has been chosen, constituting a non-isolated, bidirectional DC/DC converter. With a rated power of 10 kW, the current at 200 V DLC voltage yields 50 A in total or 12.5 A for each of the four DC/DC chopper modules.

Two versions of the DC/DC converter have been built: A circuit equipped with Si IGBTs and diodes, operated at a switching frequency of 20 kHz, serves as state of the art reference. This has been complemented by a version using GaN HEMTs operated at 100 kHz. Those have been normally-off devices; they have been driven by a gate driver ”Si8271AB” of ”SiliconLabs” [11], supplying 6 V for turn-on and -3 V for turn-off through separate gate resistors. Attention has been paid that parasitics of the drivers and the related circuitry - i. e., coupling capacity or wiring inductance respectively - remain small. Considering the tolerable ripple in the power circuit, the passive components according to Fig. 3 have been dimensioned as follows: $C1 = 7.1\,\mu\mathrm{F}, C2 = 7.1\,\mu\mathrm{F}, L = 160\,\mu\mathrm{H}$.

C. Control system

The control of the DC/DC converter is realized in digital form by using a μC. Since the switching frequency is high and a modular structure of converter is chosen, the μC should be able to perform all required calculations in a short time.The period for each module at 100 kHz is 10 µs; four modules in interleaved operation thus require a calculation within $10\,\mu\mathrm{s}/4 = 2.5\,\mu\mathrm{s}$. Because of this a digital signal processor (DSP) microcontroller TMS320F28379D of ”Texas Instruments” with a clocking frequency of 200 MHz, 16 high resolution PWM channels and 24 analogue to digital converter (ADC) inputs was chosen.

The control concept is based on the power regulation with a direct control of module currents. A power setpoint is sent from the master μC via CAN-bus to the converter’s μC, then according to the actual DLC-voltage level the setpoint of module current between maximum and minimum limits, as well as the number of active modules are set. Average current mode control (ACC) and peak current mode control (PCC) are two frequently used control strategies [12]. In contrast to ACC the PCC needs a slope compensation as is described in [13] and has a higher noise sensibility. According to this fact for the actual concept a ACC strategy was chosen. The control loop with a PI-controller for the corresponding control strategy is shown in Fig. 4.

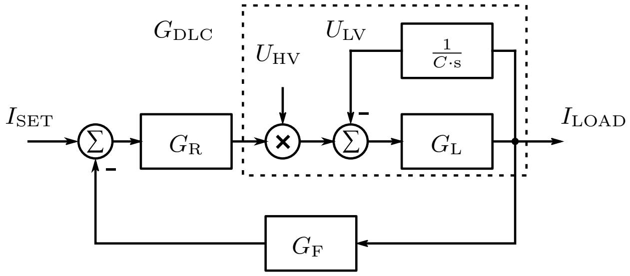

Fig. 4. Control loop of DC chopper [14]

A usual PI-controller was chosen because its characteristics fulfil the requirements regarding speed and stability of the system. The corresponding blocks of control loop are represented through the following functions, beginning from the transfer function of PI-controller:

$$G_{\mathrm{R}} = \frac{K \cdot s + 1}{T_{\mathrm{DLC}} \cdot s}, \tag{1}$$

T_{DLC} is the integral coefficient and K is the proportional coefficient. Because of the big value of DLC-capacitance the integral time constant can be sufficiently approximated [5] by

$$T_{\mathrm{DLC}} = \frac{L}{R_{\mathrm{EQ}}} \tag{2}$$

By the following steps the proportional coefficient K will be determined. Firstly, the transfer function of the filter G_{F} with a filter resistance R_{F} and capacitance C_{F} could be found as:

$$G_{\mathrm{F}} = \frac{1}{T_{\mathrm{F}} \cdot s + 1}, \text{ with } T_{\mathrm{F}} = R_{\mathrm{F}} \cdot C_{\mathrm{F}} \tag{3}$$

In the next step the transfer function G_{DLC} for the DC chopper can be calculated through

$$G_{\mathrm{DLC}} = \frac{U_{\mathrm{HV}} \cdot C \cdot s}{L \cdot C \cdot s^2 + C \cdot R_{\mathrm{EQ}} \cdot s + 1} \tag{4}$$

Finally, the transfer functions for open (5) and closed (6) control loops can be determined:

$$G_{\mathrm{O}} = G_{\mathrm{R}} \cdot G_{\mathrm{DLC}} \cdot G_{\mathrm{F}} \tag{5}$$

$$G_{\mathrm{C}} = \frac{G_{\mathrm{R}} \cdot G_{\mathrm{DLC}} \cdot G_{\mathrm{F}}}{(1 + G_{\mathrm{R}} \cdot G_{\mathrm{DLC}} \cdot G_{\mathrm{F}})} \tag{6}$$

Based on the transfer function of the closed control loop a step response of the system with various proportional coefficients was simulated, after that the open control loop was simulated and the stability of the whole system was approved regarding the stability margins on bode-diagrams. A more detailed description of the control system can be found in [5], [15].

IV. RESULTS

DC choke currents for three parallel connected power modules with a high side voltage of 365 V, low side voltage of 183 V and a current setpoint of 4 A can be seen in Fig. 5. This figure represents a controlled operation of the DC/DC converter with the DLC connected to the LV-side and a Li-ion battery on the HV-side. Deviations of the actual current from the set current could be explained through the imperfect configuration of ADC channel gain values.

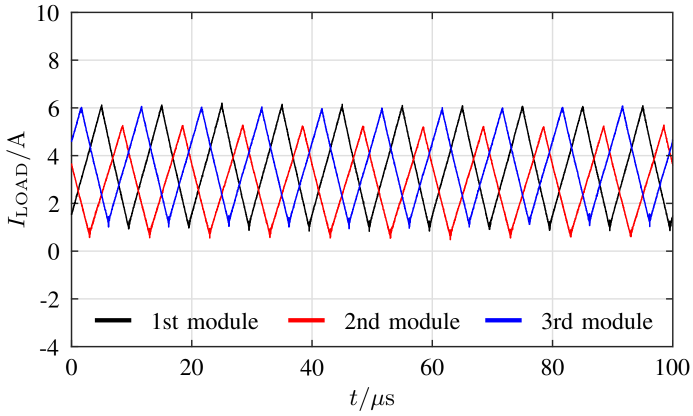

Fig. 5. Choke currents of GaN-based power modules [15]

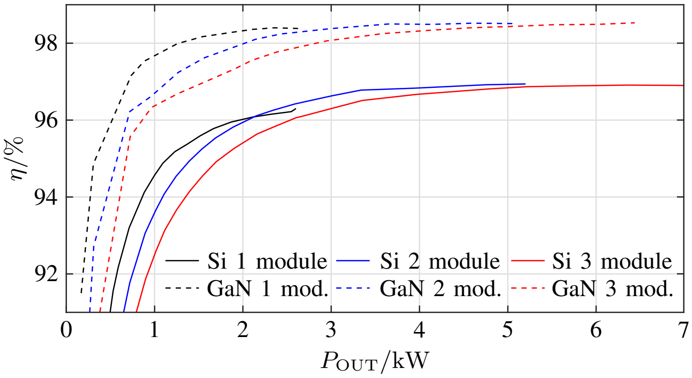

Fig. 6. Efficiency comparison of Si- and GaN-based modular DC/DC converters [15]

Fig. 6 shows the efficiency curves of the Si- and GaN-based converters with the number of parallel modules as parameter. Conditions for the efficiency measurement were same for both versions and they match with conditions for the previously described current measurement: $U_{\mathrm{HV}} = 365\,\mathrm{V}, U_{\mathrm{LV}} \approx 183\mathrm{V}$, $a \approx 50\%$. The efficiency was calculated as follows:

$$\eta = \frac{P_{\mathrm{OUT}}}{P_{\mathrm{IN}} + P_{\mathrm{AUX}}}. \tag{7}$$

P_{IN} and P_{OUT} were measured at the battery and DLC terminals of the converter and the power consumption of the external auxiliary power supply was considered by P_{AUX}. The curves show that conversion efficiency can generally be increased at partial load when the controller only activates a number of converter modules which is suitable for the required current or power respectively - i. e., less modules for low current. It is further visible that the GaN converter has a higher overall efficiency in spite of its higher switching frequency. The significantly lower switching losses of the unipolar GaN HEMTs are a prerequisite for this; further contributions may result from the circuit layout with reduced parasitic elements and the different inductor.

V. OUTLOOK

In a system architecture as outlined in Fig. 1, the battery determines the voltage of the HV grid. It however depends amongst others on battery's state of charge and temperature. The drive system in contrast would profit from a constant input voltage. It is thus promising to also connect the battery through a DC/DC converter to the HV grid as depicted in Fig. 7. This way the HV grid can be stabilised, potentially at a higher voltage level, by decoupling it from the battery, and it even seems possible to modularise the battery. Such a system shall be investigated in the future based on the aforementioned findings related to the DLC connected through a DC/DC converter.

VI. CONCLUSION

This paper deals with the design of a high voltage grid in a vehicle, where a double layer capacitor is used for intermediate energy storage, being controlled by a power electronic DC/DC converter. The system has been dimensioned and realised in a laboratory setup, including a version with a converter using

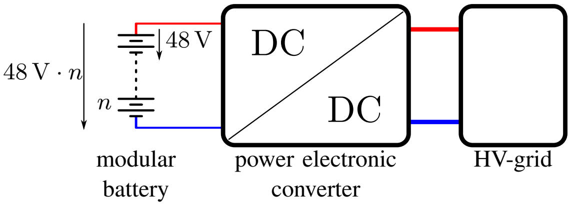

Fig. 7. Schematic representation of the HV-grid

wide bandgap GaN devices. With respect to this converter, the results do not only demonstrate its functionality but also show the advantageous properties of such a solution.

ACKNOWLEDGMENT

This research has been funded by the Federal Ministry of Education and Research of Germany in the framework of GENIAL (project number 16EMO0120K)

REFERENCES

[1] N. Medimorec, *E-Mobility Trends and Targets*.

[2] German Electrical and Electronic Manufacturers‘ Association, *Voltage Classes for Electric Mobility*, ZVEI - German Electrical and Electronic Manufacturers’ Association Centre of Excellence Electric Mobility, Lyoner Straße 9 60528 Frankfurt am Main, Germany, Dec. 2013.

[3] G. V. Research, “Gallium Nitride Semiconductor Devices Market Report, 2018-2025,” Grand View Research, Inc., research rep., 2016.

[4] A. Lidow, *GaN Transistors for Efficient Power Conversion: The EGaN FET Journey Continues*. Power Conversion Publications, 2012.

[5] B. Strauss and A. Lindemann, “A Modular DC/DC Converter to Couple a Double Layer Capacitor to the Automotive High Voltage Grid for Short Time Energy Storage,” in *PCIM Europe 2018; International Exhibition and Conference for Power Electronics, Intelligent Motion, Renewable Energy and Energy Management*, 2018, pp. 1–8.

[6] L. Middelstädt, B. Strauss, and A. Lindemann, “Project GENIAL Final Report. Project Part 1,” Institute for Electric Power Systems, Tech. Rep., May 2019.

[7] U. Nations, *Worldwide harmonized Light vehicles Test Procedure*. Global Registry, 2014.

[8] *48 Volt Module With DuraBlue — Datasheet*, Maxwell Technologies, 2015.

[9] L. Wang, D. Zhang, J. Duan, and J. Li, “Sequence coupling of inductors in multiphase interleaved bidirectional buck/boost converters,” in *2018 13th IEEE Conference on Industrial Electronics and Applications (ICIEA)*, 2018, pp. 24–29.

[10] S. Roberts, *DC/DC BOOK OF KNOWLEDGE*, Third Edition. RECOM Engineering GmbH & Co KG, Austria, 2016.

[11] *Si827x Data Sheet*, SILICON LABS, Apr. 2019.

[12] R. Sheehan, “Understanding and applying current-mode control theory,” *National Semiconductor Corporation*, Jan. 2007.

[13] M. Hallworth and S. Ali Shirsavar, “Microcontroller-Based Peak Current Mode Control Using Digital Slope Compensation,” *Power Electronics, IEEE Transactions on*, vol. 27, pp. 3340–3351, Jul. 2012.

[14] A. Chupryn, “Etwickeln und Vermessen der Regelung eines modularen Gleichspannungswandlers mit GaN-Transistoren,” Master’s thesis, Otto-von-Guericke-Universität Magdeburg, Oct. 2018.

[15] A. Chupryn, L. Middelstaedt, and A. Lindemann, “An Interleaved DC/DC Converter for Automotive Applications with GaN Power Semiconductors,” in *PCIM Europe 2019; International Exhibition and Conference for Power Electronics, Intelligent Motion, Renewable Energy and Energy Management*, 2019.

Analysis of potentials for battery electric vehicles for the implementation of V2G-technologies

Jonathan Ulbrich
Otto-von-Guericke-University
Magdeburg, Germany
jonathan.ulbrich@ovgu.de

Sebastian Helm
Otto-von-Guericke-University
Magdeburg, Germany
Chair of Electric Power Networks and
Renewable Energy Sources Magdeburg
Sebastian.helm@ovgu.de

***Abstract*— This paper shows the results of an analysis of potentials for V2G-technologies.**

In the first chapter the motivation for V2G-technologies is explained.

In the next chapter the calculation of the mechanical power of a car is shown, as well as the electrical power of the auxiliary users.

The model of the BEV is implemented into MATLAB, based on an equivalent circuit of a battery which becomes discharged by the BEV. The electrical power of the driving system is calculated with a driving cycle. The auxiliary users are simulated by the results of measurements. To determine the total capacity and electrical power for a scenario of all BEV nowadays and for a future scenario, both scenarios are simulated, using statistics of the driving behavior of car owners in Germany. The MATLAB model allows a simulation of the course of capacity, power and required charging energy of an arbitrary BEV pool.

The simulation shows the huge potential of V2G-technologies in Germany. Already nowadays but especially in the near future, there is a great amount of energy available, due to the BEVs.

***Keywords*— battery electric vehicle, lithium-ion battery, system services, vehicle to grid**

I. INTRODUCTION

The energy policies of Germany aim to ensure the availability of energy for all citizens, while increasing energy efficiency, the amount of renewable energy and reducing greenhouse gas emissions [1]. The transport sector, especially the passenger car sector, is causing a large proportion of the greenhouse emissions in Germany [2, 3]. Battery electric vehicles (BEV) can reduce this problem due to the fact that they don't emit greenhouse gases whilst on road transport. The charging of a huge number of BEVs causes a severe grid load. Potentially BEVs can divert this problem themselves because their batteries can be used for Vehicle-to-Grid-technologies (V2G) to ensure electric grid stability [4]. The V2G-technology enables the BEV to feed electrical energy from the battery back into the electric grid. In this paper the use of BEVs by car users in different driving scenarios is considered and the potential V2G-energy in Germany today and for a future scenario is determined with a MATLAB simulation.

II. SETUP BEV MODEL

The BEV model consists of two component models shown in Figure 1. The first one calculates the required or generated power of the drive system, depending on the distance of the ride and the type of roads such as city streets or motorway.

The second component model is the battery model. It becomes discharged by the first model as well as by the auxiliaries. In the outcome, the battery model shows the state of charge and the remaining capacity at the end of the ride.

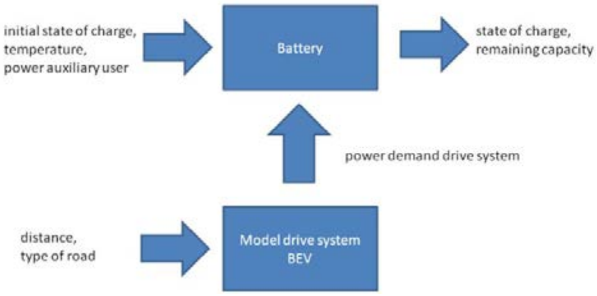

Figure 1 Overview BEV Model.

A. *Model drive system BEV*

The BEV's required power consists of the power of the drive system and the auxiliary users.

The mechanical power of the power system is calculated by the product of the forces on the BEV and the speed of the BEV [5].

$$P(t) = F(t)\cdot v(t) \tag{1}$$

The force to be overcome is made up of air-, roll- and acceleration resistance as well as the inclination of the street [5]. The inclination of the line is not further considered in this paper since a flat road for the BEV is assumed. The force of the BEV can become negative, which causes a negative power. BEV's are able to recover this energy because the machine of the BEV is able to generate power.

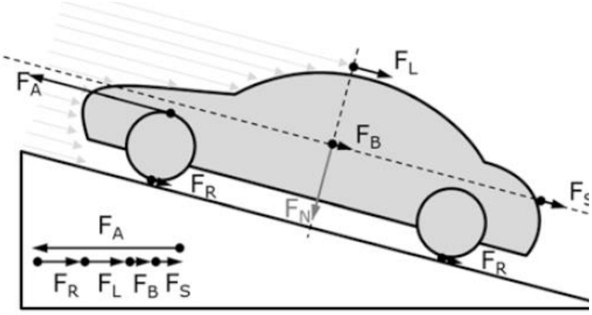

Figure 2 Forces on a car [5].

Figure 3 (blue curve) shows the worldwide harmonized light vehicle test cycle (WLTC), which is used to simulate the course of the speed of the BEV [6]. It simulates the speed of a car for various speed levels, up to 131.3 km/h, which are shown in Table 1. To simulate three different types of roads the WLTC is split into three parts in this BEV model. The first scenario is a ride through the city for which the modeled BEV is simulated with the low and medium level of the WLTC. If the BEV additionally is used for overland-roads allowing up to 100 km/h, the high level is included in the simulation. For scenarios where the BEV also is used on the motorway, the whole WLTC is used for the simulation.

Table 1 Speed Levels WLTC

Value	**Unit**	**Low (I)**	**Medium (II)**	**High (III)**	**Extra High (IV)**
Time	s	0-589	589-1012	1012-1467	1467-1800
Distance	m	3095	4759	7158	8253
Average speed	km/h	18.9	44.5	60.8	94
Maximum speed	km/h	56.5	76.6	97.4	131.3

The WLTC is a test cycle used to measure the fuel consumption of conventional cars powered by a combustion engine as well as for EV's [6].

B. *Auxiliary Users*

The electrical power of the auxiliary users is considered by measurements for various temperature scenarios shown in Figure 4 [7]. The heating and climate system require the highest electrical power of the auxiliaries. In order to reach the operating temperature of the heating or climate system, high initial power is required.

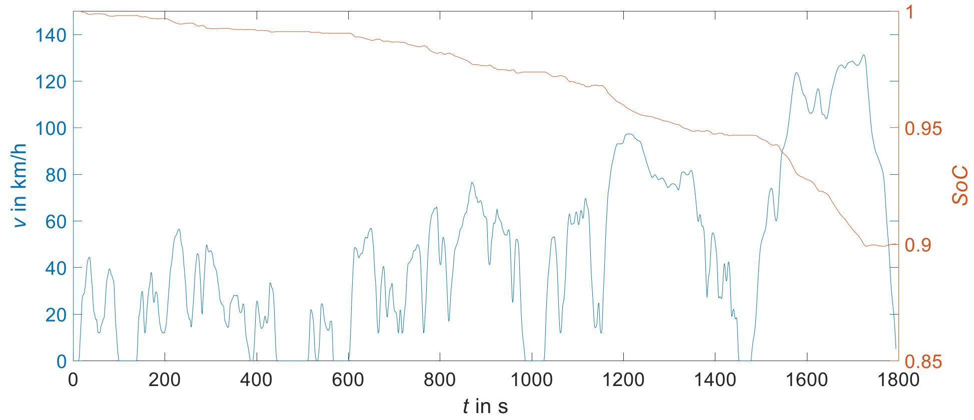

Figure 3 Course of speed WLTC and its *SoC*.

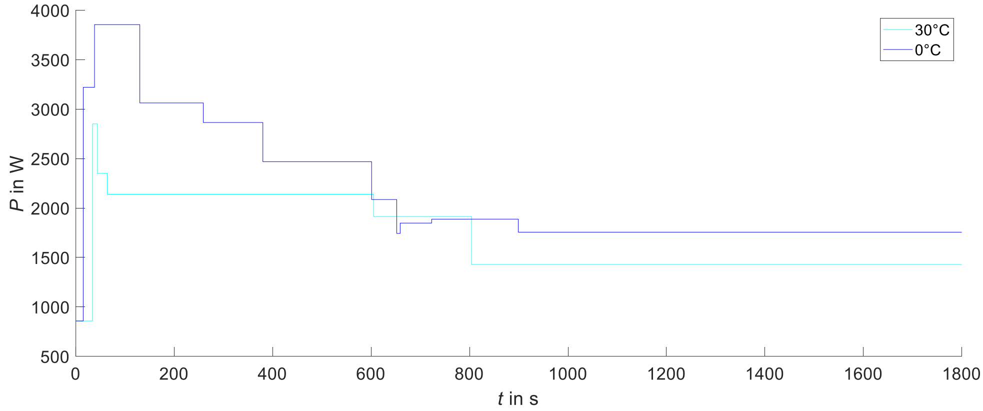

Figure 4 Electrical power auxiliaries.

C. *Equivalent circuit lithium-ion battery*

For the simulation of the electrical behavior of the BEV, an equivalent circuit is used to implement a model of the traction battery.

The dynamic behavior of a battery can be determined by the electrochemical impedance spectroscopy (EIS) [8]. To determine the impedance of the battery, an alternating voltage gets applied to the battery poles, whilst measuring the current. With voltage and current, the impedance can be calculated. With variegating the frequency of the voltage, a spectrum is built, as shown in Figure 5. The course of the spectrum depends on the temperature and the State of Charge. The impedance spectrum is showing an inductive behavior for the highest frequencies. At a point with a lower frequency, the resistance becomes ohmic. With a decreasing frequency, the spectrum shows a semicircular course. The first semicircle primarily is caused by the charge transfer resistance and the double layer capacity of the lithium-ion battery. The diffusion resistance is responsible for the second semicircular course.

The following equivalent circuit simulates the impedance spectrum of the EIS (Figure 5). For each State of Charge and temperature, there is a different spectrum, which causes varying circuit parameters.

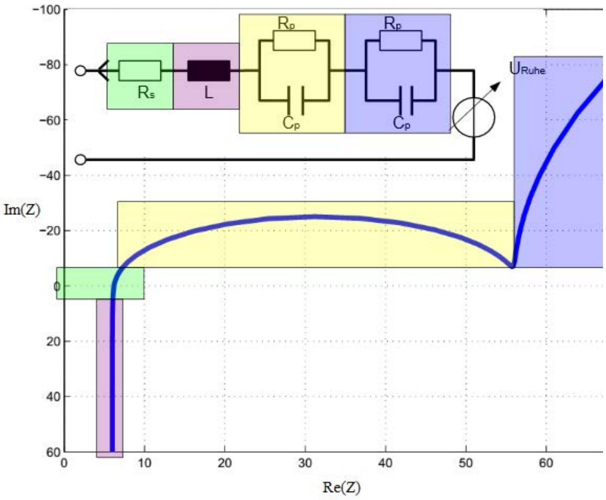

Figure 5 Impedance spectrum equivalent circuit of a battery cell [8].

The inductive behavior must not be considered in the battery model, because it's smaller than 1 µH and affects the battery only for high frequencies [9].

D. *Voltage battery*

At the beginning of the simulation, the terminal-voltage (u_{te}) is equal to the open-circuit voltage (u_{ocv}), which is a function of the batteries *SoC*.

$$u_{\text{OCV}} = f\left(SoC\right) \tag{2}$$

For operation under electrical load, the terminal voltage differs from the open-circuit voltage and can be calculated by (3). The last addend is actually split in two addends, one for each *RC* element, in the model but in this paper, they are summed up in one addend for better clarity. $U_{\text{RC}}(t_{-1})$ is the prior voltage of the *RC* element.

$$u_{\text{te}} = u_{\text{OCV}} + R_{\text{S}} \cdot i\left(t\right) + R_{\text{P}} \cdot i\left(t\right) + u_{\text{RC}}\left(t-1\right) e^{-\frac{t}{RC}} \tag{3}$$

E. *SoC battery*

For the determination of the State of Charge, an initial State of Charge (SoC_0) is required. Furthermore, the *SoC* is affected by the current, the integrated current and the capacity of the battery (4).

$$SoC = SoC_0 - \int \frac{i\left(t\right)}{Q\left(I,T\right)} \mathrm{d}t \tag{4}$$

F. *Driving behavior*

The statistic in Table 2 shows the starting time of the drives in Germany starting from the home of the car owners. The most drives start between 6-9 am.

Table 2 Starting time for drives [10]

Starting time	Share in %
0-6 am	11
6-9 am	77
9-12 am	7
12 am - 4 pm	3
4-8 pm	1
8-12 pm	1

Table 3 shows the distribution of the distance of ways to work in Germany and the WLTC level used in the MATLAB model.

Table 3 Distance way to work in Germany [11]

Distance	Share in %	WLTC level
<5 km	28	I,II
5-10 km	20	I,II
10-25 km	28	I,II,III
25-50 km	13	I, II, III, IV
>50 km	11	changing

The distances in Table 3 are one-way drives. To realize a working day, various pauses are included between the two drives. For the 11% with a distance higher than 50 km a random distance of the other four categories is chosen in the model because BEVs particularly are useful for car owners with a short drive distance.

Because 30 % of all cars aren't used every day, this 30 % are considered in the simulation as well.

G. *Types of BEV*

BEVs are categorized by the capacity of their battery. Most of the BEVs are assigned to the compact car or mid-range car segment. A few BEVs can also be assigned to top class category, which have a high range due to a high capacity battery.

Table 4 Car segments for model

Category	Capacity in kWh	Share in %
Compact car	24	50
Mid-range segment	37.5	40
Top class segment	75	10

III. RESULTS

A. *SoC for the WLTC*

In addition to the WLTC, Figure 3 shows the associated course of the *SoC* (orange curve). At the beginning of the 23.3 km WLTC, the battery is fully charged. With increasing speed and high acceleration, the *SoC* is decreasing quickly. In the first 1,470 seconds, in which the car drives 15 km with a speed lower than 100 km/h, the battery becomes discharged with 1.77 kWh. In the following 320 seconds, the battery once again is discharged with 1.77 kWh, but the BEV just drives 8.3 km with a speed up to 131 km/h. This means that for this second section the discharge is twice as high as for the first one, with regard to the covered distance. Some sectors of the curve, like the last 50 seconds, show a growth of the *SoC*, caused by energy recuperation of the BEV.

B. *SoC of a car within a day*

Figure 6 shows the *SoC* of a BEV with a capacity of almost 24 kWh within a day. In the very beginning of the day, the BEV is parked and connected to the charging station (interval I). The BEV starts a 25 km drive at 07:06 am (interval II). Afterwards, it is parking without charging (interval III) until the way back starts at 3:20 pm (interval IV). Being back home the BEV can be charged again (interval IV).

For the BEVs that aren't used during the simulated day, their entire capacity is available the whole day.

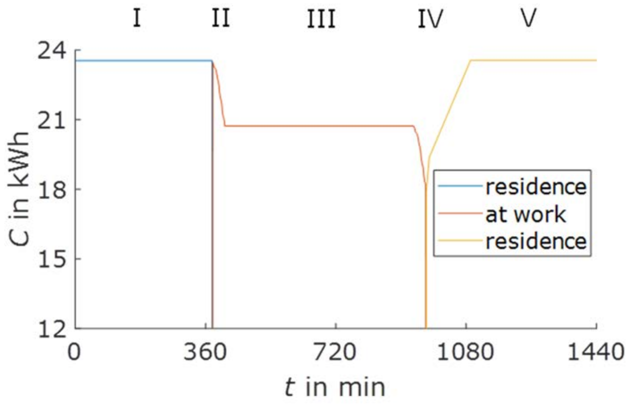

Figure 6 *SoC* of one BEV during a day.

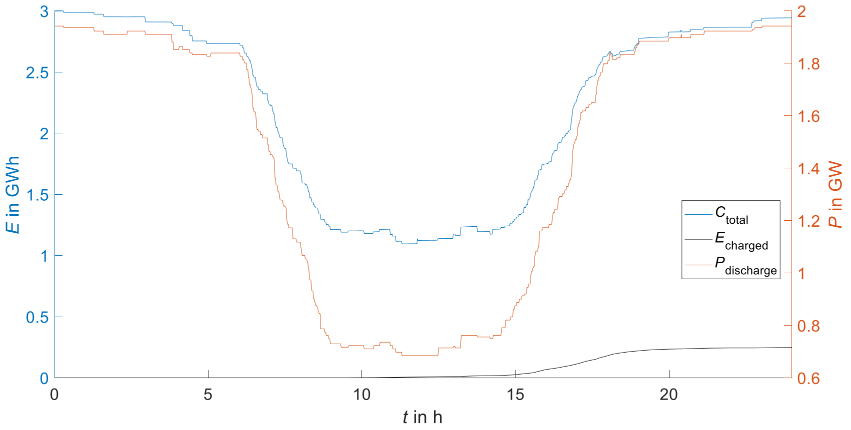

Figure 7 Simulation results for 83000 BEVs.

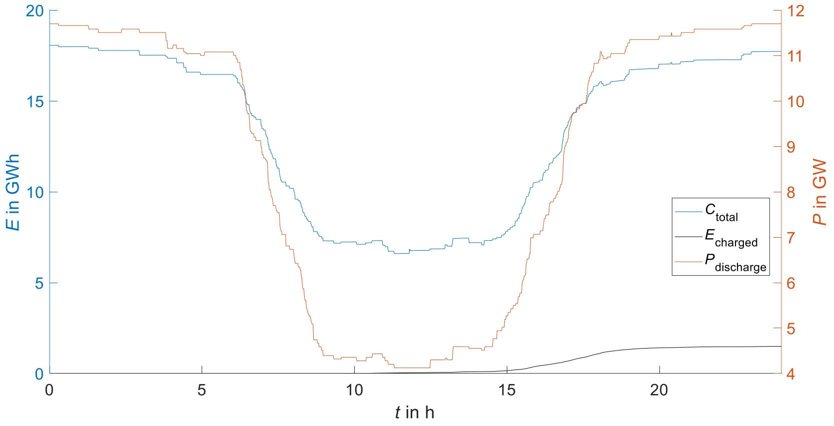

Figure 8 Simulation results for 500000 BEVs.

C. Simulation results of a current scenario

To measure the course of the potential capacity in Germany during a day the driving scenario for the currently 83,000 existing BEVs is created. The course of the *SoC* of Figure 6 is overlapped with all the BEV with the help of the statistics of Chapter II.F.

Figure 7 shows the course of the total capacity, the charged energy, and the available electrical power during a day. In the very beginning of the day, where all of the BEV are at the domestic charging point, the highest amount of energy and power is available. The total energy of 3 GWh is available for V2G technologies with a power of almost 2 GW. Until 6 am just a few people are starting their way to work, so both the energy as well as the power is decreasing slowly to 2.7 GWh respectively 1.8 GW. From 6 am to 9 am the energy is reduced to 1.2 GWh, because of the way to work of most of the people. From 9 am to 3 pm the energy is roughly on a constant level with a minimum of 1.1 GWh and a power of 0.68 MW. Starting from 3 pm the energy and power are increasing back to the approximate value from the morning 6 am, due to the way back home of the most working people. After the rest of the working people returned their BEVs and charged them, almost the starting value is achieved again. The line of E_{Charged} shows the cumulated power to charge the batteries of all of the BEVs back to the *SoC* from the beginning. In this model, the batteries become charged, right after the BEVs are plugged to the charging station. The course shows, that for the 83,000 BEV total energy of less than 250 MWh is required, to achieve, the simulated tours.

D. Simulation results of a future scenario

To give a forecast, for the time when 500,000 BEVs are available in Germany the same simulation is executed with 500,000 BEVs imaged in Figure 8. The qualitative course is similar to the course in Figure 7. In total there is a maximal value of more than 18 GWh and a minimal value of 6.6 GWh. The related power of the maximum and minimum is 11.7 GW and 4 GW. To charge all of the BEV to their starting value, charging energy of 1.5 GWh is required.

E. Conclusion of simulation results

The simulation shows the huge potential of V2G-technologies in Germany. Already nowadays in the time from 6 pm to 6 am is a lot of energy available that could be used for system services.

For the future scenario of 500,000 BEV, which will be realized within the next four years according to the German government, V2G-technologies will offer a minimal capacity of more than 6 GWh and an electrical power of 4 GW all the time. In comparison, the biggest pumped-storage plant in Germany has a capacity of 8.5 GWh with an electrical power of 1 GW [12]. Due to the distributed locations of the BEVs, the grid feed would be decentralized. Furthermore, the batteries of the BEVs can switch between charging and discharging within shortest time, whereby the feed of energy can be adjusted quickly.

IV. REFERENCES

[1] Bundesministerium für Wirtschaft und Energie , „Bundesministerium für Wirtschaft und Energie,“ [Online]. Available: https://www.bmwi.de/Redaktion/DE/Dossier/energiewende.html. [Zugriff am 16 07 2018].

[2] Das Umweltbundesamt, „Umweltbundesamt,“ 10 01 2016. [Online]. Available: https://www.umweltbundesamt.de/themen/klima-energie/klimaschutz-energiepolitik-in-deutschland/treibhausgas-emissionen/emissionsquellen#textpart-1. [Zugriff am 16 07 2018].

[3] C. Salb, S. Gül, C. Cuntz, Y. Monschauer und J. Weishäupl, „Klimaschutz in Zahlen: Fakten, Trends und Impulse deutscher Klimapolitik,“ Bundesministerium für Umwelt, Naturschutz, Bau und Reaktorsicherheit, Berlin, 2018.

[4] Bundesministerium für Wirtschaft und Energie, „Bundesministerium für Wirtschaft und Energie,“ [Online]. Available: https://www.bmwi.de/Redaktion/DE/Dossier/elektromobilitaet.html. [Zugriff am 16 07 2018].

[5] P. Komarnicki, J. Haubrock und Z. A. Styczynski, Elektromobilität und Sektorenkopplung, Berlin, Heidelberg: Springer Vieweg, 2018.

[6] „VDA.de,“ 01 09 2017. [Online]. Available: https://www.vda.de/dam/vda/publications/2017/WLTP_QundA_DE/WLTP_QA_DE.pdf. [Zugriff am 14 09 2018].

[7] H. Proff, J. Schönharting, D. Schramm und J. Ziegler, Zukünftige Entwicklungen in der Mobilität, Duisburg-Essen: Gabler Verlag Springer Fachmedien Wiesbaden GmbH, 2012.

[8] E. Mense, *Hard- und Softwareentwicklung für einen drahtlosen Batterie-Zellen-Sensor zur elektrochemischen Impedanzspektroskopie,* Hamburg, 2014.

[9] TU Clausthal, *Versuch 2: Elektrochemische Impedanzspektroskopie zur Ermittlung der Parameterfür ein Ersatzschaltbild elektrochemischer Speicher,* Clausthal, 2007.

[10] Statista, „Statista,“ [Online]. Available: https://de.statista.com/statistik/daten/studie/36312/umfrage/uhrzeit-des-aufbruchs-zur-arbeit/. [Zugriff am 10 04 2019].

[11] Statistisches Bundesamt, „destatis.de,“ 2016. [Online]. Available: https://www.destatis.de/DE/ZahlenFakten/GesamtwirtschaftUmwelt/Arbeitsmarkt/Erwerbstaetigkeit/TabellenPendler/Pendler1.html. [Zugriff am 21 09 2018].

[12] W. Mauch, „Nachhaltige Energieversorgung und Speichertechnik,“ Forschungsstelle für Energiewirtschaft e.V., München.

[13] Statista, 2018. [Online]. Available: https://de.statista.com/statistik/daten/studie/534429/umfrage/weltweite-preise-fuer-lithium-ionen-akkus/. [Zugriff am 17 07 2018].

LC Filter Design for a Voltage Controlled Grid in Uninterruptible Power Supplies

Anatolii Grydin
Institute of Electric Power Systems
Otto von Guericke University
Magdeburg, Germany
anatolii.grydin@gmail.com

Andreas Gerlach
Institute of Electric Power Systems
Otto von Guericke University
Magdeburg, Germany
andreas.gerlach@ovgu.de

***Abstract*—Three-phase inverters with LC filter are necessary in uninterruptible power supplies (UPS). The LC filter design influences the signal quality, power losses and component price. Another fact is that the control parameters depend on the LC filter design. Therefore, this paper concentrates on the procedure of LC filter components selection in such a way that the optimal design could be chosen according to the developer's requirements. Programming environment MATLAB/Simulink is applied for the analysis and the designed filter was tested on an experimental prototype.**

Keywords—three-phase inverter, LC filter, uninterruptible power supply (UPS).

I. INTRODUCTION

Renewable energy technology is developing rapidly and its market share is growing as well [1], but the energy output is not constant. The energy output depends on the environmental conditions (e.g. wind speed, sunshine duration). Another aspect is that renewable energy produces no additional emissions or requires fossil resources, which protects our environment [2]. It is necessary to accumulate energy in case of excessive energy production and to deliver it in case of reduced energy production or emergency for providing the consumer with constant electricity. The produced energy can be stored in a battery bank [3] with the conversion of the alternating current (AC) to the direct current (DC). Vice versa it is possible to convert the DC-voltage into an AC-voltage with a three phase inverter.

The output signal quality depends on the control topology for the three-phase inverter. To analyze the signal quality fast Fourier transform (FFT) analysis is used [5]. The FFT calculates the harmonic components and this enable to verify the total harmonic distortion. The analysis was performed with the programming environment MATLAB/Simulink. A simulation model was designed which contains the LC filter, inverter, resistive load and the control environment. The inverter was controlled with the space vector modulation [4].

Moreover, even when using vector control for three-phase inverter, the output signal is still of poor quality that is unacceptable for certain kinds of load. For this reason, LC filters are used in such systems. This filter effectively passes a signal frequency band that is lower than a certain frequency (cut-off frequency) and rejects the frequencies that are higher than cut-off frequency [6]. The degree of frequency rejection depends on the filter components. Therefore, the choice of filter components has an effect on the quality of the output signal. An applied load also has an influence on the output voltage. Therefore, the output voltage has to be measured and controlled. In section II the dynamic model of a LC filter is shown. It follows in section III the filter and controller design. The filter was tested in a simulation environment and with an experimental prototype in section IV. The results are shown in section V. At the end is a small conclusion in section VI.

II. DYNAMIC MODEL OF AN LC FILTER

A dynamic model of the LC filter is required to choose the optimal components. The dynamic model can be used in a simulation environment e.g. MATLAB/Simulink to test the selected elements before the components are tested in the prototype in section IV. The LC filter is shown in Fig. 1.

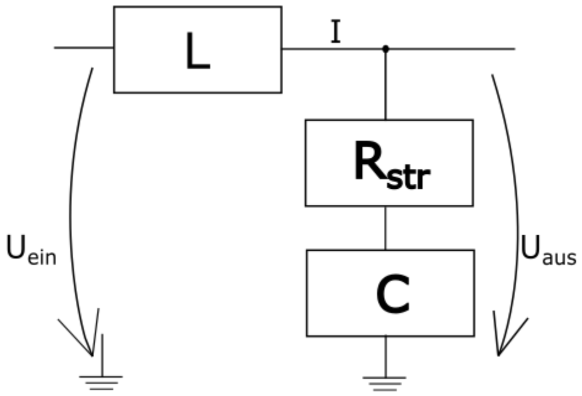

Fig. 1. Schematic of a LC Filter

The system consists of an inductance L, resistor R_{str}, and a capacitor C. The input voltage is U_{in} and the output voltage U_{out}.

$$I = \frac{U_{in}}{L\cdot s + R_{str} + \frac{1}{C\cdot s}} = \frac{U_{in}\cdot C\cdot s}{s^2\cdot L\cdot C + s\cdot R_{str}\cdot C + 1} \tag{1}$$

$$U_{out} = I\cdot\left(R_{str} + \frac{1}{C\cdot s}\right) = \frac{U_{in}\cdot(s\cdot R_{str}\cdot C + 1)}{s^2\cdot L\cdot C + s\cdot R_{str}\cdot C + 1} \tag{2}$$

$$\frac{U_{out}}{U_{in}} = \frac{s\cdot R_{str}\cdot C + 1}{s^2\cdot L\cdot C + s\cdot R_{str}\cdot C + 1} \tag{3}$$

A simplified model of a three-phase inverter is also required. To manage a three-phase inverter a vector control model with the commutation frequency of 10 kHz is used. In this paper we do not diversify modulation frequency, as when it changes, the characteristics remain similar.

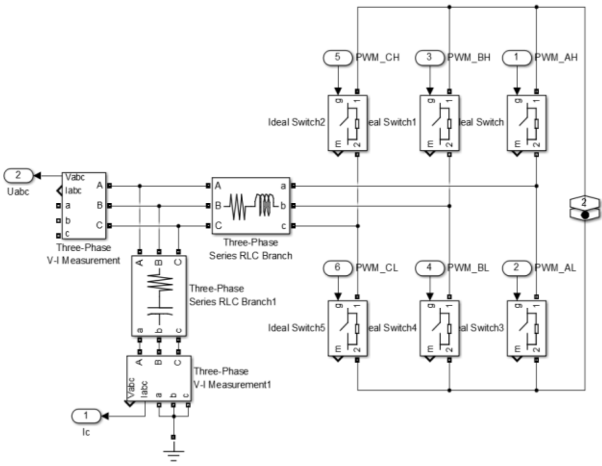

Fig. 2. Three-phase inverter model

Ideal switches are used for the simplified three-phase inverter model. The simulation model of the inverter and the LC-filter is shown in Fig. (2). The switching time is generated with the space vector modulation.

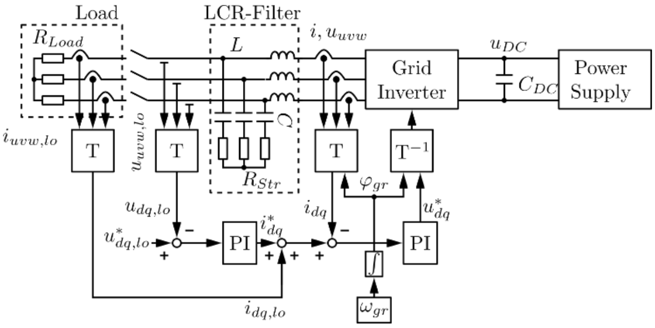

Fig. 3. Proposed control structure

The proposed control structure is shown in Fig. (3). The angle φ for vector control and the reference signal are generated so that the output signal had the frequency of 50 Hz and the input voltage of the inverter U_{dc} was 600 V. The transformation T consists of the park and clark transformation which transforms the measured currents i_{uvw} and voltages u_{uvw} in a grid oriented coordinate system (u_{dq} and i_{dq}) and the transformation T^{-1} consists of an inverse park and a space vector modulation. Two controller are used to control the current i_{dq} and the output voltage $u_{dq,lo}$. The resistive load is turned on with an additional switch.

III. DESIGN OF AN LC FILTER

With the designed dynamical model of the LC-filter (2) it is possible to optimal design the LC-filter.

First of all, we have to define the frequency band of the LC filter. E.g., given the modulation frequency of 10 kHz, the resonance frequency of the filter cannot be higher than 1 kHz (an order of magnitude smaller). Otherwise, the filter is ineffective. The resonance frequency can neither be lower than 500 Hz, as it can threaten some types of load. Then the chosen cutoff frequency band is between 750 and 1500 Hz.

Another objective of the LC filter optimization is to choose components which are accessible to the developer. Relying on the above-mentioned resonance frequency band got from Thomson formula and on the market supply, we can select respective inductors and capacitors.

$$f = \frac{1}{2 \cdot \pi \cdot \sqrt{L \cdot C}} \tag{4}$$

When selecting them, it is necessary to take into consideration the power that a consumer needs. Let us assume that the consumer needs a three-phase uninterruptible power supply with the power of 1.5 kW, and the grid line to line voltage U_{gr}=400 V the peak current is 3 A. Hence, considering 30% margin that increases the reliability of the system, it is required to select an inductance for a current bigger than 3.9 A.

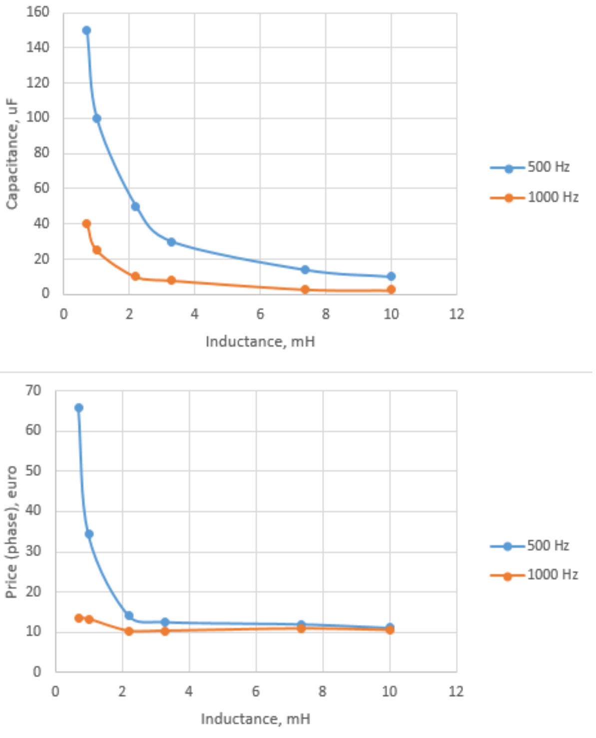

Fig. 4. The capacitance and price (phase) depending on the inductance

Therefore, inductances with 2-10 mH and capacitors with 2-55 μF capacitance are cost-effective (Fig. 4). Also, with a rising resonance frequency of the filter the range of possible values of inductance is extending.

The next problem is, that we have to increase the damping to reduce the resonance amplitude and we have to consider the efficiency of the LC-filter. If we choose 0.3% power losses of the nominal power, then the filter has to consume less than 4.5 W (1.5 W per phase). The power losses and current depending on the resistance and two different resonance frequency is shown in Fig. 5.

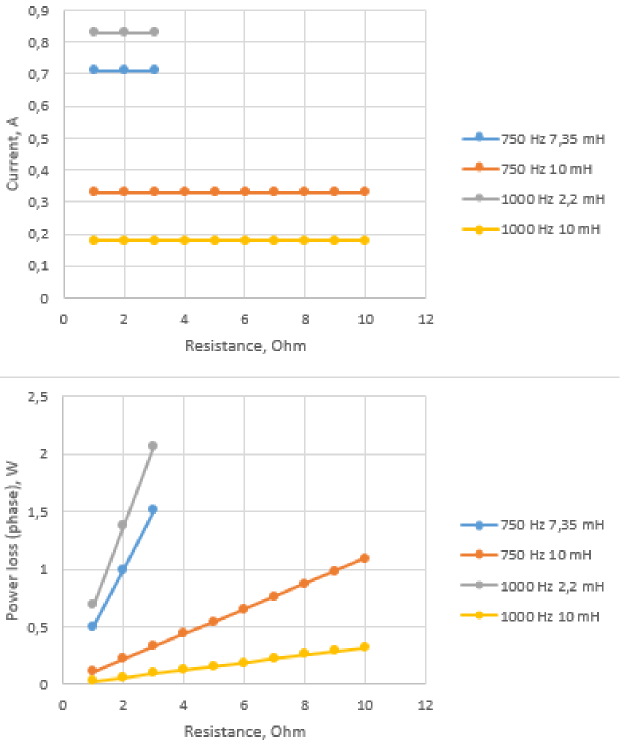

Fig. 5. The current and power loss (phase) depending on the resistance

If the resonance frequency is lower than 500 Hz, the power loss turns out to be less than 1.5 W. This results to a filter which contains: a circuit choke with 10 mH inductance, a capacitor with 10 μF capacitance and 1 Ohm resistance for every phase. The resonance frequency has to be as high as possible to increase the control dynamic but lower than the switching frequency. It was chosen to compare the LC filter with a frequency 750Hz and 1000Hz. However, such a filter has worse parameters than filters with higher resonance frequency, that is why further we are going to consider the filters with two types of frequency 750 Hz (with 7.35 and 10 mH inductance) and 1000 Hz (with 2.2 and 10 mH inductance).

It is necessary to set the quality of the output signal. The FFT analysis is used to estimate it. With its help, we can calculate the total harmonic distortion (THD) (5).

$$THD(\%) = \frac{U_2^2 + U_3^2 + U_4^2 + \cdots + U_n^2}{U_1^2} \cdot 100\% \qquad (5)$$

The analysis is evaluated up to 40 kHz. Uninterruptible power supplies with LC filter are distinguished by the high quality of the output signal, that is why let us assume THD is less than 1%. It follows from Fig. 6, that the lower is the resonance frequency of the filter, the higher is the quality of the output signal. Thus, the optimal design of an LC filter for a three-phase uninterruptible power supply with 1.5 kW includes a choke with 10 mH inductance and a capacitor with 4.5 μF capacitance. Such settings correspond to 750 Hz resonance frequency. The optimal resistance for this filter is 4 Ohm.

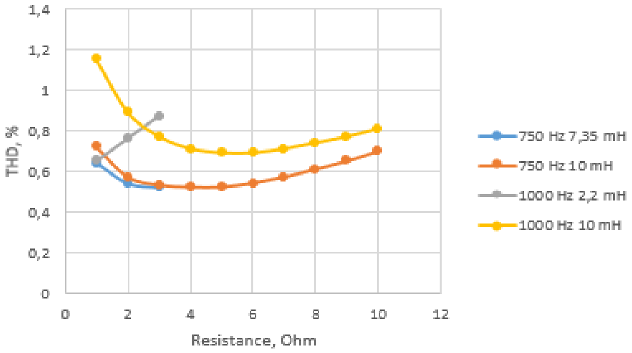

Fig. 6. THD depending on the resistance

The designed Filter is illustrated in a Bode Diagram in Fig. 7.

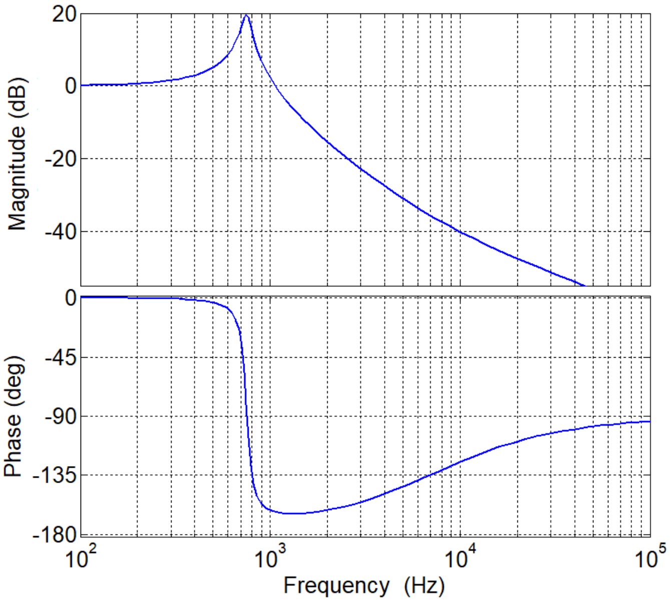

Fig. 7. Bode Diagram

It results from the magnitude and phase frequency characteristic that there is no signal enhancement with a frequency lower than 200 Hz, and there is signal attenuation -41.4 dB at 10 kHz modulation frequency, which conforms to a second-order filter.

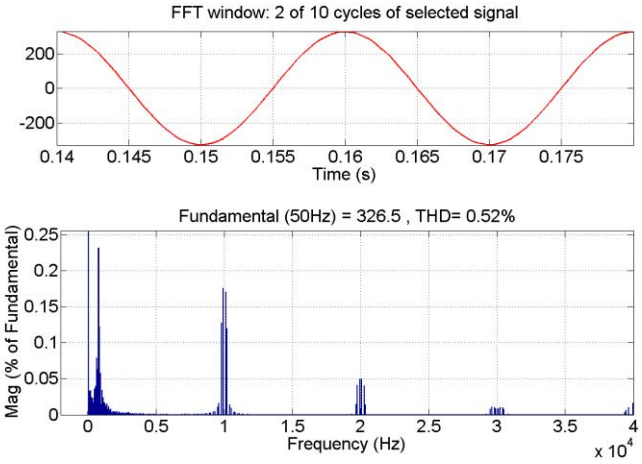

Fig. 8. FFT-analysis (10 mH inductance and 4.5 µF capacitance)

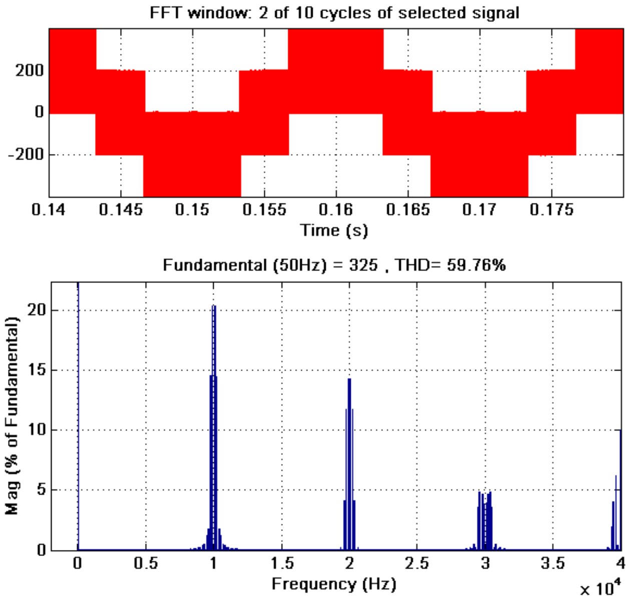

Fig. 9. FFT-analysis (without LC-Filter)

The simulated THD equals 0.52% (Fig. 8). The THD without LC-Filter was calculated with a FFT from the LCR input voltage shown in Fig. 9. In a real time system the THD is probably higher due to neglected inverter effect e.g. dead time.

IV. EXPERIMENTAL PROTOTYPE

To estimate how the simulation results agree with the practice results it is necessary to make a system consisting of an inverter, LC filter, and control system.

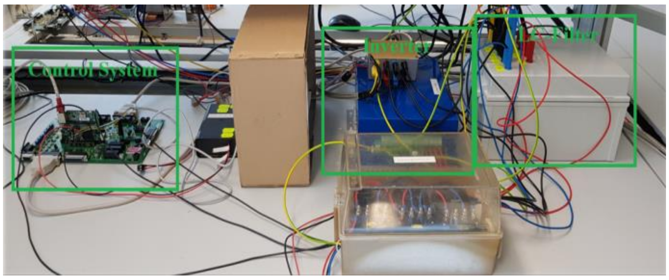

Fig. 10. Experimental prototype

The control system is based on the microcontroller F28M35H22C and MTL-CBI0020N12 (it allows to create three-phase output voltage, to pass 13 A) is chosen as the inverter. The experimental prototype is illustrated in Fig. 10. The proposed control system and the designed filter was tested and the experimental results are shown in Fig. 11. The step response U_d=325V starts at t=0.1s. The measured voltage $u_{d,load}$ rises with a constant slop because the current i_d is limited to 3.5A. After 50ms the system reached the steady state voltage. At t=0.5s a resistive load, which results to an output power P=800W, was applied to test the disturbance rejection. It is noticeable that the measured voltage is approximately constant. Only a small peak $\Delta u_{d,load}$=10V occurs. During the applied resistive load, the current i_d has to rise to supply the grid. At t=0.9s the load is turned off. The current i_d reduces to zero but the voltage $u_{d,load}$ is held constant. At t=1.3s the reference voltage u_d^* was set to zero. After a few milliseconds, the grid is turned off.

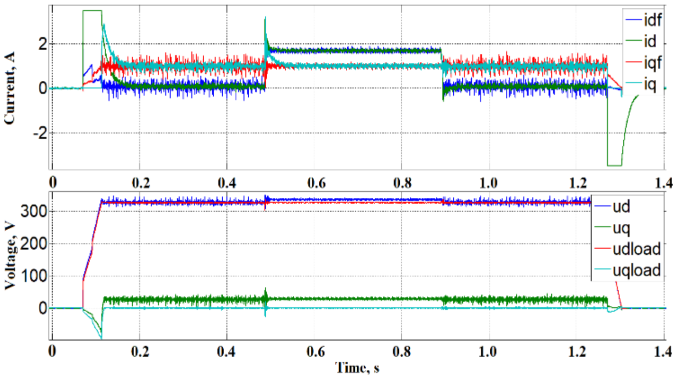

Fig. 11. FFT-analysis (10 mH inductance and 4.5 µF)

Following LC filter components were chosen for the experiment: a choke with 4.6 mH inductance, a capacitor with 10 µF capacitance and 5 Ohm resistor. The resonance frequency of the filter is 750 Hz.

For examining the model, it is necessary to find out the no-load current passing through the filter Fig. 12.

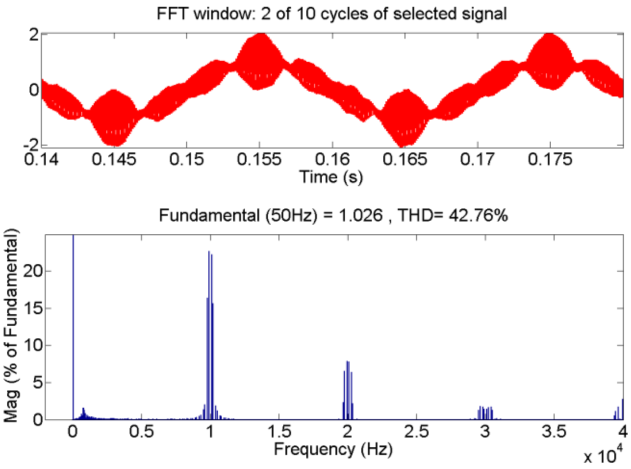

Fig. 12. FFT-analysis (10 mH inductance and 4.5 µF)

It follows from FFT analysis of the model that the rms current is 0.725 A and the peak current is 1.026 A. After that, we have to find out the current in our system. For this purpose phase currents are measured and transformed with the Clarke and Park transformation. I_q current corresponds to the peak current of the real system and is equal 1.01 A, which corresponds to 0.714 A rms current.

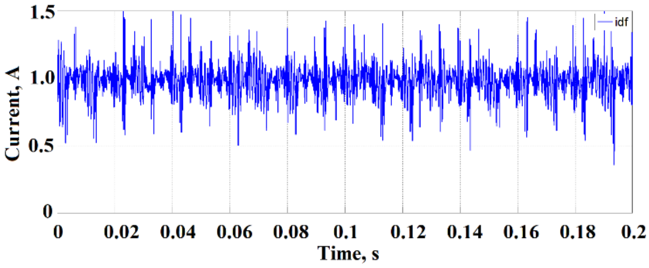

Fig. 13. Measured current of the experiemental prototype at no load

It is also necessary to compare THD of the model with THD of the realized system.

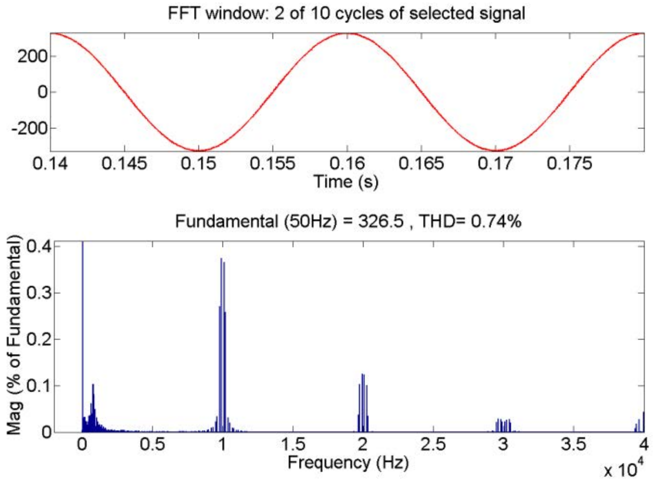

Fig. 14. FFT-analysis of the model with THD of the realized system

When simulating this filter THD equals 0.74%. Then we have to make corresponding measurements for the created system. The measurement-derived data show that THD equals 1.17%. It is also possible to stabilize the output voltage due to an applied resistive load, which is shown in Fig. 15.

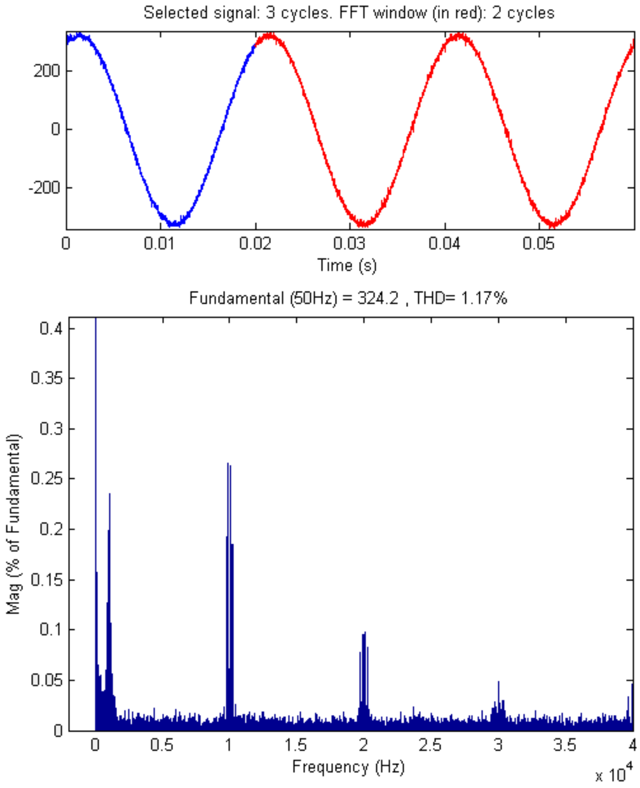

Fig. 15. FFT-analysis of the measured grid voltage

V. CONCLUSION

This paper represents the algorithm to optimize a LC filter. First of all, a set of components that can be bought according to the economic strategy is defined. Besides, the current and voltage allowing the system to work are taken into consideration. This provides system reliability. The power losses were analyzed. Then the quality of the output signal is estimated through FFT analysis. Different components were compared for an optimal filter with regard to low THD. Moreover, it is necessary to consider that THD in practice can be a little bit higher as the result of the simulation.

REFERENCES

[1] D. Elliott, T. Cook, “Renewable Energy: From Europe to Africa”, pp. 10-20, 2018.

[2] M. Kaltschmitt, W. Streicher, A. Wiese, „Renewable Energy: Technology, and Environment Economics“, pp. 1-40, 2007.

[3] C. Herbes, C. Friege, “Marketing Renewable Energy: Concepts, Business Models and Cases”, pp. 259-273, 2017.

[4] S. K. Peddapelli, “Pulse width modulation: analysis and performance in multilevel inverters”, pp. 13-22, 2016.

[5] K.R. Rao, D.N. Kim, J.-J. Hwang, “Fast Fourier Transform - Algorithms and Applications”, pp. 1-40, 2011.

[6] D. Schroder, “Elektrische Antriebe Regelung von Antriebssystemen”, pp. 463-472, 2015.

Optimization of micro-CHP systems through the integration of batteries - A theoretical analysis

Steffen Kubik
Gas- und Wärme-Institut Essen e.V.
Essen, Germany
kubik@hiwi.gwi-essen.de

Maren Wenzel
Gas- und Wärme-Institut Essen e.V.
Essen, Germany
wenzel@gwi-essen.de

Hristina Cigarida
Gas- und Wärme-Institut Essen e.V.
Essen, Germany
cigarida@gwi-essen.de

Dr. Frank Burmeister
Gas- und Wärme-Institut Essen e.V.
Essen, Germany
burmeister@gwi-essen.de

Dr. Rolf Albus
Gas- und Wärme-Institut Essen e.V.
Essen, Germany
albus@gwi-essen.de

Prof. Viktor Grinewitschus
Hochschule Ruhr West
Bottrop, Germany
Viktor.Grinewitschus@hs-ruhrwest.de

Prof. Klaus Görner
Gas- und Wärme-Institut Essen e.V.
Essen, Germany
klaus.goerner@uni-due.de

Abstract - In this paper, the impact of the integration of batteries in micro-CHP systems was investigated. For this purpose, the data of 100 existing micro-CHP systems were collected and evaluated. To simulate the battery and to retrace the state of charge a program was developed. In this program, the surplus electricity that was originally fed into the grid, can be used to charge a virtual battery with any capacity and efficiency. The battery can then be used to cover the electricity demand, at times when no electricity is produced by the CHP system. The battery increases the self-consumption and self-sufficiency rate of the systems while decreasing the consumer's necessity to buy electricity from the grid. This analysis shows, that the integration of a comparatively small battery with a storage capacity of 2 kWh results in an average increase of almost 30 % self-consumption rate in the investigated systems. At the same time, the degree of self-sufficiency increases by 21 %. Batteries with a capacity of 15 kWh can only increase the self-consumption rate by additional 5 % on average. Finally, a small, cheap and easily installed battery is necessary, to make the combination of micro-CHP systems and batteries economically feasible.

Keywords: Combined heat and power, CHP, cogeneration, battery, self-consumption, self-sufficiency

I. INTRODUCTION

In Germany, highly efficient combined heat and power (CHP) technology will have an important role in the medium term, whose expansion will save energy and avoid CO_2 emissions, as reported by the Umweltbundesamt. [1] In addition to large power plants, this technology for power and heat generation (cogeneration) can also be implemented in private households in the form of micro-CHP systems. In the project "100 KWK-Anlagen in Bottrop", Gas- und Wärme-Institut Essen e.V. (GWI) installed 100 of these highly efficient systems in the InnovationCity Bottrop. [2] All installed cogeneration systems are heat-driven. They respond to the heat demand in the building and produce electricity in addition to the required heat. If more electricity than required is produced, it can simply be fed into the public grid and will be compensated in accordance with the Kraft-Wärme-Kopplungsgesetz (KWKG). Despite this remuneration, from an economic point of view, CHP systems are primarily profitable if the highest possible proportion of the electricity generated can be used within the household itself. However, the users can implement the necessary timing of power and heat demand only to a limited extent.

A similar problem can also be seen with photovoltaic systems (PV). Due to the sun's radiation, electricity can be generated during the day, but it may not be needed until evening, when the PV system is not producing electricity. To optimize the system and to make the surplus power available later, batteries are used. Accordingly, battery storage systems could theoretically also be used in cogeneration systems in order to make the system more flexible and thus better match the power and heat requirements.

II. DETERMINATION OF REQUIRED STORAGE CAPACITY

Using the recorded data, GWI was able to create a program to investigate the theoretical impact of a battery on the existing CHP systems. In Fig. 1, the state of charge of a battery during the course of a typical day in winter is visualized. Due to the high heat demand, the CHP system produces electricity during the entire day (blue line). In this case, the battery is fully charged at 6 AM, so any additional surplus electricity has to be fed into the grid (black line). After 10 AM, the electricity demand is higher than the produced electricity by the system, so the battery is being utilized. At 3 PM, the battery is completely discharged so the power demand has to be covered with additional purchase from the grid (red line).

Since the user's heat demand determines the operation of the system, the installed systems sometimes differ depending on the building standard and type, number of residents, installed electricity and heat consumers and other influencing factors. Among the objects studied in the project "100 KWK-Anlagen in Bottrop", apart from private buildings, there are also commercial buildings and apartments with several parties to cover a wide range of building types. Only the private houses are considered for

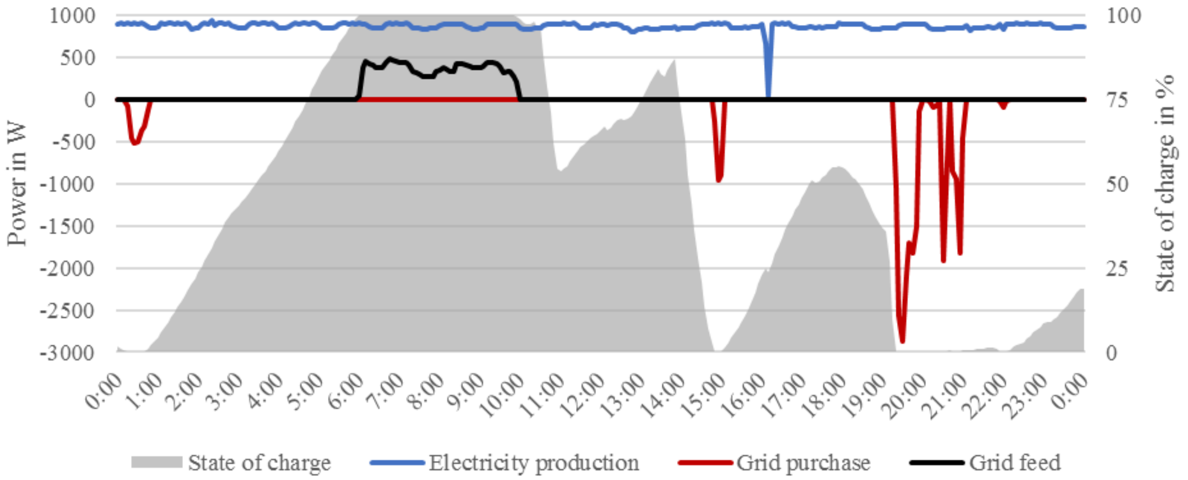

Fig. 1 State of charge of a battery during the course of a typical winter day. All values were measured in 5-minute intervals.

the following analysis, which were equipped with a heat-driven system with internal combustion or stirling engines with an electrical power of 1 kW.

Depending on the engine type, different amounts of heat are generated in relation to the produced electricity. For this reason, buildings with a comparatively high heat demand were allocated to systems with a stirling engine (about 5 kW thermal) instead of an internal combustion engine (about 2.5 kW thermal). In addition, the buildings to be considered should have no system failures or excessive differences between the two evaluated years, which are not referable to weather conditions. 37 of the 100 systems met these requirements.

The most important key figure for the analysis is the self-consumption rate. It describes how much of the produced electricity can be used locally. The investigated systems have a self-consumption rate of 48.5 % over 2 years on average. More than half of the self-generated electricity could not be used locally and was fed into the grid. A comparison of the annual balance of the systems shows variations between 18 and 80 % and illustrates the described influence of the individual user behavior and the system characteristics. Similar results can be seen when looking at the degree of self-sufficiency, which describes the share of the total electricity demand of a building that does not need to be drawn from the electricity grid. The average of 38.4 % is calculated based on values that vary between 15 and 67 %. While the average self-consumption rates for systems with stirling engines and internal combustion engines are almost identical, systems with internal combustion engines generally have a higher degree of autonomy due to their tendency of increased operation time. The high variance between the buildings suggests that completely different battery sizes could be used in order to maximize the self-consumption rate. Finally, a system with 18 % self-consumption should have a higher potential to store large amounts of unused electricity in a battery than a system with 80 % self-consumption. This system should therefore be able to utilize a much larger sized battery as long as the total amount of produced electricity is similar. Based on the batteries for photovoltaic systems available on the market, storage capacities between 2 and 15 kWh were simulated in order to determine which storage dimensioning fits for the CHP systems and to what extent the suitable battery sizes differs between the considered buildings. Instead of feeding the surplus electricity into the grid, the electricity can now be stored in a pre-dimensioned battery. The battery can then provide the power demand, which previously could only be covered by the supply of electricity from the grid. If the battery is fully charged in times of additional power production, the surplus electricity is fed into the grid. Fig. 2 illustrates the increase of self-consumption and self-sufficiency by increasing the battery size in three buildings with originally low (light blue), medium (dark blue) and high (grey) self-consumption rate.

Despite the different starting point, a significant increase in the self-consumption rate of similar proportions can be seen in all buildings even with a small battery. With a capacity of 2 kWh increases between 16 and 23 % can be achieved. A much larger battery with a capacity of 15 kWh merely increases the self-consumption rate by additional 1 to 4 %. Accordingly, in the buildings shown, the integration of a large battery does not lead to relevant benefits compared to smaller ones. The graph also reveals that although the levels of self-sufficiency and self-consumption are related in some way, they are completely different key figures. Since the self-consumption rate only indirectly refers to the total electricity consumption, a high self-consumption rate does not automatically cause a high level of self-sufficiency. Despite its high self-consumption rate, the building shown in grey has a lower degree of autonomy than the system shown in light blue due to the high power consumption and would have to draw a large proportion of the electricity from the grid even with a battery and a self-consumption rate of 100 %.

In all other systems, similar results were calculated. The simulated batteries were able to increase both the self-consumption rate and the degree of self-sufficiency significantly even with comparatively low capacities. A storage capacity of 2 kWh results in an average increase of almost 30 % from 48.5 to 77.7 % self-consumption rate. At the same time, the degree of self-sufficiency increases from 38.4 to 59.4 %. The small benefit of large batteries compared to smaller ones shown in Fig. 2, can be observed in all systems and only leads to a further increase in the self-consumption rate of 5 % on average.

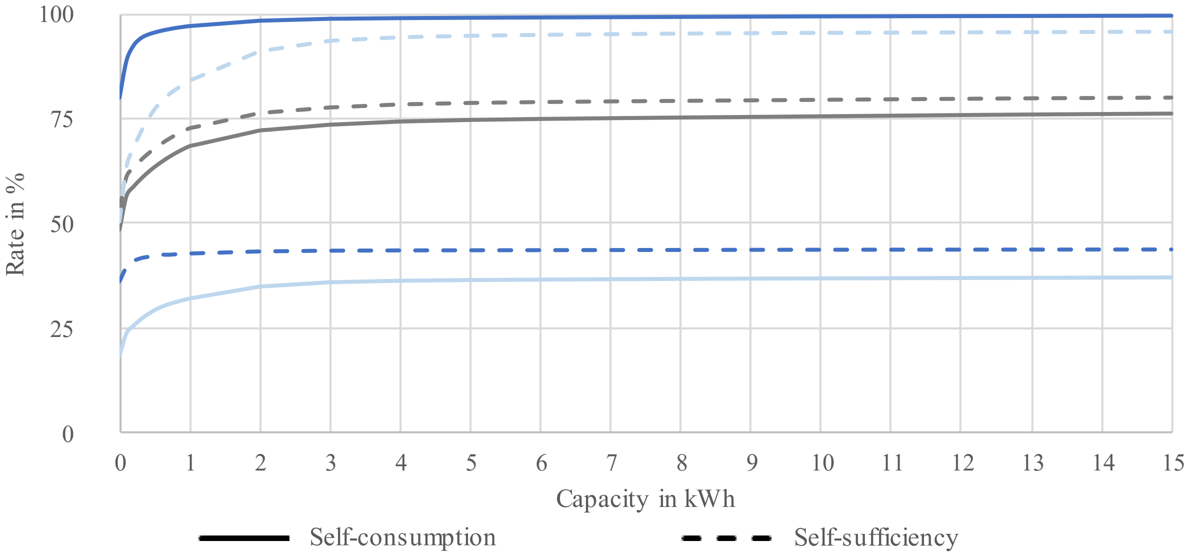

Fig. 2 Effect of different battery sizes on the self-consumption and self-sufficiency rates in systems with originally low (light blue), medium (dark blue) and high (grey) self-consumption rate

The large battery, in all of the examined buildings, cannot achieve a further increase of more than 12 %.

III. SEASONAL FLUCTUATIONS OF THE SELF-CONSUMPTION RATE AND DEGREE OF SELF-SUFFICIENCY

To understand the low impact of bigger batteries the systems have to be analyzed throughout an entire year. Due to the heat-driven mode of operation, the electricity production of CHP systems is highly dependent on the season. In the system shown in Fig. 2 in dark blue only 12.5 % of total CHP electricity yearly production was generated in the warm months between June and September. Most of the electricity is produced in the cold months due to the high heat demand and the associated high runtime of the CHP-system. Consequently, self-consumption and self-sufficiency are subject to huge seasonal fluctuations. Fig. 3 illustrates the progression of these two key figures as well as the impact of the integration of a battery over an entire year. Both diagrams illustrate the influence of the season on the respective key figure in different ways. The low electricity production in the warm months leads to the fact that even with a small storage a self-consumption rate of 100 % can be achieved (light blue line). Thus, so little surplus power is produced that the battery is never fully charged and no electricity would have to be fed into the grid. On the other hand, even in winter, the large battery cannot lead to a significant increase in the self-consumption rate (dark blue line). Due to the high runtime of the system, so much surplus electricity is produced that both the small and the large battery are fully charged over long periods and the surplus electricity would have to be fed into the grid. Only in the transition period between summer and winter, when

the battery often is in a partially filled condition, the larger battery could cause noticeable differences. A nearly mirrored image can be seen by looking at the degree of self-sufficiency. The demand for electricity in the respective building could be almost completely covered by self-produced electricity in winter using a battery. The grey curve of the self-sufficiency diagram shows the low electricity production in summer. Even if the entire amount of electricity produced could be used in the summer locally, most of the electricity demand must be covered from the electricity grid. As a result, the degree of self-sufficiency cannot be raised above 50 % even with a battery.

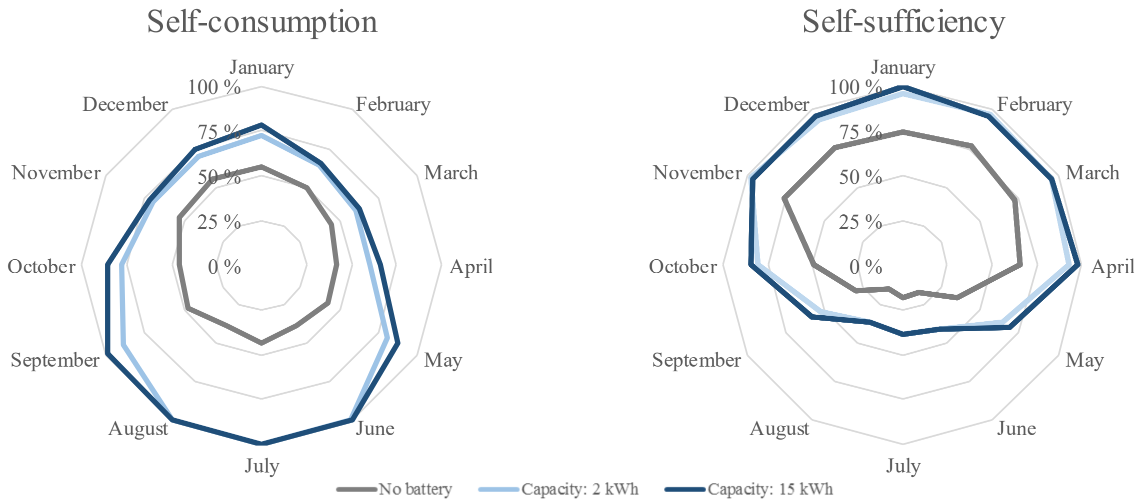

Fig. 3 Yearly trend of the self-consumption and self-sufficiency rate in micro-CHP systems with different battery sizes

Consequently, the integration of a battery causes a reduction of the need for electricity from the grid in cold month while potentially preventing surplus electricity in warm month entirely.

IV. ECONOMIC EVALUATION

In order to evaluate the increase of these key figures, an economic evaluation is mandatory. Ultimately, the savings come from the difference between feed-in tariffs and electricity costs from the public electricity grid. The former is composed of the baseload price, avoided network user charges and the CHP surcharge. It amounts to approximately 12 cents per kWh fed in, depending on the season and the network provider. Any unused kWh from the public grid in Germany can be valued with 29 cents. In addition, the user receives 4 cents for each kWh he uses locally. The integration of a battery thus leads to lowering electricity costs from the grid and additional revenue from self-used electricity. On the other hand, however, revenues are reduced by the feed-in tariff. In addition, even with highly efficient lithium batteries a certain proportion of the electricity is lost due to conversion losses. With a lifespan of the CHP system of 15 years and charge and discharge efficiencies of 95 % in each way, an amount of 2524 € can be saved in the system on average due to the integration of a 2 kWh battery. The savings in systems with an internal combustion engine tends to be higher on average, due to the higher power production compared to systems with stirling engines. The following correlation matrix (Fig. 4), which depicts the dependency of various factors with values between minus one and plus one, confirms this trend.

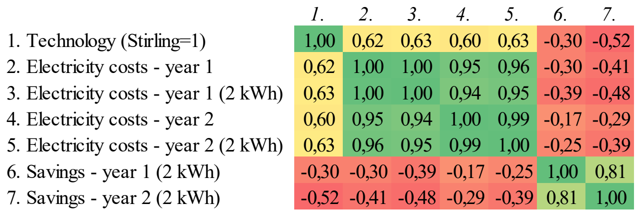

	1.	*2.*	*3.*	*4.*	*5.*	*6.*	*7.*
1. Technology (Stirling=1)	1,00	0,62	0,63	0,60	0,63	-0,30	-0,52
2. Electricity costs - year 1	0,62	1,00	1,00	0,95	0,96	-0,30	-0,41
3. Electricity costs - year 1 (2 kWh)	0,63	1,00	1,00	0,94	0,95	-0,39	-0,48
4. Electricity costs - year 2	0,60	0,95	0,94	1,00	0,99	-0,17	-0,29
5. Electricity costs - year 2 (2 kWh)	0,63	0,96	0,95	0,99	1,00	-0,25	-0,39
6. Savings - year 1 (2 kWh)	-0,30	-0,30	-0,39	-0,17	-0,25	1,00	0,81
7. Savings - year 2 (2 kWh)	-0,52	-0,41	-0,48	-0,29	-0,39	0,81	1,00

Fig. 4 Correlation matrix of economic factors regarding the evaluated CHP systems

In the first row and column, the corresponding key figure is high in systems with stirling engines if the number in the cell tends to the value of plus one. If the number tends to the value of minus one, the key figure is high in systems with internal combustion engines. As a result, owners of stirling engine systems have to spend more money on electricity from the grid and can save less money by integrating a battery. At first glance, the internal combustion engine appears as the better option. However, since this analysis only examines the integration of a battery into an existing system, but not the economics of the system itself, which would include gas and installation costs, this would be a wrong conclusion. Nevertheless, at this point the internal combustion engine can be described as more convenient for the integration of a battery, due to the higher amount of surplus electricity. After 15 years, the savings for internal combustion engines were on average 2724 € based on the data of year 1 and 3028 € based on the data of year 2. Contrary, only 2301 € and 2318 € on average can be saved in systems with stirling engines. In addition to the influence of the technology, this comparison also shows that the calculated values can change depending on the analyzed year.

In the best case, the integration of a small battery results in a saving of about 3900 € after 15 years and as long as the savings are higher than the investment costs, implementing a battery would be economic. Although the cost of lithium batteries has dropped significantly in recent years and will continue to decline, the specific cost per kWh of peripheral and installation costs is particularly high for small batteries, as pictured in Fig. 5 [3].

After the project "100 KWK-Anlagen in Bottrop", GWI was able to integrate 20 batteries into existing CHP systems in a similar project named "KWK plus Speicher". Through 33 offers that were received during the project GWI concluded that about 2100 € must be scheduled for installation costs as part of the investment costs. This amount is close to the average savings of a battery after 15 years. Even in the best system examined (savings of 3900 € after 15 years), considering the current battery prices, their integration is economically justified only at particular low installation and battery costs. This is mainly due to the described low utilization of the systems in the warm months and the small difference between feed-in tariffs and electricity procurement costs.

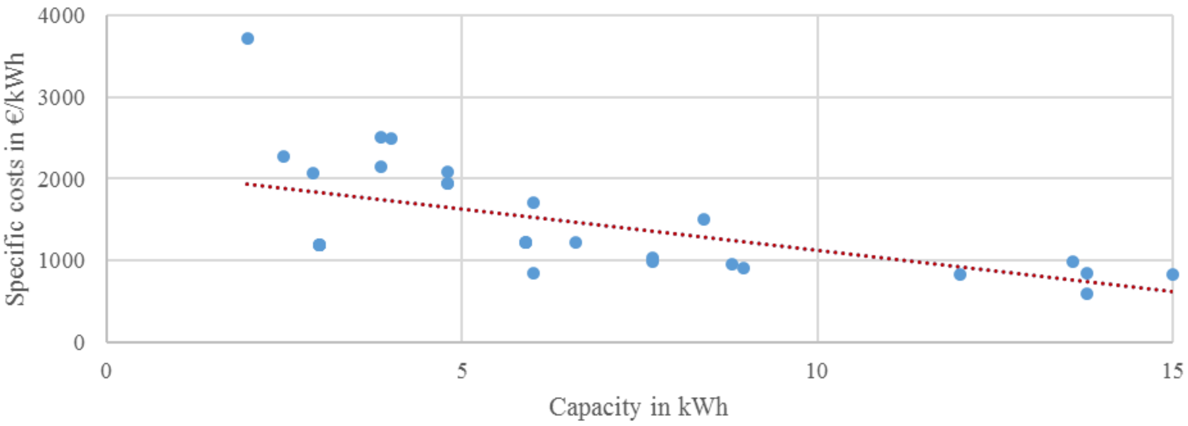

Fig. 5 Specific costs of lithium batteries for different capacities (source: GWI)

V. SCOPE OF APPLICATION AND FUTURE POSSIBILITIES FOR IMPROVEMENT

The life expectancy of 15 years assumed in this analysis, as well as the overall efficiency of approximately 90 %, must be valued as optimistic. Power limitations will not allow the batteries to cover all load peaks, so that finally less electricity can be supplied than it was assumed in this analysis. The installation cost of a battery has been crucial for the integration into an existing system. If the battery is installed at the same time as the cogeneration unit and by the same installer, the additional installation costs due to the battery could be much lower. Since only two different years were examined, the calculated values could differ significantly in other years.

For these reasons and the observed variance of the individual systems, the operating behavior of the system has to be analyzed in advance of the purchase of a battery. Because different user behavior makes each system unique, the results compiled in this paper can only be applied to the 37 buildings studied and should not be generalized. Although the assumptions made here are in part merely estimates and cannot be generalized, the results of the economic evaluation of the examined systems are definite. Even large deviations of the assumptions or the increase of electricity price on a realistic scale cannot fundamentally change the result of the investigation in economic terms. For that, a small and cheap battery would be needed, which could be integrated into a system with little effort. Only in optimal conditions, the pursuit for efficiency and more self-sufficiency can therefore justify the acquisition of a battery. However, these optimal conditions effectively mean low self-consumption and a high amount of surplus electricity in systems without a battery. In this case, a better dimensioning of the system, different cogeneration technology, switching the heat-driven to the electricity-driven or hybrid mode of operation or better timing of electricity and heat consumption might be a more economical approach than integrating a battery.

Since the cause is mainly due to the low utilization in the summer months, a combination of PV system and micro-CHP system could be reasonable. While the photovoltaic system produces electricity mainly in the summer months, the CHP system can guarantee the benefits of a battery in winter. Alternatively, pre-owned batteries of PV systems could inexpensively be purchased and integrated into CHP systems. The end of life of PV batteries is often defined by the decrease of useable capacity. Since large capacities in CHP systems are not necessary, such pre-owned batteries could be used sustainably, if safety and high efficiencies are still guaranteed.

Another approach is the combination of fuel cells and batteries that could provide fundamentally different results. Fuel cells can be assigned to the micro-CHP systems, but are operated in continuous operation and are therefore independent of the season and heat demand. Suitable fuel cells could thus circumvent the drawback of the stirling and internal combustion engines, while still providing enough electricity and heat to these households.

A verification of the assumptions and forecasts, the comparison of the results achieved by the simple model with real data presented here and the consideration of potential alternatives will follow at GWI in the project "KWK plus Speicher".

REFERENCES

[1] Umweltbundesamt, Kraft-Wärme-Kopplung (KWK). 2018. <https://www.umweltbundesamt.de/daten/energie/kraft-waerme-kopplung-kwk#textpart-1>

[2] M. Schmidt, F. Burmeister, R. Albus (Hrsg.): 100 KWK-Anlagen in Bottrop – Vom Labor in die Demonstration – KWK-Modellversuch zur CO2-Reduktion in der Innovation City; Abschlussbericht zum Verbundprojekt; Gas- und Wärme-Institut Essen e.V., Institut Energiesysteme und Energiewirtschaft der Hochschule Ruhr West, Innovation City Management GmbH. 2016.

[3] L. Goldie-Scot, A Behind the Scenes Take on Lithium-ion Battery Prices; BloombergNEF. 2019. <https://about.bnef.com/blog/behind-scenes-take-lithium-ion-battery-prices/>

Controller Optimization to Stabilize Inverter-dominated Distribution Grids

H. Cai, T. Jiang, J. Kircheis, S. Schlegel, D. Westermann
Power Systems Group
Technische Universität Ilmenau
Ilmenau, Germany
Teng.Jiang@tu-ilmenau.de

Abstract— **With the increasing use of renewable energies in the power grid, the number of converters is growing. Because of an increase in their number, the system is becoming unstable. The instability can be caused by multiple reasons, and one of the main subjects is the control structure of the inverters and their control parameters, which requires appropriate methods to parameterize and optimize the inverter controllers. This paper focuses on how the controller parameters of inverters in distribution grids can be optimized to improve system stability. This paper focuses on the parameterization of the inverter by testing five common controller parameterization methods: the Ziegler-Nichols method (ZNS), the Chien-Hrones-Reswick method (CHR), the absolute value optimum (AVO), the symmetrical optimum (SO), and the Skogestad method (SKO). The combinations of methods are investigated in the cascaded control system, and an optimal combination is selected for the best system performance. In this paper, an existing reference network is selected as the investigated network and the system stability in the small-signal range is investigated. The results show that the combination of current regulator parameterized with the SKO method and voltage regulator parameterized with the SO method provides the best small-signal behavior.**

Keywords- Cascaded control, controller parameterization method, distribution grids, inverter-dominated grids, mean-value model, mathematical model, stability

I. INTRODUCTION

Due to the accelerated energy transition in Germany, the share of renewable energies in the electrical grid has increased. The feed-in of renewable energy into the grid is predominantly based on the inverter because the inverter can convert renewable energies at the respective grid level into the desired form. From the point of view of the grid, the high proportion of converter units corresponds to a sharp increase in the current branches. The object of an inverter is to set and maintain the voltage and current at its input and output at the desired values and to maintain the predetermined magnitudes, e.g., active and reactive power. For this purpose, a control loop is necessary. Due to the control structure and control parameters, inverters have a significant impact on the system stability. System stability decreases with an increasing number of inverters in the form of an increase in intranet-network effects. Currently, in the cascade control system of the inverter, the controllers are individually arameterized in inner and outer control loops and parameterized without consideration of the influence of further connected converters in the grid. Therefore, the optimization of the control parameters of the inverters for the improvement of the system characteristics at excitations and disturbances offers itself [11].

In this paper the optimization of the controller parameters is examined. Here, the affected controller refers to the PI controller because the PI controller is the most common solution for practical control problems. There are many controller parameterization methods, including the classical method of Ziegler and Nichols [1]-[2], a modification of Ziegler-Nichols method - namely CHR method [3]-[4], the AVO method based on simplification by pole cancellation [5]-[7], the SO method capable of imposing symmetrical characteristics of the open-loop transfer function [8]-[9] and a model-based tuning method – SKO method [10]. This paper examines the best combination of the different parameterization methods in the cascaded inverter control system.

The paper is structured as follows: After the introduction, the above mentioned five controller parameterization methods are presented in chapter 2. Chapter 3 deals with a basic understanding of the converter and its control system, moreover the simulation results are illustrated. A summary of the present work and starting points for further research are provided in chapter 4.

II. CONTROLLER PARAMETERIZATION METHODS

This chapter introduces methods for a summary of the common parameterization method is given.

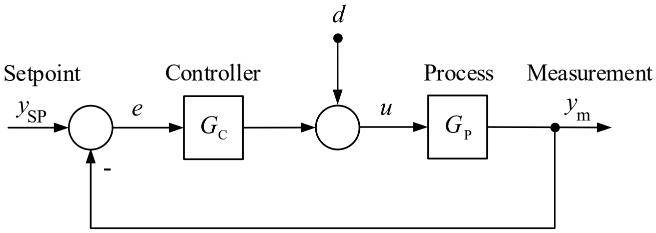

Fig 1. Block diagram of a control system [11]

A. Ziegler-Nichols Method

The method of Ziegler-Nichols (ZNS method) is based on the plant information in the form of the open-loop step response. This method can be considered as a traditional method based on modeling and control, using a process model. The step response is only characterized by two parameters n and m. The inflection point is determined first, and the tangent at that point is drawn. The intersections between the tangent and the coordinate axes yields in the parameters n and m [2]. From these parameters, the PID parameters are given directly as functions of n and m.

$$K_C = \frac{0.9}{n}, \tag{1}$$

$$T_C = 3m\,. \tag{2}$$

B. *Chien-Hrones-Reswick Method*

The Chien-Hrones-Reswick method (CHR method) is a modification of the ZNS method, and with this method, a good reference response and disturbance response can be obtained [3]-[4]. A good disturbance response is usually a relevant standard in control applications. This method results in closed-loop with slightly better robustness than the ZNS method. The design criteria used were "fastest response without overshoot" or "fastest response with 20 percent overshoot". They proposed different tuning rules for disturbances response and reference response [4]. To tune the controller according to the CHR method, first, the parameters m and n of the plant are determined as in the ZNS. The controller parameters are then specified as functions of these two parameters. Chien, Hrones, and Reswick investigated that tuning of the reference response was different than the adjustment for the disturbance's response, with controller gains generally lower.

$$K_C = \frac{0.7}{n}, \tag{3}$$

$$T_C = 2.3m\,. \tag{4}$$

C. *Absolute value optimum*

The absolute value optimum (AVO), also called modulus optimum, is a method for tuning controllers that is considered as analytical design. The goal of the AVO is a fast step response of the closed-loop. In a single-loop linear control with defined low-pass behavior, the optimum design can be set [5]-[7].

With AVO, the PI controller is selected to compensate the largest time constant of the plant. To configure the close loop optimally, the transfer functions must have the following equation:

$$G_{AVO} = G_C\, G_P = \frac{1}{(Ts+1)}\frac{1}{2Ts}\,. \tag{5}$$

By comparing the transfer function of the examined open loop with G_{AVO} , the controller parameters can be determined.

D. *Symmetrical optimum*

With the symmetrical optimum (SO) the closed-loop frequency response is also considered by the design of controllers. With SO the controller is designed so that the maximum value of the phase margin is reached by the passing frequency of the control loop [8]-[9]. The open-loop passing frequency should be in the middle between $\frac{1}{T_1}$ and $\frac{1}{T_2}$ so that the maximum of the open-loop phase response is located at the passing frequency $\frac{1}{T_s}$. After this relation the following equation can be obtained:

$$\frac{1}{a}\frac{1}{T_2} = \frac{1}{T_s} = a\frac{1}{T_1}\,. \tag{6}$$

With the SO it results in the following transfer function with a =2 [11]:

$$G_{so} = G_C G_P = \frac{1}{2T_s^2}\frac{1}{s^2}\,\frac{1+2T_s s}{1+(T_s/2)\,s}\,. \tag{7}$$

The controller parameters can be determined by comparing the transfer function of the open loop with G_{so}.

E. *Skogestad's method*

Skogestad's PID optimization method (SKO) is a model-based method in which the controller is expressed as a closed-loop function. The method is suitable for control loops with first or second order or with time delay also for integrating and pure time delay processes. The steps to use this method are:

- approximate the control loop
- Set model-based PID controllers

In the first step, the process is approximated with a first-order system plus delay:

$$G_P(s) = \frac{k}{(T_1 s + 1)}\,e^{-\theta s}. \tag{8}$$

The PI controller settings are based on the first-order system:

$$G_C(s) = K_C\,(1+\frac{1}{T_C s})\,, \tag{9}$$

with

$$K_C = \frac{T_1}{k \cdot 2\theta}, \tag{10}$$

$$T_C = \min\{T_1,\, 4(T+\theta)\}\,. \tag{11}$$

This parameterization method of the controller gives a reasonably fast response and good robustness.

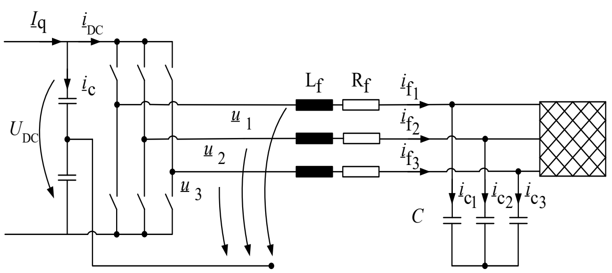

Fig. 2 Mean-value model of the inverter [11]

III. SIMULATION

The structure of the inverter control and those of the simulation model are first presented in this chapter. Subsequently, the five methods are used separately in current and voltage control, and the effects of different combinations of these methods on system stability and behavior are investigated. AVO is not suitable for voltage controller parameterization due to its controlled structure, which contains an integral part. Using AVO method in the voltage controller would lead to unstable closed loop behaviour. Finally, there are only 20 sets of combination of the parameterization methods in the cascaded control system.

From the comparison of 20 sets of results, it can be seen that the combination I_{SKO}- U_{SO} has the smallest values of integrated absolute error and the combination I_{SKO}- U_{SKO} has the highest damping ratio and the smallest overshoot. The two sets of combination lead to the overall improvement of the system behavior.

A. Inverter model and simulation model

The inverters are equipped with inner current control loops and outer DC link voltage controllers [14]. The mean-value model is used to describe the inverters. The losses in the inverters are neglected.

A simulation using the detailed grid model takes several hours. The network reduction is a solution to reduce the simulation time, at the same time the dynamics of the network is substantially emulated. The procedure of mesh reduction is shown in *Fig.* .

The dynamic behavior of the subordinate and superimposed network is simulated by a transfer function. The transfer function is determined by system identification. The system identification algorithms are presented in the following subchapters. The grid reduction is realized using the aggregated model. The behavior of the aggregated model under a small excitation signal is identical to the original system, retaining its main features but changing the structure. After the grid reduction, the aggregated models of the subordinate and superimposed network are integrated with the distribution network instead of using the compact network structures. This integration model is used for further stability investigation. The aggregated models vary depending on the type of networks to be reduced. The following sections describe two network reduction procedures: the aggregated model for replicating the superimposed or subordinate network.

In order to determine the best combination of parameterization methods in the cascaded control system, this section examines performance and stability in a three-inverter system. The structure of the model are three converters connected in parallel to the standard medium voltage Cigré network, see *Fig. 3*. To explore the overall system behavior, the grid voltage U_G is selected as the input value and the active system power P_G as the output value. The input signal U_G on the high voltage side of the transformer increases from 110 kV to $110 \cdot 1.1 = 121$ kV. The corresponding behavior of the output signal P_G is presented further below. The value increases from 4.7494 MW to 4.7495 MW.

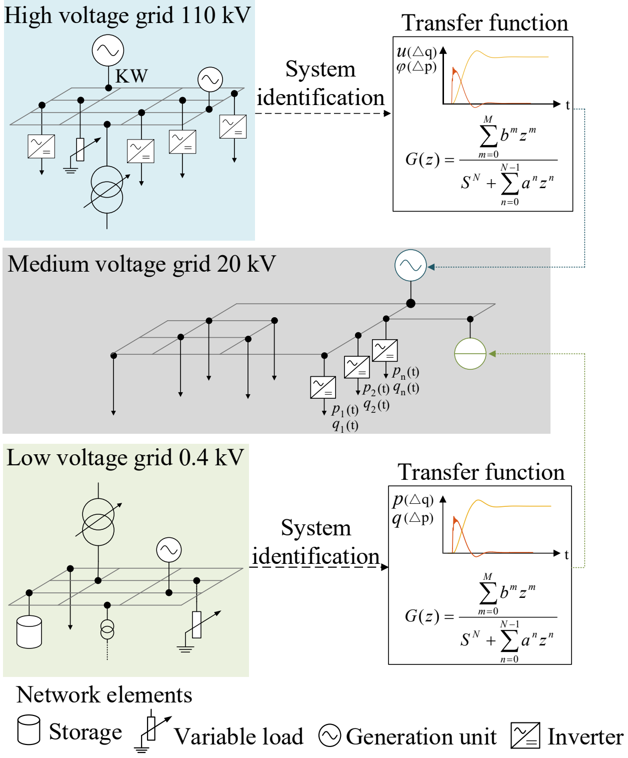

Fig. 3 Network reduction by employing the aggregated model

B. Aggregated model to emulate the overlaid network

The high-voltage grid is often built up as a mesh network to ensure a high level of supply reliability [7]. If the dynamics of the high voltage grid or the interaction of superposed networks must be considered, it is advantageous to use a simplified grid model rather than the compact model to reduce simulation time while maintaining the characteristic dynamics of the superposed network. As part of this work, the high-voltage power network is represented by the aggregated model more precisely by a controlled voltage source, because the behavior of the superposed network from the subordinate network is a non-ideal voltage source.

With the aggregated model, both the stationary behavior of the compact model and the dynamic behavior can be modeled. For this reason, the model is constructed to contain two parts, one of them represents system behavior in steady-state behavior, the other the transient behavior under a small signal.

In the aggregated model, the state variables to be considered for the observed phenomenon or the investigation focus can be selected as input or output variables. The inputs denote the operating point while the outputs are the voltage response. The stationary behavior is a measured value that can be calculated by the simulation of the compact network model. The transient behavior can be simulated by a transfer function. The topology of the aggregated model is shown in *Fig. 4*.

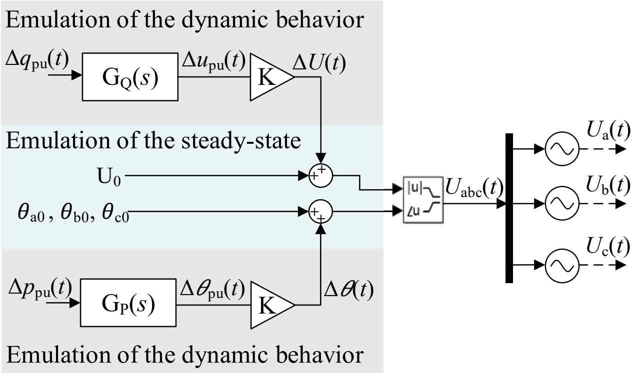

Fig. 4 Topology of the aggregated model of the overlaid network

The gray area shows the emulation of the dynamic area and the blue area the emulation of the stationary behavior of the superimposed network. The input signals $\Delta P_{\mathrm{pu}}(t)$ and $\Delta Q_{\mathrm{pu}}(t)$ denotes the temporal operating point change on the medium-voltage network in pu. The use of pu has the advantage that they are relative to a reference and thus identical for the subordinate and superimposed networks.
The transfer functions $\mathrm{G_Q}(s)$ and $\mathrm{G_P}(s)$

$$\mathrm{G_P}(s) = \frac{\Delta\theta_{\mathrm{pu}}}{\Delta P}, \tag{12}$$

$$\mathrm{G_Q}(s) = \frac{\Delta u_{\mathrm{pu}}}{\Delta Q} \tag{13}$$

and the gain K characterize the dynamic process.

The steady-state voltage amplitude $\mathrm{U_0}$ and the steady-state voltage angle θ_0 for the respective phases indicate the stationary behavior of the voltage. After combining the dynamic response and the static output into a complex voltage signal, the voltage source is driven by this voltage signal and the corresponding electrical signal is the output value.

C. Aggregated model to emulate the underlying grid

To simulate the subordinate network, a controlled power source model is constructed as an aggregated model. This controlled current source can feed the same active and reactive power as the low-voltage grid into the grid or absorb it from the grid. The aggregated model is modeled in two parts: emulation of dynamic and stationary behavior. The dynamic behavior of the subordinate network is modeled by two transfer functions.

The input signal of the transfer functions is the voltage step Δu_{pu} at the superimposed power supply and the output signals are the change of the active and reactive power. The topology is presented in *Fig. 5*.

The active power and the reactive power dynamics are determined by the composition of the stationary operating points P_{AP} and Q_{AP} by the transfer functions

$$\mathrm{G_P}(s) = \frac{\Delta P}{\Delta u_{\mathrm{pu}}}, \tag{14}$$

$$\mathrm{G_Q}(s) = \frac{\Delta Q}{\Delta u_{\mathrm{pu}}} \tag{15}$$

The input signal of the transfer function is the voltage step Δu_{pu} of the overlaid grid. With the use of the pu size, the voltage step can be generated by a high voltage network instead of a voltage source with the same voltage level, whereby the simulation time is reduced. The output signals of the transfer function are the active power ΔP_{pu} and reactive power ΔQ_{pu} response generated by the voltage step.

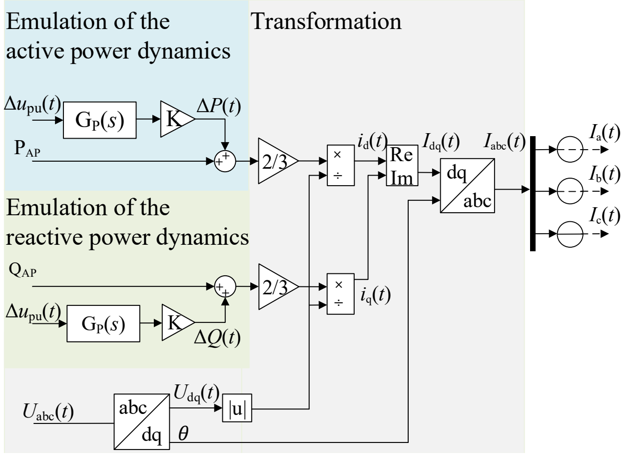

Fig. 5 Topology of the aggregated model for the emulation of the subordinate network

The gain factor K serves, on the one hand, to convert the pu values into real values, on the other hand, to adapt the output values when implementing the transfer functions.
To build the power source, the active current i_d and the reactive current i_q are calculated by the relationship between active power, reactive power and voltage and then converted by the inverse-Park transformation into three-phase current signals I_{abc}. For the calculation, the voltage is first converted into αβ -Values.

IV. RESULTS

Due to the limited space, only the results of the best eight sets of the method combinations are presented in the following. The four parameterization methods in the voltage control loop are examined using AVO and SKO method in current controllers.

From *Fig. 6* it can be concluded that with the same current controller parameters, the system behavior has the same trend in four sets of different voltage controller parameters. For the detailed oscillation analysis, the conjugate pole pair closest to the imaginary axis is selected. The results are presented in Table 1. The difference in the damping ratio between each other is less than 2%. The damping ratio at $\mathrm{U_{SKO}}$ is the highest, which indicates the better response time and the better overshoot behavior of the system. Further, the investigation is carried out under $\mathrm{I_{SKO}}$ method with a combination of four methods applied to the voltage controller.

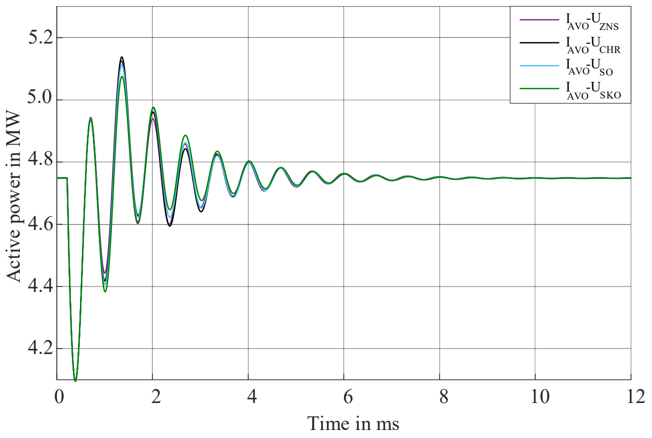

Fig. 6 Simulation results of P_G when U_G changes (Current controller: AVO)

Compared to *Fig. 6*, *Fig. 7* shows a better dynamic behavior. From Table 2 it can be concluded that the damping ratio, and the overshoot are significant lower Oscillation behavior of the investigated.

In summary, the combination I_{SKO} - U_{SKO} has the highest damping ratio and the smallest overshoot. Now, the IAE (Integrated absolute error) proves to be the most important indicator of system behavior because it represents the ability to suppress the small disturbance signal [22]. Besides, the IAE presents the entire system behavior, while the damping ratio only represents oscillation behavior of the tested pole pair. The damping ratio under I_{SKO}-U_{SO} is also high, which is only 7.69% smaller than the largest value under I_{SKO} - U_{SKO} . Because of the better IAE value the I_{SKO}-U_{SO} method is chosen as the best combination of methods.

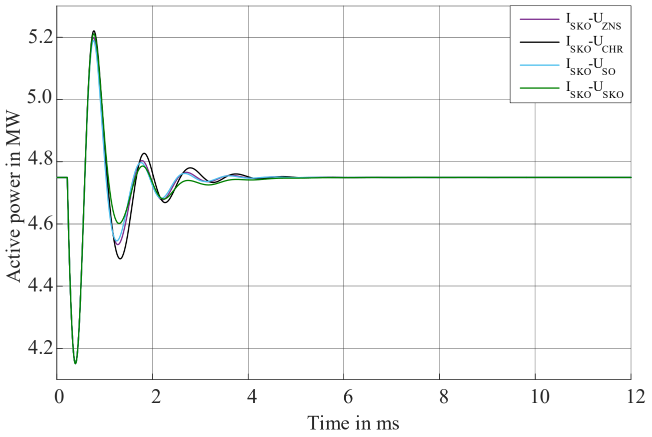

Fig. 7 Simulation results of P_G when U_G changes (Current controller: SKO)

TABLE I. POLE PAIR (CURRENT CONTROLLER-AVO)

Methods	**IAE**	**Damping ratio**	**Oscillation frequency**	**Overshoot**	**Settling time**
I_{AVO}-U_{ZNS}	492.10	0.069	1511.40 Hz	0.804	5.9 ms
I_{AVO}-U_{CHR}	504.68	0.070	1504.25 Hz	0.802	5.9 ms
I_{AVO}-U_{SO}	497.95	0.071	1503.28 Hz	0.799	5.8 ms
I_{AVO}-U_{SKO}	494.41	0.072	1501.59 Hz	0.796	5.7 ms

TABLE II. OSCILLATION BEHAVIOR OF THE INVESTIGATED POLE PAIR (CURRENT CONTROLLER-SKO)

Methods	**IAE**	**Damping ratio**	**Oscillation frequency**	**Overshoot**	**Settling time**
I_{SKO}-U_{ZNS}	390.70	0.09	2327.44 Hz	0.746	2.9 ms
I_{SKO}-U_{CHR}	439.77	0.20	1028.95 Hz	0.533	3.0 ms
I_{SKO}-U_{SO}	374.09	0.84	152.84 Hz	0.008	2.7 ms
I_{SKO}-U_{SKO}	388.67	0.91	84.12 Hz	0.001	3.3 ms

V. CONCLUSION

Due to the gradual increase of renewable energy more inverters are connected to the grid. Their influence on the system stability should be investigated. There are many influencing factors, and the controller parameters are one of them. The controller parameterization of the inverters strongly influences the behavior of the entire system. To investigate the best combination of parameterization methods in the cascaded inverter control system, a simulation of a grid developed with reference to the Cigré reference network of the European medium voltage grid was carried out. For this purpose, a mean-value inverter model is used as a modeling approach. To evaluate the results, the system stability of the test network is examined, where the system is excited by a small signal. The stability analysis is performed by integral criterion and pole analysis. The conjugate pole pair closest to the imaginary axis is selected for the analysis. 20 sets of combinations of five common parameterization methods in the inner and outer control loops in an inverter are tested. After analyzing the system stability, an optimal parameterization method is determined.

The result shows that the optimal combination of parameterization methods in the cascaded control system is a current controller parameterized with the SKO method and a voltage controller parametrized with the SO method (I_{SKO}-U_{SO}).

Also, it can be concluded that the cascaded control system with the same current controller parameters, but different voltage control parameters has similar dynamic behavior. From this, future controller parameterization should focus on the inner current loop in cascaded control system.

VI. REFERENCES

[1] J. G. Ziegler und N. B. Nichols, „Optimum Settings for Automatic Controllers“, *J. Dyn. Sys., Meas., Control*, Jg. 115, 2B, S. 220, 1993.

[2] R. Vilanova, „PID controller tuning rules for robust step response of first-order-plus-dead-time models“ in *2006 American Control Conference*, Minneapolis, MN, USA, Jun. 2006 - Jun. 2006, 6 pp.

[3] K. J. Åström und T. Hägglund, *Advanced PID control*. Research Triangle Park, NC: ISA-The Instrumentation, 2006.

[4] K. J. Åström und T. Hägglund, *PID controllers,* 2. Aufl. Research Triangle Park, N.C.: ISA, 1995.

[5] D. Schroder, Elektrische antriebe - grundlagen: Mit durchgerechneten ubungs- und prufungsaufgaben. [Place of publication not identified]: Springer Vieweg, 2013.

[6] S. N. Vukosavic, *Digital Control of Electrical Drives*. [New York]: Springer Science+Business Media, LLC, 2007.

[7] H.-W. Philippsen, Einstieg in die Regelungstechnik: Vorgehensmodell für den praktischen Reglerentwurf ; mit 17 Tabellen. München, Wien: Fachbuchverl. Leipzig im Carl-Hanser-Verl., 2004.

[8] O. Föllinger, F. Dörrscheidt und M. Klittich, *Regelungstechnik: Einführung in die Methoden und ihre Anwendung,* 8. Aufl. Heidelberg: Hüthig, 1994.

[9] O. Föllinger und F. Dörrscheidt, *Regelungstechnik: Einführung in die Methoden und ihre Anwendung,* 10. Aufl. Heidelberg: Hüthig, 2008.

[10] D. E. Rivera, M. Morari und S. Skogestad, „Internal model control: PID controller design“, *Ind. Eng. Chem. Proc. Des. Dev.*, Jg. 25, Nr. 1, S. 252–265, 1986.

[11] H. Lutz und W. Wendt, *Taschenbuch der Regelungstechnik: Mit MATLAB und Simulink,* 10. Aufl. Haan-Gruiten: Verl. Europa-Lehrmittel, 2014.

[12] Michael Schärfenberg, „Untersuchung der Wechselwirkungen zwischen leistungselektronisch integrierten Netzelementen im Verteilernetz“. Master, Technische Universität Ilmenau, Germany, 2017.

[13] C. A. Smith und A. B. Corripio, Principles and practice of automatic process control, 1985.

[14] P. Dessen, S. Blanquet, G. Zaccai und B. Jacrot, „Antico-operative binding of initiator transfer RNAMet to methionyl-transfer RNA synthetase from Escherichia coli: neutron scattering studies“ , *Journal of molecular biology*, Jg. 126, Nr. 3, S. 293–313, 1978.

Four-quadrant DC converter analysis for hoisting machine drive applications

Bartlomiej Tomasz Madura
Otto-von-Guericke Universität
Magdeburg
Magdeburg, Germany
bartlomiej.madura@ovgu.de

Abstract— **Mining hoists are machines that require high torque operation with low rotational speeds. For such applications high power direct current motor based drives can be relevant. Due to high costs connected with the investment and operation of the hoist, choice of power electronics drive converter is of high significance. Converter topology influences drive dynamics as well as initial costs and power losses. This paper presents a comparative analysis of four-quadrant converter solutions for bidirectional hoisting machine drives with separately excited DC machine. Three drive topologies, using Semiconductor Controlled Rectifier based dual-converter in armature circuit, as well as dual converter and a half-bridge DC/DC converter in excitation circuit were described. The dual-converter in armature and half-bridge in excitation circuit were simulated. Dynamic performance analysis shows that reversion of armature current leads to fastest motor response.**

Keywords—AC-DC power converters, DC-DC power converters, DC motors, Drives, Simulation

I. INTRODUCTION

High power AC/DC and DC/DC power converters that enable four-quadrant operation in current/voltage coordinate system are finding application in many systems varying from DC drives, HVDC transmission systems, electric vehicle on-board power systems and energy storage.

High power DC machine drives are still common in mining hoist applications, due to long time of operation and amortization. Because of the need of lowering as well as pulling up the mining vessel it is necessary to supply them through converters that are able to work in four-quadrant operation mode.

Reversion of DC motor can be achieved either through reversion of armature or excitation currents, which leads to different possibilities of drive topologies, characterized trough different dynamic properties.

Basic solution for bi-directional DC machine drives is Semiconductor Controlled Rectifier (SCR) based dual-converter topology described in detail in [1]. Supplying armature or excitation circuit of a separately excited DC machine leads to different dynamics of torque inversion, which may be crucial factor for choosing converter topology. Based on a DC machine mathematical model, it is to be expected that current reversion dynamics will be higher in case of bidirectional operation of armature converter, due to lower time constant associated with armature winding [2]. Further improvement of SCR dual-converter based drive solution can be achieved through application of more complex firing angle control unit [3] [4].

An alternative solution enabling four-quadrant DC drive operation is the use of transistor based DC/DC converters. Due to high switching frequencies of the state of the art self-commutated semiconductor switches, high current control dynamics and improved efficiency can be expected [5]. Additionally, novel DC/DC converter topologies [6], often implementing soft-switching techniques [7] [8] or more complex PWM control approaches, lead to further improvement of drive properties [9].

This paper presents basic analysis of three different four- quadrant DC machine drive solutions:

a) SCR dual-converter supplying armature circuit
b) DC/DC half-bridge converter supplying excitation circuit
c) SCR dual-converter in excitation circuit

For drive topologies a) and c) basic simulations using Matlab Simulink software have been implemented.

Basic description of converter topologies, with corresponding control techniques as well as supplementary information about electromagnetic interferences caused by the converter are presented in section 2. Section 3 presents separately excited DC motor mathematical model. In section 4 DC motor drive of mining hoists are described. Results of simulations and their comparison are presented in sections 5 and 6.

II. POWER CONVERTER TOPOLOGIES

A. Controlled Rectifiers

Rectifiers are power electronic converters enabling transforming AC input signals into DC output signals. Basic building block of rectifiers is a unidirectional semiconductor switch (power diode) or a thyristor in case of controlled rectifiers. Self-switching devices such as Insulated-gate bipolar transistors (IGBT) or Metal-oxide field effect transistors (MOSFET) might as well be implemented as power switches in controlled rectifier topologies.

Controlled rectifier enables smooth regulation of DC output voltage and/or current, trough adjustment of firing angle.

Delaying the activation of a thyristor in relation to zero crossing of AC supply voltage leads to reduction of DC output voltage mean value. Basic topology of controlled rectifiers permits two quadrant operation mode. In rectifier mode the current and voltage have the same direction and the energy is transported from the source to the load. If the load is able to store the energy, as in case of a DC motor and the primary source can accept the surplus energy, converter can work in inverter mode, in which the flow of energy is reversed. In both cases the current direction stays unchanged.

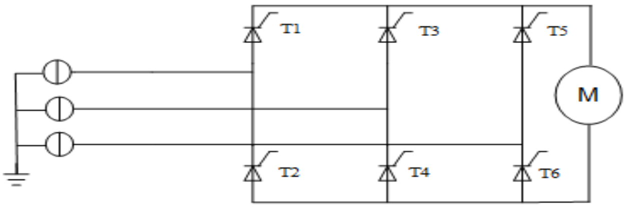

Figure 2.1 Three-phase B6C rectifier topology

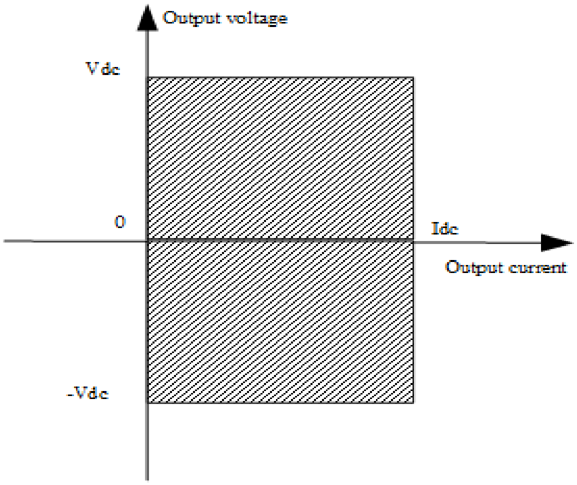

Figure 2.2 Two-quadrant operation of a rectifier

In many applications, such as DC motor drives, it is required to operate in all four quadrants, where the current flows in both directions. Bidirectional voltage and current in a rectifier can be achieved through the use of topology known as dual rectifier converter. One possible solution of such converters is antiparallel connection of two two-quadrant controlled rectifier bridges.

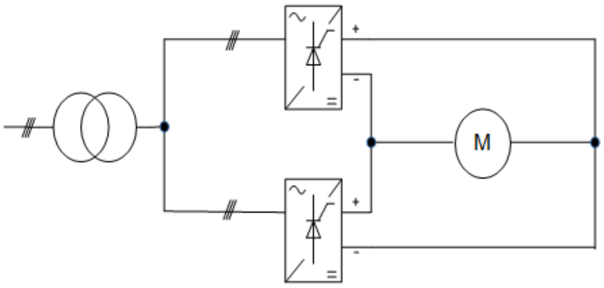

Figure 2.3 Reversing rectifier supplying a DC motor

Two bridges of dual converter can be controlled either symmetrically or alternatively, leading to two basic control schemes. In case of alternating control, only one bridge is active at a time. During reversal of the current direction, a time gap between firing the second bridge is needed, in order to prevent short-circuiting of load. In symmetrical control, both bridges can operate at the same time. This leads to the flow of balancing currents between converters, due to voltage differences at their terminals. Symmetrical operation allows higher dynamics of current reversal and causes dead time to be obsolete. Inductive filters in DC-links are necessary in order to limit the balancing currents.

Due to the switch mode working principle of power electronic converters, some level of electromagnetic interference is always generated. In high power applications like electric drive, static compensators or high voltage transmission systems, power quality associated with converter topology might be a crucial factor for choosing power converter topology. In case of thyristor based controlled rectifiers, it is possible to describe the harmonics generation level trough simple form:

$$h = n\,p \pm 1 \tag{1}$$

where:
h – order of generated harmonics
$n = \{1,2,3,\ldots\}$
p – pulse number of rectifier circuit

It can be observed that increase in output DC pulse number of converters leads to lower overall harmonics generation. Due to this observation in high power applications rectifiers with increased pulse level are being commonly used. One of such topologies is 12-pulse rectifier. This topology is based on two B6C-Thyristor bridges connected in series. Supply voltage of converter is being provided through three winding transformers, with two secondary windings connected in wye and delta. This leads to achieving of two three-phase AC voltage systems with a 30° angle difference between them. DC output voltage that is acquired has 12 sinusoidal shaped pulses in one AC supply voltage period.

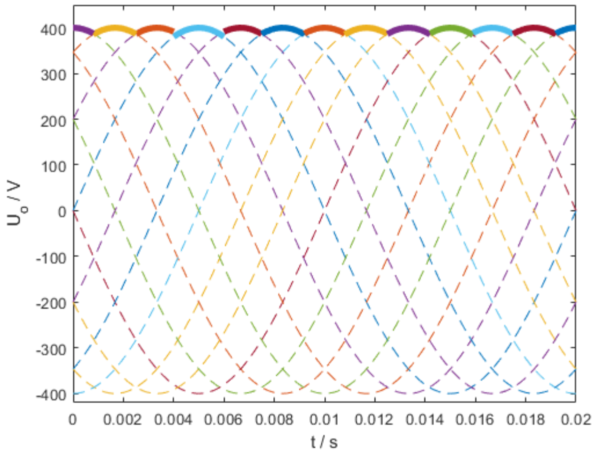

Figure 2.4 12-pulse rectifier bridge voltage output

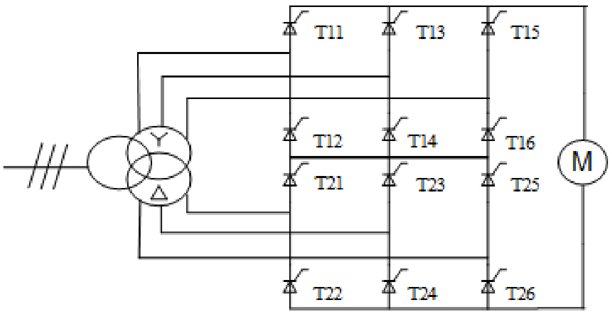

Figure 2.5 12-pulse rectifier bridge topology

Through applying equation (1) to the 12 pulse bridge, it is possible to calculate harmonics being generated:

$$h = \{11,13,22,24,\ldots\}$$

whereas for 6 pulse bridge same equation gives:

$$h = \{5,7,11,13,17,18,\ldots\}$$

It is clearly visible that the use of 12 pulse leads to elimination of harmonics of 5th and 7th order and also reduces the Total Harmonic Distortion (THD) level. Rectifier converter topologies with higher pulse levels such as 24 pulse bridges can also be achieved, although the amount of required semiconductor switches increases and it is necessary to use complicated multi-winding transformers. In practical applications increased complexity of converter topology might outweigh the reduction of electromagnetic interference levels being generated, so some kind of compromise between both factors must be found.

Control of thyristor-based converters is achieved through delaying the firing angle α in relation to the zero-crossing of voltage across the thyristor. Firing angle can be changed in range of $\alpha = <0°;\ 180°>$, where $\alpha = 0°$ corresponds to maximum power transfer from the rectifier to the load. In order to switch the device into conduction mode at required time, firing angle controller must be synchronized with the supply voltage. Proper synchronization is especially valuable when the supply voltage frequency tends to swing, which might lead to regulation errors. Synchronization of ignition controller is achieved by means of phase-locked loops (PLL), which are electronic circuits generating output signal corresponding to phase of input voltage. Triangle or saw voltage signal generator working in phase with phase-locked loop generates reference signal with frequency and phase synchronized with supply AC voltage. Reference signal is then compared with modulating voltage that is set by output signal regulators and firing pulse signal is generated. In case of high inductive loads one firing pulse might not be enough to trigger the conduction mode. A solution to that problem is supplying a longer pulse that will last for whole required conduction time of SCR. This might not be possible in case of transformer isolation between gate driver and the device. In that case two or more shorter pulses must be applied to the gate of the thyristor.

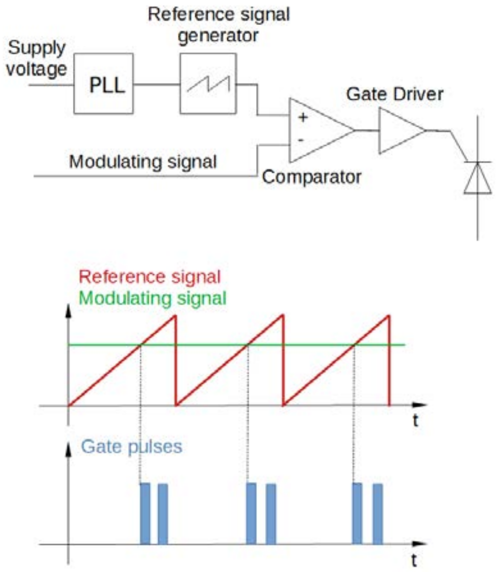

Figure 2.6 Thyristor firing controller with corresponding signals

B. *Transistor based DC/DC choppers*

Another plausible solution of controlled DC voltage source is the application of DC/DC converters controlled by means of Pulse Width Modulation (PWM). Basic topology of bidirectional DC/DC converter is a transistor based half-bridge. It contains two transistors connected between high voltage bus and ground. By applying control scheme based on modulation of periods in which one transistor is conducting, it is possible to achieve controlled DC voltage of both polarities. Due to the fact that transistor can conduct in both directions, it is possible to achieve four-quadrant operation mode, as in case of AC/DC reversing SCR based dual converter circuits.

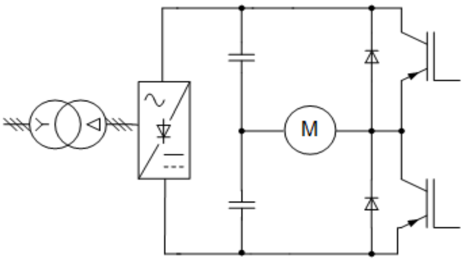

Figure 2.7 DC/DC half-bridge converter topology

Due to the fact that transistors are voltage controlled self-commutated devices, that are able to achieve high switching frequencies, control strategy known as Pulse Width Modulation (PWM) has been widely implemented in case of transistor based converters. In PWM high frequency triangle or saw carrier signal is compared with modulating signal generated by output value controllers. Frequency of carrier signal can vary, depending on type of semiconductor device being used, in range of kHz to MHz in special cases. In case of voltage source bridge and half-bridge converters, it is important to protect the converter against the possibility of short circuiting of the input voltage source. At any given time both switches of one bridge leg cannot conduct together. Protection against short circuiting can be achieved through delaying the positive edge of the gate voltage signal by the time called dead band.

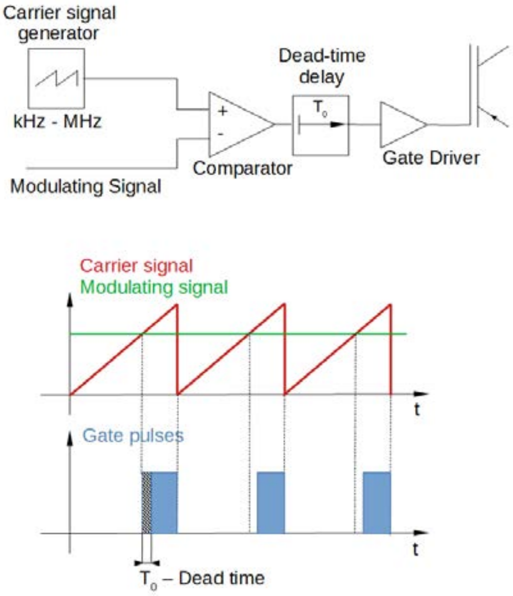

Figure 2.8 Transistor gate controller and generated pulse train

In Pulse Width Modulation control scheme switching frequencies of transistors exceeds the supply voltage frequency. This leads to injection of current harmonics of higher orders to the voltage supply. Additionally, in case of high switching frequencies magnetic interferences with sensitive electronic devices, such as computers and telecommunication devices, might become a significant problem. Trough usage of more complex PWM control schemes such as Space-PWM or Third Harmonic-Injection – PWM better results in relation to power quality and EMC can be achieved.

III. SEPARATELY EXCITED DC MOTORS

Direct current motors have been used in brought variety of drive applications, historically they were widely applied in systems requiring variable speed due to ease of regulation. Development of highly efficient AC/AC frequency converters and in consequence improved control techniques for AC motor drives caused DC motors to be exchanged by highly robust induction motor-based drives. However, in many applications DC motors are still being used.

One form of DC machines is separately excited DC motor. In this motor solution armature and excitation winding voltage is being supplied by two separate sources. This enables a wide range of speed regulation trough control of both armature voltage and excitation flux.

Armature circuit can be solved through equation:

$$U_A(t) = I_A(t)R_A+L_A(dI_A(t)/dt)+E(t) \qquad (2)$$

Where:
$U_A(t)$ – armature voltage
$I_A(t)$ – armature current
R_A, L_A – armature winding resistance and inductance
$E(t)$ – electromotoric force

Excitation circuit can be described with:

$$U_F(t) = I_F(t)R_F + d\Psi_F/dt \qquad (3)$$

Where:
$U_F(t)$ – excitation voltage
$I_F(t)$ – excitation current
R_F – excitation winding resistance
Ψ_F – excitation flux

Based on equivalent circuit of DC machine, by applying the Laplace transform, it is possible to obtain the block diagram of separately excited DC machine. Due to nonlinearity between excitation current and magnetic flux, in order to design control system, it is necessary to linearize the system.

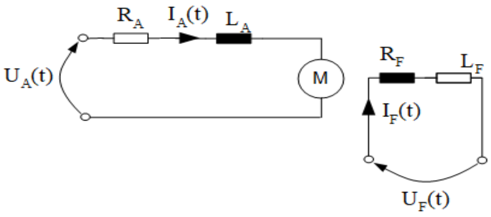

Figure 3.1 Equivalent circuit of separately excited DC machine

IV. MINING HOISTING MACHINE DRIVES

Hoisting machines require the torque in both directions in order to pull up and lower the mining vessel. Due to the mechanical construction drum should rotate with low rotational speed. This can be achieved in two ways, with use of gears between the motor shaft and drum or with application of low speed motor. Direct drives with low speed motors enable reduction of size of machine and overall increase in the efficiency due to the lack of gearing.

One of possible solutions is a DC motor drive with reversion of armature current direction. It contains two controlled rectifier systems supplying the voltage to armature and excitation. Armature winding is connected to 12-pulse dual converter trough three winding wye/wye/delta transformer. Due to large currents flowing in armature circuit alternating control mode is well suited, due to the lack of high power smoothing coils. Regulation of armature is achieved through standard cascade speed-current control circuit with two PI - controllers. Excitation winding is supplied trough 6-pulse controlled rectifier with a P - controller of excitation current.

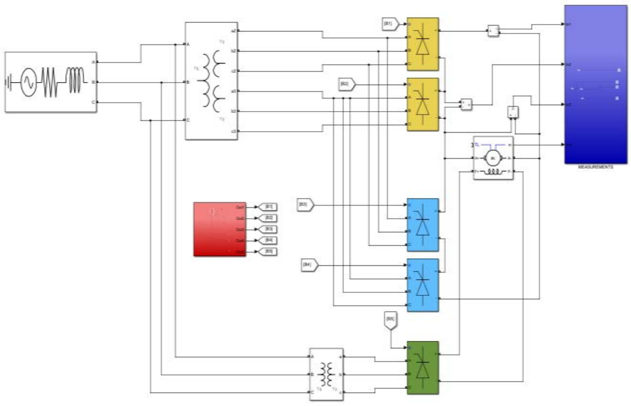

Figure 4.1 Drive system model with reversion of armature circuit created in Matlab Simulink

Alternatively, reversion of torque can be achieved through application of dual converter in excitation circuit. In this case a 6 - pulse dual rectifier is applied in excitation circuit and a 12-pulse non-reversing rectifier bridge in armature circuit.

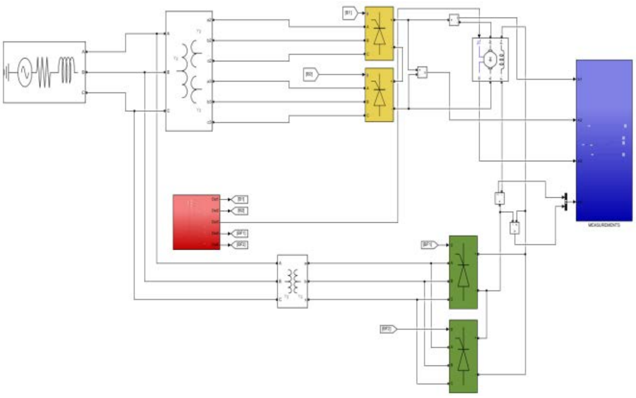

Figure 4.2. Drive system with reversion of excitation circuit trough dual-converter in Matlab Simulink

If higher dynamics of flux direction reversion is required bidirectional DC chopper as excitation power supply can be applied. Armature windings are being powered by 12-pulse rectifier bridge using same control scheme as in previous cases. Use of DC/DC chopper requires a DC voltage supply, which can be realized through standard three-phase rectifier bridge based on power diodes.

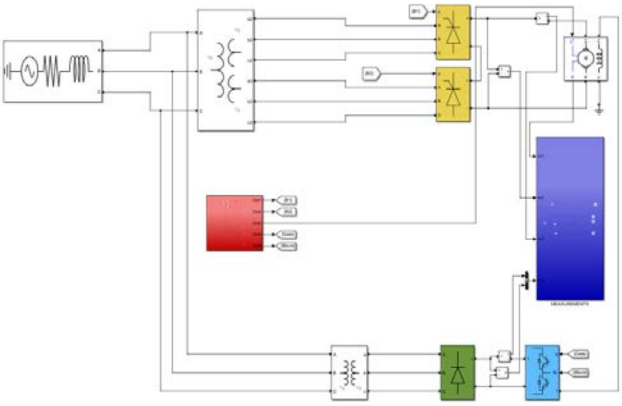

Figure 4.3. Drive model with DC/DC half bridge converter in excitation circuit in Matlab Simulink

V. SIMULATION RESULTS

Results of simulation for armature current reversion are presented in Fig. 5.1. Change of rotor direction from rated speed to rated speed requires 2.6 seconds.

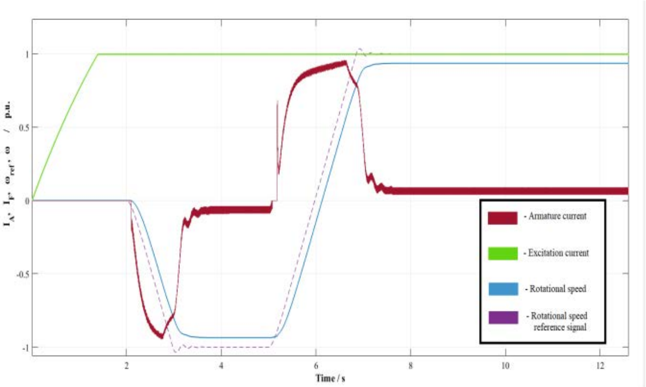

Figure 5.1. Armature current, field current and rotational speed with its reference for reversing rectifier in armature circuit

Second case being tested is excitation reversion with transistor half-bridge DC/DC converter. In this solution reversion of motor rotation direction is less dynamic, requiring 5.3 seconds to reach the rated speed in opposite direction.

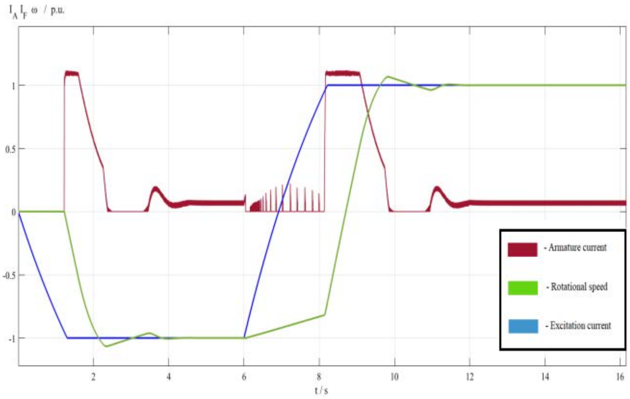

Figure 5.2. Armature current, field current and rotational speed for DC/DC converter in excitation circuit

VI. RESULTS ANALYSIS

Simulation results for two tested topologies and SCR controlled dual rectifier in excitation circuit are compared in Table 6.1.

TABLE 6.1. COMPARISON OF DRIVE CONVERTER TOPOLOGIES

Drive converter type	**Drive solution characteristics**		
	Reversion dynamics	***Number of power electronic switches***	***Current in reversing circuit***
12-pulse armature reversing rectifier	High (2.6 s)	24 SCR in armature circuit + 6 SCR in excitation circuit	High
DC/DC Half-bridge converter in excitation circuit	Medium (5.3 s)	12 SCR in armature circuit + 8 power diodes in excitation circuit + 2 power transistors in excitation circuit	Low
6-pulse excitation reversing rectifier	Low (Expected)	12 SCR in armature circuit + 12 SCR in excitation circuit	Low

Comparing the aspect of current reversion dynamics, the armature current reversion achieves the best results, in relation to tested solution of excitation reversion. Use of DC/DC transistor-based chopper is expected to improve the dynamics compared to SCR based rectifier bridge, due to high switching frequency of power transistors. Armature reversion realization requires additional bridge in armature circuit, which is a high power circuit compared to excitation and as a result would lead to increases of the overall costs of drive system. Detailed comparison of converter costs would require a more in-depth analysis of semiconductor costs. This simple analysis shows some basic tendencies in realization of bidirectional high power DC drives.

REFERENCES

[1] M.H. Rashid, "*Power Electronics Handbook*" , Academic Press, San Diego, 2001, pp.183-210.

[2] Werner Leonhard, "*Control of Electric Drives – Third Eddition*", Springer, 2001, Berlin, pp.77-93.

[3] B. Ilango, R. Krishan, B. Subramanian, S. Sadasivam, „*Firint Circuit for Three-Phase_Bridge Rectifier*", IEEE Transactions on industrial electronics and control instrumentation, vol. ieci-25, no. 1, feb. 1978, pp. 45- 49.

[4] S. C. Gupta, K. Venkatsan, K. Eapen „*A Generalized Firing Angle Controller Using Phase-Locked Loop for Thyristor Control",* IEEE Transactions on industrial electronics and control instrumentation, vol ieci-28, no. 1, february 1981, pp. 46-49.

[5] B. Axelrod, Y. Berkovich and A. Ioinovici, "*Four-quadrant bi-directional drive system based on PWM DC-DC converter,*" *2008 10th IEEE International Workshop on Advanced Motion Control*, Trento, 2008, pp. 377-381.

[6] B. V. Kumar, R. K. Singh and R. Mahanty, "*A modified non-isolated bidirectional DC-DC converter for EV/HEV's traction drive systems,*" *2016 IEEE International Conference on Power Electronics, Drives and Energy Systems (PEDES)*, Trivandrum, 2016, pp. 1-6.

[7] W. Phetphimoon and K. Bhumkittipich, "*Modeling and simulation of bidirectional half bridge dc-dc converter,*" *2016 13th International Conference on Electrical Engineering/Electronics, Computer, Telecommunications and Information Technology (ECTI-CON)*, Chiang Mai, 2016, pp. 1-6.

[8] L. Zhu, "*A novel soft-commutating isolated boost full-bridge ZVS-PWM DC-DC converter for bidirectional high power applications,*" *2004 IEEE 35th Annual Power Electronics Specialists Conference (IEEE Cat. No.04CH37551)*, Aachen, Germany, 2004, pp. 2141-2146 Vol.3.

[9] Kocalmis Bilhan, Ayse & Sunter, Sedat, "*Comparison Of Sinusoidal And Space Vector Pwm Control Techniques For Three-Level Inverter Drives*", *International Journal of Electronics, Mechanical and Mechatronics Engineering (IJEMME),* 2016, Vol 6. Num. 4

Development of an Economic Power Plant Optimization Model for Profit Maximization

Ankit Singh, André Richter
Chair of Electric Power Networks and Renewable Energy Sources
Otto von Guericke University
Magdeburg, Germany
ankit.rtps@gmail.com

***Abstract*—The objective is a new model concept which utilizes the technical and economic properties of both the conventional and the renewable power plants to schedule the power generation in such a way in order to achieve maximum profit. To accomplish that, various options of power markets are explored, such as day-ahead market, continuous intraday market and control reserve market. With all the permutations and combinations available, the one which provides the maximum profit is chosen. In this optimization model, Mixed Integer Linear Programming (MILP) method is used for optimization. This model is suited for 24-hours scheduling, that is for a single day. Hence for different days of a week or a month, different prices are considered and results are compared. The model is obviously profitable due to a large number of conventional and renewable energy sources considered in the case study. This model is capable to handle different scenarios of power generation in different times (future and current) and is, in fact, a kind of a Virtual Power Plant model.**

Keywords—power plant optimization, MILP, profit, conventional energy sources (CES), renewable energy sources (RES), virtual power plant

I. INTRODUCTION

For power plant operator, it is crucial to gain maximum profit. For researchers and power system operators, it is always important to have the knowledge about the infeed from power plants at buses to consider future power flow situations, for example for Day-Ahead Congestion Forecast (DACF) processes and grid expansion. According to the frameworks of ENTSO-E Reserve Resource Process (ERRP) [1], the power producers must provide an estimate of the ratio of power values of their generating capacity to the Transmission Systems Operator (TSO). Hence, this requires the power producer to provide a schedule, mostly to achieve maximum profit.

The main objective is the operational planning of different types of power plants, both conventional and renewable power plants with the capacity of the power plants closely resembling the current and future scenario. Power plant operational planning is done to achieve the required scheduling target for any economic reason, either cost optimization or profit optimization, with the intention of safe operation with the interconnected power system. Several types of constraints, such as technical and economic constraints must be considered while scheduling each type of power plant. Electrical power markets, such as day-ahead market, intraday market, and control reserve market have been considered for the trading of electrical power and to generate an optimized schedule. The optimal schedule development depends on the permanent change of individual market requirements, for example the change of control reserve market in 2018, and the focused markets. This is still an unfocused research question, especially in the context of quarterly hour optimization with respect to day-ahead market, continuous intraday market and control reserve market. Economic optimization in the field of virtual power plants only dealt with:

- Optimum load control
    - Load management from the end customer perspective to minimize the electricity bill [2–5].
    - Load management from a system view to reduce load peak [2,6–8].
- The composition of a virtual power plant as well as the optimal dimensioning of generation plants and storage systems, which is not convenient for the virtual power plant consideration, as a system for the bundling of existing plants [9–14].
- Provision of balancing power, but only from a technical point of view, without consideration of detailed market aspects and framework conditions [4].
- Optimum load dispatch and generation scheduling, where the virtual power plant is not operated as a pure power plant and not primarily from RES installations. The aim of this application is to balance consumption and generation as good as possible [15].
- The power plant is conceptualized in [16] with energy market based behaviour but not presented as a generic model with a defined algorithm or as an algorithm with possible systemic behaviour and subsequent market optimization. Furthermore, intraday trading with ¼-h consideration is not considered in the combined optimization with the day-ahead and reserve power market. As a result, the technical restrictions, such as power gradients in combination with market requirements, are not adequately considered.

Therefore, a power plant schedule optimization tool (MATLAB program) for profit maximization is built with the focus on large conventional power plants and virtual power plants. Also, the program gives the user an opportunity to give a schedule for each kind of generation unit in a power plant portfolio. One of the specialties of this program is that it considers 15-minutes intraday optimization and the individual schedules with respect to the markets and generation types.

II. PROBLEM FORMULATION

A. Distribution of power values for generation

The infeed from the power plants (generation units) at the buses or the grid connection point is divided in a ratio of power values which is based on the frameworks and guidelines of ERRP [1]. The design process and the scheduling of the conventional as well as renewable power plants are based on these guidelines and has been depicted in Fig. 1. Furthermore, day-ahead and intraday trading have also been pointed out.

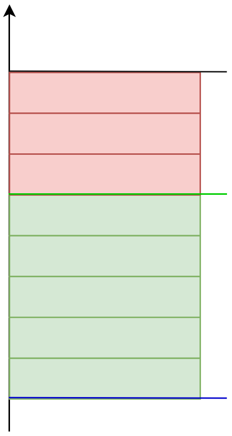

Fig. 1 Overview of the ratio of power values for generators (production) at the grid connection point

Since here the scheduled power P_{Sch} also consists of participation in the day-ahead market and cont. intraday trading, this corresponds to the following equation:

$$P_{\mathrm{Sch}} = P_{\mathrm{DA}} + P_{\mathrm{ID}} + P_{\mathrm{PCR}} + P_{\mathrm{negSCR}} + P_{\mathrm{negMCR}} \quad (1)$$

$\boldsymbol{P_{\mathrm{DA}}}$	Power generated and sold by a power plant in day-ahead auction
$\boldsymbol{P_{\mathrm{ID}}}$	Power generated and sold by a power plant in continuous intraday auction
$\boldsymbol{P_{\mathrm{PCR}}}$	Power reserved for primary control reserve (PCR)
$\boldsymbol{P_{\mathrm{negSCR}}}$	Power reserved for negative secondary control reserve (neg. SCR)
$\boldsymbol{P_{\mathrm{negMCR}}}$	Power reserved for negative minute control reserve (neg. SCR)

B. *Revenue and Costs*

The revenue generated consists of selling the scheduled power from different energy sources in day-ahead market and/or continuous intraday market. Apart from this, revenue is also generated by providing control reserves to the power network. The costs are incurred from the fixed Capital Expenditure (CAPEX), the fixed Operational Expenditure (OPEX), the variable OPEX and fuel costs, the startup costs, the day-ahead variable costs, the cont. intraday variable costs, and the annual auction costs. Equation (2) – (7) represent the revenues generated by selling energy in the auction or costs incurred in the trading and fixed costs.

$$r_{\mathrm{auc.,\,i}}(t) = P_{\mathrm{DA,\,i}}(t) \cdot p_{\mathrm{SP,\,DA}}(t) + P_{\mathrm{ID,\,i}}(t) \cdot p_{\mathrm{SP,\,ID}}(t) \quad (2)$$

$$c_{\mathrm{auc.,\,i}}(t) = P_{\mathrm{DA,\,i}}(t) \cdot c_{\mathrm{vc,\,DA}}(t) + P_{\mathrm{ID,\,i}}(t) \cdot c_{\mathrm{vc,\,ID}}(t) \quad (3)$$

$$c_{\mathrm{fuel,\,i}}(t) = P_{\mathrm{Sch,\,i}}(t) \cdot c_{\mathrm{fc,\,i}} \quad (4)$$

$$c_{\mathrm{isOn,\,i}}(t) = P_{\mathrm{Sch,\,i}}(t) \cdot OPEX_{\mathrm{i}} \quad (5)$$

$$c_{\mathrm{startup,\,i}}(t) = S_{\mathrm{i}}(t) \cdot c_{\mathrm{su,\,i}} \quad (6)$$

$$r_{\mathrm{CR,\,i}}(\mathrm{t}) = P_{\mathrm{PCR,\,i}}(\mathrm{t}) \cdot p_{\mathrm{PCR}}(\mathrm{t}) + P_{\mathrm{posSCR,\,i}}(\mathrm{t}) \cdot p_{\mathrm{posSCR}}(\mathrm{t}) + P_{\mathrm{posMCR,\,i}}(\mathrm{t}) \cdot p_{\mathrm{posMCR}}(\mathrm{t}) + P_{\mathrm{negSCR,\,i}}(\mathrm{t}) \cdot p_{\mathrm{negSCR}}(\mathrm{t}) + P_{\mathrm{negMCR,\,i}}(\mathrm{t}) \cdot p_{\mathrm{negMCR}}(\mathrm{t}) \quad (7)$$

$\boldsymbol{r_{\mathrm{auc.,\,i}}(t)}$	Revenue generated by a power plant *i* by selling power in auction at time interval *t* in €
$\boldsymbol{p_{\mathrm{SP,\,DA}}(t)}$	Selling-price in day-ahead auction at time interval *t* in €/MWh
$\boldsymbol{p_{\mathrm{SP,\,ID}}(t)}$	Selling-price in cont. intraday auction at time interval *t* in €/MWh
$\boldsymbol{c_{\mathrm{auc.,\,i}}(t)}$	Cost incurred by a power plant *i* by selling power in €/MWh
$\boldsymbol{c_{\mathrm{vc,\,DA}}(t)}$	Variable cost-price of day-ahead trading at time *t* in €/MWh
$\boldsymbol{c_{\mathrm{vc,\,ID}}(t)}$	Variable cost-price of day-ahead trading at time *t* in €/MWh
$\boldsymbol{c_{\mathrm{fuel,\,i}}(t)}$	Fuel cost incurred for power plant *i* at time *t* in €/MWh
$\boldsymbol{c_{\mathrm{fc,\,i}}}$	Fuel cost of power plant *i* at time *t* in €/MWh
$\boldsymbol{c_{\mathrm{isOn,\,i}}(t)}$	Operation cost (running cost) incurred for power plant *i* at time *t* in €
$\boldsymbol{OPEX_{\mathrm{i}}}$	Operation cost of the power plant *i* in €/MWh
$\boldsymbol{c_{\mathrm{su,\,i}}(t)}$	Startup Cost incurred for power plant *i* at time *t* in €/startup
$\boldsymbol{S_{\mathrm{i}}(t)}$	Status indicating whether the power plant has been switched on during that interval *t*
$\boldsymbol{c_{\mathrm{startup,\,i}}}$	Startup cost of the power plant *i* in €/switch
$\boldsymbol{r_{\mathrm{CR,\,i}}(t)}$	Revenue generated by a power plant *i* by selling energy as control reserve in time *t* in €
$\boldsymbol{p_{\mathrm{PCR}}(t)}$	Capacity-price for primary control reserve at time *t* in €/MW
$\boldsymbol{p_{\mathrm{pos\,SCR}}(t)}$	Capacity-price for positive secondary control reserve at time *t* in €/MW
$\boldsymbol{p_{\mathrm{neg\,SCR}}(t)}$	Capacity-price for negative secondary control reserve at time *t* in €/MW
$\boldsymbol{p_{\mathrm{pos\,MCR}}(t)}$	Capacity-price for positive minute control reserve at time *t* in €/MW

C. *Objective function*

Since the objective is the maximization of profit generated by selling the power from the generation schedule and providing control reserve services, profits are described as: *Profit = revenue - costs*, which is the basis of the whole optimization. The *revenue* and *costs* are calculated separately but the objective function *Profit* is the difference between these two.

$$\max\,(Profit) = \sum_{t=1}^{96} \sum_{i=1}^{7} r_{\mathrm{auc.,\,i}}(\mathrm{t}) + r_{\mathrm{CR,\,i}}(\mathrm{t}) - c_{\mathrm{auction,\,i}}(\mathrm{t}) - c_{\mathrm{fuel,\,i}}(\mathrm{t}) - c_{\mathrm{isOn,\,i}}(\mathrm{t}) - c_{\mathrm{startup,\,i}}(\mathrm{t}) - C_{\mathrm{fix.\,auc.}} - C_{\mathrm{fix.\,OPEX}} \quad (8)$$

Profit	Total profit obtained after the optimization process is complete
$\boldsymbol{C_{\mathrm{fix.\,auc.}}}$	Fixed annual auction or trading cost (constant and just for one time duration)
$\boldsymbol{C_{\mathrm{fix.\,OPEX}}}$	Fixed operating cost (constant and just for one time duration)

D. *Constraints*

The types of constraints that have been considered in this research paper are defined below.

1) Ramp-up and ramp-down constraints:

Mathematically, it can be described as the rate of change of net power with respect to change in time. The ramp rate is specified by MW/min or in percentage of maximum load/min (P_{Max}/min) [17]. For the sake of simplicity and to save computation time, it can be assumed from [17] and [18] that the power plant is allowed to jump from 0 to $P_{\min}$ and vice versa and therefore the equation can be defined as shown in Equation (9) – (10).

$$P(t+1)-P(t)\leq RUL+\max(P_{\min}-RUL,0)\cdot S(t+1) \qquad (9)$$

$$\begin{aligned} P(t)-P(t+1)\leq \max(P_{\min},RDL)- \\ -\max(P_{\min}-RDL,0)\cdot S(t+1) \end{aligned} \qquad (10)$$

$\boldsymbol{P(t+1)}$	Scheduled power at time interval $t+1$
$\boldsymbol{P(t)}$	Scheduled power at time interval t
RUL	Ramp-up limit of a power plant in MW/min
$\boldsymbol{P_{\min}}$	Minimum power capacity of a power plant in MW
RDL	Ramp-down limit of a power plant in MW/min

2) *Distribution of power scheduling*

As described in A and with the description of Fig. 1, the distribution of power should follow the following constraint:

$$\begin{aligned} P_{\max}\geq P_{\mathrm{DA}}+P_{\mathrm{ID}}+2P_{\mathrm{PCR}}+P_{\mathrm{posSCR}} \\ +P_{\mathrm{posMCR}}+P_{\mathrm{negSCR}}+P_{\mathrm{negMCR}} \end{aligned} \qquad (11)$$

$\boldsymbol{P_{\max}}$	Maximum power capacity of a power plant in MW
$\boldsymbol{P_{\mathrm{posSCR}}}$	Power reserved for positive secondary control reserve (neg. SCR)
$\boldsymbol{P_{\mathrm{posMCR}}}$	Power reserved for positive minute control reserve (neg. SCR)

3) *Other technical constraints*

The other technical constraints, such as minimum and maximum load constraint, start-up time constraint, minimum up time and down time constraint can be found and described in [19].

III. CASE STUDY

A case study was used and the above-mentioned process was implemented on the case to demonstrate the profit optimization algorithm. The results were documented and then a graphical user interface was designed to make the system more user-friendly and very adaptive for changing the parameters.

A. *Optimization technique*

The optimization technique has been inspired from [19] and therefore MILP (Mixed Integer Linear Programming) has been used as many of the constraints are restricted to integer values only. The detailed description of the whole process of optimization can be found in [19]. However, the difference in this research is that the problem-based method was used instead of the solver-based method. The advantage being that: creation and debugging are easier and the objective function and the constraints can be represented symbolically. An overview of the processing can be visualised from Fig. 2.

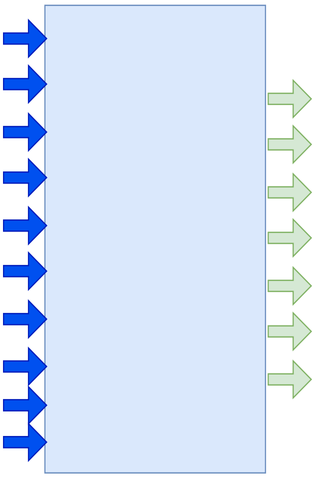

Fig. 2 Block diagram describing the whole process of optimization

B. *Power plant input characteristics*

The input consists of the different types of installed power and their technical characteristics, and other constant data which has been detailed in the section below. In TABLE I, the summarized characteristics of the seven types of power plants have been enlisted. Out of these seven, four are CES and the remaining three are RES. The installed capacity has been assumed keeping in mind the annual average distribution of energy produced by these sources in Germany, in order to be as realistic as possible according to the current scenario [20].

Along with the costs associated with the handling and operation of the power plants that has been described in the TABLE I, there are some fixed and variable costs or fees associated with the stock market which depends on the energy sold and some yearly fixed costs as specified in TABLE II. These costs can play a significant role in the scheduling of a power plant owing to its variable nature.

TABLE I TECHNICAL AND ECONOMIC CHARACTERISTICS OF POWER PLANTS

	Lignite	**Hard coal**	**CCGT**	**GT**	**Bio**	**PV**	**Wind**
Technical characteristics							
Start-up time (hours)	5	4	5	1	3	0	0
RU lim. (% of P_n/min)	4	6	5	10	11.5	100	100
RD lim. (% of P_n/min)	4	6	5	10	11.5	100	100
Min. load (% of P_n/min)	50	25	33	20	40	0	0
Max. load (% of P_n)	100	100	100	100	100	100	100
Min. up time (hours)	4	4	4	1	0.001	0	0
Min. down time (hours)	4	4	2	1	0.001	0	0
P_n or installed capacity (MW)	725	388	216	216	207	518	171
Economic characteristics							
CAPEX (€/kW)	1900	1650	950	500	3000	700	1750
OPEX fixed cost (€/MW)	36000	32000	22000	20000	120000	17500	30000
OPEX var. cost (€/MW)	5	5	4	3	5	3.59	5
Fuel costs (€/MWh)	1.8	9.6	21	21	30.3	0	0
Start-up costs (€/MW)	4.425	4.425	69.44	2.48	0.56	0	0

Amongst the RES such as PV and Wind, the amount of energy it can produce on the following day depends on the forecast of the weather i.e. amount of solar irradiation and wind speed respectively. This difference of power between the installed capacity and the forecast generation gives rise to the requirement of control reserves. But this is where the concept of a Virtual Power Plant (VPP) converts this uncertainty to stability. VPP consists of numerous types of power plants. These power plants cannot participate in the power market in their individual existence. But with the system of VPP, these power plants can be managed together as a single power producing unit, thereby having the capability in itself to provide stable power to the grid. The difference in the forecast and the installed capacity can be balanced in two ways. Firstly, this can be balanced with the help of very flexible power units such as Bio power plant or CCGT or a GT power plant which have a decent ramping and start-up capabilities. Secondly, by utilizing this difference of power to provide control reserve services, both for negative and positive power. Of course, since the goal of this research is to provide maximum profit, irrespective of what the demand is, this dynamic nature of RES like PV, wind and flexible sources such as Bio and Gas turbines can be used to supply control reserves if profitable.

TABLE II. ELECTRICITY STOCK MARKET COSTS

	Cost
Day-ahead var. cost	0.04 €/MWh
Cont. Intraday var. cost	0.08 €/MWh
Fixed auction fees	10000 €/year

A summary of the forecast data has been described graphically to get an overall idea of the system presented to the optimizer. Fig. 3 represents a graphical overview of the power forecast for PV power plant and Wind power plant. Rest of the data can be referred from [19].

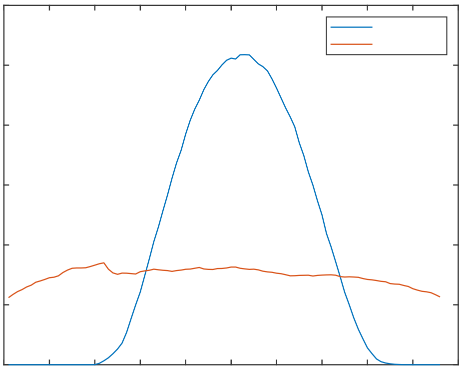

Fig. 3. PV and Wind forecast for 24 hours

C. Result of the case study

With the implementation of the day-ahead and cont. intraday optimization, the scheduling of power plants for different electricity markets along with the supply of control reserves can be determined. The unique thing about this scheduling is that it not only displays the amount of power scheduled for the respective markets, but it also determines the contribution of each power plant for the concerned market. The general structure of the results obtained through the optimization programming is as displayed in Fig. 4.

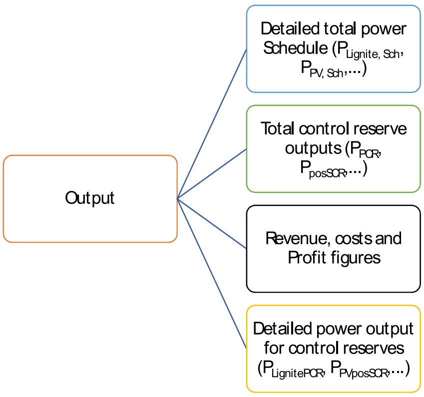

Fig. 4 Structure of the results obtained

1) Scheduled power output for P_{Sch}, P_{DA}, and P_{ID}

Fig. 5 represents the scheduled output of P_{Sch} according to the equality and inequality constraint mentioned in II.A and II.D. The graphs show the power output per quarterly hour over a day with 96-time intervals for each kind of power plant. This scheduled power is the infeed into the system and represents the sum of participation for cont. intraday, day ahead and negative control reserve. Fig. 6 and Fig. 7 represents the P_{DA} and P_{ID} respectively and according to the Equation (1). With intraday and day-ahead participation schedule, especially in the middle of the day the expected intraday, price is higher than day-ahead price.

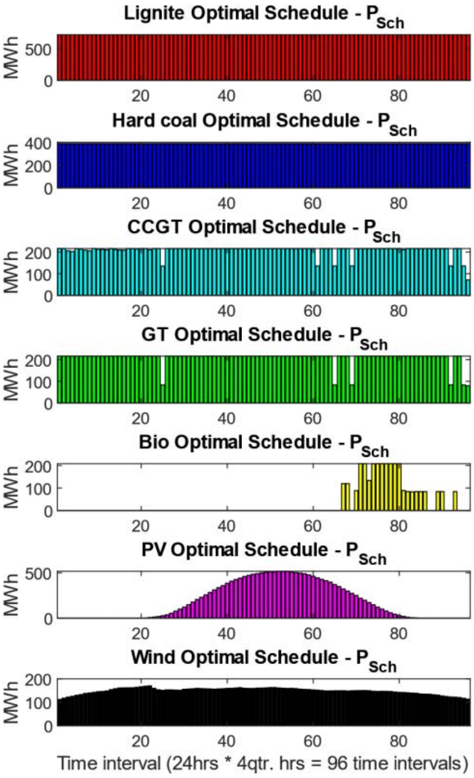

Fig. 5 Scheduled power P_{Sch} from the power plants

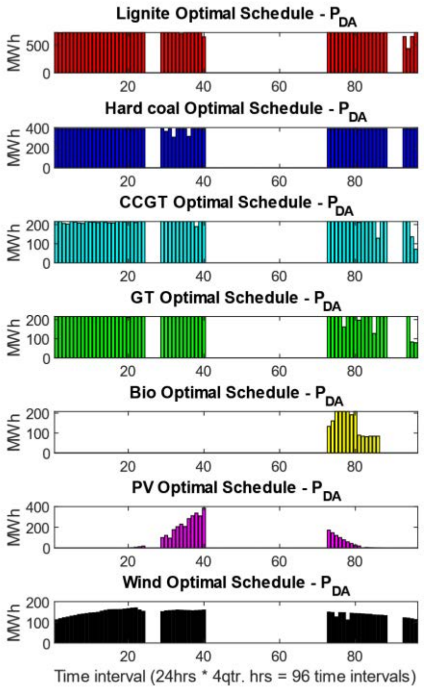

Fig. 6 Scheduled power assigned for day-ahead trading

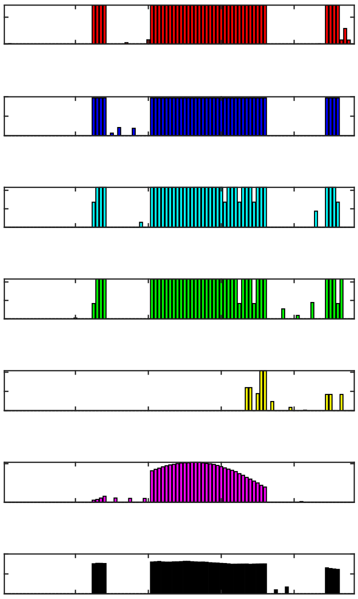

Fig. 7 Scheduled power assigned for intraday trading

2) *Generation schedule for control reserves*

As described in Equation (1), the scheduled power P_{Sch} is divided into energy traded in the day-ahead, intraday and negative control reserve market. According to the results obtained, there is no negative control reserve, which means that the whole power assigned in the P_{Sch} is distributed between P_{DA} and P_{ID}. According to the Equation (11), there is a possibility that the remaining capacity for the power plants can be used for trading for the positive control reserves. This conclusion can be made that the remaining capacity of the power plants has been used in providing positive SCR as well as positive MCR. This is done because of the high possible profit in positive control reserve market. However, at the moment in the ERRP process, it is not clear which of the power plants is serving for the respective positive control reserves. This thing is sorted out in Fig. 8 and shows exactly which of the power plants is providing for the positive control reserves.

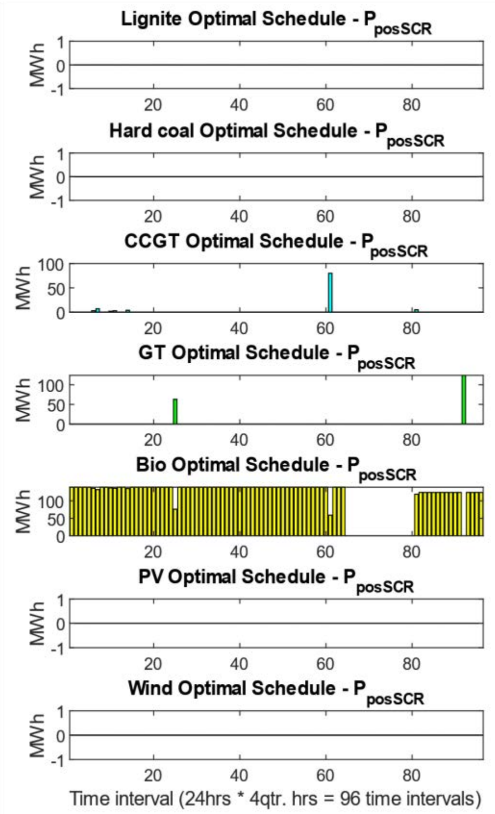

Fig. 8 Scheduled power assigned for pos. SCR

D. *Profit obtained*

The below equations are based on the equations already defined in Equation (2) – (8). As can be seen from the above calculation, the big chunk of costs belongs to the fuel cost and the variable operating cost, while the revenues generated from power sold in auctions is significantly greater than that sold for control reserves. This shows that the prices are such that it is economically and technically more profitable to sell power in the auction. The period for which the power plant is tending to generate more power seems to be the period for which price must be higher.

$$
\begin{aligned}
&R_{\mathrm{auc}} = R_{\mathrm{DA}} + R_{ID} = 1'568'710.00 \text{ €} \\
&R_{\mathrm{CR}} = R_{\mathrm{PCR}} + R_{\mathrm{posSCR}} + R_{\mathrm{negSCR}} = 20'421.70 \text{ €} \\
&C_{\mathrm{var,auc}} = C_{\mathrm{DA}} + C_{\mathrm{ID}} = 2'650.94 \text{ €} \\
&C_{\mathrm{fuel}} = 353'920.00 \text{ €} \\
&C_{\mathrm{isOn}} = 206'020,00 \text{ €} \\
&C_{\mathrm{startup}} = 33,28 \text{ €} \\
&C_{\mathrm{fix,costs}} = C_{\mathrm{fix,auc}} + C_{\mathrm{fix,OPEX}} = 787.65 \text{ €} \\
&Profit = R_{\mathrm{auc}} + R_{\mathrm{CR}} - C_{\mathrm{var,auc}} - C_{\mathrm{fuel}} \\
&\qquad - C_{\mathrm{isOn}} - C_{\mathrm{startup}} - C_{\mathrm{fix,costs}} \\
&\qquad = 1'025'719.12 \text{ €}
\end{aligned}
$$

IV. CONCLUSION AND SCOPE OF THE RESEARCH

It has been found that many studies have already dealt with optimization methods for economic power plant optimization model, but no comprehensive overall system requirements and optimizations on a detailed quarter-hourly time interval basis have been considered so far. In this paper, an overall quarterly hour optimization was presented. The functionality for pooling of conventional generation units and renewable energy sources have been demonstrated. Furthermore, the presented model can be used independently of the size of the power plant pool for optimal scheduling, for strategic portfolio management and for virtual power plant optimization.

Also, it has been found that no other research work has focused on the detailed scheduling of each of the power plants for each of the intervals in each of the different types of the electricity market, especially in the control reserve market, which is a specialty for this paper. Furthermore, this paper shows a possibility to generate a schedule for each type of generation unit, for better integration in power system planning processes. With increased knowledge concerning the infeed structure of pooling operator, the system operator gets the chance for an improved DACF planning process.

V. REFERENCES

[1] Audorff H, Azzam J, Zimmermann U, Thiele M, Schlunke S, Wozny J. Einführung des ERRP- Planungsprozesses zur Meldung von Kraftwerksdaten an die ÜNB: Implementation Guide für Deutschland;Version 1.4.

[2] Ruiz N, Cobelo I, Oyarzabal J. A direct load control model for virtual power plant management. IEEE Transactions on Power Systems 2009;24(2):959–66.

[3] Mohsenian-Rad A-H, Leon-Garcia A. Optimal residential load control with price prediction in real-time electricity pricing environments. IEEE Trans. Smart Grid 2010;1(2):120–33.

[4] Goel L, Wu Q, Wang P. Fuzzy logic-based direct load control of air conditioning loads considering nodal reliability characteristics in restructured power systems. Electric Power Systems Research 2010;80(1):98–107.

[5] Jin T-H, Park H, Chung M, Shin K-Y, Foley A, Cipcigan L. Review of Virtual Power Plant Applications for Power System Management and Vehicle-to-Grid Market Development. Korean Institute of Electrical Engineers 2016;65(12):2251.

[6] Luo Z, Kumar R, Sottile J, Yingling JC. An MILP formulation for load-side demand control. Electric machines and power systems 1998;26(9):935–49.

[7] Nehrir MH, LaMeres BJ. A multiple-block fuzzy logic-based electric water heater demand-side management strategy for leveling distribution feeder demand profile. Electric Power Systems Research 2000;56(3):225–30.

[8] Gatsis N, Giannakis GB. Residential Load Control: Distributed Scheduling and Convergence With Lost AMI Messages. IEEE Trans. Smart Grid 2012;3(2):770–86.

[9] Teleke S, Baran ME, Bhattacharya S, Huang AQ. Optimal control of battery energy storage for wind farm dispatching. IEEE Transactions on Energy Conversion 2010;25(3):787–94.

[10] Grillo S, Marinelli M, Massucco S, Silvestro F. Optimal management strategy of a battery-based storage system to improve renewable energy integration in distribution networks. IEEE Transactions on Smart Grid 2012;3(2):950–8.

[11] Chen C, Duan S, Cai T, Liu B, Hu G. Optimal allocation and economic analysis of energy storage system in microgrids. IEEE Transactions on Power Electronics 2011;26(10):2762–73.

[12] Sugihara H, Yokoyama K, Saeki O, Tsuji K, Funaki T. Economic and efficient voltage management using customer-owned energy storage systems in a distribution network with high penetration of photovoltaic systems. IEEE Transactions on Power Systems 2013;28(1):102–11.

[13] Yuan Y, Li Q, Wang W. Optimal operation strategy of energy storage unit in wind power integration based on stochastic programming. IET renewable power generation 2011;5(2):194–201.

[14] Ghavidel S, Li L, Aghaei J, Yu T, Zhu J. A review on the virtual power plant: Components and operation systems: In: IEEE International Conference on Power System Technology.

[15] Kamphuis IG, Kok J, Wamer CJ, Hommelberg MPF. Massive coordination of residential embedded electricity generation and demand response using the PowerMatcher approach: In: The 4th International Conference on Energy Efficiency in Domestic Appliances and Lighting-EEDAL06.

[16] You S, Træholt C, Poulsen B. Developing virtual power plant for optimized distributed energy resources operation and integration 2010.

[17] Wang J, Shahidehpour M, Li Z. Security-Constrained Unit Commitment With Volatile Wind Power Generation. IEEE Trans. Power Syst. 2008;23(3):1319–27.

[18] Richter A, Hauer I, Wolter M. Algorithms for Technical Integration of Virtual Power Plants into German System Operation. Adv. sci. technol. eng. syst. j. 2018;3(1):135–47.

[19] Fraunhofer Institute for Solar Energy Systems ISE. Electricity generation | Energy Charts. [October 23, 2018]; Available from: https://www.energy-charts.de/energy.htm.

Review of Components and Materials for Proton Exchange Membrane Unitized Reversible Fuel Cells

Magsud Hasanov
Mentor: Philipp Kuehne
Faculty of Electrical Engineering and Information Technology
Otto von Guericke University
Magdeburg, Germany
magsud.hasanov@ovgu.de

***Abstract*—This article is reviewing the most important components and materials used in proton exchange membrane unitized reversible fuel cells. The first section reviews the History and Working principle of fuel cells, as well as the main applications. The second section paper will be devoted particularly to the proton exchange membrane unitized reversible fuel cells and its components and materials. In the end, several conclusions are made and the used literature is given.**

***Index Terms*—history of fuel cells, membrane electrode assembly, unitize reversible fuel cell, discrete reversible fuel cell, polymer electrolyte membrane, electrodes, catalyst, gas diffusion layer, balance-of-plant.**

I. INTRODUCTION

The fuel cell is an electrochemical stationary device, that directly converts the chemical energy into the electricity. The process inside of it is simply a redox reaction, divided into two separate oxidation and reduction reactions (in one cell) [1] [2]. On practice, to obtain the required output of energy, the cells, where these processes occur, are merged in one group, called stack. The number of connected in series cells in stack depends on the required voltage output. The main features of fuel cells are:

1) the energy conversion from chemical to electrical is considered to be direct in this appliances [2];
2) fuel cell continues its operation as long as there is external ingredients supply, and productivity with the lifespan is matter of components degradation [2] [3];
3) relatively high efficiency of energy conversion, compared to the one in combustion process. Also, the efficiency is not limited to the Carnot Cycle‘s efficiency, which is the highest possible efficiency for an ordinary combustion engine [3];
4) the efficiency mainly does not depend on the load [4];
5) the lack or relatively small amount of harmful products and effects [5];
6) high energy capacity per cubical meter of volume occupied [5];
7) no rotational parts are used, therefore less power losses and more reliability [5].

Generally, for such purposes the reaction between hydrogen and oxygen is used. Hydrogen can be in pure form or within other substances, such as natural gas and etc. Which form to use is a matter of the catalyst on the anode side. Oxygen is generally taken from the air. The final product, which generally depends on the type of fuel cell, is harmless water or its vapour (depending on the operations temperature), nitrogen dioxide, heat and etc. [4]. Currently, there are many uses and applications of fuel cells as an electrical power source with the efficiency about 40 % - 60 %. Although, the heat generation is considered as a byproduct in portable and transport applications and calculated as a power loss, using the Combined Heat and Power (CHP) generation can enhance the efficiency up to 80 % - 85 % [4].

A. History of Fuel Cells

The technology of fuel cells has done a long way since it first was discovered by a Welsh physicist William Grove in 1838 [1]. The first sketch of fuel cells prototype is shown in Figure 1. Nearly at the same time the work regarding fuel cells was published in Philosophical Magazine by a German-Swiss chemist Christian Friedrich Schoenbein [2].

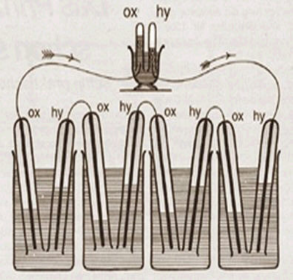

Fig. 1. William Grove‘s ”gas battery” - the first prototype of fuel cell [1].

The quick fact list in chronological sequence, provided below shows the development of the fuel cell technology throughout the years:

- **1801**. Humphry Davy discovers the principles of electrochemistry [6];
- **1838**. W. Grove invented the gas battery - the first prototype of fuel cell [7] [8]. In the same year, C. F. Schoenbein published work of first electricity generated from hydrogen and oxygen, produced from water [6] [9];
- **1889**. Ludwig Mond and Carl Langer continued the idea and officially used the term fuel cell [9];

- **1893**. Friedrich Wilhelm Ostwald - one of the founders of physical chemistry, - explained the role of each fuel cell‘s element [7];
- **1955-1958**. The first prototype of Proton Exchange Membrane (PEM) Fuel Cell was constructed by General Electric. This patent was called Grubb-Niedrach fuel cell [8] [9];
- **1959**. Francis Thomas Bacon developed first documented and working stationary fuel cell with rated capacity 5 kW [10] [11];
- **1964**. One-man underwater research vessel,that was powered by a 750-watt fuel cell, again the product of Allis-Chalmers company [8];
- **1965**. NASA‘s Project Gemini used the fuel cells to produce energy and drinkable water. It is considered as the first commercial use of this technology [9];
- **1990**. Solar-Wasserstoff-Bayern, which is the world‘s first solar-powered hydrogen production facility began its work [13];
- **2002**. The first rail way transport running on a hydrogen, so-called hydrail, was shown in Val-d’Or, Canada [12]. In the same year, Type 214 submarine, using Siemens Proton Exchange Membrane fuel cell, was built [16] ;
- **2004**. The first German Autonomous Underwater Vehicle, called DeepC and using the fuel cell to power itself, was shown [14];
- **2008**. Honda starts giving to a leasing its first Fuel Cell Electric Vehicle (FCEV) - Honda FCX-V4. It is the first step in commercialisation of hydrogen fueled automobiles [10] [12] [17];
- **2013**. Falkenhagen power to gas station - the first commercial one of its kind, starts the production of hydrogen from the power from grid [18];
- **2016**. Toyota Mirai as the first generally affordable hydrogen automobile is on the sale [19];
- **2017**. The Hydrogen Council Initiative, the platform for development and encouragement of investments in the hydrogen and fuel cells sphere, starts to function [20].

B. The working principle of fuel cell

General idea of fuel cell‘s work is to obtain the useful electrical energy from the redox reaction between two reagents. Depending on the type of the fuel cell, the components may vary, but the common ones for all types are:

1) Anode;
2) cathode;
3) and electrolyte.

The Membrane Electrode Assembly (MEA) is collective name for combination of the cathode, anode and electrolyte between them. In MEA, the main work of fuel cell is done. However, it is not the only part of whole fuel cell stack, the rest will be discussed below. One must mention, that the biggest price tag of fuel cell comes exactly from the MEA‘s cost, as it contains very expensive materials, i.e. Platinum (Pt) and ionomer electrolyte [21].

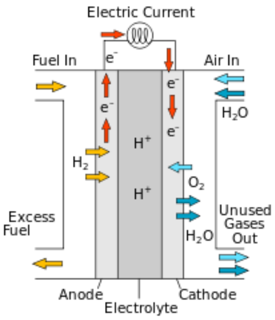

Fig. 2. Fuel cell with proton conducting electrolyte [15].

To show simple work principle the hydrogen / oxygen based fuel cell with proton conducting electrolyte is considered, as shown in Figure 2. On the anode side the Hydrogen Oxidation Reaction (HOR) occurs:

$$H_2 \rightleftharpoons 2H^+ + 2e^- \tag{1}$$

On the cathode side the Oxygen Reduction Reaction (ORR) occurs:

$$\frac{1}{2}O_2 + 2H^+ + 2e^- \rightleftharpoons H_2O \tag{2}$$

Both (1) and (2) would give the full redox reaction:

$$H_2 + \frac{1}{2}O_2 \rightleftharpoons H_2O \tag{3}$$

Both hydrogen and oxygen (from air) are fed into the fuel cell through the flow-fields plates on each side, which are specially designed to cover more area. Then gases are flowing to the Gas Diffusion Layers (GDL), that distribute reagents evenly over the entire surface of Catalysts Layers (CL). Reactions (1) and (2) occur on the hydrogen and oxygen sides, respectively. The GDL, catalyst layer and electrolyte create what is called triple-phase boundary. The ions produced in HOR, travel through the ionomer electrolyte, which actually insulate electrodes from each other, to the cathode side, where then they participate in ORR. The electrons taken from anode side, travel through the external circuit to the load, generating an electrical current.

The current generated in MEA is governed by the following equation:

$$i = nF\frac{dN}{dt} \tag{4}$$

where dN/dt is the rate of substance on reaction in mol s^{-1}, n is mols of electrons.

C. Proton Exchange Membrane Unitized Reversible Fuel Cell

The idea of reversible, or regenerative fuel cell is not new. Historically, it is bounded very tightly with PEM technology. Mostly, the idea of dual modes is motivated by creation of proper energy storage system using hydrogen. So, when the excessive amount of electricity exists, it can be used for storing the energy by creating hydrogen from water electrolysis. This device can work in two modes, in analogy to the reversible electrical machine, fuel cell mode (FC), or water electrolysis mode (WE). However, for the proper function of the unit, these two regimes should not overlap [22].

Generally speaking, reversible fuel cell can be designed in two ways:

1) Unitize Reversible Fuel Cell (URFC);
2) Discrete Reversible Fuel Cell (DRFC).

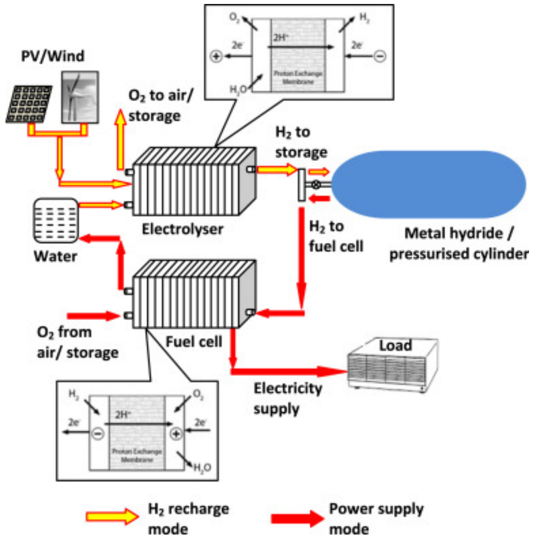

Fig. 3. Working scheme of Discrete Reversible Fuel Cell [23].

The DRFC solutions is commonly considered as conventional way and the establishment of this system is mainly system integration issue, as there will be used already existing best solutions for both appliances (fuel cell and electrolyser) in the market. The working scheme of DRFC is shown in the Figure 3. One should mention, that the most prevalent type of reversible fuel cell is exactly DRFC, due to its simplicity in operation, separable work modes, that allows to be on both FC and WE mode at the same time, and higher roundtrip energy efficiency (which is simply the efficiency of electrolyser and fuel cell operations, taken separately and summed) compared to unitized stack.

This paper will be reviewing only URFC path of fuel cell reversibility. This concept implies the use of only one unitized appliance for both purposes. The working scheme of URFC is shown in Figure 4. One should mention all the advantages of this choice, those which regarding the cost, volume and material savings, as well as the functionality gain.

In cases of confined space of vehicle or limited area, where each square meter is of a high value, the gain of mass and size savings can be crucial for installation. Therefore, the URFC will be a better solution. If achieved successfully, this concept will become a very attractive solution for space, subsea, aircraft and rural area power supply applications. But for having a good market entering, the roundtrip efficiency of unitized stack must be at least close to the roundtrip efficiency of discrete ones [21].

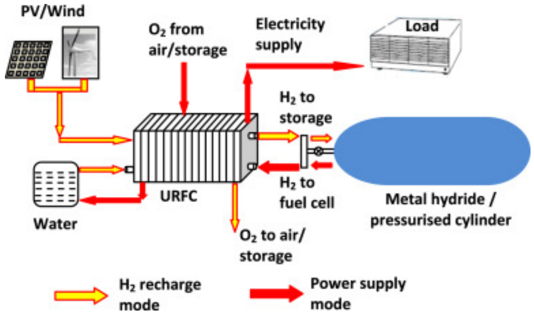

Fig. 4. Working scheme of Unitized Reversible Fuel Cell [23].

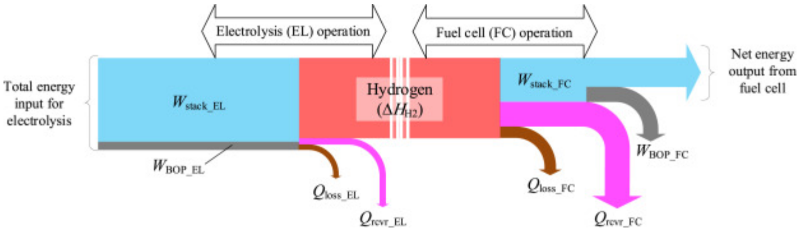

Fig. 5. Schematic of energy flow from power input into electrolysis (EL) mode (left edge) to power output from fuel cell (FC) mode (right edge). [21].

In Figure 5 the URFC‘s energy diagram is shown. From this the net roundtrip energy output can be illustrated. As it is clearly seen, the overall efficiency of URFC, depends on both FC and WE modes‘ efficiency. These notions are mutually interconnected. Therefore the complex approach to URFC components upgrade is more recommended.

II. THE COMPONENTS AND MATERIALS FOR PEM URFC

The main idea behind the fusion of electrolyser and fuel cell in one hardware stack is that these two appliances can in theory use the same components, thus decreasing the mass and volume expenses on the reversible fuel cell. Polymer electrolyte is suitable for both applications, as well as many components. The main differences of those mode remain the configuration of MEA in details, like bipolar plates‘ configuration, GDL and so on. [22]

Another thing to point the attention is that URFCs have currently mainly two configurations [23]. These configurations are mainly based on functionality of GDL and electrodes, or how it is called in some literature gas diffusion electrodes. The types of a URFC are:

1) Type A. URFC with constant anode and cathode configuration, i.e. the same electrode for both reactions is used;
2) Type B. URFC, where gas sides are switched, not the electrodes‘ functionality.

Type A has significant drawback, regarding the materials of catalyst layers and carbon supporters (GDL, gas flow channels). The used catalysts are not efficient in both directions of chemical reaction. Also on oxygen side during WE mode, the carbon-based materials are corroded rapidly. In order to solve this issue, the research of hydrophilic materials is ongoing.

Suggestions are made to use components based on Titanium, Aluminium and even Gold [22]. This type is also in the center of the paper‘s discussion.

Type B‘s special feature is that it can run on traditional fuel cell components. However, the problem is that after each switch of mode, the chambers must be fully cleaned from the used reactant gases, which leads to more complex gas management. Both types are shown in Figure 6.

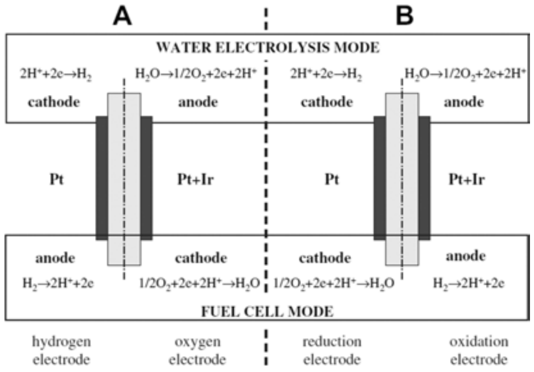

Fig. 6. Two URFC configurations [23].

A. Membrane

It is very convenient coincidence, that PEM stands for Polymer Electrolyte Membrane and Proton Exchange Membrane, as this notions describe the same material and its features, namely Nafion, which the most commonly used material for the PEMFCs [28]. As these names suggest, this membrane should be isolating electrodes electrically, should conduct protons, should block the reagents from mixing and should be with good thermal conductivity [24]. From all the variations of membranes, the common type for low-temperature PEMFC is Nafion 117, however due to its water management feature, the Nafion 112 is currently more preferable solution for the URFC [22] [23].

B. Membrane Electrode Assembly

The MEA is the heart of every fuel cell. It has the biggest contribution to the overall cost of the fuel cell. One must mention, that due to duality of URFC, the catalyst are called bi-functional catalysts. Currently the inevitable issue follows the design of this catalysts‘ layers: the catalyst, which is good for fuel cell mode, is bad for the water electrolysis mode and vice versa.

As reactions occur in triple-phase-boundary, the contact resistance should be near as possible to zero [25].

In addition to all given information, the electrode material is also a focus of controversy. Currently the most used materials are Carbon Black, Platinum, Ruthenium, Iridium and Teflon [29]. These materials have enough drawback to resist the market entry of URFC.

C. Bipolar plates

Bipolar plates are one of the most important parts in the fuel cell stack, especially in URFC design. One can mention, that unitized hardware should be capable of conduction two opposite in direction reactions. Therefore, the bipolar plates, or as sometimes they called flow fields [26], should be feasible in both fuel cell and water electrolysis modes. However, this is not so achievable with the common carbon based plates, as they are highly prone for corrosion and degradation during the WE mode [30].

The fuel cell stack hardware is shown in Figure 7. This one can also be implemented for the URFCs.

D. Gas Diffusion Layers

One should not underestimate the importance of proper diffusion media (DM) in supporting of processes in URFC. The DM is created from the combination of Gas Diffusion Layer (GDL) and Micro-Porous Layer (MPL), coated on it [22]. Both are produced from hydrophobic materials and requires good electrical and heat conductivity. The main materials of this component are carbon cloth and mixture of carbon powder polytetrafluoroethylene (PTFE), for GDL and MLP respectively [27]. In literature, other naming to these components can be applied, but the functionality remains the same: proper transport and distribution of reagents over all the CL, proper water management for preventing the membrane from dry-outs and flood-outs at lower and higher current densities during FC mode, respectively.

As it was mentioned, the materials suitable for fuel cell and electrolyser separately, can‘t be used in URFCs, due to degradation during the operation. As well as bipolar plates and CL, the problems on the oxygen side during WE mode is experienced [23].

The substitution of Carbon with Titanium [23] enables to achieve more balanced response of the hardware stack for both modes. However, in order to achieve the optimal performances of these modes, the design and material of the components should be carefully chosen.

E. Gaskets

Gaskets are vital part of the URFC. Their main role stays the same for each mode: to prevent gases going where they should not. The failure of the gasket can cause decrease of performance, damage of the appliances, and, what is the most important, safety thread. They also should be made of robust materials, as they are exposed to very aggressive environment (hydrogen, humid air, acids and etc.) and mechanical forces. Another important parameter is the thickness of the component, as it influences the performance and the stability. Generally, gaskets for URFC are made from PTFE and silicon [29].

F. Heating or Cooling plates

Depending on the temperature, the heating or cooling plates can be used. As it comes from the name the first ones are used to heat the stack, for example, in cold ambient temperature. This plates mainly use resistive heating elements [31].

Otherwise, the cooling plates are used to cool the stack, especially when the other cooling methods are not enough. The water is circulated for through this plates to cool them. The cooling plates alignment in stack hardware can be seen in Figure 7.

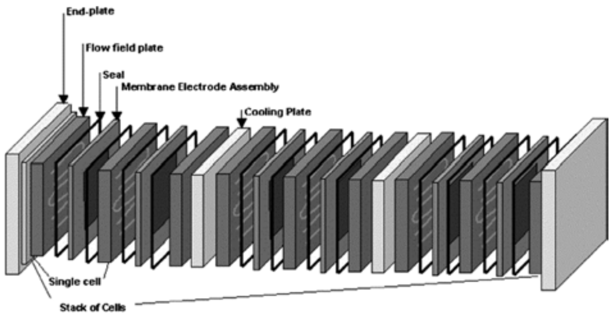

Fig. 7. Fuel cell stack hardware [15].

G. Balance-of-plant

The term Balance-of-plant (BOP) is the generalization of components‘ complex [31], containing such subsystems as:

- fuel and oxidant supply management subsystems;
- power conditioner;
- thermal management subsystem;
- water and humidification management subsystems.

The main purpose of BOP components is to support fuel cell in the achievement of the required characteristics and performance of fuel cell system [31]. These components allow fuel cell system to have the adequate dynamics, i.e. response to variable in time load demand. The overall response of the fuel cell system to such transients defines its total performance.

1) Fuel and oxidant supply management subsystems: The oxygen is supplied from the air with the help of air compressors (pumps).

It is very difficult to store the hydrogen. It is highly flammable, very light, and very low density substance. It requires pressurized and well isolated tanks. On practice, there are two dominating suggestions for storing the hydrogen - as the pressurized gas and as a metal hydrides [27]. The liquefying of hydrogen is considered as a very inefficient method.

The fuel reformer (processor) is needed, when the hydrocarbons or alcohols are used instead of pure hydrogen. The reformer will convert these fuels into high hydrogen containment gas. Also the sulfur and carbon monoxide (sometimes dioxide) filters are needed, as these gases are harmful fro the catalysts and membrane.

2) Power Conditioning: The system of electronic components, that are used to convert the output power of fuel cell stack into the desired input of the load, is called the power conditioner. Depending on the load type, this system can contain DC-DC converters (f.e. Buck-Boost converter) and/or DC-AC inverter [31]. It should also contain control scheme for connecting energy storage elements with the fuel cell.

According to the current state-of-art, the fuel cell systems can‘t satisfy the rapidly changing load demand, therefore the additional power storage devices with quick charge/discharge capacity, such as ultracapacitors or batteries should be used. The fuel cell will cover the average power demand of the load, meanwhile the control unit will decide when to refill the energy storage or use the power from it. For this purposes the power capacity of power conditioning units should be near 5 times higher that the capacity of fuel cell [26].

3) Thermal Management: Depending on application of fuel cell system, the produced heat can be used or considered as a power loss. But the requirement for cooling the fuel cell, especially the MEA will remain the same.

One can use active air cooling by using the auxiliary fans, or active liquid cooling by means of circulation of fluid with the help of pumps [1].

For the proper thermal management the components with good thermal conductivity should be used, such as carbon composite plates. In case of need the special purpose cooling plates can be used as well [31].

In case of URFC, the excessive heat can be used also in dryers of reactant gases, produced during electrolysis mode by the help of heat exchangers [23]. The need for this rises due to high humidity of gases produced at URFC, in this case the gases come out with liquefied water.

4) Water and Humidification Management: This issue has very challenging difficulty to solve, and often considered as one of the main technical problems of fuel cells, especially for URFCs [22]. The problem is that for optimal performance of fuel cell it should be sufficiently humidified, particularly the ionomer membrane, in order to achieve the best conductivity of ions through the membrane and for its longer lifespan. At the same time, the flooding of electrodes with water must be avoided as much as it‘s possible, due to reduction of reactant gas diffusion, which would lead to decreased performance of fuel cell.

Due to the heat as a product of the overall chemical reaction and the atmospheric pressure, the water inside of the membrane tends to evaporate more quickly. However, in most cases of PEM fuel cells, the heat is less than 100°C, so the water produced at the cathode as a liquid [1].

Current and most spread solutions for controlling of the water balance in the fuel cell is based on applying of excess amount of air supplied to the cathode side. Therefore, the air flow is stoichiometricaly twice more, than required for the reaction. Obviously, this leads for more self-consumption of produced energy for running the pumps and etc. Another well-known method of excessive water removal is anode water removal [1], when water from cathode side is transported through the membrane to anode side by means of the difference in concentration gradients and removed by fuel flow.

As for the humidification of the membrane, the solutions such as direct water supply to the membrane through porous material in contact with the membrane. The membrane can be fed with water internally as well, by using the produced water.

III. CONCLUSION

In this paper, the URFC‘s components and materials were discussed. Firstly, the introduction to history of fuel cells and then the working principle were given and explained. The reactions, such as HOR and ORR were defined. The required explanation of reversible fuel cell idea was shown as well. The difference between two configurations of reversible fuel cell was introduced. These two configurations are Discrete Reversible Fuel Cell and Unitized Reversible Fuel Cell. Also, the energy diagram of URFC was shown.

Then, the current state-of-art of URFCs was described. It contained the information about both two URFC‘s configurations, the explanation of both, the materials and the components of each element of URFC. These elements were MEA, Bipolar plates, Gas Diffusion Layer, Gaskets, Heating or cooling plates and the big focus was given to Balance-of-plant components, as their operation crucial for the overall performance of any fuel cell system.

Considering the all written above, several conclusions can be made:

- the careful material and construction research is needed, especially for the water electrolysis application on the oxygen side;
- the approach for the upgrade of URFC stack requires the increase in efficiency for both WE and FC modes;
- URFC system integration should also be on focus, as it can be crucial for overall performance;
- the DRFC performance can be regulated by separate development of both electrolyser and fuel cell. But the need for more smaller sizes of hardware stack stimulates the research of URFC technology. And for overall success of the fuel cells, the market entry of it should be as big as it is possible;
- another critical issue is the production process. The numerous examples from the history show us the popularization of the technology after it is easier to replicate and produce, therefore, fuel cells‘ production must be put on the conveyor;
- in portable and automotive applications the fuel cells have some serious advantages over the only battery using systems, such as robustness against different temperature and load independence. Considering this, the suggestion to use fuel cell technologies in combination with electric power storage can be made.

The literature list in the end of this article can be useful for future researches of this topic, as it is comprehensive and up-to-date.

REFERENCES

[1] Karl Kordesch, Gnter R. Simader, ”Fuel Cells and Their Applications”, Wiley, 1996, p. 375.

[2] Andrzej Wieckowski, Jens Norskov, ”Fuel Cell Science: Theory, Fundamentals, and Biocatalysis”, John Wiley and Sons, 2011, p. 640.

[3] J. Larmini, . Dicks, ”Fuel cell systems explained”, 2nd edition, John Willey and Sons Ltd., 2003, p 406.

[4] V.S. Bagotsky, ”Fuel Cells: Problems and Solutions”, NJ: Wiley, 2009, p 320.

[5] Roland Wengenmayr, Thomas Bhrke, et al.,”Renewable Energy: Sustainable Energy Concepts for the Energy Change”, 2nd ed.,WILEY-VCH Verlag GmbH & Co., 2013, p 170.

[6] Eduardo I. Ortiz-Rivera ; Angel L. Reyes-Hernandez ; Rey A. Febo, ”Understanding the history of fuel cells”,2007 IEEE Conference on the History of Electric Power,2007,p.6.

[7] Grove, William Robert (1839), ”On Voltaic Series and the Combination of Gases by Platinum”, Philosophical Magazine and Journal of Science, XIV (8687): 127130.

[8] William Robert Grove, ”On A Gaseous Voltaic Battery”, Philosophical Magazine and Journal of Science, vol. 21, no. 3, pp. 417, December 1842.

[9] P.G. Grimes,”Historical pathways for fuel cells”,IEEE Aerospace and Electronic Systems Magazine, Vol. 15, Issue 12, 2000, pp. 7-10.

[10] Bellis, Mary. ”Hydrogen Fuel Cells Innovation for the 21st Century.” ThoughtCo, Feb. 4, 2019, thoughtco.com/hydrogen-fuel-cells-1991799.

[11] ”Fuel Cell History Fuel Cell Today”, Available online, http://www.fuelcelltoday.com/history , Retrieved 28 May 2019.

[12] Eberle, Ulrich & Mller, Bernd & Helmolt, Rittmar. (2012). Fuel cell electric vehicles and hydrogen infrastructure: Status 2012. Energy & Environmental Science. 5. 8790-8798. 10.1039/C2EE22596D.

[13] https://www.bayern-innovativ.de/seite/solar-wasserstoff-bayern , Retrieved 28 May 2019.

[14] Willi Hornfeld, ”DeepC: the German AUV Development Project”, STN ATLAS Elektronik GmbH, 2004, p. 10.

[15] R.Dervisoglu - Own work, based on http://en.wikipedia.org/wiki/File:Solid_oxide_fuel_cell.svg

[16] Albert E. Hammerschmidt, ”Fuel Cell Propulsion of Submarines”, Paper was presented at: Advanced Naval Propulsion Symposium 2006, October 30-31, 2006, Arlington, VA, USA.

[17] http://www.abc.net.au/science/articles/2002/12/20/750598.htm , Retrieved 28 May 2019.

[18] https://www.uniper.energy/storage/what-we-do/power-to-gas , Retrieved 28 May 2019.

[19] https://www.edmunds.com/toyota/mirai/2016/ , Retrieved 28 May 2019.

[20] http://hydrogencouncil.com , Retrieved 28 May 2019.

[21] Hiroshi Ito, Naoki Miyazaki et al., ”Efficiency of unitized reversible fuel cell systems”, International Journal of Hydrogen Energy, Elsevier, Vol. 41, Issue 13, 2016, pp. 5803-5815.

[22] Mohamed Gabbasa, Kamaruzzaman Sopian et al., ”A review of unitized regenerative fuel cell stack: Material, design and research achievements”, International Journal of Hydrogen Energy, Vol. 39, Issue 31 Elsevier, 2014, pp. 17765-17778.

[23] Biddyut Paul, John Andrews, ”PEM unitised reversible/regenerative hydrogen fuel cell systems: State of the art and technical challenges”, Renewable and Sustainable Energy Reviews, Vol. 79, Elsevier, 2017, pp. 585-599.

[24] A. Doddathimmaiah, J. Andrews, ”Theory, modelling and performance measurement of unitised regenerative fuel cells”, International Journal of Hydrogen Energy, Vol. 34, Issue 19, Elsevier, 2009, pp. 8157-8170.

[25] Massimo Guarnieri, Piergiorgio Alotto, Federico Moro, ”Modeling the performance of hydrogenoxygen unitized regenerative proton exchange membrane fuel cells for energy storage”, Journal of Power Sources, Vol. 297, Elsevier, 2015, pp. 23-32.

[26] G. Hoogers (ed.), ”Fuel Cell Technology Handbook”, Boca Raton, FL: CRC Press, 2003.

[27] Jose Bellosta von Colbe,Jose-Ramn Ares,Jussara Barale et al., ”Application of hydrides in hydrogen storage and compression: Achievements, outlook and perspectives”, International Journal of Hydrogen Energy, Vol. 44, Issue 15, Elsevier, 2019, pp. 7780-7808.

[28] S.C. Ball, ”Electrochemistry of proton conducting membrane fuel cells”, Platin Met Rev, 49 (2005), pp. 27-32

[29] Bradley Ladewig, San Ping Jiang, Yushan Yan, G.Q. Max Lu et al., ”Materials for Low-Temperature Fuel Cells”, Wiley-VCH, 2015, p. 250.

[30] S.A. Grigoriev, P. Millet et al., ”Design and characterization of bi-functional electrocatalytic layers for application in PEM unitized regenerative fuel cells”, International Journal of Hydrogen Energy, Elsevier, 35 (2010), pp. 5070-5076.

[31] Bei Gou, Woonki Na, Bill Diong, ”Fuel Cells: Modeling, Control, and Applications”, 1st Edition, CRC Press, 2017, p. 248.

Sector coupling between different distribution grids

Kern, Alexander, Gast, Nicola
Institut für Elektrische Energiesysteme
Otto-von-Guericke-Universität
Magdeburg, Germany
alexander1kern@mailbox.org

***Abstract*— The basic idea is to ask the question: *"Can fossil energy sources such as coal, the use of which is to be reduced due to political decisions, be substituted by the conversion and storage of renewable power in other forms of energy?"* By 2025 renewable energies are to account for 40 % of the power supply in Germany, which is leading to challenges such as grid expansion and efficient storage. An alternative solution is the coupling of sectors such as power, gas and heat. The possibilities to couple different sectors is very diverse, which makes it possible to link various distribution grids with different methods. For these reasons, flexibility in the simulation of such systems is extremely important. The simulation this paper is referring to can simulate a large, central power plant located in the distribution grid or a small, decentralized system suitable for single-family homes. For reasons of optimization, parameters such as the electrical power output and the location of the system as well as the energy prices for electricity, gas and heat can be entered individually. The paper summarizes the simulation, which indicates the high potential of sector coupling.**

Keywords—Sector coupling, Power to Gas Method, Power to Heat Method, Heat pump, distribution grid

I. STATE OF THE ART

A. Motivation

The use of fossil primary energy sources is going to decrease in the future because of political decisions, which are made by the German government today. Therefore, dealing with renewable energies to secure future power supply and the possibility to store high amounts of energy are inevitable. One effective possibility among others is to connect different energy sectors. Various analyses and case studies attribute high potential to the coupling of different sectors for balancing power grids of the future. This will be necessary because the number of renewable and therefor unsteady producers will increase over time. For analysing those potentials this paper deals with the Power to Gas and Power to Heat Method. The question *"how much extra electrical energy in the power grid, which is not needed at the moment, can be stored in the gas grid or as heat so that fossil energy sources can be substituted?"* will be raised and discussed. [1]

B. Possibilities to connect the power, gas and heat sectors

The following Figure 1 shows a simplified version of the possibilities to connect different energy sources, ways of transportation, variants of storage and consumers.

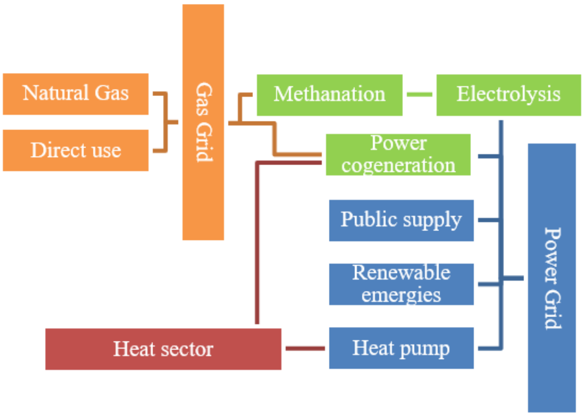

Figure 1 Sector coupling between gas, power and heat grid [2].

It can be deducted from Figure 1 that the gas grid can be used as storage when the power grid is fed with too much renewable energy and vice versa support the power grid in times with low renewable power production [2]. The following case studies uses the Power to Gas Methane Method and the heat pump for coupling the different sectors.

The Power to Gas Methane Method is based on the production of hydrogen by electrolysis. Hydrogen is not suitable for further use because of its volatility and little developed grid [3]. Methanation is an additional step to the process and produces synthetic methane, which is a substitute to fossil natural gas, from hydrogen and carbon dioxide. For a whole cycle the synthetic gas can be converted back into electrical power with e.g. a combined cycle power plant. Regarding climate change this is a neutral process because carbon dioxide is first taken from the environment and released again later. It is possible to store methane in established facilities with high efficiency and in large amounts. This makes the Power to Gas Methane Method the more functional option [2]. The efficiency of this method is about $\eta = 64$ % (80 bar). Higher numbers are expected in the future when the development of high temperature electrolysis will have been continued. In case of assuming a 60 % efficiency for combined cycle power plants the whole cycle from power to methane to power can reach approximately 38 % [4].

The second option to connect different energy sectors, which is discussed in this paper, is the Power to Heat Method represented by the compression heat pump. The different steps contain heating a refrigerant using an energy source, compress the refrigerant using electrical power (actual heat pump) and a heat sink, that heats water or rooms and cools the refrigerant back down to its starting temperature. The source and storage medium are characteristic for the different heat pumps [5 and 6]. In the following case study groundwater ($T_{\text{source}} = 10$ °C) is used as a heat source to heat water ($T_{\text{flow}} = 60$ °C) for heating and hot water. The efficiency of a water to water heat pump is measured with the coefficient of performance (COP or ε) [7].

$$\varepsilon = \frac{T_{\text{flow}}}{2 \cdot (T_{\text{flow}} - T_{\text{source}})} \tag{1}$$

The equation applied to the present case study results in $\varepsilon = 3.3$. This is an efficient heat pump compared to fossil plants, which have an efficiency of less than three. For using a heat pump in district heating the temperature of the source needs to be at least 38 °C to gain a COP higher than three, which is only possible by using process heat [8].

II. MODELLING AN INTEGRATED ENERGY SYSTEM

There are two different scenarios for using the technologies described above. On the one hand, the exported power to the transmission grid is considered in a distribution power grid, which can be used to generate gas or heat. The second Scenario considers a private home, which power production comes from local photovoltaic plants and wind turbines. These renewable power plants are used to cover the requirements of electrical power and heat of a single home and to store the remaining energy surpluses as chemical energy (gas). The observation period is one year, which makes seasonal differences visible. For the evaluation of the scenarios a MATLAB simulation has been developed.

A. Data

Part of the case study is the energy production, use and storage of one year in an hourly resolution.

The approximated wind energy is based on data of the German weather service. For the case study the eastern part of Germany was chosen and is represented by 3 weather stations: Dresden Klotzsche (01048), Magdeburg (03126) and Schwerin (04625). The hourly wind speed is the average value of the last 16 years in these three weather stations [9]. To generate electrical power a wind turbine is needed. For the following case study "Enair 70PRO with a maximum power of 4 kW was taken exemplarily. This small power plant can be stationed on top of the roof of a house [10].

The second energy source for a private home uses photovoltaic panels. For the simulation data of a real photovoltaic plant have been used. It is based in Magdeburg and consists of 26 panels with a maximum power of 240 W each. This adds up to an output of 6.24 kW. The panels are only used for power production and not for heating water [11]. Because of daily values of the photovoltaic plant the power must be split to hourly values. The highest production is around midday. In the morning and afternoon, the percentage share is much lower [1].

The other side of the energy cycle is a load profile of a single home for electrical power, heating and hot water. The data are based on VDI-Standard 4655 [12], which defines daily load profiles. This standard implies a hypothetical house with a living space of 169 m² and three inhabitants. One year is divided in three different periods: Summer, spring/autumn and winter [12]. The following case study separates these periods between the meteorological seasons begin.

Big power to gas plants or heat pumps need more electrical power than smaller plants in single homes. As a result of that a preferable solution is connecting to the local power grids [1]. The following case study uses the power transfer from the distribution to the transmission grid as energy to transform into gas or heat. The simulation is based on the high-voltage grid data for 2016 of *Mitteldeutsche Netzgesellschaft Strom GmbH (Mitnetz GmbH)* [13]. This power is currently fed back to the transmission grid but could be (and will be in the simulation) used to generate gas or heat for storing energy.

B. Matlab simulation power grid

The simulation of a power plant connected to a local power grid, is not focused on covering hourly needs, because those are already supplied by existing power plants [2]. The focus is primarily on the potentials of heat pumps in district heating grids and power to gas plants to store energy in the gas grid. The question is, therefore, what quantities of heat and gas can be generated from electrical power, which is currently provided. This applies both to a technical as well as a business consideration.

The simulation starts with asking for the electricity, gas and district heating prices. This information is needed for evaluating the economic point of view. In addition to the prices, the efficiency of the heat pump is central to the profitability of the entire system, see formula (1). The temperature levels must be selected by the user. From these quantities the ideal COP can be calculated using (1) [1]. If $\varepsilon < 3$, which indicates to an ineffective system, the program gives a warning and offers the possibility to correct the input [7]. This is followed by a user input, which decides whether the potential of the entire grid or a single plant will be considered. The second option is followed by a request to input the electrical power of the heat pump and the power to gas plant [1]. For some heat pumps and power to gas plants, a few hundred MW are possible ([14] and [15]). When combining several systems, the performance increases accordingly. This applies equally to both technologies [1]. After interrogating the available power of the considered hour, the amount of energy is calculated using the efficiency η and the coefficient of performance ε, which can be stored in the form of or methane or heat. The storages are fictitious because it considers only charging processes, but no discharges. In order to be able to analyse a real storage system, the discharging processes must be additionally implemented and simulated. Due to the focus is on the evaluation of the potential of the sector coupling and thus primarily the maximum amount of methane or heat to be produced, this simplification is justifiable. For the consideration of the entire grid potential. By offsetting the entire amount of energy for one year, following the sales prices given in advance, the revenue that could be generated in each sector is obtained.

C. Matlab simulation single home

The base of the simulation is the load profile of a single-family home [12]. The simulation starts with asking the user, whether the house is connected to the central heating grid or has its own gas heating. As an alternative to the central heating grid connection, only the gas heating can be considered, since it is theoretically possible to use the syntactical methane to generate heat using a gas heater. This is a CO_2-neutral process and thus serves the general objective of carbon dioxide reduction [16].

Following this, the user is asked for the capacity of the heat storage, the price for electrical energy and costs for district heating or gas for heating in € per kWh. The size of the storage should be based on the heat consumption of the house. In this case the household has an hourly average consumption of heat of 2.4 kWh [12].

The next step is creating the power generation profile of the home. Doing this, the user must specify the location (north-west, east or south) and the electrical power of the wind turbine. This information feeds the corresponding wind profile and the power characteristic into the program. The simulation calculates the hourly generated electrical power of the wind turbine. The generation profile of the photovoltaic system is specified regardless of location. By adding the two production profiles, the total power generation of the house is achieved in an hourly resolution for one year. The usual flow temperature of a house to provide heat and hot water is 60 °C and the source temperature of the groundwater 10 °C [17]. This results in a COP of $\varepsilon = 3.7$. Based on this information, the saving of one year can be calculated afterwards. This is based on the indicated prices for the supply of electrical power and the heat medium.

D. *Definition of parameter*

For the simulation, parameters (coefficient of performance, efficiency, storage size and degrees of effectiveness) must be provided and entered. The COP is calculated according to formula (1) and is used to calculate the power requirement of a heat pump, which is shown in formula (2) [7].

$$E_{\text{thermal}} = E_{\text{electric}} \cdot \varepsilon_{\text{real}} \tag{2}$$

A source temperature of 10 °C and a flow temperature of 60 °C are specified for the private home system, as these are the usual values for a water to water heat pump that is used for both room heating and for hot water supply [17].

As described before, the user must select the temperature levels in the case of a distribution system. Typical flow temperatures of German district heating grids are around 100 °C, which is also considered in the following scenario [18]. For this flow temperature, the source must have a temperature level of at least 38 °C to simulate an efficient heat pump, see formula (1). This can only be achieved by using industrial or power plant residual heat, which is not specified in the simulation either, since the temperature level can vary greatly depending on the source [17].

All considered solutions to store energy are assumed to be ideal and lossless with infinitely fast charging and discharging periods. In the scenario of a home, the program simulates a heat storage tank, which can be charged as well as discharged, and an infinitely large fictitious gas storage tank, which is used to store the remaining energy. The heat storage tank is assumed to be half full at the beginning of the year, as it is realistic that there is still a remaining of the previous year's production" available.

The reuse of gas is not considered, since there are multiple possibilities to use methane. In the simulation, the heat tank is designed for a storage energy quantity of 5 kWh. This assumption results from the comparison of the average hourly heat demand (2.4 kWh) and the maximum demand in one hour (6.2 kWh). The same applies to the gas storage of the private home as to the storage of the distribution grid system. Those are only "charged" to determine the amount of energy that can be converted in one year. These are therefore also fictitious energy storages.

III. CASE STUDIES

A. *Basics and parameters of the case studies*

The following parameters have been set for both case studies. They include efficiencies of different methods to produce gas or heat. They cannot be altered in the simulation process [1].

Table 1 Defined parameters of the simulation

Parameters	**Value**	**Source**
Source temperature (private home)	10 °C	[17]
Flow temperature (private home)	60 °C	[17]
COP (private home)	3,3	[7]
Efficiency power to gas-methane	65 %	[4]

The first case study (distribution grid) discusses a power to gas plant and a heat pump with 100 MW electrical power each. Table 2 shows the parameters, which have been set for the following study.

Table 2 Parameters of the distribution system

Parameters	**Value**
System type	Distribution plant
Electricity price	0,3 €/kWh [19]
Gas price	0,07 €/kWh [20]
District heating price	0,1 €/kWh [21]
Source temperature heat pump	50 °C
Flow temperature heat pump	100 °C [18]
Electrical power heat pump	100 MW [15]
Electrical power power to- as	100 MW [14]
Area	East of Germany

Since a distribution system is not operated by private individuals but is owned by the grid company, the assumptions made are primarily subject to profit maximisation. Consequently, the prices set here form the basis of the sales revenues in order to determine the earnings potential of the various sectors. These are predicated on typical prices of the recent years. Due to the tendency of the price structure to rise in the past, these are not mean values, but prices close to the maximum value of recent years ([19] to [21]).

Table 3 Parameters of the home owner system

Parameters	**Value**
System type	Private power plant
Heat storage capacity	5 kWh
Electricity price	0,3 €/kWh [19]
District heating price	0,1 €/kWh [20]
Gas price	0,07 €/kWh [21]
Area	East of Germany
Nominal power of wind turbine	4 kW [10]

After considering the distribution grid systems, the description of a scenario for a private home system is found, where a connection to the central heating grid is assumed. The parameters shown in Table 3 apply to the following case study and are based on exemplary and generally valid empirical values for a private home with a living space of 169 m² and 3 persons.

B. *Case study distribution grid*

This chapter discusses the potential of the distribution grid systems with a given performance. The production possibilities for gas and heat are shown in Figure 2.

The period under consideration extends over one year, which is shown here in a daily resolution. The curves show the respective storage levels of the gas storage (blue) and heat storage (orange). The diagram therefore shows the production potential for methane and heat in TWh [1]. The generation potential for heat is just under 600 GWh, which corresponds to approx. 13 % of the total grid potential. A similar share also exists for gas production. With a plant capacity of 100 MW, around 100 GWh of energy can be stored in the form of methane ([14] and [15]). Here the production ratio of the heat pump to the efficiency of the power to gas methane plant results in the generation of six times the amount of energy in the heating sector.

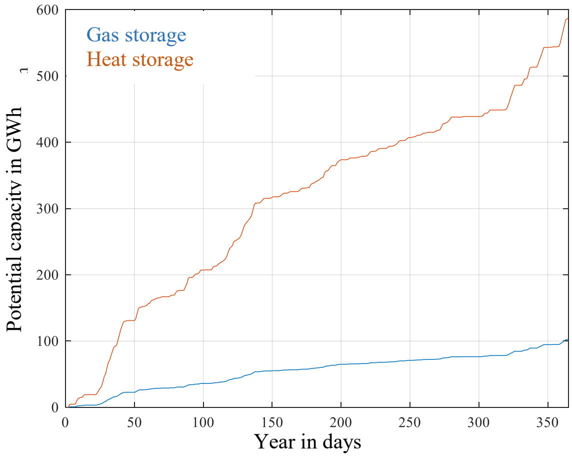

Figure 2 Production potential for methane (blue) and heat (orange) in plants with an electrical output of 100 MW ([4], [7], [9], [10], [11], [12], [13], [14], [15], [17], [18], [19], [20], [21] and [22]).

With seven such plants, the excess energy from the distribution grid can be fully utilised to produce methane and heat, which will later be used in households. Assuming that the synthetical methane and heat are used in the households, lots of homes can be heated in a climate-neutral way and supplied with renewable power.

As Figure 3 shows the financially potential in the heating sector is, as can be expected, significantly higher than in the gas sector. This is because of the higher efficiency of heat pumps and different prices for energy. Higher wind speeds prevail in eastern Germany during the winter months, which leads to a greater power and energy surplus on the one hand and, as a logical consequence, to a higher yield potential from methane and heat sales on the other [9]. This phenomenon is particularly advantageous in the heating sector, since the heating requirements of private buildings also rise sharply in the winter months together with higher production.

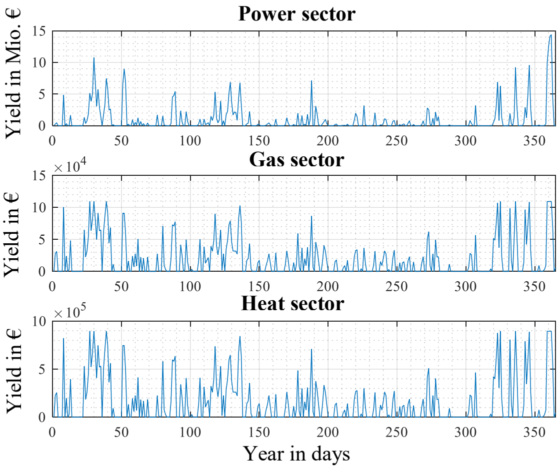

Figure 3 Yield potential split by sector over a period of one year ([4], [7], [9], [10], [11], [12], [13], [14], [15], [17], [18], [19], [20], [21] and [22]).

C. *Case study private home*

The horizontal red line in Figure 4 shows the maximum capacity of the heat storage tank. The blue graph shows the average heat storage level each day of the year. This never reaches the maximum storage level in Figure 4, which is due to the representation of daily average values. In order to achieve the capacity, the heat production would have to reach or exceed the heat demand for 24 hours. This is hardly possible due to the lack of PV production at night. In any case, it can be seen that the storage facility can be filled significantly more on summer days than on winter days.

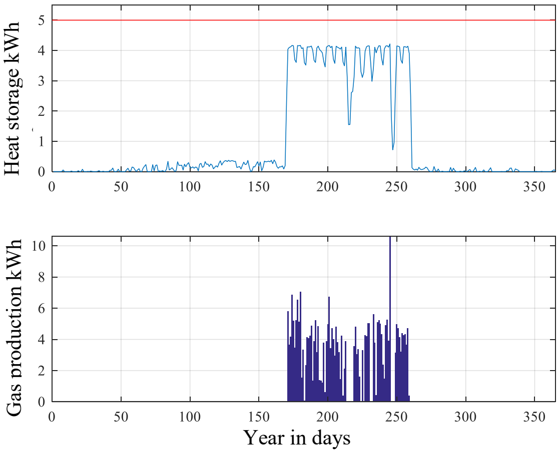

Figure 4 Average heat storage level above and daily production of gas below ([4], [7], [9], [10], [11], [12], [13], [14], [15], [17], [18], [19], [20], [21] and [22]).

As explained earlier, the charging of the heat tank has priority over gas production. For this reason, as shown in the bottom in Figure 4, gas is only produced in the summer months. A total of about 300 kWh of energy could be stored in the form of gas. At one point, a daily production volume erupts significantly upwards. This corresponds to the day of the maximum energy supply from the photovoltaic plant. On days with low generation, the distribution grid covers the remaining energy requirements for power and heat, which cannot be met by the plant. The daily course of this supply is shown in Figure 6. The total electrical power consumption is around 3000 kWh and 16,700 kWh for heating energy.

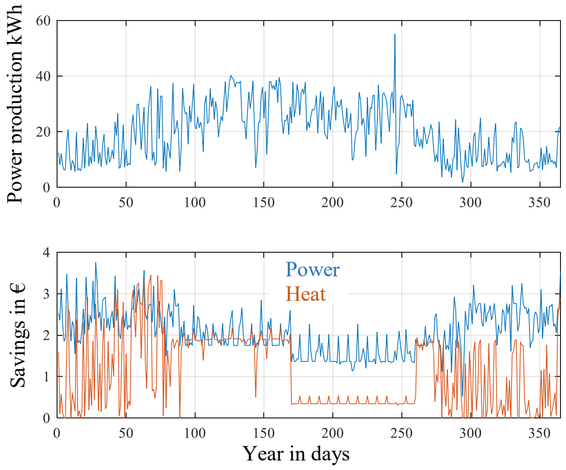

Figure 5 Power production of the owner-occupied housing system above and yield potential in power (blue) and heat (orange) below ([4], [7], [9], [10], [11], [12], [13], [14], [15], [17], [18], [19], [20], [21] and [22]).

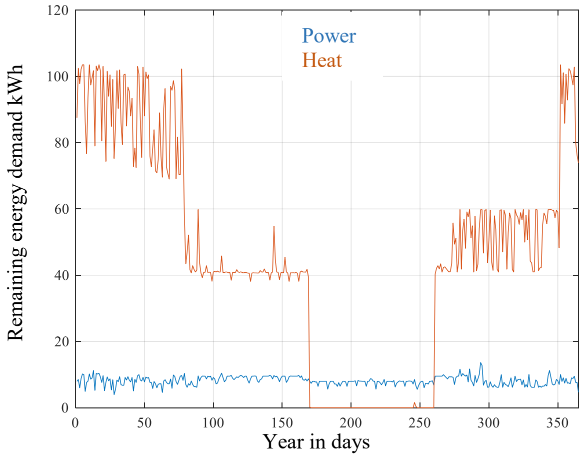

Figure 6 Daily remaining energy demand, which is covered by the distribution grids, over one year ([4], [7], [9], [10], [11], [12], [13], [14], [15], [17], [18], [19], [20], [21] and [22]).

The coverage of the heat demand depends significantly on the load profile. Figure 5 and Figure 6 confirm this, because neither the graph on cost savings nor the energy supply shows a pattern from the graph on power generation. On the other hand, the heat's load profile is clearly visible in both curves. The power loads are based on the summation of the required and generated electrical power. The blue graph both in Figure 5 (below) and in Figure 6 show a constant circulation around an average value. There are no significant breakouts up or down, regardless of the time of the year. The fluctuation between individual days is also far less pronounced than in the heat graphs. From the daily savings of electrical power and heat energy costs, results in an annual saving of altogether 1160 € (electrical power: 760 €; heating: 400 €). This results from the difference between energy procurement from the distribution grid with and without home ownership systems (wind power, photovoltaic energy and heat pump) and the multiplication by the electricity or district heating price ([19] and [21]).

Figure 6 shows the heat demand that cannot be covered by the home system. A total of around 16,700 kWh of heat is required from the grid. This leads to costs of 1670 €.

D. *Result analyses*

As a universal evaluation, this chapter summarizes the results of the scenarios. The basis for consideration is the discussed distribution system with the question: *"How many households can be supplied with heat produced?"* This is not an hourly comparison, but a general estimation of the potential for how many households the stored energy is enough for heat supply. According to formula (3), the required energy demand from the district heating grid can be determined. 16,700 kWh are required by each household in form of district heating.

$$E_{\text{consumption}} = (E_{\text{consumption}} - E_{\text{self-production}}) \cdot \eta \qquad (3)$$

This is the annual heat requirement of a household, which has its own power, gas and heat generation. The ratio to the possible generation of the distribution system results in the maximum number of households supplied with district heating, assuming an efficiency of the district heating grid of 0.85 [22]. Since the distribution grid can provide up to 600 GWh in form of heat over one year, it is possible to supply 30,500 households, which have an additional yearly demand for heating of 16,700 kWh. This energy supply is possible without additional heating using fossil resources.

E. *Potentials and limits of the simulation*

When simulating a homeownership system, it can be tested whether the hourly energy requirement of the house can be covered by a photovoltaic plant and a wind turbine. The heat storage makes a significant contribution to meeting demand, as it can bridge periods of low generation. The capacity design of a heat storage is only possible to a limited extent, because several simulations with different storage sizes would have to be compared with each other. Nevertheless, it is conceivable to check the suitability of a selected storage capacity. In addition to the capacity check, an estimate can be made of how much renewable methane can be stored with the excess energy for later use. For distribution grid plants an estimation of the storage potential in heat or gas is possible. In addition, the utilisation of specific plants with a certain capacity can be analysed and checked. Due to the lack of a load profile and the complexity of other producers, a storage design or verification is not possible. Regardless of the simulated scenario, an assessment of the technical and economic profitability can be made. In addition, at the end of the scenario the information about the methane quantity produced is available, which can be used to generate renewable power, which further increases the economic efficiency of the plant.

IV. SUMMARY

After discussing the opportunities of sector coupling in the introductory chapters, the main part of the paper deals with the description and evaluation of the simulation that represents sector coupling at the level of a home and distribution grid. As a summary of the results of a single-family house with three residents and its own power production using a photovoltaic and wind power plant, half of the power demand can be covered. In this scenario, around a quarter of the heating and hot water requirements are covered by a water to water heat pump. The remaining energy is fed from the local power grid or a central heating grid. A power to heat coupling system in the distribution grid with an electrical input of 100 MW can cover the annual residual demand of 30,500 households connected to the central heating grid. This answers the introductory question of how much energy can be stored through sector coupling.

V. FUTURE PROSPECTS

These results are based on data which, for reasons of size, are imprecise. The limitation when considering a distribution system lies primarily in the structure of the grid and its transport losses. The simulation is based exclusively on data from Mitnetz GmbH, which greatly limits the choice of location. If a distribution system in another region is to be simulated, the data of the local distribution system operator must be fed into the simulation. In addition, when selecting the location of a distribution grid system, the availability of a connection to the power, gas and central heating grid must be considered. On the other hand, transport losses from power generation to the distribution grid and from there to the consumer must also be taken into account. It is difficult to consider these losses in general, as they depend on the distance between generation and consumption. When planning a distribution grid system, the efficiency of any necessary intermediate storage and pipelines must therefore be incorporated into the simulation or included in the analysis of the results. The inaccuracy of the generation profiles of the home owned systems are due to the inaccuracy of the location. As a result, the wind power profile is very inaccurate for the wind speed conditions around a single house, despite the division of Germany into three areas. Within an area, the wind speed is approximately constant, but there are always locations with significantly higher or lower wind speed. Consequently, for an exact consideration of an explicit house project, a separate wind profile must be created and fed into the simulation. The load profile of the house is a standardised average profile, which is created by the superposition of many households. This limits the accuracy of the profile, as e.g. vacation days, are not taken into account. Based on how many households the distribution system can supply, the standardized load profile forms a good average. When considering a single-family house, the simulation must be based on an individual load profile, which is based both on the thermal insulation and the number of persons in the house, as well as on the consumption habits of the residents. By these adjustments necessary in individual cases, the simulation can calculate the potential of any distribution grid and private home. It can therefore be used to determine payback periods and potential yields.

REFERENCES

[1] A. Kern, Sektorenkopplung verschiedener Verteilnetze, Unpublished Bachelor Thesis, Magdeburg, Otto-von-Guericke University, 2018.

[2] M. Sterner und I. Stadler, Energiespeicher Bedarf-Technologien-Integration, 1st ed., Berlin, Heidelberg: Springer Vieweg, 2014.

[3] Din-Normenausschuss und Gastechnik, DIN EN 16723-2 - Erdgas und Biomethan zur Verwendung im Transportwesen und Biomethan zur Einspeisung ins Erdgasnetz - Teil 2: Festlegung für Kraftstoffe für Kraftfahrzeuge, Berlin: Beuth Verlag GmbH, 2017.

[4] M. Sterner, M. Jentsch und U. Holzhammer, Energiewirtschaftliche und ökologische Bewertung eines Windgas-Angebotes, Kassel, 2011.

[5] Stiebel Eltron, „Wärmepumpen: Technik und Funktionsweise," Baunetz Wissen, [Online]. Available: https://www.baunetzwissen.de/heizung/fachwissen/regenerative-energien/waermepumpen-technik-und-funktionsweise-161360. [Access 06 April 2019].

[6] M. Wietschel, S. Ullrich, P. Markewitz, F. Schulte und F. Genoese, Energietechnologien der Zukunft Erzeugung, Speicherung, Effizienz und Netze, Wiesbaden: Springer Fachmedien Wiesbaden, 2015.

[7] R. Paschotta, „Leistungszahl," RP-Energie-Lexikon, 22 February 2017. [Online]. Available: https://www.energie-lexikon.info/leistungszahl.html. [Access 26 April 2019].

[8] M. Fricke, „Berliner Energietage 2016," 2016. [Online]. Available: http://www.energietage.de/fileadmin/user_upload/2016/Vortragsfolien/503_Fricke_Waermepumpen_Energietage2016.pdf. [Access 21 April 2019].

[9] Deutscher Wetterdienst, „Klimadaten Deutschland - Stundenwerte (Archiv)," Deutscher Wetterdienst, [Online]. Available: https://www.dwd.de/DE/leistungen/klimadatendeutschland/klarchivstunden.html. [Access 03 April 2019].

[10] Enair Energy, „Small Wind Turbine Enair 70PRO," [Online]. Available: https://www.enair.es/en/small-wind-turbines/e70pro. [Access 03 April 2019].

[11] Private Source, Photovoltaic plant (Maximum power: 6,24 kW; alignment: south-west).

[12] VDI-Gesellschaft Energie und Umwelt, VDI 4655 - Referenzlastprofile von Ein- und Mehrfamilienhäusern für den Einsatz von KWK-Anlagen, Berlin: Beuth Verlag GmbH, 2008.

[13] Mitnetz GmbH, „Höchstentnahmelast pro Spannungsebene," Mitnetz Strom GmbH, [Online]. Available: https://www.mitnetz-strom.de/Unternehmen/ZahlenFakten/Netzdaten?standAlone=true&NavigationTarget=navurl://578aaf40b458c44d8486cb96d3457e64&sapDocumentRenderingMode=Edge&windowId=WID1512402829062&NavMode=0. [Access 03 April 2019].

[14] F. Graf, A. Krajete und U. Schmack, „Techno-ökonomische Studie zur biologischen Methanisierung bei Power-to-Gas-Konzepten," DVGW Deutscher Verein des Gas- und Wasserfachs e.V., Bonn, 2014.

[15] R. Hinterberger, „Flexibilität zwischen Strom und Wärme," 2015. [Online]. Available: https://nachhaltigwirtschaften.at/resources/e2050_pdf/reports/endbericht_201521_smart_grids_flexibilitaet_zwischen_strom_und_waerme.pdf. [Access 07April 2019].

[16] A. Pfnür, B. Winiewska, B. Mailach und B. Oschatz, „Dezentrale vs. zentrale Wärmeversorgung im deutschen Wärmemarkt," September 2016. [Online]. Available: http://www.bdh-koeln.de/fileadmin/user_upload/pressemitteilungen_pdf/summary_der_studie_dezentrale_vs_zentrale_waermeversorgung.pdf. [Access 07 April 2019].

[17] M. Schenker und I. Tiator, Wärmepumpen - Wärmepumpenanlagen, 2. Hrsg., Würzburg: Vogel Business Media GmbH, 2014.

[18] R. Paschotta, „Fernwärme," RP-Energie-Lexikon, 21 February 2017. [Online]. Available: https://www.energie-lexikon.info/fernwaerme.html. [Access 11 April 2019].

[19] L. Holm, „Strompreis in Deutschland," [Online]. Available: https://1-stromvergleich.com/strom-report/strompreis/. [Access 18 April 2019].

[20] Statista, „Entwicklung der Gaspreise für Haushaltskunden in Deutschland in den Jahren 2007 bis 2017 (in Euro-Cent je Kilowattstunde)," November 2017. [Online]. Available: https://de.statista.com/statistik/daten/studie/168286/umfrage/entwicklung-der-gaspreise-fuer-haushaltskunden-seit-2006/. [Access 18 April 2019].

[21] J. Hakenes, „Fernwärme: Technik, Nutzung, Kosten und Alternativen," 30 November 2017. [Online]. Available: https://www.co2online.de/modernisieren-und-bauen/heizung/fernwaerme/. [Access 18 April 2019].

[22] D. Wolff und K. Jagnow, „Überlegungen zu Einsatzgrenzen und zur Gestaltung einer zukünftigen Fern- und Nahwärmeversorgung," Wolfenbüttel/Braunschweig, 2011.

Modeling and experimental validation of a unitized regenerative fuel cell

Cassandra Klonz
Lehrstuhl für elektrische Netze und erneuerbare Energien
Otto von Guericke University Magdeburg
Magdeburg, Germany
cassandra.klonz@st.ovgu.de

Abstract— **The energy sector is in transition and needs new technologies to reduce the policy driven carbon emissions. Hydrogen can be used to store the surplus energy to increase the yield of clean energy sources. Unitized regenerative fuel cells (URFC) offer thereby the possibility to combine an electrolyser and a fuel cell in one system to generate and utilize the hydrogen. This paper aims to propose a performance model for the quasi-steady state behavior of a URFC based on a proton exchange membrane (PEM) working on hydrogen and air. The electrochemical behavior of the URFC has been modeled by simulating in MATLAB which offers enough precision for engineering applications. The model has been validated through voltage-current density curves with experimental measurements using a single cell URFC. It is observed that the simulated polarization behavior is in good agreement with the experimental results. Hence the influence of fitting factors such as exchange current densities, charge transfer coefficients and the degree of humidification on cell performance is analyzed.**

Keywords— URFC, electrolyser, fuel cell, hydrogen, proton exchange membrane, polarization curve

I. INTRODUCTION

Political targets, as exemplified by the UN Climate Change Conference in Paris in 2015 [1], lead to a significant reduction of the emissions of greenhouse gases, especially of carbon dioxide. One of the main producers of carbon dioxide is thereby the energy sector [2], which was based for a long time on fossil fuels and continues to grow due to the increasing world population and the growing living standards of humankind [3]. In order to achieve those climate goals, technologies with a zero carbon emission such as the renewable energies have to be further expanded. The biggest challenges currently faced by sustainable energy sources are their very volatile grid feed-in, their decentralized occurrence and the lack of direct influence on their production behavior. As a result, a stable network cannot be guaranteed. To stabilize the balance of power, there are various technologies, including the unitized regenerative fuel cell which offers the possibility to combine the electrolyser and the fuel cell in one system. The regenerative energies should primarily feed in the generated energy directly into the grid. When there is an excess of electricity, the energy can be used by converting water into oxygen and hydrogen through electrolysis. The generated hydrogen can then be stored to be converted back when needed by a fuel cell to electrical and thermal energy. The advantage of the system is that it can provide an effective, economical and compact solution by using the same components. This technology could be a key technology in the energy transition, especially due to the large area of application. Thus this paper deals with the model development and simulation of the polarization curve for the component design and operation of the URFC tested in the project RE-FLEX.

II. UNITIZED REGENERATIVE FUEL CELL CONCEPT

The PEM-URFC can operate both in fuel cell mode (1) and electrolysis mode (2).

$$4H^{+} + O_2 + 4e^{-} \rightarrow 2H_2O \tag{1}$$

$$2H_2O \rightarrow 4H^{+} + O_2 + 4e^{-} \tag{2}$$

In electrolysis mode, an external voltage source supplies a potential above the water decomposition voltage of 1.23 V to produce hydrogen. This hydrogen is used to generate energy in fuel cell mode, which is the reversed reaction to the electrolysis. Each cell of the PEM-URFC consists of an anode and a cathode separated by a membrane. The individual electrodes are composed of the bipolar plate (BPP), the gas diffusion layer (GDL) and the catalyst coating. In the following, the operation of the fuel cell mode is explained in more detail. The hydrogen and the oxygen pass through the BPP to the GDL and further to the catalyst layer in order to provide a nearly uniform distribution of the reactants over the entire active surface of the catalyst. There the electrochemical reaction of the gases takes place because the activation energy is lowered, so that the reaction rate increases. On the anode side, this leads to oxidation of the hydrogen. Due to the ionization results a potential difference between the anode and the cathode. The generated electrons migrate to the cathode side and react with the protons and the supplied oxygen or air flow to water to compensate the potential difference. The formed water, heat and residual gas are evacuated through the GDL into the corresponding channel structure of the bipolar plates [4].

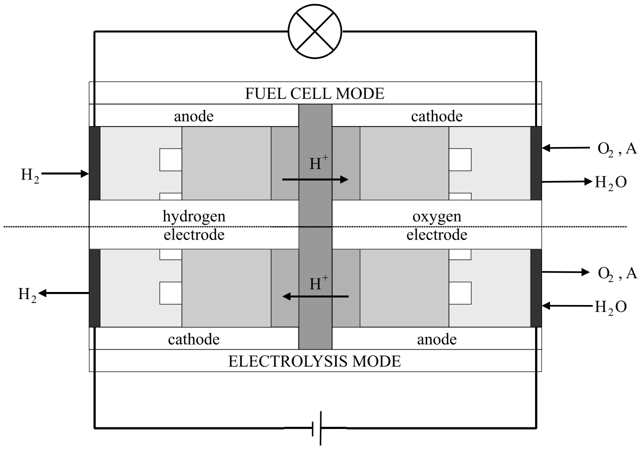

Fig. 1. Simplified structure of a PEM-URFC [7]

The investigated concept for the operation of the PEM-URFC is based on the use of bifunctional electrodes which is illustrated in figure 1. In this case, the reaction area of the hydrogen electrode is always supplied with the fuel whereas the oxygen electrode is always supplied with the oxidizing agent [5]. To increase the energy density and performance of the URFC, the cells are assembled into a stack. In addition, cooling plates are installed to ensure a nearly constant temperature in the PEM-URFC [6]. However, the biggest challenge is the oxygen evolution electrode because many materials either cause too high potentials or have poor oxygen reduction behavior. In the future, an optimization must take place, so that the efficiency increases and costs and degradation processes can be reduced. Nevertheless, the PEM-URFC could be a key technology in the future as it offers a flexible alternative for energy storage of the renewables. A major advantage is the possibility of connecting the sectors by linking the gas, electricity and district heating network. The hydrogen produced by the PEM-URFC can be stored directly or fed into the natural gas grid and if applicable in addition by methanation. In the case of energy demand, the reformed natural gas can be reconverted in a combined heat and power plant or in a combined cycle gas turbine. The resulting heat can be channeled into the district heating network. This conversion into electrical and thermal energy can also be done by using the fuel cell mode of the URFC. By building a prospective smart grid, end users could also be included in the energy grid, creating a highly flexible and effective large-capacity storage system. The energy could be used bilaterally for small-scale applications in the home as well as in the industrial or mobility sector [7].

III. SYSTEM MODELING

In the following the quasi steady state of the URFC in fuel cell mode is going to be characterized.

A. Reversible voltage

The thermodynamic maximum cell voltage U_{th} of a fuel cell, which is operated with hydrogen and oxygen, is calculated by the enthalpy of reaction and is also referred to as thermo neutral cell voltage (3).

$$U_{\mathrm{th}} = -\frac{\Delta H}{z\mathrm{F}} \tag{3}$$

In the fuel cell, only a part of the energy can be converted into electricity because losses occur due to the generation of entropy. The enthalpy of reaction and the entropy of reaction can be determined by the temperature-dependent enthalpies and entropies of formation.

$$\Delta G = \Delta H - T\Delta S \tag{4}$$

The Gibbs free energy can be used to calculate the reversible cell voltage U_{rev} (5). It is the potential difference arising in an open circuit considering the entropy of reaction. This voltage is an open circuit voltage in which no conversion of the substances and thereby no current flow takes place [8]. For water electrolysis, the reversible cell voltage describes the minimum voltage required for splitting the water [9].

$$U_{\mathrm{rev}} = -\frac{\Delta G}{z\mathrm{F}} \tag{5}$$

The reversible efficiency η_{rev} of the fuel cell is thus limited by the entropy, as shown by equation (6) [8].

$$\eta_{\mathrm{rev}} = \frac{\Delta G}{\Delta H} \tag{6}$$

The maximum efficiency can be influenced by the temperature and the pressure. This dependence of the potential on the temperature and the pressure or rather the concentration of the reactants can be described by the Nernst equation (7) [10].

$$U_N = U_{rev}^0 + \frac{\mathrm{R}T}{z\mathrm{F}} \cdot \ln\left(\frac{p_{\mathrm{H_2}} \cdot p_{\mathrm{O_2}}^{0,5}}{p_{\mathrm{H_2O}}}\right) \tag{7}$$

B. Polarization

The reversible cell voltage cannot be achieved in reality due to different polarizations. These significant losses include activation losses U_{act}, concentration losses U_{conc}, ohmic losses U_{ohm} and internal currents. The polarizations have different effects at the respective currents in the stationary operation of the fuel cell. Due to the parallel operation of the losses, the polarization curve of the fuel cell can be described by equation (8) and equation (9).

$$U_{\mathrm{FC}} = U_{\mathrm{rev}} - (U_{\mathrm{act}} + U_{\mathrm{conc}} + U_{\mathrm{ohm}}) \tag{8}$$

$$U_{\mathrm{WE}} = U_{\mathrm{rev}} + U_{\mathrm{act}} + U_{\mathrm{ohm}} \tag{9}$$

The voltage losses are explained in more detail below and related to the current density for better comparability [11].

The activation losses describe the difference between the actual voltage and the equilibrium potential. They are caused by the poor kinetics of the electrodes, as part of the voltage is used to drive the electrochemical reaction. Small current densities produce large losses at the electrodes causing a large drop in the cell voltage. The losses occur both on the anode and on the cathode side. The reaction kinetics of the reduction of oxygen is much slower, which is why it requires a higher overvoltage. Since it is the limiting factor, the activation losses of the anode can be neglected. The losses can be described by the following equation (10).

$$U_{\text{act}} = \frac{\mathrm{R}T}{2\alpha\mathrm{F}} \ln\left(\frac{i}{i_0}\right) \tag{10}$$

The critical factors are the charge transfer coefficient α and the exchange current density i_0. The exchange current density describes the reactivity of the active surface and is dependent on the temperature and concentration [10].

The concentration losses are formed due to mass transfer limitations. These occur particularly at the oxygen electrode. In fuel cell mode the oxygen is affected in its transport by the remaining air and water formed [11]. In electrolysis mode the losses are mainly caused by the oxygen molecules, as they block the surface, causing that the water does not reach the reactive area fast enough. If the electrochemical reaction is faster than the transport of the substances to the reactive surface, a concentration gradient is created. This phenomenon occurs especially at high current densities and thus high conversion rates and low surface concentration. However, these effects have little influence in commercial electrolysis, as the operating current density is never high enough to raise the limiting current and they are therefore neglected for this consideration. The losses that occur due to the concentration difference can be described by equation (11).

$$U_{\text{conc}} = -\frac{\mathrm{R}T}{z\mathrm{F}} \ln\left(1 - \frac{i}{i_{\mathrm{L}}}\right) \tag{11}$$

The theoretically maximum current density is called limiting current density i_{L}. At this point the catalyst surface does not have a concentration of reactants since they are consumed at the same moment they strike the surface. The limiting current density depends on both pressure and temperature [8].

The ohmic losses are generated by the resistance to the flow of ions R_{ion} in the electrolyte, the electrical resistance R_{el} of the electrical conductors and by the contact resistance R_{cont} between the electron-conducting materials. According to ohm's law (12) the resistances are proportional to the voltage.

$$U_{\text{ohm}} = I \cdot (R_{\text{ion}} + R_{\text{el}} + R_{\text{cont}}) \tag{12}$$

The dominant losses are caused by the ionic resistance of the membrane. They can be determined by using the thickness, conductivity and active area of the membrane as can be seen in equation (13).

$$R_{\text{Ion}} = \frac{d}{\sigma A} \tag{13}$$

But especially the conductivity is strongly influenced by the water content and the temperature in the membrane. A frequently used empirical relation for calculating the membrane conductivity is shown below [12].

$$\sigma = (0{,}005139\lambda - 0{,}00326) \cdot exp\left(1268\left(\frac{1}{303} - \frac{1}{T}\right)\right) \tag{14}$$

In the case of internal currents, a small amount of hydrogen diffuses through the membrane, even though it has high impermeability and electrical conductivity. Thus, the hydrogen does not participate in the electrochemical reaction, which causes fewer electrons to pass through the outer circuit, resulting in lower cell voltage. These losses occur especially at low current densities and at open circuit voltage. However, under operating conditions the hydrogen concentration at the catalyst layer increases, which reduces the driving force through the membrane. Therefore the internal currents can be largely neglected both in fuel cell and electrolysis mode [11].

IV. EXPERIMENTAL STUDY

The aim of the experimental investigations is to record a voltage-current density characteristic.

A. *URFC assembly*

For the PEM-URFC cell assembly a membrane electrode assembly was analyzed in the fuel cell test system quickCONNECT fixture FC25 / 100 from balticFuelCells GmbH. The system offers the possibility to test a single unitary reversible fuel cell with a Nafion 115 membrane with an active cell area of 25 cm². The hydrogen electrode is loaded with 3.0 mg/cm² platinum and contains as a gas diffusion layer a carbon cloth. The oxygen electrode on the other hand is loaded with a mixture of 1.5 mg/cm² platinum and 1.5 mg/cm² iridium ruthenium oxide followed by a platinised titanium gas diffusion layer. The bipolar plates have a parallel flow field design to feed the membrane with gases.

B. *Experimental set up*

The distribution of the measurement points was chosen accordingly to obtain a sufficiently high density in the characteristic regions. In fuel cell mode, constant currents were applied to the cell. The holding period of each measurement step is 30 seconds after the ramp has been completed so that the steady state can be set. In the electrolysis mode, a constant voltage was applied. The holding period of each measuring step is two minutes after the ramp has been completed. In order to ensure the reproducibility of the experiment, each characteristic curve is measured three times and the function value is calculated using the mean value of the respective measurement results. The supplied volume flow of water in electrolysis mode was kept constant

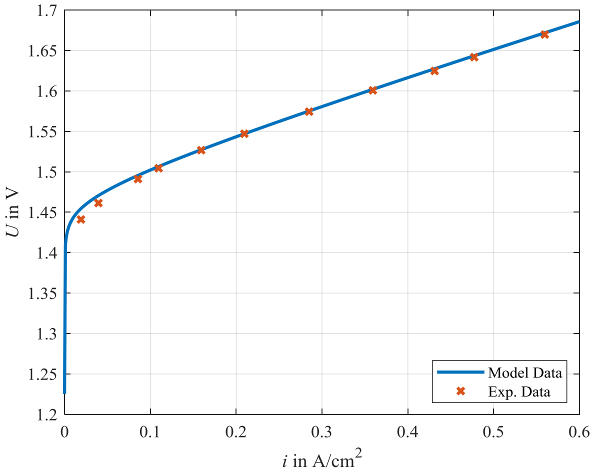

Fig. 2. Comparison of simulated and experimental polarization curve of the electrolysis mode of a PEM-URFC

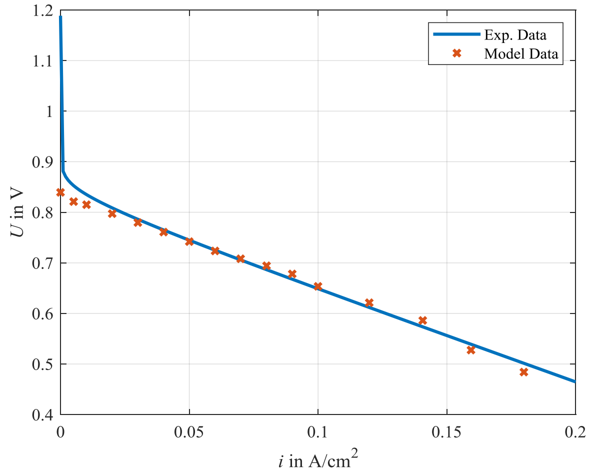

Fig. 3. Comparison of simulated and experimental polarization curve of the fuel cell mode of a PEM-URFC

at 40 ml/s. In fuel cell mode, the volumetric flow rate of oxygen is adjusted to the current density of the cell, while maintaining a range between 0.3 - 1.0 l/s. The hydrogen side is operated in dead-end mode. To prevent the gas channels from blocking with water, the hydrogen area is purged every 45 s for 500 ms. The measurements were achieved at 50°C and at atmospheric pressure.

V. RESULTS AND DISCUSSION

The i-V curves of the PEM-URFC have been modeled with dependence on cell area, cell temperature, and several internal parameters. Fig. 2 and fig. 3 show graphically the comparison between the simulated curves using the proposed model and the experimental data. Four model parameters such as the exchange current density, the charge transfer coefficient and the degree of humidification in both electrolysis and fuel cell mode could not be reliably estimated. Therefore they were allowed to vary freely. Table I lists the values assumed for the fitted parameters in the illustrated URFC model.

TABLE I. VALUES FOR THE FITTED PARAMETERS

Parameter	Value	Unit
α_{WE}	0.5	
α_{FC}	0.5	
$i_{0,\mathrm{WE}}$	9×10^{-10}	A/cm^2
$i_{0,\mathrm{FC}}$	9×10^{-14}	A/cm^2
λ_{WE}	5.1	S/cm
λ_{FC}	1.5	S/cm

The models described clearly fit the experimental data and the shape of the obtained curves is typical. The small discrepancy at low current densities is believed to arise because of some simplifying assumptions. For the electrolysis mode the fitted values of the parameters were comparable to literature data. Carmo et al. reported for a similar electrolysis assembly with a Pt-Ir anode catalysts exchange current densities between 10^{-3} - 10^{-13} A/cm² and therefore the value lies within the ranges [13]. The current exchange of the fuel cell on the other hand is poorer than reported by Doddathimmaiah et. al [14]. These deviations could also be related to the major losses that occur due to the ohmic losses. This results from the fact that during the entire experiments no statement about the humidity of the membrane could be made. The conductivity of the membrane is proportional to its water content and therefore the water management of the fuel cell is an essential part of determining the polarisation curve. However, an excessive amount of water on the cathode side causes flooding of the cell and the transport of oxygen through the GDL is restricted. Even if there is no flooding of the cell, water forms on the hydrogen side due to diffusion through the membrane. In order to prevent the clogging of the pores the cell is regularly purged. In addition, no homogeneous membrane moisture profile occurs over the active cell surface, which results in the formation of hot spots and an inhomogeneous current density distribution.

VI. CONCLUSION

A simple model to simulate a PEM-URFC has been proposed. The aim of the investigations was to achieve a sufficient precision of the characteristics with a modest computer demand for applications in the stationary area, especially in order to design the stacking of a PEM-URFC and to dimension the cooling system. The validation was carried out with experimental data from a small test bench. The details for the steady-state model, the assumptions for the calculation and the accuracy of the fitting to the experimental results issues have been presented and discussed. The results of the validation are satisfactory, the polarization curves approximately reflect the trends of the experimental data. A major remaining challenge is to integrate a model to determine the losses that occure due to the humidification of the membrane. Furthermore future testing should be done with multicellular URFC systems and with extended test conditions.

REFERENCES

[1] Bundesministerium für Umwelt, Naturschutz, Bau und Reaktorsicherheit, „Übereinkommen von Paris,“ Paris, 2015.

[2] S. Lazarou and S.Makridis, “Hydrogen Storage Technologies for Smart Grid Applications,” *Challenges*, vol. 8, pp. 1-8, May 2017.

[3] K. Stierstadt and G. Fischer, in *Energie - das Problem und die Wende in Physik, Technik und Umwelt*, Haan-Gruiten, Germany: Verlag Europa-Lehrmittel Nourney, Vollmer GmbH und Co KG, 2015.

[4] S. Geitmann, Wasserstoff & Brennstoffzellen: die Technik von morgen, Kremmen: Hydrogeit Verlag, 2004.

[5] S. Grigoriev, P. Millet, K. Dzhus, H. Middleton, T. Saetre and V. Fateev, “Design and characterization of bi-functional electrocatalytic layers for application in PEM unitized regenerative fuel cells,“ *Int. J. Hydrogen Energy,* vol. 35, pp. 5070-5076, 2010.

[6] K. Ledjeff-Hey, F. Mahlendorf and J. Roes, Brennstoffzellen: Entwicklung, Thechnologie, Anwendung, Heidelberg: C. F. Müller Verlag, 2001.

[7] P. Kühne, M. Wenske, M. Heuer and M. Wolter, „Experimentelle Charakterisierung einer reversiblen PEM-Brennstoffzelle als flexibles Energiespeichersystem,“ *25. Energie-Symposium: Nutzung Regenerativer Energiequellen und Wasserstofftechnik*, Stralsund, 2018.

[8] F. Barbir, PEM fuel cells: theory and practice, Boston: Elsevier/Academic Press, 2013.

[9] P. Kurzweil and O. Dietlmeier, Elektrochemische Speicher: Superkondensatoren, Batterien, Elektrolyse-Wasserstoff, rechtliche Grundlagen, Wiesbaden: Springer Verlag, 2015.

[10] J. Larminie and A. Dicks, Fuel Cell Systems Explained, Chichester: Wiley, 2000.

[11] J. Haubrock, Parametrierung elektrischer Äquivalentschaltbilder von PEM Brennstoffzellen, Magdeburg: Otto-von-Guericke Universität Magdeburg, 2008.

[12] H. Xiao, H. Guo, F. Ye and C. Ma, “Numerical Study of the Dynamic Response of Heat and Mass Transfer to Operation Mode Switching of a Unitized Regenerative Fuel Cell,“ *Energies,* vol. 9, 2016.

[13] M. Carmo, D. Fritz, J. Mergel and D. Stolten, “A comprehensive review on PEM water electrolysis,“ *Int. J. Hydrogen Energy,* vol. 38, pp. 4901-4934, 2013.

[14] A. Doddathimmaiah and J. Andrews, “Theory, modelling and performance measurement of unitised regenerative fuel cells,“ *Int. J. Hydrogen Energy,* vol. 34, pp. 8157-8170, 2009.

Integrated Optimization of Large Scale Power and Gas Flow Problems

Houben, Raphael
Institut für Elektrische Anlagen und Energiewirtschaft
RWTH Aachen University
Aachen, Germany
raphael.houben@rwth-aachen.de

Löhr, Lukas
Institut für Elektrische Anlagen und Energiewirtschaft
RWTH Aachen University
Aachen, Germany
l.loehr@iaew.rwth-aachen.de

Moser, Albert
Institut für Elektrische Anlagen und Energiewirtschaft
RWTH Aachen University
Aachen, Germany
info@iaew.rwth-aachen.de

Abstract— **The integrated modelling of power and gas systems is gaining importance as a result of climate policy discussions on sector coupling. Power-to-Gas-units increase existing interactions between electricity and gas networks and thus require an integrated calculation. Classic optimal power and gas flow problems (OPGF) that aim to minimize economic dispatch costs have been applied so far to small test systems. To investigate the system wide effects of sector coupling, large transmission networks must be considered. However, respecting switching decisions for power plants and the non-convexity of the pressure-loss equation results in a complex optimization problem. Therefore, the problem is decomposed. First, the OPGF as a mixed-integer linear problem with a successive linear approximation of the pressure loss equation combined to a DC power flow is solved. Then special attention is paid on the flow-pressure-subproblem by solving it using nonlinear optimization methods. The investigations contain a validation of this methodology using the Belgian H-Gas system combined to an IEEE24 power grid and a comparison of different sized test-systems regarding computation time and optimality. Furthermore, investigations show a detailed solution for the German power and gas transmission system.**

Keywords—Integrated Optimization, Power Flow, Gas Flow, DCOPF, Power-to-Gas, Gas-to-Power

I. NOMENCLATURE

Quantities

$\mathrm{N_P}$	Nodes in the electric network model
PL	Power lines
T	Transformers
$\mathrm{PST} \subseteq T$	Phase-shifting-transformers
HVDC	High voltage DC lines
PG	Power generation units
PC	Power consumers
$\mathrm{N_G}$	Nodes in the gas network model
GP	Gas Pipelines
C	Compressor stations
PV	Pressure-regulating valves
GI	Gas injections
GC	Gas consumers
PTG	Power-to-Gas transferring units
GTP	Gas-to-Power transferring units

Variables

Power flow in branches

$\mathrm{P_{ij}} \in \mathbb{R} \qquad \forall ij \in \mathrm{PL} \cup \mathrm{T} \cup \mathrm{HVDC}$

Power generation and consumption

$P_i \in \mathbb{R}_+ \qquad \forall i \in \mathrm{PG} \cup \mathrm{PC} \cup \mathrm{GTP} \cup \mathrm{PTG}$

Phase angle at nodes

$\theta_i \in \mathbb{R} \qquad \forall i \in \mathrm{N_P}$

Gas flow in branches

$\mathrm{V_{ij}} \in \mathbb{R} \qquad \forall ij \in \mathrm{GP} \cup \mathrm{C} \cup \mathrm{PV}$

Gas consumption or generation

$V_i \in \mathbb{R}_+ \qquad \forall i \in \mathrm{GI} \cup \mathrm{GC} \cup \mathrm{GTP} \cup \mathrm{PTG}$

Squared pressure at nodes

$p_i^2 = \pi_i \in \mathbb{R}_+ \qquad \forall i \in \mathrm{N_G}$

Variables of convex combination

$\lambda_{ij}^1, \lambda_{ij}^2 \in [0,1] \qquad \forall ij \in \mathrm{GP}$

Parameters

Susceptance of a power line or a transformer

$\mathrm{b_{ij}} \qquad \forall ij \in PL \cup \mathrm{T}$

Pipeline flow coefficient

$\mathrm{C_{ij}} \qquad \forall ij \in \mathrm{GP}$

Lower flow limit of a pipeline

$V_{ij}^{min} \qquad \forall ij \in \mathrm{GP}$

Upper flow limit of a pipeline

$V_{ij}^{max} \qquad \forall ij \in \mathrm{GP}$

Conversion factor of electric energy and gas flow

$\mathrm{R_{PG}}$

II. INTRODUCTION

The coupling of power and gas grids has already gained importance in recent years. Today, the coupling performed by Gas Fired Power Plants (GFPP) has mainly an unidirectional relationship. Two factors indicate a significant dependency of gas on the power system and vice versa. First, the share of electrical energy produced by Gas-to-Power-units (GtP). With 13.3 % for the German energy system in 2017 [1] this share was at a high level, even though is still at a low level compared to other countries. Closely related to this, secondly, the share of gas used for power generation in total gas consumption (11.03 % in 2017 for the German energy system [1]) shows the relevance of the electricity system for the gas infrastructure.

There are several reasons for expecting increasing interactions of those systems in the future.

To meet the targets defined in the Paris Agreement, the power generation sector needs to be reshaped from the utilization of fossil fuels to renewable energy sources (RES). In addition, secure capacity has to be partly replaced in the context of coal and nuclear phase-out in Germany.

GFPPs play an essential role in this development. They can provide flexibility, which is indispensable to equalize wind and solar power volatility. Furthermore, natural gas can contribute to meet short-term goals of reducing emissions due to lower greenhouse gas emissions compared to other fossil sources. In long-term, synthetic gas from Power-to-Gas (PtG) can replace natural gas resulting in a carbon neutral energy carrier. The increasing relevance of PtG technology will change the coupling from uni- to bidirectional [2] and thus enable to replace electric grid reinforcement by using existing transport and storage gas infrastructure.

Due to this growing coupling characteristic, the dispatch of coupling technologies (PtG and GFPPs) is strongly influenced by the states of both systems. Conversely, the use of the coupling technologies affects the dispatch of many units in both systems as well as state variables in both grids like flows, voltages or pressures. To adequately consider the existing and future synergies and dependencies between the electricity and gas system, an integrated modeling and optimization of both systems is necessary.

A variety of publications exists on this subject. The interdependency is either modelled in a linear or a nonlinear optimization problem, where the model usually includes integer variables. Therefore, it is a mixed integer linear program (MILP) or a mixed integer nonlinear program (MINLP). The following table shows a selection of different publications:

Subject	Reference	Year	Bidirectional flow	System size	Model
OPGF	[3]	2004	No	24 Nodes	MINLP
OPGF	[4]	2007	No	7 Nodes	MILP
OPGF	[5]	2014	No	44 Nodes	MILP
OPGF	[6]	2017	No	23 Nodes	MILP
OPGF	[7]	2017	Yes	44 Nodes	MINLP

Table 1: A variety of existing publications

As it can be seen in Table 1, a bidirectional coupling between power and gas grids provided by GFPPs as well as PtG is a new development and therefore rarely considered. The number of nodes is an indicator for the considered system size as every single node is usually connected to a few units. Hence, existing publication focussed on small, simple systems to perform sample calculations, because the underlying optimization problem is highly complicated. To optimize the supply in large systems such as the German power and gas grid, it is necessary to reduce this complexity. The model can be simplified by restricting the problem to single time periods, which results in the impossibility of the optimization of storage utilization. However, this is necessary in order to get practicable solving times. The previously mentioned publications use different modelling and therefore various solvers to find a solution to the OPGF-problem, but none of them shows a clear superior solving time efficiency. As a result, the selection of a suitable solver is still an open research subject.

In this paper a new method to calculate a power and gas flow respecting the interdependencies induced by a bidirectional coupling is proposed. Special focus is placed on the ability to solve large problems in practicable computation time. For this purpose, the approach uses linear and nonlinear optimization methods with the objective of minimising the operational costs of power and gas supply.

Chapter III “Model and Method” is divided into three sub-sections. In section A, a linear model similar to the one formulated in [4] containing integer variables is presented. During the described method this optimization problem is solved successively with small adjustments in each iteration, described in section B. At the end of this process a nonlinear subproblem is solved to get an accurate solution of the modelled operating state as described in section C.

The investigations in Chapter IV show a validation of this method, computational times for different networks and results for the German power and gas transmission network.

III. MODEL AND METHOD

Both power and gas grid are modelled in a graph with nodes and branches. Branches are connecting two nodes and include a flow, which corresponds to a power or a gas flow. They model power lines, (phase-shifting-) transformers, high voltage DC lines (HVDC), gas pipelines, compressor stations, pressure regulating units or coupling elements. Nodes contain state variables, the squared pressure in gas or the phase angle in power grids respectively. Consumers, generating/injecting units or storages for power or gas can be attached to these nodes. Each of them is modelled by a variable representing their demand or their generation/injection for power and gas respectively. Each variable is restricted to the associated unit’s operating limits.

A. Mixed Integer Linear Program

The flow on all AC lines and every transformer except phase shifting transformers are related to the phase angle at the beginning and the end node through equation (1). As usual for DC optimal power flow (DCOPF), b_{ij} represents the susceptance of each arc. The power flow is calculated in per-unit.

$$P_{ij} = b_{ij} \cdot (\theta_i - \theta_j) \qquad \forall ij \in \mathrm{P}L \cup (\mathrm{T} \setminus \mathrm{PST}) \qquad (1)$$

Active elements like phase-shifting transformers provide the flexibility to influence the power flow by changing the tap position. This is modelled by an additional phase angle related to the supplementary voltage of the transformer (2).

$$P_{ij} = b_{ij} \cdot (\theta_i - \theta_j + \alpha_{s1,i} - \alpha_{s2,i}) \qquad \forall ij \in \mathrm{PST} \qquad (2)$$

The continuity equation (3) connecting power flow branches, suppliers and electricity consumers completes the electrical network model. $\delta^+(i)$ refers to outgoing branches, $\delta^-(i)$ refers to incoming branches of node i. $\delta(i)$ is a quantity containing every unit connected to node i.

$$\begin{array}{c}\sum\limits_{\substack{ij\in(\mathrm{PL}\cup\mathrm{HVDC}\cup\mathrm{T})\\ \cap\delta^{+}(i)}} P_{ij} + \sum\limits_{\substack{i\in(\mathrm{PC}\cup\mathrm{PTG})\\ \cap\delta(i)}} P_i \\ - \\ \sum\limits_{\substack{ij\in(\mathrm{PL}\cup\mathrm{HVDC}\cup\mathrm{T})\\ \cap\delta^{-}(i)}} P_{ij} + \sum\limits_{\substack{i\in(\mathrm{PG}\cup\mathrm{GTP}\cup)\\ \cap\delta(i)}} P_i \end{array} = 0 \qquad \forall i\in \mathrm{N_P} \qquad (3)$$

Gas pipelines establish – similar to AC lines in the electrical network – a link between flow and state variables. The pressure-loss equation (4) links gas flow and the (squared) pressure at the beginning and the end node for gas pipelines.

$$|V_{ij}|\cdot \mathrm{V}_{ij} = C_{ij}\cdot(\pi_i-\pi_j) \qquad \forall ij\in \mathrm{GP} \qquad (4)$$

The non-convexity of this equation (shown in Fig. 1 to 3) complicates a linearization. The piecewise linearization is a suitable method to do it, as applied in [4, 5, 8]. This paper describes a similar approach restricting the total number of linearization points to two. This corresponds to approximating the pressure-loss curve through one single straight line. Two extreme points with their corresponding gas flow V_{ij}^{min} and V_{ij}^{max} define this line. The selected gas flow-pressure loss relation is a convex combination of these points as stated in (5)-(7):

$$V_{ij}^{min}\cdot\lambda_{ij}^{1} + V_{ij}^{max}\cdot\lambda_{ij}^{2} = V_{ij} \qquad ij\in \mathrm{GP} \qquad (5)$$

$$\begin{array}{c}|V_{ij}^{min}|\cdot V_{ij}^{min}\cdot\lambda_{ij}^{1}\\ + \\ |V_{ij}^{max}|\cdot V_{ij}^{max}\cdot\lambda_{ij}^{2}\end{array} = C_{ij}\cdot(\pi_i-\pi_j) \qquad \forall ij\in \mathrm{GP} \qquad (6)$$

$$\lambda_{ij}^{1}+\lambda_{ij}^{2} = 1 \qquad \forall ij\in \mathrm{GP} \qquad (7)$$

Compressors are modelled by two nodes connected through a compressor branch that can increase the pressure level at its end node by mechanical work. Due to the wide operating range of compressors, the relation between flow and pressure is neglected (8).

$$\pi_i \le \pi_j \qquad \forall ij\in \mathrm{C} \qquad (8)$$

In contrast, a pressure regulating valve can decrease the pressure at its end to control pressure or gas flow (9).

$$\pi_i \ge \pi_j \qquad \forall ij\in \mathrm{PV} \qquad (9)$$

The continuity equation for the gas network model (10) is analogous to the electrical network. Gas flow of incoming branches and injections connected to a node has to meet the demand of attached consumers and the outflowing gas.

$$\begin{array}{c}\sum\limits_{\substack{ij\in(\mathrm{GP}\cup\mathrm{C}\cup\mathrm{PV})\\ \cap\delta^{+}(i)}} V_{ij} + \sum\limits_{\substack{i\in(\mathrm{GC}\cup\mathrm{GTP})\\ \cap\delta(i)}} V_i \\ - \\ \sum\limits_{\substack{ij\in(\mathrm{GP}\cup\mathrm{C}\cup\mathrm{PV})\\ \cap\delta^{-}(i)}} V_{ij} + \sum\limits_{\substack{i\in(\mathrm{GI}\cup\mathrm{PTG})\\ \cap\delta(i)}} V_i \end{array} = 0 \qquad \forall i\in \mathrm{N_G} \qquad (10)$$

Coupling technologies as GFPPs or PtG units are connected to one electrical and one gas node. The transfer between gas and power is modelled by a constant unit specific efficiency multiplied by the calorific value of gas (11), (12).

$$P_i = R_{\mathrm{PG}}\cdot\frac{1}{\eta_i}\cdot V_i \qquad \forall i\in \mathrm{PTG} \qquad (11)$$

$$P_i = R_{\mathrm{PG}}\cdot\eta_i\cdot V_i \qquad \forall i\in \mathrm{GTP} \qquad (12)$$

The objective of this optimization is to minimise operating costs of the system, in particular fuel costs.

B. Successive linearization

The first stage of the described method: “successive sub-optimization”, is a linearization of the gas flow-pressure loss relationship through one straight line. By this, the pressure loss is estimated vaguely. Therefore, this process is repeated successively. In the first iteration, the flow limits V_{ij}^{min} and V_{ij}^{max} equal the original pipeline limits. The first optimization considering this flow limits determines an operating point with a specific gas flow for this pipeline. A reduction parameter regressively sets new flow limits at the next iteration. The new limits V_{ij}^{min} and V_{ij}^{max} are formed equidistant around the fixed operating point resulting from the previous iteration. During each iteration, pressure limits at each node can be exceeded due to the inaccuracy of linearization, however, this is punished in the objective function with penalty costs. Consequently, the solution process resembles an optimization with pressure relaxation, where only flow limits for the gas network model exist. The penalty costs force the optimization to find a feasible solution that does not exceed any pressure limit. The successive process is represented in Fig. 1 to 3 for a regressive reduction of 33 % in each iteration. Within this process, the new calculated flow limits never exceed the initial limits.

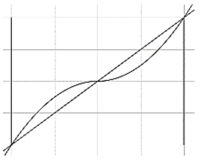

Fig. 1: Linearization (Iteration 0)

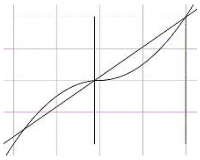

Fig. 2: Linearization (Iteration 1)

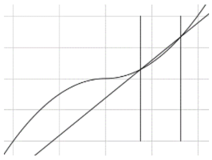

Fig. 3: Linearization (Iteration 2)

Fig. 1, 2 and 3 show, how this approximation gets more precise with each iteration. The parameters “flow-limits-reduction” and “pressure-penalty-costs” enable adjusting the successive linearization.

Small reductions of the flow-limits do not restrict the solution space much, resulting in better solutions. However, it needs more iterations to get a solution with adequately approximated pressure values. Therefore, if the solution time is fixed, the objective value is worse for smaller reduction parameters. On the other hand, if the reduction is too restrictive, better or even every feasible solution regarding pressure limits may be skipped.

Higher penalty costs have a greater impact on the objective function and therefore push the solver to find solutions complying the pressure limits. Conversely, lower penalty costs do not change the objective function much, resulting in better solutions regarding the original objective. However, if the costs are too low, only solutions that break the pressure limits can be obtained.

The optimal parameter set is depending on the grid topology and the operating situation.

C. *Gas flow and pressure loss subproblem*

Since the converging process of the successive linearization depends essentially on the parametrization of the flow-limit-reduction and the pressure-penalty-costs, the accuracy of the solution is depending on these parameters. To avoid inaccuracies, a gas flow-pressure sub-problem is solved using the precise pressure loss equation (4) in a nonlinear program solved by SCIP and IPOPT. Thus, an accurate solution for the pressure is obtained. The sub-problem consists of pipeline flow, compressor flow and pressure regulating valves flow additionally to the node pressure. They are linked through the pressure-loss-equation (4), the continuity equation for gas nodes (10) as well as the pressure relations at starting and ending nodes of compressors (8) or valves (9). Other variables of the MILP in III like gas injections or demand and supply of coupling units are fixed to the values obtained by the successive linearization. The resulting optimization problem has two major advantages, it contains no integer variables and the problem is significantly less extensive than the whole OPGF problem. This results in a tremendous reduction of solving time compared to the general nonlinear optimization problem.

IV. INVESTIGATIONS

A. *Test systems*

Three distinct networks, each with a different number of nodes and assets, were used for comparison in the investigations. Each model represents a mixture of gas - and power transmission network. They model the Belgian system, a part of the German system, and the whole German system. The three models are differentiated by the number of nodes. Table 2 describes the number of assets present in each network.

	44 nodes	253 nodes	1066 nodes
N_P	24	118	542
PL	29	177	950
T	5	9	198
$PST \subseteq T$	1	0	10
HVDC	0	0	6
PG	26	206	1418
PC	17	99	362
N_G	20	135	524
GP	21	141	537
C	3	29	59
PV	0	0	159
GI	6	10	30
GC	9	99	524
PTG	2	19	92
GTP	2	10	228

Table 2: Number of assets in the different networks

The network topology of the 44 nodes-system is depicted in Fig. 4.

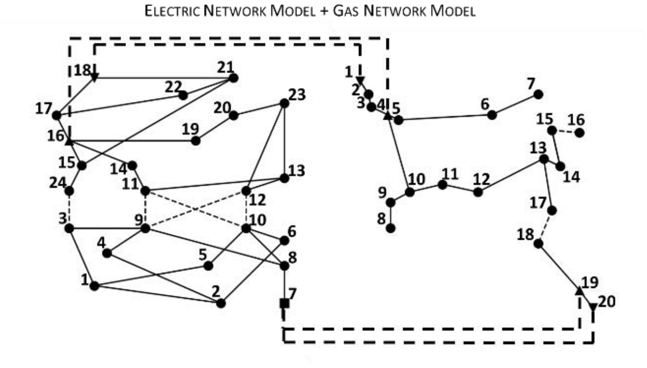

Fig. 4: 44 nodes coupled electric and gas network

B. *Validation*

To validate the explained method, the solutions of a simple test system, the 44 nodes network are compared. One of the solutions is calculated through the described method called successive sub-optimization and the other solution derives from the exact nonlinear equations representing the referred system with the same supply and demand for every single unit solved by the Newton-Raphson-method. In that case electric state variables are calculated using the nonlinear equations constituting the AC power flow also modelling reactive power opposite to the successive sub-optimization that uses simplified equations referred to as DCOPF. These equations do not determine the injected or consumed reactive power. The fact of not knowing the values for generated reactive power is solved by the simplification that consumed reactive power is generated locally at each node so that only reactive losses must be satisfied by the slack bus. Additionally, the resistance of all lines and transformers are neglected as the value is usually small compared to the reactance for an electric transmission system.

A comparison of the results shows a total deviation of 0.002 % for the pressure of all nodes. This small difference derives from the usage of the exact power equations for compressors with the Newton-Raphson calculation, in contrast to using a simplification for compressors and can be observed at node 18 to 20 in Fig. 5.

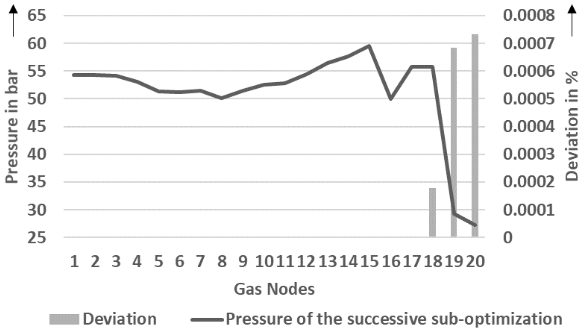

Fig. 5: pressures of the successive sub-optimization

The gas flow in every pipeline and compressor calculated by the successive sub-optimization does not differ from the one calculated using the Newton-Raphson-method. The respective gas flows are represented in Fig. 6.

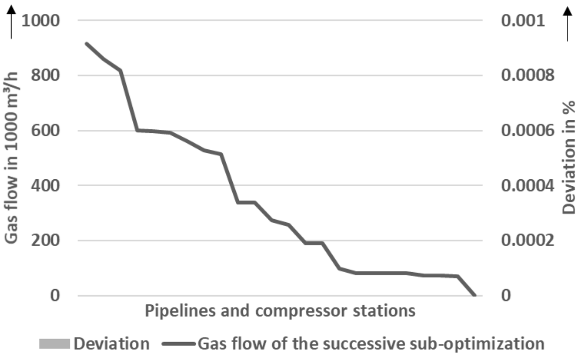

Fig. 6: pipeline and compressor utilization of the successive sub-optimization

In general, an AC power flow only shows small deviations from the results of a DC power flow for a transmission system. However, the computation of a DCOPF is depending on the systems size up to 60-times faster as stated in [9]. The deviations of AC vs. DC power flow calculation can be observed in this interconnected system at every electric bus, as shown in Fig. 7.

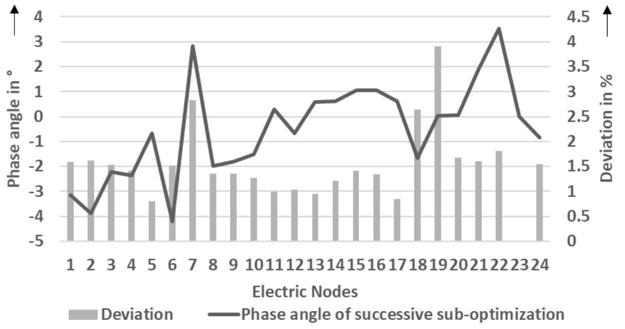

Fig. 7: Phase angles of the successive sub-optimization

As reactive power flow is not considered in the optimization, line utilization is generally underestimated. Fig. 8 displays that the observable deviation is small. Lines that are only used to a low degree in a DCOPF mainly transport reactive power and therefore show higher deviations in the line utilization. The outlying line with a utilization of 26.5 % and a deviation of approximately 3 % is connected to the slack bus and therefore transports reactive power needed by a part of the grid.

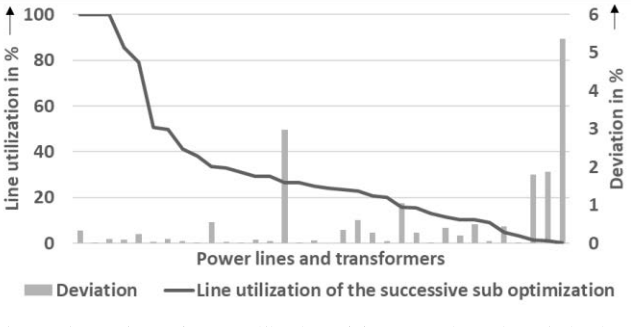

Fig. 8: Line and transformer utilization of the successive sub-optimization

The operating costs including fuel prizes determined by the successive sub-optimization for 24 exemplary operating situations for this small network and the one with 253 nodes are the same as found by a closed nonlinear optimization.

This proves that the successive sub-optimization is able to calculate a supply with small operating costs and that the state variables in the gas system satisfies all nonlinear equations with the exception of the power consumption of compressors.

C. Performance

Table 3 shows a comparison of the computation time for different methods applied on three differently sized networks described in section A of this chapter. The gained solutions have the same operating costs for each grid. Every value represents the total computation time for 24 sample operating situations. The methods MILP and MINLP describe the closed optimization of a linear or a nonlinear formulation of the OPGF respectively. Both methods do not lead to a solution in a practical computation time for the grid model with 1066 nodes.

	MILP	MINLP	Successive Sub-optimization
44 nodes	0.96 s	8.86 s	7.58 s
253 nodes	123.65 s	5145.28 s	31.67 s
1066 nodes	-	-	219.85 s

Table 3: Comparison of computation times for different coupled networks

These calculations show that for small systems a closed optimization provides an optimal solution very quickly but if a larger system with more units is considered a closed optimization is slow. Even in the network model with 253 nodes, the successive sub-optimization is able to discover the optimal solution for all 24 operating situations approximately 4 times faster than a closed optimization.

A comparison of different available solvers shows that compared to CPLEX and SCIP, Gurobi provides the shortest computation times for the successive linearization and to find an optimal solution of the MILP formulation of this problem.

D. Case study: German power and gas transmission

In this section, exemplary results regarding the interdependency of power and gas system calculated using the successive sub-optimization approach are presented. For this purpose, the German power and gas transmission system is modelled in a Graph with 1066 nodes, described in section A. The analysed supply scenarios originate from a forecast for a summer day in 2050 derived from [10]. The total electric energy demand for all 24 use cases is 1080.24 GWh and the gas demand 189.08 Mio. m³/h. Additional RES with a total available energy of 965.8 GWh are available during these cases. Fig. 9 shows the usage of the coupling elements and the power of electric loads subtracted by volatile feed-in of RES (the residual load) during those periods.

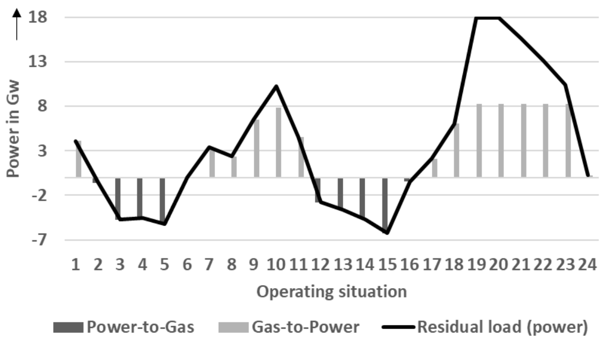

Fig. 9: Usage of PtG and GFPP for 24 operating situations in 2050 German power and gas transmission system

The capacity of RES leads to some operating situations with a higher generation by this RES than the actual demand for electric energy. PtG-units offer the advantage to meet this higher energy production with a flexible operation and therefore avoid curtailment of RES. This advantage is demonstrated in Fig. 10. Synthetic gas from avoided RES curtailment can substitute gas, that would have been imported for a gas price of 0.141 €/m³. This leads to operating cost savings of 337 667.05 €. Therefore, PtG is expected to be present in future energy systems resulting in system cost savings [10].

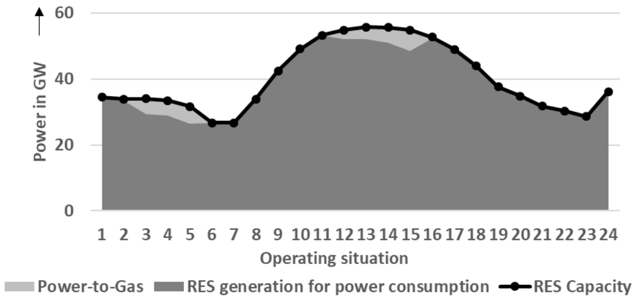

Fig. 10: Usage of RES for 24 operating situations in 2050 German power and gas transmission system

CONCLUSION

GFPPs cause increasing interdependencies between electric and gas systems. Furthermore, changes in the whole energy sector lead to a stronger coupling of both grids through the expected industrial scaled integration of PtG units. This strong coupling is characterised by a mutual influence of electric energy and gas flow. In order to take full advantage of those interdependencies and to obtain a transport capacity as large as possible with no need for extensive grid reinforcement, a coordinated operation of both systems is required. The integrated optimization of power and gas flows is an important tool in the pursuit of this goal. Various methods for integrated optimization of power and gas flows are presented in existing publications. However, none of them allows to calculate large energy systems in a practically usable solving time. Therefore, a new approach the successive sub-optimization is proposed. The exemplary investigations show that this method is the only present approach that allows the computation of an accurate solution with low operating costs for large systems in a short computation time. Moreover, the calculated state variables show minor deviations compared to state-of-the-art network calculations. In an exemplary case study, the integrated optimization of the German power and gas transmission system is presented.

The resulting system operation and the economic dispatch costs determined by the successive sub-optimization can further be improved by a closed optimization started with the obtained solution, or by a meta-heuristic started with a solution pool obtained by different parametrization of the explained successive linearization.

REFERENCES

[1] BMWI, *Energiedaten-gesamt,* Stand: 01.08.2018.

[2] Amprion, Open Grid Europe, Gasunie, Tennet, Thyssengas *Pressemitteilung: Netzbetreiber stellen Investitionsanträge für Power-to-Gas-Projekte,* 2019.

[3] S. An, Natural Gas and Electricity Optimal Power Flow, Oklahoma, 2004.

[4] M. Urbina and Z. Li, „A Combined Model for Analyzing the Interdependency of Electrical and Gas Systems," in *IEEE- 39. North American Power Symposium*, 2007.

[5] C. Correa-Posada and P. Sanchez-Martin, „Security-Constrained Optimal Power and Natural-Gas Flow," *IEEE Transactions on Power Systems Vol. 29,* pp. 1780-1787, 04.07.2014.

[6] D. Ojeda-Esteybar and R. Rubio-Barros, „Integrated operational planning of hydrothermal power and natural gas systems with large scale storage," *J. Mod. Power Syst. Clean Energy,* pp. 299-313, 2017.

[7] G. Sun, S. Chen, Z. Wei and S. Chen, „Multi-period integrated natural gas and electric power system probabilistic optimal power flow incorporating power-to-gas units," *J. Mod. Power Syst. Clean Energy,* pp. 412-423, 2017.

[8] A. Martin, M. Möller and S. Moritz, „Mixed Integer Models for the Stationary Case of Gas Network Optimization," *Math. Program. Ser. B,* pp. 563-582, 2006.

[9] T. Overbye, X. Cheng and Y. Sun, „A Comparision of the AC and DC Power Flow Models for LMP Calculations," 2004.

[10] Deutsche Energie-Agentur (dena), *Leitstudie: Integrierte Energiewende,* Berlin, 2018.

[11] I. Marjanovic, T. Bongers, J. Lichtinghagen and A. Moser, „Influence of Power-to-Gas-Technology on Unit Commitment and Power System Operation," *International Conference on Clean Electrical Power,* pp. 536-540, 2017.

[12] C. Coffrin and P. Van Hentenryck, „A Linear-Programming Approximation of AC Power Flows," 06 08 2013.

[13] A. Gleixner, M. Bastubbe, L. Eifler,et al. „The Scip Optimizstion Suite," 2 Juli 2018. [Online]. Available: http://www.optimization-online.org/DB_FILE/2018/07/6692.pdf. [Accessed 27.03.2019].

Impact of wind turbines on power system dynamics

Hani AL Aghawani
Chair of Electric Power Networks and Renewable Energy
Otto von Guericke University
Magdeburg, Germany
hani.alaghawani@ovgu.de

Hazem Mohammad
Chair of Electromagnetic Theory
Wuppertal University (BUM)
Wuppertal, Germany
1613060@uni-wuppertal.de

Dr. Ing. Hassan Sowidan
Electric Power Engineering Department
Damascus University
Damascus, Syria

Abstract **—In this paper, the effect of Double Fed Induction Machine (DFIM) on the transient stability of the electric power system has been analyzed by the gradual increase of power, which is generated by the wind turbines and the change of turbines position in the system, with defining the Critical Clearing Time (CCT) for each case. The results of the work show, that the effect of wind turbines on the dynamic behavior of the electric power system varies according to the percentage of contribution of the wind turbines in the total capacity of the generated power and the location difference of the wind farm to the topographic plan of the electric network. In some cases, these turbines have a significant effect on the rotor angle and speed of synchronous generators, bus voltages and thus the transient stability of the electric system.**

Keywords—Double Fed Induction Machine, Power System, Transient Stability, Wind Power

I. INTRODUCTION

The increase of interest in environmental issues and the decline in traditional energy sources lead to an increased focus on renewable sources of power generation. Some sources of renewable energies are economic competitors for conventional energy systems, especially wind energy systems, which is one of the most promising sources in this area. Hence, the concept of distributed generation is defined by IEEE as an electrical generation by smaller units of central generating units, can be connected to any point in the power system. The addition of wind turbines to electrical networks, affects the power quality and requiring operators in the transmission control centers to make additional efforts to maintain this power. Therefore, connecting groups of distributed generation to the network must be carried out with care and planning [1].

Another set of problems is the instability resulting from power generation from wind turbines, which in turn affect the power system determinants, especially the dynamic determinants of stability. From this point of view, it is important to study and understand the dynamic processes of the system after connecting the wind turbines to it and its integration with other types of generation e.g. thermal and hydropower plants. The wind energy systems add additional inertia of the power system when a fault occurs, which directly affects the dynamic stability of the system [2]. Wind power plants use different technologies compared to conventional power plants. Most of the wind turbines use induction generators, due to the advantages of these generators. With the development of power electronics recently, the use of Double Fed Induction Machine (DFIM) has become increasingly widespread due to the ability to control separately the active and reactive power and high energy output, as well as the low capability of the necessary power electronics circuits [3].

This highlights the definition of the stability of power system, which is the ability of the system to return to a normal operating state after exposure to a disturbance. Thus, the stability can be classified into three categories: Rotor stability, Voltage stability, and Frequency stability. The rotor stability can be classified into:

1) Steady state stability: The generators can return to synchronization, when small and slow disturbances occur such as gradual changes in generation or load. Then the generators will be static stable.
2) Transient Stability: The generators can return to synchronization, when large and sudden disturbances occur such as a three-phase fault or unplanned switching off lines. Then the generators will be transient stable [4].

Stability studies help to identify very important things such as the level of voltage of interconnection networks and the amount of energy transferred between them. As well as the Critical Clearing Time (CCT) of the circuit breakers, which is the maximum time during which a disturbance can be applied without the system losing his stability. The aim of this calculation is to determine the characteristics of protections required by the power system [4].

Some observations emerge from the preceding discussion that motivates the work in this paper, which is analyzed in section III:

1) The focus on the use of DFIM in wind power generation when connected to the electric grid.
2) The effect of DFIM on the transient stability of synchronous generators after disturbances occur such as a three-phase fault, especially those adjacent to the disturbance zone.
3) Defining the CCT for the system.

II. PROBLEM FORMULATION

A. Synchronous Generator

Fig.1 Shows the equivalent circuit of the synchronous machine. Equation (1) describes the synchronous machine in a stable state and fig. 2 shows the phasor diagram. The complete mathematical model of synchronous machine in the transient case can be found in detail in [5].

$$\underline{E}_{\mathrm{t}} = -(\mathrm{r_s} + j\,\mathrm{X_s})\,I_t + jE_{\mathrm{fd}} \qquad (1)$$

$\underline{E}_{\mathrm{t}}$: terminal voltage
$\mathrm{r_s}$: armature resistance
$\mathrm{x_s}$: synchronous reactance
I_{t} : armature current
E_{fd}: armature voltage

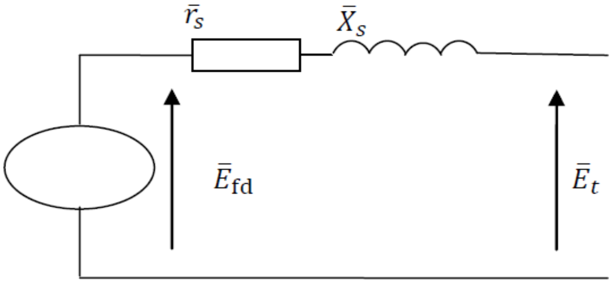

Fig. 1 Equivalent circuit of synchronous machine [5]

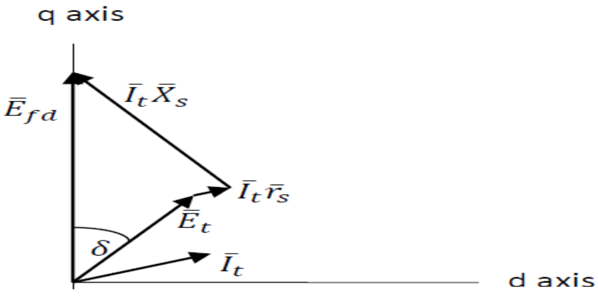

Fig. 2 Phasor diagram of synchronous machine [5]

B. Double Fed Induction Machine

The DFIM in generator mode is the same as the three-phase wound rotor induction generator in which the rotor coils are connected with three slip rings. Rotor coils in the induction generator are fed by three-phase variable alternating voltage and frequency systems through electronic switches (AC/DC/AC), which are usually connected to the same electrical network like the stator coils as shown in fig. 3. This generator can work in both cases above and below synchronization. The difference between the two modes of synchronization is, that the power provided to the network is the same in both cases, knowing that if operating below synchronization, the rotor will be fed from the network and the power injection through the stator, but in the case of operation above synchronization, the power injection into the network is through the stator and rotor together [5].

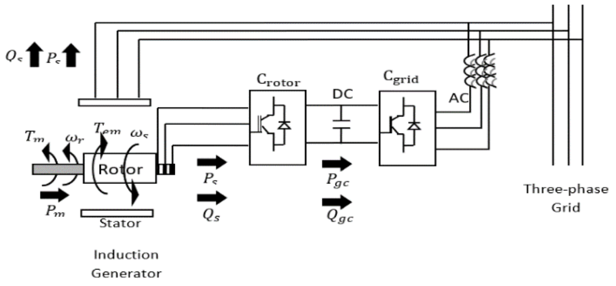

Fig. 3 Double fed induction machine [5]

Fig. 4 shows the equivalent circuit of the DFIM in a stable state and the complete mathematical model of DFIM in the transient case, the mathematical model of power transformer and transmission line can be found in detail in [5].
Equivalent circuit equations can be written as follows:

$$\underline{V}_s = R_s I_s + j\omega_1 L_{s\lambda} I_s + j\psi_s \tag{2}$$

$$\frac{V_r}{s} = \frac{R_r}{s} I_r + j\omega_1 L_{r\lambda} I_r + j\omega_1 \psi_r \tag{3}$$

$$0 = R_m I_{Rm} + j\omega_1 \psi_m \tag{4}$$

$$P_r = -sP_s \tag{5}$$

V_s: stator voltage
V_r: rotor voltage
R_s: stator resistance
R_m: magnetizing losses
R_r: rotor resistance
I_{Rm}: magnetizing current
I_s: stator current
I_r: rotor current
$L_{s\lambda}$: stator leakage inductance
$L_{r\lambda}$: rotor leakage inductance
ω_1: stator angular speed
s: slip
ψ_s: stator magnetic flow
ψ_r: rotor magnetic flow
ψ_m: air gab magnetic
P_r: rotor electric power
P_s: stator electric power

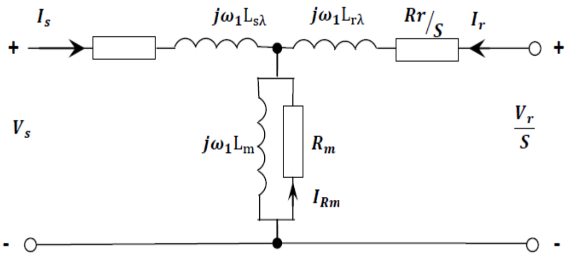

Fig. 4 Equivalent circuit of the DFIM in a stable state [5]

C. The Transient Stability

In transient stability studies, attention is focused on the amount of the deviation of the rotor speed from the synchronous angular speed ω_s. Thus, the swing equation gives the relative angular acceleration $\frac{d^2\delta}{dt}$ in terms of the mechanical power P_m provided by the turbine, the electric power P_e and inertia constant H like in (6) [4].

$$\frac{H}{\pi f_0}\frac{d^2\delta}{dt^2} = P_{m(pu)} - P_{e(pu)} = P_m - P_{max}\sin\delta \tag{6}$$

In the synchronous machine, the rotor accelerates during the turbulence, when the mechanical torque is greater than the electric torque. On the contrary, the rotor slows down when the mechanical torque is less than the electric torque as shown in fig. 5 [4]. Active and reactive power injected by the voltage source is given by (7) and (8). The amount of active power increases with the increase of δ up to 90 degrees, reaching the maximum value. Thus, δ is used to represent both, the mechanical swing of the rotor and the angle of the electromotive force of the generator E [6]. In practice to maintain the dynamic stability of the electrical system the phase angle should be 20° [1].

$$P_e = \frac{EV}{X}\sin\delta \tag{7}$$

$$Q_e = \frac{E^2}{X} - \frac{EV}{X}\cos\delta \tag{8}$$

V: grid voltage

X: reactance between the generator and the grid

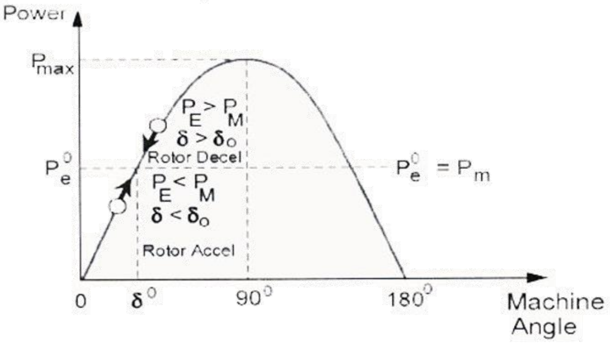

Fig. 5 Active power transferred from the generator [6]

The system response is affected by the nonlinear relationship between the torque angle or load and power, usually the field of study for this type of stability in the first seconds after turbulence. And after solving the differential equations (6) and calculate the electric system along the field of study, curves d(δ) can be built to judge the stability of the system. In addition, curves can be built for speed and voltage in terms of time [6]. Multi-machine system equations can be written similarly to single-machine connected to an infinite bus. The following assumptions will simplify the analysis of transient stability [4]:

1. Each synchronous generator represents as constant voltage source directly behind the transient reactance.
2. We neglect the response of the governor and the income power is almost constant during the representation period.
3. Transfer all loads to equivalent admittance using bus bar voltages before the fault occurs.
4. Damping is neglected.
5. The angle of each generator (angle of stability) equal to the angle of the electromotive force behind the generator's impedance.
6. All generators in any power plant swing together.

The first step to analyze the transient stability is by solving the load flow to determine the voltage of the buses and their angles. We get the voltage behind the transient reactance E' from (9):

$$\underline{E_i'} = V_i + j\,\mathrm{X}_{\mathrm{d}}'\,I_i \tag{9}$$

i = 1, 2..number of generators

X_{d}': direct axis transient reactance

I : generator current

Then we transfer all loads to equivalent admittance. To include the voltages behind transient reactance, we add m-buses to the n-buses network like in fig. 6. Where n+1……. m are bus voltages behind transient reactance.

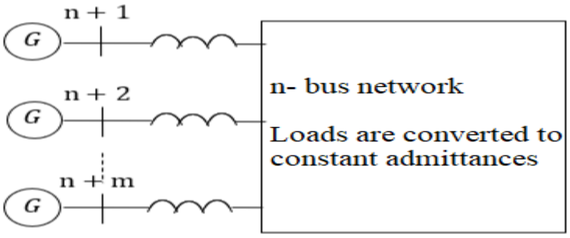

Fig. 6 Representing the power system [4]

The transmission network is represented with transformers by impedances, which connected the different nodes. Bus voltages matrix (10) is given by the following:

$$\begin{bmatrix} I_1 \\ I_2 \\ \vdots \\ I_{\mathrm{n}} \\ I_{\mathrm{n+1}} \\ \vdots \\ I_{\mathrm{n+m}} \end{bmatrix} = \begin{bmatrix} Y_{11} & \cdots & Y_{1\mathrm{n}} & Y_{1(\mathrm{n+1})} & \cdots & Y_{1(\mathrm{n+m})} \\ Y_{21} & \cdots & Y_{2\mathrm{n}} & Y_{2(\mathrm{n+1})} & \cdots & Y_{2(\mathrm{n+m})} \\ \vdots & \ddots & \vdots & \vdots & \ddots & \vdots \\ Y_{\mathrm{n}1} & \cdots & Y_{\mathrm{nn}} & Y_{\mathrm{n(n+1)}} & \cdots & Y_{\mathrm{n(n+m)}} \\ Y_{(\mathrm{n+1})1} & \cdots & Y_{(\mathrm{n+1})\mathrm{n}} & Y_{(\mathrm{n+1})(\mathrm{n+1})} & \cdots & Y_{(\mathrm{n+1})(\mathrm{n+m})} \\ \vdots & \ddots & \vdots & \vdots & \ddots & \vdots \\ Y_{(\mathrm{n+m})1} & \cdots & Y_{(\mathrm{n+m})\mathrm{n}} & Y_{(\mathrm{n+m})(\mathrm{n+1})} & \cdots & Y_{(\mathrm{n+m})(\mathrm{n+m})} \end{bmatrix} \begin{bmatrix} V_1 \\ V_2 \\ \vdots \\ V_{\mathrm{n}} \\ E'_{\mathrm{n+1}} \\ \vdots \\ E'_{\mathrm{n+m}} \end{bmatrix}$$

This matrix is like the admittance matrix for power flow and the only difference is that the generator and transformer reactance's enter this matrix. In addition, the diagonal components are modified to include load admittance. The admittance matrix is calculated for the three situations before, during and after fault. In the final step, delete all nodes except the generation nodes and putting load buses in the upper lines [4]. By taking the voltage and admittance into polar values, we get the generated active power P_{e}.

$$P_{\mathrm{e}i} = \sum_{j=1}^{m} |E_i'||E_j'||Y_{ij}|\, cos(\theta_{ij} + \delta_i + \delta_j) \tag{11}$$

The swing equation of a generator without damping will be:

$$\frac{H_i}{\pi f_0}\frac{d^2\delta_i}{dt^2} = P_{\mathrm{m}i} - \sum_{j=1}^{m} |E_i'||E_j'||Y_{ij}|\, cos(\theta_{ij} + \delta_i + \delta_j) \tag{12}$$

H: inertia of the generator based on the rated power S_{MVA}

Equations (13) is the swing equation after converting it to the model of the state variable.

$$\begin{gathered} \frac{d^2\delta_i}{dt^2} = \Delta\omega_i \\ \frac{d\Delta\omega_i}{dt} = \frac{H_i}{\pi f_0}(P_{\mathrm{m}i} - P_{\mathrm{e}i}) \end{gathered} \tag{13}$$

Therefore, there are two differential equations for each generator that can be solved by mathematical methods, such as the modified Euler or Euler or Runge-Kutta to obtain angle values and speeds with time [4]. When the fault is cleared, the admittance matrix is recalculated to consider changes in the network, then in a subsequent step, the shorted admittance matrix is recalculated and defines the generator power after the fault. After that, power angle and angular speed are calculated in terms of time, until it becomes clear whether is stable or not. One generator is usually used as reference and the phase angle difference for each generator is calculated relative to this reference. If the angle differences are not increasing then it can be said that the system is stable, but if these differences are increasing, it indicates that the system is unstable. In order to remain stable, the fault must be cleared before arriving δ to the critical value δ_{cr}. And the protection devices should work during the clearing time t_c less than the CCT, which corresponded to the critical angle δ_{cr} [6].

III. CASE STUDY

Based on the theoretical study in the previous sections and the mathematical model of the power system elements, an analytical study on the electric power system as shown in fig. 7 is performed with Neplan program [7] to show the effect of wind turbines on the dynamic performance of this system, specifically the transient stability after occurring a three-phase fault on one of the lines and defining the CCT. The system consists of nine buses, four synchronous generators, four power transformers and a range of transmission lines. Generator buses at 20 kV and the transmission network are at 230 kV. The total amount of the generated power is 2735.15+j748.72 MVA und the total amount of loads is 2651.01+j199.55 MVA. The system frequency is 60 Hz. The length of transmission lines and the generators properties are listed below in the tables I, II, where the impedance of the transmission line is 0.0529+j0.529 Ω\km.

TABLE I. length of lines

Line	Length in Km
L (5-6)	25
L (6-7)	10
LA (7-8) = LB (7-8)	110
LA (8-9) = LB (8-9)	110
L (9-10)	10
L (10-11)	25

TABLE II. SYNCHRONOUS GENERATORS PROPERTIES

Generator no.	1 and 2	3 and 4
Rated power in MVA	900	900
Voltage in kV	20	20
Inertia H in s	6.5	6.175
Power factor	0.77	0.7
Type	Steam	
X_d%	180	
X'_d%	30	
X_q%	170	
X'_q%	55	
X_l%	20	
T'_{do}%	8	
T'_{qo}%	0.4	

X_d:	direct axis reactance
X_q:	quadrature axis reactance
X'_q:	quadrature axis transient reactance
X_l:	leakage reactance
T'_{do}:	direct axis transient time constant
T'_{qo}:	quadrature axis transient time constant

A. *Study the transit stability without wind turbines*

This case represents the basic operating state of the power system without wind generating sources connected to the system. A three-phase fault causes significant power imbalance where the voltage in the faulted branch is almost zero. In addition, the generators accelerate over the duration of the fault due to the low generated electric power as a result of the voltage decrease, which may lead to the possibility to lose generators synchronization, especially during the faults with long CCT. The CCT is performed by assuming a three-phase fault, which cleared after x ms, without losing synchronization of generators. Redoing this process with a new fault time, until reaching the CCT [8].

A three-phase fault occurred on the line LA (8-9) and the CCT is 0.98 s. As shown in fig. 8 the effect of the fault does not significantly affect the rotor angle stability, where it remained stable. The reference generator is the generator number three. Fig. 9 shows some of the bus voltages, which decrease after the fault in different values depending on the Thevenin impedance [4].

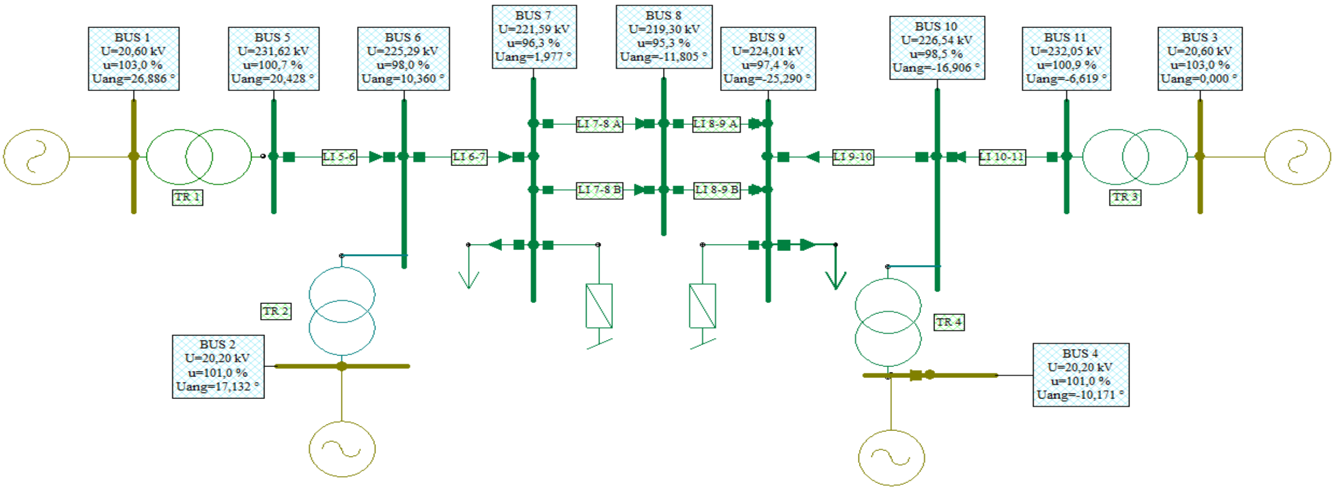

Fig.7 The studied system [7]

The fault does not affect the voltage stability too. Fig. 10 shows the speed of the generators. It is clear from this figure that the generators are synchronous although they swing in different scales due to their different determinants. But they remain synchrony and close to nominal speed. The system will be unstable after this time, when the CCT is 0.99 s as shown in fig.11, fig. 12 and fig. 13.

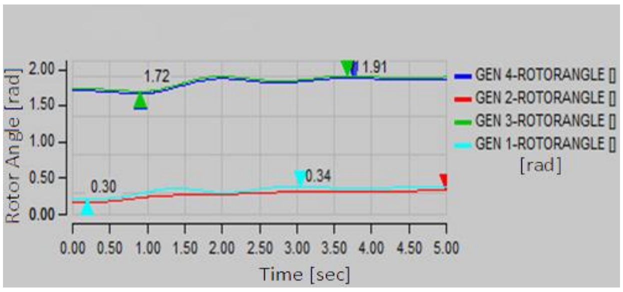

Fig. 8 Rotor angles for CCT = 0.98 s

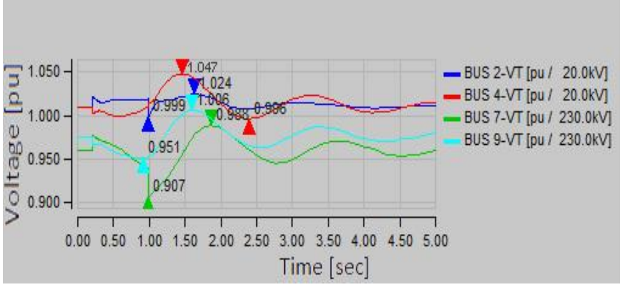

Fig. 9 Bus voltages for CCT = 0.98 s

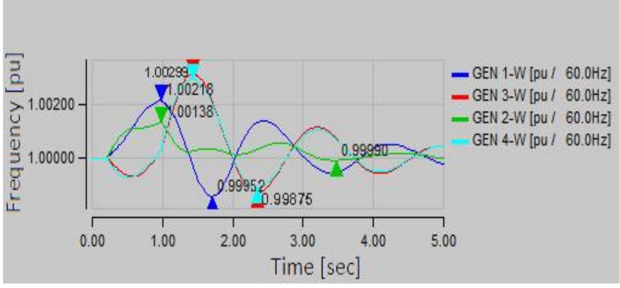

Fig. 10 Generators speed for CCT = 0.98 s

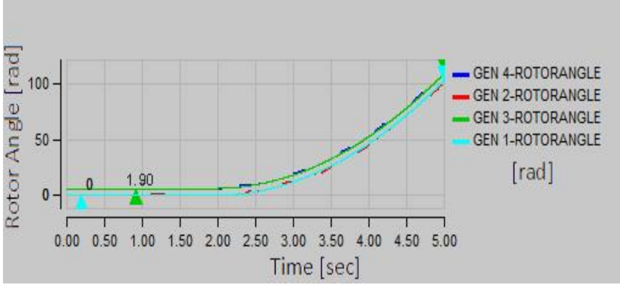

Fig. 11 Rotor angles for CCT = 0.99 s

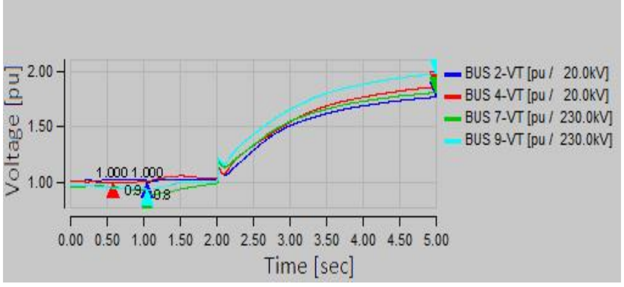

Fig. 12 Bus voltages for CCT = 0.99 s

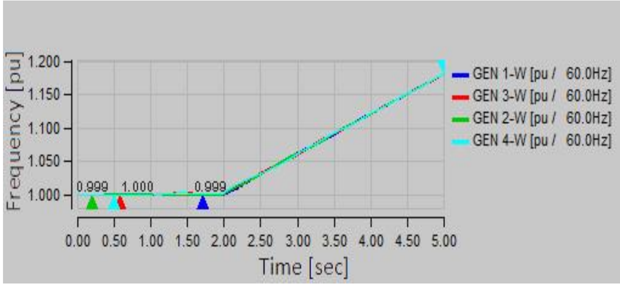

Fig. 13 Generators speed for CCT = 0.99 s

B. *Study the transit stability with wind turbines*

To demonstrate the effect of wind turbines on transient stability of the electric system. Wind farm is connected to the bus 9 through power transformers in two steps 20 kV\66 kV and 66 kV\230 kV. And the wind farm has rated power of 50 MW. All wind turbines have the same properties as shown in Table III. The same previous fault is applied after connecting the wind farm. But this time the CCT has increased to 1.1 s. Therefore, connecting the wind farm to bus 9 has led to improve system stability as shown in fig. 14, fig. 15 and fig. 16. With taking into account that the generators swing with each other with a slight deviation from what was before due to differences in the inertia of wind generators from those of synchronous generators [8]. The system will be unstable after this time, when the CCT become 1.11 s in the same manner as before, which means generators rotor angles increase, indicating that the system is unstable.

TABLE III. DFIM PROPERTIES

Generator type	DFIM
Rated power in MW	2
Voltage in V	690
Frequency in Hz	50\60
No of poles	4
R_s%	0.00706
X_s%	1.074
X_m%	18.22
R_r%	0.005
X_r%	0.98
X_s%	1.074

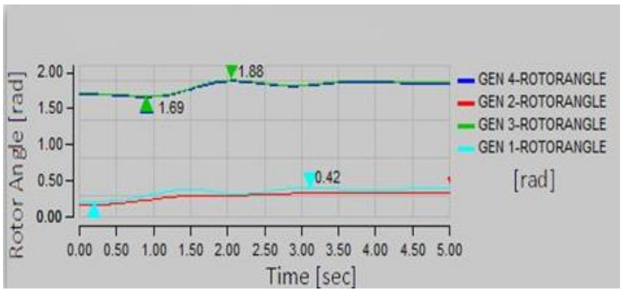

Fig. 14 Rotor angles for CCT = 1.1 s

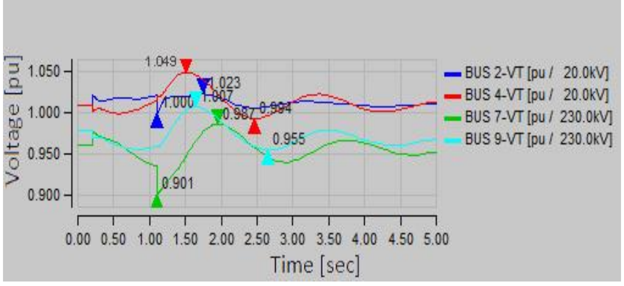

Fig. 15 Bus voltages for CCT = 1.1 s

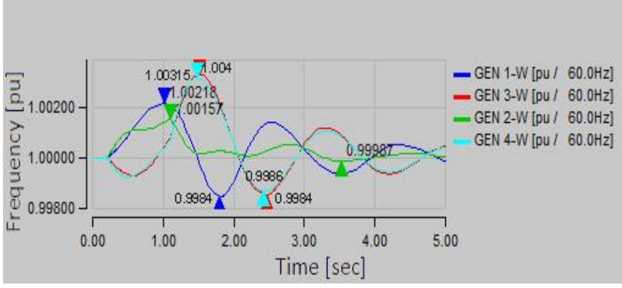

Fig. 16 Generators speed for CCT = 1.1 s

C. *Study the impact of increasing the wind farm power on transient stability*

To demonstrate the effect of increasing the power of wind turbines on the transient stability. The wind farm power is gradually increased from 50 MW to 150 MW and the CCT is determined for each case. The results are shown in table IV. The margin of stability is slightly reduced when the generated power from wind turbines is increased to 150 MW, which can be explained by a decrease in total system inertia due to adding more lower torque generators [6]. From another point, the DFIMs in generator mode often do not deliver as much reactive power as synchronous generators do and dynamically, they cannot produce the same short circuit current. Thus, synchronous generators give stronger support to the grid voltage. Therefore, DFIM during transients can reduce voltage stability limit. In some countries, the grid codes are so rigid, that the DFIMs must be combined with reactive power compensation station in order to achieve a similar behavior as the one of synchronous generators [9].

TABEL IV. CCT FOR DIFFERENT GENERATED POWER

Wind farm power in MW	50	100	150
CCT in s	1.1	1.16	1.08

D. *Study the location impact of wind farm on the transit stability*

The transient stability is followed when the wind farm is connected to different buses. The CCT is improved only when the wind farm is connected to buses 8 and 9 than in the basic case as shown in table V.

TABEL V. CCT FOR DIFFERENT GENERATED POWER

Bus	8	9
CCT in s	1.03	1.11

IV. CONCLUSION

The impact of DFIM wind turbines on transient stability has been studied in this work after a three-phase fault has occurred. The following results have been reached:

1) Connecting the wind farm at bus 9 has led to improve system stability better than the original case without the wind farm.
2) The system maintains stable into certain limits when the power of the wind farm is increased.
3) Some locations provide a better margin of stability than other locations. Therefore, before connecting the wind turbines, it is recommended to do a dynamic study on the system to select the best location for wind turbines within the map of the available wind locations.

In conclusion, there are several factors that improve the transient stability of the synchronous generator:

1) Using of high-speed control excitation systems in power generation plants [4] and fast turbine-value control [10].
2) Reactance reduction of the system e.g. series compensation of some lines with attention to avoid the resonance phenomenon [6].
3) Using digital protection devices and fast circuit breakers [4].

REFERENCES

[1] Deutsches wind energy Institute," Wind Turbine Grid Connection and Interaction", Germany, 2001.

[2] Hamzeh.A, Nagi.K, "Introduction to renewable energies", University of Damascus Publications, 2010.

[3] Sun.T, "Power Quality of Grid-Connected Wind Turbines with DFIG and Their Interaction with the Grid", Aalborg University, Denmark, 2004.

[4] Hamzeh.A, Zeidan.K , "Analysis of Power Systems", University of Damascus Publications, 2007.

[5] Larao.A., Jenkins N, "Wind Energy Generation Modelling and Control", John Wiley and Sons, Ltd, Publication, UK, 2009.

[6] Sowidan.H , "Impact of Wind Turbines on the Stability of Electrical Power Systems", Damascus University Journal of Engineering Sciences, Vol 29, No. 1, 2013

[7] www.neplan.ch

[8] Sowidan.H, " Study the effect of short circuits on the transit stability in the Syrian electrical system ", Damascus University Journal of Engineering Sciences, Volume 26, No. 2, 2010.

[9] Hossain. M. J. , Pota. H. R. , Mahmud. M. A. and Ramos. Rodrigo A, "Investigation of the Impacts of Large-Scale Wind Power Penetration on the Angle and Voltage Stability of Power Systems ", Pages 76-84, IEEE system journal , 2012.

[10] Jabbour.E, Al-Jazi.A, "Synchronous Machines", University of Damascus Publications, 2008.

Robust and Optimized Voltage Droop Control consindering the Voltage Error

Thomas, Friederike
Chair of Electrical Energy Supply
Technische Universität Dresden
Dresden, Germany
Friederike.Thomas@tu-dresden.de

Krahmer, Sebastian
Chair of Electrical Energy Supply
Technische Universität Dresden
Dresden, Germany
Sebastian.Krahmer@tu-dresden.de

Schegner, Peter
Chair of Electrical Energy Supply
Technische Universität Dresden
Dresden, Germany
Peter.Schegner@tu-dresden.de

***Abstract*— Distributed voltage control using centrally supervised reactive power setpoints is a means of operating distribution grids to the specific demands. However, this way highly depends on the structural integrity of the communication link. To maintain the optimized setpoints even when the link is broken, this paper proposes a *Q(U)*-fallback solution. The presented methodology aims at the necessary tuning of the reference voltage with explicit consideration of the steady state error inherent in the *Q(U)*-control. Furthermore, this approach is extended for a set of forecasts. In addition a stability assessment of the *Q(U)*-characteristic is included. Based on this, the performance is presented using simulations in a benchmark grid.**

***Keywords*— reactive power management, renewable integration, fallback, *Q(U)*, distribution grid**

I. INTRODUCTION

The integration of fluctuating renewable energy sources (RES) into the electricity grid is becoming an important issue in the wake of the energy revolution. One of the main challenges is the distributed infeed of most of the RES, especially wind and solar power. This defines new requirements for grid control and declares the need for new control schemes.

Distributed voltage control (DVC) based on distributed reactive power management supports the operation of distribution grids driven by RES and is a means to facilitate higher penetrations of distributed generators (DGs). There are different studies presenting coordinated distributed reactive power management, like [1], [2], [3] and [4]. One possibility is to use periodically optimized reactive power set points as presented in [4]. This concept has the advantage of an easy parametrization and does not lead to stability issues but the drawbacks are the inability to react to sudden load changes and the need for periodical communication. Therefore, a fallback solution is essential to ensure a working voltage control in the case of loss of communication. As the effectiveness of the *Q(U)*-control as autonomous control is showed, e. g. in [5], [6], this control scheme is examined more closely. Hence, the objective of this paper is to derive an algorithm for a robust and optimized controller parametrization to use the *Q(U)*-control as a fallback solution for a global[1] optimization scheme. In Germany, a main part of the wind power is connected to the 110-kV-distribution grid [7], therefore this paper focus on this voltage level.

Firstly, the *Q(U)*-control is explained in relevant detail and the steady-state response of the controller is examined. In section III, a method to calculate the steady-state voltage error considering the nonlinearity of the *Q(U)*-characteristic is presented. Based on this, an algorithm is derived in section IV to optimize the parameters of the characteristic for a precise time interval defined by k-forecasts of load and generation, where k defines the forecasting horizon. Finally, the results are demonstrated using a 110-kV-benchmark grid.

II. DISTRIBUTED VOLTAGE CONTROL BASED ON *Q(U)*

A widely used method for implementing DVC is the use of coordinated *Q(U)*-control in which the DGs provides reactive power corresponding to the voltage at the point of common coupling (PCC). This section presents the main features of this control mechanism.

A. Control Characteristic

The control scheme is based on two characteristics: the *Q(P)*-characteristic defines the operational reactive power limits, Q_{min} and Q_{max}, according to the current active power infeed and is of secondary importance for this work. The *Q(U)*-characteristic defines the reactive power infeed according to the voltage at PCC and is shown in Fig. 1. The reference voltage U_{q0} denotes the voltage set point, while the width of the dead band is fixed within bounds according to national regulations and protects type 3 turbines from mechanical stress [8].

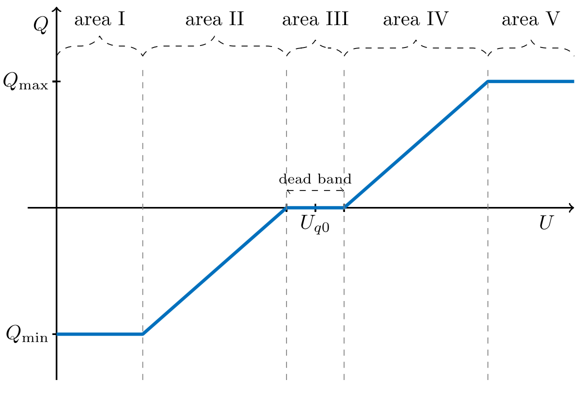

Fig. 1 *Q(U)*-characteristic with dead band and reactive power limits

B. Modeling of distributed generation with coordinated Q(U)-control

For the analysis of the performance, the model presented in [8] is used. Fig. 2 shows a so-called SISO (single input, single output) system a single wind farm (WF) connected to the grid consisting of the farm voltage controller, the reactive power control loop and the grid model. Of further importance

---

[1] This has to be seen in context of one single distribution grid optimization area.

is the nonlinear *Q(U)*-characteristic of the farm voltage controller. If several wind farms are connected to the grid, the resulting model is a so-called MIMO (multiple input, multiple output) system.

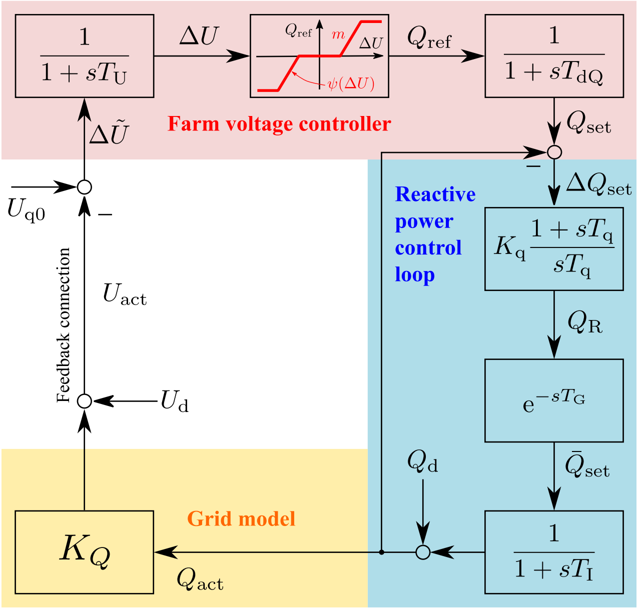

Fig. 2 SISO control loop of a WF. All quantities in this signal flow graph has to be interpret as deviations in respect to reference voltage U_{q0}.

C. *Behaviour and characteristic of control system*

The system response is decisive for the optimization algorithm presented in section IV, in particular the controller stability and the steady-state response. In [8] a robust small-gain-based stability criteria was derived, focusing on the gain m of the *Q(U)*-characteristic. Because of the nonlinearity of the *Q(U)*-characteristic the circle criterion was used. The stability analysis showed that the stability depends on the nodal voltage sensitivity K_Q at the PCC. The paper presents a calculation method to identify stable slopes m for several WFs connected to the grid for a known K_Q and given controller parameters. The use of this method ensures the stability of the system.

Another important information is the steady-state response of the system. For a droop controller a steady-state voltage error ΔU_{error} is inherent. Many publications do not mention the steady-state voltage error and assume that a change of voltage ΔU_{R0} leads to a reactive power in-feed of mK_Q. This assumption can leads to major errors, as shown in the next section. For generality of analysis and optimization respectively within section III and IV, all voltages are related to the nominal voltage of the grid.

III. CALCULATION OF STEADY-STATE VOLTAGE ERROR

To discuss the steady-state voltage error, several variables must be introduced. Fig. 3 shows an exemplary voltage curve over time, starting with u equal to the reference voltage u_{q0}. A change in load leads to a change in voltage Δu_{R0}. After the time delay e^{-sT_G} of the reactive power control loop, the WF starts to inject reactive power, which counteracts the change in voltage and causes the steady-state voltage u_∞ retaining a steady-state voltage error Δu_{error}. For the subsequent optimization, it is essential to know this steady-state voltage error.

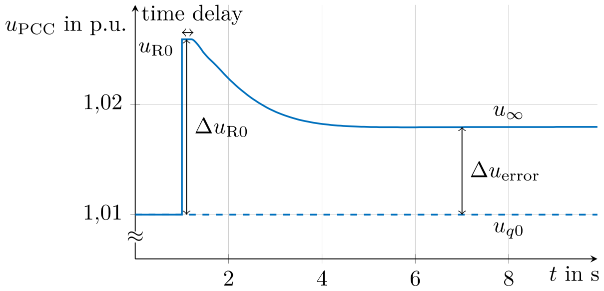

Fig. 3 Exemplary voltage curve during load change and subsequent regulation with designation of the different voltages

A. *SISO-System*

For a linear SISO-System, with the open loop transfer function G_0 and a stepwise change of the input x_0 the steady-state value for a stable system is calculated using the limit theorem:

$$x_\infty = \lim_{t\to\infty} y(t) = \lim_{s\to 0} sY(s) = \lim_{s\to 0}[G_0(s)x_0] \qquad (1)$$

with $G_0(s)$ as the open loop transfer function.

As already mentioned, the examined control loop is a nonlinear system due to the nonlinear *Q(U)*-characteristic, which is why the limit theorem is not valid. In a first step, the steady-state error neglecting the non-linearity is calculated. For a change of the disturbance u_d by Δu_{R0}, the steady-state voltage error is

$$\Delta u_{error} = \lim_{s\to 0}\frac{1}{1+G_0(s)} = \Delta u_{R0} - \frac{mK_Q}{1+mK_Q}\Delta u_{R0}. \qquad (2)$$

A connection that can be seen in (2) is that to reduce Δu_{error} the slope m of the *Q(U)*-characteristic needs to be increased. The slope is on the other hand limited by stability reasons, as the stability analysis already showed. Therefore, a certain steady-state voltage error is inherent to this kind of control loop.

To calculate the steady-state voltage for the non-linear system, the characteristic can be divided into its linear parts as shown in Fig. 1. Thus, there are five different cases to be taken into account in the calculation, whereas case 2 and case 4 as well as case 1 and case 5 are quite similar. In case 3 the slope and the reactive power are equal to zero and the steady-state voltage $u_\infty = u_{R0}$. In case 1 and 5 the controller works at its maximum limitation, so in this cases the slope is zero, too and the steady-state voltage is given by the reactive power limits. Therefore, the only cases to consider are case 2 and case 4. The steady-state voltage error for these cases is calculated by taking (2) and introducing a new variable $u_{R0\,dead}$ defined as:

$$\Delta u_{R0\,dead} = \begin{cases} \Delta u_{R0} + \Delta u_{dead} & \text{for } \Delta u_{R0} < -\Delta u_{dead} \\ \Delta u_{R0} - \Delta u_{dead} & \text{for } \Delta u_{R0} > \Delta u_{dead} \\ 0 & \text{else.} \end{cases} \qquad (3)$$

With this definition the steady-state voltage error for the nonlinear system in case 2 and case 4 is:

$$\Delta u_{\text{error}} = \Delta u_{\text{R0}} - \frac{mK_Q}{1+mK_Q}\Delta u_{\text{R0 dead}}. \tag{4}$$

B. *MIMO-System*

For the calculation steady-state voltage error $\Delta \boldsymbol{u}_{\text{error}}$ of the MIMO-system, the same approach is used. Fig. 4 shows the model of a grid with n WPs connected to it [8].

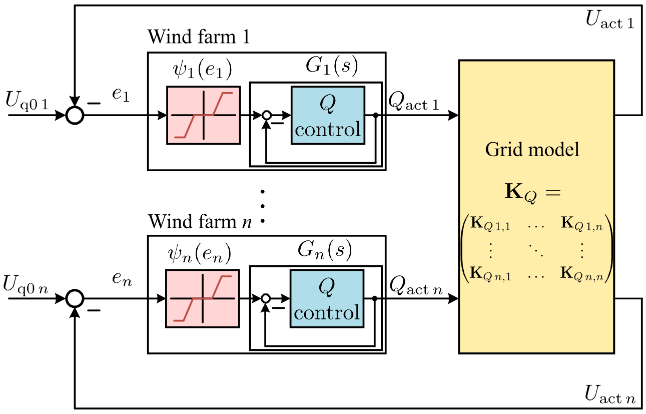

Fig. 4 MIMO control loop of a several WFs with grid model

$\boldsymbol{K}_Q$ is a $n \times n$ matrix that models the grid response to a change in reactive power. The steady-state voltage error $\Delta \boldsymbol{u}_{\text{error}}$ is in this case a vector with n elements. It is computed as:

$$\Delta \boldsymbol{u}_{\text{error}} = \Delta \boldsymbol{u}_{\text{R0}} - \boldsymbol{M}\boldsymbol{K}_Q\left(\boldsymbol{I} + \boldsymbol{M}\boldsymbol{K}_Q\right)^{-1}\Delta \boldsymbol{u}_{\text{R0 dead}}. \tag{5}$$

$\boldsymbol{M}$ is a $n \times n$-Matrix with the slope m_i as the ith main diagonal element and $\boldsymbol{I}$ the identity matrix.

This approach allows the calculation of the voltage in a system with *Q(U)*-controlled DGs. Based on this, in the next section an algorithm is derived to optimize the parameters of the *Q(U)*-characteristic considering $\Delta \boldsymbol{u}_{\text{error}}$.

IV. OPTIMIZATION OF *Q(U)*-CHARACTERISTIC

For the characteristic curve to be used as a backup solution, the parameters of the characteristic must be set according to the higher-level optimization. This must be done for several forecasts to ensure continuous operation in the event of a prolonged loss of communication.

A. *Optimization parameters*

The free parameters of the *Q(U)*-characteristic are the slope m, the reactive power limits $\boldsymbol{q}_{\text{min}}$ and $\boldsymbol{q}_{\text{max}}$, the dead zone $\Delta \boldsymbol{u}_{\text{dead}}$ and the reference voltage u_{q0}. The slope m is limited by the stability criteria. For the reactive power limits, there are only three variants in the standard [9], whereby the network operators must commit itself to one of these variants. The dead band serves to protect the generator and therefore cannot be chosen arbitrarily small. Thus, not all these parameters are useful if an exact voltage operating point is to be maintained. Just the reference $\boldsymbol{u}_{q0}$ meet this condition. Therefore this optimization approach focusses on $\boldsymbol{u}_{q0}$.

B. *Optimization goal*

The higher-level optimization determines a reactive power set point for a specific use case, e.g. loss-optimization with specified reactive power at CPs [4]. A certain voltage distribution $\boldsymbol{u}_{\text{opt}}$ is associated with this state. At this point, it should be pointed out that $\boldsymbol{u}_{\text{opt}}$ and $\boldsymbol{u}_{q0}$ are two different variables, $\boldsymbol{u}_{\text{opt}}$ is the result of the higher-level optimization and $\boldsymbol{u}_{q0}$ is the references voltage of controller. The approach in this paper is to adjust the reference voltage $u_{q0\,i}$ of each DG to decrease the individual deviation from an optimal voltage $u_{\text{opt}\,i}$ considering several forecast intervals. Fig. 5 visualizes the approach for a SISO-system for a time horizon of 4 forecasts. In this example, selecting $u_{q0} < u_{\text{opt}}$, increases the voltage error indicated by the dashed area for the first forecast but decreases it for the others. The aim of the optimization is therefore to minimize the dashed area by finding an optimized offset for u_{q0}.

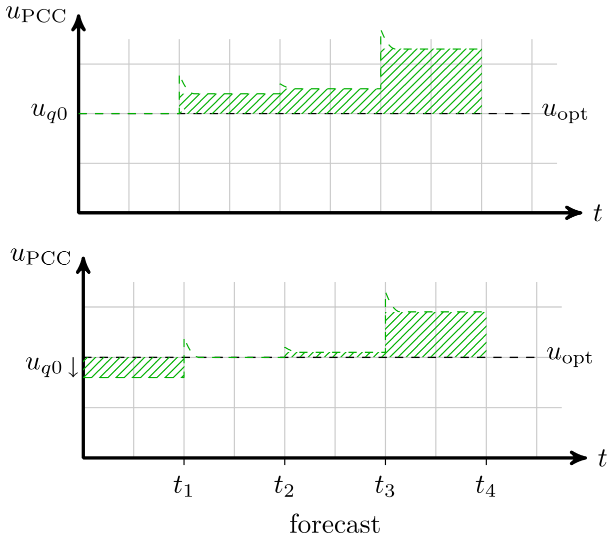

Fig. 5 Principle of optimizing u_{q0}; dashed area visualize the steady-state voltage error before (upper diagram) and after optimization (lower diagram)

C. *Optimization problem*

To simplify the optimization a linear system is assumed, so an optimization function for a linear system is used. The reactive power limits are represented by the constraints and the death band can be neglected. The optimization objective for a MIMO-system is to choose $\boldsymbol{u}_{q0}$ in such a way that the difference between $\boldsymbol{u}_{\infty}$ and $\boldsymbol{u}_{\text{opt}}$ is minimized. The optimization problem is as follows:

$$\min_{x \epsilon D} |\boldsymbol{f}(\boldsymbol{x})|^2 \tag{6}$$

The function $\boldsymbol{f}(\boldsymbol{x})$ is the optimization function and the set D defines the constraints in the form of:

$$\boldsymbol{A}\boldsymbol{x} \le \boldsymbol{b} \text{ and } \boldsymbol{b}_{\text{l}} \le \boldsymbol{x} \le \boldsymbol{b}_{\text{u}}. \tag{7}$$

The variable $\Delta \boldsymbol{u} = \boldsymbol{u}_{\infty} - \boldsymbol{u}_{\text{opt}}$ is introduced and with this, the optimization function for the jth forecast is:

$$\boldsymbol{f}_{Uj}(\boldsymbol{u}_{\text{offset}}) = \boldsymbol{C}_U \boldsymbol{u}_{\text{offset}} - \Delta \boldsymbol{u}_j. \tag{8}$$

The vector $\boldsymbol{u}_{\text{offset}}$ is the adjustment of $\boldsymbol{u}_{q0}$ and $\boldsymbol{C}_U$ results from equation (5):

$$\boldsymbol{C}_U = \boldsymbol{K}_Q\boldsymbol{M}\left(\boldsymbol{I} + \boldsymbol{K}_Q\boldsymbol{M}\right)^{-1}. \tag{9}$$

The constraints specify on the one hand the reactive power limits, $\boldsymbol{q}_{\min}$ and $\boldsymbol{q}_{\max}$. For this $\boldsymbol{q}_{\text{res}}$ is defined that gives the reactive power reserve. The optimized offset must be below this limit:

$$\boldsymbol{M}\left(\boldsymbol{I} + \boldsymbol{M}\boldsymbol{K}_Q\right)^{-1}\boldsymbol{u}_{\text{offset}} \leq \boldsymbol{q}_{\text{res}}. \tag{10}$$

On the other hand the solution space is constrained by the voltage limits, $\boldsymbol{u}_{\min}$ and $\boldsymbol{u}_{\max}$, defined by the grid code:

$$\boldsymbol{u}_{\min} \leq \boldsymbol{u}_{\text{offset}} + \boldsymbol{u}_{q0} \leq \boldsymbol{u}_{\max}. \tag{11}$$

D. Algorithm

Fig. 6 illustrates the flowchart of the optimization algorithm. As explained above, the voltage controller has a non-linear characteristic, so the additional steps explained in section III must be taken to include the non-linearity of the controller. This is done in the first part of the algorithm.

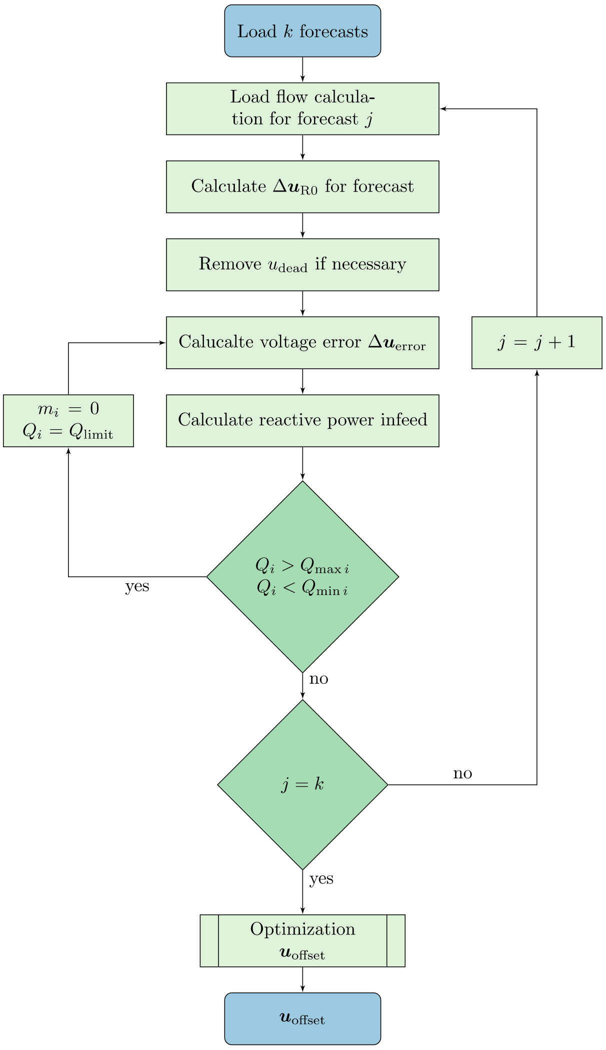

Fig. 6 Flowchart of the optimization algorithm of $\boldsymbol{u}_{\text{offset}}$ for k forecasts

The first part of the algorithm calculates the steady-state voltage for k load forecasts including the dead band and the reactive power limits that varies with the current active power. The second part appraises the optimal reference voltage for k load forecast and the given optimal voltage distribution $\boldsymbol{u}_{\text{opt}}$. For this, the equation (8) is solved using the linear least-squares solver of MATLAB with the Interior-Point Algorithm. To calculate the offset for all k-forecast intervals a matrix-structure is used:

$$\boldsymbol{f}_U(\boldsymbol{u}_{\text{offset}}) = \begin{pmatrix}\boldsymbol{C}_U\\ \vdots\\ \boldsymbol{C}_U\end{pmatrix}\boldsymbol{u}_{\text{offset}} - \begin{pmatrix}\Delta\boldsymbol{u}_1\\ \vdots\\ \Delta\boldsymbol{u}_k\end{pmatrix}. \tag{12}$$

V. DEMONSTRATION ON A BENCHMARK GRID

A. Setup

To prove the chosen approach, simulations on a 61-bus-system developed in the SimBench project [10] were made. Fig. 7 shows the high voltage grid with a high penetration of wind power and three connecting points (CPs). The CPs are connected with the slack by an impedance that models the overlain networks.

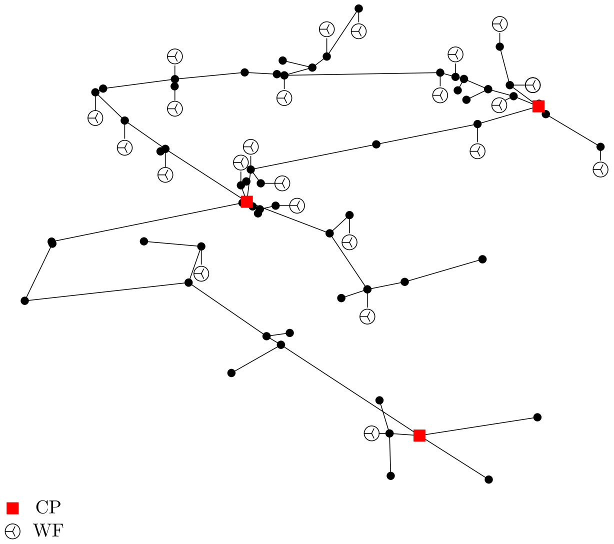

Fig. 7 110-kV-benchmark grid with 61 busbars and 23 WFs [10]

For the demonstration, k is set to four, which means that the parameters are optimized for four different forecasts. TABLE I lists the total power of the forecasts, whereby FC 3 is a high load case and FC 4 a high-infeed case.

To demonstrate the functionality in a simplified way, $\boldsymbol{u}_{\text{opt}}$ is the voltage distribution for an additional load case and a reactive power infeed of $Q_i = 0.3 \cdot Q_{\max\,i}$ at each WF instead of the result of higher-level optimization.

TABLE I OVERVIEW OF FORECAST SETUPS

Forecast	**Load *P* in MW**	**Load *Q* in Mvar**	**Infeed *P* in MW**
FC 1	337	118	-297
FC 2	369	108	-272
FC 3	474	150	-247
FC 4	263	88	-305

For the slope $\boldsymbol{M}$ the stability criteria of [8] is used to find effective and robust slopes m_i for all WF. The reactive power limits are set according to variant 2 in the standard [9]. For reasons of clarity, all values are with units again.

B. Results

The simulation results with the optimized $\boldsymbol{u}_{q0}$ are compared to the standard (not optimized) setting $\boldsymbol{u}_{q0} = \boldsymbol{u}_{\mathrm{n}}$, where $\boldsymbol{u}_{\mathrm{n}}$ is the nominal voltage of the system, as well as $\boldsymbol{u}_{q0} = \boldsymbol{u}_{\mathrm{opt}}$. For the three different settings of the reference voltage, the voltage at each busbar and for the four forecasts is simulated and the deviation from the optimal voltage $\boldsymbol{u}_{\mathrm{opt}}$ is calculated for every busbar and every forecast:

$$F_i = U_i - U_{\mathrm{opt}\,i}. \tag{13}$$

To visualize F_i for all busbars of one forecast a boxplot is used. Fig. 8 is the boxplots for the four forecasts. The boxplot visualizes the median of F_i (red line in the middle of the bar) as well as the upper and lower quartiles (the box). Without any optimization, the voltage at all busbars is very low and the voltage drops between the busbars are very high, which is a sign for high losses. To set the reference voltages to $\boldsymbol{u}_{\mathrm{opt}}$ already reduce the voltage drops and decreases the voltage error of all busbars. Nevertheless, almost none of the busbars reach the optimum voltage, which was to be expected due to the steady state voltage error. With the optimized reference voltages, it is possible to increase the overall voltage and reduce the voltage error. The fact that the reference voltages are optimized for all forecasts limits the possibility to optimize the reference voltages for a specific case, but it also increases the robustness, as shown below.

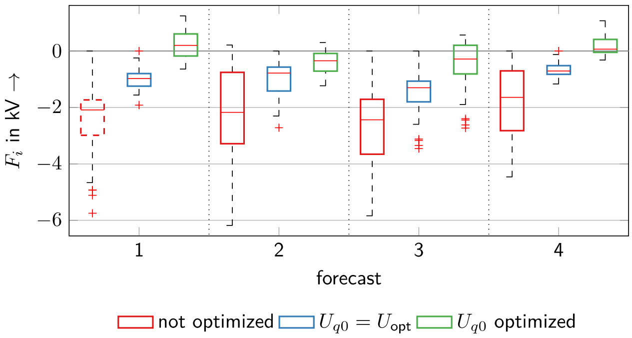

Fig. 8 Boxplot of voltage error F_i of all busbars for the four forecasts, with 4-quantiles

To get an overall impression of the effectiveness of the optimization the mean error F_{G} is introduced. F_{G} is evaluated separately for every forecast and for the n busbars of the grid and calculated as:

$$F_{\mathrm{G}} = \frac{1}{n}\sum_{i=1}^{n}\left|U_i - U_{\mathrm{opt}\,i}\right|. \tag{14}$$

In Fig. 9 it can be seen that the optimization of $\boldsymbol{u}_{q0}$ helps to decrease the mean error (green bar). F_{G} is decreased between 87 % and 77 % compared to the not optimized settings. The method is more effective in case of high infeed, as was to be expected. To prove the robustness of the method against forecast error, the simulation is re-run with the same reference voltages and slightly different load cases. The mean error for this deviating forecast is the purple bar in Fig. 9. It is not significantly affected by the forecast error. Therefore, it is not sensible to optimize the reference voltage just for one forecast because this would make the optimization more sensitive to forecast errors.

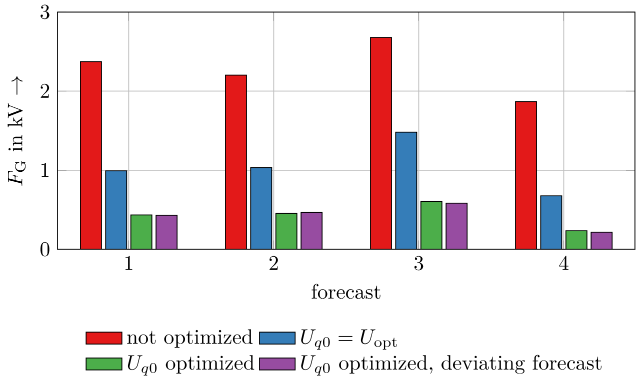

Fig. 9 Mean error for the four forecasts as well as deviating forecasts

VI. CONCLUSION

This paper presented an approach to use the *Q(U)*-control as an efficient and robust fallback solution for a distributed reactive power control scheme. It was shown that a steady state voltage error is inherent to the control system. With the presented algorithm, the steady-state error is taken into account when calculating an optimized reference voltage. Simulations on a benchmark grid showed that with the optimized reference voltage the deviation from the optimal state can be decreased for all forecast. Observing several forecast intervals makes the method more robust against forecast errors.

REFERENCES

[1] A. Kulmala et al., “Coordinated Voltage Control in Distribution Networks Including Several Distributed Energy Resources,” IEEE Transactions on Smart Grid, 2014.

[2] M. Meyer, M. Cramer, P. Goergens and A. Schnettler, “Optimal use of decentralized methods for volt/var control in distribution networks,” IEEE PowerTech, 2017.

[3] O. Marggraf, S. Laudahn, B. Engel et al., “U-Control – Analysis of Distributed and Automated Voltage Control in current and future Distribution Grids,” Internationaler ETG Kongress, 2017.

[4] M. Kreutziger, P. Schegner, S. Wende-von-Berg, M. Braun und N. Bornhorst, “Reactive power management of distributed generators for selective voltage optimization in 110-kV-subtransmission grids,” Conference: NEIS 2019 - Conference on Sustainable Energy Supply and Energy Storage Systems, 09/20/2018 - 09/21/2018 at Hamburg, Deutschland

[5] O. C. Rascon, B. Schachler, J. Bühler, M. Resch and A. Sumper, „Increasing the hosting capacity of distribution grids by implementing residential PV storage systems and reactive power control,“ Conference: 2016 13th International Conference on the European Energy Market (EEM)

[6] FNN Forum Netztechnik, “Vergleich von technischer Wirksamkeit sowie Wirtschaftlichkeit zeitnah verfügbarer Verfahren zur Sicherung der statischen Spannungshaltung in Niederspannungsnetzen mit starker dezentraler Einspeisung,“ Schlussbericht, 2014.

[7] Bundesnetzagentur (2019, Januar 28), EEG in numbers 2017, [online].Available:https://www.bundesnetzagentur.de

[8] S. Krahmer, A. Saciak, J. Winkler, P. Schegner and K. Röbenack, “On robust stability criteria for nonlinear voltage controllers in electrical supply networks,“ Power Systems Computation Conference (PSCC), 2018.

[9] VDE-AR-N-4120:2018-11 Technical requirements for the connection and operation of customer installations to the high voltage network (TAR high voltage)

[10] S. Meinecke (2018, July). *SimBench* [Online]. Available: https://www.simbench.de.

Flexible tariffs for optimal operation of storage in a microgrid

Muhammad Tayyab, Jun.-Prof. Dr.-Ing. Ines Hauer
Chair Electric Power Networks and Renewable Energy (LENA)
Otto-von-Guericke-Universität Magdeburg (OvGU)
Magdeburg, Germany
Muhammad.tayyab@ovgu.de

***Abstract*—Energy storage is used to store the excess energy generated from renewable energy sources. However, due to economic unfeasibility, different design and operation strategies should be analyzed. In the present paper, a flexible tariff (White tariff) will be introduced alongside with different battery operation strategies in a settlement with a grid-connected photovoltaic system. The operation strategies are compared under the white and flat tariff for a storage feasibility check. The results show a significant increase in the savings using white tariff in these types of systems. However, considering the investment cost of the storage, 5 years of payback time is required.**

Keywords—Microgrid, battery energy storage, direct usage, optimal storage operation, white tariff

I. INTRODUCTION

The storage is used to mitigate the intermittent generation of renewable energy sources. The advantages of the storage systems are several. However, the cost of the battery increases with each kWh. Therefore, the profitability of the battery energy storage should be analyzed in a microgrid application. There are different ways of such analysis including the application of flexible tariffs because the smart meters will allow the application of flexible tariffs [1]. The flexible tariffs have different prices at on-peak and off-peak consumption level. The battery is often charged in the off-peak time and discharged at an on-peak time to avoid high price purchase of electricity [2]. As a flexible tariff, the white tariff will be used which is already implemented in the Brazilian network, where low voltage customers can choose this tariff. The implementation of the white tariff in Germany with a different load and PV production can be beneficial.

Another factor of interest in a microgrid application is self-consumption. The utilization of the local generation of the produced energy is recommended which enable the reduction of the grid stress. The self-consumption has been triggered by the introduction of incentives such as feed-in tariffs and energy tariffs [1].

In literature, the grid-connected microgrids have been studied excessively. The use of battery energy storage has been found to be efficient in peak shaving, voltage support, reliability, and integration of renewable energy sources [3]. Storage of energy at an off-peak time and discharging it at an on-peak time has been studied in [3]. Furthermore, the use of the battery energy storage system to support the distribution grid has been analyzed in [4]. Grid-connected microgrids with Battery energy storage system (BESS) in a different configuration and under consideration of time-of-use tariffs got more attention [5,6]. The BESS studies in terms of self-consumption based on demand forecasting have been studied in [7- 12,13]. Similarly, self-consumption with different electricity prices has been analyzed in [14]. A combination of the different distributed energy resources (DER) with respect to BESS to gain technical and economic benefits are still to be analyzed [15]. Investigation of BESS coupled with PV to facilitate the consumer to get the benefit of feed-in tariffs incentive has been done in [16]. The study uses mixed integer linear programming (MILP) to solve the optimization problem. The studies [17,18] consider the optimization for different tariff structures. Furthermore, BESS with PV and time-varying tariffs to decrease the operational cost has been studied in [19,20,21,22,23]. However, a study on the comparison of battery charging with PV and grid usage, along with PV under white tariffs to decrease the grid usage ultimately at the peak price time is lacking.

The study in the present paper investigates a settlement area with photovoltaic and storage systems. The electrical loads of the settlement houses include the electrical profile of heat pumps. Different battery operation strategies have been analyzed and compared under consideration of the white tariffs with the optimization goal to decrease the grid supply. The results have been compared with the flat electricity tariffs to analyze the effect of the white tariff on these types of systems.

The paper is organized as follows. Firstly, the settlement area is defined. Secondly, a methodology is presented and finally, the results followed by discussion and conclusion based on the comparison of different scenarios are presented.

II. METHODOLOGY

A. Description of the settlement area

The settlement area investigated is located in Magdeburg, Germany. The settlement was assumed to consist of five single-family (SFH) houses and six multi-family (MFH) houses. The single-family houses occupied by one to five persons, while two MFH houses consist of twelve dwellings and four MFH sixteen dwellings. The SFH area is supposed to be 140 m^2 and the MFH area is 950 m^2 and 1170 m^2 respectively with 12 dwellings and 16 dwellings [24]. The houses in the settlement are assumed to be passive houses with an annual heating requirement of 15 kWh / m^2 and equipped with photovoltaic systems [27,30].

B. Load profiles

Heating demand (water and space heating) was calculated depends on the number of persons and the area of the houses in the settlement. A heat pump was used in the settlement to cover the houses heating load. Based on the settlement heating requirement, the electrical energy required for the heat pump was calculated [26,27]. The seasonal coefficient of performance (SCOP) is needed for this purpose which has been calculated by using VDI4655.

HTW Berlin University of Applied Sciences electrical loads database has been selected for the settlement area [25].

Load profiles are available between 1.4 MWh and 8.6 MWh. For a single-person household, the electric load with annual electricity consumption of 1.4 MWh is assumed. The number of persons and their electricity consumptions are given in Table 1.

TABLE I. ANNUAL ELECTRICITY CONSUMPTION [27,28,29]

Household size (Number of persons)	**1**	**2**	**3**	**4**	**5**
Annual electricity consumption in MWh	1.20-1.97	2.70-3.33	3.00-4.50	3.60-5.50	4.90-6.00

C. PV production profile

The rated PV production is calculated in (1) [31],

$$PV_{\mathrm{PV,inst}} = G \cdot \eta_{\mathrm{M}} \cdot PR \cdot A_{\mathrm{PV}} \qquad (1)$$

where G represents the irradiance, which is assumed to be 1000 W/m^2, η_{M} refers to the solar module efficiency, PR shows the complete system performance ratio and A_{PV} is the total PV area. Module efficiency of 19.1 % and a performance ratio of 85 % is assumed [32]. The total PV area (A_{PV}) is given in (2) [33],

$$A_{\mathrm{PV}} = A_{\mathrm{R}} \cdot GCR \qquad (2)$$

where A_{R} is the total roof's area and GCR is the ground coverage ratio assumed to be 75 %. Different tilting mechanisms increase PV production by 15 % compared to the horizontal surface [34]. The total rated PV capacity installed in the settlement is 224 kW. The roof's area of the SFH and MFH has been assumed to be 90 m^2 and 0 m^2, respectively. The PV details are shown in Table 2.

TABLE II. TOTAL PV AREA AND INSTALLED CAPACITY

House type	**Number of Houses**	**Total Roof's area**	**Total PV area**	**PV Production capacity in kW**
SFH	5	450	337.5	54.5
MFH	6	1500	1125	182

D. Storage and Converter rated capacity

The rated storage capacity can be selected on the basis of the rated PV production. According to the storage monitoring carried out by the Institute of Power Electronics and Electric Drives (ISEA) at the RWTH Aachen, the rated storage capacity has approximately a 1:1 ratio as compared to the rated PV production as shown in Fig. 1.

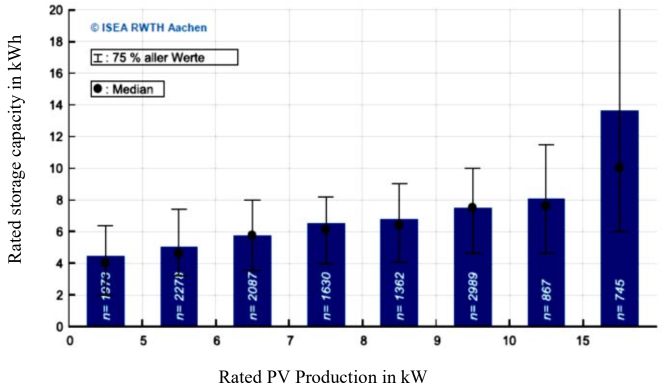

FIG. 1. RATED STORAGE CAPACITY VERSUS RATED PV PRODUCTION [41]

The capacity of the converter is selected based on the rated capacity of the battery. In the present study, it is assumed with 50 % of the rated capacity of battery [35].

E. Tariffs

The white tariff has been implemented in Brazil for low voltage consumers and is shown in Fig 2.

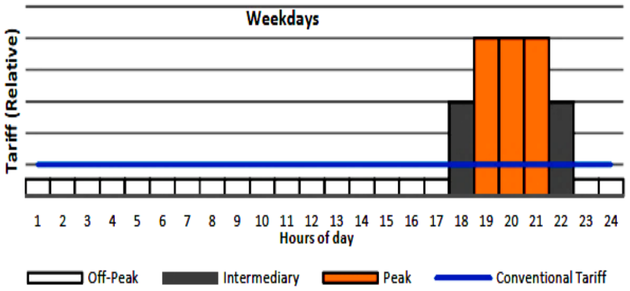

FIG 2 WHITE TARIFF [2]

The tariffs have distinctive values within the weekdays as well as on weekends. The rate of electricity for off-peak, mid-peak and on-peak time is assumed to be 20 Cents, 50 Cents and 90 Cents per kWh for weekdays and a flat value of 30 Cents on the weekend and on holidays. For comparison, the system is also analyzed with a flat rate as implemented in Germany. A flat rate of 30 Cents/kWh has been assumed [2].

F. problem formulation

The optimization objective is to increase the discharge of the battery at peak price and decrease the use of the grid. Linear programming is used for this purpose for implementation. The objective function of increasing profits is shown in (3)

$$\max \sum_{t=1}^{h} (P_{\mathrm{GF}} C_{\mathrm{GF}} - P_{\mathrm{CT}} C_{\mathrm{GF}} - P_{\mathrm{GS}} C_{\mathrm{GS}} + P_{\mathrm{BD}} C_{\mathrm{GS}}) \quad (3)$$

Where, h is the hours, C_{GF} are the costs of selling energy and C_{GS} are the costs of electricity purchased from the grid. P_{GF} is the grid feed-in power, P_{GS} is the grid supply power, P_{BD} is the battery discharge power and P_{CT} is the curtailed power. Extra costs related to the operation of district storage systems (EEG-levy) are not considered.

The load should be always covered by PV direct usage, battery discharge, and grid supply. Similarly, PV production should be totally utilized in direct usage, battery charge, grid feed-in, and curtailment. The constraints are given in (4,5).

$$P_{\mathrm{Load}}(t) = P_{\mathrm{DU}}(t) + P_{\mathrm{BD}}(t) + P_{\mathrm{GS}}(t) \qquad (4)$$

$$PV_{\mathrm{PV,inst}}(t) = P_{\mathrm{DU}}(t) + P_{\mathrm{BC}}(t) + P_{\mathrm{GF}}(t) + P_{\mathrm{CT}}(t) \qquad (5)$$

Here, P_{DU} is direct usage power and P_{BC} is the battery charge power. The battery charge and discharge power are bounded by the capacity of the battery. The battery discharge energy cannot exceed the battery charge energy. Furthermore, the battery discharge power has to be less than the battery charge power given as follows.

$$0 \le P_{\mathrm{BD}}(t) \le P_{\mathrm{max,CON}} \qquad (6)$$

$$0 \le P_{\mathrm{BC}}(t) \le P_{\mathrm{max,CON}} \qquad (7)$$

$$\sum P_{\mathrm{BD}} - P_{\mathrm{BC}} \le 0 \qquad (8)$$

Here, $P_{\max,\text{CON}}$ is the converter capacity. In the scenario where the battery will be charged from PV and from the grid, P_{BC} will be the accumulated value for the day. The grid feed-in limitation is assumed to be 50 % of the installed PV capacity [36,37,38]. The constraint for the grid feed-in, grid supply, and curtailment are given in (9).

$$\begin{cases} 0 \le P_{\text{GF}}(t) \le 0.5 \cdot PV_{\text{PV,inst}} \\ 0 \le P_{\text{GS}}(t) \le P_{\text{Load}} \\ 0 \le P_{\text{CT}}(t) \le PV_{\text{PV,inst}} \end{cases} \tag{9}$$

Here, the $PV_{\text{PV,inst}}$ is the rated capacity of the PV system installed.

G. Self-consumption and self-sufficiency

The local use of energy, in the settlement, is referred to self-consumption (*SC*) and the ability of the settlement to provide energy without grid intervention is referred to self-sufficiency (*SS*) [41].

$$SC = \frac{(P_{\text{DU}} + P_{\text{BD}})}{PV_{\text{PV,inst}}} \tag{10}$$

$$SS = \frac{(P_{\text{DU}} + P_{\text{BD}})}{P_{\text{Load}}} \tag{11}$$

III. RESULTS AND DISCUSSION

The analyzed scenarios for the grid-connected microgrid in this settlement has been described in section (II, A). The one-hour resolution has been considered in the present paper. three cases have been considered for the evaluation based on white tariffs and flat tariff as given below.

Case 1: PV without battery storage as a reference case

Case 2: PV with battery storage and the battery will be charged only from PV

Case 3: PV with battery storage and the battery will be charged from PV as well as the power systems

A. Case 1

In this case, grid feed-in and direct usage are the main parameters to been considered. At the start of the PV production, the electricity imported from the grid is decreased gradually until it becomes zero at approximately 8 AM. The energy is sold to the grid as soon as the PV production becomes higher than the load. The remaining energy must be curtailed.

In figure 3, the curtailed energy is 305 kWh on this day and the energy purchased from the grid are 237.5 kWh. The grid feed-in is 588.2 kWh. The power balance at summer and winter is shown in Fig 3 and Fig 4 respectively.

The PV production is low on a winter day, a small amount of grid feed-in has been noticed. There is no curtailment on the day Most of the produced energy has been self-consumed by direct usage. The grid supply is 514 kWh for the day which means that an average of 154 € of electricity should be purchased from the grid to fulfill the load of the settlement considering a flat rate of 30 Cents/kWh. The grid feed-in on the day is 12 kWh.

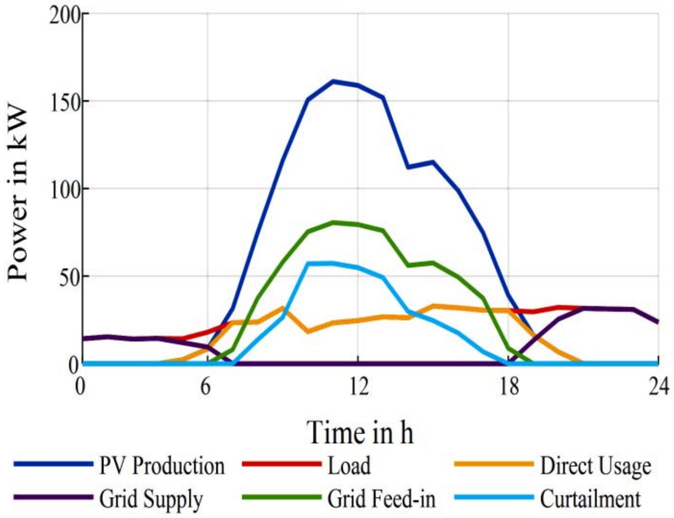

FIG 3 POWER BALANCE SUMMER DAY (JULY, 19TH)

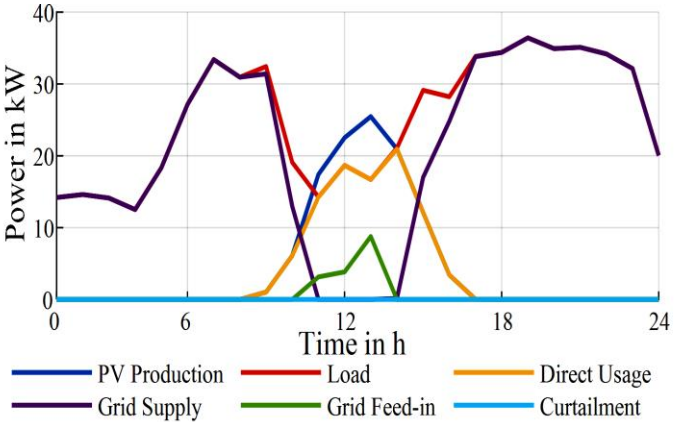

FIG 4 POWER BALANCE FOR WINTER CASE 1 (JANUARY, 15TH)

B. Case 2

The battery capacity is 224 kWh. On January, 15th, the PV production is low and is not enough to charge the battery. However, the battery has covered a part of the load at the peak price. Due to which, a high amount of grid supply is needed to cover the load. The power balance for a winter day is shown in Fig 5.

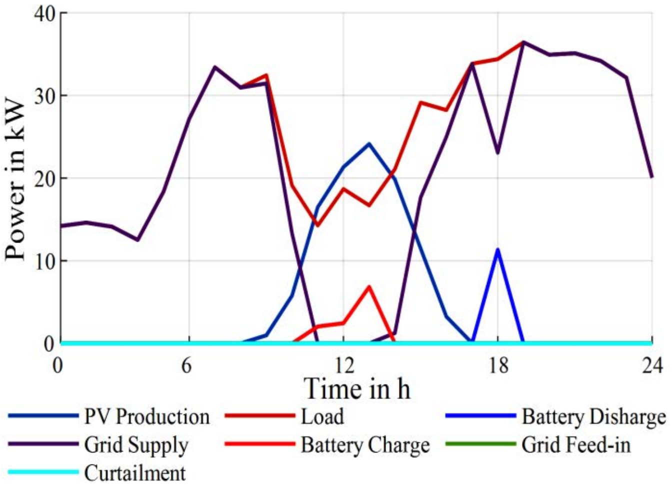

FIG 5 OPTIMAL POWER BALANCE FOR CASE 2 IN WINTER (JANUARY, 15TH)

The PV production becomes higher than the direct usage and the remaining power directed to battery storage. The battery has been discharged at around 6 PM where the prices were high. On a summer day, to cover the total load by the battery. discharge, an increase in battery capacity is recommended. Furthermore, charging from the grid should be included to use the total capacity, which will be discussed in the next section. The grid feed-in, grid supply, and curtailment on 19th July are 588 kWh, 80 kWh, and 81 kWh respectively. The curtailments and grid usage have been decreased as compared to case 1. The grid feed-in is the same, because of the high PV production and the energy needed to charge the battery is taken from the curtailment

C. *Case 3*

A battery with a capacity of 224 kWh is placed and the battery is also charged from the grid. In the context of reducing the grid import at the peak price, this type of system will be useful as shown in Fig 6.

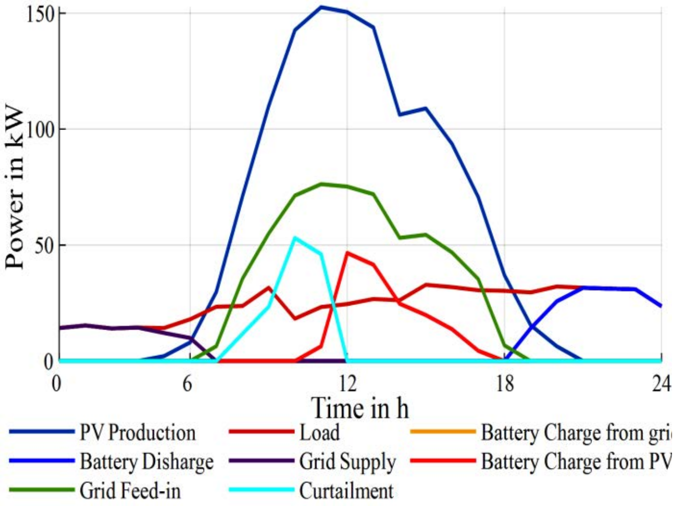

FIG 6 OPTIMAL POWER BALANCE FOR CASE 3 IN SUMMER (JULY, 19TH)

It has been assumed that the battery is empty at the start of the day. The PV production is high, and it can charge the battery completely. The purchased energy from the grid on this particular day is 80 kWh, 85 % less compared to case 1. The grid feed-in and curtailment on this day are 588 kWh and 137 kWh, respectively. Power balance on a winter day is shown in Fig 7.

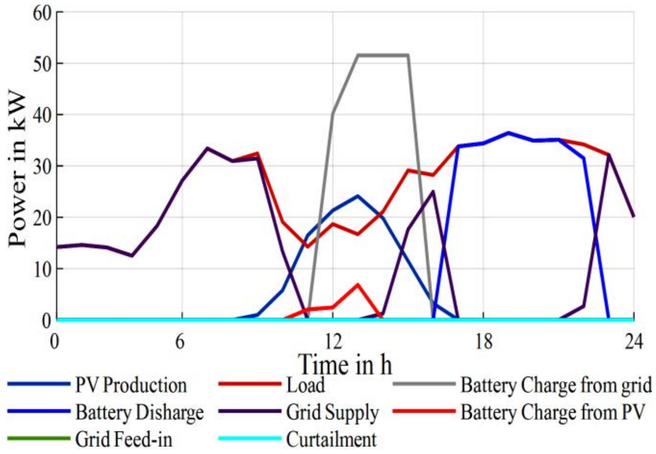

FIG 7 POWER BALANCE FOR WINTER (JANUARY, 15TH)

On a winter day, the grid will be used to charge the battery completely, as shown in Fig 7. The battery is empty at the start of the day. The battery is slightly charged from PV production. Most of the PV production has been used as direct usage. Using the grid and PV, the battery has been fully charged and the load at peak price time has been covered by the battery discharged as shown in Fig 7. The purchased energy to cover the load is 308 kWh and 194 kWh is needed from the grid to charge the battery. The curtailment and grid feed-in are 0 at the day.

D. *Comparison*

Fig 8 shows the results of a one-year simulation. The grid supply and grid feed-in are much more in case 1. Furthermore, case 3 provides more flexibility in term of battery full capacity usage. The average state of charge is 33 % for case 3 while it is 20 % for case 2. Which means that the battery in case 3 has utilized its capacity more times compared to case 2. Technically, case 3 has more potential to decrease grid stress. The curtailment is also low in case 3 compared to another case.

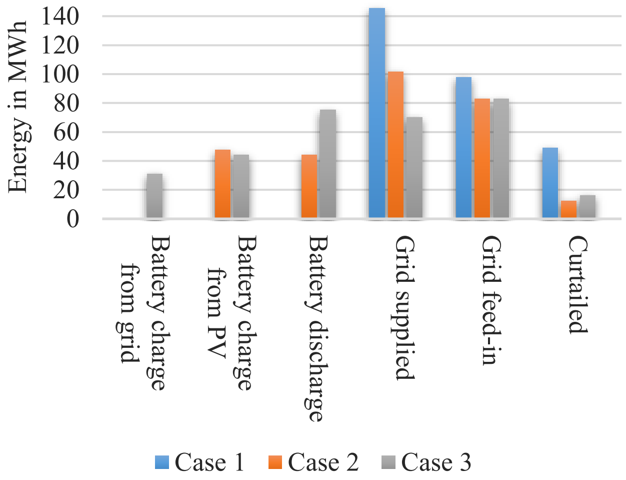

FIG 8 YEARLY ENERGY BALANCE

The objective function value for one year considering the white tariff (see section IV) and a selling price of 11 Cents/kWh for the energy fed into the grid is shown in Table 3. The flat rate as implemented in Germany with 0.30 €/kWh assumption is also considered and compared with the white tariff is Table 3.

TABLE III OBJECTIVE FUNCTION VALUE

Cases	**Objective function value using white tariff (€)**	**Objective function value € using flat rate (€)**
Case 1	-48 933	-37 874
Case 2	2916	-8893
Case 3	27 243	-9390

Table 3 shows that the case 2 and 3 has positive value when operated in the white tariff. The value will be positive when the grid feed-in and battery discharge is greater than the grid supply and curtailment. The benefit of case 3 includes the full capacity usage of the battery on a daily basis. The revenue and cost of the amount of energy purchased, sold and curtailed are shown in Table 4.

TABLE IV PURCHASED, SOLD AND CURTAILED ENERGY REVENUE/COST UNDER WHITE TARIFFS

Cases	**Energy purchased (€)**	**Energy sold (€)**	**Cost of the Curtailed amount (€)**
Case 1	54 687	11 572	5818
Case 2	30 051	9802	1471
Case 3	20 301	9812	1926

The usage of scenario three, where the battery is charged form the grid is beneficial as shown in Table 4. In case three, the cost of the energy required to fulfill the demand has been decreased as it will be charged in peak time and discharged at an off-peak time. The cost of the curtailment in case 3 is higher than the case 2 because the battery is charged from the grid and when it started charging from the grid, the battery has already a little bit of energy content. Assuming an annual fixed cost of the battery system of 66 €/kWh and a battery life of 10 years [39]. For the case, 2 and 3 investment cost become 135520 € is required which bring a payback time of 5 years for case 3. It means that after 5 years of profit, the battery would be amortized. By the inclusion of PV system fixed cost of 40 €/kW, the payback time will be 8 years [40].

It can be seen that the implementation of the battery in Case 2 is not feasible, because the savings are low per year and the battery is expensive. With a flat rate, in all cases, the cost of purchased and curtailed energy is greater than the sell or self-consumption as shown in Table 5. Due to a flat rate of energy purchased, Case 3 and Case 2 has identical values.

TABLE V PURCHASED, SOLD AND CURTAILED ENERGY REVENUE/COST UNDER FLAT TARIFFS

Cases	**Energy purchased (€)**	**Energy sold (€)**	**Cost of the Curtailed amount (€)**
Case 1	43 627	11 572	5818
Case 2	30 426	9802	1471
Case 3	30 452	9812	1926

The self-consumption of reference case 1 is low due to the missing battery. The introduction of the battery in case 3 does not help in the promotion of self-consumption and self-sufficiency due to the higher curtailment compared to case 2 as shown in Figure 9.

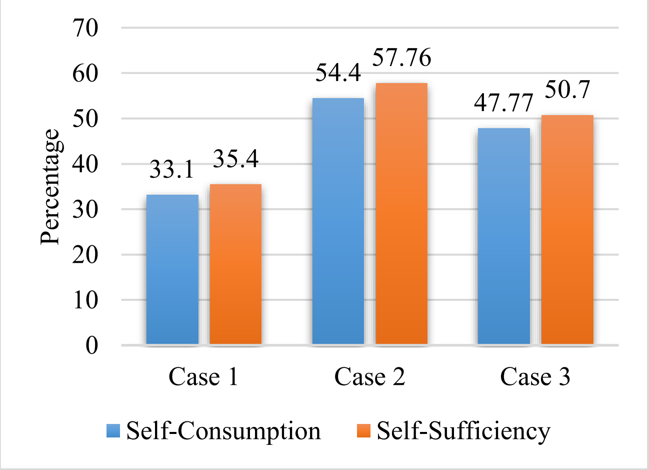

FIG 9 SELF-CONSUMPTION AND SELF-SUFFICIENCY

The self-consumption has been increased from 33% to 54.4% in case 2 as compared to the reference case. Similarly, an increase of 22% has resulted in self-sufficiency for case 2.

There is no major difference is the change in self-sufficiency as well as self-consumption when analyzed in the flat or white tariff. The increase of self-consumption and self-sufficiency will increase the profitability of PV system in countries where the subsidies on PV are less [41]. These will also decrease the grid stress subject to an increase in storage capacity.

IV. CONCLUSION

The case study of a new settlement area has been investigated. The electrical and heating load profile taking into account a heat pump has been computed for the settlement area. Time-varying electricity prices specifically the white tariff has been implemented in the settlement area. Furthermore, optimal storage operation to decrease the grid stress at the peak price of electricity has been implemented with linear programming.

Three cases have been analyzed. Firstly, the reference case without any storage has been studied. Secondly, a scenario with storage and the storage will be charged only from the PV. Finally, the energy storage charged from the PV as well as the grid has been analyzed. The three scenarios have been compared keeping in mind the battery life, cost, and time-varying prices. The implementation of the white tariff with case three is beneficial but still, a 5 year of payback time is required. By the comparison of three scenarios on the basis of self-consumption and self-sufficiency, it is noticed that scenario 2 has a higher potential in self-consumption and self-sufficiency due to less curtailment as compared to scenario 3.

V. REFERENCES

[1] G. Subramani, V. K. Ramachandaramurthy, S. Padmanaban, L. Mihet-Popa, F. Blaabjerg, and J. M. Guerrero, “Grid-tied photovoltaic and battery storage systems with Malaysian electricity tariff - A review on maximum demand shaving,” Energies, vol. 10, no. 11, 2017.

[2] D. De Campos, E. A. C. A. Neto, R. C. Fernandes, I. Hauer, and A. Richter, “Optimal tariff system for integration of distributed resources based on a comparison of Brazil’s and Germany’s system,” 2016 IEEE Symp. Ser. Comput. Intell. SSCI 2016, pp. 0–7, 2017.

[3] Muhammad Faisal et al, “Review of energy storage system technologies in microgrid applications: Issues and challenges,” SPECIAL SECTION ON ADVANCED ENERGY STORAGE TECHNOLOGIES AND THEIR APPLICATIONS,IEE,2018

[4] J. Tant, F. Geth, D. Six, P. Tant, and J. Driesen, “Multiobjective battery storage to improve PV integration in residential distribution grids,” IEEE Trans. Sustain. Energy, vol. 4, no. 1, pp. 182–191, 2013.

[5] F. A. Inthamoussou, J. Pegueroles-Queralt, and F. D. Bianchi, ‘‘Control of a supercapacitor energy storage system for microgrid applications,’’ IEEE Trans. Energy Convers., vol. 28, no. 3, pp. 690–697, Sep. 2013.

[6] Teng F, Miles J, Thomson A, Strbac G, Brandon N, Pudjianto D. Potential value of energy storage in the UK electricity system. Proc ICE - Energy 2015; 168:107–17. http://dx.doi.org/10.1680/ener.14.00033.

[7] Bertsch V, Geldermann J, Lühn T. What drives the profitability of household PV investments, self-consumption and self-sufficiency?; 2017.

[8] Weniger J, Tjaden T, Quaschning V. Sizing of residential PV battery systems. Energy Procedia 2014;46:78–87. http://dx.doi.org/10.1016/j.egypro.2014.01.160.

[9] Brusco G, Burgio A, Menniti D, Pinnarelli A, Sorrentino N. The economic viability of a feed-in tariff scheme that solely rewards self-consumption to promote the use of integrated photovoltaic battery systems. Appl Energy 2016;183:1075–85. http://dx.doi.org/10.1016/j.apenergy.2016.09.004.

[10] Castillo-Cagigal M, Caamaño-Martín E, Matallanas E, Masa-Bote D, Gutiérrez A, Monasterio-Huelin F, et al. PV self-consumption optimization with storage and Active DSM for the residential sector. Sol Energy 2011;85:2338–48. http://dx. doi.org/10.1016/j.solener.2011.06.028.

[11] Linssen J, Stenzel P, Fleer J. Techno-economic analysis of photovoltaic battery systems and the influence of different consumer load profiles. Appl Energy 2017;185:2019–25. http://dx.doi.org/10.1016/j.apenergy.2015.11.088.

[12] Ratnam EL, Weller SR, Kellett CM. Scheduling residential battery storage with solar PV: Assessing the benefits of net metering. Appl Energy 2015;155:881–91. http://dx.doi.org/10.1016/j.apenergy.2015.06.061.

[13] Pyrgou A, Kylili A, Fokaides PA. The future of the Feed-in Tariff (FiT) scheme inEurope: The case of photovoltaics. Energy Policy 2016; 95. doi:10.1016/j.enpol.2016.04.048.

[14] Quoilin S, Kavvadias K, Mercier A, Pappone I, Zucker A. Quantifying selfconsumption linked to solar home battery systems: Statistical analysis and economic assessment. Appl Energy 2016;182:58–67. http://dx.doi.org/ 10.1016/j.apenergy.2016.08.077.

[15] Ruth M, Pratt A, Lunacek M, Mittal S, Wu H, Jones W. Effects of home energy management systems on distribution utilities and feeders under various market structures 2015;15(18).

[16] Ratnam EL, Weller SR, Kellett CM. An optimization-based approach to scheduling residential battery storage with solar PV: Assessing customer benefit. Renew Energy 2015;75:123–34. http://dx.doi.org/10.1016/j.renene.2014.09.008.

[17] Jayawardana HPAP, Agalgaonkar AP, Robinson DA. Novel control strategy for operation of energy storage in a renewable energy-based microgrid. In: 2015 Australasian Universities Power Engineering Conference (AUPEC), IEEE; 2015, p. 1–6. doi:10.1109/AUPEC.2015.7324891.

[18] Ratnam EL, Weller SR, Kellett CM. An optimization-based approach for assessing the benefits of residential battery storage in conjunction with solar PV. In: 2013 IREP symposium bulk power system dynamics and control - IX optimization, security and control of the emerging power grid, IEEE; 2013, p. 1–8. doi:10.1109/IREP.2013.6629420.

[19] Tazvinga H, Xia X, Zhang J. Minimum cost solution of photovoltaic–diesel–battery hybrid power systems for remote consumers. Sol Energy 2013;96:292–9. http://dx.doi.org/10.1016/j.solener.2013.07.030.

[20] Tazvinga H, Xia X, Zhu B. Optimal energy management strategy for distributed energy resources. Energy Procedia 2014;61:1331–4. http://dx.doi.org/10.1016/j.egypro.2014.11.1093.

[21] Tazvinga H, Zhu B, Xia X. Optimal power flow management for distributed energy resources with batteries. Energy Convers Manage 2015;102:104–10. http://dx.doi.org/10.1016/j.enconman.2015.01.015.

[22] Hove T, Tazvinga H. A techno-economic model for optimising component sizing and energy dispatch strategy for PV-diesel-battery hybrid power systems. J Energy Southern Africa n.d.; 23: p. 18–28.

[23] Wu Z, Tazvinga H, Xia X. Demand side management of photovoltaic-battery hybrid system. Appl Energy 2015; 148:294–304. http://dx.doi.org/10.1016/j.apenergy.2015.03.109. ´

[24] M. Fernandez and B. Cener, “Heating and cooling energy demand and loads for building types in different countries of the EU,” ENTRANZE project, March 2014.

[25] T. Tjaden, J. Bergner, J. Weniger, and V. Quaschning,“Represen tative electrical load profiles of residential buildings in Germany with a temporal resolution of one second,” Work. Pap. HTW Berlin -HTW Berlin - Univ. Appl. Sci. Res., pp. 1–7, 2015.

[26] Association of German Engineers VDI, "progress report VDI - No. 560 Refernezlastprofile of single and multi-family dwellings for the use of CHP plants," VDI Verlag, Düsseldorf 2007.

[27] Muhammad Tayyab, Ines Hauer,Christian Klabunde and M. Wolter,’’Optimal storage design and operation in a new settlement area under consideration of sector coupling and renewable energy generation,2018,Glasgow, Schottland, September

[28] Bundesministerium für Umwelt, Naturschutz, Bau und Reaktorsicherheit,“Stromspiegel für Deutschland 2014 - Vergleichswerte für Ihren Stromverbrauch“,Bundesministerium für Umwelt, Naturschutz, Bau und Reaktorsicherheit, 2014.

[29] M. Bost, B. Hirschl, and A. Aretz, “Effekte von Eigenverbrauch und Netzparität bei der Photovoltaik,” Berlin, Hamburg, pp. 1– 96, 2011.

[30] B.Environmental, “Energy consumption and Passive Houses.” 2014 [online] Available:http://passipedia.passiv.de/passipedia_en/start [Accessed Dec 2017].

[31] T. Lang, D. Ammann, and B. Girod, “Profitability in absence of subsidies: A techno-economic analysis of rooftop photovoltaic self-consumption in residential and commercial buildings,” Renew. Energy, vol. 87, pp. 77–87, 2016.

[32] Energysage, “What are the most efficient solar panels on the market?.”2017 [online] Available:"https://news.energysage.com/what-are-the-most-efficient-solar-panels-on-the-market" [Accessed Nov,2017]

[33] M. Culligan and J. Botkin, “Impact of Tilt Angle on System Economics for Area Constrained Rooftops,” 22nd Eur. Photovolt. Sol. Energy Conf. Exhib., p. 3278, 2007.

[34] H. Wirth, “Recent facts about photovoltaics in Germany,” Fraunhofer ISE, Berlin, Hamburg p. 92, 2015.

[35] J. Weniger, T. Tjaden, J. Bergner, and V. Quaschning, “Sizing of Battery Converters for Residential PV Storage Systems,”Energy Procedia, vol. 99, pp. 3–10, 2016.

[36] J. Bergner, J. Weniger, T. Tjaden, “Algorithmus zur Umsetzung der prognosebasierten Batterieladung für PV-Speichersysteme mit messewertbasierten PV-und Lastprognosen (Version 1.1) Berlin Forschungsgruppe Hochschule für Technik und Wirtschaft HTW Berlin 2016

[37] J. Bergner et al.,“Verbesserte Netzintegration von PVSpeichersystemen durch Einbindung lokal erstellter PV- und Lastprognosen,” Symposium Photovoltaische Solarenergie, Kloster Banz, Bad Staffelstein vol. 1, 2015.

[38] J. Bergner, J. Weniger, T. Tjaden, and V. Quaschning, “ Feed-in Power Limitation of Grid-Connected PV Battery Systems with Autonomous Forecast-Based Operation Strategies,” 29th European PV Solar Energy Conference and Exhibition Amsterdam, 2014.

[39] J. Dancker, M. Wolter, J. Rosberg, and E. Tsotsas, “Increasing self-sufficiency in a micro grid: Integrated vs. non-integrated energy system approach,” Proc. - 2018 53rd Int. Univ. Power Eng. Conf. UPEC 2018, pp. 1–6, 2018.

[40] Christian Ziegler, André Richter, Ines Hauer, Martin Wolter, “Technical Integration of Virtual Power Plants enhanced by Energy Storages into German System, Operation with regard to Following the Schedule in Intra-Day” Proc. - 2018 53rd Int. Univ. Power Eng. Conf. UPEC 2018, pp. 1–6, 2018.

[41] Rasmus Luthandera, Joakim Widéna, Daniel Nilssonb, Jenny Palm “Photovoltaic self-consumption in buildings: A review” 2016.available’’https://doi.org/10.1016/j.apenergy.2014.12.028’’Volume 142, 15 March 2015, Pages 80-94 Applied Energy

Automated use of wired measures in grid planning for solving current and voltage band problems

M.Sc. Hermann Kraus
Forschungsstelle für Energienetze und Energiespeicher (FENES)
OTH Regensburg
Regensburg, Bavaria
hermann.kraus@oth-regensburg.de

Prof. Dr.-Ing. Oliver Brückl
Forschungsstelle für Energienetze und Energiespeicher (FENES)
OTH Regensburg
Regensburg, Bavaria
oliver.brueckl@oth-regensburg.de

Abstract—**This work deals with the use of cable exchange and parallel cabling as network expansion measures in the context of an automated grid planning for the elimination of current and voltage band problems in a distribution network. Inter alia, reference is made to a higher-level program, which is being developed in the EU project "CrossEnergy", and the procedures for remedying the limit value violations are presented.**

Keywords—grid planning, automation, cable exchange, parallel cabling, network expansion

I. Introduction

The changes in the power grid, that accompany the energy revolution, pose new challenges for many network participants. In future, distribution system operators will also have to reckon with an increased number of renewable energy sources in their electricity grids and continue to guarantee safe operation. It is not uncommon that, with the connection of photovoltaic (PV) stations or wind turbines, limits are exceeded in terms of voltage or current. Changes in consumer behavior, demographic change or the integration of e-mobility can also cause network bottlenecks in distribution networks. In order to detect these difficulties and their consequences and to develop appropriate measures, it is necessary for the network operators to carry out detailed investigations. Automated calculations in grid planning can serve as a major support in planning a technically meaningful and at the same time economical network expansion [1].

II. Automation of Grid Planning Processes

When designing an automated grid planning program, it is crucial to develop concepts and algorithms that include generalized methods. This enables the handling of any network topologies and occurring problems. The calculated solutions should ideally represent a global optimum. It is possible to achieve this goal by means of probabilistic calculations, however, this is based on an enormous computing power as well as the determination of many partial results, which represent an inefficient problem solution. In order to reduce computing power and time, heuristics can be used to sort out irrelevant solution variants in advance. The problem with the mere integration of heuristics is often the limited application to the problem cases. Thus, there is the risk that an algorithm with a pure heuristic method can no longer filter out the best result from a separate solution pool or even finds a local optimum. Consequently, solution variants, that would be better, are not included and are not shown in the final results. To eliminate this inefficiency, heuristics are included in the proposed grid planning tool in order to keep the solution set as small as possible, but then supplemented by mathematical optimizations. Therefore, this method should ensure that the global optimum is taken into account in the final results. The search for the best results involves technical and economic aspects. Thus, it is also possible to search specifically for different optima, such as the solution with the lowest cost or greatest technical benefit.

III. Grid Planning Tool Included in the EU-Project CrossEnergy

The conception of the automated network planning arises in the course of the project CrossEnergy. This funded EU research project, created under the ETC goal, is concerned with the development of a decision support system (DSS) for the strategic development of electricity grids at the distribution grid level. The focus is on a common grid expansion planning in the Bavarian-Czech border region with regard to future scenarios for load and generation development. The main target groups are network operators and network subscribers, but the program is also intended to appeal to political decision-makers or other interest groups who would like to gain insight into the future development of electrical energy systems in a region [1].
The research project covers three topics with the Ostbayerische Technische Hochschule (OTH) Regensburg, the Technische Hochschule Deggendorf (THD) and the University of West Bohemia (UWB) in Pilsen: prognosis, grid planning and grid operation (see Fig. **1**). For this purpose, the THD provides energy data in the form of time series and installed power for current and future years as well as forecasts for load and generation development. In the course of a given scenario, OTH Regensburg implements the corresponding grid planning which is calculated fully automatically. Finally, the UWB compiles key figures and status assessments for the networks planned by OTH Regensburg, whereby a specially developed load-flow calculation program is utilized here. All three partners use a platform developed by UWB for communication and data exchange. The same data platform also has an interface to the user, who can, among other things, transmit his network and scenario data and then also receive the results of the DSS [1].

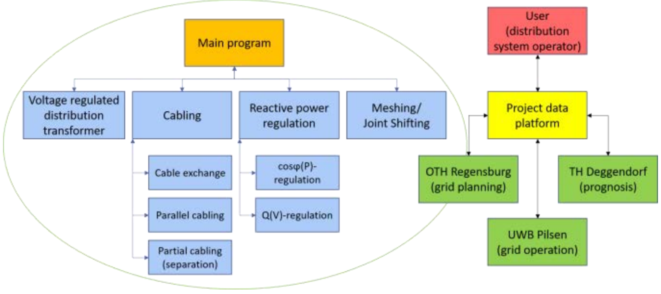

Fig. 1. System architecture of the DSS [1]

Fig. **1** shows an overview of the system architecture of the grid planning tool developed by OTH Regensburg. The main program manages the input and the output via the interface with the project database as well as the control of the individual network expansion measures. Depending on the selection of network expansion methods (e.g., cable exchange, Q(V)-regulation, etc.), load and generation development scenarios are calculated accordingly and a completed network model is returned to the platform. Thus, at the end the user has several options for a network expansion ready, which are accordingly occupied with technical and economic figures as a decision-making aid [1]. The measures can also provide several solution variants (see IV.A and IV.B). A distribution system operator then uses the final results to select, which expansion variant is best for his network. The focus of this work is on the wired measures.

IV. AUTOMATED USE OF CABLE-BONDED GIRD EXTENSIONS

In this work, the cabling measures for network planning are categorized as follows: cable exchange, parallel cabling and partial cabling. The cable exchange represents the pure replacement of lines with a larger cross section (Fig. 2). The parallel cabling provides an additional line that is installed along a critical string (Fig. 3). The partial cabling is a modified version of the parallel cabling, which also installs a parallel cable, but adds a separation at the end node of the parallel cable (Fig. 4).

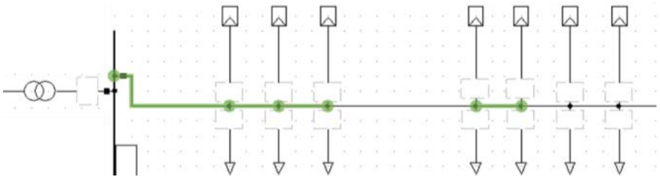

Fig. 2. Grid extension measure “cable exchange”

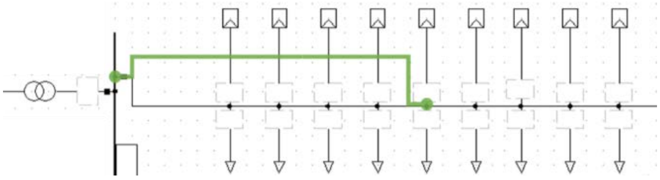

Fig. 3. Grid extension measure “parallel cabling”

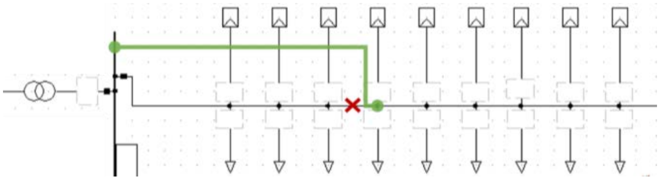

Fig. 4. Grid extension measure “partial cabling” (parallel cabling with separation)

All cable-specific measures can be used for solving current and voltage problems. In principle, when current and voltage limits are exceeded at the same time, current problems are always solved first, since this reduces or resolves in most cases the voltage problem, too. Solving the voltage problem first can also reduce or resolve the current problem, but experience shows that the chances are lower. In addition, the procedure "current problem before voltage problem" also covers a worst-case issue, which occurs with a voltage band, where most of load and generation power appear on different grid points in a string. This will be explained in more detail later (see section A). In order to present the heuristics and mathematical methods that have emerged in the development of an automated use of wired measures, the cable exchange and the parallel cabling will be discussed here deeper.

A. Cable exchange

After the routine made the load flow calculation of a distribution network, all faulty lines are sorted by error intensity. This means that the cable pieces and network nodes, which have the highest utilization or the largest deviation from the voltage limits, are first returned to a permissible network state (see Fig. 5).

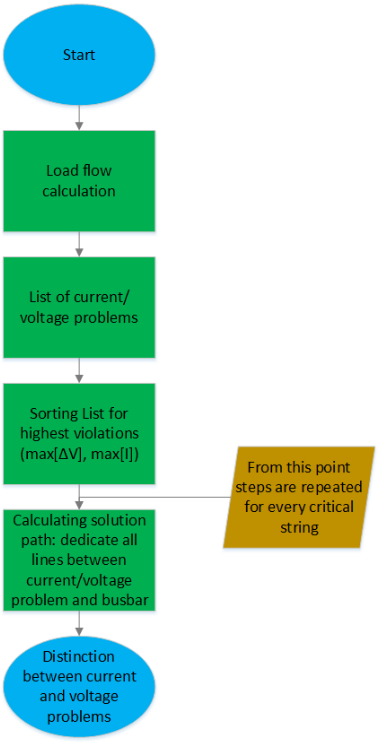

Fig. 5. Flow chart for identification of grid problems, sort of violated lines/nodes in error intensity and calculation of the solution path

To solve the current/voltage problems, the algorithm reads out additionally a solution path, which is extracted from the critical string. All lines from the affected path are then available for the routine to solve the problem by cable exchange. Fig. 6 shows how the solution path is detected.

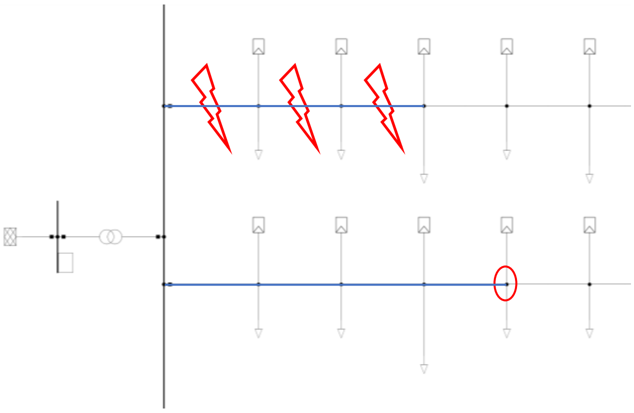

Fig. 6. Visualization of the solution path (upper string: current problem, lower string: voltage problem)

The sections with the red flashes represents lines, which are too heavily loaded. The point encircled in red depicts a network node with an impermissible voltage, and the lines marked in blue then reproduce the corresponding solution paths. The procedure is as follows: the algorithm is reading out all lines that are on the way to the nearest busbar beginning from the critical line or critical node.

From this point on, a distinction is made between the treatment of a current or voltage problem (see Fig. 7). Exceeding current limits are solved by replacing all lines that have too high utilization. In this work cable exchange always means the use of cables with a higher cross section. The exchange is done until the current problem is solved or no cable type with higher cross section is available, as on left flow chart of Fig. 7 depicted. The user can specify how many and which cable types are available for usage. If the user does not want to give input, then a default library will be used.

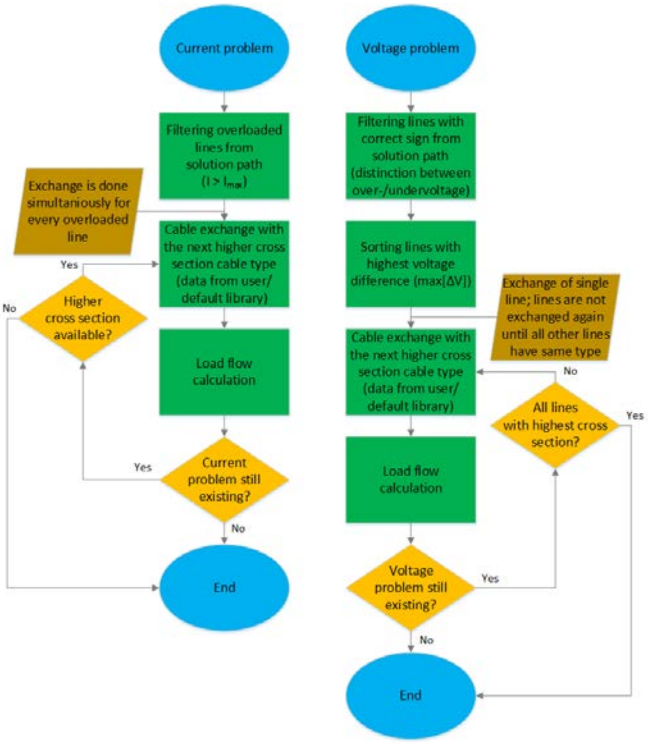

Fig. 7. Flow chart for current (left) and voltage (right) problems with cable exchange

The solution of voltage-related violations is more complicated to implement than current problems. Because here it is important to know the voltage band along the solution path and then to exchange appropriate lines. If a voltage problem is to be solved as technical effectively as possible, then firstly the lines must be replaced, which cause the highest voltage differences (Fig. 7, from second green shape on the right flow chart). Therefore, the exchange of the lines goes further from the highest occurring voltage difference to the line with the lowest, until the voltage problem is resolved or all lines from the solution path have the highest possible cross section. However, it would not be useful to hand this procedure over to the routine. As shown in Fig. 8, the cable exchange on the section with the highest voltage difference may even worsen the existing problem. In this example the cable exchange of the line, which causes the highest voltage difference (between nodes 2 and 3 in the blue curve), reduces the voltage increase at the beginning of the voltage band, but does not solve the low voltage problem in node 19 (orange curve), while the dashed lines (green) the voltage limits represent. Quite the contrary, the cable exchange aggravates the existing problem (form 0.885 p.u. to 0.865 p.u.). Therefore, only the lines that have a solution-relevant sign on the slope may be considered here, as at the beginning on the right flow chart in Fig. 7 illustrated. In the case of a low voltage problem, these are the line sections, where the voltage drops occur (in Fig. 8 lines between nodes 5 to 19).

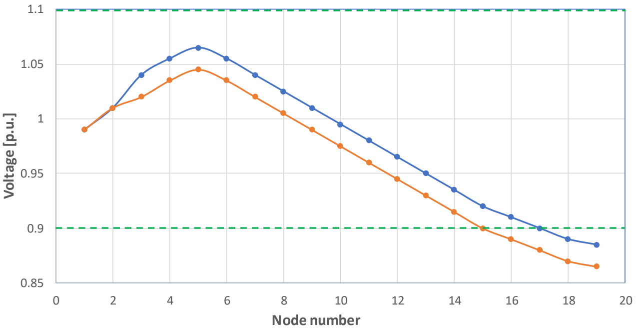

Fig. 8. Voltage band course before (blue) and after (orange) the cable exchange of the line with the highest voltage difference (between nodes 2 and 3); dashed lines (green) represent the voltage limits

The algorithm can further differentiate the results here. Because in the just described procedure, the lines, which cause the highest voltage differences with the correct sign, are replaced without considering whether the line sections are behind each other or if they are spread over the string. This can be expressed economically, for example, in authorization procedures and construction site costs. Furthermore, it would not be sufficient for the optimal result search, only to use the next higher cable cross section. So the algorithm should calculate the most economical solution by the use of the available cable types. These different optima can be limited by concrete specifications that the user makes. Thus, it is well conceivable, that the user gives, for example, the input for the replacing of several line sections that they must be behind each other.

B. Parallel cabling

As in the case of cable exchange, the critical lines and the solution paths are also determined here first and a distinction is made between solving current or voltage problems. The most effective solution to handle with a current problem in this routine is the pure parallel cabling of the overloaded lines. The line is not laid over each cable section parallel, but over the entire length of the problematic string part. The algorithm only deviates from this procedure if there is a branch between the overloaded lines (see Fig. 9).

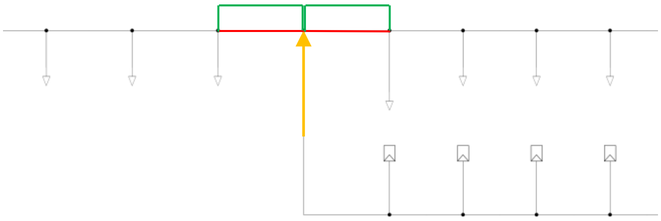

Fig. 9. Parallel cabling with crossing a branching point

Here is the parallel cable interrupted at the branch point (green marked lines) to make sure that the routine is, e.g. in the case of a high infeed from the lower string (orange arrow), able to solve the overload of the two red marked line sections.

The previously described concept of the shortest parallel cabling does not take account of cable distribution cabinets (CDC) that are present in the network. If they are now to be integrated into the solution process, a second implementation is obtained in addition to direct parallel cabling of overloaded lines. In this variant, the parallel cables are installed from busbar (BB) to CDC or from CDC to CDC. Technically, the resolution of the current problem is worse in this solution variant, but, inter alia, the installation of new stations can be prevented, which is economically better. However, this solution type requires an expansion of the considered equipment, which are used to solve the problem. So not only the CDC of the returned solution path are included, but all CDC of the string up to the next branch. Fig. 10 shows the described situation: the critical lines are marked with red flashes and the lines highlighted in blue corresponds to the solution path that the routine reads out. The orange encircled network nodes represent the relevant CDC, which are included in the solution finding. In order to calculate the solution here, all connection possibilities between the BB and the CDC as well as the CDC among each other are calculated and the shortest connection, which solve the current problems, is rated as the best result (see (1)). In the formula represents L_{PL} the solution of parallel cabling, which is from all connections between BB and CDC ($L_{BB,CDC}$) the shortest and coincident solving the current problem.

$$L_{PL} = \min(L_{BB,CDC}),\ \forall L: I < I_{max} \qquad (1)$$

Here can be an important input from the user, how many connection ports are still available at the CDC, to take into account whether the distribution station has to be extended because of the parallel cables and how this would be expressed in the economic terms of the results. In the example shown in Fig. 10, it could be important to have this input to answer the question, if there should be a completely continuous cable from the busbar to the rear CDC, or if the parallel cable should be divided into two lines with connection to the first CDC.

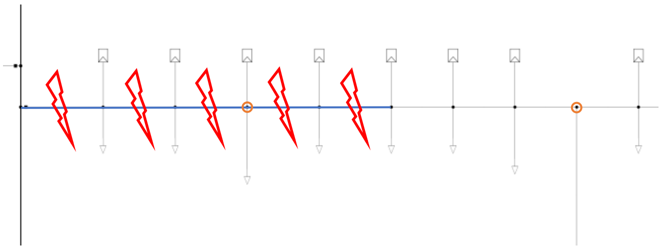

Fig. 10. Parallel cabling with consideration of CDC (orange encircled grid nodes) in the string (red flashes: current problems, blue marked lines: solution path)

The algorithm solves voltage problems in consideration of CDC with the analogous concept, which is used for current problems. In the variant of the shortest parallel cabling with regard to violated voltage limits, first the line section with the greatest sign-correct slope is chosen. If the voltage is exceeded, a parallel cable will only be laid in those parts of the string, which are increasing the voltage. From the line with the largest gradient (marked red in Fig. 11) the routine compares the adjacent lines (marked in orange) and considers this section for parallel cabling, which shows the greater slope. The algorithm will continue this procedure until either the voltage problem is resolved or no more sign-correct cable sections are left.

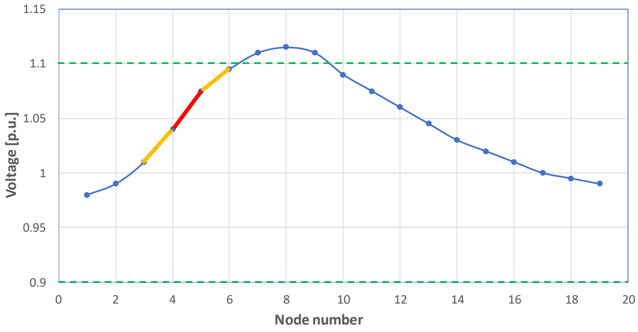

Fig. 11. Voltage band course with visualization of the approach of the measure "parallel cabling" with handling a high voltage problem; dashed lines (green) represent the voltage limits

V. SUMMARY AND OUTLOOK

Automated grid planning is a suitable tool to show distribution system operators possibilities for future grid expansion. The combination of heuristics and mathematical optimization is more efficient than the pure probabilistic approach. The biggest challenge in the automation of network planning processes is the generalized procedure of the routine, so that any network condition, topology and problem in terms of voltage and current can be treated and the best possible solution is found. The EU project CrossEnergy is developing a grid planning program that implements inter alia the automated use of cable exchange and parallel cabling. The procedure for the detection of the problem areas and the strings, in which a corresponding measure is then implemented for the solution, is the same for both expansion technologies. Differences are mainly to be seen when dealing with current and voltage problems between cable exchange and parallel cabling. The treatment of overloaded lines is implemented in the cable exchange by replacing it with a cable type having a higher cross section. The resolution of voltage problems is realized by the systematic replacement of lines with the largest and sign-correct slope. In the parallel cabling measure, in case of a current problem, the cable is directly laid parallel on the overloaded line sections in order to obtain the best technical efficiency. In the case of a voltage problem, the line with the largest gradient is identified and again only those sections are considered, which have a sign-correct slope. From this line piece then the adjacent lines are compared with each other and the routine adds the line with the larger gradient to the pool for parallel cabling. The algorithm continues this procedure until the voltage problem is solved or no lines are left.

Automated network planning shows a great deal of potential in supporting network operators. The results are supported by technical and economic figures, so the user can decide, which expansion variant should be used for the future grid extension. The algorithm presented in this paper can be further developed in many ways. In order to get even better solutions in the case of wired measures, for example, land use can be included. With this additionally information, it is possible to give the line sections a weighting factor that indicates how expensive an exchange or a parallel installation is. This can serve as additional input for even more economic network development.

REFERENCES

[1] H. Kraus, D. Gschoßmann and O. Brückl, "Automatisierung von Netzplanungsprozessen in der Verteilnetzebene – Q(U)- und cosφ(P)-Blindleistungsregelung dezentraler Anlagen als spannungshaltende Netzausbaumaßnahmen", transcript of the conference *Zukünftige Stromnetze für Erneuerbare Energien*, p. 407-420, Berlin, January 2019.

Ein neuer Ansatz zur variablen Ventilsteuerung bei Motoren mit einer einzigen Nockenwelle

Martin Fritsch
Institut für Elektrische Energiesysteme (IESY)
Otto-von-Guericke-Universität Magdeburg
Magdeburg, Deutschland
martin.fritsch@ovgu.de

***Kurzfassung*—Auf Basis einer permanenterregten Synchronmaschine wird ein innovativer Ansatz für eine variable Ventilsteuerung am Beispiel eines Einzylinder-Ottomotors vorgestellt. Anstelle eines Zahnriemens werden Nockenwelle und Ventile direkt von dem Elektromotor angetrieben. Durch Ansteuerung der Nockenwelle mit ungleichförmiger Bewegung, kann somit Einfluss auf die Steuerzeiten der Ventile genommen werden. Hierfür werden zunächst sinnvolle Geschwindigkeitsverläufe für einen späteren Betrieb mit Steuerzeitenvariation entwickelt. Anschließend wird ein entsprechendes Regelungstechnik-Konzept für den Nockenwellenmotor vorgestellt. Die variable Ventilsteuerung ist abschließend durch Tests an einem Prototyp validiert worden. Es ist gelungen die Steuerzeiten sowohl des Auslass- als auch des Einlassventils unabhängig voneinander in einem weiten Bereich zu variieren, obwohl beide von einer gemeinsamen Nockenwelle angetrieben werden.**

Keywords—PMSM, Nockenwellenantrieb, variable Steuerzeiten, variable Ventilsteuerung, Regelungstechnik, Energieeffizienz, Verbrennungsmotor

I. HINTERGRUND

Zur Erreichung der ambitionierten Pläne der Bundesregierung hinsichtlich einer nachhaltigen und umweltverträglichen Energieerzeugung, bedarf es einer alle Bereiche erfassenden Senkung des Energiebedarfs. Hinsichtlich konventioneller Verbrennungsmotorentechnik konnten die Hersteller in den letzten Jahren bereits beachtliche Potentiale zur Steigerung der Energieeffizienz heben. Erwähnt werden soll in diesem Zusammenhang die Einführung variabler Ventilsteuerungen bei mit Ottokraftstoff betriebenen Saugmotoren. Das verfügbare Drehmoment solcher Motoren verhält sich proportional zur durch ein geöffnetes Einlassventil angesaugten Menge an Luft-Kraftstoff-Gemisch (Zylinderladung). Entsprechend wird die Leistungsregelung üblicherweise quantitativ, durch Drosseln der angesaugten Ladungsmenge mit Hilfe einer Drosselklappe im Ansaugtrakt, bewerkstelligt. Dieser Vorgang hat einen negativen Einfluss auf das Druckniveau im Saugrohr, weshalb zusätzliche Kolbenarbeit beim Ansaugen anfällt. Diese sogenannten Drosselverluste lassen sich vermeiden, wenn die einströmende Ladungsmenge stattdessen über variable Einlassventilhübe geregelt wird, sodass eine Drosselklappe nicht weiter notwendig ist. Die Entdrosselung von Saugmotoren durch variable Ventilsteuerungen stellt eine wesentliche Maßnahme zur Steigerung der Energieeffizienz (12 % Verbrauchsabsenkung laut *BMW* [1]) und somit einen Schritt zur Schonung fossiler Energieträger dar [2][3].

Nachfolgend soll ein neuartiger Ansatz zur variablen Ventilsteuerung mit Hilfe eines hochdynamischen Elektromotors präsentiert werden. Die Entwicklung basiert auf einem Einzylinder-Ottomotor. Da variable Ventilsteuerungen bisher beinahe ausschließlich in hubraumstarken Mehrzylindermotoren verwendet werden, bergen Einzylindermotoren nach wie vor große Potentiale zur Steigerung ihres Wirkungsgrades. In diesem Sinne soll die vorliegende Arbeit einen Beitrag zur rationellen und nachhaltigen Verwendung fossiler Energie leisten.

II. STAND DER TECHNIK UND KONZEPT

Abbildung 1 stellt linksseitig den konventionellen Aufbau eines Viertakt-Ottomotors mit einem Zylinder dar. Durch das zyklische Ansaugen, Verdichten, Zünden und Ausspülen eines zündfähigen Luft-Kraftstoff-Gemisches wird im Zylinderraum fortwährend Energie freigesetzt, welche den zylindrischen Kolben **1** verdrängt. Die resultierende Hubbewegung wird mittels Pleuel **2** und Kurbelwelle **3** in eine Rotation umgeformt und steht als Antrieb für eine Arbeitsmaschine zur Verfügung. Über einen Zahnriemen **4** treibt die Kurbelwelle zusätzlich die Nockenwelle **5** im Verhältnis 2:1 an. Diese wiederum aktiviert die im Zylinderkopf angeordneten Tellerventile **6**. Die eröffneten Ventilhübe Y von Einlass- und Auslassventil folgen der Kontur des jeweiligen Nockens **7** und sind in Abbildung 2 über einen Verbrennungszyklus, das heißt über zwei Kurbelwellenumdrehungen $\theta_{\mathrm{KW}} = 0-720^{\circ}$, aufgetragen. Indem während der Öffnung des Einlassventils frische Ladung angesaugt und nach der Verbrennung über das Auslassventil ausgespült wird, hält sich der Verbrennungsprozess selbstständig am Leben. Es ist ersichtlich, dass diese Art des Zahnriemen-Antriebs keine variable Ventilsteuerung ermöglicht, da die Nockenwelle stets mit halber Kurbelwellengeschwindigkeit rotiert [2].

Ein alternatives Konzept stellt der Direktantrieb der Nockenwelle mit Hilfe eines permanenterregten Synchronmotors **8** dar, welches auf Abbildung 1 rechts zu sehen ist. Auf diese Weise sind beide Motorwellen voneinander entkoppelt. Diese neu gewonnene Freiheit wird zur Drehzahlvariation der

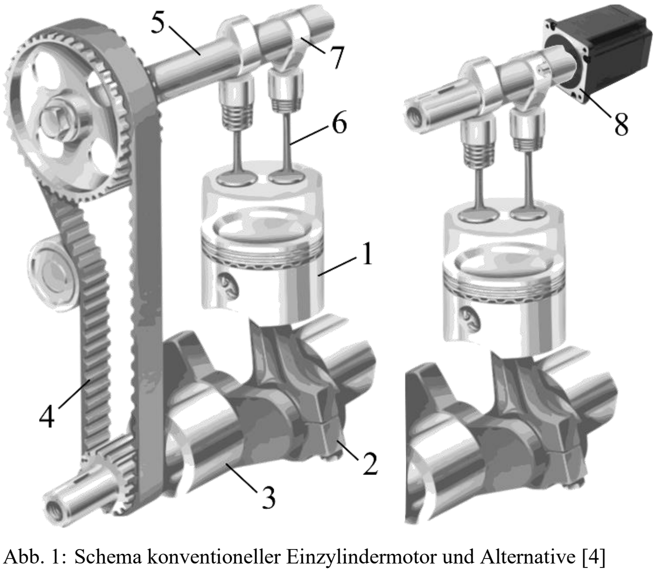

Abb. 1: Schema konventioneller Einzylindermotor und Alternative [4]

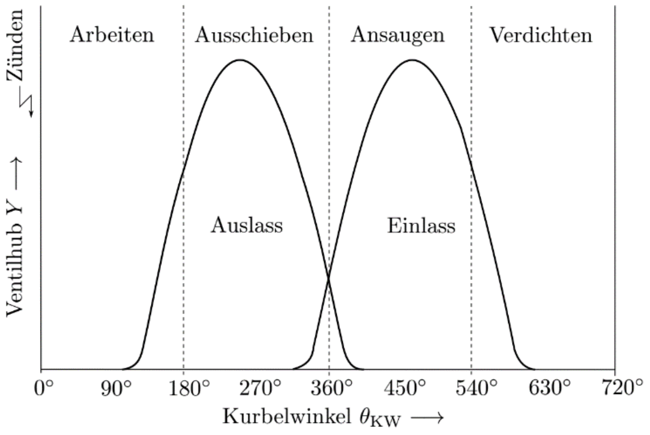

Abb. 2: Steuerzeitendiagramm eines Viertakt-Prozesses [5]

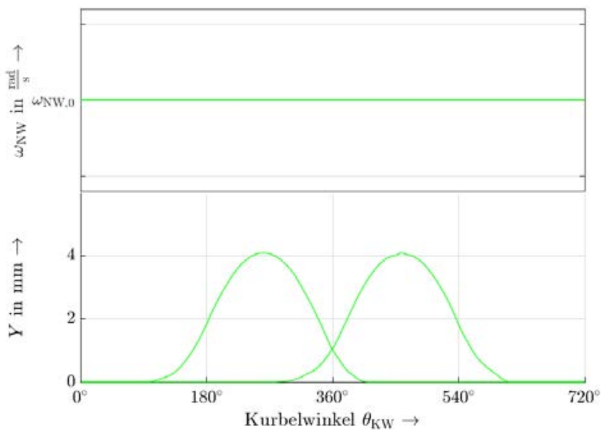

Abb. 3: Standard-Ventilhübe bei gleichförmiger Nockenwellendrehzahl

Nockenwelle genutzt. Das heißt durch gezieltes Beschleunigen und Abbremsen innerhalb einer Umdrehung werden die Ventilhübe relativ zum Verbrennungsprozess verkürzt oder verlängert. Durch den Wegfall des Zahnriemens und da nur ein einziger Elektromotor als Nockenwellenaktor notwendig ist, zeichnet sich dieses System durch geringe mechanische Komplexität aus. Aufwendige Umbauten an Zylinderkopf oder Nockenwelle sind im Gegensatz zu anderen variablen Ventilsteuerungen nicht notwendig. Wegen der genannten Simplizität ist bei Anwendung des gezeigten Ansatzes nur mit geringen Kosten zu rechnen, wenngleich auf Grund der entkoppelten Wellen höhere Herausforderungen an die Regelungstechnik gestellt werden.

III. STEUERZEITENVERSTELLUNG DURCH DREHZAHLVARIATION

Der Viertakt-Prozess bedingt ein zyklisches Austauschen der verbrannten Abgase durch frisches Luft-Kraftstoff-Gemisch. Zur Steuerung dieses Ladungswechsels ist im Zylinderkopf entsprechend Abbildung 1 jeweils ein Auslass- und Einlassventil verbaut, welche über zwei separate Nocken betätigt werden. Die resultierenden Ventilhübe Y für eine Umdrehung der Nockenwelle werden einzig durch die Nockenkonturen vorgegeben und sind in Abbildung 2 über den Kurbelwinkel θ_{KW} der Kurbelwelle aufgetragen. Vorteil dieser Darstellung als Steuerzeitendiagramm ist die zeitliche Gegenüberstellung des Viertakt-Verbrennungsprozesses mit den Öffnungsdauern der Ventile, welche Steuerzeiten genannt werden. Prinzipiell gilt, dass Einlass- und Auslassventil nur zum korrespondierenden Takt öffnen dürfen, damit der Kreisprozess nicht zum Erliegen kommt. Beide Motorwellen müssen hierzu synchron zueinander laufen, wobei die Nockenwelle ω_{NW} stets mit halber Kurbelwellendrehzahl ω_{KW} rotiert.

$$\omega_{NW,0} = \frac{1}{2}\,\omega_{KW} \tag{1}$$

Dieser Betriebsfall wird beim Zahnriemen-Antrieb durch die starre Kopplung immer gewährleistet. Bei korrekter Einbaulage der Wellen zueinander gilt der entsprechende Zusammenhang auch für die Wellenwinkel.

$$\theta_{NW,0} = \frac{1}{2}\,\theta_{KW} \tag{2}$$

Bei Nutzung eines Zahnriemens wird der geforderte synchrone Lauf mechanisch stets gewährleistet.

Um diesen Standardbetrieb auch bei Nutzung eines Elektromotors als Nockenwellenantrieb zu realisieren, muss entsprechend (1) und (2) die Winkelgeschwindigkeit ω_{KW} und der Winkel θ_{KW} der Kurbelwelle bekannt sein, damit ein synchroner Lauf der entkoppelten Wellen gewährleistet werden kann. Beide Werte werden daher messtechnisch präzise erfasst und der Nockenwellen-Regelung als Führungsgrößen übergeben. Diese berechnet dann die Basis-Winkelgeschwindigkeit $\omega_{NW,0}$ und den Leitwinkel θ_{NW} zum Antrieb der Nockenwelle. Es resultieren die bekannten Standard-Ventilhübe, welche im unteren Diagramm von Abbildung 3 zu sehen sind. Das obere Diagramm zeigt, dass der Nockenwellenmotor mit der berechneten Basis-Winkelgeschwindigkeit $\omega_{NW,0}$ gleichförmig rotiert. Dieser Betriebszustand entspricht dem Fall ohne variable Ventilsteuerung und ist äquivalent zum Zahnriemen-Antrieb.

Da der Zahnriemen im vorliegenden Fall fehlt, ist die Nockenwelle jedoch entkoppelt und es besteht kein Zwang sie mit gleichförmiger Drehzahl anzutreiben. Durch eine einfache Änderung der Basis-Winkelgeschwindigkeit $\omega_{NW,0}$ innerhalb einer Umdrehungsperiode $\Delta\theta_{KW} = 720^\circ$ kann die Steuerzeit variiert werden. Abbildung 4 zeigt, dass eine Beschleunigung der Nockenwelle bei geöffnetem Einlassventil (rosa Verlauf zwischen 360 – 560°) zu einer Verkürzung seiner Steuerzeit führt. Um den synchronen Lauf nicht zu beeinflussen, darf eine Nockenwellenumdrehung nicht von der Periodendauer des Viertakt-Prozesses abweichen. Das heißt das Zeitfenster τ für eine Rotation des Nockenwellenmotors wird von der Kurbelwelle vorgegeben und berechnet sich wie folgt.

$$\tau = \frac{2\pi}{\omega_{NW,0}} \tag{3}$$

Da die Periodendauer der Nockenwelle umgekehrt proportional zur Winkelgeschwindigkeit ist, führt die gezeigte Beschleunigung während ein Ventil geöffnet ist zu einer verkürzten Periodendauer. Im Sinne der Synchronität wäre dieser Betriebszustand unzulässig. Zur Vermeidung wird die Nockenwelle nach der Beschleunigungsphase zusätzlich im selben Maße abgebremst, sobald das entsprechende Ventil wieder geschlossen ist (rosa Verlauf zwischen 560 – 720°), sodass die Periodendauer zum Ursprungswert zurückkehrt. Auf diese Weise wird ein synchroner Lauf von Nockenwelle- und Kurbelwelle sichergestellt und dennoch eine verkürzte Steuerzeit gewonnen. Allgemein ist Synchronität gegeben, sobald eine Umdrehung der Nockenwelle gleich dem Zeitfenster τ des

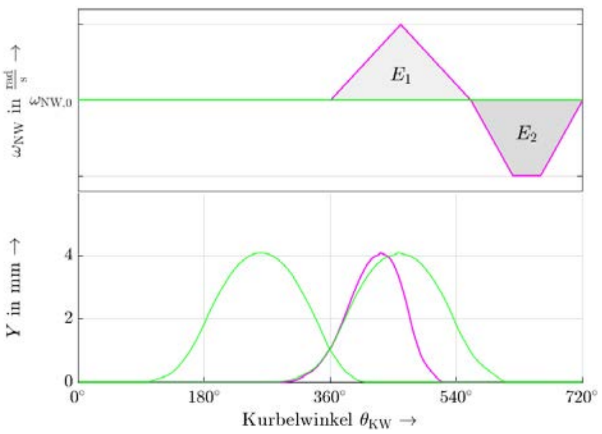

Abb. 4: Ventilhübe bei ungleichförmiger Nockenwellendrehzahl

Verbrennungsprozesses ist, trotz der vorgenommenen Geschwindigkeitsänderungen. Graphisch ist diese Bedingung immer erfüllt, wenn die entstehenden Flächen E_1 und E_2 in Abbildung 4, ober- und unterhalb der Basis-Winkelgeschwindigkeit $\omega_{\mathrm{NW},0}$, gleich groß sind. Das heißt jede Beschleunigung bedingt einer gleichwertigen entgegengesetzten Beschleunigung während derselben Rotationsperiode. Alle Winkelgeschwindigkeitsverläufe welche diese Regel erfüllen, sind im Sinne der Synchronität zulässig.

Der Nockenwellenmotor treibt beide Ventile über eine gemeinsame Nockenwelle an. Um die Steuerzeit von Einlass- und Auslassventil unabhängig voneinander variieren zu können, kann das verfügbare Zeitfenster in zwei Hälften geteilt werden, wie in Abbildung 5 zu sehen ist. Um die Öffnungsdauer des Auslassventils zu verändern wird die Nockenwellendrehzahl im Bereich 0 – 360° verändert. Beschleunigungen in der zweiten Hälfte 360 – 720° können die Steuerzeit des Einlassventils variieren. Gilt für beide Zeitfenster die Synchronitätsbedingung gleichermaßen, beeinflussen sich die Ventile nicht gegenseitig und sind unabhängig voneinander variierbar, trotz gemeinsamer Nockenwelle. Graphisch interpretiert gilt dann wieder A_1=A_2 und E_1=E_2.

Abbildung 5 zeigt weiterhin, dass eine Abbremsung der Nockenwelle bei geöffnetem Auslassventil (roter Verlauf zwischen 160 – 360°) zu einer Verlängerung der Steuerzeit führt. Die Öffnungsdauer beider Ventile kann also nicht nur verkürzt, sondern auch verlängert werden.

Abbildung 6 stellt die vier sinnvollen Winkelgeschwindigkeitsverläufe dar, welche die Grundlage der variablen Ventilsteuerung bilden. Diese Verläufe werden später als Sollwerte der Nockenwellen-Regelung benötigt und müssen hierfür mathematisch beschrieben werden. Entsprechend den zwei Periodenhälften für Auslass- und Einlassventil ergibt sich eine Beschreibung der folgenden Form.

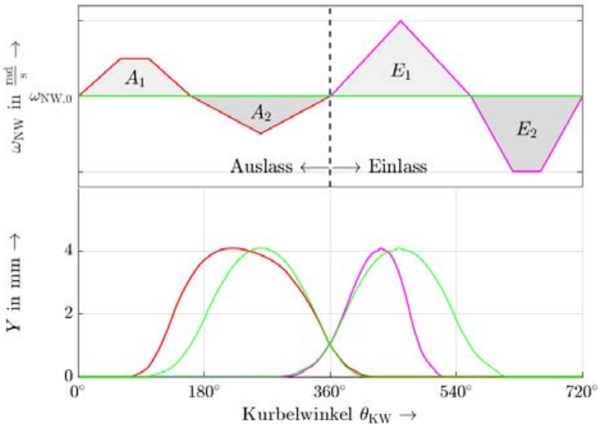

Abb. 5: Getrennte Ansteuerung für Einlass- und Auslassventil

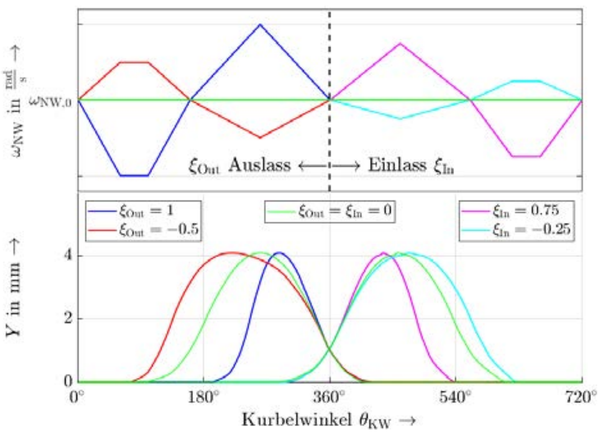

Abb. 6: Einige Winkelgeschwindigkeitsverläufe zur Steuerzeitenvariation

$$\omega_{\mathrm{NW}}(\theta_{\mathrm{KW}}) = \omega_{\mathrm{NW},0} + \xi_{\mathrm{Out}} R_{\mathrm{Out}}(\theta_{\mathrm{KW}}) + \xi_{\mathrm{In}} R_{\mathrm{In}}(\theta_{\mathrm{KW}}) \quad (4)$$

Die Winkelgeschwindigkeit der Nockenwelle setzt sich aus der Basis-Winkelgeschwindigkeit $\omega_{\mathrm{NW},0}$ und den rampenförmigen Beschleunigungen zusammen. R_{Out} beschreibt die Beschleunigungsrampen des Auslassventils und R_{In} entsprechend die des Einlassventils. Die Intensität mit der die Rampen aufaddiert werden, kann über die beiden Stellgrößen ξ_{Out} und ξ_{In} reguliert werden. Für ξ_{Out}=ξ_{In}=0 rotiert die Nockenwelle mit gleichförmiger Basis-Winkelgeschwindigkeit $\omega_{\mathrm{NW},0}$ und es werden die grünen Standard-Steuerzeiten von Abbildung 6 erzeugt. Durch Verstellung der Stellgrößen im Bereich $-1 \leq \xi \leq 1$ können die Rampen in unterschiedlicher Stärke zur Basis-Drehzahl addiert werden, um die Steuerzeiten zu variieren. Der Stellbereich der Steuerzeiten wird durch die maximal mögliche Winkelbeschleunigung $\alpha_{\max}$ des Nockenwellenmotors begrenzt. Bei $\xi = 1$ wird mit maximaler Beschleunigung gearbeitet und es wird die kleinstmögliche Steuerzeit gestellt. Für $\xi = -1$ ergibt sich die gegenteilige Aussage. Eine detaillierte mathematische Beschreibung von R_{Out} kann für die verschiedenen Rampenintervalle abschnittsweise wie folgt angegeben werden.

$$R_{\mathrm{Out}} = \begin{cases} -\alpha_{\max} \frac{\theta_{\mathrm{KW}}}{720°}\,\tau & ,[0°,60°), \\ -\alpha_{\max} \frac{60°}{720°}\,\tau & ,[60°,100°), \\ \alpha_{\max} \frac{\theta_{\mathrm{KW}}-160°}{720°}\,\tau & ,[100°,160°), \\ \frac{3}{5}\,\alpha_{\max} \frac{\theta_{\mathrm{KW}}-160°}{720°}\,\tau & ,[160°,260°), \\ -\frac{3}{5}\,\alpha_{\max} \frac{\theta_{\mathrm{KW}}-360°}{720°}\,\tau & ,[260°,360°), \\ 0 & ,[360°,720°) \end{cases} \quad (5)$$

Hier zeigt sich der Vorteil der gewählten Rampenfunktionen, welche mit linearen Funktionen beschreibbar sind. Der Vorfaktor $\frac{3}{5}$ mancher Rampen resultiert aus der genannten Synchronitätsbedingung. In jedem Intervall beinhaltet die abschnittsweise definierte Funktion die maximale Winkelbeschleunigung $\alpha_{\max}$ als Faktor. Bei Vergleich mit (4) zeigt sich deutlich wie ξ_{Out} Einfluss auf die gefahrene Beschleunigung beziehungsweise die Dynamik des Nockenwellenantriebs nimmt. Für das Einlassventil ergibt sich eine ähnliche Beschreibung.

$$R_{\mathrm{In}} = \begin{cases} 0 & ,[0°,360°), \\ \frac{3}{5}\,\alpha_{\max}\,\frac{\theta_{\mathrm{KW}}-360°}{720°}\,\tau & ,[360°,460°), \\ -\frac{3}{5}\,\alpha_{\max}\,\frac{\theta_{\mathrm{KW}}-560°}{720°}\,\tau & ,[460°,560°), \\ -\alpha_{\max}\,\frac{\theta_{\mathrm{KW}}-560°}{720°}\,\tau & ,[560°,620°), \\ -\alpha_{\max}\,\frac{60°}{720°}\,\tau & ,[620°,660°), \\ \alpha_{\max}\,\frac{\theta_{\mathrm{KW}}-720°}{720°}\,\tau & ,[660°,720°) \end{cases} \qquad (6)$$

Je nach Vorgabe der Stellgrößen ξ_{Out} und ξ_{In} kann nach (4) der Verlauf der Soll-Winkelgeschwindigkeit ω_{NW} für den Nockenwellenmotor berechnet werden.

Abschließend sei bemerkt, dass es Betriebspunkte gibt für die sich $\omega_{\mathrm{NW}} < 0$ berechnet. In diesem Fall würde die Nockenwelle anfangen rückwärts zu rotieren. Zur Vermeidung dieses unzulässigen Zustandes wird $\alpha_{\max}$ in diesen Fällen begrenzt, sodass ω_{NW} stets positiv bleibt.

IV. REGELUNG UND SOLLWERTRECHNER

Zur grundlegenden Funktionsweise des Nockenwellenmotors entsprechend (1) muss die Basis Winkelgeschwindigkeit der Nockenwelle $\omega_{\mathrm{NW},0}$ stets gleich der halben Drehzahl der Kurbelwelle ω_{KW} sein. Zwei Umdrehungen der Kurbelwelle führen also zu einer Umdrehung der Nockenwelle, wie beim Viertakt-Prozess typisch. Zum Sicherstellen des synchronen Laufs beider Wellen gemäß (2) muss weiterhin der Kurbelwinkel θ_{KW} bekannt sein. Führungsgröße der auf Abbildung 7 dargestellten Regelung des Nockenwellenmotors ist folglich der Kurbelwinkel θ_{KW} und seine Ableitung ω_{KW}. Er wird mit einem Drehgeber präzise am Verbrennungsmotor (VM) erfasst und der Regelung als Leitwert vorgegeben. Damit die permanenterregte Synchronmaschine (PMSM) der Führungsgröße folgen kann, wird eine kaskadierte Lageregelung verwendet, das heißt es sind mehrere Regelkreise ineinander verschachtelt. Von innen nach außen sind dies ein Strom- oder Drehmomentenregelkreis sowie ein Drehzahl- und ein Lageregelkreis. Die Sollgrößen ω^*, i_{q}^* der inneren Regler werden vom jeweils überlagertem Regelkreis vorgegeben. Die PMSM wird feldorientiert geregelt, das heißt die Stromregelung wird in rotorfesten d/q-Koordinaten durchgeführt. Hierzu werden die dreiphasigen Ströme i_{U}, i_{V}, i_{W} und Spannungen u_{U}, u_{V}, u_{W} der Drehfeldmaschine zuerst mit Hilfe der Clarke-Transformation in ein ständerfestes, zweiachsiges α/β-Koordinatensystem transformiert. Durch Messung des elektrischen Rotorwinkels θ_{el} der PMSM kann anschließend ein sich fest mit dem Rotor drehendes d/q-Koordinatensystem berechnet werden, wie [6] ausführlich beschreibt. Vorteil dieser Koordinatentransformation ist, dass das Drehfeld mit Hilfe konstanter Größen beschrieben werden kann. Die Ständerströme der PMSM i_{U}, i_{V}, i_{W} werden gemessen, zu i_{d} und i_{q} transformiert und den zugehörigen Stromreglern als Istwerte zugeführt. Die Komponente i_{d} entspricht der magnetischen Flussdichte im Rotor. Im vorliegenden Fall wird die Synchronmaschine von Permanentmagneten erregt, weshalb der Sollwert $i_{\mathrm{d}}^* = 0$ gewählt wird. Die Stromkomponente i_{q} ist proportional zum erzeugten Drehmoment T_{PMSM} des Rotors.

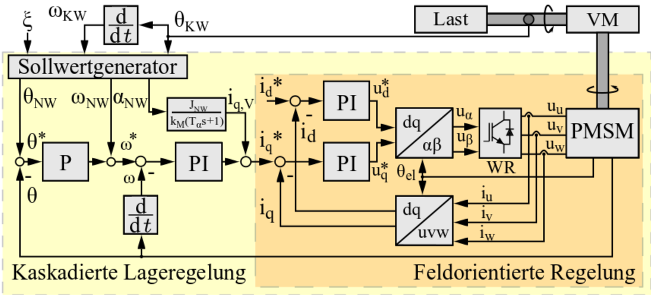

Abb. 7: Lageregelung des Nockenwellenmotors

$$T_{\mathrm{PMSM}} = \frac{3}{2}\,p\,\psi_{\mathrm{PM}}\,i_{\mathrm{q}} = k_{\mathrm{M}}\,i_{\mathrm{q}} \approx \alpha_{\mathrm{NW}}\,J_{\mathrm{NW}} \qquad (7)$$

Sowohl Polpaarzahl p als auch der magnetische Fluss der Permanentmagneten ψ_{PM} sind konstant und abhängig von der gewählten PMSM und können in der Maschinenkonstanten k_{M} zusammengefasst werden. Das Drehmoment zum Nockenwellenantrieb entspricht weiterhin ungefähr dem Produkt aus Massenträgheitsmoment J_{NW} und Winkelbeschleunigung α_{NW} der Nockenwelle. Die Ausgangsgrößen der Stromregler sind die Sollwerte der Ständerspannung u_{d}^*, u_{q}^*. Diese werden zunächst zu u_α, u_β transformiert und mittels einer Raumzeigermodulation über einen selbstgeführten Wechselrichter (WR) der PMSM aufgeschaltet, sodass sich das geforderte Drehmoment einstellt. Der Sollwert i_{q}^* wird vom überlagerten Drehzahlregler vorgegeben. Dessen Sollwert ω^* wird wiederum vom äußeren Lageregler erzeugt. Der Istwert des mechanischen Rotorwinkels θ wird analog zum elektrischen Rotorwinkel θ_{el} per integriertem Drehgeber der PMSM erfasst, wobei der Zusammenhang $\theta_{\mathrm{el}} = \theta \cdot p$ gilt. Der Istwert ω ist als zeitliche Ableitung ebenfalls bekannt. Die Auswahl und Auslegung der einzelnen Regler erfolgt ebenfalls von innen nach außen und ist in [7] und [8] ausführlich beschrieben.

Um die entwickelte variable Ventilsteuerung in die Regelung einzubinden, wird ein zusätzlicher Sollwertrechner implementiert. Zur Steuerzeitenvariation der Ventile ist der Sollwert der Winkelgeschwindigkeit der Nockenwelle ω_{NW} entsprechend (4) bereits bekannt. Durch Integration und Differentiation kann nun ebenfalls der zugehörige Sollverlauf des Nockenwellenwinkels θ_{NW} und der Winkelbeschleunigung α_{NW} ermittelt werden.

$$\theta_{\mathrm{NW}} = \frac{\theta_{\mathrm{KW}}}{2} + \xi_{\mathrm{Out}} \int R_{\mathrm{Out}}\,\mathrm{d}t + \xi_{\mathrm{In}} \int R_{\mathrm{In}}\,\mathrm{d}t \qquad (8)$$

$$\omega_{\mathrm{NW}} = \frac{\omega_{\mathrm{KW}}}{2} + \xi_{\mathrm{Out}} R_{\mathrm{Out}} + \xi_{\mathrm{In}} R_{\mathrm{In}} \qquad (9)$$

$$\alpha_{\mathrm{NW}} = \xi_{\mathrm{Out}} \frac{\mathrm{d}R_{\mathrm{Out}}}{\mathrm{d}t} + \xi_{\mathrm{In}} \frac{\mathrm{d}R_{\mathrm{In}}}{\mathrm{d}t} \qquad (10)$$

Die Ableitungen und Integrale von (5) und (6) können für die einzelnen Intervalle einfach analytisch gebildet werden. Sie sind aus Platzgründen nicht detailliert abgedruckt. Weiterhin wird noch die maximale Winkelbeschleunigung $\alpha_{\max}$ der PMSM benötigt, welche sich mit (7) und dem maximal zulässigen Stoßstrom $i_{\mathrm{q,peak}}$ berechnet.

$$\alpha_{\max} \approx \frac{k_{\mathrm{M}}\, i_{\mathrm{q,peak}}}{J_{\mathrm{NW}}} \qquad (11)$$

TABELLE I. PARAMETER DER PMSM

Polpaarzahl p	4
Nennspannung U_N	48 V
Nennstrom I_N	10,77 A
Spitzenstrom I_{peak}	32,31 A
Nenndrehzahl n_N	3000 $\frac{1}{s}$
Nenndrehmoment M_N	1,4 Nm
Spitzendrehmoment M_{peak}	4,2 Nm
Massenträgheitsmoment J_{NW}	0,00016 $\frac{kg}{m^2}$

Die drei Referenzfunktionen können in einem Sollwertrechner programmiert werden. Dieser berechnet entsprechend den Eingangsgrößen θ_{KW}, ω_{KW}, ξ_{Out}, ξ_{In} die Referenzwerte der variablen Ventilsteuerung. Die Führungsgröße θ^* der Lageregelung entspricht dann direkt dem berechnetem Winkelverlauf θ_{NW} zur Stellung der gewünschten variablen Ventilöffnungszeiten. Um das Führungsverhalten und damit die Dynamik des Nockenwellenmotors zu optimieren werden zudem Drehzahl und Drehmoment vorgesteuert. Hierzu wird der Referenzverlauf ω_{NW} zusätzlich dem Drehzahlregler aufgeschaltet. Somit steht dem Regler der zugehörige Sollverlauf direkt zur Verfügung und muss nicht erst durch den überlagerten Regelkreis erzeugt werden. Selbiges gilt für den Stromregler, wobei der berechnete Sollverlauf der Winkelbeschleunigung α_{NW} entsprechend (7) wieder in einen Strom zurück gerechnet werden muss.

$$i_{q,V} \approx \frac{\alpha_{NW} J_{NW}}{k_M} \tag{12}$$

Dieser Strom wird zur Vorsteuerung auf den q-Stromregler aufgeschaltet. Bei korrekter Vorsteuerung müssen Lage- und Drehzahlregler nur noch anfallende Störgrößen ausregeln, wovon die Dynamik erheblich profitiert [6][7][8].

Als Ableitung der unstetigen Winkelgeschwindigkeitsrampen, weist die Winkelbeschleunigung α_{NW} einen sprunghaften Verlauf auf und wird daher vor der Vorsteuerung zusätzlich über ein Tiefpass PT$_1$-Filter mit einer kleiner Zeitkonstante $T_\alpha = 1\,\text{ms}$ geglättet. Die komplette Regelung kann auf einem Mikrocontroller mit integriertem dreiphasigem Wechselrichter implementiert werden.

V. PRÜFSTANDERGEBNISSE

Die entwickelte variable Ventilsteuerung wurde prototypisch an einem Einzylindermotor in Betrieb genommen. Tabelle I enthält einige technische Spezifikationen der gewählten PMSM. Die Steuerzeitenvariation ist für beide Ventile bis zu einer Basis-Winkelgeschwindigkeit der Nockenwelle von $\omega_{NW,0} = 60\,\frac{rad}{s}$ getestet worden. Abbildung 8 zeigt die erreichbare Schar an einstellbaren Steuerzeiten. Die Öffnungsdauer beider Ventile kann um etwa 29 Prozent verkürzt und um circa 12 Prozent verlängert werden gegenüber den Standard-Ventilhubkurven. Für Drehzahlen größer $\omega_{NW,0} > 60\,\frac{rad}{s}$ ist die Dynamik der PMSM nicht mehr vollständig ausreichend und sie würde ohne Reduzierung von α_{max} überlastet werden. Die erreichbaren Grenzen der Steuerzeitenvariation nehmen daher mit zunehmender Winkelgeschwindigkeit langsam ab.

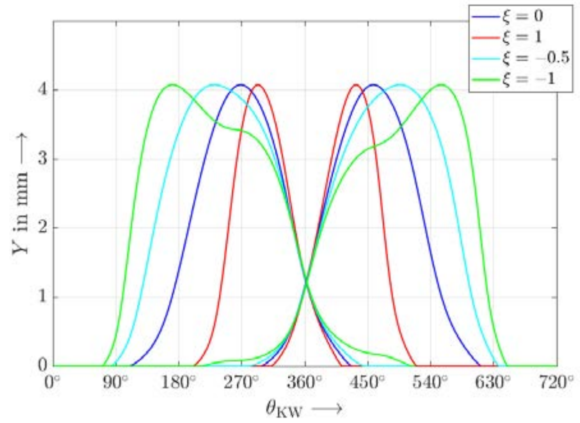

Abb. 8: Gemessener Stellbereich der variablen Ventilsteuerung

VI. FAZIT

Die entwickelte variable Ventilsteuerung kann die Steuerzeiten der Ventile in einem weiten Bereich verstellen. Dies gelingt allein durch den Verbau einer PMSM als Nockenwellenantrieb und anschließender ungleichförmiger Rotation. Weitere Umbauten des Verbrennungsmotors sind nicht notwendig. Die Steuerzeiten von Auslass- und Einlassventil können unabhängig voneinander verstellt werden trotz gemeinsamer Nockenwelle. Als möglicher Anwendungsfall des Systems ist die teilweise Entdrosselung des Ansaugtraktes von Motoren mit gemeinsamer Nockenwelle für alle Ventile denkbar (erste Versuche sind in [9] enthalten). Die Idee kann theoretisch auch auf Motoren mit zwei Nockenwellen angewendet werden, wodurch die Stellfreiheiten weiter profitieren würden. Die variable Ventilsteuerung ist nicht zuletzt auch für Freikolbenmaschinen ohne Kurbeltrieb geeignet.

LITERATURVERZEICHNIS

[1] H. Unger, C. Schwarz, J. Schneider, K.-F. Koch.: Die Valvetronic. Erfahrungen aus sieben Jahren Großserie und Ausblick in die Zukunft. In: MTZ – Motortechnische Zeitschrift 69.7-8 (Juli 2008), S. 598-605.

[2] R. van Basshuysen; F. Schäfer: Handbuch Verbrennungsmotor – grundlagen, Komponenten, Systeme, Perspektiven. 7. Auflage. Wiesbaden: Springer Vieweg, 2015, S. 566-598.

[3] D. Wabbals: Potenziale der Kombination von kontinuierlich verstellbarem Verdichtungsverhältnis und variabler Ventilsteuerung. Als Ms. Gedr. VKM-Schriftenreihe 13. Kaiserslautern: TU, 2013.

[4] A. Muir: The engine – how the valves open and close. Hrsg. von How a car works. Eingesehen am: 14.05.2019. URL: https://howacarworks.com/basics/the-engine-how-the-valves-open-and-close .

[5] J. Stoffregen: Grundlagen und Konzepte von Motor, Antrieb und Fahrwerk, 8., vollst. Überarb. u. erg. Aufl. 2012. ATZ/MTZ-Fachbuch. Wiesbaden: Vieweg+Teubner Verlag, 2012.

[6] D. Schröder: Elektrische Antriebe – Regelung von Antriebssystemen. 4. Auflage. Heidelberg: Springer Vieweg, 2015.

[7] J. Teigelkötter: Energieeffiziente elektrische Antriebe: Grundlagen, Leistungselektronik, Betriebsverhalten und Regelung von Drehstrommotoren. Wiesbaden: Vieweg+Teubner Verlag, 2013, S. 135-145.

[8] A. Gerlach, S. Zeilinga, H. Rottengruber, R. Leidhold: Regelungsstruktur und Realisierbarkeitsanalyse für den Betrieb eines direktangetriebenen Freikolbenmotors. In: 13. Magdeburger Maschinenbau-Tage: autonom–vernetzt–nachhaltig, 27. und 28. September 2017: Tagungsband (2017), S. 409-418

[9] A. Gerlach, M. Fritsch, S. Benecke, H. Rottengruber, R. Leidhold: Variable valve timing with only one camshaft actuator for a single-cylinder-engine. In IEEE/ASME Transactions on Mechatronics, unpublished

Two-phase immersion cooling system to validate impulsive loaded solid-state power controllers

Kevin Alexander Egle*, Florian Grumm*, Holger Benecke+, Marc Florian Meyer*, Detlef Schulz*

*Electrical Power Systems
Helmut-Schmidt-University / University of the Bundeswehr
Hamburg, Germany
+Central Mechanic Design and Development Lab
Helmut-Schmidt-University / University of the Bundeswehr
Hamburg, Germany

***Abstract*—Most conventional heat sinks are not sufficient to dissipate the occurring heat during impulsive loading of solid-state power controllers: an alternative cooling system has to be developed. A possible solution, to increase the transient power capacity of power electronic switches of solid-state power controllers, is a two-phase immersion cooling system. This contribution describes the principle function, the design and a first laboratory test of such a system. Furthermore, the basics of a model are described to calculate the unknown thermal resistance of the systems intercooler.**

***Keywords*—two-phase cooling, power electronic device, solid-state power controller**

I. INTRODUCTION

In onboard power supply systems of aircrafts solid-state power controller (SSPC) replace the traditional fuses or electromechanical circuit breakers in the secondary power distribution boxes of the aircraft grid [1-5]. SSPCs consist of power semiconductor switches - MOSFETs, IGBTs or thyristors - controlled by a micro controller with a bus interface that connects several SSPCs. Besides there traditional protection function against over/ under voltage and over current, they are used to balance the phases of an ac system [3] or to manage the system's power by switching of loads [4].

SSPCs are highly flexible and adaptable to requirements of power systems. Hence, a SSPC may be used to protect low voltage power systems – $U_{\mathrm{Grid}} \leq 1\ \mathrm{kV}$ –, which have the following two operation modes:

- *Islanding operation*: The power system is supplied by the sources in the islanded grid section during black outs or security matters
- *Normal operation*: The power system is directly connected to the public mains.

Between the two operation modes the short circuit current capacity of the power system changes immense [5]. Hence, the SSPC for such an application require a special design that is presented in [5]. During the design of SSPC occurred several difficulties regarding adequate cooling.

Typically, the steady state loading of the power electronic switches is designed to be below the manufacturer's maximum specifications. However, the usage of the SSPC as a protective device in the *normal operation* mode of the power system requires a cooling system to cope with transient impulsive loads like short-circuits. Conventional heat sinks do not represent an appropriate solution due to their low heat transfer coefficients; an alternative cooling system for SSPCs has to be constructed. Hence, this contribution presents laboratory test setup of a two phase immersion cooling system (TPICS) to analyse the SSPC behaviour under impulsive load conditions.

A. Thermal stress of power electronics

Power electronics like insulated-gate bipolar transistors (IGBT), metal-oxide-semiconductor field-effect transistors (MOSFET), power diodes, impulse resistors or thyristors have very high power-densities. The occurring thermal energy has to flow through various layers into the cooling fluid. The number and dimension of the layers depends on the specific device. In an IGBT module for example, as shown in Fig. 1

The heat flow emerging in the depletion layer has to flow through six different layers of copper, solder and ceramics to the cooling plate. Each layer has a specific thermal resistance R_{th}. The heat-flow though the layers is the same but the temperature difference across the layers are different due to different thermal resistances. Additionally, each material has a different coefficients of thermal expansion (CTE). Thus, every temperature cycle leads to tensions within the layers. The higher the temperature difference during one cycle the higher the tensions. Exemplary length changes of the different layers are illustrated in Tab. I.

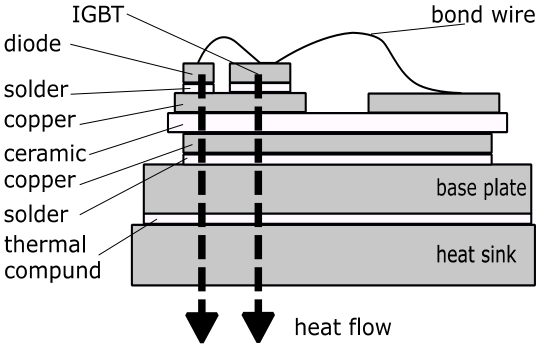

Figure 1: heat flow through the different layers of IGBT module

The leading cause of a thermal stress failure is brought about solder and bonding wire fatigue caused by tension induced defects. The thermal stress during impulsive loads or short circuits is sharply increased compared to steady-state operation, because the thermal impedance, determined by pythagorean addition of the thermal resistance and the specific heat capacity, delays the heat-flow to the cooling plate. The material tensions increases further. As a consequence, reduced thermal stress extends the lifespan of electronics and increases the reliability.

TABLE I. LINEAR EXPANSION OF DIFFERENT LAYERS DUE TO POWER CYCLING AND TEMPERATURE CYCLING ACCORDING TO [6]

Layer	CTE (10^{-6}/K)	Power cycling			Temperature cycling		
		T (°C)	ΔT (K)	Δl (µm)	T (°C)	ΔT (K)	Δl (µm)
Chip (IGBT) SI	3.5	125	100	**3.5**	125	100	**3.5**
AIN-DCB	8.2	105	80	**6.6**	125	100	**8.2**
AL_2O_3 DCB	10.7	105	80	**8.6**	125	100	**10.7**
ALSiC base plate	7	80	55	**3.8**	125	100	**7**
Cu base plate	17	80	55	**9.4**	125	100	**17**
Bond wire Al	23	100	75	**17.2**	125	100	**23**

II. BASICS OF COOLING SYSTEMS

Thermal energy is transferred from one surface to another by *conduction*, *convection* and *radiation*.

A. Thermal radiation

Every solid with an absolute temperature above absolute zero emits *thermal radiation* in form of electromagnetic radiation. The typical wavelength of the *thermal radiation* emitted by power electronics ranges from 0.8 µm to 400 µm [7]. For calculations the black body can be taken as a reference adjusted by the emissivity ε. With the radiation constant C_s=5.67 W/m^{-2}K^{-4} of the black body the heat flow $\dot{Q}_\mathrm{r}$ is calculated by [7]:

$$\dot{Q}_\mathrm{r} = \epsilon \cdot C_\mathrm{s} \cdot \left(\frac{T}{100}\right)^4 . \tag{1}$$

Typically, the body also absorbs *thermal radiation* from the ambiance. Hence, the net emitted thermal radiation is calculated by (2).

$$\dot{Q}_\mathrm{r} = \epsilon \cdot C_\mathrm{s} \cdot \left(\left(\frac{T_\mathrm{case}}{100}\right)^4 - \left(\frac{T_\mathrm{amb}}{100}\right)^4\right) \tag{2}$$

Taking an exemplary power MOSFET in a TO-220-3 case, Infineon IRFZ44NPBF, see parameters of Tab. 1, the emitted *thermal radiation* power under the assumption of an ideal emissivity of ε=1 is

$$\begin{aligned}\dot{Q}_\mathrm{s} &= 1 \cdot 5.67 \frac{\mathrm{W}}{\mathrm{m}^2\mathrm{K}^4} \cdot 5.38 \cdot 10^{-4}\mathrm{m}^2 \\ &\quad \cdot \left(\left(\frac{373.15\ \mathrm{K}}{100}\right)^4 - \left(\frac{298.15\ \mathrm{K}}{100}\right)^4\right) \\ &= 0.35\ \mathrm{W}\,.\end{aligned}$$

This represents only 0.42% of the maximum rated power, thus the effects of thermal *radiation* can be neglected.

TABLE II. PARAMETERS OF MOSFET IRFZ44NPBF

Parameter	Value
case surface	538 mm²
rated power	83 W
case temperature	100°C

B. Thermal conduction and convection

The heat transfer via *thermal conduction* is limited by the material-specific thermal conductivity λ, compare Fourier's law (3), which describes the local heat flux density vector $\boldsymbol{q}_\mathrm{C}$ in dependence of the negative local temperature gradient $-\nabla\boldsymbol{T}$.

$$\boldsymbol{q}_\mathrm{C} = -\lambda\nabla\boldsymbol{T}. \tag{3}$$

Furthermore, λ depends on:

- the pressure,
- the temperature and,
- eminently on the aggregation state [8].

For the considered application high heat transfer coefficients are important. The heat transfer coefficient is a constant expressing the ability of heat to transfer from one object to another across their mutual boundary layer; it is proportional to the size of the boundary layer and the temperature difference. Heat transfer coefficients are essential to evaluate thermal convection at boundary layers.

Thermal convection can be forced or natural. Both methods can lead to higher heat transfer compared to *thermal conduction* due to the additional mass transfer. A consequence of heat transfer within a fluid– gas or liquid– is the expansion caused by higher temperatures: the resulting different densities of the fluid cause *natural convection.* This effect can be enhanced by using fans or pumps, depending on the aggregate state of the fluid, which increase the flow. This *forced convection* occurs as a laminar or turbulent flow, depending on the so-called Reynolds number *Re*. Fig. 2 shows the difference between laminar and turbulent flow. A low Reynolds number leads to a laminar flow, which is characterized by fluid particles flowing in smooth layers with little or no mixing. Whereas, a turbulent flow is characterized by chaotic changes in pressure and flow velocity. These changes in flow velocity lead to a higher possible heat transfer compared to the laminar flow.

During the fault current interruption the full amount of power loss accumulates in the semiconductor switches in form of heat energy. Due to the low mass of the depletion layer the specific heat capacity is not sufficient. Hence, the maximum allowed temperature is quickly reached. As a result the high current leads to a thermal runaway. The common heat transfer coefficients of usual cooling systems based on conduction and convection are orders of magnitude too low to be able to transfer the transiently occurring heat energy away from the depletion layer.

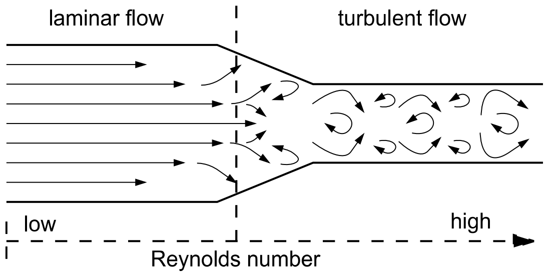

Figure 2: Difference between laminar an turbulent flow

C. Cooling methods

There are several commonly used cooling methods depending on various factors:

- passive air cooling (natural convection)
- active air cooling (forced convection)
- water cooling (forced convection).

Especially, active air cooling and water cooling are important methods to transfer the dissipated heat from the electronics. The implementation of an air-cooling system is easy and inexpensive. If the power densities are too high and the required heat transfer coefficient is too low, for example in the case of high-voltage, direct current electric power transmission systems, water cooling based systems have to be used. Water cooling is implemented by aluminium plates with water channels mounted to the power electronic devices. Cold water flows through the channels of the plates. The heat is transferred away. The used water has to be cooled down by using active air cooling in separate heat exchanger. Alternatively, fresh water can be used and transmitted back into the water source.

A common problem of traditional cooling methods is the necessity of using heat-conductive paste. Typically, baseplates of power electronics have an unevenness of up to 50 µm per 10 cm and a depth of roughness of 10 µm. Moreover, the surface of the cooling element suffers of fabrication tolerances as well. This leads to the problem of air inclusion. Air has a lower heat conductivity than commonly used metals of heat sinks like aluminium or copper. Thus, the heat cannot flow properly from the heat source to the heat sink.

The air inclusion is an unwanted heat insulation. To avoid or decrease the air inclusion problem heat paste has to be applied between the layers to fill the macroscopic gaps. Additionally, the plates have the disadvantage that their surface is either plane or adapted to a specific device or printed circuit board. Hence, they are neither versatile nor adaptive to random surfaces.

Although, water cooling systems have high heat transfer coefficients of up to 5000 W/(m²K), the different discrete layers of power electronics still lead to a high resulting thermal resistance. Furthermore, the heat transfer coefficient is too low to cope with the high transient currents occurring in the case of short circuits.

A new and not yet established cooling method is cooling though boiling or the immersion cooling. According to the Nukiyama-curve boiling liquids can reach heat transfer coefficients of up to 10^6W/(m²K). To immerge the electronics into the liquid, it has to be a dieletric. Water cannot be used due to autoprotolysis, therefore different special liquids based on perfluorcarbone are commercially available. By using a liquid, fabrication tolerances do not matter and can be neglected.

III. DESIGN AND CONSTRUCTION OF THE TWO PHASE IMMERSION COOLING SYSTEM (TPICS)

The two-phase immersion cooling system, see Fig. 3, requires a specific design and construction measures to implement an impermeable case and solutions addressing isobaric or isochoric boundary conditions. To ensure a constant boiling point, the pressure has to be constant and as a consequence, a certain construction has to guaranty isobaric status changes. The boiling point of the fluid has to be low enough to ensure that the allowed temperatures of the power electronic device is not exceeded. Yet, it has to be high enough, so partial pressure does not lead to evaporation at room temperature. The heat has to be transferred out of the closed system with a heat exchanger working as a condenser.

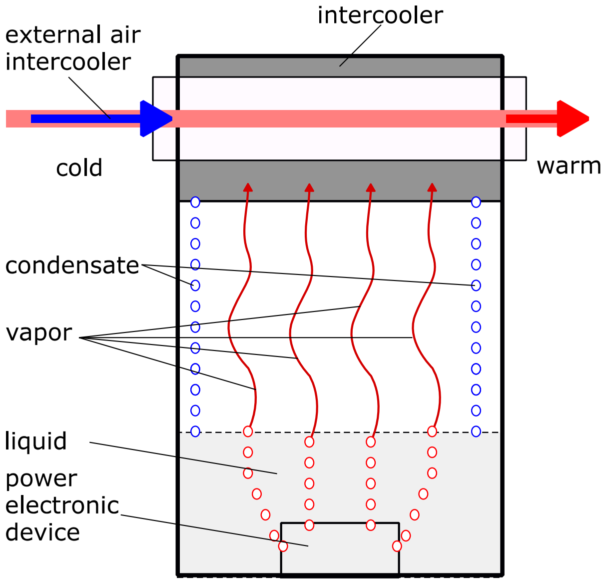

Figure 3: Principle function of the two phase immersion cooling system

A. Cooling liquid

To sum up, the liquid has to be compatible with regularly used materials in electronics, needs a boiling point adequate for power electronics and has to have a hazard-free health and safety profile due to a non-dangerous handling in the laboratory. The 3M™ Novec™ 7200 Engineered Fluid (NOVEC) fulfils all specifications: boiling point of 76°C and suitability for use on most surfaces and compatibility of materials. Moreover, it is chemically stable, not flammable and not toxic.

B. Cooling circuit

The cooling circuit is subdivided in two systems. The outer system, consisting of air, and the inner system, consisting of air and NOVEC-vapor.

The outer system –system II– transfers the heat through a heat exchanger out of the inner system –system I–. The whole system is dimensioned for 3 kW dissipative power to ensure a broad field of application. To accelerate condensation the air and NOVEC-vapor in system I have to circulate by forced convection. Three fans with a total volume flow of 480 m³/h limit the proportion of NOVEC-vapor below 2.5% of the total volume flow, if the cooling system is loaded with up to 3 kW resulting in a Novec-vapor volume flow of 9.66 m³/h or a mass flow of 90.7 kg/h.

C. Method to approximate the thermal resistance of the intercooler

Usual heat sinks cannot be used due to the necessity of total imperviousness; the heat exchanger has to separate the systems and transfer heat from system I to system II, without any leakage. Intercoolers have to fulfil high standards and are a cost-efficient alternative to established electronic coolers. Because manufacturers do not publish any data regarding the thermal resistance of their intercoolers, the thermal resistance has to be approximated by modelling the component. The model breaks the intercooler down into the smallest unit of heat transfer as shown in Fig. 4.

Figure 4: Part of the intercooler (left) and the corresponding smallest unit (right)

Subsequently, the resulting thermal resistance can be calculated by upscaling the thermal resistance of the smallest unit –the unit cell–. The unit cell consist of a *wall* and two *ribs*. The thermal resistance of such an unit cell ($R_{\text{th cell}}$) is calculated by:

$$R_{\text{th cell}} = \frac{1}{\alpha_{\text{G }1}A_{\text{G }1} + \alpha_{\text{R }1}\eta_{R\ 1}A_{\text{R }1}} + \frac{\delta_{\text{W}}}{\lambda_{\text{W}}\,A_{\text{W}}} + \frac{1}{\alpha_{\text{G }2}A_{\text{G }2} + \alpha_{\text{R }2}\eta_{\text{R }2}A_{\text{R }2}} \tag{4}$$

η_{R} represents the rib efficiency (5), including the parameter *m* (6).

$$\eta_{1,2} = \frac{\tanh(m_{1,2}h_{1,2})}{m_{1,2}h_{1,2}} \tag{5}$$

$$m_{1,2} = \sqrt{\frac{2\ \alpha_{\text{R1,R2}}}{\lambda_R\delta_{\text{R}}}} \tag{6}$$

Fig. 5 illustrates the different heat flows in the unit cell. The thermal resistance is calculated assuming that the heat is transferred via convection through the intercooler and not condensation. This simplification has to be made because the exact condensation in the intercooler cannot be calculated analytically, and to ensure that the thermal resistance is low enough for the application and the power of 3 kW.

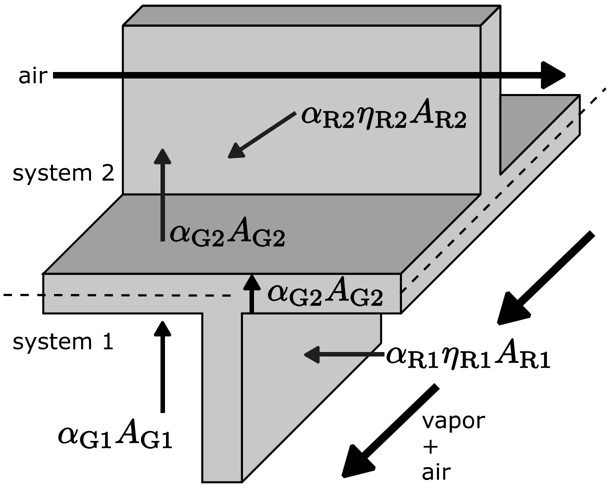

Figure 5: Heat flows in the unit cell

The heat transfer coefficient cannot be calculated without adjustments due to the fluid in system I consisting of vapor and air. The mixing of both leads to another viscosity and thermal conductivity. The dynamic viscosity of the air and NOVEC-vapor mixture η_{mix} is calculated after Wilke or Herning and Zipperer (6) with the correction factors (7) [9].

$$\eta_{\text{mix}} = \sum_{i=1}^{n}\frac{x_i\eta_i}{\sum_{k=1}^{n}x_k\phi_{i,k}} \tag{6}$$

$$\phi_{i,k} = \frac{\left(1+\left(\frac{\eta_i}{\eta_k}\right)^{1/2}\cdot\left(\frac{M_k}{M_i}\right)^{1/4}\right)^2}{\sqrt{8\left(1+\frac{M_k}{M_i}\right)}} \tag{7}$$

The thermal conductivity of the air and NOVEC-vapor mixture λ_{mix} is calculated similarly after Wassiljewa-Mason-Saxena (8) with the correction factors (9) [10].

$$\lambda_{\text{mix}} = \sum_{i=1}^{n}\frac{x_i\lambda_i}{\sum_{k=1}^{n}x_k\phi_{i,k}} \tag{8}$$

$$\phi_{i,k} = \frac{\left(1+\left(\frac{\lambda_i}{\lambda_k}\right)^{1/2}\cdot\left(\frac{M_k}{M_i}\right)^{1/4}\right)^2}{\sqrt{8\left(1+\frac{M_k}{M_i}\right)}} \tag{9}$$

After calculating the Reynolds Re number and the Prandtl number Pr, the Nusselt number can be calculated by (13) [11]. The Reynolds Number (10) is calculated via the kinematic viscosity ν_{mix} (11), which depends on the dynamic viscosity of the mixture (6) and its density. The Prandtl number depends on ν_{mix} and thermal diffusivity a.

$$\text{Re} = \frac{v_{\text{flow}}\,L}{\nu_{\text{mix}}} \tag{10}$$

$$\nu_{\text{mix}} = \frac{\eta_{\text{mix}}}{\rho_{\text{mix}}} \tag{11}$$

$$\text{Pr} = \frac{\nu_{\text{mix}}}{a} \tag{12}$$

$$\text{Nu}_m = \left(3.66^3 + 0.7^3 + \left(1.615\left(\text{Re}\,\text{Pr}\frac{d}{L}\right)^{\frac{1}{3}} - 0.7\right)^3\right)^{1/3} \tag{13}$$

Finally, the heat transfer coefficients α_{G1} and α_{R1} are equal and can be derived from (13).

$$\alpha_{\text{G1}} = \alpha_{\text{R1}} = \frac{\text{Nu}_m\,\lambda_{\text{mix}}}{d} \tag{14}$$

The heat transfer coefficients α_{G2} and α_{R2} of system II can be determined by (13) and (14) as well. The difference is, that Pr and ν_{air} can be taken from [11]. The systems can be brought together, with regard to the physical dimensions, in the unit cell, compare (4). The amount of parallel unit cells can be calculated by dividing the volume of the intercooler by the volume of the unit cell (15).

$$k_{\text{cell}} = \frac{V_{\text{intercooler}}}{\text{V}_{\text{cell}}} \qquad (15)$$

Hence, the thermal resistance of the unit cell is 2588 K/W, the total thermal resistance of the intercooler is 0.010155K/W, compare (16).

$$R_{\text{th intercooler}} = \frac{R_{th\ cell}}{\text{k}_{\text{cell}}} \qquad (16)$$

Finally, it can be stated that the thermal resistance is small enough for 3 kW dissipative power.

IV. First Testing of the TPICS

Fig. 6 shows the laboratory test setup. A first measurement to validate the TPICS has been done with two power resistors of 10 Ω by heating them up with a series of different currents, so that a comparison can be drawn.

The measurement procedure was the following: It was started with an initial current and increased stepwise until the maximum temperature was reached. Each current step was held for a specific heating duration.

The measurement Parameters are:

- Initial current: 1 A
- Current steps: 1A
- Heating duration: 60 sec
- Stop if the surface temperature reaches 80°C.

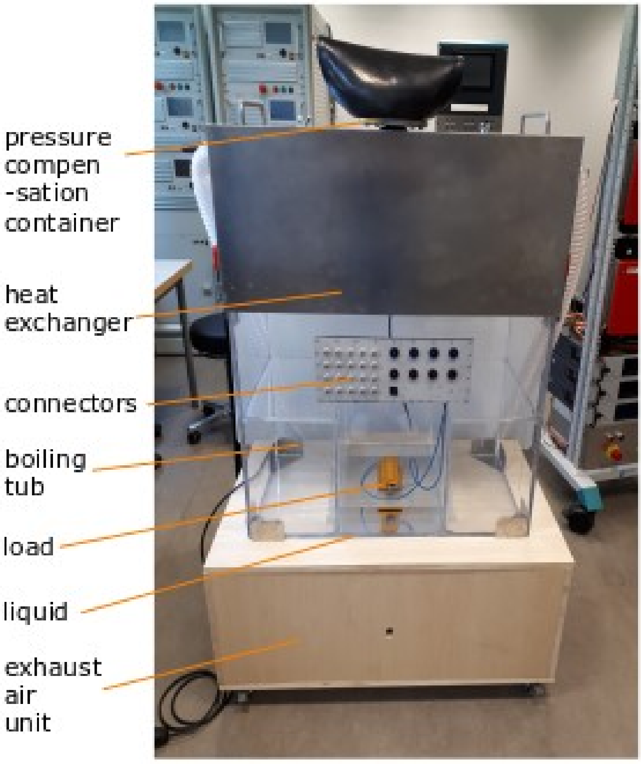

Figure 6: Laboratory test setup of the two phase emersion cooling system

To measure the temperature of the resistors, thermocouples were mounted with screws on the surface of the resistor.

The measurement results is shows Fig. 7. The trend curves of the measurement series proceed inverse of each other. As can be seen, the air cooled data points increase linear with the dissipated power or quadratic with the current, whereas the immersion cooled resistors temperature starts increasing likewise, but seems to settle when the liquid starts boiling. Fig. 8 shows the boiling at the resistor's surface. The air-cooled resistor has to be switched off at 6 A or 360 W because the maximum allowed temperature of 80°C was exceeded. The immersion cooled resistor was switched off at 12 A or 1,44kW due to the already highly exceeded power limitation.

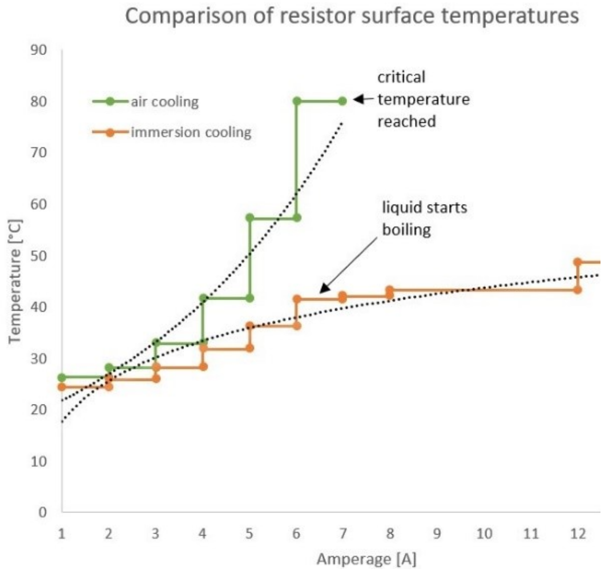

Figure 7: Measurement results of the laboratory test setup

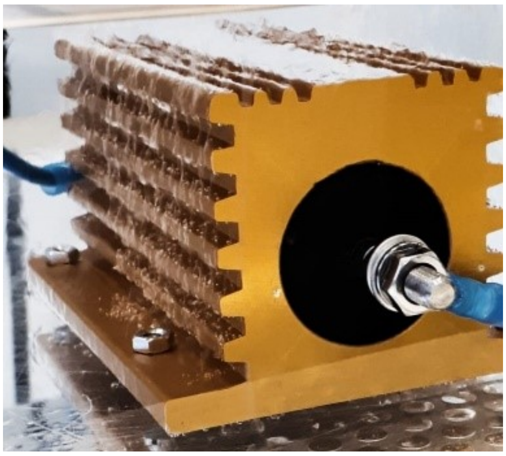

Figure 8: Boiling liquid at the resistors surface

V. Conclusion

This contribution describes the design and test of a two phase immersion cooling systems. This cooling system is needed to cool the power electronic switches of solid-state power controllers during a short-circuit event in the public energy supply. A conventional heat sink topology cannot fulfil the requirements regarding the transient heat transfer behavior.

Because the heat transfer coefficients are several orders of magnitude too low.

The two phase cooling system consists of a special liquid in a hermitic housing with an intercooler as a heat exchanger. The special liquid boils at 75°C, so the heat is transferred via evaporation cooling to the intercooler.

Evaporation cooling is more effective than convection and conduction cooling. To design the system the thermal resistance of the intercooler had to be modeled, as it was not known. A final measurement shows that the system is working according to its design. As shown in the test, it is possible to increase the power capacity of a power resistor by factor greater than three. The power was increased from 360°W to about 1400°W. This system can enable the design of solid-state power controller for high short circuit currents. Hence, further research has to be conducted to down size the cooling system to the smallest possible size.

REFERENCES

[1] Terörde, M., Grumm, F., Schulz D., Wattar, H., Lemke, J.,"Implementation of a Solid-State Power Controller for High-Voltage DC Grids in Aircraft", IEEE Power and Energy Student Summit (PESS 2015), TU Dortmund University, 13 – 14 January 2015, Dortmund, Germany, DOI: http://dx.doi.org/10.17877/DE290R-7742

[2] Grumm, F.; Meyer, M.; Waldhaim, E.; Schulz, D., "Self-testing Solid-State Power Controller for High-Voltage-DC Aircraft Applications", Conference on Sustainable Energy Supply and Energy Storage Systems (NEIS 2016), Hamburg, Germany, 15-16 September 2016, Springer Vieweg, Wiesbaden 2017, pp 26-31, DOI 10.1007/978-3-658-15029-7

[3] Terörde, M., „Lastumverteilungsverfahren in elektrischen Bordnetzen von Verkehrsflugzeugen", Dissertation Helmut-Schmidt-Universität / Universität der Bundeswehr Hamburg 2015, VDE Verlag, ISBN 978-3-8007-4142-7

[4] Brombach, J., „Methoden zur Gewichtsreduktion in elektrischen Flugzeugkabinennetzen", Dissertation Helmut-Schmidt-Universität / Universität der Bundeswehr Hamburg 2014

[5] Egle, K. A.; Grumm, F.; Meyer, M. F. ; Plenz, M.; Schulz, D. "Concept of an Adaptable Protection Device for Low Voltage Networks",VDE/IEEE Power and Energy Student Summit 2018, Kaiserslautern , Germany, 2-4 July 2018, pp 115-119

[6] Wintrich, A; Nicolai, U.; Tursky, W. and Reimann,T., Application Manual Power Semiconductors, ISLE Verlag, Ilmenau 2015

[7] Von Böckh, P. and Wetzel, T, Heat Transmission (in German: Wärmeübertragung), Springer Vieweg, 2013.

[8] Baehr, H. D. and Stephan, K., heat and mass transfer (in German: Wärme und Stoffübertragung), Springer, 1994.

[9] Geurtz, H. J., Research to validate fluid characteristics of fuel-vapor-air-mixtures of motor vehicle during refueling. Research in engineering (in German Untersuchung zur Bestimmung der Fluideigenschaften von Kraftstoffdampf-Luft-Gemischen von Kraftfahrzeuganlagen währen der Betankung. Forschung im Ingenieurwesen),2011

[10] Udoetok, E. "Thermal conductivity of binary mixtures of gases. Frontiers in Heat and Mass Transfer (FHMT)",4(2), 2013.

[11] VDI, Wärmeatlas, 11 Auflage,VDI-Verlag 2013.